

AU NO.

AD A 056931

DDC FILE COPY

14

AFGL-TR-77-0369,
AFGL-SR-209

LEVEL II



B.S.

Contributed Papers to the Study of
Travelling Interplanetary Phenomena/1977.

(Proceedings of COSPAR Symposium B,
Tel Aviv, Israel, June 1977)

Editors

M. A. SHEA,
D. F. SMART
S. T. WU

29 Dec [REDACTED] 77

9 Special rept.,

DDC

REF ID: A64121
AUG 2 1978

12 412 p. 1

Approved for public release; distribution unlimited

16 2311

17 G1

SPACE PHYSICS DIVISION PROJECT 2311
AIR FORCE GEOPHYSICS LABORATORY
HANSCOM AFB, MASSACHUSETTS 01731

AIR FORCE SYSTEMS COMMAND, USAF



AIR FORCE (1) MAY 17, 1978--1496

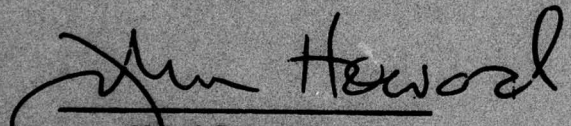
409 578 78 07 31 006

Yan

This report has been reviewed by the ESD Information Office (OI) and is
releasable to the National Technical Information Service (NTIS).

This technical report has been reviewed and
is approved for publication.

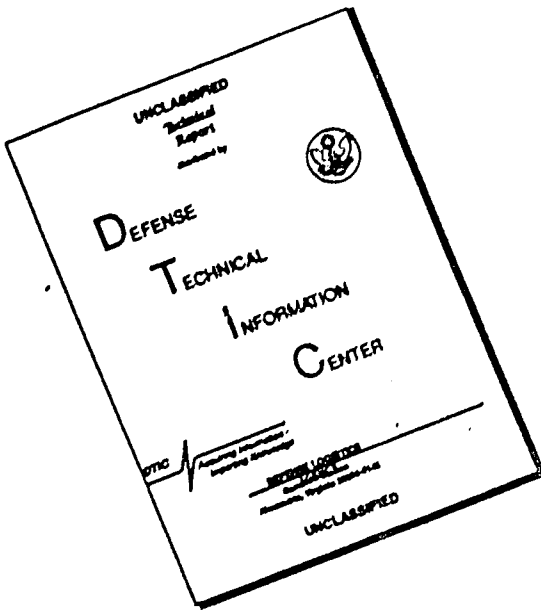
FOR THE COMMANDER



John Howard
Chief Scientist

Qualified requestors may obtain additional copies from the
Defense Documentation Center. All others should apply to the
National Technical Information Service.

DISCLAIMER NOTICE



**THIS DOCUMENT IS BEST
QUALITY AVAILABLE. THE COPY
FURNISHED TO DTIC CONTAINED
A SIGNIFICANT NUMBER OF
PAGES WHICH DO NOT
REPRODUCE LEGIBLY.**

Unclassified

SECURITY CLASSIFICATION OF THIS PAGE (When Data Entered)

REPORT DOCUMENTATION PAGE		READ INSTRUCTIONS BEFORE COMPLETING FORM
1. REPORT NUMBER AFGL-TR-77-0309	2. GOVT ACCESSION NO.	3. RECIPIENT'S CATALOG NUMBER
4. TITLE (and Subtitle) CONTRIBUTED PAPERS TO THE STUDY OF TRAVELLING INTERPLANETARY PHENOMENA/1977 (Proceedings of COSPAR Symposium B, Tel Aviv, Israel, June 1977)		5. TYPE OF REPORT & PERIOD COVERED Scientific. Interim.
7. AUTHOR(s) Editors: M. A. Shea, D. F. Smart and S. T. Wu*		6. PERFORMING ORG. REPORT NUMBER Special Reports, No. 209
9. PERFORMING ORGANIZATION NAME AND ADDRESS Air Force Geophysics Laboratory (PHG) Hanscom AFB Massachusetts 01731		10. PROGRAM ELEMENT, PROJECT, TASK & WORK UNIT NUMBERS 61102F 2311G101
11. CONTROLLING OFFICE NAME AND ADDRESS Air Force Geophysics Laboratory (PHG) Hanscom AFB Massachusetts 01731		12. REPORT DATE 29 December 1977
14. MONITORING AGENCY NAME & ADDRESS(if different from Controlling Office)		13. NUMBER OF PAGES 411
16. DISTRIBUTION STATEMENT (of this Report)		15. SECURITY CLASS. (of this report) Unclassified
		15a. DECLASSIFICATION/DOWNGRADING SCHEDULE
17. DISTRIBUTION STATEMENT (of the abstract entered in Block 20, if different from Report)		
18. SUPPLEMENTARY NOTES Contributed papers to the L. D. de Feiter Memorial Symposium, Tel Aviv, Israel, June 7-10, 1977.		
* University of Alabama in Huntsville, Huntsville, Alabama 35807		
19. KEY WORDS (Continue on reverse side if necessary and identify by block number)		
Solar physics Solar radio astronomy Interplanetary scintillations Solar wind	Solar particles Interplanetary medium Cosmic rays Comets	Solar X-rays
20. ABSTRACT (Continue on reverse side if necessary and identify by block number) This report is a compilation of 36 papers contributed to the L. D. de Feiter Memorial Symposium on the Study of Travelling Interplanetary Phenomena, one of the specialized symposia held in conjunction with the XX COSPAR meeting, Tel Aviv, Israel, June 7-10, 1977. These papers span the entire range of multi-disciplinary studies of transients propagating from the sun through the interplanetary medium and represent a current assessment of theoretical		

Unclassified

SECURITY CLASSIFICATION OF THIS PAGE(When Data Entered)

20. Abstract (Continued)

studies and analyses, computer simulation, and in situ measurements of these phenomena. This includes solar phenomena as the source of transient events propagating through the solar system, and theoretical and observational assessments of the dynamic processes involved as these transients propagate through the interplanetary medium. The subjects covered are solar physics, solar radio astronomy, interplanetary scintillation measurements, cometary studies, direct spacecraft observations from Venera 9, Venera 10, Helios 1 and Helios 2, energetic particle propagation in the interplanetary medium and shock-particle interactions. Also included are reports on coronal hole and solar wind studies during STIP Interval I (September-October 1975) and the dynamic solar-Terrestrial events that occurred during STIP Interval II (15 March-15 May 1976).

Unclassified

SECURITY CLASSIFICATION OF THIS PAGE(When Data Entered)

ACCESSION for	
NTIS	White Section <input checked="" type="checkbox"/>
DOC	Buff Section <input type="checkbox"/>
UNANNOUNCED	<input type="checkbox"/>
JUSTIFICATION	
.....	
BY	
DISTRIBUTION/AVAILABILITY CODES	
Dist.	AVAIL. and/or SPECIAL
A	

Foreword

The Study of Travelling Interplanetary Phenomena (STIP) was formally established by the International Council of Scientific Union's Special Committee on Solar-Terrestrial Physics (SCOSTEP) in August 1973 with M. Dryer as Convenor and M. A. Shea as Secretary. The scientific objectives of STIP are the study and search for understanding of quiet (i.e. normal or background) and active periods in the interplanetary medium. The concepts of informal, extemporaneous interdisciplinary research are continuously emphasised, and these concepts have proven to be extremely successful in conducting the very productive studies undertaken by the members.

About 200 scientists are actively participating in STIP, their interests ranging from solar physics (insofar as it concerns the initiation of phenomena which move out from the Sun) to the observation and study of comets and planetary magnetospheres and ionospheres. Solar radio astronomy and interplanetary scintillations of discrete radio sources, solar and galactic cosmic rays, solar wind plasma and interplanetary magnetic fields, and interstellar interactions are among the topics of interest.

A number of subgroups within STIP have been organized and are headed by coordinators from several different countries. Almost all of the coordinators conduct and carry out informal studies, quickly and efficiently within their groups, with a minimum of formalities. Both the informal character of the entire STIP program and the enthusiastic response to the interdisciplinary approach of the various studies, have contributed to the productivity and success of this group over the past four years. For example, two scientific sessions devoted to travelling interplanetary phenomena studies were held in conjunction with the XVIII COSPAR Meeting in Varna, Bulgaria in 1975; a special issue of *Space Science Reviews* was published in 1976 presenting review papers on the August 1972 solar-terrestrial phenomena; and four special periods for scientific studies, STIP Intervals I, II, III, and IV, have been designated, with selection of these intervals based upon unique opportunities generated by interplanetary spacecraft configurations. So far unique observations have been possible during STIP Intervals II, III, and IV, primarily because of the solar activity (and hence related interplanetary effects) that occurred at those times.

The L. D. de Feiter Memorial Symposium on the Study of Travelling Interplanetary Phenomena was still another successful activity conducted by STIP participants. Held in conjunction with the XX COSPAR Meeting and co-sponsored by SCOSTEP,

COSPAR, and the IAU, the symposium was named in honor of the memory of Leen Dirk de Feiter, who actively encouraged and participated in the organization and initial activities of STIP.

The Proceedings of the L. D. de Feiter Memorial Symposium on the Study of Travelling Interplanetary Phenomena are published in two parts. The contributed papers are contained in this publication. The invited papers have been published in the book *Study of Travelling Interplanetary Phenomena/1977*, also edited by M. A. Shea, D. F. Smart, and S. T. Wu, published by the D. Reidel Publishing Company of Dordrecht, Holland, as Volume 71 of their Astrophysics and Space Science Library. Since these two publications are complimentary to each other, we feel it is appropriate to give a listing of the topics and individual papers published in the volume of invited papers. These are as follows:

SOLAR PHYSICS AS IT CONCERNs THE STUDY OF TRAVELLING INTERPLANETARY PHENOMENA (STIP)

- Mass Ejections from the Solar Corona into Interplanetary Space
E. Hildner
Energetic Solar Flare Particles and Interplanetary Shock Waves
R. P. Lin
Dynamic Modeling of Coronal and Interplanetary Responses to Solar Events
S. T. Wu, Y. Nakagawa, and M. Dryer

SOLAR RADIO ASTRONOMY AND INTERPLANETARY SCINTILLATIONS

- Solar Stereo Radioastronomy
J.-L. Steinberg
Measurements of the Solar Wind Using Spacecraft Radio Scattering Observations
R. Woo
Observations of Interplanetary Scintillation: Solar Wind Velocity Measurements
T. Kakinuma
Scintillation Observations of the Interplanetary Plasma
Z. Houminer

SOLAR WIND THEORY AND OBSERVATIONS

- The Three-Dimensional Structure of the Interplanetary Medium
W. I. Axford
Theoretical Contributions to Solar Wind Research - A Review
S. Cuperman
The Large Scale and Long Term Evolution of the Solar Wind Speed Distribution and High Speed Streams
Devrie S. Intriligator
Pioneer 10, 11 Observations of Evolving Solar Wind Streams and Shocks Beyond 1 AU
E. J. Smith and J. H. Wolfe
Wave-Particle Interaction Phenomena Associated with Shocks in the Solar Wind
F. L. Scarf

COMETARY TOPICS

- Comets in the STIP Context
Max K. Wallis
The Comet-Solar Wind Interaction
D. A. Mendis
Solar Wind Interaction with Type-I Comet Tails
A. I. Ershkovich

SOLAR COSMIC RAY PROPAGATION, MODULATION, AND INTERPLANETARY ACCELERATION

Signatures of Solar Cosmic Ray Events and Their Relation to Propagation and Acceleration Processes

G. Wibberenz

Solar Energetic Particles Below 10 MeV

E. C. Roelof and S. M. Krimigis

Acceleration and Modulation of Electrons and Ions by Propagating Interplanetary Shocks

T. P. Armstrong, G. Chen, E. T. Sarris, and S. M. Krimigis

STUDY OF TRAVELLING INTERPLANETARY PHENOMENA - STIP INTERVAL I AND STIP INTERVAL II

A Summary of Significant Solar-Initiated Events During STIP Intervals I and II

M. A. Shea, D. F. Smart, and H. E. Coffey

Overview of the HELIOS 1 and HELIOS 2 Missions and Their Participation in STIP Intervals I and II

H. Porsche

To avoid the delays normally encountered in type setting a conference proceedings of this magnitude, all authors were requested to prepare their manuscripts in a camera ready format, in accordance with general guidelines provided to them. The discussion after each presentation was transcribed at the conference and added at the end of each manuscript by the editors. In the process of reviewing each manuscript some changes were necessary in an effort to achieve a standardized format. Whenever these changes were minor in nature, corrections were made to the original manuscript, sometimes using the "cut and paste" technique. In a few cases, complete manuscripts were retyped. In this regard the typing services of Ms. Carol Holladay of the University of Alabama are gratefully acknowledged. Finally, the editors gratefully acknowledge the cooperation given to them by each of the authors throughout the preparation of this conference proceedings.

M. A. Shea

D. F. Smart

S. T. Wu

Contents

Foreword

I. SOLAR PHYSICS AS IT CONCERN'S THE STUDY OF TRAVELLING INTERPLANETARY PHENOMENA (STIP)	1
Long Duration Soft X-Ray Transients: Physical Parameters and Morphology Jesse B. Smith, Jr., David M. Speich, Robert M. Wilson, and Edwin J. Reichmann	3
The Effect of the Magnetic Field on Coronal Transients R. S. Steinolfson, S. T. Wu, M. Dryer, and E. Tandberg-Hanssen	23
Relation Between Moreton Waves, Type II Shocks and Interplanetary Shock Waves S. Pintér	35
Local Accelerations in the Corona During Type II - Type IV Emission; Observational and Theoretical Evidence Yolande Leblanc and Monique Aubier	49
Timing of Beginnings of Type II Radio Bursts by Energetic Particle Flares L. Křivský	59
Faraday Rotation Transients Observed During Solar Occultation of the Helios Spacecraft M. K. Bird, H. Volland, C. T. Stelzried, G. S. Levy, and B. L. Seidel	63
II. SOLAR WIND STUDIES	77
A Multi-Fluid Model for Stellar Winds Nathan Metzler	79
Propagation Velocities of Small Amplitude Disturbances in Multi-ion Plasmas E. J. Weber	93

Contents

A Model for the Interaction of Solar Wind Streams Raphael Steinitz and Menashe Eyni	101
New Evaluation of Spacecraft Solar Wind Plasma Data Menashe Eyni and Raphael Steinitz	109
The Interaction Between the Solar Wind and the Interstellar Hydrogen Beyond the Heliosphere P.W. Blum and R. Lang	117
Travelling Phenomena in the Heliosphere Induced by Solar Activity S. Grzędzielski and R. Ratkiewicz	127
III. INTERPLANETARY SHOCK WAVES	137
IPS Observations of Flare-Associated Shock Waves in 1972-1974 Takashi Watanabe	139
The Shape and the Energy of the Interplanetary Shock Waves Associated With the August 1972 Solar Flares C. D'Uston, G.N. Zastenker, V.V. Temny, and J.M. Bosqued	151
Directional Properties of the Propagation of Solar Flare-Generated Shock Waves in Interplanetary Space Stephen Pintér	161
IV. COMETARY STUDIES	189
Viscous Interaction Between the Solar Wind and Cometary Plasmas H. Pérez-de-Tejada, A. Orozco, A. Ershkovich, and M. Dryer	191
"Secondary Tail Events" in the Plasma Tail of Comet Kohoutek 1973 XII K. Jockers	201
V. COSMIC RAY MODULATION AND ACCELERATION	207
Cosmic Ray Perturbations Produced by Fast Streams Coming from Quiet Solar Regions - Coronal Holes N. Iucci, S. Orsini, M. Parisi, M. Storini, and G. Villoresi	209
Modulation of Energetic Solar Particle Fluxes by Interplanetary Shock Waves Manfred Scholer and Gregor Morfill	221
Solar Cosmic Ray Diffusion Coefficient Behind Interplanetary Shock Waves Gregor Morfill and Manfred Scholer	231
Acceleration of Low-Energy Solar Protons at Interplanetary Shocks E. Amata, V. Domingo, R. Reinhard, K.-P. Wenzel, and H. Grünwaldt	243
Storage of Solar Cosmic Rays by Shock Wave Ensemble J. Otaola, R. Gall, and R. Pérez Enríquez	253

Contents

VI. STUDY OF TRAVELLING INTERPLANETARY PHENOMENA - STIP INTERVAL I (SEPTEMBER-OCTOBER 1975)	261
A Coronal Hole Observed by λ 8-cm Radioheliograph Kiyoto Shibasaki, Masato Ishiguro, Shinzo Enome, and Haruo Tanaka	263
Solar Wind Parameters During STIP Intervals I and II According to Venera-9 and Venera-10 Measurements G. N. Zastenker, J. M. Bosqued, A. V. Djatchkov, C. D'Uston, S. A. Romanov, V. V. Temny, and O. L. Vaisberg	275
VII. STUDY OF TRAVELLING INTERPLANETARY PHENOMENA - STIP INTERVAL II (15 MARCH-15 MAY 1976)	285
Type II Radio Bursts Originating from Well Behind the Solar Limb G. J. Nelson and D. J. McLean	287
Evolution of the X-ray Emitting Corona Preceding and After Major Solar Events C. J. Wolfson, L. W. Acton, D. T. Roethig, and M. Walt	295
Fast Flux and Polarization Periodic Time Structure of Microwave Solar Bursts Pierre Kaufmann, L. Rizzo Piazza, and J. C. Raffaelli	307
Estimation of Exciter Length of Type IIIb Bursts Near Two Solar Radii Derived from Microscopic Solar Decametric Spectral Features H. S. Sawant, R. V. Bhonsle, S. S. Degaonkar, and S. K. Alurkar	313
Radio Evidence of Travelling Coronal Electron Density Irregular- ties Near Two Solar Radii R. V. Bhonsle, H. S. Sawant, S. S. Degaonkar, and S. K. Alurkar	321
Solar Radio Burst Energies for March-April 1976 J. P. Castelli, and G. L. Tarnstrom	329
Radio and Optical Evidence of Mass Ejections from Solar Flares and Solar Decametric Noise Storm Activity During March 1976 (STIP Interval II) A. Bhatnagar, G. M. Ballabh, Rajmal Jain, S. S. Rao, R. V. Bhonsle, and H. S. Sawant	341
The Solar Wind During STIP II Interval: Stream Structures, Boundaries, Shocks and Other Features as Observed by the Plasma Instruments on Helios-1 and Helios-2 R. Schwenn, H. Rosenbauer, and K. H. Mühlhäuser	351
Characteristic Features of Coronal Propagation as Derived from Solar Particle Observations by Helios 1 and 2 During STIP Interval II H. Kunow, G. Wibberenz, G. Green, R. Müller-Mellin, M. Witte, H. Hempe, and J. Fuckner	363
The Composition of Low Energy Solar Cosmic Rays During the Active Period March 76-May 76 M. Scholer, B. Klecker, D. Hovestadt, G. Gloeckler, and C. Y. Fan	373

Contents

The Time Behaviour of the Galactic Cosmic Ray Intensity During the Period, March 20-June 8, 1976 N. Iucci, M. Parisi, M. Storini, and G. Villoresi	383
Multidisciplinary Event-Oriented Data Collection for 30 April 1976 D. B. Bucknam and H. E. Coffey	395

**CONTRIBUTED PAPERS
TO THE STUDY OF TRAVELLING
INTERPLANETARY PHENOMENA/1977**

(PROCEEDINGS OF COSPAR SYMPOSIUM B,
TEL AVIV, ISRAEL JUNE 1977)

**I. SOLAR PHYSICS AS IT CONCERNs
THE STUDY OF TRAVELLING
INTERPLANETARY PHENOMENA (STIP)**

Long Duration Soft X-ray Transients: Physical Parameters and Morphology

**Jesse B. Smith, Jr.*
David M. Speich***
**NOAA/Space Environment Laboratory
Boulder, CO 80302, USA**

**Robert M. Wilson
Edwin J. Reichmann
NASA/Marshall Space Flight Center
Huntsville, AL 35812, USA**

Abstract

Results of analysis of Skylab soft X-ray, low-coronal observations of coronal transient-related events are presented. Both spatially resolved photographic images obtained by the X-Ray Telescope (X-RT) and high-temporal resolution proportional counter data obtained by the X-Ray Event Analyzer (X-REA) have been used in these analyses. The structure and evolution of the low-coronal events and the morphology of the associated eruptive prominences/disparitions brusques are briefly discussed. X-REA reported results include time profiles of flux at various wavelengths and physical parameters (average temperatures and emission measures), as determined using a channel-ratioing technique. Typical peak temperatures deduced are $6-14 \times 10^6$ K and peak volume emission measures are approximately $5 \times 10^{47} \text{ cm}^{-3}$.

*Now at: NASA/Marshall Space Flight Center, ES52, Huntsville, AL 35812

1. INTRODUCTION

The observation of long-duration X-ray transient events (LDEs), having X-ray flux signatures similar in shape to the "gradual-rise-and-fall" phenomenon observed at microwave wavelengths, was originally reported by Kreplin *et al.* (1962). At that time, it was also suggested that these LDEs may be associated with rising limb prominences. More recently, Sheeley *et al.* (1975) and Kahler (1977), using Skylab and groundbased observations, confirmed the relationship between LDEs and disparitions brusques and showed that LDEs are frequently associated with coronal transients. Munro *et al.* (1974) and Gosling *et al.* (1974) found a correlation between eruptive prominences and coronal transients. In this paper, we will examine the H_α, XUV and X-ray morphology and evolution of selected LDEs, and we will present results of analysis regarding the determination of temperature (T), volume emission measure ($EM = \int N_e^2 dV$, where N_e is the electron density and V the volume), and thermal energy content ($E_{th} = 3k \int TN_e dV$, where k is Boltzmann's constant) for these events. The X-ray data are those obtained with the ATM/S-056 X-ray experiment aboard Skylab (Underwood *et al.*, 1977), and the events discussed herein include the slow-accelerating events of 21 August 1973 (eruptive limb prominence) and 18 January 1974 (disparition brusque) and the contrasting fast-accelerating event of 17 January 1974 (eruptive limb prominence, probably flare related).

2. INSTRUMENTATION

The primary data source was the NASA-Marshall Space Flight Center/The Aerospace Corporation X-ray experiment (S-056) onboard Skylab. The experiment consisted of two instruments, the X-Ray Telescope (X-RT) and the X-Ray Event Analyzer (X-REA). The X-RT, a Wolter Type-I glancing-incidence imaging telescope, obtained high spatial resolution (~ 2") photographic data through five metallic filters of different passbands in the 6-18 Å and 27-40 Å range, permitting comparison for the determination of spectral hardness and, hence, physical parameters. Exposure times (generally 1.3 s - 280 s) were variable to optimize the observation of features and events of widely different X-ray intensity. The X-REA utilized two proportional counters with spectral ranges of 2.5-7.25 Å and 6.1-20 Å and employed pulse-height analyzers for spectral resolution. The instrument viewed the full sun with a temporal resolution of 2.5 s. The S-056 experiment is described in detail by Underwood *et al.* (1977) and Wilson (1976, 1977).

3. PLASMA DIAGNOSTICS

Physical parameters are determined from the X-ray telescope filterheliograms following a technique similar to that described by Vaiana *et al.* (1973) and from the X-ray proportional counter data following a technique similar to that described by Horan (1971). At any point in a given X-ray image the exposure Φ_n (in photons cm⁻², where n denotes the filter) is related to the specific intensity I_λ by

$$\Phi_n = \frac{A_T t}{f^2} \int \eta_n(\lambda) \frac{I_\lambda(\lambda)}{h\nu} d\lambda, \quad (1)$$

where A_T is the telescope collecting area, t the exposure time, f the telescope focal length, $\eta_n(\lambda)$ the combined filter-telescope transmission for photons of wavelength λ , and $h\nu$ the energy per photon. For an optically thin, thermal plasma of coronal composition and temperature, assumed to be isothermal along the line of sight, we write

$$\int \eta_n(\lambda) \frac{I_\lambda(\lambda)}{h\nu} d\lambda = \int \eta_n(\lambda) \frac{\epsilon_\lambda(\lambda)}{N_e^2 h\nu} d\lambda \int N_e^2 ds, \quad (2)$$

where $\epsilon_\lambda(\lambda)$ is the emission coefficient, N_e the electron density, s the distance along the line of sight, and $\int N_e^2 ds$ the linear emission measure. (Values of $\epsilon_\lambda(\lambda)$ are due to Walker (1972) and Tucker and Koren (1971); see also Underwood and McKenzie (1977).) By ratioing the right-hand sides of Eq. (2) for two different filters, one obtains a value which is dependent only upon temperature. Thus, we determine the temperature of the X-ray emitting source from the observed ratio of the left-hand side of Eq. (2) using two different filters. Once the temperature is known, the linear emission measure is found by the use of Eq. (2). The electron density is then obtained from the linear emission measure following an assumption about the geometrical extent along the line of sight.

For X-ray proportional counters (like the X-REA) with fields of view including the entire sun, the number of counts ψ_j (where j denotes the channel) is related to the solar flux incident on the counter ϕ_λ by

$$\psi_j = A_c \Delta t \int \eta_j(\lambda) \phi_\lambda(\lambda) d\lambda, \quad (3)$$

where A_c is the aperture area of the counter, Δt the integration time, and $\eta_j(\lambda)$ the number of counts in channel j per photon at wavelength λ (analogous to $\eta_n(\lambda)$ used in Equations 1 and 2). Using the same assumptions as above, except now the plasma is isothermal over the volume of the X-ray-emitting region (i.e., event), we obtain

$$\int \eta_j(\lambda) \phi_\lambda(\lambda) d\lambda = \frac{1}{(AU)^2} \int \eta_j(\lambda) \frac{\epsilon_\lambda(\lambda)}{N_e^2 h\nu} d\lambda \int N_e^2 dV \quad (4)$$

where AU is the astronomical units, V the volume, and $\int N_e^2 dV$ the volume emission measure. The ratio of Equation (4) evaluated for two different channels (or wavelength bands) is a function of temperature alone and, thus, is used for determining

the temperature of the X-ray event. Knowing the temperature allows one to determine the volume emission measure (from Eq. 4) which in turn yields the electron density after an assumption about the volume is made.

Another parameter of interest is the thermal energy content of the event, denoted E_{th} , which is related to the electron density by

$$E_{th} = 3k \int T N_e dV, \quad (5)$$

where k is Boltzmann's constant. Another useful form of Eq. (5) based on our observation is

$$E_{th} = 3k T(EM)^{1/2} V^{1/2}, \quad (6)$$

where EM is the volume emission measure ($EM = \int N_e^2 dV$).

4. OBSERVATIONS AND ANALYSIS

The three coronal X-ray events (all LDEs) selected for this analysis were associated with eruptive or disappearing prominences and, in the case of the two limb events, had associated white light coronal transients, observed by the Skylab borne High Altitude Observatory White Light Coronagraph (WLC). The third event, a disparition brusque, was near disk center - probably making any white light coronal transient unobservable. (Among others, Sheeley *et al.*, 1975, and Kahler, 1977, have discussed the correlation between long duration X-ray events and coronal transients.) These three events are summarized in Table 1.

The eruptive prominence of 21 August 1973 was clearly a slow acceleration event with a velocity profile similar to Valněček's Curve II (Valněček, 1964) and typical of the eruption of quiescent prominences. For reasons to be discussed, the disparition brusque of 18 January 1974 is also believed to be in this category. The very rapid acceleration and the high velocity of the 17 January 1974 eruptive are typical of Valněček's Curve I for sprays, which Bruzek (1969) and Tandberg-Hanssen (1974) relate to other flare-related fast ejections. Brief descriptions of the three events follow.

4.1 21 August 1973 Eruptive Prominence

4.1.1 Morphology

The location producing the 21 August event was the source of at least 3 other eruptives in just over a month - including a disparition brusque and large (3B) flare on 29 July, a west limb eruptive on 10 August, and the disk disparition brusque of 1 September, accompanied by a large area of relatively weak X-ray enhancement, as reported by Rust and Webb (1977).

Table 1. Selected H-alpha, Soft X-ray, and Radio Data for the Three Events

		21 AUGUST 1973	18 JANUARY 1974	17 JANUARY 1974
	EVENT	ERUPTIVE PROMINENCE	FLARE (1F)	DISPARITION BRUSQUE
H-ALPHA	BEGIN MAXIMUM END	~1300 UT >1410 UT	<1344 UT 1407 UT 1433 UT	<1811 UT ~1915 UT
SOLRAD	CLASS	C 0.7		C 0.3
X-REA	BEGIN (25-725Å) MAXIMUM " END "	1344 UT 1444 UT 1950 UT	1830 UT 1932 UT 2300 UT	1920 UT 1934 and 1944 UT 2400 UT
	RISE (HRS)	-	1.0	1.0
	T (K) PEAK	14.3 x 10 ⁶	7.4 x 10 ⁶	11.8 x 10 ⁶
	VOLUME PEAK (X-RAY) (cm ³)	4.1 x 10 ²⁹	1.6 x 10 ²⁹	10 ²⁹
	N _e PEAK (cm ⁻³)	9.5 x 10 ⁸	1.7 x 10 ⁹	1.7 x 10 ⁹
RADIO	THERMAL ENERGY PEAK (ERGS S ⁻¹)	CONT (IMP2) 1440-1650 TYPE IV(IMP3) 1442-1734 TYPE IV(IMP1) 1825-1919	7.8 x 10 ²⁹	6.1 x 10 ²⁹
			NONE REPORTED	TYPE III N(IMP1) 1701-1926 TYPE III(IMP1) 1931-1948 TYPE III(IMP2) 1933-1936 TYPE II(IMP2) 1937-1949

The eruptive prominence of 21 August and its associated X-ray event have been discussed and its coronal response modeled by Smith *et al.* (1977). The white light coronal transient was analyzed in detail by Poland and Munro (1976) and its relationship to the He II (304 Å) eruptive prominence was discussed by Bohlin *et al.* (1974).

The quiescent tree-shaped H α prominence, apparently based about 8 to 17 degrees behind the northeast limb, was slowly lifting ($\sim 10 \text{ km s}^{-1}$) at 1300 UT, with leading elements gradually accelerated to greater than 200 km s^{-1} by 1410 UT. (The position, and hence, velocity may be underestimated due to a loss of H α visibility with increasing temperatures.) Figure 1d and 1e show the H α prominence pre-event and during its eruptive phase. At ~ 1344 UT, a weak H α flare appeared in the prominence base, just above the limb, and possibly related material infall into this area was observable at 1358 UT. The enhancement remained weak, returning to prominence intensity by about 1433 UT. In Figure 1c, the He II 304 Å at 1441 UT is seen to extend much further outward from the sun - to approximately 1.8 R_\odot - but, as reported by Poland and Munro (1976), the prominence brightened later in He II than in H α and remained visible longer than in H α - indicating increasing temperatures.

The weak pre-event X-rays in Figure 1a (a factor of 3 greater exposure than for the X-ray event in Figure 1b) had been visible for several hours and were probably associated with weak chromospheric enhancement near the prominence. The X-ray enhancement, recorded by the X-REA (Figure 2a and 2b), began at 1340 UT, very near the time of onset of the observable H α enhancement. At 1442 UT, about the time of the soft X-ray maximum, the first observational sequence by the X-RT revealed a large, bright arcade of loops (Figure 1b) in the area of the previously faint X-ray emission (mostly to the north of the eruptive prominence foot-point as seen in Figures 1c and 1e). The foot-points of the X-ray loops were clearly occulted by the disk, and it appears likely that they were situated above the filament-associated neutral line and that the unseen chromospheric event was similar to the 29 July event (discussed by Michalitsanos and Kupferman, 1974). The coronal event was also observed in Fe XV and Fe XVI, where the loop arcade structure was clearly visible in observations by the NRL XUV spectroheliograph (R. Tousey, private communication).

4.1.2 Physical Parameters

As is shown in Figure 2a and 2b, the harder 2.5 - 7.25 Å X-rays (plotted in one minute averages of 2.5 s data samples) began about 3 or 4 minutes before the softer 6-20 Å flux. The resultant calculated maximum temperature (for assumptions, see section 3) was $14 \times 10^6 \text{ K}$, occurring well before peak X-ray flux and, as has generally been the case, before the peak emission measure (indicating that the density was increasingly significant in X-ray emission). By measuring the event area on the imaged X-RT data and making some symmetric geometry assumptions, we deduce an average density of $\sim 9.5 \times 10^8 \text{ cm}^{-3}$, somewhat lower than the spatially resolved peak of $3.5 \times 10^9 \text{ cm}^{-3}$ deduced from the imaged data.

4.2 18 January 1974 Disparition Brusque

4.2.1 Morphology

The disparition brusque of 18 January also occurred in a historically active location. The north-south oriented polarity-reversal (neutral) line along which lay the disrupted filament was the location of a frequently active filament the preceding month.

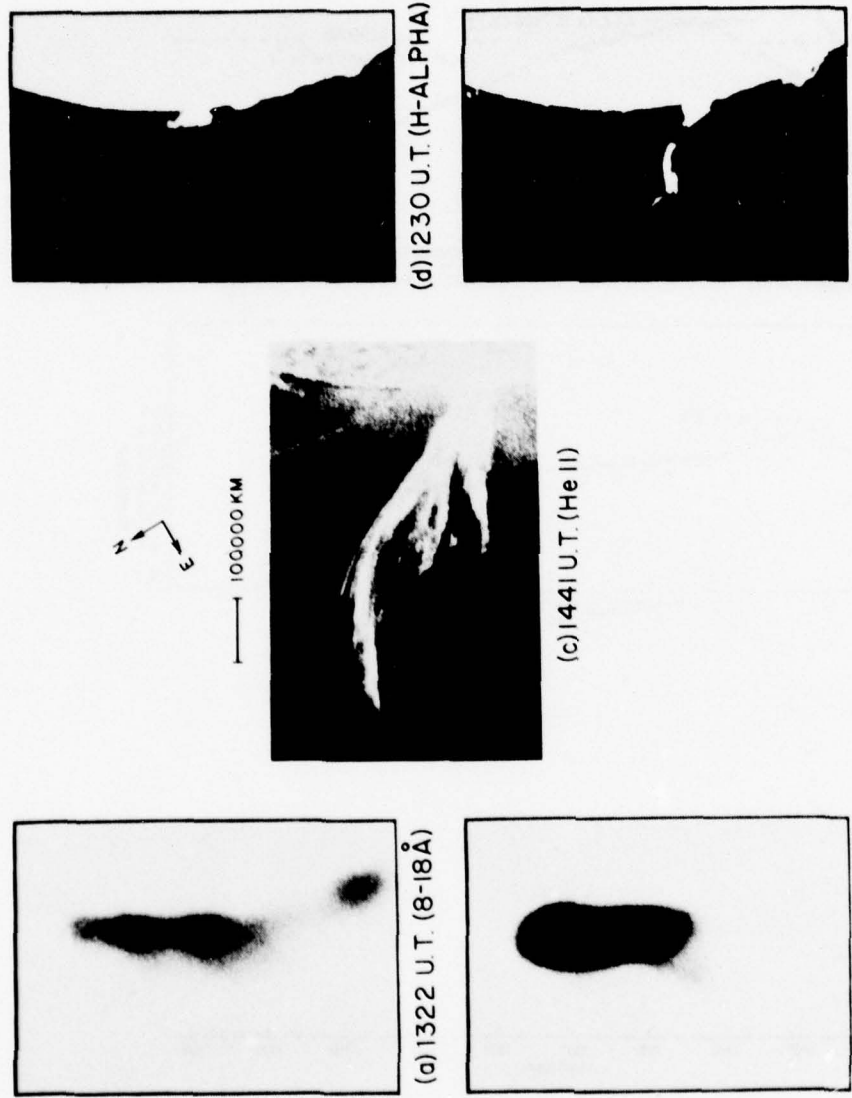


Figure 1. 21 August 1973 eruptive prominence and associated low coronal enhancement.
 (a) Pre-event soft X-rays, (b) soft X-rays at near X-ray maximum, (c) He II (304 \AA), late in the eruptive, (d) H α pre-event and (e) during the prominence eruption. (The He II picture is courtesy the Naval Research Laboratory.)

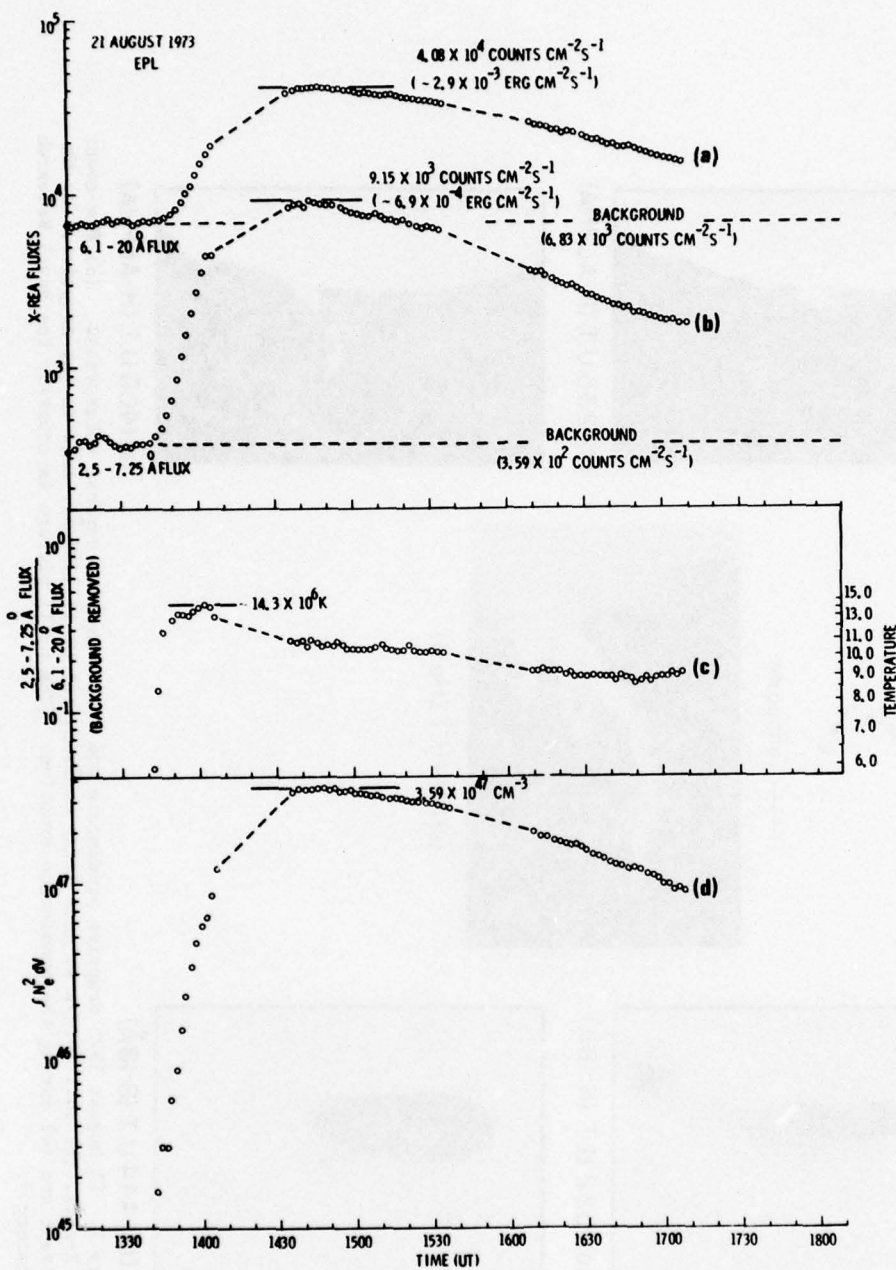


Figure 2. 21 August 1973 X-REA observed flux profiles at (a) $6.1 - 20 \text{ \AA}$ and (b) $2.5 - 7.25 \text{ \AA}$. Derived values are (c) the temperature profile and (d) the emission measure profile.

Figures 3a and 3c clearly show the expected similarity between the pre-event soft X-ray and Fe XV structure. An unusual and interesting common feature is the reverse S-shaped filamentary structure, composed of generally north-south loops nearly parallel to the underlying H_α filament. As pointed out by Sheeley *et al.* (1975), comparison with the magnetogram (Figure 3g) confirms that the sharply defined western edge of this linear structure was nearly parallel to the magnetic neutral line and was bordered by an area of suppressed emission - clearly seen in soft X-rays but more pronounced in Fe XV. This sharp western edge was also found to be nearly parallel with the southern portion of the pre-event H_α filament.

At 1606 UT (Figure 3e), the north-south filament was narrow and fragmentary between the two small bipolar regions, but larger and dense to the north. By 1630 UT, the north-south portion of the filament had become active. By ~ 1800 UT, it had undergone major geometry changes, breaking away from the northern, east-west portion and curving westward toward a small bipolar region, and had begun to disappear from on-band H_α. Doppler shifted material remained strongly visible in both wings at ~ 1905 UT but, at 1920 UT, only a small segment of the absorption feature was visible in the blue wing. The filament remained visible in a He II (304 Å) spectroheliogram taken with the NRL XUV spectroheliograph (S-082A) at 1852 UT (Sheeley *et al.*, 1975).

The evolution of the soft X-ray event, which began at ~ 1830 UT, is shown in a series of filtergrams in Figure 4. At 1449 UT, only the small active region to the east of the linear X-ray feature is clearly visible in this short exposure. By 1837 UT, the event had clearly begun with the brightening of the apparently non-potential north-south loops. (Late in the event, the X-ray structure appeared composed of more potential appearing loops oriented approximately east-west across the neutral line.) During its early development, we deduce that the X-ray emission expanded east-west at about 15 km s⁻¹ (~ 7.5 km s⁻¹ on either side), in a reasonable agreement with the 5 km s⁻¹ reported by Rust and Webb (1977) as the vertical expansion velocity of the August 21st loops. During the time of the soft X-ray event, there was no such enhancement in Fe XV (with a maximum response at ~ 2.3 x 10⁶K) where the primary change was a further reduction in emission and possible narrowing of the areas of suppressed emission paralleling the sinuous coronal structure (Sheeley *et al.*, 1975).

4.2.2 Physical Parameters

The beginning and maximum of the X-ray event were not recorded by the X-REA (Figures 5a and 5b) but the time of maximum flux can be estimated as ~ 1940 UT. Data are complete for the time of probable maximum spectral hardness - yielding a calculated peak temperature of ~ 7.4 x 10⁶K (Figure 5c). Again, the maximum emission measure (Figure 5d) occurs later than the maximum temperature and yields a particle density of ~ 10⁹ cm⁻³. These physical parameters, deduced from X-REA data, can be compared with those calculated using spatially resolved X-RT data: T ~ 6 x 10⁶K and N_e ~ 2.5 x 10⁹ cm⁻³. The absence of significant enhancement in Fe XV, combined with the absence of emission in the hotter XUV lines such as Fe XXIV, which maximizes at ~ 2 x 10⁷K (Widing and Cheng, 1974), although not quantitatively verifying the X-ray derived temperature, does appear to restrict the coronal event temperature range and to place the X-ray calculated temperatures within that range of acceptable values.

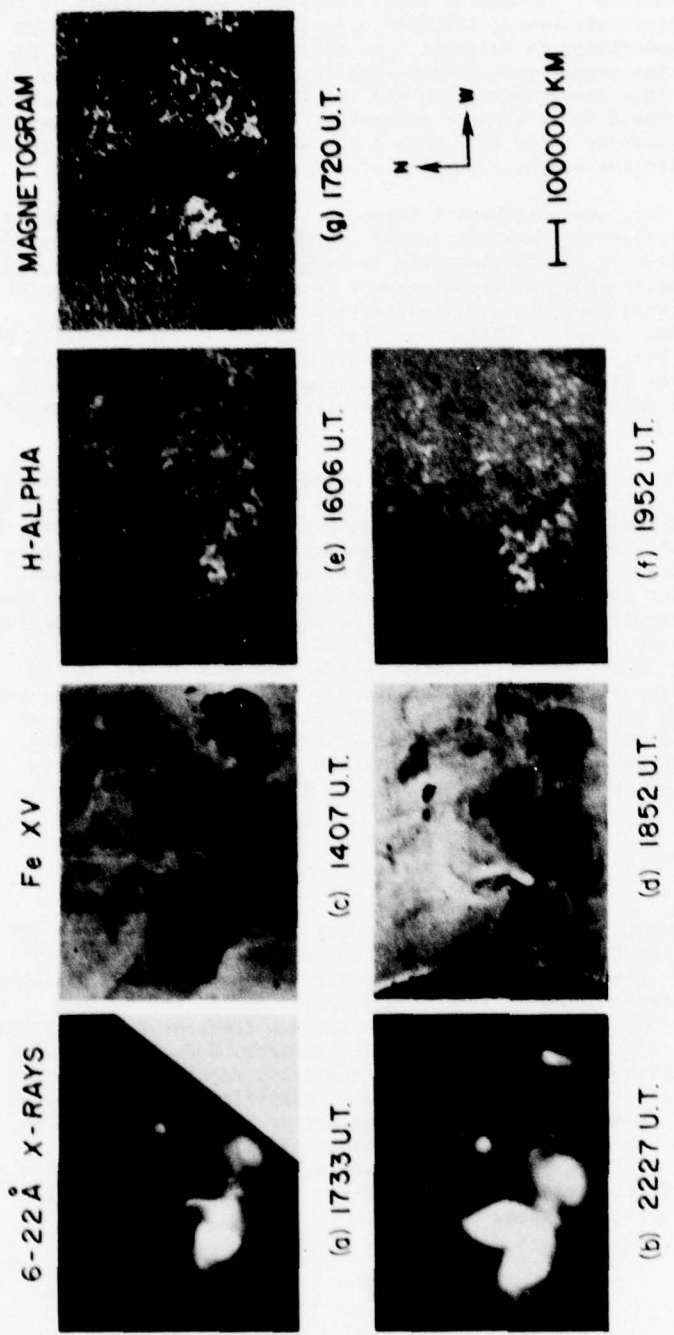
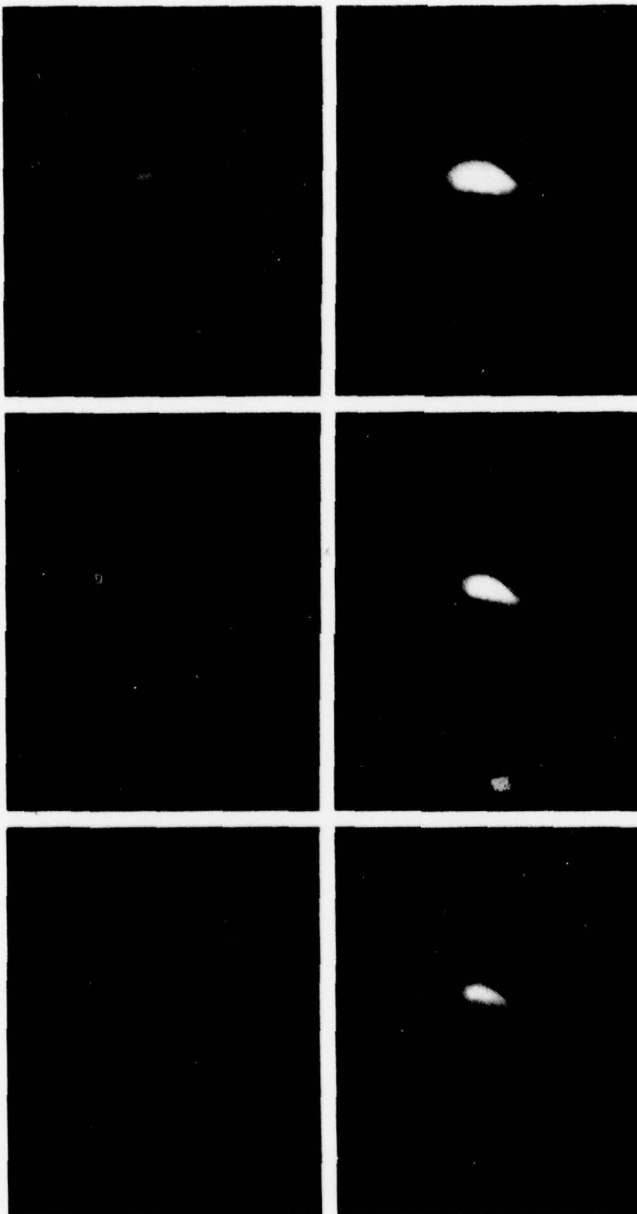


Figure 3. 18 January 1974 disappearance brusque. (a) Pre-event soft X-rays, (b) soft X-rays late in the event, (c) Fe XV (284 Å) pre-event, (d) Fe XV during the X-ray event, (e) H₂ pre-event and (f) post-disappearance brusque, and (g) a magnetogram prior to the event. (The magnetogram is courtesy Kitt Peak National Observatory and Fe XV spectroheliograms are courtesy the Naval Research Laboratory.)

N
W
1449 U.T.

1837 U.T.

1849 U.T.



1854 U.T. 1908 U.T. 2015 U.T.
1837 U.T. 1849 U.T. 1837 U.T.

Figure 6. 18 January 1974. The soft X-ray ($\sim 18 \text{ \AA}$) evolution of the X-ray event associated with the disappearance of the filamentary structures.

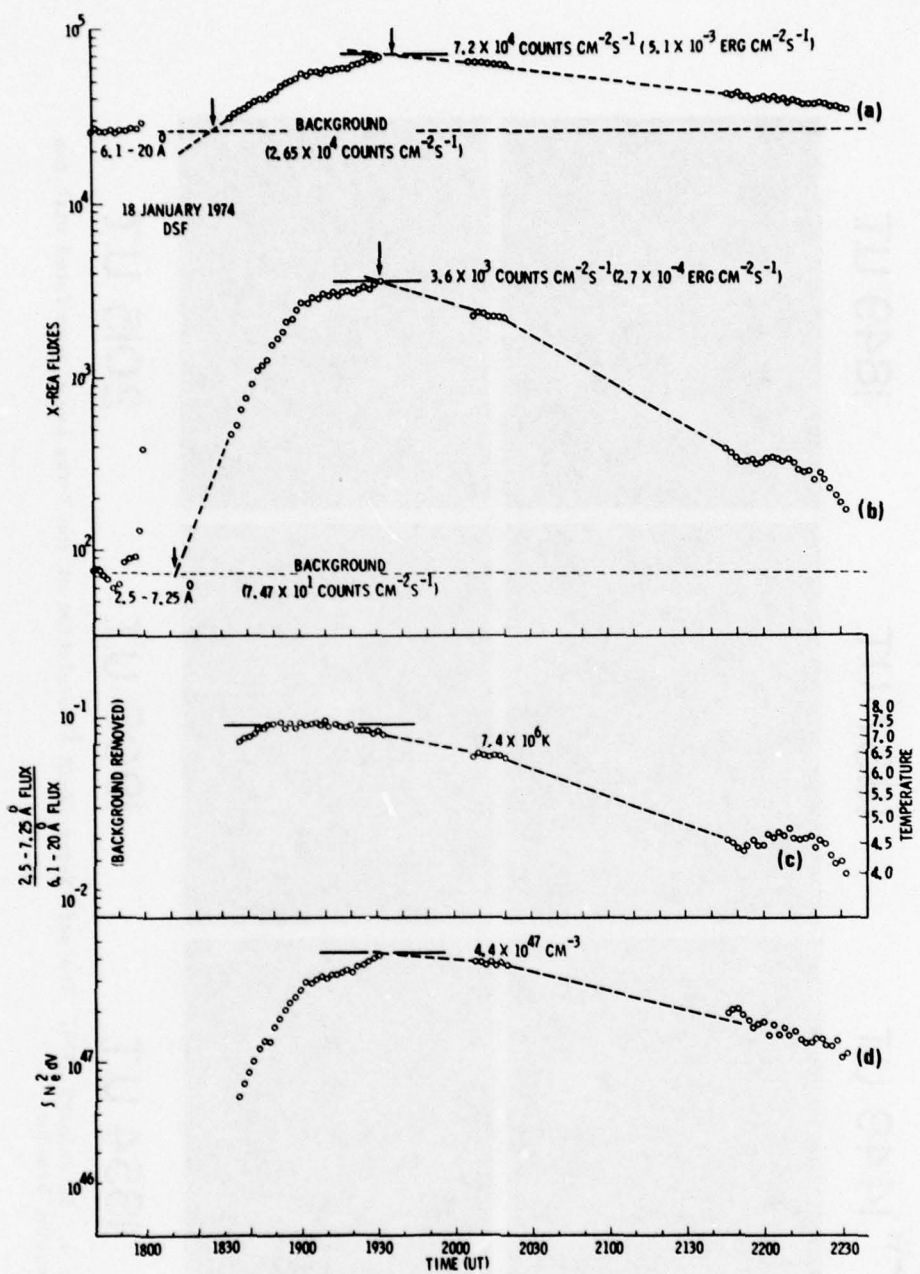


Figure 5. 18 January 1974 X-REA observed flux profiles at (a) 6.1-20 Å and (b) 2.5-7.25 Å. Derived values are (c) the temperature profile and (d) the emission measure profile.

4.3 17 January 1974 Spray

4.3.1 Morphology

The energetic limb event of 17 January probably originates in Boulder Active Region 314 (AR 314) (McMath Flare No. 12686), which had transited the west limb on the 15th of January. The region was growing as it approached the west limb and had produced a moderately large flare (optical 1B, X-ray M1) while very near the west limb on 15 January. This flare was also accompanied by a spray which was followed by a high speed coronal transient.

At the time of the 17 January spray (seen in Figure 6), the source region (AR 314) was about $0.065 R_s$ ($\sim 45,000$ km) occulted by the west limb. The H α event was first observed as a spray by the Ramey AFB observatory at ~ 1925 UT and was also observed by Mauna Loa Observatory, where high quality photographic images were made with a 10 \AA pass-band filter centered on H α . The spray appeared as a thick loop which rose rapidly and became very tenuous in its southern leg and foot point. This faint leg of the loop was laminated in structural appearance and some possible downflow was observed there (Hansen, private communication). At 1951 UT (Figure 6e), the H α ejected material was visible to about $2 R_s$, still appearing attached to the disk with both legs but becoming more tenuous. The loop shape of the chromospheric prominence is more clearly seen in the NRL He II, 304 \AA image (Figure 6f). (In a general discussion of the morphology and dynamics of flare sprays, Tandberg-Hanssen *et al.* (1978) have found the ejected spray material to be confined to a rapidly expanding loop-shaped magnetic envelope.)

The 17 January soft X-ray event began at ~ 1920 UT, either simultaneously with or a few minutes before the chromospheric spray prominence was seen at the limb. (Conversely, soft X-ray emission began tens of minutes after the eruption onset in the other two events.) The comparatively sharp rise of the $2.5 - 7.25 \text{ \AA}$ X-rays in the 17 January event is also indicative of an energetic onset. Tousey (1975, 1976) reports the 17 January event to be the only S-082A observed eruptive prominence to be seen in the high transition and coronal lines. (The 21 August event, for comparison, is seen in Fe XV, but only as a low coronal enhancement; the prominence itself is not observed.)

Soft X-ray images pre-event and during the event are seen in Figure 6a and 6b. The weak pre-event enhancement is associated with AR 314, about one and one half days behind the west limb. The event X-ray enhancement in Figure 6b is centered to the north of the major leg of the prominence as seen in H α and He II, and is a low coronal event which is believed to be primarily associated with the unseen chromospheric flare - occulted by the west limb.

XUV observations of the prominence ejection have been discussed in depth by Tousey (1975, 1976) and representative images are shown in Figures 6c, 6d, and 6f. He II 304 \AA emission (Figure 6f) maximizes at chromospheric temperatures and is quite similar to H α . Mg IX 369 \AA (Figure 6d) maximizes at about 10^6 K , but has a broad temperature range, and is therefore convenient for seeing transition region and coronal structure. The southern, low level loops seen in Fe XV 283 \AA (Figure 6c) are seen as an open loop and the long spur of the prominence is also still visible here. The elongated northern loop extends to well above the soft X-ray coronal event. At 1945 UT (Figure 6c), the Fe XV emission is strongest in the low lying southern loops (below the eruptive prominence) and along the spur to the north. The soft X-ray emission at 2007 UT is approximately co-spatial with the Fe XV faint northern emission and the spur.

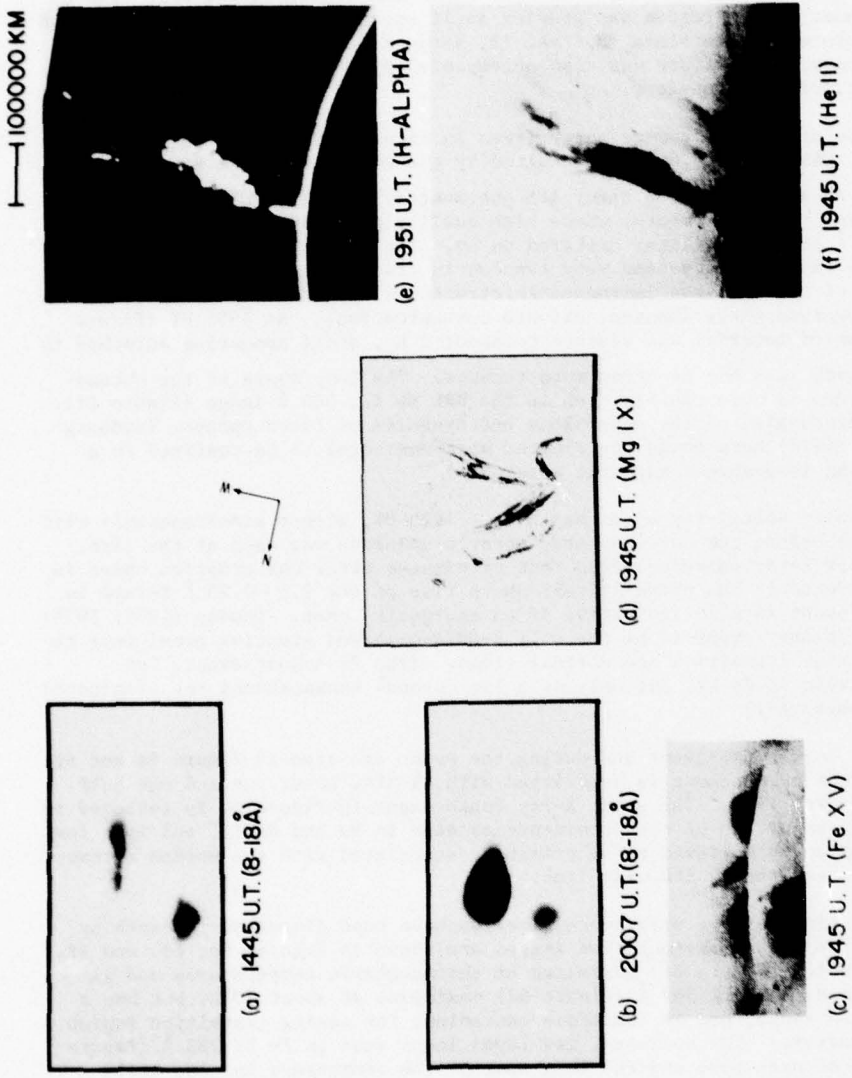


Figure 6. 17 January 1974 spray. (a) Pre-event soft X-rays, (b) soft X-rays near X-ray maximum, (c) Fe X V at X-ray maximum, (d) sketch of Mg IX (369 Å) at X-ray maximum, (e) H_α and (f) He II during the eruptive. (He II, Mg IX, and Fe X V spectroheliograms are courtesy the Naval Research Laboratory. The Mauna Loa 10 Å pass-band H_α photograph is courtesy the High Altitude Observatory.)

The associated white light coronal transient was first observed in progress by the HAO White Light Coronograph at 1943 UT, when the tops of the expanding diffuse loops were at about $2.5 R_s$. Jackson (private communication) and Hildner (1977) report the initially observed velocity as $\sim 850 \text{ km s}^{-1}$, apparently followed by deceleration at approximately the rate determined by gravity, in the absence of other forces.

Sweep frequency observed radio bursts included Type III (Importance 2), observed by Boulder at 1933.4 to 1934.7 UT and Type II, which was observed by Harvard (Importance 1, 1931-1948 UT) and by Boulder (Importance 2, 1936.7-1948.5 UT). Type I continuum was also reported by Boulder (Importance 1, 1515-1805 UT) and Type III was reported by Harvard (Importance 1, 1701-1926 UT).

4.3.2 Physical Parameters

X-REA observed time profiles of X-ray flux are shown in Figure 7. The softer X-rays (6.1-20 Å) were slow to rise and fall and only increased by about a factor of 2 over the pre-event background. However, the higher energy (2.5-7.25 Å) flux increased rapidly by $\sim X 35$ between 1920 and 1934 UT. This rapid increase in spectral hardness resulted in a sharp rise (8-10 minutes) to a maximum calculated temperature of $11.8 \times 10^6 \text{ K}$. Based on these X-REA observations, the maximum emission measure ($\int N_e^2 dV$) is calculated as $\sim 2.8 \times 10^{47} \text{ cm}^{-3}$. Assuming a volume of 10^{29} cm^3 , the maximum particle density, averaged over the event volume, is therefore $\sim 1.7 \times 10^9 \text{ cm}^{-3}$. By way of comparison, the imaged X-RT data yield a maximum density of $\sim 2.3 \times 10^9 \text{ cm}^{-3}$.

5. DISCUSSION

The events have in common that all were associated with ascending prominences (or disparitions brusques) of the type usually having associated coronal transients, that all were accompanied by soft X-ray enhancements in the low corona, and that all were of the general Long Duration Event (LDE) class in X-rays. However, their differences are perhaps most interesting. The three events are compared in Table 1.

The 18 January disparition brusque was of relatively low calculated coronal temperature ($\sim 7 \times 10^6 \text{ K}$ compared to $\sim 12 \times 10^6 \text{ K}$ and $14 \times 10^6 \text{ K}$ for the 17 January and 21 August events, respectively) and only a small, very faint chromospheric brightening was observed. Although the other two source regions were well obscured by the solar disk, the 21 August event exhibited faint H α limb brightening and, if it was indeed similar to the event which occurred at approximately that same heliographic location on 29 July, there was probably a chromospheric flare behind the limb of the type frequently associated with spotless regions and large ascending prominences.

In the case of the 17 January event, the evidence is strong that it was of energetic flare origin. The 2.5-7.25 Å X-ray enhancement began at $\sim 1920 \text{ UT}$, about five minutes before the chromospheric spray prominence was seen at the limb. If we assume the spray origin was occulted $\sim 45,000 \text{ km}$ by the west limb, and we assume a velocity of 400 km s^{-1} , the chromospheric material would have required only about two minutes to become visible at the limb. This near simultaneity indicates the heating of the plasma to coronal flare temperatures at

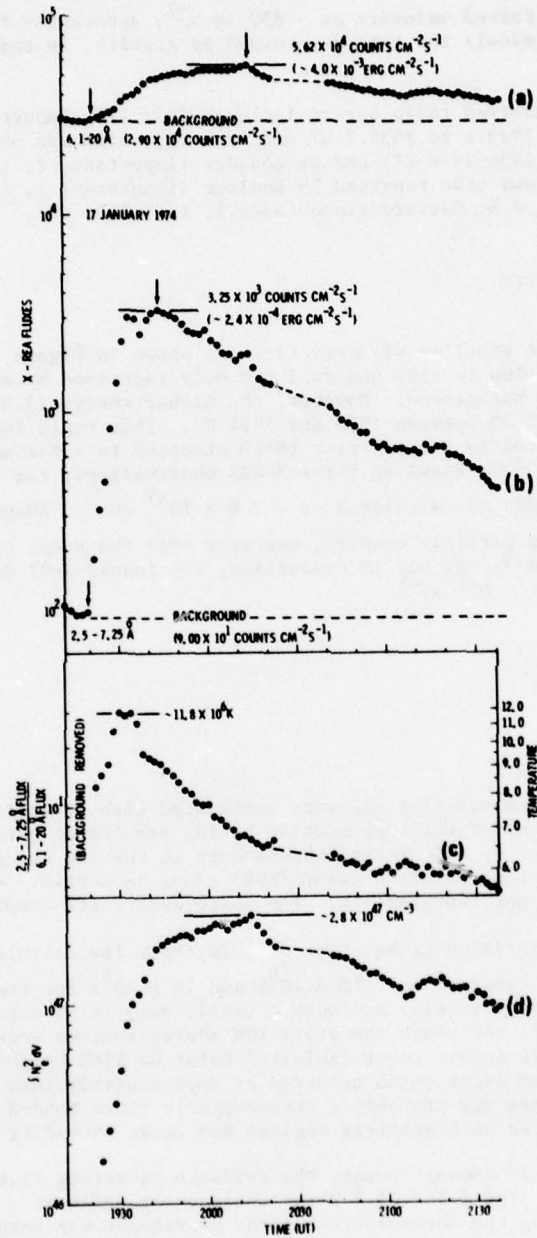


Figure 7. 17 January 1974 X-REA observed flux profiles at (a) $6.1 - 20 \text{ \AA}$ and (b) $2.5 - 7.25 \text{ \AA}$. Derived values are (c) the temperature profile and (d) the emission measure profile.

about the time of the spray eruption. Conversely (Table 1), X-ray emission began tens of minutes after the eruption onset in the other two events. The comparatively sharp rise of the 2.5-7.25 Å X-rays in the 17 January event (although perhaps due in part to the event origin being occulted) also appears indicative of an energetic onset. Tousey (1975, 1976) reports the 17 January event to be the only S-082A observed eruptive prominence to be seen in the high transition and coronal lines. The 21 August event, for comparison, is seen in Fe XV, but only as a low coronal enhancement; the prominence itself is not observed.

Another very striking difference in the 17 January and the 21 August eruptives is in the radial velocities of the H α prominence material. Gradual acceleration to a maximum observed velocity of 200 km s $^{-1}$ for the 21 August eruptive is reported by Smith *et al.* (1977), while the velocity of the 17 January spray was observed by Hansen and Jackson (private communication) to be 400 to 600 km s $^{-1}$. (This difference may be partially attributed to the difference in instrument sensitivity.) The association of initially high-speed (rapid acceleration) ejecta of Valniček's Type I (such as sprays) with flares was recognized by Warwick (1957) and the dynamics of sprays have been discussed by Tandberg-Hanssen *et al.* (1978).

The initially observed speed of 850 km s $^{-1}$ for the 17 January white light coronal transient required very high initial accelerations. At a slightly greater initially observed height, the projected speed of the leading edge of the 21 August white light coronal transient was observed as 450 km s $^{-1}$, followed by slow acceleration to 530 km s $^{-1}$ during about 3 hours of observations (Poland and Munro, 1976). Gosling (1976) has compared velocities of white light coronal transients and found that flare associated transients averaged 775 km s $^{-1}$ versus 330 km s $^{-1}$ for eruptive prominence associated events.

Acknowledgments

We are indebted to Dr. R. Tousey for the use of several NRL XUV spectrograms and for discussions of the January 17 event. We also wish to thank Dr. J. Harvey for supplying the KPNO magnetogram. We are grateful to Dr. E. Tandberg-Hanssen for reading the manuscript and for helpful discussions of event morphology. This study was stimulated by participation in the Skylab Workshop Series B on Solar Flares and was supported by the National Aeronautics and Space Administration under Government Work Order H-12261B, NASA/MSFC.

References

- Bohlin, J. D., G. E. Brueckner, J. D. Purcell, V. E. Sherrer, N. R. Sheeley, R. Tousey, and A. I. Poland, The eruptive prominence and coronal transient of 21 August 1973, *EOS*, 55, p. 409, 1974.
- Bruzek, A., Motions in arch filament systems, *Solar Phys.*, 8, p. 29, 1969.
- Gosling, J. P., E. Hildner, R. M. MacQueen, R. H. Munro, A. I. Poland and C. L. Ross, Mass ejections from the Sun: A view from Skylab, *J. Geophys. Res.*, 79, p. 4581, 1974.

- Gosling, J. T., Transient phenomena in the solar atmosphere and solar wind, Proc. International Symposium on Solar-Terrestrial Physics, June 7-18, 1976, Boulder, Colorado, ed. by D. J. Williams, Publ. by Am. Geophysical Union, p. 286, 1976.
- Hildner, E., Mass ejections from the solar corona into interplanetary space, in Study of Travelling Interplanetary Phenomena/1977, in the series Astrophys. and Space Sci. Library, ed. by M. A. Shea, D. F. Smart and S. T. Wu, p. 3, D. Reidel Publ. Company, Dordrecht, Holland, 1977.
- Horan, D. M., Electron temperature and emission measure variations during solar X-ray flares, Solar Phys., 21, p. 188, 1971.
- Kahler, S., The morphological and statistical properties of solar X-ray events with long decay times, Astrophys. J., 214, p. 891, 1977.
- Kreplin, R. W., T. A. Chubb, and H. Friedman, X-ray and Lyman-Alpha emission from the Sun as measured from the NRL SR-1 satellite, J. Geophys. Res., 67, p. 2231, 1962.
- Michaliskanos, A. G., and P. Kupferman, Spectrograph, filtergraph and magnetograph observations of the two-ribbon flare of 29 July 1973, Solar Phys., 36, p. 403, 1974.
- Munro, R. H., J. T. Gosling, E. Hildner, R. M. MacQueen, A. I. Poland and C. L. Ross, Observations of flare associated coronal dynamics above $2R_\odot$, Flare-Related Magnetic-Field Dynamics, NCAR, Boulder, Colorado, p. 139, 1974.
- Poland, A. I., and R. H. Munro, Interpretation of broad-band polarimetry of solar coronal transients: Importance of $H\alpha$ emission, Astrophys. J., 209, p. 927, 1976.
- Rust, D., and D. F. Webb, Soft X-ray observations of large-scale coronal active region brightenings, Solar Phys., 54, p. 403, 1977.
- Sheeley, N. R., Jr., J. D. Bohlin, G. E. Brueckner, J. D. Purcell, V. E. Sherrer, R. Tousey, J. B. Smith, Jr., D. M. Speich, E. Tandberg-Hanssen, R. M. Wilson, A. C. deLoach, R. B. Hoover, and J. P. McGuire, Coronal changes associated with a disappearing filament, Solar Phys., 45, p. 377, 1975.
- Smith, J. B., Jr., D. M. Speich, R. M. Wilson, E. Tandberg-Hanssen, and S. T. Wu, Prominence mass ejections and their effects on the corona. I. The eruptive prominence of 21 August 1973 and the surge of 4 December 1973, Solar Phys., 52, p. 379, 1977.
- Tandberg-Hanssen, E., Solar Prominences, 12, Geophysics and Astrophysics Monographs, ed. by B. M. McCormac, D. Reidel, Dordrecht, The Netherlands, 1974.
- Tandberg-Hanssen, E., S. F. Martin, and R. T. Hansen, Dynamics of flare sprays, Solar Phys. (submitted), 1978.
- Tousey, R., XUV emission from above the solar west limb near 20:00 UT, January 17, 1974, Astrophys. and Space Sci., 38, p. 327, 1975.
- Tousey, R., Eruptive prominences recorded by the XUV spectroheliograph on Skylab, Phil. Trans. R. Soc. Lond. A., 281, p. 359, 1976.
- Tucker, W. H., and M. Koren, Radiation from a high-temperature, low-density plasma: The X-ray spectrum of the solar corona, Astrophys. J., 168, p. 283, 1971.

- Underwood, J. H., J. E. Milligan, A. C. deLoach, and R. B. Hoover, The S-056 X-ray telescope on the Skylab-Apollo Telescope Mount, Appl. Opt., 16, p. 858, 1977.
- Underwood, J. H. and D. L. McKenzie, The analysis and interpretation of solar X-ray photographs, Solar Phys., 53, p. 417, 1977.
- Vaiana, G. S., A. S. Krieger, and A. F. Timothy, Identification and analysis of structures in the corona from X-ray photography, Solar Phys., 32, p. 81, 1973.
- Valnicek, R. Escape of matter from chromosphere and active regions, Bull. Astron. Inst., 15, p. 207, 1964.
- Walker, A. B. C., Jr., The coronal X-spectrum: Problems and prospects, Space Sci. Rev., 13, p. 672, 1972.
- Warwick, J. W., Flare-connected prominences, Astrophys. J., 125, p. 811, 1957.
- Widing, K. G., and C. C. Cheng, On the Fe XXIV emission in the solar flare of 1973 June 15, Astrophys. J. (Letters), 194, p. L111, 1974.
- Wilson, R. M., The Skylab ATM/S-056 X-ray event analyzer: Instrument description, parameter determination, and analysis example, NASA TM X-73332, Marshall Space Flight Center, AL., 1976.
- Wilson, R. M., The analysis of the X-ray event analyzer proportional counter data: A comment, NASA TM X-73367, Marshall Space Flight Center, AL., 1977.

Discussion

H. Hudson: Your plasma particle density of $\sim 1.5 \times 10^9 \text{ cm}^{-3}$ for the January 17 event appears low when compared with other X-ray flares.

J. Smith: I agree. Three comments: a) The event is partially occulted by the limb. b) The N_e you refer to was calculated using full sun proportional counter data which, with the background subtracted, averages over the total volume of the enhancement. The spatially resolved data yield a slightly higher density. c) The volume estimate over which the integration is made (Emission Measure = $\int N_e^2 dV$), based on the area of the spatially resolved event data and the assumed geometry, may be too large.

H. Hudson: What would you estimate to be the amount of occultation?

J. Smith: The active region assumed to be the source of the flare was about one and one-half days behind the west limb.

The Effect of the Magnetic Field on Coronal Transients

R. S. Steinolfson and S. T. Wu
School of Science and Engineering
The University of Alabama in Huntsville
Huntsville, AL 35807, USA

M. Dryer
Space Environment Laboratory
NOAA/ERL
Boulder, CO 80302, USA

E. Tandberg-Hanssen
NASA/MSFC
Space Sciences Laboratory
Marshall Space Flight Center
Huntsville, AL 35812, USA

Abstract

The dynamic interaction between the magnetic field and the material ejected during a solar event is examined in the meridional plane with the use of numerical solutions of the complete nonlinear, two-dimensional, time-dependent magnetohydrodynamic (MHD) equations of motion. The solar event is simulated by perturbations in the thermodynamic variables (pressure, density and temperature) at the base of the atmosphere. Two magnetic field configurations are considered: One configuration allows the ejected material to flow directly along the field lines to the outer corona (open configuration), and the other tends to retard the outward motion by the build-up of Lorentz forces (closed configuration). The effect of the magnitude of the magnetic field is also considered. We use magnetic fields with magnitudes at the base of the initial equilibrium atmosphere such that the values of β (the ratio of thermal pressure to magnetic pressure) are 1 and 0.1 at the base in the "preflare" state. The closed configuration does not allow any of the ejected material to flow to the

outer corona; however, a perpendicular MHD shock ($\beta = 1$) or a fast MHD wave ($\beta = 0.1$) does propagate upward. Most of the ejecta does reach the outer corona in an open configuration for both values of β .

I. INTRODUCTION

The intriguing and often changing shape of coronal transients has been studied extensively during the last several years, especially using Skylab observations (e.g., see MacQueen et al., 1974 and Hildner et al., 1975). It is now generally considered that it is the preexisting coronal magnetic field that largely determines the shape of the transient as it propagates through the lower corona. Also, the magnetic field has a dominating influence on the physical conditions in the plasma of the coronal transient. In some instances the magnetic field prevents transients from propagating more than a few tenths of a solar radius from the solar surface. Although the importance of the coronal field is well-recognized, it cannot be measured directly. As a result, one must resort to theory in order to gain a better understanding of the role of the field. One-dimensional models are of little use since they cannot account for the tensile effect of the magnetic field. The simplest model which can be used to realistically study the dynamic interaction between the fluid and the magnetic field is a two-dimensional, time-dependent MHD model which includes the complete nonlinear equations of motion. Unfortunately, in this case the equations are so cumbersome that they must be solved numerically. Such a model written in Cartesian coordinates was used by Nakagawa et al. (1976) to calculate the build-up of magnetic energy in the solar atmosphere. Another model applicable to the equatorial plane has been used by Wu et al. (1977) to study the effect of the field configuration on a coronal transient.

In the present paper we present results obtained with a two-dimensional, time-dependent MHD model applicable to the meridional (latitudinal) plane. Our interest is in the effect of the magnetic field on coronal transients - both in the topology of the field overlying the solar event which produces the transient and in the magnitude of the field. Two magnetic field configurations are considered: One which is essentially radial and one which is essentially parallel to the solar surface. For given thermodynamic conditions the magnitude of the field is given by the parameter β . Values for β of 1 and 0.1 are considered.

2. BASIC EQUATIONS AND SOLUTION PROCEDURE

We assume that the solar atmosphere can be treated as a single fluid with negligible dissipative effects (except at shock waves). By further neglecting radiation, the time-dependent equations that describe the flow in the meridional plane can be written in MKS units as follows:

$$\frac{\partial p}{\partial t} + \frac{\partial}{\partial r} (\rho u) + \frac{\partial}{\partial \theta} \left(\frac{\rho v}{r} \right) = - \frac{2\rho u}{r} - \frac{\rho v}{r} \cot \theta \quad (1a)$$

$$\frac{\partial u}{\partial t} + u \frac{\partial u}{\partial r} + \frac{B_\theta}{\mu \rho} \frac{\partial B_\theta}{\partial r} + \frac{1}{\rho} \frac{\partial p}{\partial r} + \frac{v}{r} \frac{\partial u}{\partial \theta} - \frac{B_\theta}{\mu \rho r} \frac{\partial B_r}{\partial \theta} = - \frac{GM_\odot}{r^2} + \frac{v^2}{r} - \frac{B_\theta^2}{\mu \rho r} \quad (1b)$$

$$\frac{\partial v}{\partial t} + u \frac{\partial v}{\partial r} - \frac{B_r}{\mu \rho} \frac{\partial B_\theta}{\partial r} + \frac{v}{r} \frac{\partial v}{\partial \theta} + \frac{B_r}{\mu r \rho} \frac{\partial B_r}{\partial \theta} + \frac{1}{r \rho} \frac{\partial p}{\partial \theta} = \frac{B_r B_\theta}{\mu r \rho} - \frac{uv}{r} \quad (1c)$$

$$\frac{\partial B_r}{\partial t} - \frac{\partial}{\partial \theta} \left(\frac{u B_\theta - v B_r}{r} \right) = \frac{1}{r} (u B_\theta - v B_r) \cot \theta \quad (1d)$$

$$\frac{\partial B_\theta}{\partial t} + \frac{\partial}{\partial r} (u B_\theta - v B_r) = - \frac{1}{r} (u B_\theta - v B_r) \quad (1e)$$

$$\frac{\partial p}{\partial t} + \gamma p \frac{\partial u}{\partial r} + u \frac{\partial p}{\partial r} + \frac{\gamma p}{r} \frac{\partial v}{\partial \theta} + \frac{v}{r} \frac{\partial p}{\partial \theta} = - \frac{\gamma p}{r} (2u + v \cot \theta), \quad (1f)$$

where the dependent variables are the density ρ , radial velocity u , meridional velocity v , pressure p , radial magnetic field B_r and the meridional magnetic field B_θ . The independent variables are the radius r and the meridional (or latitudinal) coordinate θ . The constants are the polytropic index γ , magnetic permeability μ , solar gravitational constant G and the solar mass M_\odot .

Prior to the solar event we assume that the atmosphere is stationary and can be described by a polytropic law; that is,

$$\frac{p}{\rho^\gamma} = \text{constant}. \quad (2)$$

The initial thermodynamic conditions at the base of the atmosphere are taken to be: temperature $T = 1.5 \times 10^6 \text{ K}$ and number density $n = 3 \times 10^8 \text{ cm}^{-3}$ (where $\rho = n m_p$ and m_p is the proton mass). The solution of the equation for hydrostatic equilibrium along with the polytropic law uniquely defines the initial atmosphere. In order for stationary conditions to exist, it is necessary that the Lorentz force vanish. This condition and the equation for the absence of free magnetic poles determine the initial magnetic field configuration, which is given in terms of Legendre polynomials of order 1. For the configuration selected, the magnetic field components are given by

$$B_r = \frac{1}{r^5} \cos \theta (5 \cos^2 \theta - 3), \quad (3a)$$

$$B_\theta = \frac{3}{4r} \sin \theta (5 \cos^2 \theta - 1). \quad (3b)$$

This configuration is obtained by using the Legendre polynomial of degree 3, which results in a global magnetic field with six lobes. One advantage of this configuration is that β increases with radius as would be expected in a realistic ambient atmosphere. In a dipole configuration, for instance, β decreases with radius. Two different portions of the global magnetic field are sketched in Figure 1. In the open configuration β increases away from the equator, while it decreases away from the equator in the closed configuration. If the solar event

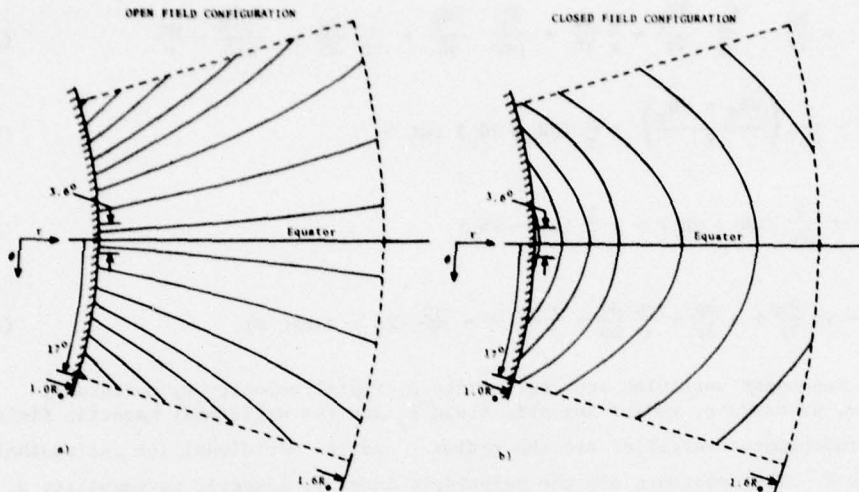


Figure 1. Schematic diagrams of open and closed magnetic field configurations in the meridional plane

occurs near the equator, the field configuration in Figure 1a allows material to flow along the field lines to the outer corona and hence is referred to as an "open" field configuration. The configuration in Figure 1b will tend to restrain material ejected near the equator and consequently is referred to as a "closed" field configuration.

The simulated solar event is assumed (1) to occur at the base of the atmosphere within 1.8° (i.e., within 2.2×10^4 km - see Figure 1) of the equator and (2) to be symmetrical about the equator. The event is represented by simultaneous perturbations in the density, temperature and pressure and is assumed to last for 5 minutes. The pressure is increased by a factor of 5 above the ambient pressure ($\delta p = 5$), which is achieved by a density increase of $\delta \rho = 1.2$ and a temperature increase of $\delta T = 4.17$. The perturbation is the same for every case considered in the following section in order to isolate the effects of β and of magnetic topology (i.e., open vis-à-vis closed magnetic field configurations).

Once the perturbation has been introduced, the time-dependent solution of Eqs. (1) simulates the coronal response. The equations are solved numerically using the modified Lax-Wendroff finite difference scheme given by Rubin and Burstein (1967). The radial grid spacing is $0.01 R_\odot$, and the latitudinal grid spacing is chosen to be equal to the radial grid spacing at $1.0 R_\odot$. The solution is obtained within the region bounded by the solar surface ($1.0 R_\odot$) and the dashed lines in Figure 1. Due to the symmetry of the solution about the equator, the computations are only performed for the region below the equator. Since the solution is only calculated out to a maximum of $1.6 R_\odot$, the neglect of the velocity in determining the initial state is not a serious limitation.

The atmospheric base is not treated as a solid wall in the present study as it was by Wu et al. (1977). We allow fluid to pass through the base, and hence, in analogy with the one-dimensional work of Nakagawa and Steinolfson (1976) and

Steinolfson and Nakagawa (1976), the flow variables must satisfy some sort of compatibility relations at the base. For the present case four variables can be specified arbitrarily at the base, and the remaining two must be calculated from the compatibility relations. We choose to specify the thermodynamic variables and magnetic field components and to calculate the velocity components. This procedure is followed so that the fluid can flow outward from the simulated solar event at whatever velocity is required by the pressure forces. The specified variables are held constant at the base except, of course, for the thermodynamic variables in (and during) the perturbation.

3. NUMERICAL RESULTS

The governing equations (Eqs. 1) can be nondimensionalized in such a way that the only parameters are γ , β and a parameter involving the reference temperature. Since γ and the reference temperature are kept constant, the only parameter in the equations is β . Steinolfson and Dryer (1977) have shown for a one-dimensional problem that the character of the solution depends on whether β is greater or smaller than one. Further theoretical evidence for the importance of β has been provided by Nakagawa et al. (1976) who showed that the magnetic energy build-up in the solar atmosphere depends critically on β . In order to determine what effect β has in the present problem, we use two values (i.e., $\beta = 1$ and $\beta = 0.1$). The only remaining parameter (since the perturbation is not changed) is the magnetic field configuration; both open and closed configurations, as defined in the previous section, are considered.

3.1 $\beta = 1$ Case

The results for a closed magnetic field configuration 10 min after introduction of the perturbation (at $t = 0$) are shown in Figure 2. The plots in Figure 2 and in all subsequent figures were computer-generated. Since we currently do not have the capability to generate these type of plots in polar coordinates, all results are presented in Cartesian coordinates. The amount of distortion involved in translating from polar to Cartesian coordinates is shown on the plot of velocity vectors in Figure 2 where the portion of the meridional plane on which the computations were performed is overlaid on the corresponding Cartesian plane.

The same quantities as in Figure 2 are presented in Figure 3 for an open field configuration. The density ratio is the density at each point divided by the ambient density at that point. The darkness of the shading increases with increasing density ratio. The velocity vector points in the direction of the velocity at the origin of the vector and its length is proportional to the velocity magnitude at its origin. The well-known result that weak disturbances travel faster across field lines than along them (due to the larger characteristic speed across field lines) is clearly illustrated on the density plots in Figures 2 and 3. The disturbance has traveled further radially near the symmetry axis in the closed configuration and further laterally near the base in the open configuration. In both the above cases the faster disturbance was traveling more nearly perpendicular to the field lines. For the two field configurations we immediately note the following similarities: (a) A well-defined shock forms at the leading edge of the disturbance, (b) the density compression behind the shock wave travels away from the perturbation as an expanding loop, (c) the density compression is followed by a density

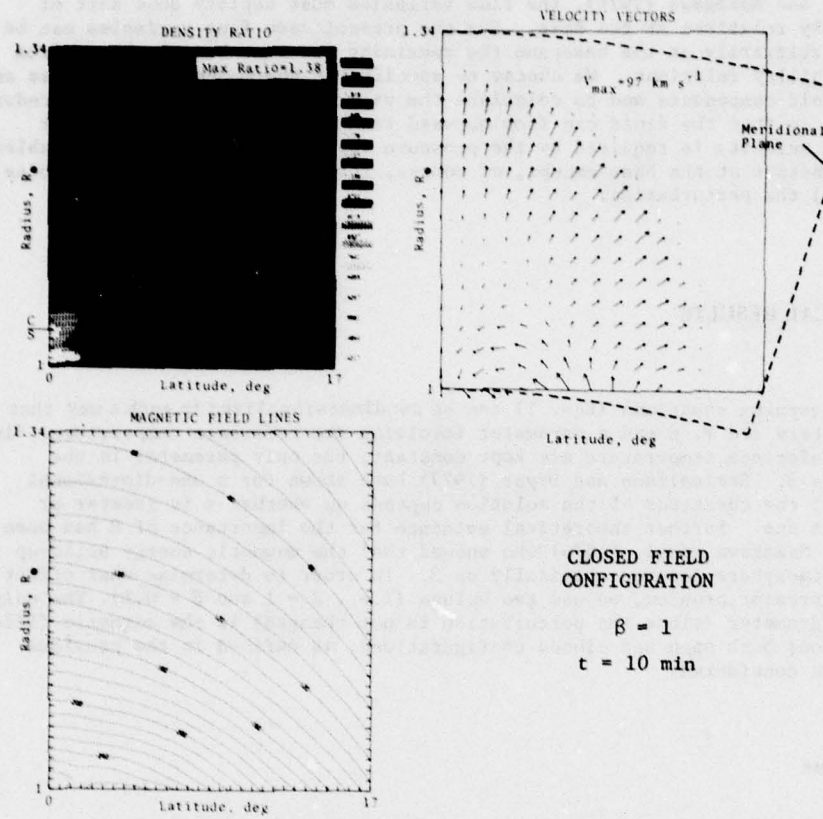


Figure 2. Selected results for a closed field configuration after 10 min for $\beta = 1$. The latitude is measured in degrees below the equator, which is at latitude = 0. The tic mark at the left edge of the density ratio plot labeled CS is the radial location of the contact surface on the symmetry axis (latitude = 0). The "Max Ratio" on the density plot (and on similar plots of other thermodynamic variables) is the maximum value on the plot. V_{\max} is the maximum velocity, as indicated by the length of the velocity vector, on the plot. The solution is actually calculated in the meridional plane indicated on the plot of the velocity vectors; however, as shown, all plots are in Cartesian coordinates.

rarefaction, (d) a swirling motion develops as seen on the plot of the velocity vectors, and (e) some fluid is flowing downward through the base; however, time-sequence plots show that the downward flow is continually decreasing and that the original ambient state is being restored. The following differences are also apparent: (a) The density enhancement is considerably less and broader in the closed configuration, (b) the density enhancement for the open configuration is concentrated near the top of the loop, while for the closed configuration the density enhancement is nearly constant along the loop, (c) the swirling motion is counter-clockwise in the closed configuration and clockwise in the open configuration, (d) a time-sequence of velocity vector plots shows that the center of the

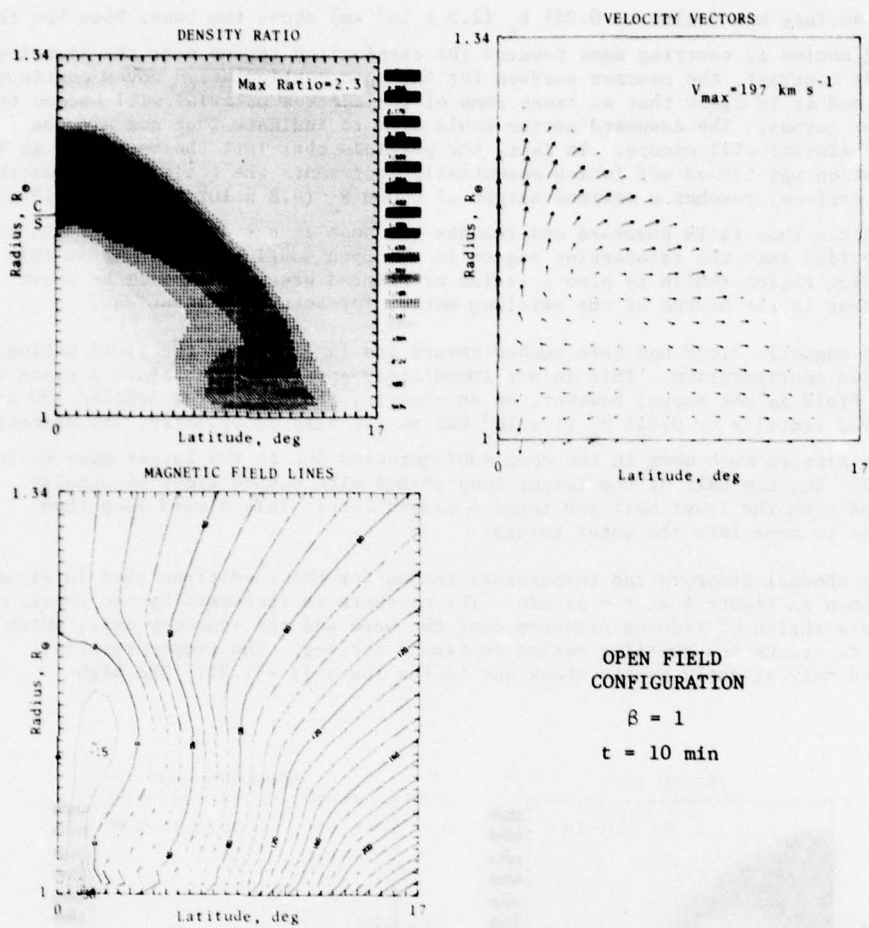


Figure 3. Selected results for an open field configuration after 10 min for $\beta = 1$ (See the caption for Figure 2.)

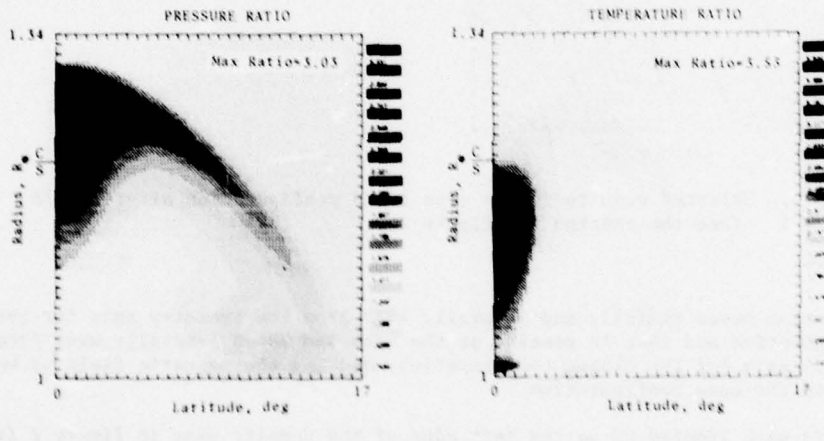
swirling motion moves radially and laterally away from the symmetry axis for the open configuration and that it remains at the base and moves laterally away from the symmetry axis for the closed configuration, and (e) the magnetic field is more distorted in the open configuration.

The tic mark labeled CS on the left edge of the density plot in Figure 2 (and on the left edge of the plots of all thermodynamic variables in other figures) indicates the radial location of the contact surface on the axis of symmetry. The contact surface represents the leading edge of fluid ejected during the simulated solar event. The fluid between the contact surface and the shock is ambient fluid that has been compressed, heated and accelerated by the shock. For the closed configuration in Figure 2, the leading edge of the ejected fluid reaches a maximum height of $0.051 R_\oplus$ ($3.6 \times 10^4 \text{ km}$, the distance between each tic mark is $0.01 R_\oplus$) above the base at $t = 6 \text{ min}$ and then begins falling downward until at $t = 10 \text{ min}$ the

contact surface has fallen to $0.041 R_s$ (2.9×10^4 km) above the base. Note how the swirling motion is carrying mass towards the rarefaction region near the symmetry axis. By contrast, the contact surface for the open configuration moves continuously upward, and it is clear that at least some of the ejected material will escape to the outer corona. The downward motion would seem to indicate that not all the ejected material will escape. In fact, the particle that left the base just as the perturbation was turned off (which essentially represents the trajectory of another contact surface) reaches a maximum height of $0.068 R_s$ (4.8×10^4 km) at $t = 12$ min; the particle then falls downward and reaches the base at $t = 16$ min. Fluid is also being carried into the rarefaction region in the open configuration. It is this rarefaction region (which is also a region of reduced pressure as will be shown later) that is the source of the swirling motion for both configurations.

The magnetic field has been pushed upward and laterally by the fluid motion in the closed configuration. This is not immediately apparent from Figure 2 since the initial field is not shown; however, as an example, the field line labeled 120 has been moved radially by $0.015 R_s$ (1×10^4 km) on the axis of symmetry. The magnetic field is altered much more in the open configuration due to the larger mass motion involved. The top half of the larger loop formed with dashed lines eventually separates from the lower half and forms a closed loop. This closed loop then continues to move into the outer corona.

The thermal pressure and temperature ratios for the conditions used in Figure 3 are shown in Figure 4 at $t = 12$ min. The pressure is increased by the shock, but there is a region of reduced pressure near the base and the symmetry axis, which is helping to create the swirling motion mentioned earlier. The temperature is increased only slightly by the shock due to the low γ ($\gamma = 1.2$). The high



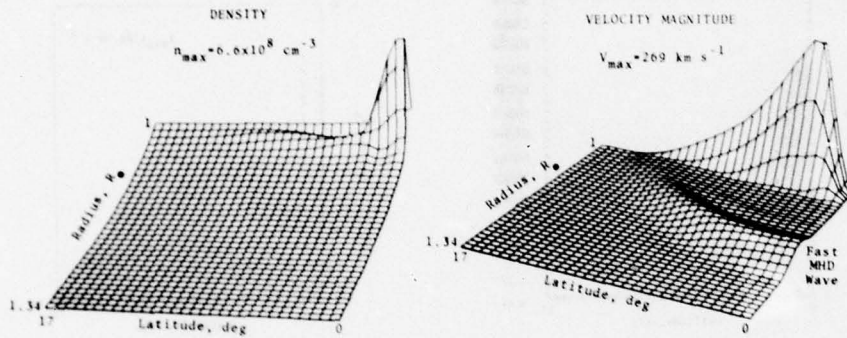
OPEN FIELD CONFIGURATION - $\beta = 1$, $t = 12$ min

Figure 4. Pressure and temperature ratios for the same conditions as in Figure 3

temperature fluid is the fluid that was ejected during the simulated solar event. The perturbation at the base extended about 2 1/2 tic marks laterally indicating that the fluid is being guided by the field despite the relatively high β . By comparison with Figure 3, one can see that the temperature is high where the density is low. A similar plot of temperature ratio for the closed configuration would show that the only high temperature region (the ejected material) is in the small rarefaction below the contact surface in Figure 2.

3.2 $\beta = 0.1$ Case

In the closed configuration the ejected material did not flow out to the interplanetary medium for $\beta = 1$, and consequently, one would not expect it to do so for a lower β . Indeed it doesn't, as shown in Figure 5; however, a fast MHD wave is formed. The fluid is accelerated in this wave, but the density and other thermodynamic variables remain unchanged. The wave is a fast MHD wave since its leading



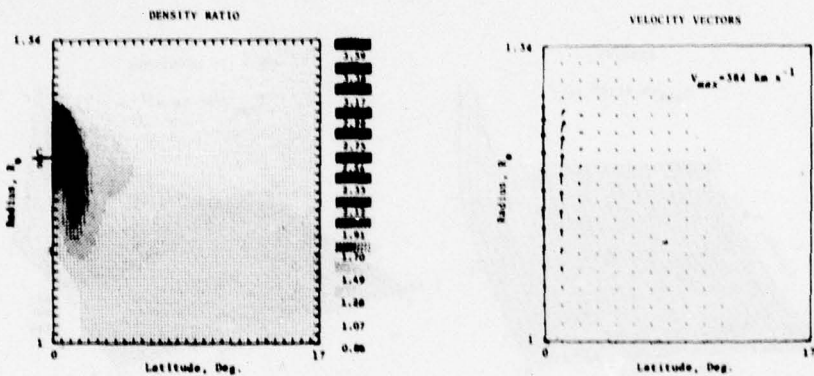
CLOSED FIELD CONFIGURATION - $\beta = 0.1$, $t = 4$ min

Figure 5. Density and velocity magnitude ($\sqrt{u^2 + v^2}$) for a closed field configuration after 4 min for $\beta = 0.1$. The maximum values on the plots are indicated. The right edge of each plot now represents the equator, and the top represents the solar surface.

edge is traveling along the symmetry axis at 530 km s^{-1} , which is approximately equal to the relevant characteristic speed of propagation of small amplitude (i.e., linearized) disturbances (the square root of the sum of the squares of the Alfvén and sound speeds). The fast wave is traveling radially almost twice as fast as the shock for $\beta = 1$ in the closed configuration. The large velocity near the base in Figure 5 is once again caused by a spiral motion similar to that for the corresponding larger β case.

Some of the results for an open configuration are shown in Figure 6 after 8 min. The magnetic field is so strong that it is not appreciably affected by the flow and retains the initial configuration in Figure 1. The main coronal response in this case is confined to a region near the equatorial axis comparable in latitudinal extent to the size of the solar event. The transient properties near the equatorial axis are similar to those for the open configuration for $\beta = 1$,

although the leading edge travels faster for the lower β . The leading edge in Figure 6 is traveling radially at 470 km s^{-1} which is the same as the relevant propagation speed of small amplitude disturbances (the Alfvén speed since $\gamma\beta/2 < 1$). This is true despite the fact that the jump in velocity and density across the leading edge are certainly not of small amplitude. The disturbance propagating laterally is so weak that it is lost in the numerical noise and doesn't appear on the figure. In analogy with the previously considered open configuration case, one would expect the disturbance to travel faster laterally than radially. There is a downflow behind the disturbance for times later than the time used for the figure. The downflow is very small, and eventually the original ambient atmosphere is restored.



OPEN FIELD CONFIGURATION - $\beta = 0.1$, $t = 8 \text{ min}$

Figure 6. Selected results for an open field configuration after 8 min for $\beta = 0.1$ (See the caption for Figure 2.)

4. DISCUSSION AND SUMMARY

The propagation of coronal transients through the lower corona is investigated in the meridional plane with numerical solutions of the time-dependent MHD equations of motion. The importance of the topology of the initial coronal magnetic field is demonstrated by considering two configurations: One which is essentially radial (open) and another which is essentially parallel to the solar surface (closed). The effect of the magnitude of the magnetic field is demonstrated by using values for the parameter β of 1 and 0.1 at the coronal base. The solar event responsible for the transient is simulated by a step-function increase in the pressure at the base of an initially hydrostatic atmosphere by a factor of 5 for a period of 5 min. For all cases investigated a disturbance propagates upward and laterally through the corona with the leading edge of the disturbance having the shape of an expanding loop. The lateral motion is appreciably less for the low β , open configuration than for the other cases with the major portion of the

disturbance being confined to a region directly over the solar event. The leading portion of the disturbance contains only coronal material whose properties have been altered by the preceding waves (which may strengthen into shocks) created by the explosive nature of the solar event. For both values of β the closed configuration does not allow any of the material ejected in the event to flow to the outer corona; the ejecta merely rises above the surface for a short time and then falls downward. In the open configuration the disturbance is preceded by a fast-mode MHD shock for $\beta = 1$ and a fast-mode MHD wave for $\beta = 0.1$. The coronal medium is set in motion by the MHD wave, but the wave does not alter the thermodynamic variables by a perceptible amount. The ejecta does reach the outer corona for both values of β in an open configuration with little lateral motion. A shock forms ahead of the radial motion of the disturbance but weakens rapidly with increased latitudinal distance from the equator and becomes little more than a wave propagating in the lateral direction. The present results corroborate the results of Wu et al. (1977) in that coronal transients which propagate to the outer corona and contain material ejected in the solar event appear to occur in open field regions. It must be kept in mind, however, that if the perturbation is of a larger magnitude than used herein, it is possible that material may reach the outer corona even in a closed field configuration.

When some of the ejected material does reach the outer corona the ambient medium which has been compressed by the shock ahead of the transient is followed by the high temperature ejecta from the solar event. It is the compression region which may become visible to instruments such as the white light coronograph on Skylab, and the high-temperature region which may be seen in the lower corona in X-ray (providing the density is high enough). Of course, the material from the solar event may be observed in X-ray and other wavelengths in the lower corona even if it returns to the solar surface.

Acknowledgments

Two of the authors (RSS and STW) express their appreciation to NASA/Marshall Space Flight Center which sponsored this work under Contract NAS8-28097. Acknowledgment is made to the National Center for Atmospheric Research, which is sponsored by the National Science Foundation, for the use of its computer facilities. In carrying out this research, the authors have benefited considerably from the Skylab Solar Workshop Series on Solar Flares. The workshops are sponsored by NASA and NSF and managed by the High Altitude Observatory, National Center for Atmospheric Research.

References

- Hildner, E., J. T. Gosling, R. M. MacQueen, R. H. Munro, A. I. Poland and C. L. Ross, The large coronal transient of 10 June 1973 I. Observational description, Solar Phys. 42, 163, 1975.
- MacQueen, R. M., J. A. Eddy, J. T. Gosling, E. Hildner, R. H. Munro, G. A. Newkirk, Jr., A. I. Poland and C. L. Ross, The outer solar corona as observed by SKYLAB: Preliminary results, Astrophys. J. 187, L85, 1974.

- Nakagawa, Y., and R. S. Steinolfson, Dynamical response of the solar corona. I. Basic formulations, Astrophys. J. 207, 296, 1976.
- Nakagawa, Y., R. S. Steinolfson and S. T. Wu, On build-up of magnetic energy in the solar atmosphere, Solar Phys. 47, 193, 1976.
- Rubin, E. L., and S. Z. Burstein, Difference methods for the inviscid and viscous equations of a compressible gas, J. Comp. Phys. 2, 178, 1967.
- Steinolfson, R. S., and M. Dryer, Numerical simulation of MHD shock waves in the solar wind, submitted to J. Geophys. Res., 1977.
- Steinolfson, R. S., and Y. Nakagawa, Dynamical response of the solar corona. II. Numerical simulation near the sun, Astrophys. J. 207, 300, 1976.
- Wu, S. T., M. Dryer, Y. Nakagawa and S. M. Han, Magnetohydrodynamics of atmospheric transients II. Two-dimensional numerical results for a model solar corona, submitted to Astrophys. J., 1977.

Discussion

Bird: In your simulation with $\beta = 1$ (open field configuration), the largest disturbance in the ambient magnetic field seemed to occur in a region behind the peak in the density enhancement. Does this trend continue out to higher altitudes ($> 2.5 R_s$) where the coronal transients are observed? Could it be further assumed that the magnetic field is only weakly perturbed within the high density region?

Dryer: The deformation of the ambient magnetic field continues to the larger distances from the sun in our simulation. We believe that the magnitude of the magnetic fields' perturbation will be strongly enhanced close to the high density region (as found in separate 1D, MHD computations by Steinolfson, Dryer, and Nakagawa, J. Geophys. Res., 80, 1989, 1975) and are presently in the process of examining this question in more detail.

Armstrong: What is the effect of the isotropic equation of state on the calculated density and temperature profiles? For example, allowing high thermal conductivity along \vec{B} might reveal field controlled patterns in the white light emission.

Dryer: Although we have not examined an anisotropic equation of state, we believe that the basic features (effect of Beta and magnetic topology confinement of the initial perturbation) will remain unchanged. Certainly, the magnitudes of the profiles would be expected to differ from the isotropic case. We have also ignored thermal conductivity. However, in the presence of high thermal conductivity along \vec{B} , we would expect an efficient cooling process to preclude white light observations.

Relation Between Moreton Waves, Type II Shocks and Interplanetary Shock Waves

S. Pinter

Geophysical Institute of the Slovak Academy of Sciences
947 01 Hurbanovo, Czechoslovakia

Abstract

There are twenty cases of flare-associated waves, usually referred to as Moreton waves. These were studied to determine their relation to the type II radio bursts and interplanetary shock waves. Fourteen of the twenty Moreton wave events (70.0%) were associated with type II bursts and also with interplanetary shock waves observed around the Earth. We used the velocity as a key parameter in the interpretation of Moreton waves. The mean chromospheric velocity was calculated assuming that the wave effect is propagating along or just above the surface of the chromosphere. The comparison of the mean chromospheric velocities of the Moreton waves with the associated radial velocities of the coronal shock waves computed from the frequency drift of type II radio bursts and with the associated mean velocities of the interplanetary shock waves indicated that there is a close relation between them, i.e., the larger the Moreton wave velocity, the larger the type II shock velocity and the interplanetary shock wave velocity. In an earlier study we found a linear relationship between type II coronal shock wave velocities and interplanetary shock wave velocities. Clearly, if there is a linear relation

between Moreton wave velocities and type II shock velocities, there must be a relation between Moreton wave velocities and interplanetary shock velocities. These relationships strongly suggest a basic physical similarity between these three phenomena.

We can conclude that the Moreton waves, type II shocks and interplanetary shock waves have not only similar mechanisms, but also a common source of disturbance. Observed Moreton waves represent the early phase of shock before they arrive at the coronal levels emitting type II bursts, and later the shock waves persist into interplanetary space and produce, for example, discontinuities in the solar wind.

I. INTRODUCTION

Solar flare-associated fast travelling waves, propagating along the surface of the chromosphere, were first discovered by Moreton (1960) and they drew attention from the point of view of the observer, as well as from the point of view of the theoretical solar physicist (Athay and Moreton, 1961; Dodson and Hedeman, 1964; Moreton, 1965; Anderson, 1966; Meyer, 1966; Uchida, 1960, 1968, 1969, 1970, 1974; Smith and Harvey, 1971). These flare-associated chromospheric wave events, which are usually called after their discoverer "Moreton waves", are triggered by explosive flares and can be observed in the centre of the line and/or in the wings of the H-alpha line. Moreton waves and the usually subsequent coronal and interplanetary shock waves represent extreme cases in the whole series of flare-associated fast travelling solar and interplanetary phenomena. The origin, characteristic and interpretation of these events are of key importance in solar physics and in the physics of solar-terrestrial relationships, because understanding them may provide certain possibilities of forecasting, e.g., of such geophysical events as sudden commencements of geomagnetic storms.

A whole series of studies, concerning Moreton waves, have appeared in the literature. Most of them concentrated on detailed analysis of specific events or on describing the general phenomenology of the events. However, so far the relation of Moreton waves to coronal and interplanetary shock waves has not been studied statistically or in detail for individual events.

The primary purpose of this paper is to summarize briefly the materials which have so far been published about the observed characteristics of Moreton waves and to find their relation to radio bursts of type II and interplanetary shock waves.

2. DEFINITION AND DESCRIPTION OF MORETON WAVES

Systematic photography of the solar chromosphere in the centre and at the wings of the H-alpha line with high time and space resolution enabled Moreton (1960) to discover new properties of solar flares which are characterized by a sudden explosion or expansion. These flares are usually called explosive flares (Moreton, 1961). These explosive flares, as we shall see later, are connected with such fast travelling disturbances as shock waves, type II, III and IV radio bursts, etc. (Bruzek, 1969).

With explosive flares, we are clearly able to identify a short sudden increase in the H-alpha flux at the time of the "flash" phase of the flare (area \propto intensity), and this takes place before the flare maximum is reached. The fundamental factor in the explosive development is the sudden expansion of the flare area, at the time of which the whole or part of the peripheral bright regions of the flare spread in a certain direction with a velocity sometimes exceeding 100 km/s (Moreton, 1965). The interval of this acceleration development, i.e., the duration of the explosive phase is only about 10 seconds and, as Moreton maintains, shorter than 30 seconds.

Athay and Moreton (1961) reported the first direct proof of the existence of fast travelling chromospheric disturbances, which were identified on Lockheed flare films taken in the H-alpha line in 1959 and 1960. Later Smith and Harvey (1971) summarized all the available facts on wave effects also observed on Lockheed films between 1959 and 1967. The latest aspects of the optical effects of Moreton waves, which were found on H-alpha filtergrams with a resolution of about one second of arc, were discussed by Martin and Harvey (1974). Besides these papers of substantial significance, concerning the description and interpretation of the observational effects of Moreton waves, there exists a whole series of papers, the authors of which deal with the description of the characteristics of the individually observed explosive flares in various connections, which generate the Moreton wave (Zirin and Werner, 1967; Dodson and Hedeman, 1968; Zirin and Russo Lackner, 1969, and Harvey et al., 1974).

At present there exist four different types of optically observed direct or indirect evidence in favour of the existence of flare-associated Moreton waves (Smith and Harvey, 1971 and Martin and Harvey, 1974), i.e.:

Wave fronts (WF): Fast travelling diffusive wave front, observable in the emission of the centre of the H-alpha line and/or in the dark wave in the wings of the H-alpha line.

Filament oscillation (FO): A sudden oscillation or activating of a filament located outside the flare region, in some cases, which leads to "disparition brusque".

Chromospheric brightening (CHB): Short-lived brightening of small points (spots) occurring in the chromosphere outside the flare centre at locations passed by the wave.

Filament turbulence (FT): Filaments show abruptly initiated turbulence instead of a distinct oscillation of its mass.

Table 1 contains some of the most important information on 20 Moreton waves, known from the literature (Smith and Harvey, 1971; Moreton, 1965). The first four columns of Table 1 give the data on explosive flares which produced a Moreton wave, identified via one of the effects mentioned above. The table indicates that in most cases the Moreton wave generated an oscillation of a filament and only in very few cases was chromospheric brightening observed. It is possible that the mentioned effects of the Moreton wave are only manifestations of the interaction of the wave with a certain chromospheric or coronal structure most accessible to us. We are convinced that, given a suitable observational technique, further phenomena will be discovered which will enable us to study Moreton waves.

Table I. A Comparison of Various Solar and Interplanetary Phenomena in Association with Observed Moreton Waves

Solar Flare Data				Moreton Wave Data				Type II Radio Burst				Interplanetary Shock Waves			
Date	Start UT	Explosive Phase UT	Position	Type*	Angular extent degrees	Mean velocity \bar{V}_h km sec $^{-1}$	Start UT	Frequency range MHz	Start UT	Radial velocity \bar{V}_R km sec $^{-1}$	Date	SSC UT	Mean speed km sec $^{-1}$		
1960 June 25	20 37	20 41:45		WF, FO	165	810	20 45	20-180	1100	June 27	16 30	950			
1960 Sep. 07	23 09	23 09:00		WF, FO, CHB	35	710	No Observed	-	-	-	-	-			
1960 Oct. 12	17 40	17 45:45		WF, FO	115	680	17 51	50-180	1530	Oct. 13	2147	1480			
1961 Mar. 18	19 08	19 08:30		-	70	630	No Observed	-	-	-	-	-			
1961 Sep. 03	20 39	20 41:00		WF, CHB	60	440	No Observed	-	-	-	-	-			
1963 Sep. 20	23 50	23 56:15		WF, FO	70	750	20 59	20-200	1200	Sep. 22	16 01	970			
1966 Aug. 28	15 21	15 28:00	22N 05E	WF, FO	90	1250	15 31	20-120	6200	Aug. 29	13 15	1650			
1966 Dec. 30	22 31	22 33:00	23S 37E	WF, FO	75	440	22 36	50-280	1140	Jan. 01	24 00	840			
1967 Feb. 04	16 40	16 44:00	11N 40E	WF, FO	125	750	16 48	30-100	1200	Feb. 07	16 40	560			
1967 Feb. 27	16 37	16 43:15	27N 01E	WF, FO	115	650	16 41	10-30	990	Mar. 02	05 00	690			
1967 Mar. 27	21 07	21 11:00	23N 23W	WF	80	620	21 26	30-300	-	Apr. 01	08 07	500			
1967 May 03	15 37	16 15:45	21N 51E	FT	-	530	15 47	30-300	-	May 07	01 00	515			
1967 May 23	18 34	18 37:10	31N 25E	WF, FO	85	1125	18 38	25-180	5000	May 24	17 30	1760			
1967 July 30	15 54	15 59:45	13N 06W	WF, FO, CHB	60	500	-	-	-	-	-	-			
1967 July 31	17 15	17 21:00	10N 21W	WF, CHB	65	560	-	-	-	-	-	-			
1967 Aug. 01	00 56	01 17:00	11N 27W	WF, FO	45	710	01 20	30-300	1280	Aug. 04	07 02	650			
1967 Aug. 24	10 06	00 11:00	19S 00E	WF, FO	70	490	00 17	30-300	700	Aug. 29	17 32	460			
1967 Aug. 29	20 36	20 50:45	22N 50E	FO	-	-	20 54	30-300	1500	Sep. 01	04 00	730			
1969 Apr. 16	20 30	20 51:30	17S 02E	FO, CHB	-	-	-	-	-	-	-	-			
1969 Apr. 26	22 58	23 01:15	07N 38E	FO, CHB	45	1210	23 06	30-300	1270	Apr. 28	02 52	1490			

• See text for definitions of WF, etc.

3. MORETON WAVE PROPAGATION VELOCITY

The velocity of propagation is the key parameter in interpreting Moreton waves and in determining their relation to various events connected with the flare wave. The velocity of propagation of fast travelling flare-associated disturbances is determined by accurate measurements of the time interval and distance between the beginning of the explosive phase of the flare and the subsequent observation of the disturbance appearing in the centre or at the wings of the H-alpha line spectrum as it moves away from the explosive flare region. The transverse component of velocity is measured, and it is assumed that the wave propagates along or directly above the chromosphere.

The values of the velocity of propagation of Moreton waves, \bar{V}_{ch} , for individual events, obtained by different authors, are given in column 7 of Table 1 (Athay and Moreton, 1961; Smith and Harvey, 1971; Martin and Harvey, 1974). The velocities of propagation, given in the table, vary from 440 to 1250 km/s, the mean velocity of Moreton waves propagation being 730 km/s.

It is interesting to compare, in actual cases, the velocity of propagation of Moreton waves in different directions, determined for the same events on the basis of various effects, e.g., from chromospheric brightening and from sudden oscillations of a filament which appears at various longitudes and latitudes. Such comparisons may provide an answer to the question of the existence of isotropic or anisotropic velocity of propagation of flare-generated Moreton waves. A comparison of this kind can be made with the event which occurred at 22 58 UT on 26 April 1969 (Harvey and Martin, 1974). After the explosive phase which was observed at 23 01:15 UT, oscillations of filaments were observed as well as chromospheric brightening. The velocity of the Moreton wave, which produced the filament oscillations, was determined as 1210 ± 400 km/s. This velocity is nearly identical with the velocity of the wave derived from chromospheric brightening, i.e., 1210 ± 230 km/s. With a view to the position of the chromospheric brightening and the oscillations of the filament relative to the flare it may be assumed that in this case the wave was propagating isotropically within a range of 45° .

A typical case of anisotropic propagation of a Moreton wave is the event of 3 May 1967, which was observed at 15 37 UT at $21^\circ N$ $51^\circ E$ (Martin and Harvey, 1974). The Moreton wave, generated at the time of the explosive phase (16 15:45 UT) of this flare, was responsible for the turbulent motion of the filament. The velocity derived from three points of the filament turbulence A, B and C (e.g., see Fig. 5 in the paper by Martin and Harvey, 1974) amounted to 500, 630 and 780 km/s. Further evidence of anisotropic propagation of a Moreton wave is provided by the event of 23 May 1967 (De Mastus and Stover, 1967; Smith and Harvey, 1971). Figure 1 is a schematic drawing of the progress of the wave front from the time of the flare explosion. One can see that the wave did not propagate spherically, which implies anisotropic distribution of the propagation velocity. The emission front represents a wide scale of velocities from 340 to 1250 km/s.

A graph of the transverse component of the mean velocity was constructed for several exclusive events of the observed Moreton wave front. Figure 2a shows the mean velocity of propagation of the leading edge of the wave front, observed between 18 37 and 18 45 UT on 23 May 1967. Until the explosive phase of the flare the wave propagated at 1250 km/s, and at a distance of about 20×10^4 km its velocity had decreased to 750 km/s.

The Moreton wave front, observed on 20 September 1963, could only be observed in the wings of the H-alpha line spectrum (Figure 2b). As can be seen in Figure 2b, the leading edge of the wave in the observed direction propagated at a constant

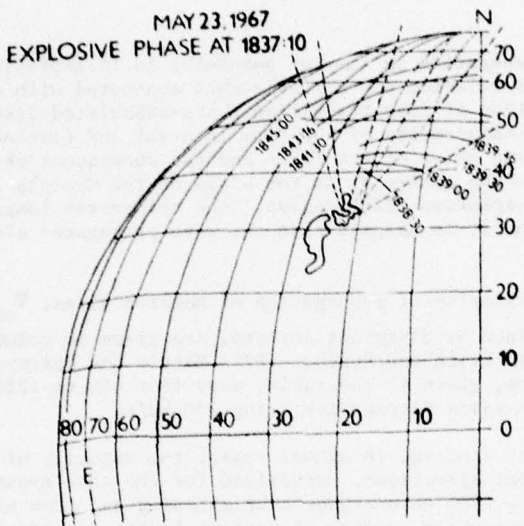


Figure 1. The Moreton wave event of May 23, 1967,
traced with time lapse from the sequence of films by
S. F. Smith (Uchida, 1970)

velocity of 750 km/s to a distance of 35×10^6 km.

The analysis of these data indicates that the velocity of propagation of Moreton waves is, in many cases, strongly anisotropic. This anisotropy is clearly caused by the conditions under which the wave propagates and that the anisotropy of a wave front may vary across the front. As we have seen, the velocity varies from 440 to 1250 km/s. These velocities are supersonic and the wave represents some type of MHD shock wave. M. Dryer has suggested (private communication, 1977) that - depending on the local Alfvén speeds - these waves are either fast MHD shocks or fast MHD waves, the latter having been studied by Uchida as noted above.

4. THE DIRECTION OF MORETON WAVE PROPAGATION

Another important characteristic of Moreton waves is that they are highly directional. In many cases the angular width of the effects observed is equal to or smaller than 90° (Smith and Harvey, 1971). In many cases, as indicated by Table 1, this angle is larger. For example, with the events of the wave front of 25 June 1960 the angular range amounted to 165° . The most accurate data of angular width of propagation of a disturbance were obtained from a wave front in which emission or absorption could be observed directly. In the case of the Moreton wave, observed in connection with the proton flare of 28 August 1966, the wave front encompassed a concave arc with an angle of 90° with its apex near the main spot closest to the flare. The Moreton wave propagated away from the flare across the

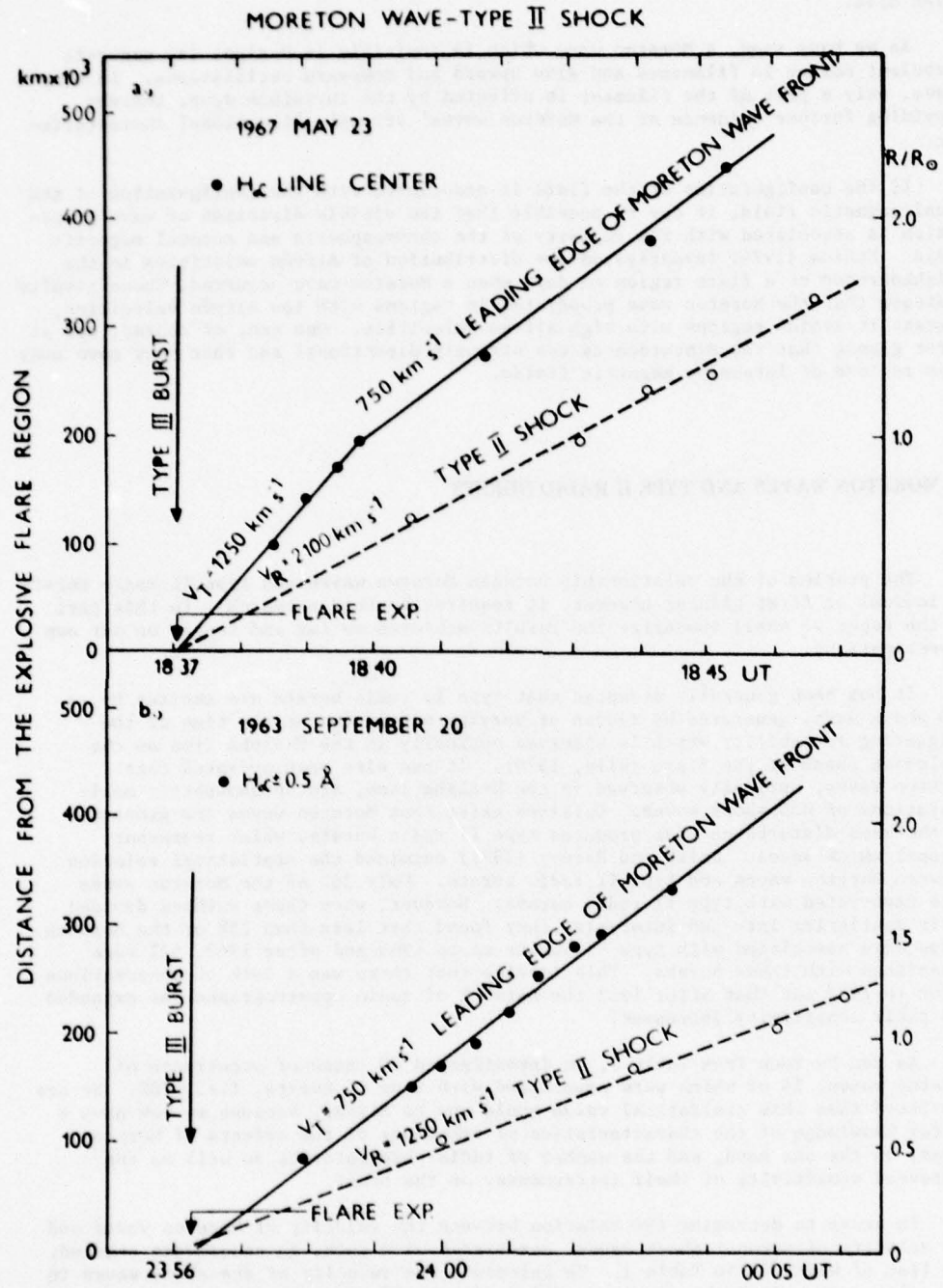


Figure 2. Velocities of Moreton waves and type II shocks associated with the major flares of May 23, 1967 and September 20, 1963.

solar disk.

As we have seen, a Moreton wave which is invisible in H-alpha may generate turbulent motion in filaments and also upward and downward oscillations. In many cases, only a part of the filament is affected by the invisible wave, thereby providing further evidence of the Moreton waves' strongly directional characteristic.

If the configuration of the flare is associated with the configuration of the local magnetic field, it may be possible that the visible direction of wave propagation is associated with the geometry of the chromospheric and coronal magnetic field. Uchida (1974) investigated the distribution of Alfvén velocities in the neighbourhood of a flare region on days when a Moreton wave occurred. These results indicate that the Moreton wave propagates in regions with low Alfvén velocities, whereas it avoids regions with high Alfvén velocities. One can, of course, see at first glance that the disturbances are strongly directional and that they move away from regions of intensive magnetic fields.

5. MORETON WAVES AND TYPE II RADIO BURSTS

The problem of the relationship between Moreton waves and type II radio bursts is logical at first glance; however, it requires further research. In this part of the paper we shall summarize the results achieved so far and report on our own investigations.

It has been generally accepted that type II radio bursts are excited by an MHD shock wave, generated by flares of varying magnitudes at the time of the triggering instability which is observed optically in the H-alpha line as the explosive phase of the flare (Wild, 1970). It has also been accepted that Moreton waves, optically observed in the H-alpha line, are chromospheric manifestations of MHD shock waves. Opinions exist that Moreton waves are generated by the same disturbance that produces type II radio bursts, which represent coronal shock waves. Smith and Harvey (1971) examined the statistical relation between Moreton waves and type II radio bursts. Only 36% of the Moreton waves were associated with type II radio bursts. However, when these authors divided their statistics into two intervals, they found that less than 25% of the Moreton waves were associated with type II bursts up to 1963 and after 1963, 52% were associated with these bursts. This implies that there was a lack of observations prior to 1963 and that after 1963 the network of radio spectrographs was expanded and their sensitivity increased.

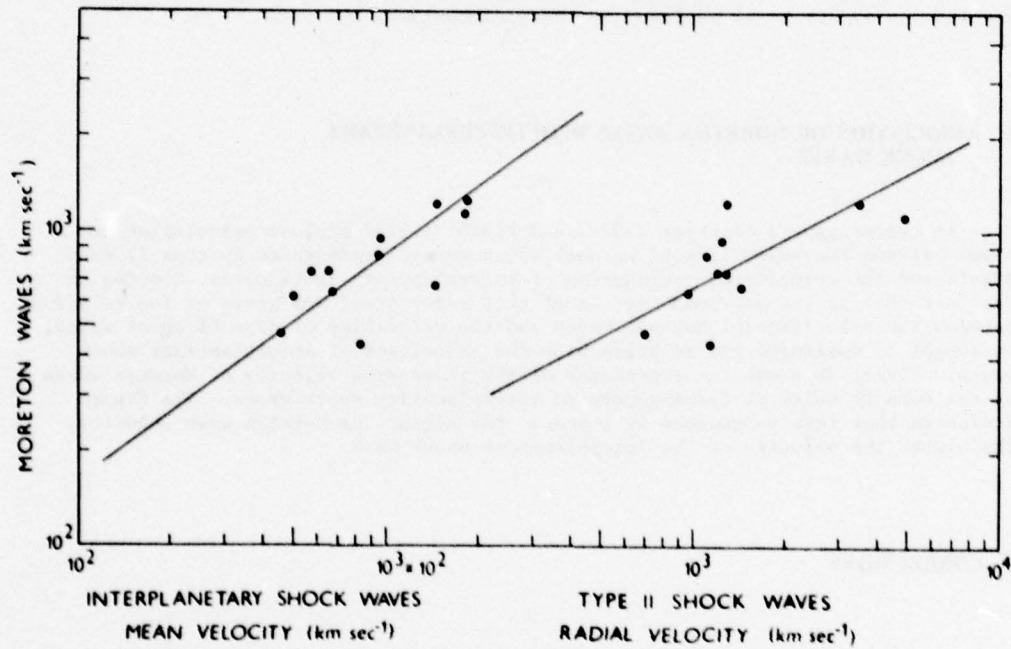
As can be seen from Table 1, we investigated 20 cases of occurrence of Moreton waves, 14 of which were associated with type II bursts, i.e., 70%. We are convinced that this statistical value would now be higher, because we now have a better knowledge of the characteristics of behaviour of the effects of Moreton waves, on the one hand, and the number of radio observatories as well as the increased sensitivity of their instruments, on the other.

In order to determine the relation between the velocity of Moreton waves and the velocity of coronal shock waves, associated with them, 13 cases were studied, the list of which is in Table 1. To calculate the velocity of the shock waves in the solar corona from the frequency drift of type II radio bursts, we used the 10 Baumbach-Allen density model of the corona. The calculated velocities of these coronal type II burst shock waves are also given in Table 1. The table indicates

that the velocity of the type II burst shock is between 700 and 5000 km/s. In all cases considered, the velocity determined exceeds the local escape velocity.

The comparison of the transverse velocities of Moreton waves with the radial velocities of the coronal shock waves, associated with the latter and as derived from type II radio bursts, implies a close relation between them. Figure 3 illustrates the dependence between the velocity of Moreton waves and the radial velocity, derived from type II bursts. Figure 3 shows that the higher the velocities of the Moreton waves, the higher the velocities of the coronal shock waves, represented by type II radio bursts. This relationship is indicative of a fundamental physical association between these two phenomena.

Apart from the statistical dependences mentioned above, there are several well documented examples which proved that a Moreton wave in the H-alpha line is a visible manifestation of a mobile source which also exists in the form of a type II radio burst. The most remarkable example of the relation of a Moreton wave to a type II radio burst occurred on 20 September 1963 (Smith and Harvey, 1971). The Moreton wave was observed at the Lockheed Observatory, USA, in H-alpha $\pm 0.5 \text{ \AA}$ and



the radio spectrogram is from the Fort Davis Observatory in Texas (Figure 4). Figure 4, which represents a mounted picture of optical and radio observations, shows that the visible front of the Moreton wave and of the type II radio shock wave are in exact time coincidence. Whereas the Moreton wave front travels across the surface of the chromosphere, the type II shock wave travels radially outwards. Assuming that both observations involve the same shock wave, one is able to obtain a two-dimensional idea of the source of propagation in a complicated magnetic field. In Fig. 2b one can see the time dependence of the propagation of the wave front. The figure indicates that the mean velocity is constant and amounts to 750 km/s. The explosive phase commenced at 23 56:15 UT \pm 15 seconds and at the same time a type II radio burst was recorded on the radio spectrogram, i.e., the occurrence of a type II burst represents the commencement of the explosive phase, at the time of which the shock wave is generated. Evidence of this is also provided in Fig. 2b, in which we can see that the beginning of the generation of the Moreton wave coincides with the explosive phase. The frequency drift of the type II burst also implies that the shock wave was generated at the time of the explosive phase of the flare, and it was even found that there is a certain agreement in height in generation with the Moreton wave. This example allows one to draw the conclusion that the type II shock wave and the Moreton wave not only have the same physical foundation, but also the same source of generation.

A similar characteristic of the relation of the Moreton wave to the type II radio burst was also observed with explosive proton flares which were observed on 23 May 1967 and 28 August 1966.

Further evidence in favour of the relation between the Moreton wave and the type II shock wave was provided by observations of the time and propagation velocity of the individual events, with which radio bursts were observed by means of 80 MHz Culgoora radioheliographs (Kai, 1969; Dulk, 1971). These observations enabled the events to be analysed in three dimensions.

6. ASSOCIATION OF MORETON WAVES WITH INTERPLANETARY SHOCK WAVES

In recent papers of Dryer (1974) and Pintér (1973) a close association was shown between the velocities of coronal shock waves, represented by type II radio bursts and the velocity of propagation of interplanetary shock waves. Drawing on the fact that in the previous Section of this paper proof was given of the relation between the velocities of Moreton waves and the velocities of type II shock waves, we sought to determine the relation with the velocities of interplanetary shock waves. Figure 3b shows the dependence of the transverse velocity of Moreton waves on the mean velocity of flare-generated interplanetary shock waves. The figure indicates that this dependence is linear: the higher the Moreton wave velocity, the higher the velocity of the interplanetary shock wave.

7. CONCLUSIONS

At the time of the explosive phase of a flare the generated shock wave of a suitable chromospheric and coronal magnetic configuration is capable of propagating across the solar disk (this is observed as a Moreton wave) as well as upward into

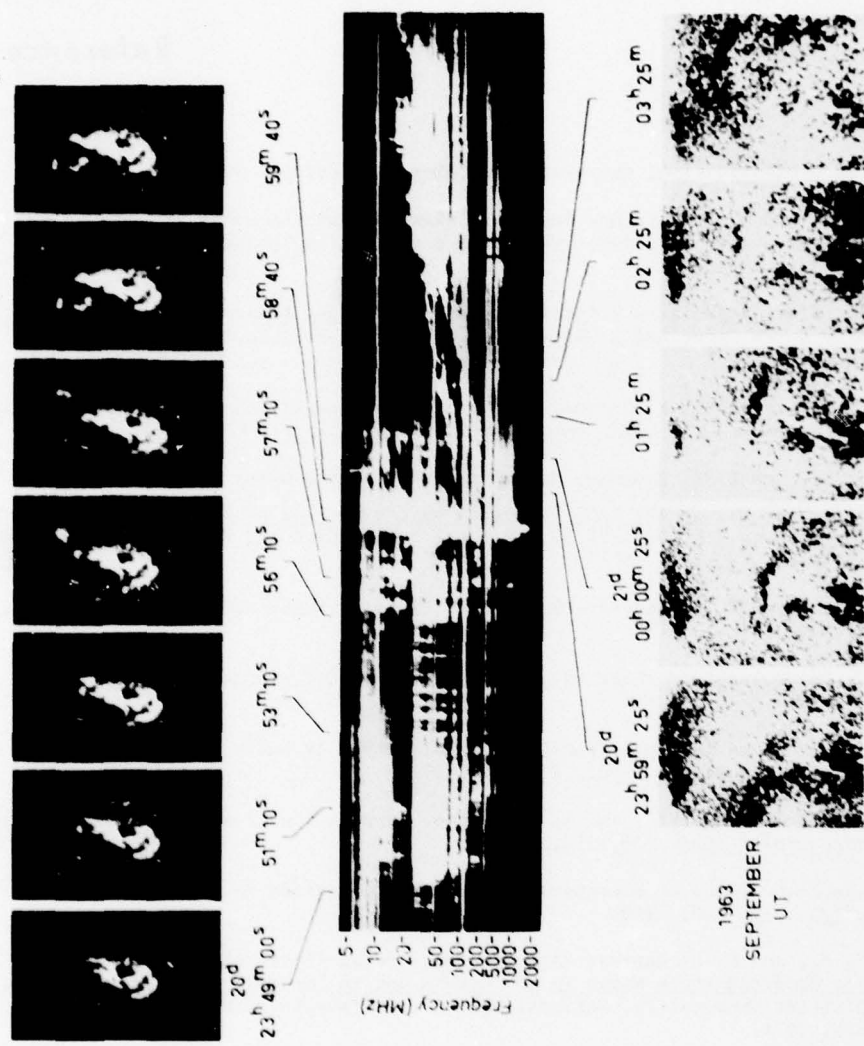


Figure 4. Optical and radio records of the flare on September 20-21, 1963 (after Moreton, 1965)

the corona where it excites type II radio bursts. In many cases the disturbance travels further through the corona into interplanetary space where, for example, it generates a discontinuity in the solar wind. The complex detailed study of the relation of Moreton waves to various solar and interplanetary phenomena will be published elsewhere.

References

- Anderson, G., Dissertation, University of Colorado, Boulder, 1966.
- Athay, R. G., and G. E. Moreton, Impulsive phenomena of the solar atmosphere. I. Some optical events associated with flares showing explosive phase, Astrophys. J., 133, 935, 1961.
- Bruzek, A., Flare associated optical phenomena, in Solar Flares and Space Research, edited by C. de Jager and Z. Švestka, p. 61, North-Holland Publishing Company, Amsterdam, 1969.
- De Mastus, H. L., and R. R. Stover, Visual and photographic observations of a white-light flare on May 23, 1967, Proc. Astron. Soc. Pac., 79, 615, 1967.
- Dodson, H. W., and E. R. Hedeman, Moving material accompanying the flare of 1959 July 16^d21^h14^m UT, in AAS-NASA Symposium on the Physics of Solar Flares, Edited by W. N. Hess, p. 15, NASA SP-50, National Aeronautics and Space Administration, Washington, D. C., 1964.
- Dodson, H. W., and E. R. Hedeman, The proton flare of August 28, 1966, Solar Phys., 4, 229, 1968.
- Dryer, M., Interplanetary shock waves generated by solar flares, Space Sci. Rev., 15, 403, 1974.
- Dulk, G. A., Motions and polarization of a solar type IV burst related to a magnetic arch, Aust. J. Phys., 24, 217, 1971.
- Harvey, K. L., S. F. Martin, and A. C. Riddle, Correlation of a flare wave and type II bursts, Solar Phys., 36, 151, 1974.
- Kai, K., Radio evidence of directive shock-wave propagation in the solar corona, Solar Phys., 10, 460, 1969.
- Martin, S. F., and K. L. Harvey, Rare observations of flare-related wave effects, in Flare-Produced Shock Waves in the Corona and in Interplanetary Space, p. 39, High Altitude Observatory, National Center for Atmospheric Research, Boulder, Colorado, 1974.
- Meyer, F., Flare produced coronal waves, in Structure and Development of Solar Active Regions, edited by K. O. Klepenheuer, p. 485, IAU Symp. 35, D. Reidel Publishing Co., Dordrecht, 1966.
- Moreton, G. E., H_α observations of flare-initiated disturbances with velocities ~ 1000 km/sec, Astron. J., 65, 494, 1960.

- Moreton, G. E., Fast-moving disturbances on the sun, Sky and Telescope, 21, 145, 1961.
- Moreton, G. E., Kinematics of solar flares, in Proc. of the Plasma Space Science Symposium, edited by C. C. Chang and S. S. Huang, p. 24, D. Reidel Publishing Company, Dordrecht, 1965.
- Pintér, S., Close connection between flare-generated coronal and interplanetary shock waves, Nature, 243p, 96, 1973.
- Smith, S. F., and K. L. Harvey, Observational effects of flare-associated waves, in Physics of the Solar Corona, edited by C. J. Macris, p. 156, D. Reidel Publishing Company, Dordrecht, 1971.
- Uchida, Y., On the excitors of Type II and Type III radio bursts, Publ. Astron. Soc. Japan, 12, 376, 1960.
- Uchida, Y., Propagation of hydromagnetic solar corona and Moreton's wave phenomenon, Solar Phys., 4, 30, 1968.
- Uchida, Y., A mechanism for the acceleration of solar chromospheric spicules, Publ. Astron. Soc. Japan, 21, 128, 1969.
- Uchida, Y., Diagnosis of coronal magnetic structure by flare associated hydromagnetic disturbances, Publ. Astron. Soc. Japan, 22, 341, 1970.
- Uchida, Y., Manifestation of flare-induced coronal MHD waves as Moreton waves and Type II bursts, in Flare-Produced Shock Waves in the Corona and in Interplanetary Space, p. 53, High Altitude Observatory, National Center for Atmospheric Research, Boulder, Colorado, 1974.
- Wild, J. P., Some investigations of the solar corona: The first two years of observation with the Culgoora radioheliograph, Proc. Astr. Soc. Australia, 1, 365, 1970.
- Zirin, H., and D. Russo Lackner, The solar flares of August 28 and 30, 1966, Solar Phys., 6, 86, 1969.
- Zirin, H., and S. Werner, Detailed analysis of flares, magnetic fields and activity in the sunspot group of Sept. 13-26, 1963, Solar Phys., 1, 66, 1967.

RECOMMENDED

about 500 second RTI pages in microfiche and over 100000 to 150000 full page
size RTI pages in microfiche and over 1000000 to 1500000 full page size
RTI pages in microfiche.

Estimated time required for RTI conversion of the entire collection would be
about 1000 hours at current rates of conversion.

Local Accelerations in the Corona During Type II - Type IV Emission; Observational and Theoretical Evidence

Yolande Leblanc and Monique Aubier
Observatoire de Meudon
92190 Meudon, France

Abstract

Radio observations with a high spectral and temporal resolution allowed us to show that local accelerations in the corona occurred in relationship with type II-type IV burst emission. These accelerations appeared as an emission of drifting structures superimposed on the continuum emission of the type IV burst.

All the observations gathered in the optical range lead us to conclude that we are dealing with a transient propagating through an arch magnetic configuration.

We have identified these drifting structures: in the high frequency range (25+ 45 MHz) beams of electrons of high energy propagating downwards in the arch magnetic field give rise to type III burst emission with a positive drift rate. Some of these beams, after reflection in a mirror region, have characteristics such as a cyclotron beam plasma instability emission occurring near this region. Narrow-band short lived bursts are then observed (60+70 MHz). We have derived from theoretical approaches the parameters of the beam and of the medium and we conclude that in the beam: the initial energy $U_0 \geq 0.46 c$ (or 63 kev); the velocity dispersion $V_b \approx 2V_e = 14000 \text{ Km s}^{-1}$; the density $N_b \approx 10^{-5} N_0$. In the medium the local magnetic field is

found to be equal to about 9 gauss between 1.5 and $2 R_{\odot}$ in the arch and to decrease very steeply between $2 R_{\odot}$ and $3 R_{\odot}$.

1. INTRODUCTION

In the range of 80-20 MHz, very few observations of type IV bursts are made with high resolution receivers, and this is due to the low sensitivity of the instruments used at these frequencies.

At Nançay Observatory, since 1970, receivers with high spectral and temporal resolutions are operating in the range of 25-70 MHz.

In this paper two type II - type IV events observed in this range are described. They appear with fine structures drifting positively (towards high frequencies) in the low frequency range and negatively (towards low frequencies) in the high frequency range (Figure 1).

An interpretation in terms of local acceleration at the top of an arch is given to explain the formation of high energy beams of electrons which give rise to type III-like bursts propagating downwards in the corona (positively drifting structures or p.d.s.) and after reflection in a mirror region, they give rise to an emission (negatively drifting structures or n.d.s.) which can be described by a cyclotron beam plasma instability.

2. THE OBSERVATIONS

2.1 The Equipment

The observations are made with two swept-frequency spectrographs covering the range 24.4 MHz to 38.8 MHz and 38.8 MHz to 70 MHz, with a bandwidth resolution of 20 KHz and 200 KHz respectively. In addition four fixed frequency receivers are operating at 30, 38, 60 and 76 MHz. The time resolution is about 0.1 s.

2.2 Observational Data

2.2.1 THE 29 JULY 1973 EVENT

Between 13.00 and 13.24 UT a large 3 N two ribbon flare was recorded at Tel-Aviv and Big Bear Observatories at the heliocentric coordinates N13, E45 (McMath region 12461), and a coronal transient was observed by the Skylab coronograph (MacQueen et al., 1974).

The radio-emission is characterized by a type II burst starting at 13.23 UT; the fundamental and the harmonic emission were observed in our frequency range. The

type IV burst appeared at 13.26 UT and three minutes later are observed p.d.s. in the low-frequency range and n.d.s. in the high-frequency range. These later structures are much less numerous than the others.

2.2.2 THE 7 SEPTEMBER 1973 EVENT

Many flares of importance 2N and 3N were recorded between 11.30 and 14.00 UT. Their heliocentric coordinates were S18 W45 (McMath region 12507). A coronal transient was observed by the Skylab coronograph when observations began at 13.06 UT (MacQueen et al., 1974). This mass ejection was associated with a large interplanetary shock wave disturbance observed at 1 A.U. (Gosling et al., 1975).

In our records a first type IV burst started at 11.54 UT and covered the whole range of the receivers (25 - 70 MHz). At 12.00 UT a type II burst with fundamental and harmonic emissions was observed. We notice that only the harmonic emission appears with fast variations of intensity with time as in the other event. This time variability of type II burst had already been studied (Leblanc and Lecacheux, 1976).

At 12.07 UT the type II burst was followed by a continuum emission of a type IV burst on which are superimposed drifting structures as those observed in the first event.

An analysis of the data allows us to conclude that:

- We are dealing with an arch configuration, probably transequatorial, since the two events are associated with active centers in the equatorial region, and loop-shaped transients were observed by the coronograph.
- The positively drifting structures recalls type III emission. Their frequency drift varies from 2 to 4 MHz/s.
- The negatively drifting structures are observed in the frequency range 60-70 MHz. Their bandwidth and mean frequency remain constant for the whole duration of the emission. The frequency-drift of the structures is nearly constant and equal to 1 or 2 MHz/s. The duration of each individual structure is about 4 to 5 seconds.

A correlation in time between these two sets of structures exist probably if we compare the relative intensity of some structures. We think that the end of a p.d.s. is associated in time with the beginning of a n.d.s. and it appears that many p.d.s. are not followed by n.d.s. We shall show that this representation may be explained theoretically.

3. THEORETICAL INTERPRETATION

Kopp and Pneuman (1976) explain in a theoretical model how the rising loop prominence systems seen after coronal transients are the result of magnetic field reconnection in the corona: the transient event tears open the closed field lines and a solar wind expansion is set up which extends well out in the corona. This explains the high speed streams observed at 1 A.U. Just before reconnection of the magnetic field, the upward mass flow is very enhanced and this material will be captured in the closed loops and compressed downwards in the corona.

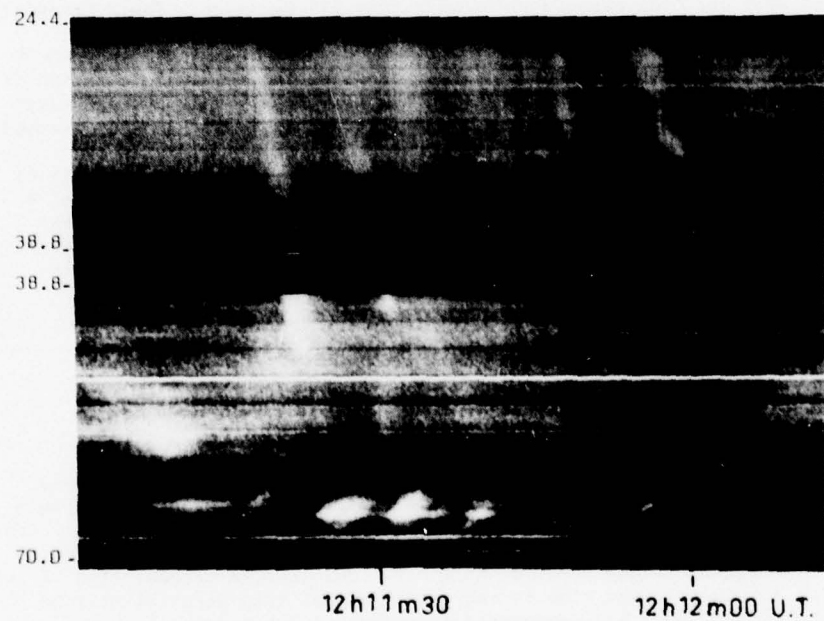
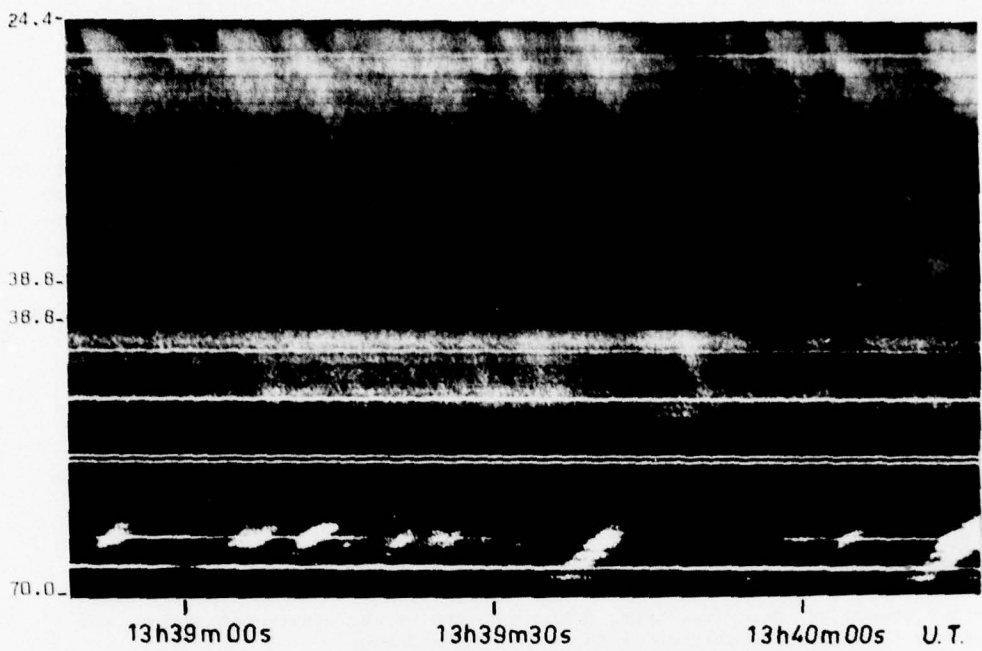


Figure 1. A part of the two events recorded in the decameter range at Nançay.
Top panel: 29 July 1973. Bottom panel: 7 September 1973.

Then it is probable that local accelerations at the top of the loop are set up since the magnetic field changes drastically in the region located near the neutral point while the reconnection goes up.

The accelerated beams of electrons propagate downward and excite at each level a plasma emission which gives rise to a type III burst drifting positively. As the magnetic field B is increasing the parallel velocity component ($v_{||}$) decreases and the perpendicular one (v_{\perp}) increases. When $v_{||}$ is such as there is no more positive slope in the velocity dispersion function, then the plasma type III emission disappears.

The electrons still go down in the corona with $v_{||}$ decreasing as B increases until they are reflected in a mirror region. Then they will propagate upwards (Figure 2).

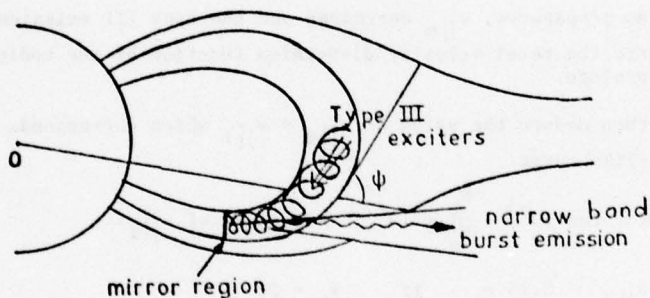


Figure 2. The physical representation of the type III excitors and of the narrow burst emission in an arch magnetic field configuration.

Therefore the beam just after reflection is such as $v_{\perp} \gg v_{||}$. We shall show that the conditions in the medium as well as in the beam are such that a cyclotron beam plasma instability, according to the Mangeney and Veltri theory (1976a, b) can occur. This emission gives rise to short lived narrow-band bursts, the characteristics of which are in agreement with the "negatively drifting structures".

3.1 Type III Emission

We define the medium by a model of density $N_o(r) = 10 \times 3.6 \cdot 10^{4+4/r}$ (Leblanc et al., 1973) and the thermal velocity v_e .

The beam is defined by an electron density N_b , an initial average energy U_o which is supposed to be constant along the propagation, and a non-zero average pitch-angle. We call $F_o(v_{||})$ and $F_b(v_{||})$ the velocity distribution function of the medium and of the beam along the direction of propagation. $v_{||m}$ is the average value of $v_{||}$ at a given altitude and v_b the velocity dispersion of the beam.

$$F_o(v_{||}) = \frac{N_o(r)}{(2\pi v_e^2)^{1/2}} \exp \left(-\frac{v_{||}^2}{2v_e^2} \right) \quad (1)$$

$$F_b(v_{||}) = \frac{N_b}{(2\pi v_b^2)^{1/2}} \exp \left(-\frac{[v_{||} - v_{||m}]^2}{2v_b^2} \right) \quad (2)$$

While the beam propagates, $v_{||m}$ decreases and the type III emission disappears near the point where the total velocity dispersion function of the medium $F_t(v_{||})$ has no more positive slope.

We can then deduce the value of $v_{||m} = v_{||f}$ which corresponds to the end of the type III-like burst.

We obtain, for $10^{-3} < \frac{N_b}{N_o} < 10^{-7}$, two ranges of $v_{||f}$:

$$0.12 < v_{||f} < 0.15 \text{ c} \quad \text{if} \quad v_b = 2v_e$$

$$0.20 < v_{||f} < 0.23 \text{ c} \quad \text{if} \quad v_b = 6v_e.$$

We test these values from another approach. We write the relationship between the variation of the magnetic field in the arch and the observed frequency drift:

$$\frac{B(r)}{B_m} = 1 - \left(\frac{0.12 \times r^2}{U_o \times 10^{2/r} \times \cos \Psi} \right)^2 \quad (\text{Figure 3}). \quad (3)$$

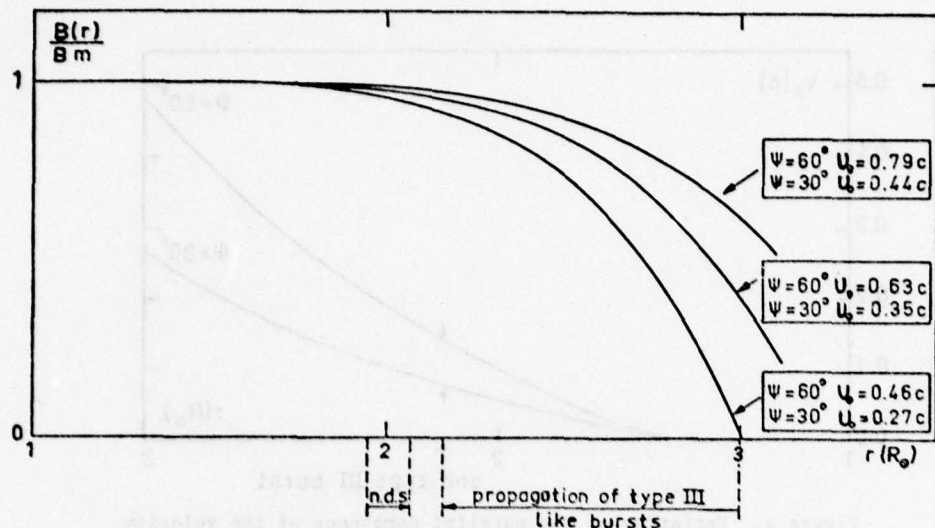


Figure 3. Variation of the magnetic field $B(r)/B_m$ along the arch. Three curves are computed for two sets of values of Ψ and U_o . The regions where the n.d.s. and the p.d.s. are observed are indicated.

B_m is the magnetic field in the mirror region and Ψ the angle between the magnetic field and the radial. This relation gives us the lower limit to the velocity U_o since the term in brackets must be less or equal to 1 at the altitude where the emission occurs.

$$\text{We find } U_o \geq 0.27 \text{ c} \quad (\Psi = 30^\circ)$$

$$U_o \geq 0.46 \text{ c} \quad (\Psi = 60^\circ).$$

Now the variation of the parallel component of the velocity $v_{||}(r)$ in the region where the type III emission occurs is:

$$v_{||}(r) = U_o \sqrt{1 - \frac{B(r)}{B_m}} \quad (\text{Figure 4}) \quad (4)$$

$$v_{||}(r) = \frac{0.12 r^2}{10^2/r \cos \Psi}, \quad (5)$$

relation independent of U_o ($v_{||}(r)$ is expressed in units of c, and r in solar radii).

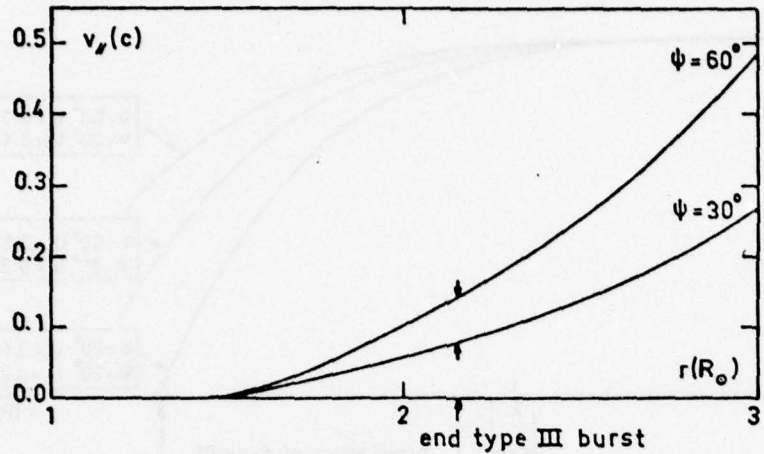


Figure 4. Variation of the parallel component of the velocity $v_{||}(r)$ along the arch. The two curves are computed for two values of Ψ . The end of type III emission is indicated by an arrow.

We then compute $v_{||f}$ at the altitude (r) where the type III emission stops. We compare this value with that computed previously. We find that the agreement is good for large values of Ψ ($\Psi \sim 60^\circ$), small beam dispersion velocity ($v_b \sim 2v_e$) and low density beam $\frac{N_b}{N_0} \sim 10^{-5}$ (although this parameter is not too severe).

To sum up this part we find that the accelerated electrons have energies higher or equal to $0.46c$ (63 kev), that the parallel component of the velocity is of the order of $0.14c$ when the type-III emission disappears (at an altitude of $\sim 2.15 R_\odot$ for a given model of density).

3.2 Narrow-Band Burst Emission

- After reflection in the mirror region, the characteristics of the beam are:
- the perpendicular component of the velocity is much larger than the parallel one ($v_{\perp} \gg v_{||}$).
 - the average pitch angle θ is non zero at the altitude $r > 1.5 R_\odot$.
 - the average energy of the beam is higher than 63 kev.
 - the beam density ratio (N_b/N_0) is small ($< 10^{-5}$) since after propagation and reflection it becomes less and less dense.
 - the relative dispersion of the beam velocity is small.

In the medium the magnetic field in the arch is probably very high since a type IV emission implies a synchrotron mechanism, and magnetohydrodynamic

fluctuations are present since the studied coronal region lies above sunspots.

Mangeney and Veltri (1976a, b) show that if all these conditions are fulfilled, a beam plasma instability occurs and a burst of electromagnetic radiation is emitted at a frequency slightly higher than the local plasma frequency and close to v times the electron gyrofrequency (in our frequency range $v = 2$). Then the particles escape from the emission region with almost no perpendicular momentum. The characteristics of the emission are in agreement with the observed short lived, narrow band bursts (n.d.s.).

By using this theory, we may derive:

- the altitude of this emission: $1.95 R_\odot < r < 2.07 R_\odot$
- the velocity dispersion of the reflected beam: $V_{br} = 8.400 \text{ Km s}^{-1}$
- the turbulent fluctuations within the source: $\frac{\delta B}{B} \sim 3\%$
- the local magnetic field in the arch: $B \sim 9 \text{ gauss}$ between $1.5 R_\odot$ and $2 R_\odot$ and $3 R_\odot$. Moreover we explain why we don't observe type III bursts after the narrow-band short lived bursts as the beam goes upward. Indeed after this burst emission the particles will escape from the emission region with almost no perpendicular momentum so that the parallel component of the velocity cannot reach a value high enough to give rise to type III burst emission in our frequency range.

Acknowledgments

The authors wish to express their thanks to Drs. Robert Smith, André Mangeney and André Boisshot for many fruitful discussions and comments on this work.

References

- Gosling, J. T., E. Hildner, R. M. MacQueen, R. H. Munro, A. I. Poland, and C. L. Ross, Direct observations of a flare related coronal and solar wind disturbance, Solar Phys., 40, 439, 1975.
- Kopp, R. A., and G. W. Pneuman, Magnetic reconnection in the corona and the loop prominence phenomenon, Solar Phys., 50, 85, 1976.
- Leblanc, Y., J. L. Leroy, and P. Pecantet, Quiet corona density model for the last maximum of solar activity, Solar Phys., 31, 343, 1973.
- Leblanc, Y., and A. Lecacheux, Time variability of Type II solar bursts and 1+ ν conversion processes, Astron. Astrophys., 46, 257, 1976.
- MacQueen, R. M., Private communication, 1974.
- Mangeney, A., and P. Veltri, On the theory of Type I solar radio bursts, I. Beam plasma instabilities in a turbulent magnetized plasma, Astron. Astrophys., 47, 165, 1976a.

Mangeney, A., and P. Veltri, On the theory of Type I solar radio bursts, II. A model for the source, Astron. Astrophys., 47, 181, 1976b.

ability of small冕冕型耀斑等的简单推论。在这些事件中，我们发现，当它们的亮度增加时，它们的射电辐射强度也增加，而且，当它们的亮度开始下降时，它们的射电辐射强度也下降。

最近，我们利用了“1955—1969年太阳粒子事件目录”(Dodson et al., 1975)中的数据，对上述结论进行了检验。结果表明，对于所有的冕冕型耀斑，其射电辐射强度与亮度变化是相关的，即，当亮度增加时，射电辐射强度也增加，而当亮度开始下降时，射电辐射强度也下降。

虽然，上述结论只适用于冕冕型耀斑，但，它还是可以应用于其他类型的耀斑。因此，我们希望，通过研究不同类型的耀斑，我们可以得到更广泛的应用。同时，我们还希望，通过研究不同类型的耀斑，我们可以得到更广泛的应用。同时，我们还希望，通过研究不同类型的耀斑，我们可以得到更广泛的应用。

Timing of Beginnings of Type II Radio Bursts by Energetic Particle Flares

L. Křížský
Astronomical Institute
Czechoslovak Academy of Sciences
251 65 Ondřejov, Czechoslovakia

Abstract

In this paper we have studied the problem of the onset of the shock-wave radio emission in the development of a solar energetic particle flare. It is evident that the shock wave is generated with most flares in the so-called explosive phase of the flare, between the time of its brightening and the time of the H α maximum, or close to it.

The recently published "Catalog of Solar Particle Events 1955–1969" (Dodson et al., 1975), based on extensive observational data and measurements of flare emissions at terrestrial observatories, on interplanetary probes and satellites, is a source of data for further investigation of these phenomena and of the relations between some of the parameters. The Catalog enabled us to answer the

question as to the phase of development of the high-energy particle flare in which identification of the type II radio emission is made, which reflects the generation and passage of a shock wave from the flare via the corona into outer space (Kai, 1969; Harvey et al., 1974; Dodge, 1975; Křivský and Pintér, 1975b).

Earlier Švestka and Fritzová (1974) have studied the time connection between the onset of type II bursts and the occurrence of the microwave burst maxima: on an average, the onset of the metric type II was delayed by 2 min relative to the microwave burst maxima; in all cases the type II followed the onset of microwave bursts.

Type II radio emission can be determined from spectrograms, constructed from the records of individual frequencies in the metre and dekametre ranges by radio meters, or much more reliably by means of radio spectrographs (where the axes are time and frequency). The Catalog in question gives the commencements of type II emissions; this emission may be generated by a shock wave at various altitudes of the solar corona above the flare (and, therefore, may be manifest at different frequencies with a view to the different plasma concentration values) and also recording it at terrestrial stations must depend on complicated and variable (and not fully known) conditions of the index of refraction and propagation of radio waves (McLean, 1974). Whether the emission will be received on Earth should be determined by the distance of the flare from the solar disk centre. (A radio emission from a shock wave, generated by flares near the solar disk limb, should not be recorded on Earth at all, however, this is not always true.) The shock wave will probably be generated earlier than would correspond to the individual date of radio observations; the radio emission will in fact be recorded at a time when the shock wave is at a certain altitude from which the radiation is able to penetrate the corona towards the Earth. Determining the time of onset of the type II emission may also be affected on spectrograms by being obscured by another type of emission, e.g., type IV (plasma cloud emission), or even by different record sensitivities. At least these main items should be pointed out for us to realize that the actual generation of the shock wave may in fact take place earlier than the beginnings of type II radio emissions, adopted from observations at the observatories given in the Catalog.

In order to treat this problem, which may be investigated statistically, it is necessary to select a physically significant phenomenon in the development of the flare, which can be determined with sufficient accuracy and which can be evaluated sufficiently reliably from observations or a film record. As a result of extensive practical experience we may say that this is not the beginning of the flare (there is a larger inaccuracy in determining the time here), much less the end of the flare, but only the maximum of the flare brightness, determined according to the photographs of the flare in the H α hydrogen line. The time of the maximum of the flare brightness is usually nearly identical with the maximum width of the H α line, which is sometimes also measured in determining the development of the flare. The data on the maximum of the flare brightness, given in the Catalog, may display a minor inaccuracy in time, ± 2 min. As regards this maximum of flare brightness it should be added that this is a culmination of the emission processes from the point of view of physical processes mostly of a secondary nature, when the flare plasma has already been extensively thermalized and when the so-called impulsive phase of the flare has already reached its peak, i.e., when the intensity of the short burst of the hard X-emission and of the radio emission in the GHz range is already decreasing; this also reflects the triggering and impulsive phases of the main acceleration of the particles of energies of $10^6 - 10^{11}$ eV (Křivský and Pintér, 1975a).

These uncertainties in the type II radio emission data and the flare brightness maxima had to be pointed out, in order to allow us to evaluate critically the statistical result of the relation being investigated.

The Catalog contains 380 cases (100%) of all identified flares with ejections of very fast particles. Of these 162 (43%) flares were accompanied by type II emissions; with some other flares, emissions of this type were also probably in evidence, however, they could not be determined for various reasons. For the statistics 143 cases (38%) were used for which the data on the type II commencements and H_a brightness maxima were relatively reliable. If several cases of repeating type II emissions with a single flare were identified, the commencement of the first occurrence and the main first flare brightness maximum were considered. If several separate bursts in H_a and, therefore, also brightness maxima (as well as several type II emissions) were observed with a flare, which was quite exceptional, the separate cases were considered to represent individual cases in the statistical treatment.

The data were processed as follows: at minute intervals prior to and after the occurrence of the flare brightness maximum in H_a the numbers of type II onsets were recorded. Figure 1 shows the histogram with 3-minute intervals, which eliminates the excessive 1-minute interval fluctuations. The histogram indicates that the natural scatter is within the range of plus-minus 19 minutes relative to the occurrence of the flare maximum; there are 6 values not given on the histogram which are removed by more than 22 minus minutes, and 2 removed by more than 22 plus minutes. The mean value is -3 min, the median -2 min, and the modulus ~ 0 min.

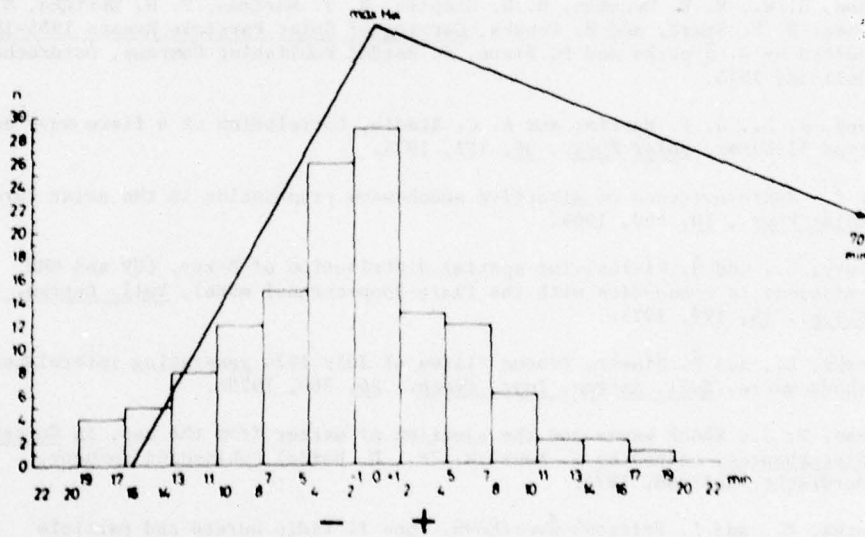


Figure 1. The occurrence of the beginning of the type II radio bursts before (-) and after (+) maxima of energetic particle flares in H_a. Maxima in H_a $t = 0$ min. This histogram was treated for three-minute intervals. Number of cases before $t = 0$ was 87, after $t = 0$ was 56; mean value -3 min, median -2 min, modulus ~ 0 min. Typical development of flares of this kind is given in the curve: mean duration from beginning to maximum 16.7 min from maximum to end 70.0 min; number of cases 246.

This result should be considered as a first attempt of this kind to solve the problem statistically. It is clear and indubitable that the generation of a shock wave within a high-energy particle flare from the point of view of their duration and development is not distributed randomly over the whole duration of the flare, lasting from several tens of minutes to several hours. Using the same Catalog, the average duration of the phase from flare commencement to maximum and from maximum to the end was determined to characterize the average development of high-energy particle flares. The curve, constructed from 246 cases (using only reliable time data) is also shown in Figure 1. It is indubitable that the concentration of the main occurrence of type II emissions is associated with the flare brightness maximum with a slight tendency to precede this maximum (the number of type II occurrences prior to the flare brightness maximum is 87, after the maximum 56). If one considers that, for reasons given in the discussion of type II emission at the beginning, the actual generation of the shock wave will precede the time of the first recording of the type II radio emission for several reasons, it is evident that the shock wave is generated with most flares in the so-called explosive phase of the flare, between the time of its brightening and the time of the H α maximum, or close to it.

References

- Dodge, J. C., Source regions for type II radio bursts, Solar Phys., 42, 445, 1975.
- Dodson, H. W., E. R. Hedeman, R. W. Kreplin, M. J. Martres, V. N. Obrikko, M. A. Shea, D. F. Smart, and H. Tanaka, Catalog of Solar Particle Events 1955-1969, edited by Z. Švestka and P. Simon, D. Reidel Publishing Company, Dordrecht, Holland, 1975.
- Harvey, K. L., S. F. Martin, and A. C. Riddle, Correlation of a flare-wave and type II burst, Solar Phys., 36, 151, 1974.
- Kai, K., Radio evidence of directive shock-wave propagation in the solar corona, Solar Phys., 10, 460, 1969.
- Křížský, L., and Š. Pintér, The spatial distribution of X-ray, EUV and GHz emissions in connection with the flare-loop-channel model, Bull. Astron. Inst. Czech., 26, 199, 1975a.
- Křížský, L., and Š. Pintér, Proton flares of July 1974 generating interplanetary shock waves, Bull. Astron. Inst. Czech., 26, 360, 1975b.
- McLean, D. J., Shock waves and the ejection of matter from the sun, in Coronal Disturbances, edited by G. Newkirk, Jr., D. Reidel Publishing Company, Dordrecht, Holland, 1974.
- Švestka, Z., and L. Fritzová-Švestková, Type II radio bursts and particle acceleration, Solar Phys., 36, 417, 1974.

Faraday Rotation Transients Observed During Solar Occultation of the Helios Spacecraft

**M. K. Bird and H. Volland
Radioastronomisches Institut
Universität Bonn
5300 Bonn, FRG**

**C. T. Stelzried, G. S. Levy, and B. L. Seidel
Jet Propulsion Laboratory
Pasadena, CA 91103, USA**

Abstract

The plane of polarization of the S-band carrier signal of the Helios spacecraft is rotated along its downlink ray path according to the Faraday effect. Measurable Faraday rotation from the solar corona is observed at times of superior conjunction at solar offsets between 2-15 solar radii. The effects of the quiescent corona on the time profile of the measured Faraday rotation are limited to variations on a large time scale ($\tau = \text{days}$) due to the slowly changing solar offset and/or the rotation of the coronal structure. On a number of occasions, however, the recorded signature was interrupted by characteristic excursions from the presumed baseline in a manner similar to the Faraday rotation transients first seen with Pioneer 6 in 1968. The events observed during the Helios missions occurred much less frequently than during the solar maximum experiment on Pioneer 6, and cannot always be directly correlated with H α flares. Particularly interesting activity was seen on day number 200 (18 July, 1976) when two large events were registered at the Effelsberg ground station during the outbound occultation of Helios-2 on the solar west limb.

1. INTRODUCTION

The heliocentric orbits of the spacecraft Helios-1 and Helios-2 are ideally suited for radio science investigations during solar occultation. The 6 month period and zero inclination of the Helios orbit results in at least one short-duration interval annually, in which the Helios/Earth ray path is physically occulted by the photosphere. Additional long-duration occultations occurred on both satellites approximately 4 months after launch. The Faraday rotation of the linearly polarized S-band carrier signal of the spacecraft was monitored at receiving stations in Effelsberg, Germany and Goldstone, California in 1975 and 1976 during these occultations. A measurable effect from the quiescent solar corona becomes noticeable for solar offsets (the closest approach of ray path to the Sun) less than about $10 R_\odot$. The large-scale time variation of the Faraday rotation, which can be used under certain assumptions to infer radial and longitudinal structure in the corona, has been discussed by Volland et al. (1977).

Short-time scale variations in the Faraday rotation, which cannot be attributed to either rigid rotation of the coronal material or motion of the Helios ray path, have also been observed during the Helios mission. On at least one occasion, the magnitude, duration and signature of the Faraday profile were astoundingly similar to those of the events seen by Levy et al. (1969) with Pioneer 6. A description of this Helios Faraday rotation transient together with some other remarkable events are presented in this report. As with the transients observed on Pioneer 6 (Schatten, 1970; Pintér, 1973), outstanding occurrences of radio emission and observed H α flares are examined for their possible roles in causing such Faraday events. In particular, it is demonstrated that the nature and occurrence frequency of the Faraday rotation transients are exactly those expected from the passage of a coronal mass ejection cloud through the line-of-sight. There has been a dramatic improvement in the statistical data base for mass ejection events after the synoptic white light coronograph observations on board Skylab. Many results of investigations describing the phenomenology and general characteristics of the mass ejection event are now available (e.g. Gosling et al., 1974; Hildner et al., 1975a; Hildner et al., 1975b; Gosling et al., 1975; Hildner et al., 1976; Gosling et al., 1976; Poland and Munro, 1976; and Dulk et al., 1976).

2. HELIOS FARADAY ROTATION TRANSIENTS

The measured signal Faraday rotation on day 241 (29 AUG 1975) during the second solar occultation of Helios-1 is presented in Fig. 1. The solar offset is given at the top of the figure. The dashed line at zero degrees is the nominal baseline of the Helios signal for large solar offsets (no coronal contribution). The times of significant single frequency radio bursts are designated with coded letters. The key to the code with information on each burst event for the Figures 1-4 is given in Table 1.

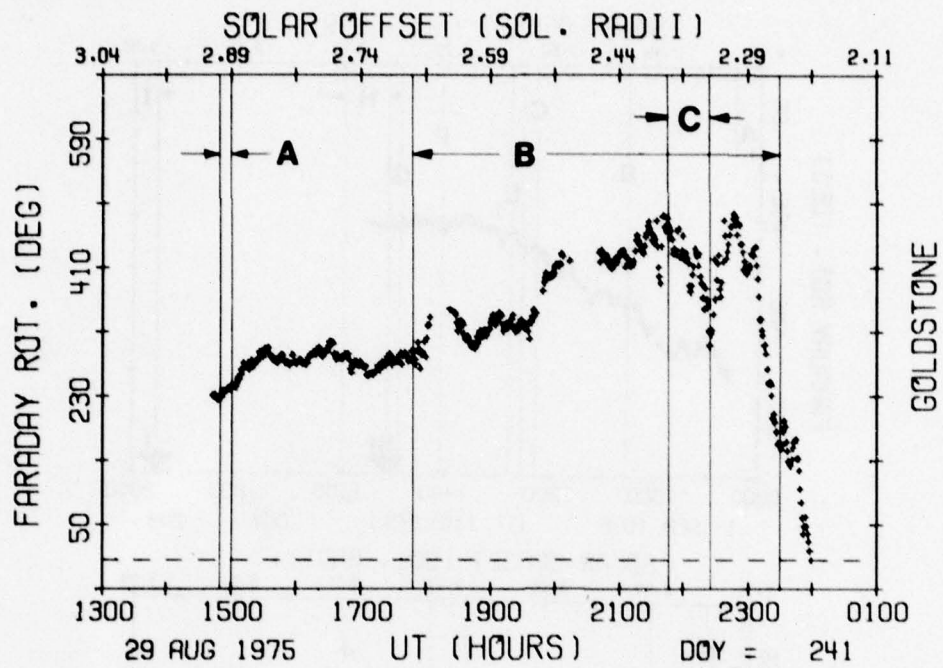


Figure 1. Helios-1 Signal Faraday Rotation at Goldstone on 29 AUG 1975 (Day of Year: 241; Solar Limb: West). The vertical lines with coded letters denote the times of solar radio bursts reported in Solar-Geophys. Data. See Table 1 for listing.

Aside from a few minor disturbances, the measured Faraday rotation increased monotonically to higher positive values in accordance with the ray path's decreasing distance to the Sun. The profile becomes abruptly erratic at about 2140 UT, moving down about 200° , returning briefly to the baseline, and then plunging down again to "zero" over about one hour's time. The tracking pass at Goldstone unfortunately ended at 2400 UT during this unusual event.

Only two small H α flares were reported in Solar-Geophys. Data on 29 AUG 1975, both occurring much too early to be correlated with the Faraday transient. A solar noise storm was in progress most of the day. Since the majority of reported white light transients are not flare induced, but more likely the coronal reaction to an eruptive prominence (Gosling et al., 1974; Hildner et al., 1975b), a search should be made for the fate of prominences near the west limb late on 1975 day 241. Solar filaments were observed above McMath active region 13808, which was located about 10° beyond the west limb at the time of the event. A limb prominence associated with this region is noted on the NOAA Boulder H α patrol map for 29 AUG 1975 (Solar-Geophys. Data, OCT 1975), but is missing on the following day.

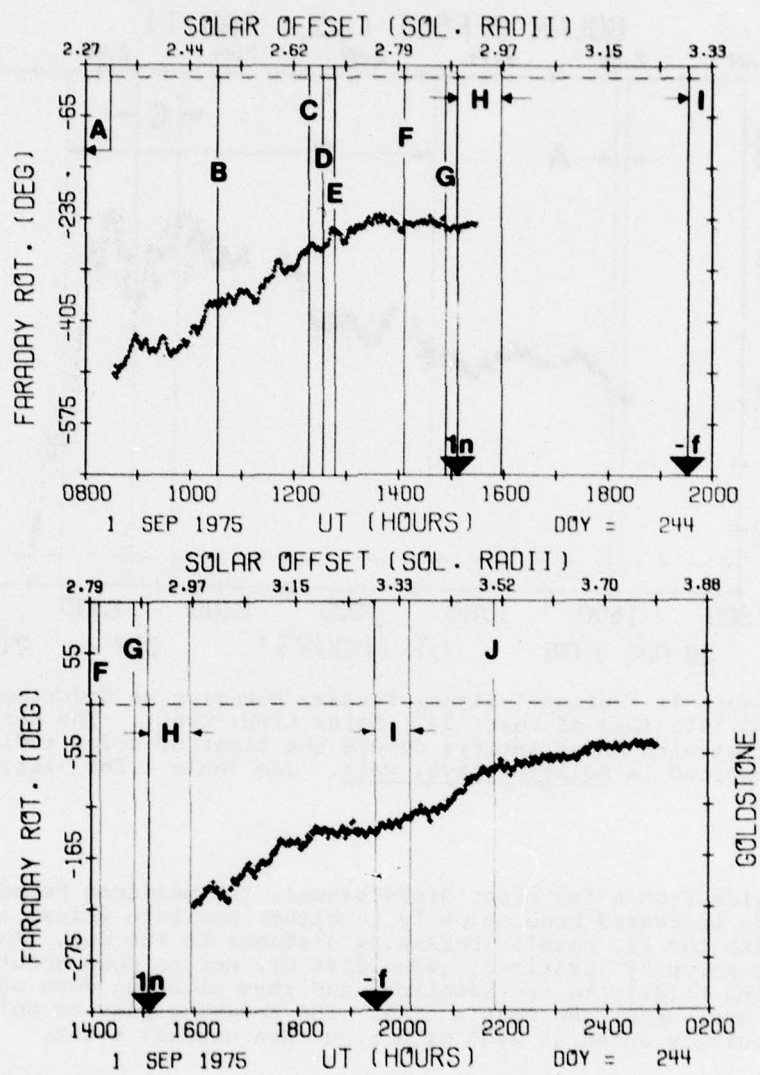


Figure 2. Helios-1 Signal Faraday Rotation at Effelsberg (top) and at Goldstone (bottom) on 1 SEP 1975 (DOY: 244; Limb: East)

Fig. 2 shows the east limb continuation of the experiment on 1 SEP 1975 upon recovery of Helios-1 after the blackout imposed by the occultation. Considerable structure is seen at small solar offsets, but no fluctuations are pronounced enough to be justly proclaimed "coronal transients". The main reason for showing the passes for this day is to display the reaction of the Faraday rotation, or more accurately, its lack of reaction to the largest flare reported during the occultations of both Helios spacecraft. A flare of importance in loca-

ted at N03, E53 was seen at 1507 UT. Assuming radial propagation of the disturbance from this flare, the traversal of the Helios/Earth line-of-sight would occur as early as 1530 UT (for a propagation velocity $\approx 1000 \text{ km s}^{-1}$) with a most probable time-of-arrival around 1550 UT using the mean velocity of flare-initiated transients from Gosling et al. (1976) of 775 km s^{-1} . Although an unfortunate data gap exists from 1530-1600 UT, it is apparent from the remaining Faraday profile that this flare exerted very little if any influence on the medium probed by the Helios ray path. Either not every flare is capable of producing a coronal transient, or (more likely) the propagation direction was removed far enough from the radial, that the disturbance effectively missed the Helios/Earth ray path.

An unusual wiggle in the recorded Faraday trace with peak-to-peak amplitude of 20° and duration of 6 hours is shown in Fig. 3. This plot is for the Effelsberg pass of 22 MAY 1976 when the apparent position of Helios-2 was $5 R_\odot$ from the solar east limb. Some radio burst activity occurred concurrently with the disturbance in the Faraday profile. Furthermore, a -f flare located at S07,E30 was observed at 0455 UT with the remark "probably the end of a more important flare". Again assuming radial propagation from this flare, the Faraday anomaly beginning at 0800 UT could have arisen from such a flare induced disturbance if the propagation speed were about 500 km s^{-1} , a not unrealistic value (see Gosling et al., 1976).

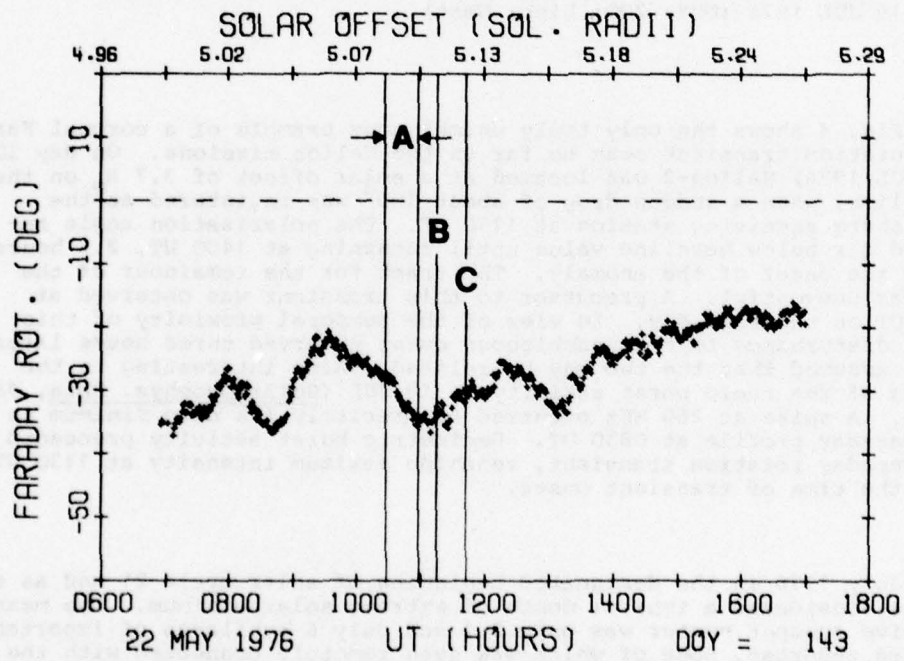


Figure 3. Helios-2 Signal Faraday Rotation at Effelsberg on 22 MAY 1976 (DOY: 143; Limb: East)

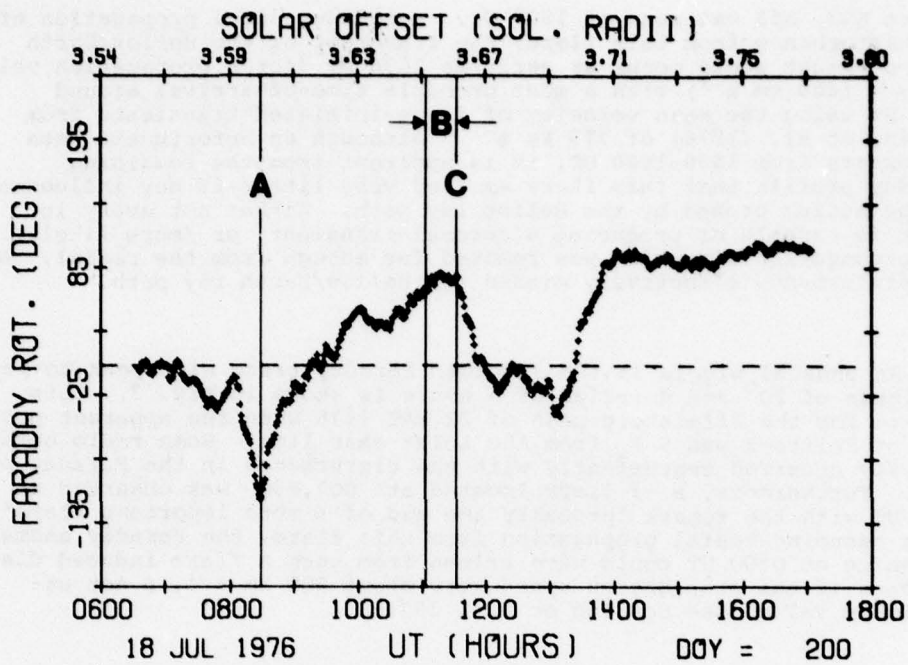


Figure 4. Helios-2 Signal Faraday Rotation at Effelsberg on 18 JUL 1976 (DOY: 200; Limb: West)

Fig. 4 shows the only truly unambiguous example of a coronal Faraday rotation transient seen so far on the Helios missions. On day 200 (18 JUL 1976) Helios-2 was located at a solar offset of $3.7 R_{\odot}$ on the west limb, when a sudden drop of about 100° was registered at the Effelsberg receiving station at 1130 UT. The polarization angle remained far below baseline value until returning at 1400 UT, 2.5 hours after the onset of the anomaly. The track for the remainder of the day was uneventful. A precursor to this transient was observed at 0800 UT on the same day. In view of the temporal proximity of this first disturbance to the unambiguous event observed three hours later, it is assumed that the two may be related. Also interesting is the timing of the radio burst activity on 18 JUL (Solar-Geophys. Data, JAN 1977). A spike at 260 MHz occurred at precisely the deep minimum in the Faraday profile at 0830 UT. Decimetric burst activity preceded the Faraday rotation transient, reaching maximum intensity at 1130 UT, i.e. the time of transient onset.

July 1976 is the designated beginning of solar cycle 21 and as such may be considered a typical month of extreme solar minimum. The mean relative sunspot number was only 2.1 and only 6 subflares of importance were reported, none of which was even remotely connected with the Faraday anomaly on 18 JUL. A fairly large equatorial filament was seen at Central Meridian Passage (CMP) over the McMath region 14307 on 10

Table 1. Radio Events Indicated in Figures 1-4

Fig/Event	f (MHz)	Station	Burst Type	UT Time Start	Max	Duration (min)	Peak Flux Dens. (10^{-22} Wm $^{-2}$ Hz $^{-1}$)
1/A	930	BORD	3 S	1453	1456	10	13
1/B	245	SGMR	43 NS	1747	1914	332D	16.5
1/C	9400	HUAN	20 GRF	2150	2214	33	13.4
2/A	260	ONDR	8 S	0711	0711	0.2	8
2/B	260	ONDR	3 S	1034	1035	2	5
2/C	550	KIEV	41 F	1217	1217	1.9	39
2/D	550	KIEV	6 S	1235	1235	0.4	32
2/E	550	KIEV	41 F	1248	1250	2.7	33
2/F	550	KIEV	8 S	1407	1407	0.1	32
2/G	550	KIEV	8 S	1452	1452	0.2	32
2/H	2800	OTTA	21 GRF	1505	1510	50	4.8
	2800	OTTA	2 S/F	1507	1509	2	2
2/I	2800	OTTA	20 GRF	1932	1935	40	0.8
2/J	18	MCMA	6 S	2142	2144	3	
3/A	550	KIEV	42 SER	1027		31.5	6
3/B	550	KIEV	3 S	1113	1114	2	5
3/C	550	KIEV	40 F	1144	1147	4	3
4/A	260	ONDR	8 S	0826	0826	0.2	17
4/B	550	KIEV	41 F	1104		30.5	4.5
4/C	550	KIEV	42 SER	1135	1136	5	40

Notes: Station and burst type codes are from Solar-Geophys. Data, 378.

Figure 1: Helios-1 West Limb 29 AUG 1975.

Figure 2: Helios-1 East Limb 1 SEP 1975.

Figure 3: Helios-2 East Limb 22 MAY 1976.

Figure 4: Helios-2 West Limb 18 JUL 1976.

JUL 1976 (Carrington longitude 150°). At the next CMP on 6 AUG 1976, the magnetic structure at this heliographic longitude had been significantly rearranged. One must consider the possibility that the filament underwent disparition brusque during its west limb passage (McMath 14307 was 25° behind the limb at time of transient).

3. A SIMPLE MODEL

A survey of the possible causes of the Faraday rotation transients on Pioneer 6 and Pioneer 9 has been given by Bird (1976). Among the suggestions are kinks in the magnetic field, coronal magnetic bottles and moving solar plasma clouds with constant radial magnetic field. Recent work by Dulk et al. (1976) suggests that the mass ejections are magnetically controlled. Magnetic energy densities derived assuming that the metric radiation associated with the transient arises from the gyro-synchrotron process were over 10 times greater than thermal energies in the cloud, and even marginally greater than the kinetic energy

density. Since the magnetic field \vec{B} cannot be separated from the electron density N in a determination of the Faraday rotation, the two quantities will be considered together. The direction of \vec{B} will be considered to be approximately radial within the transient.

The quasi-longitudinal approximation for the Faraday rotation of the Helios signal ($f = 2.29$ GHz) is given by

$$\Omega = K \int N \vec{B} \cdot d\vec{s} \quad \text{degrees} \quad (1)$$

where $K = 2.58 \times 10^{-13}$ in gaussian units. Assuming that the product $N \cdot B$ falls off radially as $r^{-\delta}$, the excess Faraday rotation from the transient will be given by

$$\Omega_t = -KnLN_0 B_0 (\sin\phi_0/a)^\delta \cos\phi_0 \quad (2)$$

where n = transient enhancement factor (increase in $N \cdot B$ over ambient)
 L = thickness of transient along line-of-sight
 N_0 = ambient electron density extrapolated to coronal base
 B_0 = ambient magnetic field strength at coronal base
 ϕ_0 = heliographic longitude of transient (Fig. 5)
 a = solar offset

Fig. 5 is a schematic drawing of the corona at the time of the transient on 18 JUL 1976. The magnetic field polarities of the regions in heliographic longitude, which agree with the inferred polarities taken from polar cap magnetograms (Solar-Geophys. Data, SEP 1976), are indicated by arrows. The numbers indicated in each region are the value of $N \cdot B$ (in units of 10^6 g cm $^{-3}$) derived from the large-scale Faraday data in July 1976 using a simplified technique developed by Volland et al. (1977). Comparing Eq. (2) with Fig. 5, it becomes apparent that the negative Faraday rotation transient could only occur for the combination $B_0 < 0$ and $\cos\phi > 0$ (i.e. behind the limb). Using the observed values $\Omega_t = -100$ and $a = 3.6 R_\odot$, one may obtain the value of nL required for transients originating at all values of ϕ . As mentioned, only values in the range $30^\circ < \phi < 90^\circ$ yield the correct sign for the transient, and at these longitudes nL has the value 1.5-5.0 R_\odot . For example, if the quiescent prominence at $\phi = 65^\circ$ really did erupt and cause the transient observed here, $nL = 1.7 R_\odot$. This would indicate that the thickness of the loop transient would have to be well under 1 R_\odot in order to have a density enhancement close to values observed by Hildner et al. (1975a).

4. TRANSIENT OCCURRENCE FREQUENCY

A study of the spatial distribution of coronal transients by Hildner et al. (1976) has determined that the occurrence frequency

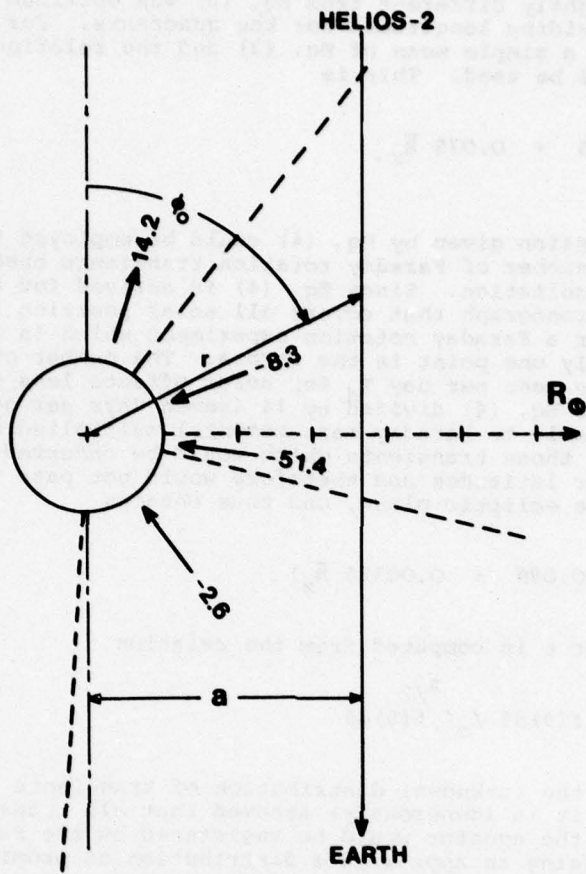


Figure 5. Schematic representation of Coronal Configuration at Time of Helios-2 Faraday Rotation Transient on 18 JUL 1976. The view is of the ecliptic plane from the north solar pole. The west limb is divided into four regions as indicated by the radial dashed lines. See text for details.

tends to maximize at certain preferred longitudes. Although the experimental restraints do not allow a finer resolution in heliolongitude than quadrants, a remarkable high correlation exists between the number of transients seen and the 7-day running average of the Zurich sunspot number in each quadrant. Hildner et al. (1976) derive the following linear relation

$$T = 0.96 + 0.084 \bar{R}_z \quad (3)$$

where T is the number of transients seen per solar rotation in one quadrant, and \bar{R}_z is the mean relative sunspot number in that quadrant.

A relation slightly different from Eq. (3) was obtained using different (arbitrary) dividing longitudes for the quadrants. For the purposes of this paper, a simple mean of Eq. (3) and the relation for arbitrary longitudes will be used. This is

$$T = 1.25 + 0.075 \bar{R}_z. \quad (4)$$

The expression given by Eq. (4) could be employed to determine the most probable number of Faraday rotation transients observed during a given solar occultation. Since Eq. (4) is derived for the Skylab white light coronograph that covers all solar position angles, it must be modified for a Faraday rotation experiment which is monitoring essentially only one point in the corona. The number of Faraday rotation transients seen per day T_d for solar offsets less than $10 R_\odot$ is estimated to be Eq. (4) divided by 14 (seven days per quadrant, only one limb available to Faraday measurements) multiplied by a factor ϵ accounting for those transients which would be observed on Skylab, but occur at higher latitudes and therefore would not pass through a line-of-sight in the ecliptic plane. One thus obtains

$$T_d = \epsilon(0.089 + 0.00535 \bar{R}_z). \quad (5)$$

The factor ϵ is computed from the relation

$$\epsilon = \frac{\int_0^1 f(\theta) d\theta}{\int_0^{\pi/2} f(\theta) d\theta} \quad (6)$$

where $f(\theta)$ is the (unknown) distribution of transients in heliographic latitude, and it is (generously) assumed that all transients within one radian of the equator would be registered by the Faraday rotation experiment. Using an approximate distribution of prominences rather than the transients themselves for $f(\theta)$, one obtains different values of ϵ for solar maximum and solar minimum. This occurs because about twice as many prominences occur at low solar latitudes during solar maximum as opposed to equal probability over all θ at minimum. If then $f=1$ at solar minimum, and $f=2$ ($0 < \theta < 1$), $f=1$ ($1 < \theta < \pi/2$) at solar maximum, one obtains

$$\epsilon = \begin{cases} 0.64, & \text{solar minimum (Helios, 1975, 1976)} \\ 0.78, & \text{solar maximum (Pioneer 6, 1968)} \end{cases} \quad (7)$$

A tabulation of the number of transients expected for intervals during the Pioneer 6 and Helios missions is displayed in Table 2. Only days for which the solar offset was less than $10 R_\odot$ are considered. Also given are the mean of the values of \bar{R}_z used over the interval, the total days of actual observation, and the number of transients actually seen. It now becomes clear why the solar minimum occultations of Helios were so "uneventful".

Table 2. Theoretical Transient Observations from Eq. (5)

Mission (year)	Occultation Time Interval	Total Actual Observation Time (days)	Mean \bar{R}_z over Interval	Nr. of Transients	
				Pred.	Obser.
Pioneer 6 (1968)	3 NOV-8 DEC	7.18	105.5	3.6	3
Helios-1	15 APR-29 APR	3.56	2.7	0.2	0
Helios-1	26 MAY-14 JUN	1.51	4.3	0.1	0
Helios-1	25 AUG-4 SEP	4.07	16.0	0.5	1?
Helios-1 (1975)	all data	9.14	8.9	0.8	0 or 1
Helios-2	9 MAY-14 MAY	2.05	18.4	0.2	0
Helios-2	19 MAY-30 MAY	3.80	1.1	0.2	1?
Helios-2	1 JUN-30 JUN	4.46	12.0	0.4	0
Helios-2	16 JUL-30 JUL	4.00	0.3	0.2	1
Helios-2 (1976)	all data	14.31	6.8	1.1	1 or 2

5. CONCLUSIONS

Short-duration deviations from the slowly varying baseline have been observed in the Faraday rotation profiles of the Helios space-craft during solar occultation. It is concluded that this anomalous behavior results from outward moving electron density and magnetic field irregularities in the solar corona, which when observed in white light are denoted "mass ejection events" or simply "coronal transients".

The typical mass content, velocity and structure of the coronal transients are compatible with the magnitude, duration and signature registered in the Faraday profile during such an event. The Faraday rotation transients, like their optical alter ego, are not always triggered by flares. It is speculated, although the evidence is inconclusive, that eruptive prominences are responsible for the most conspicuous events seen on Helios. Finally, the occurrence frequency of optical coronal transients and the Faraday counterparts are in good agreement both for the solar minimum occultations of Helios and the pre-Skylab observations on Pioneer 6. If the two Helios satellites can continue to survive their perilous perihelions (at last report, they were alive and well), a series of solar occultations over the ascending phase of the present solar cycle would yield valuable information on the transient occurrence frequency and other solar activity dependent relations.

References

- Bird, M.K., Coronal transient events observed by S-band Faraday rotation measurements during solar occultation, Space Res., 16, 711, 1976.
- Dulk, G.A., S.F. Smerd, R.M. MacQueen, J.T. Gosling, A. Magun, R.T. Stewart, K.V. Sheridan, R.D. Robinson and S. Jacques, White light and radio studies of the coronal transient of 14-15 September 1973, Solar Phys., 49, 369, 1976.
- Gosling, J.T., E. Hildner, R.M. MacQueen, R.H. Munro, A.I. Poland and C.L. Ross, Mass ejections from the Sun: A view from Skylab, J. Geophys. Res., 79, 4581, 1974.
- Gosling, J.T., E. Hildner, R.M. MacQueen, R.H. Munro, A.I. Poland and C.L. Ross, Direct observations of a flare related coronal and solar wind disturbance, Solar Phys., 40, 439, 1975.
- Gosling, J.T., E. Hildner, R.M. MacQueen, R.H. Munro, A.I. Poland and C.L. Ross, The speeds of coronal mass ejection events, Solar Phys., 48, 389, 1976.
- Hildner, E., J.T. Gosling, R.M. MacQueen, R.H. Munro, A.I. Poland and C.L. Ross, The large coronal transient of 10 June 1973 I: Observational description, Solar Phys., 42, 163, 1975a.
- Hildner, E., J.T. Gosling, R.T. Hansen and J.D. Bohlin, The sources of material comprising a mass ejection coronal transient, Solar Phys., 45, 363, 1975b.
- Hildner, E., J.T. Gosling, R.M. MacQueen, R.H. Munro, A.I. Poland and C.L. Ross, Frequency of coronal transients and solar activity, Solar Phys., 48, 127, 1976.
- Levy, G.S., T. Sato, B.L. Seidel, C.T. Stelzried, J.E. Ohlson and W.V.T. Rusch, Pioneer 6: Measurement of transient Faraday rotation phenomena observed during solar occultation, Science, 166, 596, 1969.
- Pintér, S., Observations of moving solar plasma clouds at $10 R_{\odot}$, Bull. Astr. Inst. Czech., 24, 337, 1973.
- Poland, A.I. and R.H. Munro, Interpretation of broad-band polarimetry of solar coronal transients: Importance of H α emission, Astrophys. J., 209, 927, 1976.
- Schatten, K.H., Flare identification associated with coronal disturbances, Science, 168, 395, 1970.
- Volland, H., M.K. Bird, G.S. Levy, C.T. Stelzried and B.L. Seidel, HELIOS-1 Faraday rotation experiment: Results and interpretations of the solar occultations in 1975, submitted to J. Geophys., 1977.

Discussion

Dryer: Can you say anything about the direction of the field within the transients?

Bird: Using Faraday data alone, the most honest answer is no. If we were ever to observe a coronal transient both in white light and in the Faraday rotation from an occultating satellite, we could separate the contributions due to enhanced electron density from those due to perturbations in the direction and strength of the magnetic field along the line-of-sight.

II. SOLAR WIND STUDIES

A Multi-Fluid Model for Stellar Winds

Nathan Metzler*
Space Environment Laboratory
ERL-NOAA
Boulder, CO 80302, USA

Abstract

A multi-fluid model describing the time-independent plasma flow in stellar winds is formulated. This plasma includes electrons and different types of ions which are allowed to have different streaming velocities as well as different non-isothermal temperatures. This flexibility means that the various energy equations are explicitly incorporated in the model. Analytical explicit expressions for the ion momentum equations make it possible to analyze the various conditions for the critical points even in this complicated multi-fluid case.

*NRC Resident Research Associate

Recursion relations, enabling modifications of the existing equations, are found for more general cases when an extra ion species is introduced. Through these relations it is possible to determine the conditions in which the extra ion type will not significantly change the behavior of the other, already existing species. This will happen when the extra ion charge density is much smaller than that of the electrons. Finally, it is shown analytically that, in order to accelerate heavier ions to streaming velocities above those of lighter ions (as observed in the solar wind for the alpha-particles), heavier ions will be hotter during the accelerating region.

1. INTRODUCTION

The basic theory of supersonic expansion of an extended stellar atmosphere treated as simple fluid has been successfully started by Parker (1958) and further investigated by Noble and Scarf (1963). Next, Sturrock and Hartle (1966) developed a two-fluid model in which electrons and protons were allowed to have different temperatures. Then, three-fluid models were used by Yeh (1970) in which temperature variations were ignored, and by Geiss et al. (1970) in which equal and polytropic temperatures for all species were assumed. The three-fluid model was improved by Cuperman and Metzler (1975), allowing different temperatures as well as different streaming velocities for the different species.

Recent data analysis (Geiss, 1972, 1973; Zinner et al., 1974; Hodges and Hoffman, 1974) indicate the presence of minor species, besides alpha-particles, in the solar wind. It is important to investigate the general nature of the multi-fluid equations, before using them for the specific study of the composition of the solar wind. Because of the special nature of the equations, an introduction of an extra ion, even of a minor species can cause a significant change in the solutions for the already existing species. The first study of a multi-fluid plasma in astrophysics was done by Weber (1973a,b), who determined conditions for the existence of critical points. But, because his expressions for the velocity gradients were inexplicit, these conditions were only special cases for more general conditions, which are derived in this paper.

2. THE BASIC EQUATIONS

It is assumed that the plasma which flows in a spherically-symmetric steady state, has an infinite electric conductivity, scalar pressure and no viscosity. The plasma consists of electrons and n different types of ions. The continuity and momentum equations can be written in the form:

$$n_a v_a r^2 = J_a = \text{const.} \quad (1)$$

$a = e, 1, 2, \dots, n$

$$\frac{n_a m_a v_a}{r} \frac{dv_a}{dr} + \frac{d}{dr} (n_a k T_a) + \frac{GM_e \rho_a n_a}{r^2} = Z_a e n_a E + R_a \quad (2)$$

where r is the radial distance from the star, m_a the mass, Z_a the charge number ($Z_e \equiv -1$), n_a the density, v_a the streaming velocity, and T_a the temperature of "a-type particles." Also, e is the electron charge, k is Boltzmann's constant, G the gravitational constant, M the star's mass, E the radial electrostatic field which develops as a result of the gravity-induced charge polarization, $R \equiv \sum_{ab} R_{ab}$ with R_{ab} being the mean rate of momentum exchange between a-type particles and b-type particles. In principle, R_a can include any other unspecified forces, acting on a-type particles.

The assumptions of electric quasi-neutrality and absence of net electric currents can be written in the form:

$$\sum_a Z_a n_a = 0 \quad (3)$$

$$\sum_a Z_a J_a = 0 \quad (4)$$

Eliminating the electric field E , by writing the electron momentum equation separately, and using conditions (3) and (4), one can rewrite the equations in the form of the following linear system of equations:

$$a_{ij} x_j = b_i \quad i, j = 1, 2, \dots, n \quad (5)$$

(summation on the double index j) for the unknowns

$$x_j = \frac{1}{v_j} \frac{dv_j}{dr} \quad (6)$$

where

$$a_{ij} \equiv \alpha_i \delta_{ij} - \beta_j \quad (\delta_{ij} \text{ is the Kronecker delta})$$

$$\alpha_i \equiv (m_i v_i^2 - kT_i) / Z_i kT_e$$

$$\beta_i \equiv \frac{Z_i J_i / v_i}{\sum_k Z_k J_k / v_k} = \frac{Z_i n_i}{n_e} \quad (\text{the relative charge density}) \quad (7)$$

$$b_i \equiv \left[2 \frac{kT_e + kT_i / Z_i}{r} - \frac{d}{dr}(kT_e + kT_i / Z_i) - \frac{GM_e m_i / Z_i}{r^2} + \frac{R_i}{Z_i n_i} + \frac{R_e}{n_e} \right] / kT_e$$

after neglecting for simplicity the electron mass. We now direct attention to the solution of Eqs. (5) in the next section.

3. THE RECURSION RELATIONS AND THE EXPLICIT SOLUTIONS

The solutions of Eqs. (5) can be written in the form

$$x_{j,n} = N_{j,n} / D_n \quad j = 1, 2, \dots, n \quad (8)$$

where the subscript n indicates the number of different ion species. D_n is the determinant of the coefficients $D_n \equiv |a_{ij}|$, and $N_{j,n}$ is the determinant of the coefficients a_{ij} with the j column replaced by b_i as shown by Weber (1973a,b). We now examine general explicit expressions for the above-mentioned numerators and denominators. It can be proven that the denominators and numerators satisfy the following new recursion relations:

$$D_{n+1} = \alpha_{n+1} D_n - \beta_{n+1} \prod_{i=1}^n \alpha_i \quad (9)$$

$$N_{j,n+1} = \alpha_{n+1} N_{j,n} - \beta_{n+1} (b_j - b_{n+1}) \prod_{k \neq j}^n \alpha_k ; \quad j = 1, 2, \dots, n+1 \quad (10)$$

if we introduce an extra $(n+1)$ -type ion to the already existing plasma. Here we use the notation:

$$\sum_{i=1}^n A_i \prod_{k \neq i}^n B_k = A_1 B_2 B_3 \dots B_n + B_1 A_2 B_3 \dots B_n + \dots + B_1 B_2 \dots B_{n-1} A_n .$$

Using these new recursion relations, one can find the following explicit expressions for the denominators and the numerators of Eqs. (8):

$$D_n \equiv \prod_{k=1}^n \alpha_k - \sum_{i=1}^n \beta_i \prod_{k \neq i}^n \alpha_k \quad (11)$$

$$N_{j,n} \equiv b_j \prod_{k \neq j}^n \alpha_k - \sum_{i \neq j}^n \beta_i (b_j - b_i) \prod_{k \neq i,j}^n \alpha_k , \quad j=1, 2, \dots, n . \quad (12)$$

The above explicit relations, not known before, enable us to make a general investigation of the critical points involved in the multi-fluid problem.

4. THE CRITICAL POINTS

The gradients of the streaming velocities (Eqs. 8) will have singularities when the denominator D_n vanishes. In order to have continuous streaming velocities, all the numerators $N_{j,n}$ must vanish simultaneously at these points. Such a point is called a "critical" point. Solutions which pass through critical points are called critical solutions. One gets a critical solution by choosing the proper boundary conditions. In a case of one or two-fluid model, there is only one set of conditions to be satisfied ($a_1 = 0, b_1 = 0$ from Eqs. 5 and 7) in order to get a critical point. Because of the monotonic behavior of the solutions, one expects only one critical point. However, in a fluid containing more than one type of ion, we shall see that there will be more than one critical point. The purpose of this work is to determine explicitly, without reducing the generality of the situation, the conditions for the existence of critical points.

Equations (11) and (12) can be rewritten in the form:

$$D_n = \sum_{i=1}^n \{ [\beta_i + \frac{1}{n} (1-n\beta_i)] \alpha_i - \beta_i \} \prod_{k \neq i}^n \alpha_k \quad (13)$$

$$N_{j,n} = \sum_{i \neq j}^n [b_j (\frac{\alpha_i}{n-1} - \beta_i) + \beta_i b_i] \prod_{k \neq i,j}^n \alpha_k, \quad j=1, 2, \dots, n \quad (14)$$

where n is a parameter which can have arbitrary real values.

From Eq. (13) one can see that

$$\alpha_i = \frac{n\beta_i}{n\beta_i + (1-n\beta_i)} \quad i=1, 2, \dots, n \quad (15)$$

is the general condition for a singular point. Insertion of condition (15) into Eq. (14) gives us

$$\sum_{i=1}^n [n\beta_i + (1-n\beta_i)] b_i = 0 \quad (16)$$

as a condition to be satisfied simultaneously with Eq. (15), in order to have a critical point. Conditions (15) and (16) define critical surfaces. The exact determination of the actual critical points depends on the specific problem involved, namely, the specific composition, the assumed energy equations, and the boundary conditions.

Taking the parameter $\eta \rightarrow \infty$ one gets

$$\alpha_i = 1 ; \sum_{i=1}^n \beta_i b_i = 1 ; \quad i=1, 2, \dots, n \quad (17)$$

to be the conditions for a critical point. Or, in physical variables this can be written in the form:

$$\frac{m_i v_i^2 - kT_i}{z_i kT_e} = 1 ; \sum_{i=1}^n \frac{z_i n_i}{n_e} b_i = 1 \quad i=1, 2, \dots, n \quad (18)$$

which are the conditions found by Weber for one special family of critical points. Taking $\eta=0$, one gets

$$\alpha_i = 0 ; \sum_{i=1}^n (1 - n\beta_i b_i) = 0 \quad i=1, 2, \dots, n \quad (19)$$

which means that all the ion-species will have their Mach number simultaneously equal to 1. Weber found that it is sufficient that only two of the ion species will have their Mach number simultaneously equal to 1 which can be seen from Eq. (11) for the denominator. If, let's say, that only $\alpha_1 = \alpha_m = 0$, we will need $b_1 = b_m$ as an additional condition for a critical point in that case.

Let us consider now as an example the special case of a three-fluid ($n=2$) plasma in the next section.

5. THE THREE-FLUID ($n=2$) CASE

Because it is possible now to write the conditions for critical points in an explicit form, considering the case of three fluids will not reduce the general properties of the problem.

Inserting $n=2$ in conditions (15) and (16) one gets:

$$\alpha_1 \equiv \frac{m_1 v_1^2 - kT_1}{z_1 kT_e} = \frac{n\beta_1}{n\beta_1 + (\beta_2 - \beta_1)} \quad (19)$$

$$\alpha_2 \equiv \frac{m_2 v_2^2 - kT_2}{z_2 kT_e} = \frac{n\beta_2}{n\beta_2 + (\beta_1 - \beta_2)} \quad (20)$$

$$[n\beta_1 + (\beta_2 - \beta_1)]b_1 + [n\beta_2 + (\beta_1 - \beta_2)]b_2 = 0 \quad (21)$$

recalling the definition of b_i in Eqs. (7) and that $\sum_{i=1}^n \beta_i = 1$.

Conditions (19)-(21) define the critical surfaces which are plotted in Figure 1 for $\beta_1 = 0.9$, $\beta_2 = 0.1$ in parametric form. The variable $\beta_2 b_2 / \beta_1 b_1$ was chosen rather than b_2/b_1 , simply because of scaling convenience. For any arbitrary value of n one can find the corresponding values of α_1, α_2 and the ratio b_2/b_1 in order to have a possible critical point, without any further assumptions on the types of ions and energy equations involved. For convenience, α_2 is plotted versus α_1 in Figure 2, for the same values of β_1 and β_2 . One can see that independently of the values of the relative abundances, the curves will always pass through the points $(0,0)$ and $(1,1)$ in the (α_1, α_2) plane. The first point represents a Mach number which is simultaneously equal to 1 for both ion species. The second point represents the condition

$$m_i v_i^2 = kT_i + Z_i kT_e \quad i=1, 2 \quad (22)$$

which is the only possibility for a critical point in the one and two fluid ($n=1$) cases. Stated differently, the two solid curves in Figure 2 collapse to a single point for the special cases of 1- or 2-fluid plasmas. Because one expects the flow to start subsonically, the first critical point will occur for

$$\frac{\beta_2 - \beta_1}{\beta_2} < n < \frac{\beta_1 - \beta_2}{\beta_1} \quad \text{which are the values of the asymptotes. For } \beta_1 = 0.9,$$

$\beta_2 = 0.1$ one has $-8 < n < 8/9$ in Figure 1. In Figure 2 it will be a point on the lower branch. Because one expects to have a monotonic change of variables, and in particular the temperatures going to zero at infinity, the path of $\alpha_1 - \alpha_2$ should pass through the higher branch too (Fig. 2). So, one expects two critical points under the assumption of monotonic behavior which will be the first in the neighborhood of $(0,0)$ and the second, in the neighborhood of $(1,1)$ in the (α_1, α_2) plane. Obviously, the exact points will be determined by the actual problem involved. We now examine an explicit numerical computation of a 3-fluid plasma.

A numerical self-consistent computation was performed for a solar wind containing electrons, protons and alpha-particles. The alpha-particle flux was taken to be 3.5% of the total ion-flux. The heat-flux term was neglected in the ion energy equations only at distances larger than $100 R_\odot$ from the sun. The momentum exchange rate was taken to be about five times the collisional one in order to get an appropriate alpha-particle acceleration relative to the proton's acceleration beyond the second critical point. The integration away from the sun was started at the second critical point; here the conditions are taken to be:

$$(a) \quad m_p v_p^2 - kT_p = 0.5 (m_\alpha v_\alpha^2 - kT_\alpha) = kT_e; \quad \beta_1 b_1 + \beta_2 b_2 = 0$$

and

$$(b) \quad T_e = 0.45 T_p; \quad m_\alpha v_\alpha^2 = 2.5 m_p v_p^2.$$

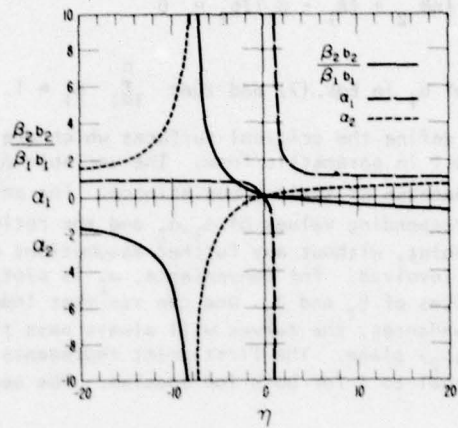


Figure 1. The parametric topology of the critical points for a general three-fluid case, with relative ion charge densities $\beta_1=0.9$; $\beta_2=0.1$. The simultaneous values of the variables $\alpha_i \equiv (m_i v_i^2 - kT_i)/(z_i kT_e)$, ($i=1,2$); and $(\beta_2 b_2 / \beta_1 b_1)$ can be found for any arbitrary value of η .

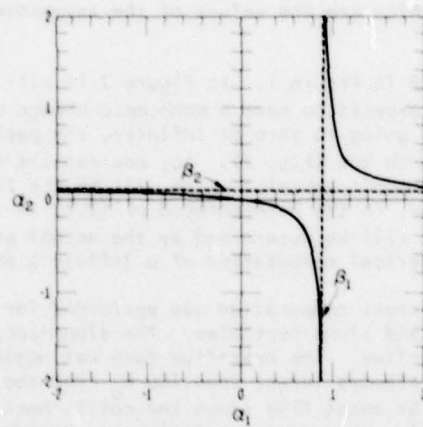


Figure 2. The plot of $\alpha_2 \equiv (m_2 v_2^2 - kT_2)/(z_2 kT_e)$ versus $\alpha_1 \equiv (m_1 v_1^2 - kT_1)/(z_1 kT_e)$, for the relative charge densities $\beta_1=0.9$ and $\beta_2=0.1$ in a general three-fluid case.

Conditions (a) follow from the specification: $\alpha_i = 1$, $i = p, \alpha$ for a critical point. Conditions (b) were taken in an arbitrary manner. Conditions alternative to (b) could have been chosen by an iterative process in order to select the solution which also passes through the first critical point nearer to the Sun. However, such a procedure would take too much computer time because other iterative processes involving condition (a) are involved in the selection of the solutions with monotonic decrease of the temperatures to zero at infinity. In order to insure the passage of the solution through the first critical point, a proper modification was done on the momentum exchange rate between the protons and the alpha-particles in the range between the second critical point and the Sun. This modification involved the gradual reduction of the rate of momentum exchange from five times the collisional one (at the second critical point) to the collisional value near the Sun.

The first critical point was at $3.19 R_\odot$ while the second was at $3.83 R_\odot$. Typical values of the α_i 's are $(0.34, -0.03)$ at the first critical point. At the second critical point the values were chosen to be $(1, 1)$ as indicated by Condition (a). We have $B_1 = 0.909$, $B_2 = 0.091$ at the first critical point and $B_1 = 0.915$, $B_2 = 0.085$ at the second. The equivalence of the B_1 's and B_2 's justifies the neglect of the variations of the relative charge densities near the critical points in the discussion. Calculated profiles of velocities and temperatures are presented in Figure 3. The alpha-particle temperature is the only parameter which does not agree with observations. The high alpha-particle temperature was chosen (through Conditions (b)) in order to show a case in which alpha velocities are larger than those of the proton.

6. ADDITION OF ANOTHER ION SPECIE TO AN $(n+1)$ -FLUID

We recall (Section 2) that n refers to the number of ions. Thus an $(n+1)$ -fluid refers to that which includes, of necessity, the electrons. If one adds an additional ion specie to an $n+1$ -fluid, one will have from Eqs. (8)-(10)

$$x_{j,n+1} = \frac{N_{j,n+1}}{D_{n+1}} = \frac{\alpha_{n+1} N_{j,n} - \beta_{n+1} (b_j - b_{n+1})}{\alpha_{n+1} D_n - \beta_{n+1} \sum_{i=1}^n \alpha_i} \quad j \leq n. \quad (23)$$

One can see that, if the relative charge density β_{n+1} of the extra ion specie is very small ($\beta_{n+1} \ll 1$) the logarithmic gradient of the streaming velocities of the existing ion species will not change considerably due to the addition of the extra ion specie. But this condition can be applicable only if $N_{j,n} \neq 0$ and $D_n \neq 0$; as a result, the new critical points may not be at the previous critical points. So, it is not obvious that one can consider an extra, minor ion specie as a small perturbation to the $(n+1)$ -fluid solution, and the equations should be solved in a self-consistent manner.

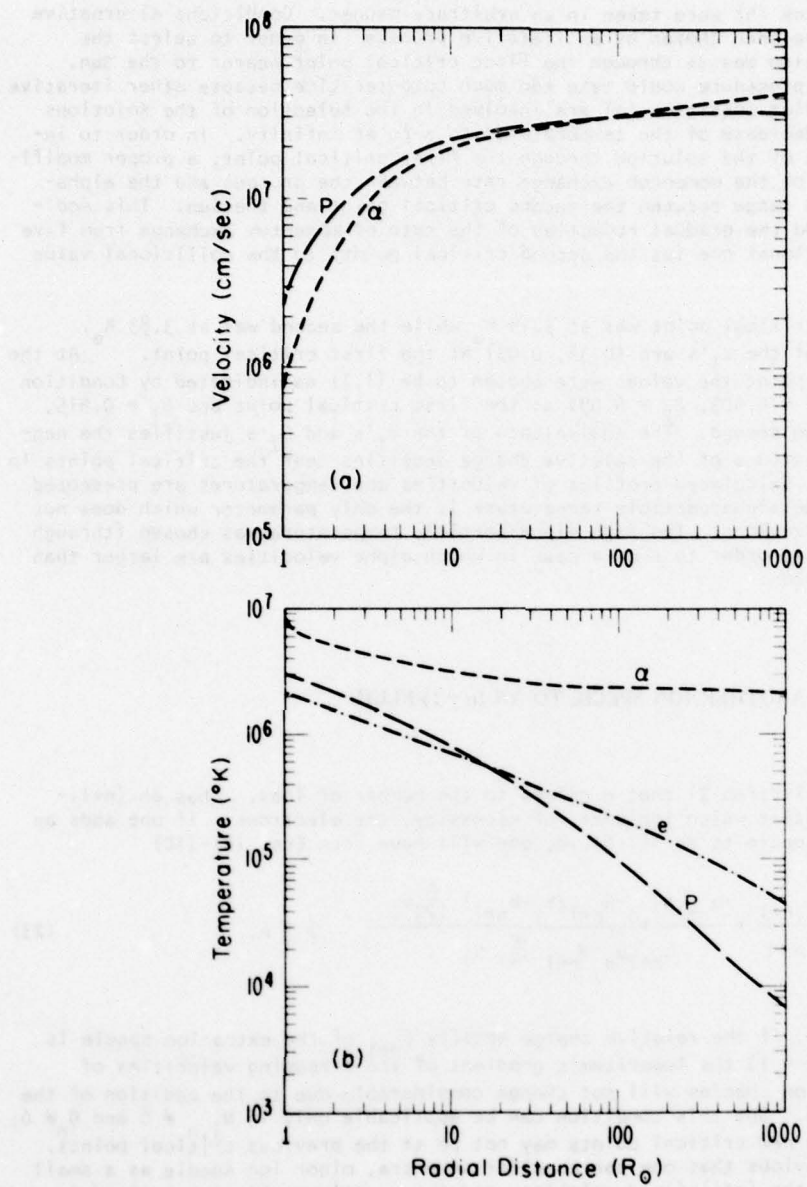


Figure 3. Calculated velocity and temperature profiles for the three-fluid solar wind (electrons, protons and alpha-particles). This case of extreme high alpha temperature was chosen in order to demonstrate a possibility of alpha velocities higher than proton velocity.

7. THE ENERGY EQUATIONS

The energy equations, after elimination of forces through the electron momentum equation, can be written in the form:

$$\frac{d}{dr} \left(\frac{3}{2} k T_a + \frac{r^2 q_a}{J_a} \right) + k T_a \left(\frac{1}{v_a} \frac{dv_a}{dr} + \frac{2}{r} \right) = \frac{r^2 Q_a}{J_a} \quad a = e, 1, 2, \dots, n \quad (24)$$

where the heat fluxes (q_a) can be written in the form (Spitzer, 1962)

$$q_a = -K_{o,a} T_a^{5/2} \frac{dT_a}{dr}, \quad (25)$$

$K_{o,a}$ being the heat conduction coefficients. $Q_a \equiv \sum_{b \neq a} Q_{ab}$ with Q_{ab} being the mean rate of exchange of energy between a-type particles and b-type particles. In principle, Q_a may include any other unspecified energy addition to a-type particles.

Because of the terms $\frac{1}{v_a} \frac{dv_a}{dr}$, one can see that the temperature gradients have singularities too. The temperature gradients cannot be written explicitly because the heat fluxes cause the energy equations to be of second order. For the same reason, the temperature gradients, which appear in the inhomogeneous terms b_i in Eqs. (5), cannot be eliminated from Eqs. (7).

If one neglects the ion heat fluxes, solution of Eqs. (5) together with Eq. (24) gives the velocity gradients the new expressions:

$$x_{j,n} = \frac{\bar{N}_{j,n}}{\bar{D}_n} \quad j=1, 2, \dots, n \quad (26)$$

where, similarly to Eq. (11) and (12),

$$\bar{D}_n = \pi \sum_{k=1}^n \bar{\alpha}_k - \sum_{i=1}^n \beta_i \sum_{k \neq i} \pi \bar{\alpha}_k \quad (27)$$

$$\bar{N}_{j,n} = \bar{b}_j \sum_{k \neq j} \pi \bar{\alpha}_k - \sum_{i \neq j} \beta_i (\bar{b}_j - \bar{b}_i) \sum_{k \neq i,j} \pi \bar{\alpha}_k \quad j=1, 2, \dots, n \quad (28)$$

where now

$$\bar{a}_i = (m_i v_i^2 - \frac{5}{3} kT_i) / Z_i kT_e \quad (29)$$

$$\bar{b}_i = [2 \frac{kT_e + \frac{5}{3} kT_i / Z_i}{r} - \frac{d(kT_e)}{dr} - \frac{GM_\odot m_i / Z_i}{r^2} + \frac{R_i}{Z_i n_i} + \frac{R_e}{n_e} - \frac{2r^2 Q_i}{3 Z_i J_i}] / kT_e \quad (30)$$

The neglect of the ion heat flux enables one to see qualitatively the effect of different temperatures on the relative streaming velocities.

It is observed in the solar wind that alpha-particles near 1 AU have larger average streaming velocities than those of the protons (Ogilvie and Zwally, 1972; Asbridge et al., 1973, 1974; Hirshberg et al., 1974; Ogilvie, 1975). These observations may now be explained on the basis of this self-consistent analysis. The friction like exchange of momentum $R_\alpha \sim -(v_\alpha - v_p)$ can at most equalize the alpha-particles streaming velocity v_α to that of the protons v_p . But the contribution from the exchange of energy $Q_\alpha \sim -(T_\alpha - T_p)$ can make v_α larger than v_p if the alpha-particle temperature T_α is sufficiently larger than the proton temperature T_p . This can be seen explicitly only by neglecting the ion heat flux, and numerically, only if the equations are solved in a self-consistent manner. In fact, we found that v_α exceeds v_p at 1 AU by 10% only if T_α is about 50 times larger than T_p , (see Fig. 3) rather than 4 times as observed. This numerical result indicates that there are additional contributions to the acceleration of alpha-particles, but basically the fact that $v_\alpha > v_p$ is observed can, in principle, be understood even without additional arbitrary heating as in the three-fluid model of Ryan and Axford (1975).

8. CONCLUSIONS

The explicit relations derived in this work for the streaming velocity gradients enable us to make a general analysis for a multi-fluid steady state plasma flow. From the analysis presented here, one concludes that an extra ion species, introduced to a fluid cannot be treated *a priori* as a small perturbation even if this ion type has a very small abundance. So, one should solve this as a new problem in a self-consistent manner. In a multi-fluid plasma one will have more than one possible critical point, and the actual critical points should be determined by the specific problem involved. Finally, consideration of the multi-fluid problem in a self-consistent manner gives a possible explanation for heavier ions to have velocities which are larger than those of the lighter ions if they also have larger temperatures. The self-consistent solution presented here is, then, a likely explanation for the observations which show $v_\alpha/v_p \gtrsim 1.1$ when the special case of the 3-fluid (protons, electrons, alphas) solar wind is considered.

Acknowledgments

I would like to express my gratitude to M. Dryer and J. Joselyn for useful discussions and for a critical reading of this paper, to P. Rosenau for useful mathematical suggestions and to S. Suess for useful discussions.

References

- Asbridge, J. R., S. J. Bame and W. C. Feldman, Variations in the helium component of the solar wind, Trans. Amer. Geophys. Union, 54, 440, 1973.
- Asbridge, J. R., S. J. Bame, W. C. Feldman and M. D. Montgomery, Helium and hydrogen velocity differences in the solar wind, EOS (Transactions, American Geophysical Union), 56, 1180, 1974 (abstract).
- Cuperman, S., and N. Metzler, Solution of three-fluid model equations with anomalous transport coefficients for the quiet solar wind, Ap. J., 196, 204, 1975.
- Geiss, J., P. Hirt and H. Leutwyler, On acceleration and motion of ions in corona and solar wind, Solar Phys., 12, 458, 1970.
- Geiss, J., Elemental and isotopic abundances in the solar wind. The Solar Wind, Ed. C. P. Sonett, P. J. Coleman, Jr. and J. M. Wilcox, NASA SP-308, 559, 1972.
- Geiss, J., Solar wind composition and implications about the history of the solar system, 13th Inter. Cosmic Ray Conf., Conference Papers, 5, 3375, 1973.
- Hirshberg, J., J. R. Asbridge and D. E. Robbins, The helium component of solar wind velocity streams, J. Geophys. Res., 79, 934, 1974.
- Hodges, R. R. Jr., and J. H. Hoffman, Measurements of solar wind helium in the lunar atmosphere, Geophys. Res. Letters, 1, 69, 1974.
- Noble, L. M., and F. L. Scarf, Conductive heating of the solar wind I, Ap. J., 138, 1169, 1963.
- Ogilvie, K. W., Helium abundance variations, J. Geophys. Res., 77, 3957, 1972.
- Ogilvie, K. W., and H. J. Zwaay, Hydrogen and helium velocities in the solar wind, Solar Phys., 24, 236, 1972.
- Ogilvie, K. W., Differences between the bulk speeds of hydrogen and helium in the solar wind, J. Geophys. Res., 80, 1135, 1975.
- Parker, E. N., Dynamics of the interplanetary gas and magnetic fields, Ap. J., 128, 604, 1958.
- Ryan, J. M., and W. I. Axford, The behavior of minor species in the solar wind, J. Geophys. Res., 41, 221, 1975.

- Spitzer, L., Jr., Physics of Full Ionized Gases, 2nd revised ed., Interscience, New York, 1962.
- Sturrock, P. A., and R. E. Hartle, Two-fluid model of the solar wind, Phys. Rev. Letters, 16, 628, 1966.
- Weber, E. J., Multi-ion plasmas in astrophysics I: General requirements for the existence of critical points, Astrophys. Sp. Sci., 20, 391, 1973a.
- Weber, E. J., Multi-ion plasmas in astrophysics II: Motion of Isothermal plasmas in a gravitational field, Astrophys. Sp. Sci., 20, 401, 1973b.
- Yeh, T., A three-fluid model of solar winds, Plan. Sp. Sci., 18, 199, 1970.
- Zinner, E., R. M. Walker, J. Borg and M. Maurette, Measurement of heavy solar wind particles during the Apollo 17 mission, Solar Wind Three, C. T. Russell, Ed., p. 27, 1974.

Propagation Velocities of Small Amplitude Disturbances in Multi-Ion Plasmas

E. J. Weber
Pure and Applied Science Division
Global Enterprises, Inc.
P. O. Box 49216
Tucson, AZ 85717, USA

Abstract

Since astrophysical plasmas behave in most aspects like fluids, they represent media through which small amplitude disturbances or signals are propagated. In the case of the expansion of such plasmas from a central stellar body as typified by the solar wind, the only steady state flow configuration possible is one in which the plasma moves "subsonically" in the vicinity of and "supersonically" at large distances from the central star. However, while these terms have well defined meanings in ordinary gas dynamics, they have to be defined in a special manner for plasmas, especially when they are made up of different ion species. In this paper it is shown how plasma Mach numbers and small signal propagation velocities can be defined consistently in such cases. For illustrative purposes, these properties are developed numerically for a two-ion isothermal plasma model.

1. INTRODUCTION

The great majority of theoretical models used to describe the steady state bulk motion of plasmas in interplanetary space are essentially hydrodynamic in nature. As such they treat these ionized gases as conducting fluids which are quasineutral electrically. The presence in such gases of electrons as well as ions produces effects which cannot be found in ordinary non ionized gases such as air. This was demonstrated clearly when the interplanetary motion of hydrogen was calculated using such a fluid model some twenty years ago. Yet while hydrogen represents the major ion constituent of the solar wind, it also contains other ions which can affect the overall flow regime. This might be even more so in the case of other central body problems where ions such as helium might exist in larger abundances. Thus it behooves the researcher to understand the effects other ions can have on the overall plasma behaviour.

During the past five to seven years, significant progress has been made in our attempts to understand these multi-ion plasmas and their motions. One has to remember that were it not for the effects produced by viscosity and by electric fields, each ion constituent, major or minor, would essentially travel through space completely on its own irrespective of the presence of the other ions. The most fundamental coupling between the different ion fluids is produced by the electric field in the plasma. In the theoretical models, however simplified they may be, this electric field results in the presence of all ion velocity gradient terms in the equations of motions of every ion species. It is also important to note that this coupling not only influences the bulk properties of the plasma, it has also a significant effect on the velocities with which small amplitude disturbances or signals are able to propagate in such media, as we will show below.

2. MATHEMATICAL RELATIONSHIPS

The model which we wish to utilize is a standard spherically symmetrical n-ion plasma model as described in the literature (e.g. Weber, 1972a). With it, we can show that the set of n coupled ion momentum equations are most conveniently represented in matrix notation as

$$\mathbf{A} \mathbf{x} = \mathbf{y} \quad (1)$$

from which, using Cramer's rule, we obtain immediately the solutions for the individual ion equations as

$$x_i = \frac{1}{u_i} \frac{du_i}{dr} = \frac{\sum_j A_{ij}}{|A|} \quad . \quad (2)$$

However, astrophysical plasmas expanding from a central body can have conditions where $|A|$, the determinant of A becomes zero and this will result in physically unacceptable solutions unless the numerator of Eq.2 vanishes identically at the same place. While it is probably quite obvious, we would nevertheless emphasize the fact that where singularities occur, they do so at the same point in all individual ion momentum equations.

Analogous situations are also encountered in ordinary gas dynamics. There we find that the denominator goes to zero whenever the bulk velocity of the fluid and its soundspeed, defined by $\sqrt{\gamma kT/m}$, become equal which implies that the Mach number M goes to unity

$$M = \frac{u}{\sqrt{\gamma kT/m}} = 1 . \quad (3)$$

For plasmas similar, but not identical, relationships exist at singularities. The reason for these differences is due to the fact that the electrons as well as the ions participate in the propagation of signals. This can readily been seen for a single ion gas, where at the singularity the ion Mach number M_i has to equal

$$M_i = 1 + \epsilon Z_i \sqrt{\gamma_e / \gamma_i} \quad (4)$$

where $\epsilon = T_e/T_i$ and the subscripts refer to the electrons and ions respectively. In deriving this equation we have neglected terms in u_e^2 as compared to terms in $\gamma_e kT_e/m_e$. For Parker's hydrogen ion model with $T_e = T_i$, $\gamma_e = \gamma_i$ and $Z_i = 1$, the singularity occurs when $M_i^2 = 2$. Thus the speed with which signals are transmitted in a hydrogen ion plasma is $\sqrt{2}$ times that of a neutral hydrogen gas. If we were dealing with ionized helium, M_i^2 would be equal to 3 at the singularity. The expression on the RHS of Eq.4 is the dimensionless "soundspeed" in the medium.

The mathematical relationships defining the points where singularities are found become progressively more complicated as the number of ions in the plasma increases. Already for a simple isothermal ($\gamma_e = \gamma_1 = \gamma_2 = 1$) two-ion model (Weber, 1972b) we find that

$$(M_1^2 - 1 - \epsilon Z_1 \frac{Z_1 n_1}{n_e}) (M_2^2 - 1 - \epsilon \frac{Z_2}{\alpha_2} \frac{Z_2 n_2}{n_e}) - \epsilon^2 \frac{Z_1 Z_2}{\alpha_2} \frac{Z_1 n_1}{n_e} \frac{Z_2 n_2}{n_e} = 0 \quad (5)$$

where $\alpha_2 = T_2/T_1$ and where the subscripts 1, 2 and e refer to hydrogen ions, helium ions and electrons, respectively. An infinite number of pairs of (M_1, M_2) exists for which this equation is satisfied as is indicated in Figure 1.

Quantities which seem to be analogous to the soundspeed as defined above are given by

$$\alpha^2 = 1 + \epsilon Z_1 \frac{Z_1 n_1}{n_e} \quad (6)$$

and

$$\beta^2 = 1 + \epsilon \frac{Z_2}{\alpha_2} \frac{Z_2 n_2}{n_e} \quad (7)$$

from which it is apparent that they again depend on the total number of particles and on their temperature. However, in contrast to the previously discussed single ion case, a condition where $M_1^2 = \alpha^2$ and/or $M_2^2 = \beta^2$ will not produce singularities. Thus α and β do not represent true signal propagation speeds in this two-ion plasma. It is quite easily shown that the same holds for general n-ion plasmas.

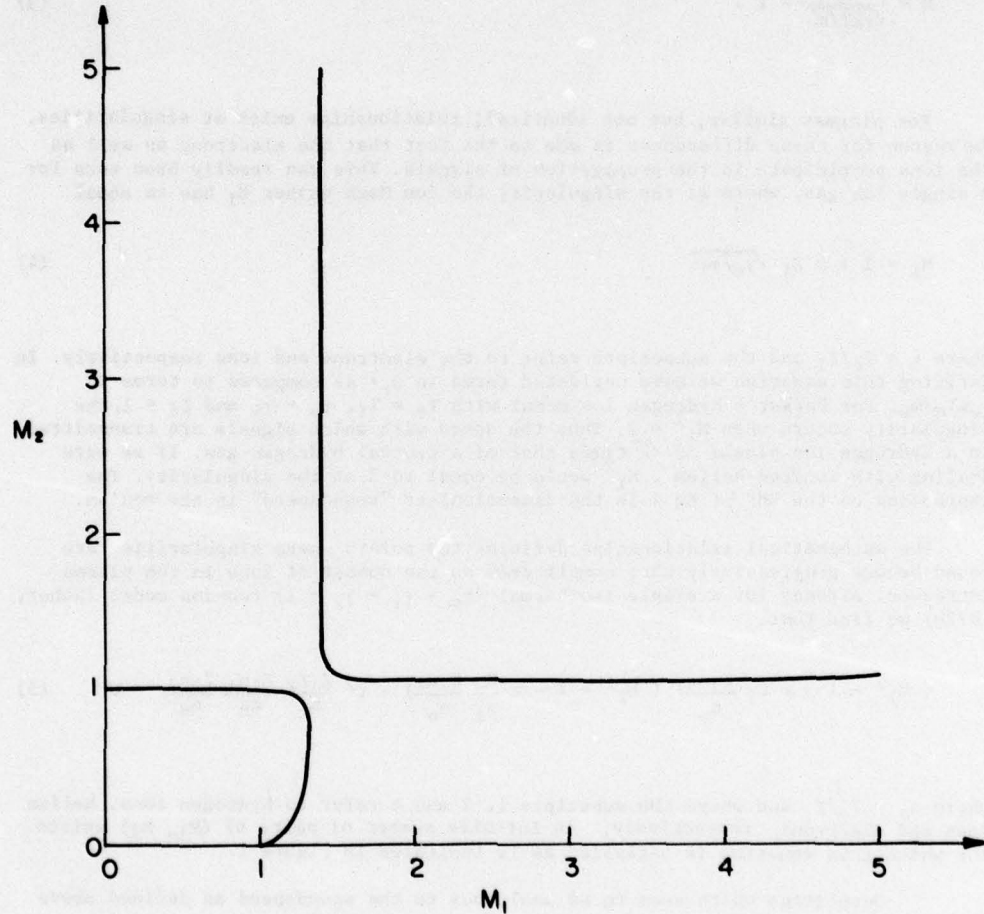


Figure 1. The loci of pairs of (M_1, M_2) for which the ion momentum equations possess a pole for a hydrogen-helium gas with $u_2 n_2 / u_1 n_1 = 0.05$, $T_1 = 10^6$, $T_e/T_1 = 1$, $T_2/T_1 = 4$. These values apply also to Figure 2.

3. PLASMA SOUNDSPEEDS

The important question which we have to face is whether n-ion plasmas have properties which can be attributed to them because they behave like single fluids or whether they are just a collection of n individual fluids each acting more or less as if it were alone. In particular, will small amplitude disturbances originating in any given ion species remain essentially confined to that constituent and will they travel with a speed characteristic of that ion? Alternatively, are they truly fluid disturbances which affect the overall plasma as a whole and are they propagated with a speed which is truly characteristic of the plasma itself and not of only some of its member ions? We could try to obtain an answer to this problem in many different ways, the most obvious being a perturbation analysis. However, there is a much quicker and more novel approach to obtain an answer. In this we rely on the general property of fluids that singularities occur only wherever their bulk speed equals their local soundspeed, the speed with which small amplitude disturbances or signals are transmitted or propagated. Mathematically this happens if and only if $|A|$ becomes zero. Yet as we have seen above, this does not occur when the individual ion flow speeds become equal to their respective soundspeeds. Thus the true soundspeeds of the plasma must be associated with the fluid as a whole. A detailed analysis of the matrix A indicates that a fluid Mach number M may be defined as the geometric mean of all the individual ion Mach numbers M_i

$$M = (M_1 \cdot M_2 \cdot M_3 \cdot M_4 \cdot M_5 \cdots \cdots \cdot M_n)^{1/n} \quad (8)$$

which then allows us to express the determinant of A very simply as

$$|A| = (M^2 - a^2)(M^2 - b^2)(M^2 - c^2) \cdots \cdots (M^2 - p^2) \quad (9)$$

where we have a total of n factors in this product. This expression is now in a form which implies that whenever the fluid Mach number is equal to either a , b , c , \cdots , p , the determinant of A vanishes identically, i.e. a singularity occurs. Thus the quantities a , b , c , \cdots , p are the real dimensionless soundspeeds of the medium.

As an example we wish to develop these quantities for the simple two-ion hydrogen-helium plasma which we have used to obtain Figure 1. In this case

$$M = (M_1 \cdot M_2)^{1/2} \quad (10)$$

and

$$|A| = (M^2 - a^2)(M^2 - b^2). \quad (11)$$

A few simple algebraic operations give us the following expressions for a and b

$$b^2 = \left(x^2 + y^2 - \left[(x^2 - y^2)^2 - 4 \epsilon^2 \frac{Z_1 Z_2}{\alpha_2} \frac{Z_1 n_1}{n_e} \frac{Z_2 n_2}{n_e} \right]^{1/2} \right) / 2 \quad (12)$$

and

$$a^2 = \left(x^2 y^2 - \epsilon^2 \frac{Z_1 Z_2}{\alpha_2} \frac{Z_1 n_1}{n_e} \frac{Z_2 n_2}{n_e} \right) / b^2 \quad (13)$$

where the quantities x and y are defined as

$$x^2 = \frac{M_2}{M_1} \alpha^2 \quad (14)$$

and

$$y^2 = \frac{M_1}{M_2} \beta^2 . \quad (15)$$

The functional behaviour of M, a and b, and of M₁ and M₂ for reference, are indicated in Figure 2. All numerical values have been obtained by means of the two-ion isothermal plasma model described by Weber (1972b). As all other such models, this particular one has great difficulties in predicting reasonable densities in the vicinity of the sun, i.e. for small values of h. This in turn gives rise to the sharp rise and rapid decline in the values of a and b, respectively, as we approach the solar corona. Yet while the actual numerical values for these quantities derived with this model are not too accurate in the coronal region, the general behaviour of these functions is correct and represents the soundspeeds in the plasma.

4. CONCLUSIONS

In this paper we recapitulated the physical significance of singularities in fluids. Their general property that they occur whenever the local bulk speed equals the speed of propagation of small amplitude disturbances in the medium allowed us to define "soundspeeds" in a consistent, logical fashion. These speeds, derived here heuristically, are real and their existence should be verified by analyzing suitable data from spaceprobes or from terrestrial laboratory experiments. The most important and significant result, though, is not that we were able to find definitions for these plasma properties, but that their existence allows us to gain additional insight into the nature and behaviour of multi-ion plasmas.

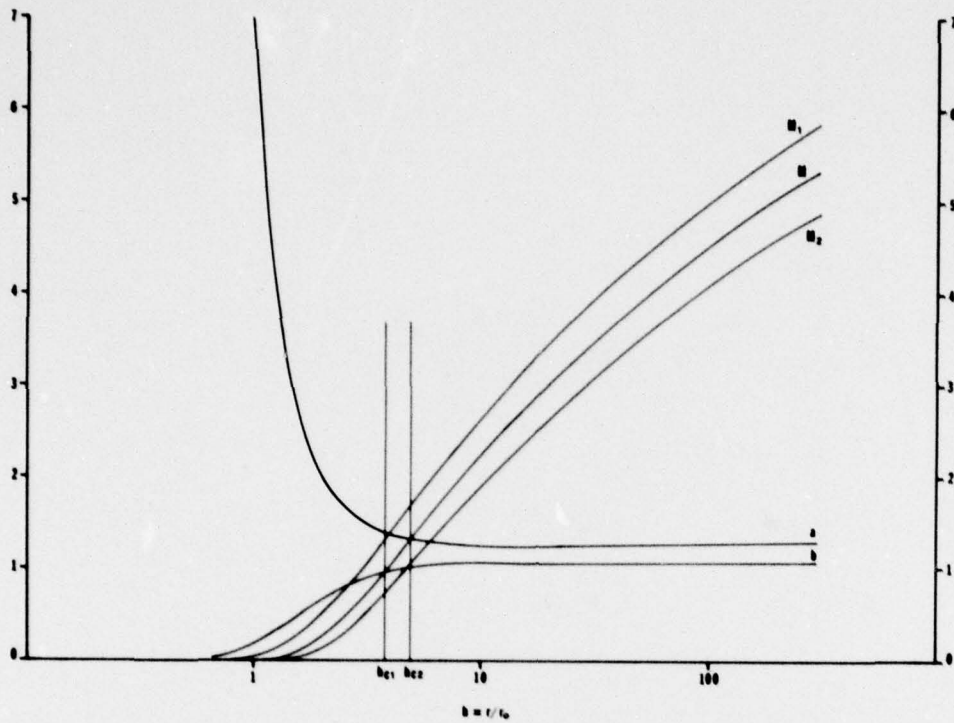


Figure 2. Mach numbers and soundspeeds in a two-ion isothermal plasma. Fine vertical lines indicate the locations of the two critical points. The reference distance r_0 equals 10^9 m.

References

- Weber, E. J., Multi-ion plasmas in astrophysics, I: General requirements for the existence of critical points, Astrophys. Space Sci., 20, 391, 1972a.
- Weber, E. J., Multi-ion plasmas in astrophysics, II: Motion of isothermal plasmas in a gravitational field, Astrophys. Space Sci., 20, 401, 1972b.
- Yeh, T., A three-fluid model of solar winds, Planet. Space Sci., 18, 199, 1970.

A Model for the Interaction of Solar Wind Streams

Raphael Steinitz and Menashe Eyni
Department of Physics
Ben Gurion University of the Negev
Beer Sheva, Israel

Abstract

Of the phenomena observed in proximity of the interaction region of plasma streams in the solar wind, we discuss here the heating of the plasma and the α -particle flow velocity u_α which is larger than the proton flow velocity u_p . We first mention the difficulties with previous models in accounting for the observations. As an alternative, we examine the consequences of a model in which one stream diffuses into the other. The heating of the interacting streams is thus in part due to compression, but to a larger extent is the result of mixing of different velocity streams. The model explains the details of the phase relationship between the observed compression and temperature. A quantitative estimate of $u_\alpha - u_p$ is obtained from the model with the interaction of streams having different helium abundance. Finally, it is proposed that the problem of the heating of the solar wind may be resolved by applying the model as developed in this paper.

1. INTRODUCTION

Early solar wind models predicted the rate of cooling of the plasma as it recedes from the sun. Since the expected cooling rates were not observed, heating mechanisms were incorporated in later models. It has been suggested that such heating may, for example, be the result of interaction of adjacent streams, which have different flow velocities. However, it appears that there is no general agreement as to the details of the heating mechanism (Coleman, 1968; Jokipii and Davis, 1969; Papadopoulos, 1973; Goldstein and Eviatar, 1973). Independent of the details of the models, there remain some general difficulties, which we discuss in the next section. Subsequently, a model is proposed which may circumvent the difficulties discussed previously.

Since it has been firmly established that He and H do sometimes indicate different flow velocities, our model is applied to this case, and numerical estimates are compared with observations. The model is further used to estimate the width of the heating zone connected with the interacting streams, and finally we show why cooling could not be found in the Mariner 2 data for velocities in excess of 500 km/sec.

2. SOME GENERAL DIFFICULTIES

2.1 The Asymmetry of the Temperature Profile

Examples of the heating mechanisms proposed for the interaction of streams, are turbulent heating as discussed by Goldstein and Eviatar (1973), and Papadopoulos (1973). According to these models, heating results from thermalization of waves generated at the interface of adjacent plasma flows. We first note that the density enhancement profile (Gosling et al, 1972, Figure 2) at the interface is approximately a symmetric function of time to within one day before and after phase zero (defined by maximum density). Therefore, if only heating modes as mentioned above are operative, the temperature profile is expected to be symmetric about phase zero. However, Figure 5 in the paper by Gosling et al (1972) clearly indicates that the temperature profile is not symmetric with respect to phase zero: from about 0.25 day prior to phase zero temperature rises steeply from 4×10^4 K to 12×10^4 K at phase zero, whence it continues to rise to 20×10^4 K attained at 0.5 day after phase zero. From then on, temperature drops slowly during the next three days. So it is difficult to see how the proposed mechanisms would account for the observed asymmetric temperature profile.

2.2 Velocity Differences Between He and H

Here we first discuss flow conditions associated with $(u_\alpha - u_p) > 0$, where u_α and u_p are respectively the He and H flow velocities. Furtheron we quote explanations for $(u_\alpha - u_p) > 0$ suggested in the literature, and argue that they are inadequate.

Asbridge et al (1976) show that $(u_\alpha - u_p) > 0$ is associated with the occurrence of double peaked velocity distributions (DPVD). Feldman et al (1973a,b) have suggested that the DPVD may be the result of interpenetrating plasma streams, due to inhomogeneities in bulk velocity of ions spiraling about the same magnetic line. Thus, $(u_\alpha - u_p) > 0$ can be understood in terms of (a) bulk velocity inhomogeneities, (b) higher He abundance in the faster stream (Asbridge et al, 1976). However, $(u_\alpha - u_p) > 0$ is also associated both with high velocity streams following density enhancements (Hirshberg et al, 1974), as well as with high velocity streams in general (Asbridge et al, 1976). Such high velocity streams seem to be stationary corotating structures (Gosling et al, 1972). Thus, $(u_\alpha - u_p) > 0$ can be a stationary condition associated with certain flow parameters, and would not be the result of passing bulk velocity inhomogeneities flowing along one and the same field line (i.e. originating from the same location close to the sun but at different times). Therefore, we propose in the next section a model which may resolve the difficulties mentioned here.

3. THE MODEL

We propose a model in which two adjacent plasma streams partially interpenetrate. Each stream is characterized by three flow parameters: the bulk velocity u , the proton density n_p and the He abundance $x = n_\alpha/n_p$, where n_α is the He particle density. It is suggested that the particles retain their flow characteristics during partial interpenetration. We regard the density enhancement regions, as discussed by Gosling et al (1972), as a realization of this model, where a fast, low density stream is overtaking a slow, high density stream. We now examine some consequences of this model.

3.1 Heating

In section 2.1 we mentioned that while the density profile at the interface of the two streams is symmetric within one day prior until one day after density maximum (Gosling et al, 1972, Figure 2), the temperature profile is not symmetric. We note first that the density enhancement on both sides of phase zero (= density maximum)

could be due to different processes: prior to phase zero, the density increase may be the result of true compression, while after phase zero - due to mixing of the two streams. Accordingly, heating prior to phase zero is essentially due to adiabatic compression, and after phase zero it is the result of mixing of two velocity populations.

Denoting by primes conditions during compression, we have

$$(T^1/T) = (n^1/n)^{2/3} \quad (1)$$

Taking $(n^1/n) = (20/6)$, we have $(T^1/T) = 2.23$, so that with an initial temperature $T = 4 \times 10^4$ K we obtain $T^1 = 9 \times 10^4$ K.

For the mixing process we have

$$(3/2)kT = (1/2)m_p(\Delta u/2)^2, \quad (2)$$

where the relative velocity is Δu and m_p is the proton's mass. With $\Delta u = 150$ km/sec we find $T = 2.3 \times 10^5$ K, which is the observed value. The results demonstrate that the temperature increase due to the mixing is in excess of the compressional heating, giving rise to an asymmetric temperature profile.

3.2 ($u_\alpha \cdot u_p$)

Hirshberg et al (1972) found that the He abundance (n_α/n_p) increases with proton velocity u_p . So we add now the assumption that the fast stream is characterized by a higher He abundance. We expect then that $(u_\alpha - u_p) > 0$ after phase zero, as is indeed observed (Hirshberg et al, 1974, Figure 5).

Let S and F denote the slow and fast streams, and M the mixed region. Before mixing we have $(u(S), n_p(S), n_\alpha(S))$ and $(u(F), n_p(F), n_\alpha(F))$, where we have assumed implicitly that the He bulk velocity is identical with the proton velocity prior to mixing.

After mixing,

$$u_p(M) = (n_p(S)u(S) + n_p(F)u(F))/(n_p(S) + n_p(F)), \quad (4)$$

$$u_\alpha(M) = (n_\alpha(S)u(S) + n_\alpha(F)u(F))/(n_\alpha(S) + n_\alpha(F)), \quad (5)$$

with some algebra we obtain

$$\frac{u_\alpha(M)}{u_p(M)} = \frac{1 + (u(F)/u_p(M))z}{1 + z}, \quad (6)$$

where

$$z = \frac{n_p(F)}{n_p(S) + n_p(F)} \cdot \left(\frac{n_\alpha(F)}{n_p(F)} \cdot \frac{n_p(S)}{n_\alpha(F)} - 1 \right), \quad (7)$$

and finally

$$u_p(M) = u(F) - \frac{n_p(S)}{n_p(S) + n_p(F)} \cdot (u(F) - u(S)). \quad (8)$$

Clearly $u(F) > u_p(M)$, so that from Eq.(6) it follows that $u_\alpha(M) > u_p(M)$.

Taking from Gosling et al (1972) $u(S) = 325$ km/sec, $n_p(S) = 6$; $u(F) = 475$ km/sec, $n_p(F) = 4$, and from Hirshberg et al (1972) the corresponding values for the abundance $(n_\alpha(S)/n_p(S)) = 0.030$; $(n_\alpha(F)/n_p(F)) = 0.045$, we find $u_\alpha(M) = 1.038 u_p(M)$. The experimental values (Hirshberg et al, 1974, Figure 5) are: $u_\alpha(M) - u_p(M) = 15$ km/sec; $u_p(M) = 450$ km/sec, so that $u_\alpha(M) = 1.033 u_p(M)$.

Thus we have shown that the asymmetric temperature profile can be obtained, with a quantitative estimate of the heating. Moreover, the model yields in a simple manner a numerical estimate for $u_\alpha \approx u_p$.

4. FURTHER COMMENTS

4.1 Width of Heating Zone

The width of the heating zone (neglecting compressional heating) is determined by the width of the velocity mixing zone. This, in turn, will depend on the slow and fast radial flow velocities, the heliocentric distance r and the distance r_0 , where the two streams first intersect. In a plane polar coordinate system (r, φ) in the ecliptic plane, corotating at angular velocity Ω with the sun, a flow line is described by

$$r - r_0 = \left(\frac{u}{\Omega}\right)(\varphi - \varphi_0), \quad (9)$$

where u is the radial flow velocity.

The angular width $\Delta\varphi$ of the mixing region is therefore

$$\Delta\varphi = \Omega(r - r_0) \left(u(S)^{-1} - u(F)^{-1} \right). \quad (10)$$

Here $u(S)$ and $u(F)$ are the slow and fast flow velocities. The time Δt spent by a satellite in the mixing zone, moving around the sun with angular velocity Ω^1 , is:

$$\Delta t = \Delta\varphi / (\Omega - \Omega^1). \quad (11)$$

Assuming $r_0 \ll r$, and taking $u(S) = 325$ km/s, $u(F) = 500$ km/s, we find at 1 AU that typically $\Delta t \approx 2$ days. This compares favorably with Figure 5 of the paper by Gosling et al (1972). The estimate for Δt could in fact be an underestimate, since diffusion effects were neglected.

4.2 High Velocity and Heating

Large velocity differences ($u_\alpha - u_p$), between He and H, may be taken as indicators for mixing of velocity populations with large velocity differences. Such mixing will manifest itself as strong heating.

Asbridge et al (1976, Figure 17) indicate that $(u_\alpha - u_p)$ increases monotonically with proton velocity u_p . One may therefore expect that strong heating is associated with high velocity streams. This may be the reason for the failure to detect the cooling of solar wind plasma with heliocentric distance, for flow velocities in excess of 500 km/sec (Eyni and Steinitz, 1977).

5. CONCLUSION

To account for the different velocities of He and H that are sometimes observed, interpenetration of different velocity and abundance populations has been suggested before by Asbridge et al (1976), but there it has been assumed explicitly that the two interpenetrating streams spiral along the same magnetic line. In our model, this topological constraint has been eliminated altogether, enabling us to explain some of the finer details associated with density enhancement regions. However, it is not necessary to confine oneself to the regions where population mixing is more or less evident. If $u_\alpha \neq u_p$ is taken as an indicator for mixing of different velocity and abundance populations, then it follows that mixing is often associated with high velocity streams. Thus heating of the plasma may be the result of population mixing, even in

those cases in which the mixing itself is not obvious. This may explain, as mentioned above, why cooling has not been detected in the Mariner 2 data for high velocity streams. Moreover, all this suggests the possibility that the heating mechanism one is looking for quite in general is simply the mixing of velocity populations.

References

- Asbridge, J.R., S.J. Bame, W.C. Feldman, and M.D. Montgomery, Helium and hydrogen velocity differences in the solar wind, J. Geophys. Res., 81, 2719-2727, 1976.
- Coleman, P.J., Jr., Turbulence, viscosity and dissipation in the solar wind plasma, Astrophys. J., 153, 371-388, 1968.
- Eyni, M., and R. Steinitz, Mariner 2 data: cooling of the solar wind protons, Bull. Israel Phys. Soc., 23, 110, 1977.
- Feldman, W.C., J.R. Asbridge, S.J. Bame, and M.D. Montgomery, Double ion streams in the solar wind, J. Geophys. Res., 78, 2017-2027, 1973a.
- Feldman, W.C., J.R. Asbridge, S.J. Bame, and M.D. Montgomery, On the origin of solar wind proton thermal anisotropy, J. Geophys. Res., 78, 6451-6468, 1973b.
- Goldstein, M.L., and A. Eviatar, Turbulent heating of colliding streams in the solar wind, Astrophys. J., 179, 627-636, 1973.
- Gosling, J.T., A.J. Hundhausen, and V. Pizzo, Compressions and rarefactions in the solar wind: Vela 3, J. Geophys. Res., 77, 5442-5454, 1972.
- Hirshberg, J., J.R. Asbridge, and D.E. Robbins, Velocity and flux dependence of the solar-wind helium abundance, J. Geophys. Res., 77, 3583-3588, 1972.
- Hirshberg, J., J.R. Asbridge, and D.E. Robbins, The helium component of solar wind velocity streams, J. Geophys. Res., 79, 934-938, 1974.
- Jokipii, J.R., and L. Davis, Jr., Long-wavelength turbulence and heating of the solar wind, Astrophys. J., 156, 1101-1106, 1969.
- Papadopoulos, K., Electrostatic turbulence at colliding plasma streams as the source of ion heating in the solar wind, Astrophys. J., 179, 931-938, 1973.

New Evaluation of Spacecraft Solar Wind Plasma Data

Menashe Eyni and Raphael Steinitz
Department of Physics
Ben Gurion University of the Negev
Beer Sheva, Israel

Abstract

Spacecraft data are re-examined in order to find possible relationships between flow parameters of the solar wind, such as temperature, flow velocity and density. To reduce the fluctuations, Mariner 2 data were smoothed by averaging over time intervals of one to five days. We obtained 80 sets of averaged densities n , averaged velocities u and averaged temperatures T . Plotting $\log(n)$ against $\log(u)$ we find that the scattered points are bounded on one side by an envelope $\log(n) \approx 3 \log(u) + \text{const.}$ A similar plot for Vela 3 spacecraft data yields a larger dispersion, which might be attributed to the proximity of the spacecraft to the earth's magnetosphere.

In examining the relation between T and u we find that the points in a $\ln(T)$ vs. $\ln(u)$ plot cluster around the straight line $\ln(T) = 2 \ln(u) + \text{const.}$, so that $T \propto u^2$. Moreover we find in the same plot that (a) the dispersion of $\ln(T)$ for

$u > 500$ km/sec is larger than for $u < 500$ km/sec, and (b) that the data exhibit cooling of solar wind protons with heliocentric distance, for $u < 500$ km/sec. The different behaviour for high and low velocities is further discussed in another paper in this conference (Steinitz and Eyni, 1977).

1. INTRODUCTION

In establishing empirical relations between flow parameters of the solar wind, one encounters the difficulty that large fluctuations are present in the data. Such fluctuations may mask the relations one is looking for. This prompted us to re-examine anew spacecraft data, after properly smoothing the data.

There appears to be some disagreement among various authors as to the relationship the data indicate. For example, Neugebauer and Snyder (1966) find a relation between proton density n and flow velocity u , while Hundhausen et al (1970) find a different result. This controversy has been further discussed by Formisano et al (1974).

According to theoretical models one expects that the solar wind plasma cools as it recedes from the sun, yet Neugebauer and Snyder (1966) could not confirm this prediction. Accordingly, we describe in the next section the preparation of the data for our analysis, which is then discussed in the subsequent sections.

2. DATA PROCESSING

For our analysis we used the Mariner 2 data published by Neugebauer and Snyder (1966) and the Vela 3 data published by Bame et al (1970). These data were averaged over time intervals of about one to five days, where the intervals were chosen so as to reduce the variance without losing too much information. In this manner we obtained for Mariner 2 80 sets of averaged (n, u, T) data, covering 4 months, and 90 sets of (n, u, T) data, averaged from Vela 3 observations, and covering about 15 months. Here n and u are the proton density and flow velocity respectively, and T is the proton temperature.

3. THE (n, u) RELATION

Figure 1 is a plot of $\log(n)$ against $\log(u)$ for the Mariner 2 data. It can be seen that the points are bounded on one

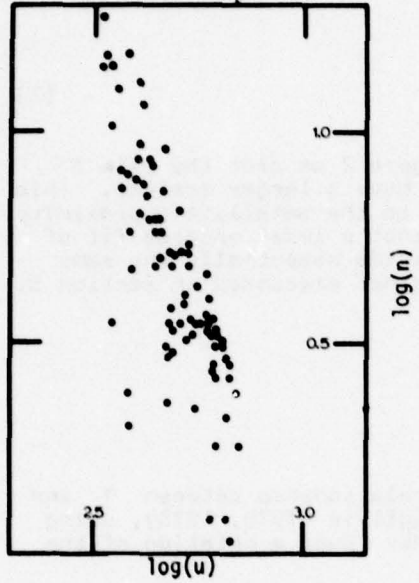


Figure 1. Mariner 2: n is the particle density (cm^{-3}) normalized to its value at 1 AU, and u is the flow velocity (km/s)

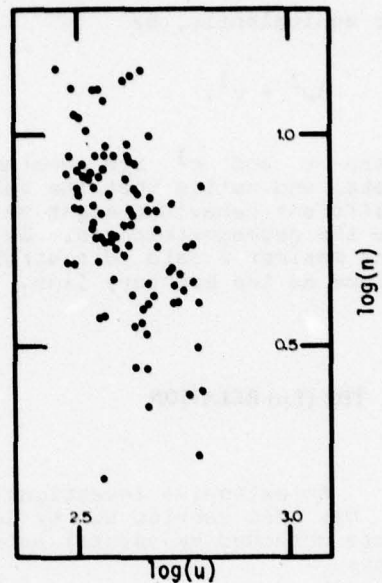


Figure 2. Vela 3: n is the particle density (cm^{-3}) and u is the flow velocity (km/s)

side by the line

$$\log(n) = -3 \log(u) + c, \quad (1)$$

or equivalently, by

$$nu^3 = c^1. \quad (2)$$

Here c and c^1 are constants. In Figure 2 we plot the Vela 3 data, and notice that the Vela 3 points have a larger scatter. This different behaviour might be attributed to the satellite's proximity to the geomagnetosphere. We also note that a least squares fit of the Mariner 2 data to a straight line yields essentially the same slope as the boundary line. This is further discussed in section 5.

4. THE (T,u) RELATION

An extensive investigation of the relationship between T and u has been carried out by Burlaga and Ogilvie (1970, 1973), using data obtained by several satellites. They found a relation of the form

$$\sqrt{T} = au + b, \quad (3)$$

where a and b are constants. Burlaga and Ogilvie (1973) also examined Mariner 2 data but concluded that the uncertainties in this case are larger than the scatter of other satellite data.

In Figure 3 we have plotted $\ln(T)$ against $\ln(u)$ for the smoothed Mariner 2 data. It appears that the straight line fit

$$\ln(T) = 2 \ln(u) + \text{const.} \quad (4)$$

is a good approximation. It follows that

$$T = Ku^2 \quad (5)$$

where K is a constant.

We have also indicated in Figure 3 the points measured at heliocentric distance $r < 1.25 \times 10^8$ km (circles) and $r > 1.3 \times 10^8$ km (triangles). For the velocity range below $u = 500$ km/sec (indicated in the figure by long bars) we find that

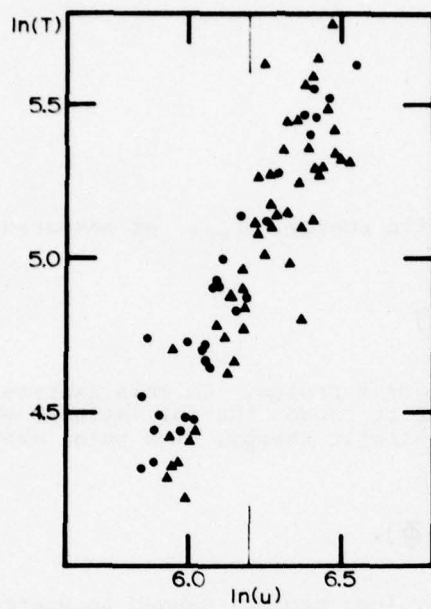


Figure 3. Mariner 2: the temperature T is in 10^3K , and u is the flow velocity (km/s). The bars correspond to $u=500\text{km/s}$. Circles for distances $r < 1.25 \times 10^8 \text{km}$ and triangles for $r > 1.3 \times 10^8 \text{km}$.

in general the triangles lie below the circles, indicating that velocities below 500 km/sec exhibit cooling of the plasma with increasing heliocentric distance. A detailed regression analysis of this cooling has already been reported (Eyni and Steinitz, 1977).

5. DISCUSSION

5.1 Energy Flux

The flux of kinetic energy, F_{KE} , as measured by a satellite, is given by

$$F_{KE} = (nu)(mu^2/2) \quad (6)$$

where m is the mass of a proton. In this expression we have neglected the flux due to random thermal motions, which is less than 5% of the total kinetic energy. The total mechanical flux, F_T , is given by

$$F_T = nu (mu^2/2 + \Phi). \quad (7)$$

Here Φ is the energy (per proton) needed to overcome gravitation. Mariner 2 data show a tendency towards constant nu^3 (c.f. section 3 and Figure 1), which is less evident in the Vela 3 data. With this tendency, that is with constant kinetic energy flux, we see that the total flux supplied by the sun decreases with increasing velocity. We have used the typical amplitude in the Mariner 2 data along the boundary line (Figure 1) to evaluate the typical variations in total mechanical flux close to the sun. It is of interest to note that these variations are of the same magnitude as typical variations in the UV solar flux.

5.2 Masking by Interference Effects

In section 4 we mentioned that the Mariner 2 data exhibited cooling for $u < 500$ km/sec. In another paper in this conference (Steinitz and Eyni, 1977) it is argued that the interaction of high velocity streams with other streams manifests itself in the form of heating. Thus it is perhaps not surprising that we could not find the plasma cooling with heliocentric distance in the high velocity data. Interaction of streams may also account for the larger dispersion in Figure 3 present for $u > 500$ km/sec.

6. CONCLUDING REMARKS

The foregoing analysis demonstrates that it may be useful to average over sufficiently long time intervals, and thus reduce the noise in the data. Also, we found the log-log representation to be efficient in exhibiting the relationships between the various flow parameters and suggest their use in future analyses.

References

- Bame, S.J., J.R. Asbridge, H.E. Felthauser, H.E. Gilbert, A.J. Hundhausen, D.M. Smith, I.B. Strong, and S.J. Sydoriak, A compilation of Vela 3 solar wind observations, 1965 to 1967, Rep. LA-4536, vol.1, Los Alamos Sci. Lab., Los Alamos, New Mexico, 1970.
- Burlaga, L.F., and K.W. Ogilvie, Heating of the solar wind, Astrophys. J., 159, 659-670, 1970.
- Burlaga, L.F., and K.W. Ogilvie, Solar wind temperature and speed, J. Geophys. Res., 78, 2028-2034, 1973.
- Eyni, M., and R. Steinitz, Mariner 2 data: cooling of the solar wind protons, Bulletin of the Israel Physical Society, 23, 110, 1977.
- Formisano, V., G. Moreno, and E. Amata, Relationship among the interplanetary plasma parameters: Heos 1, December 1968 to December 1969, J. Geophys. Res., 79, 5109-5117, 1974.
- Hundhausen, A.J., S.J. Bame, J.R. Asbridge, and S.J. Sydoriak, Solar wind properties: Vela 3 observations from July 1965 to June 1967, J. Geophys. Res., 75, 4643-4657, 1970.
- Neugebauer, M., and C.W. Snyder, Mariner 2 observations of the solar wind, I. Average properties, J. Geophys. Res., 71, 4469-4483, 1966.
- Steinitz, R., and M. Eyni, A model for the interaction of solar wind streams, in Contributed Papers to the Study of Traveling Interplanetary Phenomena/1977, edited by M. A. Shea, D. F. Smart, and S. T. Wu, AFGL-TR-77-0309, p. 101, Air Force Geophysics Laboratory, Bedford, Massachusetts, 1977.

Discussion

Intriligator: I agree that it would be very interesting to look for cooling in the solar wind between the sun and 1 AU. However, because of the problems in sorting out temporal and spatial variations it is preferable to use simultaneous data from at least two locations (preferably radially aligned). For example, compare the Helios data (obtained between 0.3 and 1 AU) with the HEOS or IMP data at 1 AU.

Eyni: Yes, I fully agree that it will be useful to obtain simultaneous data from two locations to substantiate our finding that cooling is present in the Mariner 2 data.

The Interaction Between the Solar Wind and the Interstellar Hydrogen Beyond the Heliosphere

P. W. Blum and R. Lang
Institut für Astrophysik und
extraterrestrische Forschung
Universität Bonn
5300 Bonn, FRG

Abstract

Solar wind protons and interstellar neutral hydrogen atoms may interact in the solar system via charge-exchange reactions. Accordingly, three categories of interstellar hydrogen atoms in interplanetary space can be defined: (a) H-atoms which did not take part in any charge-exchange reaction, (b) H-atoms which have undergone a charge-exchange reaction within the heliosphere, and (c) H-atoms which have suffered a charge-exchange reaction with the decelerated solar wind protons beyond the heliosphere. The latter type of H-atoms amounts in interplanetary space to about 10% of the H-atoms of type (a). Interplanetary H-atoms scatter the solar Lyman- α radiation. From the distribution of the scattered radiation we may infer the distribution of the H-atoms in interplanetary space. Previously, difficulties have arisen in explaining the Lyman- α radiation that is observed from the so-called downwind cone of the interstellar wind. Our model, which takes into account the presence of H-atoms of type (c), offers a better interpretation of the observational results obtained from space probes and satellites.

1. INTRODUCTION

In recent years satellite measurements of interplanetary Lyman- α backscatter radiation have been carried out repeatedly. Several models were developed to explain the measured intensity distributions. Blum and Fahr (1970) have shown that the observed radiation is caused mainly by neutral hydrogen of the interstellar gas entering the solar system. When approaching the sun, these neutral hydrogen atoms are experiencing ionizational and gravitational effects. Due to their low velocity relative to the sun, absorption of solar Lyman- α radiation can take place. The observed Lyman- α backscatter radiation in interplanetary space is explained well by the neutral hydrogen density distribution. An exception is the radiation which originates in the direction opposite to the entering particles. One would expect only small radiation intensities on the downwind side of the sun if, on the average, the radiation pressure on the hydrogen particles is larger than the solar gravitation. Such a ratio of radiation pressure to gravitation is expected. Therefore, although hardly any radiation is anticipated, more than 10% of the maximum intensity is observed on the downwind side. Several explanations have been suggested, e.g. radiation pressure effects, high temperatures of the interstellar gas, radiation of galactic origin, and multiple scattering of Lyman- α photons. Since all of these explanations are contradictory to some extent, they are not satisfactory.

2. CHARGE EXCHANGE BETWEEN SOLAR WIND PROTONS AND INTERSTELLAR HYDROGEN

Some of the neutral hydrogen atoms entering the solar system are interacting with solar wind protons. In a charge-exchange process neutral hydrogen atoms of solar wind proton velocity are being created. Patterson et al. (1963) conjectured that these hydrogen atoms produced by charge exchange contributed most to the observed Lyman- α backscatter radiation. It was shown subsequently, though, that the Lyman- α backscatter radiation is produced mainly by entering interstellar hydrogen. Thus the backscatter radiation of hydrogen atoms produced by charge exchange was considered negligible (Hundhausen, 1968; Axford, 1972; Holzer, 1972). This assumption, however, seems to be correct only if one looks exclusively at charge-exchange processes taking place within the heliosphere. That is to say, since the properties of the hydrogen atoms mainly depend upon their point of origin, one has to distinguish between particles produced inside and outside the heliosphere, respectively. It will be shown in this paper that those hydrogen atoms produced outside the heliosphere in a charge exchange with protons are an additional source of Lyman- α radiation. As the pattern of this Lyman- α component is almost isotropic, it will also be observed from the downwind direction.

According to the interaction of interstellar neutral hydrogen with solar protons one can distinguish three "types" of hydrogen atoms observed in interplanetary space:

(a) The entering hydrogen atoms experience no charge exchange with solar wind protons. Their velocities do not change appreciably. Their density is altered by focusing and ionization processes (Blum et al., 1975).

(b) The entering hydrogen atoms experience charge exchange processes with fast solar protons inside the heliosphere. They assume the proton velocities of about 400 km s^{-1} and move radially away from the sun (Figure 1). Their maximum density is about 1% of the particles described in (a).

(c) The entering hydrogen atoms experience a charge exchange with strongly decelerated solar protons outside the heliosphere. They assume the proton velocities, which in this case are between 200 km s^{-1} and 20 km s^{-1} . Their maximum density is about 10% of the particles described in (a) (Figure 2).

3. CHARGE EXCHANGE BEYOND THE SHOCK FRONT

Due to the width of the solar Lyman- α line (almost 1\AA) and the low velocities of the hydrogen atoms produced beyond the shock front (particles of "type" (c)) these atoms can scatter the solar Lyman- α radiation. The velocities of the hydrogen particles which underwent charge exchange are composed of the solar wind bulk velocity and the proton thermal velocities (Lang, 1977). They are equivalent to the proton velocities depicted in Figure 3 as a function of heliocentric distance. The velocity vector directions of the neutral particles are undetermined due to the inclusion of the thermal velocities. In principle any direction is possible, since the isotropic proton thermal velocities are higher than the bulk velocity. Due to the superimposed solar wind plasma velocity in the radial direction, however, higher velocities of the produced neutral particles are found in the direction of the positive radius vector. Figure 3 shows that if the ratio μ of radiation pressure to gravitation is $1/3$, the proton velocity in the upwind direction ($\theta = 1^\circ$) is larger than in the downwind direction ($\theta = 179^\circ$). Under the condition of $\mu > 1$ (dominant radiation pressure) a wide region free of slow hydrogen atoms is formed in the downwind direction. In this case the solar wind is decelerated considerably less in the downwind direction, and the proton velocities there always remain higher than in the upwind direction. The proton velocities in the upwind direction are almost identical for $\mu = 1/3$ and $\mu = 5/3$, and thus only the curve for $\mu = 1/3$ is shown in Figure 3.

The hydrogen atoms produced by charge exchange therefore will move away from their origins in random directions (Figure 2). Some of these atoms that impinge on the heliosphere from all directions will traverse it. Since their velocities are of the same magnitude as those of the slow hydrogen atoms, they also contribute to the Lyman- α backscatter radiation. Their density is therefore of special interest. In Figure 2 it is shown how the "fast" hydrogen atom density is produced by particles originating outside the heliosphere (Lang, 1977). Displayed in this figure are a heliosphere assumed to be elliptical (Bird and Fahr, 1973), the upwind direction of the interstellar gas, and the location \vec{r} where the density is to be determined. The position of \vec{r} can be located inside or outside the heliosphere.

**CHARGE EXCHANGE WITHIN
HELIOSPHERE**

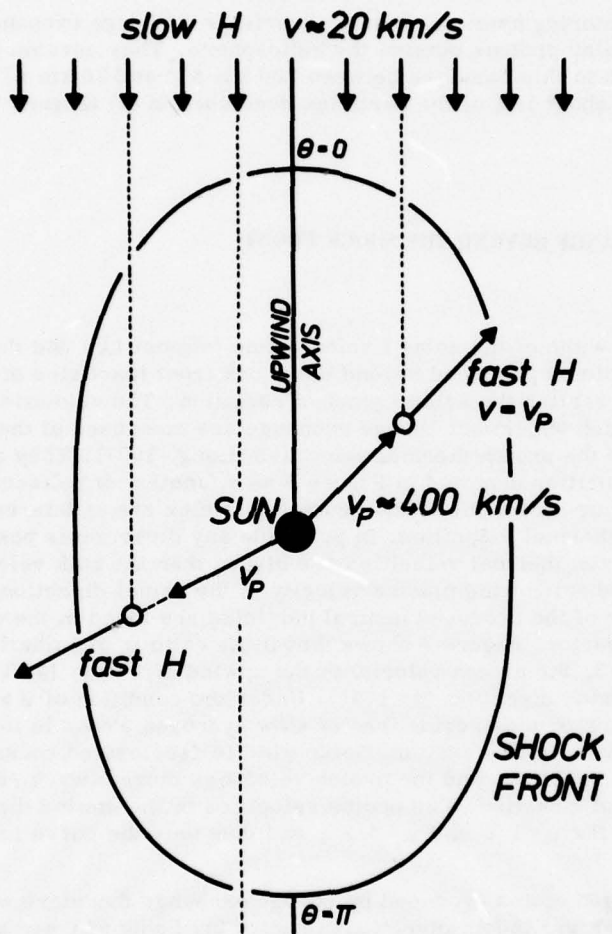


Figure 1. Schematic Representation of the Interaction between Interstellar Hydrogen Atoms Entering the Heliosphere and Solar Wind Protons. This is the charge-exchange process which occurs inside the shock front and produces fast hydrogen particles of "type" (b).

CHARGE EXCHANGE BEHIND HELIOSPHERE

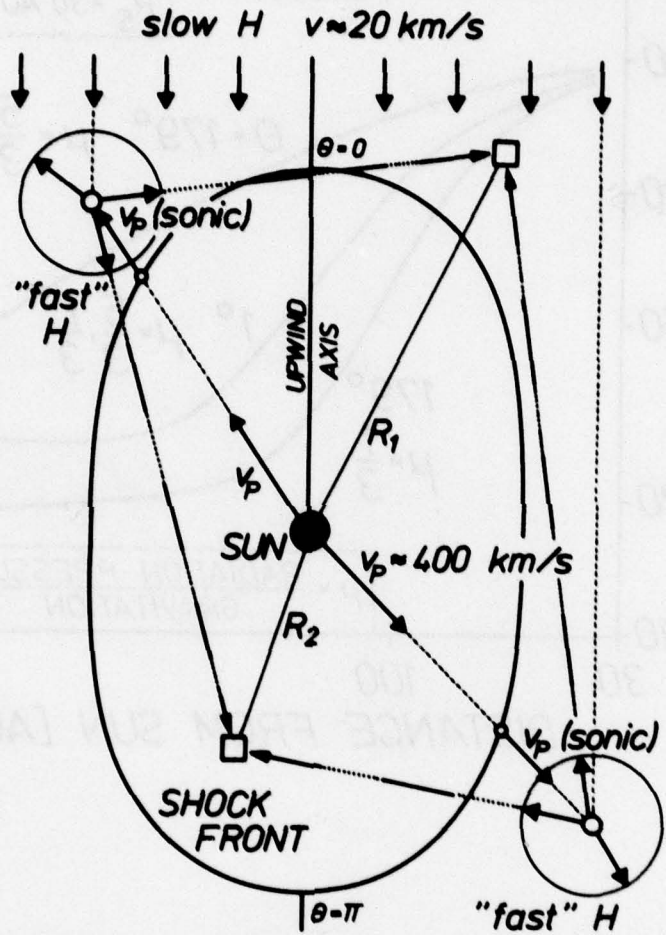


Figure 2. Schematic Representation of the Interaction between Interstellar Hydrogen Atoms and Solar Wind Protons. This is the charge-exchange process which occurs outside the shock front and produces "fast" hydrogen particles of "type" (c).

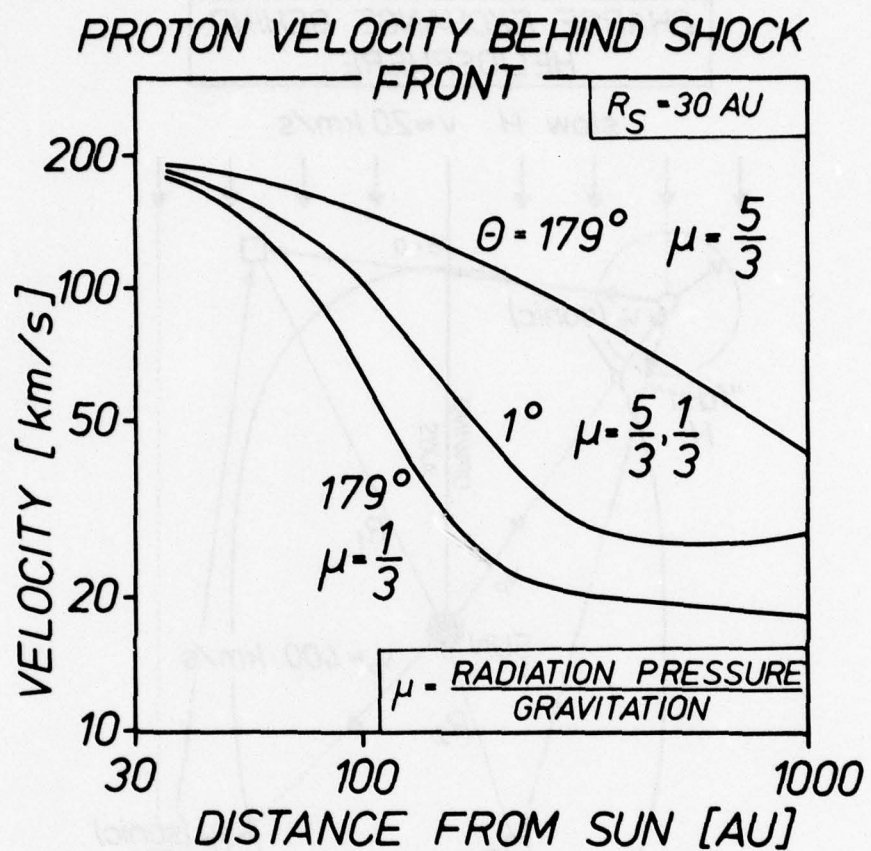


Figure 3. Dependence of the Proton Velocity Beyond the Shock Front on Heliocentric Distance. The proton velocity consists of a solar wind velocity component and a proton thermal velocity component.

Figure 4 shows the computed density values of "fast" hydrogen versus heliocentric distance. This is to demonstrate the influence of radiation pressure and of the distance between the sun and the shock front on the density. An examination of only one heliocentric direction is sufficient; the downwind direction ($\theta = 180^\circ$) has been selected. The distance between the shock front and the sun was taken to be 30 AU and 60 AU, respectively. Three values of the ratio μ of radiation pressure to gravitational attraction have been chosen: $\mu = 1/3$, $\mu = 1$, and $\mu = 5/3$. Figure 4 thus shows six curves. It is obvious from these curves that radiation pressure affects the density of the "fast" hydrogen only very little. The location of the shock front, however, cannot be neglected. The density increases for smaller heliospheric shock front distances. Consider the case of a small heliosphere. Here charge-exchange processes are taken into account in regions where the solar wind proton density is still high. Also the volume contributing to the density of the "fast" hydrogen is larger. Both effects become negligible at large heliocentric distances; thus the curves for different shock front distances tend to converge there.

4. LYMAN- α BACKSCATTER RADIATION

The Lyman- α backscatter radiation has been calculated in the downwind direction in Figure 4 (Lang, 1977). Radiation pressure and gravitation were of equal magnitude, i.e. the particles moved on straight lines. A Lyman- α backscatter radiation intensity of about 160 Rayleigh resulted from an elliptical shock front main axis 60 AU in length. Enlargement of the main axis by a factor of 2 reduced the intensity by 50%. The Lyman- α backscatter radiation is thus very sensitive to the location of the shock front, analogous to the "fast" hydrogen atom density. Calculated intensities were in the range of 40 to 160 Rayleigh, while measured Lyman- α intensities in the downwind direction were between 50 and 200 Rayleigh (Fahr, 1974). Table 1 compares observed intensities to possible contributions by other sources of Lyman- α backscatter radiation. The Lyman- α backscatter radiation observed in the downwind direction thus can be explained by the presence of "fast" hydrogen atoms. Slow hydrogen will produce Lyman- α backscatter radiation in this region only if the radiation pressure is smaller than the gravitation or if the interstellar gas is very hot.

Combined density distributions of particles of "type" (a) and "type" (c) result in a distribution of the Lyman- α backscatter radiation that is in accordance with the existence of an interplanetary shock front. This distribution does not contradict any observed Lyman- α backscatter radiation intensities and thus avoids some of the difficulties of other models.

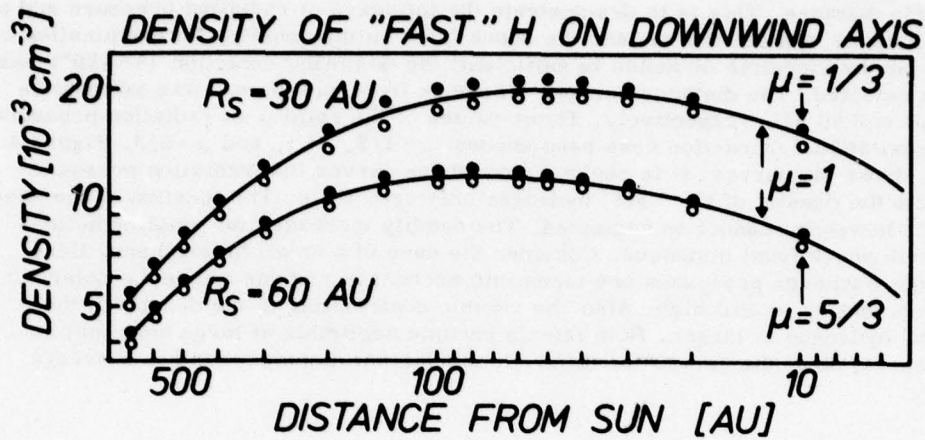


Figure 4. Density of "Fast" Hydrogen in the Downwind Direction versus Heliocentric Distance, given for Shock Front Locations at 30 AU and 60 AU Distance, respectively. Different ratios of radiation pressure to gravitational attraction are taken into account.

Table 1. Comparison of Possible Contributions by Different Sources to Lyman- α Backscatter Radiation. The observed intensities are also included.

		<i>Ly-α-Radiation Downwind Direct.</i>	<i>Velocity [km/s]</i>
<i>Observation</i>		<i>50 - 200 R</i>	
<i>possible contr. to observ., u₂₁</i>			
<i>slow H</i>		<i>0 R</i>	~ 20
<i>fast H</i>		<i>0 R</i>	~ 400
" <i>fast</i> " H		<i>40 - 160 R</i>	<i>20 - 200</i>
<i>Galactic Rad.</i>	<i>probably none</i>		

References

- Axford, W.I., The interaction of the solar wind with the interstellar medium, in Solar Wind, NASA SP-308, p. 609, 1972.
- Bird, M.K., and H.J. Fahr, The effect of the interstellar magnetic field on the size and shape of the heliosphere, preprint, Astronomical Institutes, University of Bonn, 1973.
- Blum, P.W., and H.J. Fahr, Interaction between interstellar hydrogen and the solar wind, Astron. Astrophys., 4, 280, 1970.
- Blum, P.W., J. Pfleiderer, and C. Wulf-Mathies, Neutral gases of interstellar origin in interplanetary space, Planet. Space Sci., 23, 93, 1975.
- Fahr, H.J., The extraterrestrial UV-background and the nearby interstellar medium, Space Sci. Rev., 15, 483, 1974.
- Holzer, T.E., Interaction of the solar wind with the neutral component of the interstellar gas, J. Geophys. Res., 77, 5407, 1972.
- Hundhausen, A.J., Interplanetary neutral hydrogen and the radius of the heliosphere, Planet. Space Sci., 16, 783, 1968.
- Lang, R., Dichteverteilung und Lyman-Alpha-Streustrahlung des durch Ladungsaustausch mit Sonnenwindprotonen entstandenen Wasserstoffs, Ph.D. Thesis, University of Bonn, 1977.
- Patterson, T.N.L., F.S. Johnson, and W.B. Hanson, The distribution of interplanetary hydrogen, Planet. Space Sci., 11, 767, 1963.

Discussion

Wallis: I refer to the figure (Wallis and Dryer, Astrophys. J., 205, 895, 1976) which shows the heliosphere embedded in the larger region of interstellar plasma flowing around the heliospheric obstacle. The neutral interstellar hydrogen undergoes charge exchanging collisions in this denser and cooler plasma region and would surely result in an additional source of neutral hydrogen atoms.

Blum: The process described in the paper of Wallis and Dryer is certainly possible and might be responsible for some heating of the interstellar gas that penetrates into the solar system. But in my opinion it is unlikely that it is a dominant process that radically changes the properties of the interstellar gas. This view is supported by the observations of the interplanetary scattered resonance radiation which clearly indicates that there exists a well-defined bulk velocity of the interstellar gas that penetrates into the solar system. If the majority of the H-atoms suffered one or more charge-exchange reactions with the deflected ionized component of the interstellar gas, it would mean that the interstellar neutrals would have lost all information on their original bulk velocity, similar to the state of the ionized component of the interstellar gas according to the hypothesis of the above mentioned paper by Wallis and Dryer. But the clearly defined velocity vector of the interstellar neutrals, as deduced

by the Lyman-alpha and He-584 Å radiation, shows that this is not the case.

Bird: How does the contribution from the "fast" hydrogen atoms to the Lyman-alpha backscatter radiation vary with your assumed distance to the shock front?

Blum: The nearer the shock front is to the sun, the more "fast" hydrogen atoms there are that reach regions near the sun. This is also seen in the figure where the density of fast hydrogen atoms on the downwind axis is shown as a function of the ratio of solar radiation pressure and gravitational attraction. The reason for this behaviour is that the space region where the "fast" hydrogen atoms are created moves closer to the sun when the shock front becomes nearer.

**Travelling Phenomena in the
Heliosphere Induced by Solar Activity**

S. Grzedzinski
Space Research Centre, Polish Academy of Sciences,
Warsaw Astronomical Observatory, Warsaw University
Warsaw, Poland

R. Ratkiewicz
Space Research Centre, Polish Academy of Sciences
Warsaw, Poland

Abstract

Solar activity induced variations in the ionization rate of neutral galactic gas inside the heliosphere influence the deceleration rate of the solar wind and cause wave-like phenomena in the distant solar wind with temperature variations of 10 - 20% at the orbits of Saturn - Neptune.

1. INTRODUCTION

The aim of the present paper is to study the possible time-dependent phenomena in the heliosphere due to coupling between the solar activity and the neutral gas (mostly hydrogen) of galactic origin moving with $\vec{v}_{\text{is}} = 20 \text{ km/s}$ relative to the Sun (Fahr, 1974). The neutral particles inside the heliosphere become ionized by $\lambda < 912 \text{ Å}$ photons and by charge exchange with solar wind protons. The newly born ions are rapidly picked-up and thermalized by the solar wind plasma (Feldman et al., 1972, Wu et al., 1973). The ensuing frictional drag slows down the hypersonic solar wind and the kinetic energy of bulk motion gets converted into thermal energy thus increasing markedly the temperature of the distant solar wind primarily in the (hydrogen-) apex hemisphere. In contrast, the scarcity of neutral atoms in the anti-apex direction allows the temperature to stay low (Grzędzielski and Ratkiewicz, 1975). Thus the temperature variation along, for instance, Neptune's orbit amounts to 1 to 2 times $10^5 \text{ }^{\circ}\text{K}$ between the apex and the anti-apex directions for hydrogen density at infinity equal to 0.1 at/cm^3 . The above description corresponds to a time - independent case.

2. THE TIME-DEPENDENT SITUATION

Changes in solar activity, in plasma flux and EUV flux, cause variations in local ionization rate and thus perturb the density distribution of neutral gas $n_H(\vec{r}, t)$. This feeds back on the solar wind via frictional drag variations and in consequence generates temperature and pressure wave-like phenomena in the distant solar wind .

The general approach used in the present paper develops the line adopted in an earlier paper (Grzędzielski and Ratkiewicz, 1975),

namely, the effect of interaction of the solar wind and solar photons with the galactic H is treated as a small perturbation of the non-magnetic, spherically symmetric solar wind. This zero-order flow is assumed to be an "average" solar wind, evolving with the solar cycle through a sequence of quasi-stationary states, whose properties change on a time scale (\sim few years) which is large as compared to the time scale required by the solar wind in the heliosphere to attain a new quasi-stationary state (\sim few months).

3. BASIC EQUATIONS FOR THE TIME-DEPENDENT CASE

The equations for $n_H(\vec{r}, t)$ are

$$\vec{v}_{is} = \text{const}$$

/1/

$$\partial n_H / \partial t + \text{div}(n_H \vec{v}_{is}) = -q/m_H - L$$

/2/

where q/m_H and L describe the mass loss terms corresponding to photoionization and charge exchange. The solar wind is described by the equations

$$\partial q / \partial t + \text{div}(q \vec{v}) = q$$

/3/

$$\rho \partial \vec{v} / \partial t + \rho (\vec{v} \cdot \text{grad}) \vec{v} + \text{grad } p = \vec{F}_i + \vec{F}_c$$

/4/

$$\partial (\rho \epsilon + \rho v^2/2) / \partial t + \text{div}[\rho \vec{v}(\epsilon + v^2/2 + p/\rho)] =$$

$$= (\vec{F}_i + \vec{F}_c) \cdot \vec{v} + \xi (G_i + G_c) + qv^2/2 \quad /5/$$

$$p = k\xi T/m_H^m, \quad , \quad \epsilon = kT/[(\gamma - 1) \cdot m_H^m] \quad /6/$$

where ξ denotes the internal energy per gram, \vec{F}_i, \vec{F}_c are the drags due to photoionization and charge exchange and G_i, G_c denote the thermal energy supplied by thermalization of new ions. For details see Grzędzielski and Ratkiewicz (1975). The RHS of Eqs. /3/ - /5/ describe the mass, momentum and energy sources due to the interaction of two media. Putting the RHS equal to zero one gets the zero-order flow. Solutions to the described set of equations were obtained analytically and evaluated numerically using standard perturbation techniques.

4. EFFECTS DUE TO SOLAR ACTIVITY

The changes in solar activity taken into consideration were the following:

1/ 11-year cycle variations of solar wind flux as given by Diodato et al., (1974) and the corresponding variations in EUV flux compiled by Smith and Gottlieb (1974). Both effects were described by sinusoidal variations superposed upon the "average" flux, as given in Fig.2.

2/ Sudden impulse in solar EUV flux due to August 1972 series of solar flares. The photoionization rate increase was estimated from Solrad 1 - 8 Å and 8 - 20 Å data using EUV energy distribution based on Donnelly's (1976) flare spectrum models.

The interplay between 1/ and the stream of H produces a complex pattern of fluctuating n_H -distribution. In Fig.1 the time evolution of n_H -distribution is shown for one-half of the solar cycle. The modulation is particularly strong in the antiapex direction. For angular distance from the apex $\vartheta = 154^\circ$, the hydrogen



Figure 1. Time Evolution of Neutral Hydrogen Distribution in the Heliosphere During One-Half of the Solar Cycle. The blank/dark regions correspond to n_H -values higher/lower than values of n_H corresponding to the stationary case (no modulation). Arrows indicate the flow of neutral gas. For the second half of the cycle blank becomes dark and vice versa. Diameter of picture = 90 AU

density n_H changes by factor ~ 3 at $r = 8$ AU and by 18% at $r = 26$ AU. In the apex-hemisphere the modulation is much weaker : 16% and 2% for $\vartheta = 26^\circ$ and same values of r as above. Hydrogen density at infinity was always 0.1 at/cm^3 . This complex pattern interacting with the solar wind leads to solar wind temperature variations : at $r = 29$ AU $\Delta T/T \approx 15 - 20\%$ (Figure 2).

A series of intense solar flares 2/ increases the ionization

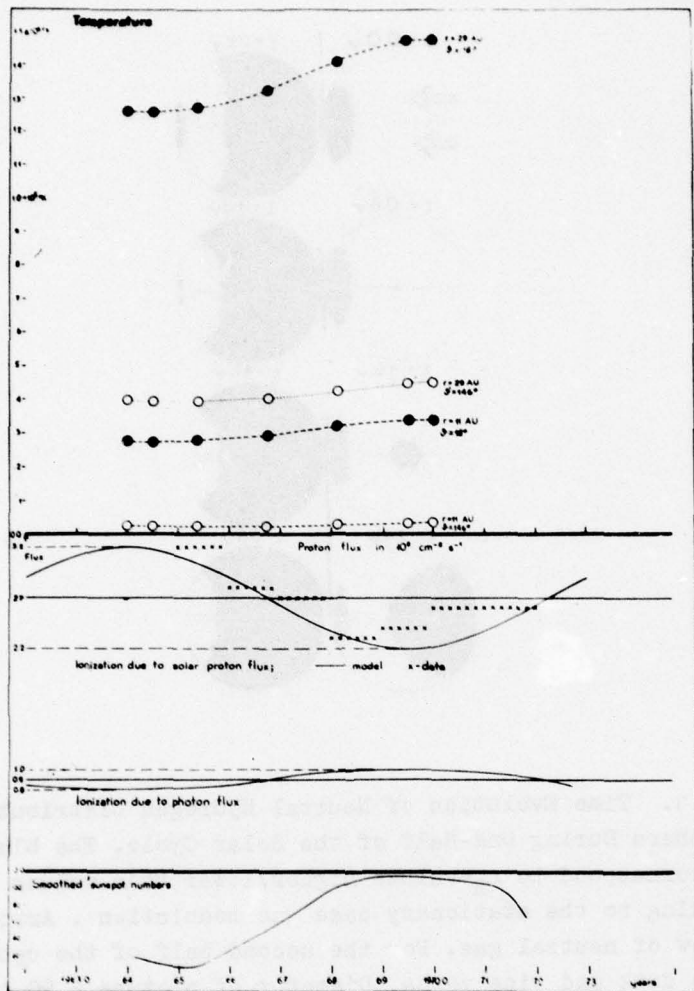


Figure 2. Upper Panel: Temperature Variations of the Distant Solar Wind Due to Solar Modulation of the Galactic Gas. r - heliocentric distance, ϑ - angle from apex. Middle panel: modulation of the ionization rates

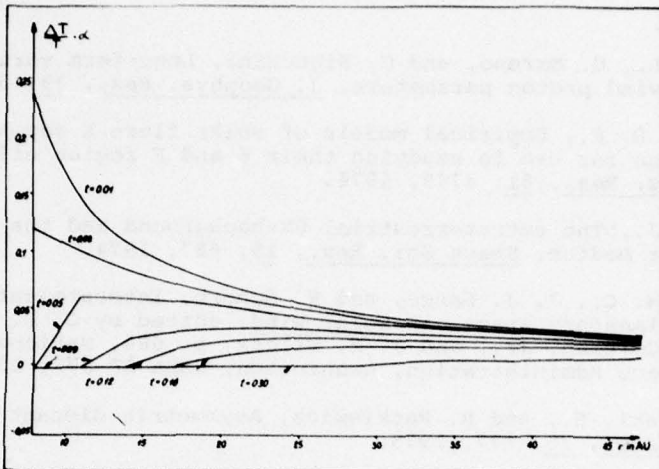


Figure 3. Relative Changes of Distant Solar Wind Temperature Due to EUV Flux from Flares. For Aug. 2 - 7, 1972 $\alpha \approx 1/4$ in case of Donnelly's model Z. For model X $\alpha \approx 1/25$. Time in 0.01 years after flare

rate in the heliosphere. It results from the present calculations that although the direct heating by photoelectrons is negligible, the additional deceleration of the solar wind due to picking up excess ions gives rise to a precursor temperature wave well ahead of the shocked gas. $\Delta T/T$ in the wave may attain 6% at $r = 8$ AU for Aug. 2 - 7, 1972 flares (Figure 3). The wave is most intense in the downwind direction.

References

- Diodato, L., G. Moreno, and C. Signorini, Long-term variations of the solar wind proton parameters, J. Geophys. Res., 79, 5095, 1974.
- Donnelly, R. F., Empirical models of solar flare X ray and EUV emission for use in studying their E and F region effects, J. Geophys. Res., 81, 4745, 1976.
- Fahr, H. J., The extraterrestrial UV-background and the nearby interstellar medium, Space Sci. Rev., 15, 483, 1974.
- Feldman, W. C., J. J. Lange, and F. Scherb, Interstellar helium in interplanetary space, in Solar Wind, edited by C. P. Sonett, P. J. Coleman, Jr., and J. M. Wilcox, p. 684, National Aeronautics and Space Administration, Washington, NASA SP-308, 1972.
- Grzędzielski, S., and R. Ratkiewicz, Asymmetric distant solar wind, Acta Astr., 25, 177, 1975.
- Smith, E. V. P., and D. M. Gottlieb, Solar flux and its variations, Space Sci. Rev., 16, 771, 1974.
- Wu, C. S., R. E. Hartle, and K. W. Ogilvie, Interaction of singly charged interstellar helium ions with the solar wind, J. Geophys. Res., 78, 306, 1973.

Discussion

Blum: In your talk you described a time-dependent density distribution of the interplanetary neutral hydrogen atoms. The time-dependence is ascribed to a variable solar EUV and corpuscular flux. What deviations from the time-dependent density would you obtain in a steady state model where you use your momentary EUV and corpuscular fluxes as the steady state values of the solar radiation?

Grzędzielski: In the apex hemisphere the situation would be much the same, i.e., the expected modulation would be of the order of 10-30% depending on spatial position. In the anti-apex hemisphere, however, one would obtain modulation smaller by a factor of 10 or more than that which results from the time-dependent calculations. This is due to the fact that in order to enter the down-wind tail of the solar cavity, the galactic gas has to flow first past the Sun where it is subjected to strong modulation. This results in a very strong modulation (by a factor of 2 to 5) close to the anti-apex direction.

Blum: The charge exchange processes dominate photoionization, so why do you get modulation due to solar EUV?

Grzędzielski: The modulation due to solar EUV emission may become important in case of strong solar flares. For instance in the

period of the August 1972 flares the increase in the solar EUV flux may enhance the total ionization rate by 5-10% for a period of a few days. This suffices to produce a precursor temperature wave with $\Delta T/T$ of the order of 3-5%.

III. INTERPLANETARY SHOCK WAVES

IPS Observations of Flare-Associated Shock Waves in 1972-1974

Takashi Watanabe
The Research Institute of Atmospherics
Nagoya University
Toyokawa, 442, Japan

Abstract

The flare-associated shock waves which were detected by the IPS observations in 1972-1974 are examined. The shock wave generated by the solar flare on Aug. 2/20h, 1972 was accompanied by the turbulent piston. The motion of this piston was strongly decelerated in the region west of the flare normal. Because of the strong deceleration, this shock wave was degenerated into the density fluctuations which were convected by the ambient solar wind of 350 km/sec at 1.4 AU from the Sun. The shock wave produced by the solar flare on Aug. 7/15h, 1972 was also accompanied by the turbulent piston. There was no significant deceleration of the piston. Another piston-driven shock wave was observed in early July 1974.

1. INTRODUCTION

In this report, we discuss the flare-associated shock waves which were detected by the IPS observations in 1972-1974. Among them, the shock waves observed in early August 1972 and in June-July 1974 are discussed in detail. For the shock waves in early August 1972, we demonstrate a capability of the IPS method in the investigations of the structure and the dynamical behavior of post-shock plasma.

2. SHOCK WAVES IN EARLY AUGUST 1972

2.1 IPS Observations

In early August 1972, several flare-associated shock waves were detected by the IPS observations (e.g., Kakinuma and Watanabe, 1976). The locations of the lines of sight to 3C48 and 3C144 are shown in Figure 1. The positions of Pioneer 9 and Pioneer 10 are also shown.

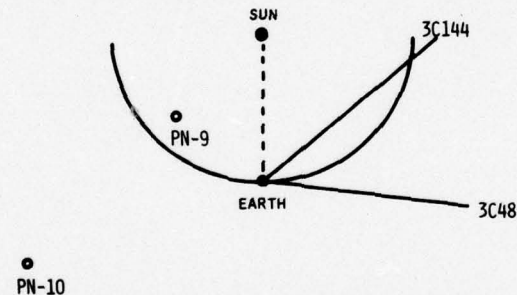


Figure 1. Ecliptic plane projections of the lines of sight and the space crafts in early August 1972

The pattern speeds and IPS levels obtained by the IPS observations in early August 1972 at our institute (TYKW) are shown in Figure 2. The pattern speeds provided by the IPS group at Univ. of California, San Diego (UCSD) are also plotted (Armstrong et al., 1973). We estimate the pattern speed under the assumptions of radial solar wind and isotropic diffraction pattern (Coles and Rickett, 1975). The IPS level is the rms intensity fluctuations normalized by the galactic background noise level.

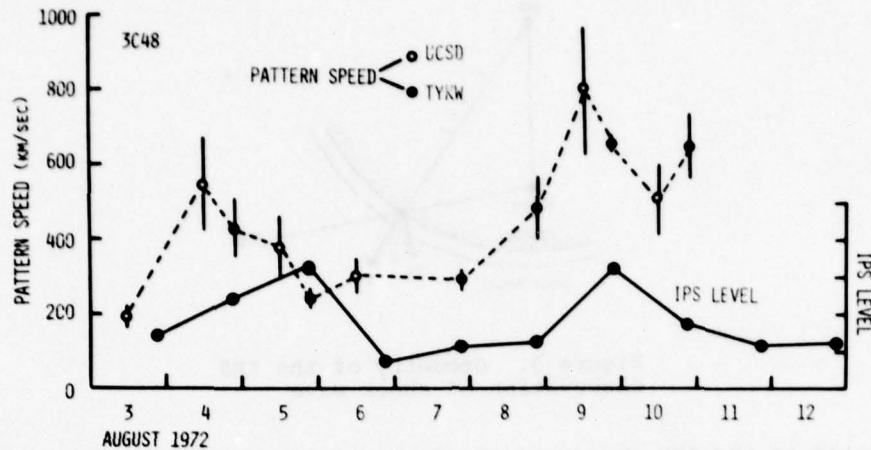


Figure 2. Pattern speeds and IPS levels obtained by the IPS observations of 3C48 in early August 1972. The pattern-speed measurements were made at Nagoya Univ. (TYKW) and at Univ. of California, San Diego (UCSD). The unit of the IPS level is arbitrary.

Two well-defined enhancements in IPS level accompanied by the increase in pattern speed can be seen in Figure 2. First one was observed on Aug. 4, and this enhancement was due to the shock wave generated by the solar flare on Aug. 2/20h, 1972. Second one which was observed on Aug. 9 is attributed to the shock wave generated by the solar flare on Aug. 7/15h. The shock wave generated by the solar flare on Aug. 4/06h was missed by the IPS observations of 3C48.

According to Figure 2, each increase in pattern speed caused by the flare-associated shock wave was followed by the gradual decrease, and lasted at least 24 hours. If we consider that the highly turbulent post-shock plasma still existed on the line of sight during one or two days, the observed decreases in pattern speed can be explained by a combination of the following three effects: (1) projection of radial flow vector, (2) deceleration of flow speed with heliocentric distance, and (3) anisotropic expansion. Since we observed the shock waves propagating beyond the Earth's orbit by IPS of 3C48 in early August 1972, the expected pattern speed is obtained by the formula:

$$v_p = v_o (1 + r)^{-k} \cos \theta \quad (r > 0) \quad (1)$$

where v_p is the speed of diffraction pattern produced by the turbulent post-shock plasma propagating at $(1 + r)$ AU from the sun, v_o is the flow speed at 1 AU ($r = 0$), k is the deceleration power law index, and θ is the projection angle. When we cannot neglect the anisotropic expansion, v_o and k become the functions of latitude and longitude. The index K will also depend on r . This formula can be directly

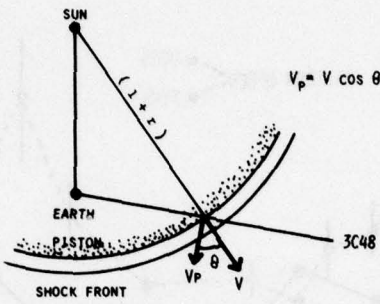


Figure 3. Geometry of the IPS observation of shock wave

applied to the IPS observations of the piston of the shock wave. The geometry is shown in Figure 3. If we were observing the shocked gas just behind the shock front, a modification of Eq. 1 is required.

2.2 Shock Wave Generated by the Solar Flare on August 2/20h, 1972

At first we try to examine the dynamical behavior of the post-shock plasma of the disturbance generated by the solar flare on Aug. 2/20h, 1972 in the outer region of the Earth's orbit by applying Eq. 1 to the IPS observations of 3C48 during Aug. 4-5. As shown in Figure 4, the IPS observations seem to be fitted by the curve given by the formula:

$$v_p \text{ (km/sec)} = 610 (1 + r)^{-1.3} \cos \theta. \quad (2)$$

The flow speed of 610 km/sec at 1 AU is the approximate solar wind speed observed by the Prognoz satellites (e.g., Vaisberg and Zastenker, 1976) about two hours after the shock-front passage when the proton number density reached the maximum ($\sim 150/\text{cc}$). This high density post-shock plasma is considered to have been the piston. The successful prediction of the pattern speed by Eq. 2 suggests that the turbulent level in post-shock plasma reached the maximum at the piston, and that the expansion of the piston was locally isotropic in the region about $30^\circ\text{W} - 70^\circ\text{W}$ of the flare normal. The IPS observations and the shock model given by Eq. 2 indicate that on Aug. 5/19h, the flow speed of the piston plasma was slowed down to that of the ambient solar wind of about 350 km/sec at 1.4 AU from the sun and at 70° west of the flare normal. High IPS level on Aug. 5/19h (see Figure 2) shows that the piston was degenerated into the plasma density fluctuations which were convected by the ambient solar wind.

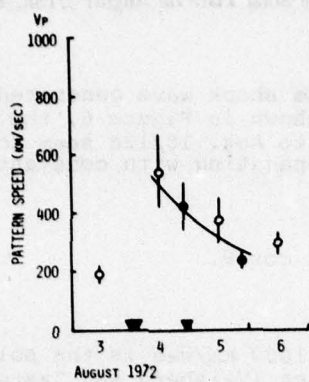


Figure 4. Comparison of the pattern speed (V_p) predicted by Eq. 2 with the IPS observations during Aug. 4-5, 1972

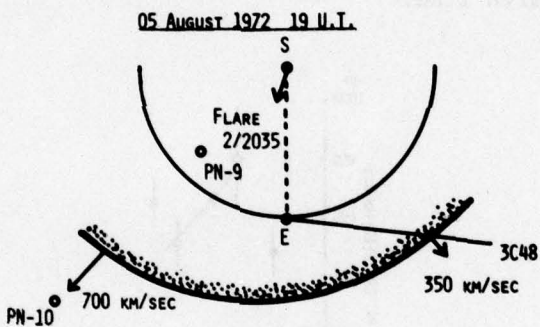


Figure 5. An estimated geometry of the piston on Aug. 5/19h, 1972.

Strong deceleration of this shock wave in the region west of the flare normal forms a contrast with the conclusion given by Intriligator (1976) that there was no significant deceleration of this shock wave between Pioneer 9 at 0.8 AU and Pioneer 10 at 2.2 AU. Since the Pioneers were situated at about 20° east of the flare normal, it is also concluded that the deceleration of the piston in the region west of the flare normal was strong as compared with that in the region east of the flare normal. We can draw a possible gross geometry of the piston in the outer region of the Earth's orbit on the basis of the observations by Pioneers and IPS of 3C48. The result is shown in Figure 5.

2.3 Shock Wave Generated by the Solar Flare on August 7/15h, 1972

We next examine the shock wave generated by the solar flare on Aug. 7/15h, 1972. As shown in Figure 6, the IPS observations in the period from Aug. 9/12h to Aug. 10/12h seem to be well fitted by the model of shock wave propagating with constant speed:

$$V_p \text{ (km/sec)} = 1000 \cos \theta. \quad (3)$$

The flow speed of 1000 km/sec is the solar wind speed observed by Prognoz satellites (Vaisberg and Zastenker, 1976) about six hours after the shock-front passage when the proton number density reached the maximum ($\sim 20/\text{cc}$). If we consider that this relatively high density post-shock plasma was the turbulent piston, it is concluded that this piston expanded as far out as 1.7 AU from the Sun in the region east of the flare normal without significant deceleration. A good agreement seen in Figure 6 indicates the locally isotropic expansion of the piston in the region between the flare normal and the Sun-Earth line.

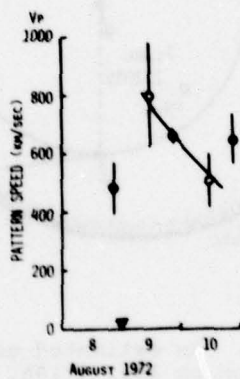


Figure 6. Same as Figure 4 but for the shock wave generated by the solar flare on Aug. 7/15h, 1972

The observations at Pioneer 9 and Pioneer 10 located at 80° east of the flare normal showed no significant deceleration of this shock wave (Intriligator, 1976). A possible gross geometry of the piston of this shock wave is shown in Figure 7. The slower expansion along the Sun-Pioneers line seems to have been due to the existence of ambient low speed stream (Kakinuma and Watanabe, 1976).

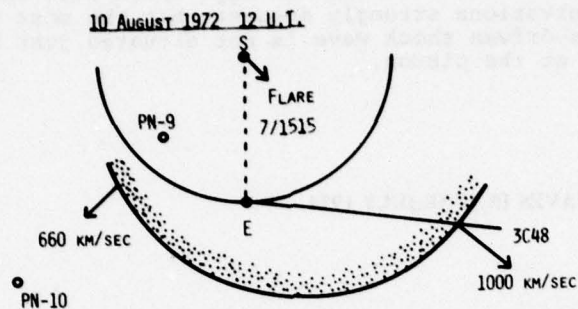


Figure 7. Same as Figure 5 but for Aug. 10/12h

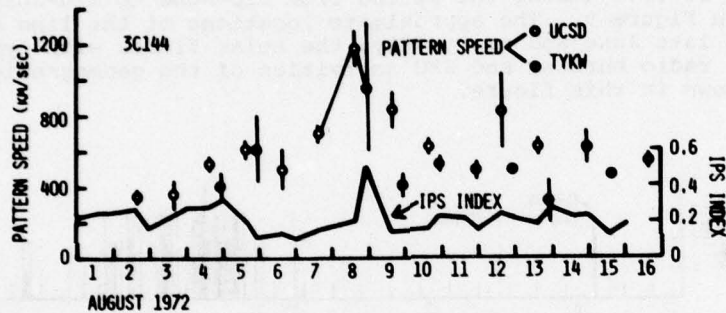


Figure 8. Pattern speeds and IPS indices obtained by IPS observations of 3C144 in early August 1972 (see text)

The existence of the turbulent piston driving the shock wave generated by the solar flare on Aug. 7/15h, 1972 seems to be confirmed by the IPS observations of 3C144. As shown in Figure 1, the line of sight to 3C144 was situated inside the Earth's orbit in this period. The pattern speeds obtained at TYKW and at UCSD, and the IPS indices obtained at UCSD (Rickett, 1975) and at Adelaide Univ. (Ward, 1975) are shown in Figure 8. Daily IPS index obtained at UCSD is halved to adjust to the base level of IPS activity observed at Adelaide. As shown in Figure 8, very high pattern speed of about 1000 km/sec was observed at UCSD on Aug. 8/16h while the IPS activity was not enhanced (Rickett, 1975). If we estimate the position of the shock front at the time of IPS observations of 3C144 assuming the constant shock speed of 1100 km/sec (Vaisberg et al., 1975), it is concluded that the IPS observation at UCSD on Aug. 8 was made immediately after the shock-front passage of the disturbance generated by the solar flare on Aug. 7/15h. On the other hand, the IPS observation at Adelaide which was made about seven hours after the UCSD observation on Aug. 8 shows the prominent increase in IPS index. The IPS

observation of 3C144 at TYKW on Aug. 8/23h also showed high IPS level. These observations strongly suggest that the most turbulent region in the piston-driven shock wave is not situated just behind the shock front but at the piston.

3. SHOCK WAVES IN JUNE-JULY 1974

3.1 IPS Observations

The pattern speeds and IPS levels obtained by the IPS observations of 3C48 during the period from mid-June to mid-July 1974 are shown in Figure 9. The approximate locations of the line of sight to 3C48 in late June and early July, the solar flares with type II and/or type IV radio bursts, and SSC activities of the geomagnetic field are also shown in this figure.

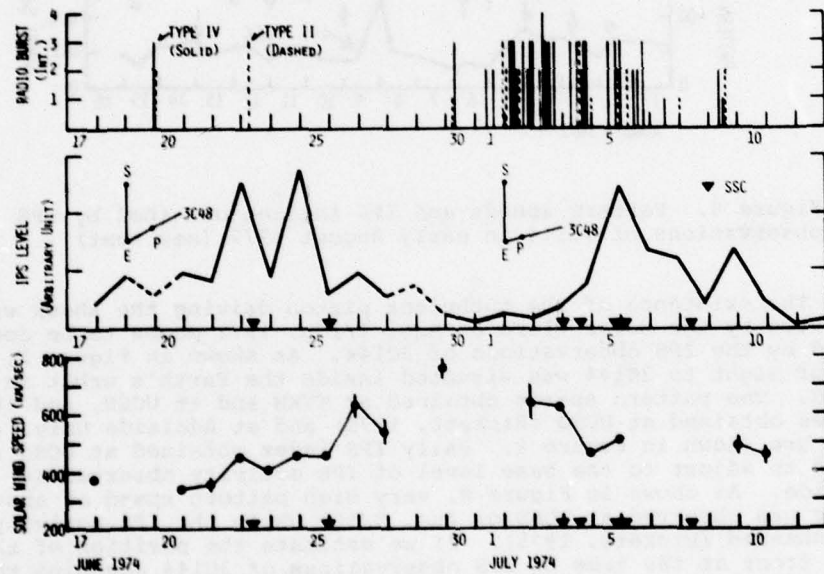


Figure 9. Solar flares with type II and/or type IV radio bursts, IPS level of 3C48, pattern speed obtained by the IPS observations of 3C48, and SSCs in June-July 1974

3.2 Shock Waves in Late July 1974

As shown in Figure 9, the prominent enhancements in the IPS level, observed late on June 22 and on June 24, 1974, were followed by an SSC in the geomagnetic field. The first enhancement in the IPS level was accompanied by the increase in pattern speed up to 450 km/sec, and this enhancement was probably due to the shock wave generated by the solar flare with type II and type IV radio bursts on June 19/23h, 1974. The enhancement in IPS level was very prominent while the magnitude of SSC activity was small.

The second enhancement in IPS level accompanied by the small increase in pattern speed up to 450 km/sec was observed about 24 hours before the onset of SSC on June 25/23h. This enhancement seems to have been due to the shock wave generated by the solar flare on June 23/06h. However, as shown in Figure 9, the IPS level fell down to the normal level about one hour before the SSC. This situation cannot be explained by the model of uniformly expanding shock wave. The expanding speed along the flare normal situated at about 50° west of the Sun-Earth line must have been much faster than that along the Sun-Earth line, and that highly turbulent region must have been confined in the vicinity of the flare normal.

3.3 Shock Waves in Early July 1974

A number of intense proton flares and associated solar-terrestrial events were observed in early July 1974 (e.g., NOAA Technical Memo-random ERL SEL-38, ed., S.J. Mangis). As shown in Figure 9, a sharp increase in IPS level accompanied by the increase in pattern speed up to 500 km/sec was observed on July 5/22h. This enhancement was followed by the SSC on July 6/03h. Krivsky and Pinter (1975) suggested that this SSC was caused by the shock wave generated by the solar flare with type II and type IV radio bursts on July 4/21h. On the basis of the observations at Pioneer 10 and Pioneer 11, they also suggested that this shock wave propagated as far out as Jupiter's orbit without strong deceleration. Estimated deceleration power law index of the mean propagating speed between 0.5 and 2.2 AU from the Sun is about 0.3. Because of small deceleration index as compared with that of the theoretical blast wave (see the review given by Dryer, 1974), this shock wave is considered to have been the driven-type disturbance. Therefore, observed enhancement in IPS level was probably due to the turbulent piston.

There exists no appreciable increase in IPS level corresponding to the shock waves which produced the SSC activities on July 4. These shock waves must have propagated in the high speed stream which was observed by IPS observation of 3C48 during June 25 - July 4. Thus it is suggested that some shock waves propagating in the high speed streams do not produce appreciable increase in IPS level.

4. CONCLUSIONS

The IPS observations in early August 1972 show that the shock waves accompanied by the high density piston produced high IPS activity. The turbulence level in the post-shock region was the maximum at the piston.

The IPS observations in early August 1972 also show that the deceleration of the piston in the region west of the flare normal was strong as compared with that in the region east of the flare normal. Such a difference in deceleration rate will produce an asymmetric expansion of the flare-associated disturbance (e.g., Sakurai and Chao, 1973).

According to the IPS observations in 1972-1974, violent shock waves of a driven type produced high IPS activity. As shown in section 3.2, two minor shock waves propagating in the low speed stream also produced high IPS activity. On the other hand, as shown in section 3.3, the shock waves propagating in the high speed stream did not produce appreciable increase in IPS level. To find a causal relationship, it is required to collect more examples of the shock observations by the IPS method.

Acknowledgments

The author is grateful to Professor T. Kakinuma for many valuable discussions. His thanks especially due to Dr. J. D. Mihalov for kindly providing unpublished Pioneer 9 data and helpful discussions. Thanks are also due to Dr. H. Washimi and Mr. M. Kojima for discussions.

References

Armstrong, J. W., W. A. Coles, J. K. Harmon, S. Maagoe, B. J. Rickett, and D. J. Sime, Radio Scintillation Measurements of the Solar Wind Following the Flares of August 1972, Collected Data Reports on August 1972 Solar-Terrestrial Events, Rep. UAG-28, part 2, edited by H. E. Coffey, World Data Center A, Boulder, Colo., 371, 1973.

Coles, W. A., and B. J. Rickett, Solar Wind Speed from IPS Measurements at UC San Diego, Solar-Geophysical Data, 366 (supplement), US Department of Commerce, Boulder, Colo., p. 15, 1975.

Dryer, M., Interplanetary Shock Waves Generated by Solar Flares, Space Sci. Rev., 15, 403, 1974.

Intriligator, D. S., The August 1972 Solar-Terrestrial Events: Solar Wind Plasma Observations, Space Sci. Rev., 19, 629, 1976.

Kakinuma, T., and T. Watanabe, Interplanetary Scintillation of Radio Sources During August 1972, Space Sci. Rev., 19, 611, 1976.

Krivsky, L., and S. Pinter, Proton Flares of July 1974 Generating Interplanetary Shock Waves, Bull. Astron Inst. Czech., 26, 360, 1975.

Rickett, B. J., Disturbances in the Solar Wind from IPS Measurements in August 1972, Solar Phys., 43, 237, 1975.

Sakurai, K., and J.-K. Chao, Expanding Pattern of Helium-Enriched Shell Associated with Solar Flares, Nature, Phys. Sci., 246, 72, 1973.

Vaisberg, O. L., and G. N. Zastenker, Solar Wind Magnetosheath Observations at Earth During August 1972, Space Sci. Rev., 19, 687, 1976.

Vaisberg, O. L., G. N. Zastenker, F. Cambou, V. V. Temnyi, and M. Z. Khokhlov, Solar-Wind Parameters and Shock Wave Generated by the Strong Flares of August 1972, Cosmic Res., 13, 765, 1975.

Ward, B. D., Radio Wave Scattering in the Interplanetary Medium, Univ. of Adelaide, South Australia (Ph. D. Thesis), 1975.

The Shape and the Energy of the
Interplanetary Shock Waves Associated
with the August 1972 Solar Flares

C. D'Uston[†]
G. N. Zastenker^{††}
V. V. Temny^{††}
J. M. Bosqued[†]

[†]Centre d'Etude Spatiale des Rayonnements, (C.E.S.R.)
9 avenue du Col. Roche
B.P. 4346 - 31029 Toulouse, France

^{††}Space Research Institute, (I.K.I.)
USSR Academy of Sciences
Prosoyusnaya, 88
117810, Moscow, USSR

Abstract

The shape of solar flare-associated shock waves in August 1972 was studied by comparing the solar plasma observations on Prognoz, Prognoz-2, Pioneer-9 and Pioneer-10 spacecrafts with type II radio burst observations and observations of radiosource scintillations. This study showed that the first shocks were almost spherical and displayed strong deceleration (blast waves). Two subsequent shocks were highly nonspherical with low deceleration (piston-driven waves). Energy and mass-ejected quantities obtained from Prognoz-2 measurements are $10^{32} - 10^{33}$ ergs and $10^{16} - 10^{17}$ g, respectively.

PRECEDING PAGE BLANK

1. INTRODUCTION

During early August 1972 the sun displayed very intense activity, the greatest in the twentieth solar cycle. This activity was associated with the passage of the Mc Math region N° 11976 across the solar disc, a phenomenon visible from the Earth. This period has been investigated by many direct observations which reveal four major flares :

- Event 1 : 2 August at 03.10 U.T.
- Event 2 : 2 August at 19.58 U.T.
- Event 3 : 4 August at 06.20
- Event 4 : 7 August at 15.05 U.T.

This group of flares represents the most intense solar activity recorded in space experiment history. The data obtained during this period are thus of particular interest in studying the development of flare-associated disturbances.

The development of the plasma characteristics and the interplanetary magnetic field in the shock waves detected at different points in interplanetary space has been given in many publications and reports (Cattaneo et al., 1974 ; Mihalov et al., 1974 ; Bezrukikh et al., 1975 ; Cambou et al., 1975 ; Dryer et al., 1975, 1976 ; Hakura, 1976 ; Intriligator, 1976 ; Smith, 1976 ; Vaisberg and Zastenker, 1976). In order to improve the interpretation of these observations, the geometrical structure and energy distribution within a shock wave must be taken into account. These parameters are important and may be used as criteria for testing two dimensional theoretical models. In this paper we present the overall values obtained for the August 1972 disturbances, i.e., the energy released and the matter ejected during each of the solar events, as well as an estimate of the volume of the disturbance. This volume will be indicated only by its extension along the ecliptic plane.

2. DATA AND INFORMATION

The data used in this paper come from the Franco-Soviet Calipso and RIP experiments aboard earth-orbiting satellites Prognoz and Prognoz 2 (Temny et al., 1974 ; Cambou et al., 1975 ; Vaisberg and Zastenker, 1976 ; d'Uston et al., 1977). Measurements have also been made by Pioneer 9 at 0.8 A.U. and Pioneer 10 at 2.2 A.U. on the same heliocentric radius at 45° east of the Sun-Earth line (Mihalov et al., 1974 ; Dryer et al., 1975, 1976 ; Intriligator, 1977 ; Smith et al., 1977). The chronology of the events seen at these different points is given in Table 1. This table is arranged to indicate the associations we have made between detected shock waves and solar events. Other combinations have been proposed for the shock waves detected by Pioneer 10 (Intriligator, 1977, Smith et al., 1977). We have also used observations of the scintillation of radiosources whose line of sight is near the ecliptic plane. In order to simplify the figures we have placed the interaction of the plasma and the radio wave at a point corresponding to the maximum efficiency of this interaction on the line of sight (Figure 1).

Table 1. Summary of satellite, comet and radiosource observations

Object	Coordinates			Registration of shock waves (UT)							
	R (A.U.)	θ°	ϕ°	1 st flare		2 nd flare		3 rd flare		4 th flare	
				Day	Time	Day	Time	Day	Time	Day	Time
Pioneer-9	0.78	2N	45E	3	4.20	3	11.17	4	23.23	9	7.10
Prognоз	1.0	6N	0	4	1.19	4	2.20	4	20.54	8	23.52
Pioneer-10	2.2	0	45E	-	-	-	-	6	15.20	13	3.00
Comet G/Z	0.99	4N	58W	-	-	-	-	-	-	9	15.
3C 48	1.1	12N	15W	-	-	4	13.	5	13.	8	19.
3C 144	0.80	6N	40W	-	-	4	17.	5	17.	8	16.
3C 273	0.82	6N	39E	-	-	-	-	-	-	9	6.
3C 298	0.95	10N	19E	4	1.	-	-	5	1.	9	1.

3. EXTENSION AND PROPAGATION

Considering the work already done elsewhere (Dryer et al., 1975 ; Grigoryeva et al., 1976 ; Rickett, 1975 ; Kakinuma and Watanabe, 1976) and using these data we have attempted to find the shape of the shock wave at the moment of detection by the Prognоз satellites near the Earth. Since the observations were made at different points and different times, it is necessary to provide a radial propagation model to study the longitude-dependence. We have considered three different cases :

- a constant propagation speed along a given heliocentric radius,
- an average propagation speed inversely proportional to the heliocentric distance travelled, and
- an average speed following a law of the form $R^{-\alpha}$, where the exponent has been determined from work previously published by Zastenker et al.(1976).

These three hypothesis lead to similar results concerning their dominant features. More specifically we have retained the third model, since it can be used to separate the shock waves into two types depending on the exponent alpha.

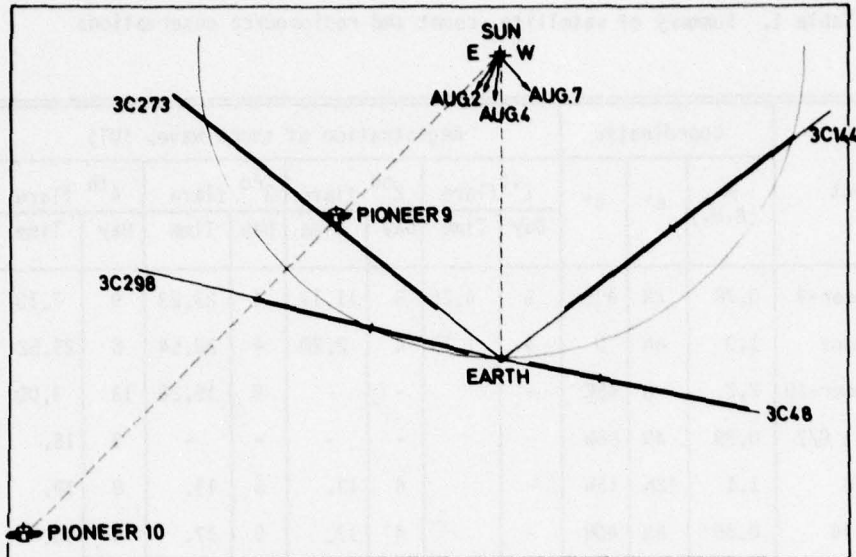


Figure 1. Positions of Pioneer 9 and Pioneer 10 and lines of sight of radiosources projected on to the solar-equatorial plane. The longitudes of the August 2, 4 and 7 major solar flares are shown by arrows (adapted from Rickett, 1975).

In this model the propagation speed of the shock front at a point located at distance R from the Sun, is expressed as :

$$U = U_{int} (R / R_{int})^{-\alpha} \quad (1)$$

where R_{int} is the distance at which the deceleration begins and U_{int} the speed of propagation at this point. For each direction $\Delta\phi$ with respect to the central meridian of the flare we have calculated U_{int}

$$U_{int} (\Delta\phi) = (R_{obj}^{1+\alpha} / R_{int}^\alpha + \alpha R_{int}) / \Delta t_{obj} (1 + \alpha) \quad (2)$$

using the arrival time (Δt_{obj}) of the shock wave at one point in space ($\Delta\phi$, R_{obj}). The values obtained are generally in agreement with the speeds found from measurements of type II radio bursts in the solar corona. These estimates are quite accurate since the calculation uses observations made closest to the central meridian of the burst. This criterion, however, should not be given too much importance since we have taken a value of R_{int} at around 70 to $90 R_\odot$ in agreement with the results presented by Dryer et al., (1975), while the source of the type II radio bursts observed is located at less than $20 R_\odot$.

The position R' and the propagation speed U' of the shock wave in different directions $\Delta\phi$ with respect to the Sun at the time Δt_0 of their detection at the Earth have been calculated using this same model :

$$R' = R_{int} \left[(1 + \alpha) (U_{int} \cdot \Delta t_0 / R_{int} - 1) + 1 \right]^{-\frac{1}{1+\alpha}} \quad (3)$$

and

$$U' = U_{int} (R' / R_{int})^{-\alpha} \quad (4)$$

Figure 2 gives the results obtained using this method for propagation speeds.

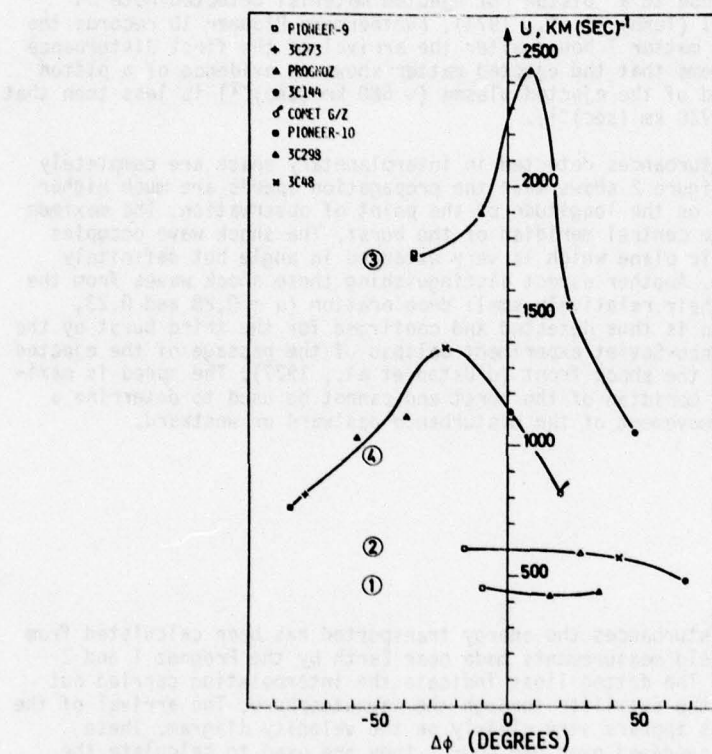


Figure 2. The shock wave velocity (U') dependence versus the angular deflection from the flare meridian. Figures in circles are numbers of the flares.

Taking into account the normalization at 1 AU, performed on the positions, the results indicate a shape which like the speeds depends on the heliocentric longitude. This calculation shows that the same speeds are obtained whether one uses Pioneer 9 observations or those of Pioneer 10, using the associations given at the beginning of this paper. In the case of differing associations, there is a substantial disagreement on this particular point. Furthermore, the speeds found are

in good agreement with those determined near the Earth using measurements of plasma characteristics before and after the passage of the shock front (Cattaneo et al., 1974, Vaisberg and Zastenker, 1976).

Generally speaking, the figure given shows several interesting characteristics. The first two shock waves propagated at a speed independent of the longitude, at least in a wide region of the ecliptic plane ; this leads to an almost spherical shape of the shock waves. Many authors have shown that these two disturbances underwent a strong deceleration ($\alpha = 1.4$ and 1.7 , respectively) which gave them the character of a blast. However, it is certain that the second event also has a different character due to a "piston" of ejected material detected both on Pioneer 9 and Prognoz 1 (Temny et al., 1974). Furthermore Pioneer 10 records the passage of the ejected matter 7 hours after the arrival of the first disturbance on 6 August, but it seems that the ejected matter shows no evidence of a piston, since the maximum speed of the ejected plasma ($\sim 680 \text{ km (sec)}^{-1}$) is less than that of the shock front ($\sim 720 \text{ km (sec)}^{-1}$).

The two other disturbances detected in interplanetary space are completely different in nature. Figure 2 shows that the propagation speeds are much higher and strongly dependent on the longitude of the point of observation. The maximum speed is found near the central meridian of the burst. The shock wave occupies a region in the ecliptic plane which is very extended in angle but definitely non-spherical in shape. Another aspect distinguishing these shock waves from the two preceding ones is their relatively small deceleration ($\alpha = 0.28$ and 0.23 , respectively). A piston is thus detected and confirmed for the third burst by the observation of the Franco-Soviet experiment Calipso of the passage of the ejected matter two hours after the shock front (d'Uston et al., 1977). The speed is maximum around the central meridian of the burst and cannot be used to determine a possible preferential movement of the disturbance eastward or westward.

4. ENERGIES

In all of these disturbances the energy transported has been calculated from plasma and magnetic field measurements made near Earth by the Prognoz 1 and 2 satellites (Figure 3). The dotted lines indicate the interpolation carried out during the passage of the satellite through the magnetosphere. The arrival of the successive disturbances appears very clearly on the velocity diagram. These parameters are values averaged over one hour ; they are used to calculate the kinetic (bold face), thermal (fine line), and potential (not shown) energy fluxes (Figure 4). The measured value of the total magnetic field is used to calculate the magnetic energy flux (dotted line).

Since the second disturbance quickly follows the first, it is impossible to separate the energies involved in each. We shall thus consider the sum of the contributions for these two events.

Generally speaking, the observations made by Prognoz present characteristics in agreement with measurements made at 0.8 A.U. 45° east of the Sun-Earth line by Pioneer 9. The detailed structure has already been studied in other publications (Dryer et al., 1976 ; d'Uston et al., 1977). It may be noted that the three components of the energy flux exhibit a similar behavior during the "return to quiet" phase following the third disturbance.

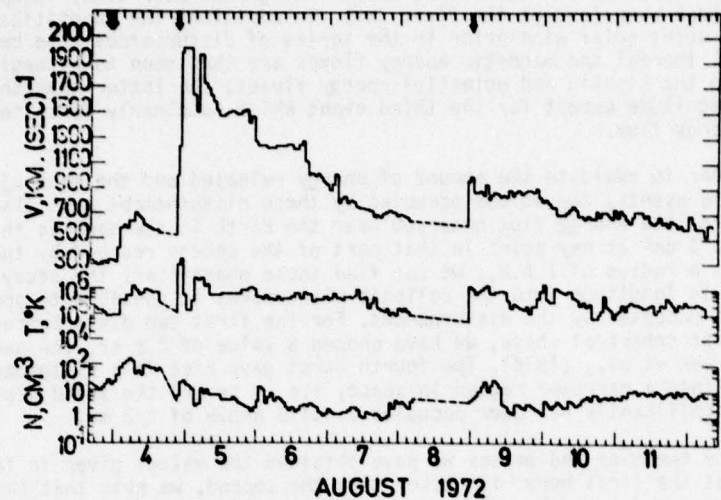


Figure 3. The solar wind plasma parameters from Prognoz and Prognoz-2 data for August 3-12, 1972. The arrows show the arrival of four shock waves at the Earth. Interpolation is denoted by a dotted line.

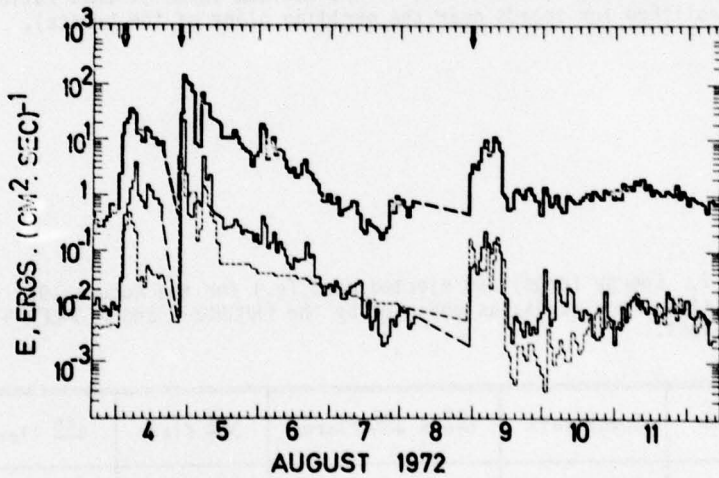


Figure 4. Time variations of the flux density for kinetic (solid line), thermal (thin) and magnetic (dashed line) energies for August 1972 events.

The values shown in Figure 4 have been integrated over time, independently for each shock wave (except the first two). In addition, the quantities corresponding to the quiet solar wind prior to the series of disturbances have been left out. The overall thermal and magnetic energy fluxes are then seen to be negligible compared to the kinetic and potential energy fluxes. The latter have the same order of magnitude except for the third event which is clearly dominated by the kinetic energy flux.

In order to evaluate the amount of energy released and the mass ejected during these events, the volume occupied by these disturbances must also be found. Assuming that the energy flux observed near the Earth is the same as that which has crossed 1 cm^2 at any point in that part of the sphere reached by the disturbance at a radius of 1 A.U., we can find these quantities. The study made on the extent in longitude into the ecliptic plane makes it possible to specify the solid angle occupied by the disturbances. For the first two disturbances presenting an almost spherical shape, we have chosen a value of $2\pi \text{ sr}$, the same as that taken by Dryer et al., (1976). The fourth burst gave rise to a disturbance which propagated into a narrower region in space, i.e. $\pi \text{ sr}$ and the third disturbance which is significantly narrower occupies a solid angle of $\pi/2 \text{ sr}$.

For the energies and masses we have obtained the values given in Table 2. Knowing that the first burst is weaker than the second, we note that the second is the more powerful and has the greater quantity of ejected mass. It can also be noted that the second burst ejected about 10 times more matter than the third while the energy released is only twice as great. Assuming a predominance of kinetic energy in the third disturbance and an equal distribution between kinetic and potential energy in the second, the ratio of speeds should be $\sqrt{10}$. This ratio is actually about 4, which is in rather good agreement with our hypothesis, particularly if we consider that this is the maximum value of this ratio (it was in fact established for speeds near the meridian plane of the bursts).

Table 2. Energy (ergs) and ejected mass (g.) for the August 1972 flare associated shock waves, as observed by the PROGNOZ-2 and PIONEER-9 satellites.

Parameter	Spacecraft	1 st + 2 nd flares	3 rd flare	4 th flare
Energy (erg)	Prognoz-2	2.6×10^{33}	1.3×10^{33}	2.9×10^{32}
	Pioneer-9	5.5×10^{32}	1.1×10^{32}	3.8×10^{32}
Mass (g)	Prognoz-2	6.0×10^{17}	4.0×10^{16}	4.5×10^{16}
	Pioneer-9	1.4×10^{17}	1.6×10^{16}	9.4×10^{16}

5. CONCLUSION

By studying each event of this series of disturbances independently, we have shown that a single outline of behavior cannot be applied. This is due to the fact that while the initial propagation speed most likely depends only on the energy released by the burst (Hundhausen and Gentry, 1969), the average propagation speed depends in fact on the medium through which it has travelled. During the first half of August 1972 this study was very complex because of the disturbed state of the interplanetary medium.

A classification can however be made with respect to the deceleration rates of these shock waves. The first two disturbances are blast waves ($\alpha > 1$) and have an approximately spherical shape, unlike the two following bursts which are instead driven shock waves, with a non-spherical shape. It can thus be noted that for the same energy the propagation speed of a driven shock wave is greater than that of a blast wave.

Acknowledgments

This study was carried out as part of the French-Soviet space sciences program. The authors would like to thank Professor Cambou and Doctor Vaisberg for their constant support in this cooperative effort. The French part of this project was supported by the Centre National d'Etudes Spatiales (CNES contract 212). One of us (C.U.) is supported by a research grant from CNES.

References

- Bezrukikh, V.V., K.I. Gringauz, G.N. Zastenker, M.Z. Khokhlov, Certain characteristics of the solar wind, the position of bow shock waves, magnetopause and plasmapause during the period of high solar activity in August 1972, Cosmic Res. USSR, Engl. Transl., 13, 304, 1975.
- Cambou, F., O.L. Vaisberg, H. Espagne, V.V. Temny, C. d'Uston, G.N. Zastenker, Characteristics of interplanetary plasma near the earth observed during the solar events of August 1972, Space Res., 15, 461, 1975.
- Cattaneo, M.B., P. Cerulli-Irelli, L. Diodato, A. Egidi, G. Moreno, P.C. Hedgecock, Observation of interplanetary shocks of August 1972, in Correlated Interplanetary and Magnetospheric Observations, edited by D.E. Page, pp. 555-562, D. Reidel, Dordrecht, Netherlands, 1974.
- Dryer, M., A. Eviatar, A. Frohlich, A. Jacobs, J.H. Joseph, E.J. Weber, Interplanetary shock waves and comet brightness fluctuations during June-August 1972, J. Geophys. Res., 80, 2001, 1975.

- Dryer, M., Z.K. Smith, R.S. Steinolfson, J.D. Mihalov, J.H. Wolfe, J.K. Chao, Interplanetary disturbances caused by the August 1972 solar flares as observed by Pioneer 9, J. Geophys. Res., 81, 4651, 1976.
- d'Uston, C., V.V. Temny, G.N. Zastenker, E.G. Eroshenko, J.M. Bosqued, O.L. Vaisberg, F. Cambou, Energetics properties of interplanetary plasma at the earth following the August 4, 1972, solar flare, Solar Phys., 51, 217, 1977.
- Grigoryeva, V. P., G. N. Zastenker, V. V. Temny, Motions of interplanetary shock wave generated by solar flare on 4 August 1972 derived from solar wind the Type II radio-burst observations, Space Res., XVI, 693, 1976.
- Hakura, Y., Interdisciplinary summary of solar/interplanetary events during August 1972, Space Sci. Rev., 19, 411, 1976.
- Hundhausen, A.J., R.A. Gentry, Numerical simulation of flare associated solar wind disturbances, J. Geophys. Res., 74, 2908, 1969.
- Intriligator, D.S., The August 1972 solar terrestrial events : solar wind plasma observations, Space Sci. Rev., 19, 629, 1976.
- Intriligator, D.S., Pioneer 9 and Pioneer 10 observations of the solar wind associated with the August 1972 events, J. Geophys. Res., 82, 603, 1977.
- Kakinuma, T., T. Watanabe, Interplanetary scintillation of radio sources during August 1972, Space Sci. Rev., 19, 611, 1976.
- Mihalov, J.D., D.S. Colburn, H.R. Collard, B.F. Smith, C.P. Sonett, J.H. Wolfe, Pioneer solar plasma and magnetic field measurements in interplanetary space during August 2-17, 1972, in Correlated Interplanetary and Magnetospheric Observations, edited by D.E. Page, pp. 545-553, D. Reidel, Dordrecht, Netherlands, 1974.
- Rickett, B.J., Disturbances in the solar wind from IPS measurements in August 1972, Solar Phys., 43, 237, 1975.
- Smith, E.J., The August 1972 solar terrestrial events : interplanetary magnetic field observations, Space Sci. Rev., 19, 661, 1976.
- Smith, E.J., Leverett Davis, Jr., P.J. Coleman, Jr., D.S. Colburn, P. Dyal, D.E. Jones, August 1972 Solar Terrestrial events : Observations of interplanetary shocks at 2.2 A.U., J. Geophys. Res., 82, 1077, 1977.
- Temny, V.V., A.A. Zertzelov, O.L. Vaisberg, Y.E. Berezin, Measurements of the proton and alpha component of plasma by the Prognoz satellite during high solar activity (August 1972), Cosmic Res. USSR, Engl. Transl., 12, 66, 1974.
- Vaisberg, O.L., G.N. Zastenker, Solar wind and magnetosheath observations at Earth during August 1972, Space Sci. Rev., 19, 687, 1976.
- Zastenker, G. N., O. L. Vaisberg, F. Cambou, V. V. Temny, M. Z. Khokhlov, Study of propagation of solar-flare-generated shock waves in August 1972 using solar wind measurements, Space Res., XVI, 699, 1976.

Directional Properties of the Propagation of Solar Flare-Generated Shock Waves in Interplanetary Space

Stephen Pinter
Geophysical Institute of the Slovak Academy of Sciences
947 01 Hurbanovo, Czechoslovakia

Abstract

We have examined multiple spacecraft plasma and magnetic field observations at different heliocentric longitudes to determine the directional properties (the angular distribution of shock velocities) of the propagation of the flare-generated interplanetary shock waves at a distance of 1 AU. It was found that the shock waves mostly do not propagate isotropically in the interplanetary medium, i.e. the wave front emitted by a flare explosion moves with different velocities in different directions of propagation. The highest average velocity of the shock waves is observed in the direction close to the meridional plane which crosses the position of an associated flare, i.e. the average wave velocities decrease with increasing angular distance between the flare meridian and the direction to the observer. This feature is associated with an anisotropic angular distribution of shock wave velocities.

To determine the shape of the shock wave we used normalized average velocities up to 1 AU. The results indicate that the shock expands on a broad front which is not spherical, but nearly symmetrical with respect to the meridional plane of an

associated flare. These non-spherically symmetric shock waves, however, have a limited angular extent.

Two possible patterns of generation and propagation of flare-associated shock waves in interplanetary space, explaining these properties, are discussed:

(i) A piston-driven shock wave is generated by the flare, probably persisting to a distance of 0.3 - 0.6 AU; the radially ejected plasmoid probably ceased at that time, thereby leaving the shock to decelerate like a blast wave, i.e. the effective region of generation of blast-like waves is situated at a large distance from the flare (Dryer et al., 1976).

(ii) The flare generates a shock wave, the velocity of the front decreasing on moving away from the radial direction. In the conclusion of the paper the directional properties of the shock wave velocity are studied with the aid of diagrams for which the values of the so-called angular coefficient were computed.

1. INTRODUCTION

The available data on the angular distribution of the propagation velocity of flare-generated interplanetary shock waves were mostly obtained by studying the shape of the shock fronts observed close to the Earth's orbit. The primary source of information on the configuration of shock-wave fronts in the plane of the ecliptic comes from a statistical analysis of a large number of observations of geomagnetic storm SSC's (Hirshberg, 1968) and Forbush decreases of cosmic rays (Sakurai, 1973, 1974). In order to determine the shape of the shock-wave front Hirshberg (1968) used the magnitudes of geomagnetic storms which were studied as a function of the heliographic longitude of solar flares, causing the SSC's. The central meridian effect, determined from all the cases investigated, includes information on some of the mean properties of the shape of the shock wave in the plane of the ecliptic close to the Earth. Hirshberg (1968) reached a very important conclusion: The shock is expanding on a broad front but the shape deviates considerably from spherical symmetry. The velocity of the shock at large angles is approximately six-tenths the velocity at zero degrees.

In another effort to determine the shape of the front of interplanetary shock waves close to the Earth's orbit, Sakurai (1973, 1974) statistically analysed the time lag of the SSC after the generation of the SSC of geomagnetic storms and of Forbush effects of cosmic rays as a function of the heliographic longitude of the corresponding flares. The resulting time intervals yield information on the velocity of the propagation of interplanetary shock waves as a function of the heliographic longitude. By employing mean time intervals Sakurai (1973) determined the angular distribution of the mean velocity of shock waves which indicates that the shock waves do not propagate isotropically through interplanetary space and that the largest velocity was observed about 30° west of the central meridian plane.

Recently a number of papers has been published (Taylor, 1969; Landt and Croft, 1970; Chao and Lepping, 1974; Savassano et al., 1973) in which the authors determined the shape and characteristics of flare-generated interplanetary shock waves by using satellite observations of the plasma and magnetic field. These papers present a statistical study of the gross geometry of a "typical" or average shock surface based on multiple spacecraft sightings and their relative orientation with respect to the parent flare.

Apart from these statistical studies there exist several papers (Mariani et al., 1970; Lepping and Chao, 1976; Ness and Taylor, 1969) dealing with a detailed study of the ecliptic plane geometry of a single shock surface near 1 AU on the following dates: July 8, 1966; February 15-16, 1967; February 25, 1969.

The facts about the spatial distribution of the velocity of the flare-generated interplanetary shock waves form the foundation for understanding their dynamics, energy and also the processes by which the plasma is ejected from the solar flare region. In principle, this knowledge is best obtained from observing a certain flare-generated interplanetary shock wave at various heliocentric longitudes by means of spacecraft.

The purpose of the present paper is to examine the angular distribution of the velocities of the propagation of flare-generated shock waves with the help of multiple spacecraft observations and using well-documented events. To determine the angular distribution of the shock wave propagation velocity the observations from the solar orbiting Pioneer space probes constituted our principle data source. Occasional observations from the Venera and Mariner interplanetary probes were also used. This paper represents the first large collection of selected flare-generated shock wave data as observed simultaneously by several spacecraft in interplanetary space.

2. PROPAGATION OF FLARE-GENERATED SHOCK WAVES, AUGUST 2 TO 13, 1972

2.1 Velocity Anisotropy in the Propagation of Flare-Generated Waves, Observed Between August 2 and 13, 1972

In this initial part of the paper we shall discuss the properties of the propagation of shock waves, generated by sequential solar flares in McMath region 11976, between August 2 and 13, 1972 (see Table 1). Although the solar and interplanetary events, produced by this active region, have already been examined sufficiently from various aspects in the papers of Dryer et al. (1975, 1976), Zastenker et al. (1976), and Pintér and Dryer (1977), we consider it important to point out in greater detail some of the angular properties of the propagation of these shock waves in order to understand better their mechanism of propagation in interplanetary space.

Region 11976 was quite active in producing solar coronal and interplanetary waves, which generated strong SSC effects and Forbush decreases in the cosmic ray intensity (Venkatesan et al., 1975). Direct observations of interplanetary shock waves were obtained by five spacecraft: Prognoz 1 and 2, Heos B, Pioneer 9 and 10 (Mihalov et al., 1974; Cambou et al., 1975; Vaisberg et al., 1975). We shall not consider the Pioneer 10 observations, because we will only study the velocity of propagation out to about 1.0 AU. The spacecraft Prognoz 1 and 2, and Heos B had a circumterrestrial orbit; Pioneer 9 was located about 47°E of the Sun-Earth line. Very important additional information about the propagation of shock waves was obtained from interplanetary scintillations of discrete radio sources (Rickett, 1975; Watanabe et al., 1973). In addition the transition of the shock wave at a heliocentric distance of 0.993 AU and 56.7°W of the Earth was identified on August 3 and 8 from the sudden brightening of the comet P/Giacobini-Zinner (Dryer et al., 1975; D'Uston, 1975).

Table 1. Properties of the Shock Waves Generated by Sequential Flares in McMath Region 11976

EVENT	SHOCK I	SHOCK II	SHOCK III	SHOCK IV
Solar Flare	0316 UT, August 2	1959 UT, August 2	0621 UT, August 4	1505 UT, August 7
Location	14°N, 35°E	13°N, 28°E	15°N, 09°E	14°N, 38°W
Optical Importance	1B	2B	2B	3B
Radio Emission	Type II/IV	Type II/IV	Type II/IV	Type II/IV
Pioneer 9	0440 UT, August 3	1117 UT, August 3	2323 UT, August 4	0710 UT, August 9
Average Shock Velocity \bar{V}_{S-P9} (km/sec)	1284*	2118*	1893*	808*
Average Shock Velocity Normalized to 1 AU \bar{V}_{S-P9} (km/sec)	1020	1678	1476	640
Local Shock Velocity V_{S-P9} (km/sec)	431*	667*	1183*	672*
Earth	0119 UT, August 4	0221 UT, August 4	2054 UT, August 4	2354 UT, August 8
Average Shock Velocity \bar{V}_{S-E} (km/sec)	910	1389	2864	1290
Local Shock Velocity V_{S-E} (km/sec)	465	771	~1800	~1100

*Dryer et al. (1976)

Table 1 contains some important data on the solar flares which very probably causes interplanetary shock waves (Dryer et al., 1975). This table also gives information on the velocity of propagation of the flare-generated shock waves.

Using these data we determine the angular distribution of the mean velocities of shock waves (Shock I-IV) in relation to the heliocentric longitude of the associated flares from observations made close to the Earth, as well as from those made by Pioneer 9. Figure 1 shows:

- (i) the dependence of the mean velocity \bar{V}_{S-Pg} of the shock waves between the Sun and the Earth on the heliographic longitudes of the corresponding associated flares (illustrated by the solid curve),
- (ii) the dependence of the mean velocity \bar{V}_{S-Pg} also on the heliocentric longitude of the flares (illustrated by the dot-dashed curve), and

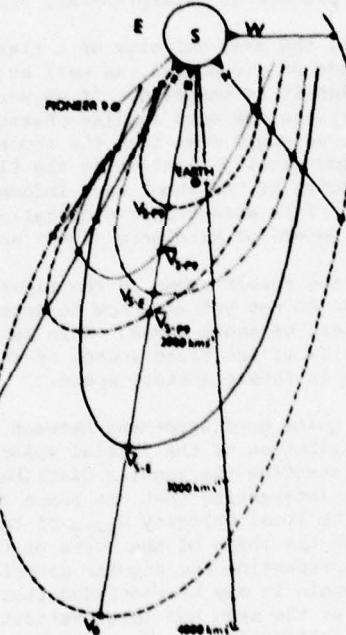


Figure 1. Solar Longitude Dependence of the Interplanetary and Coronal Shock Velocities Emitted by Solar Flares Between August 2 and 11, 1972. V_{S-Pg} (dashed curve) and V_{S-g} (illustrated by the curve composed of sequences of three dots and three dashes) are the local velocities of the shock waves, recorded by Pioneer 9 and close to the Earth by Prognos 1 and 2, Heos B, and Explorer 41. V_{S-Pg} (illustrated by the dot-dashed curve) and V_{S-g} (illustrated by the solid curve) are the mean velocities of the propagation of shock waves between the Sun and Pioneer and the Earth, respectively. \bar{V}_{S-Pg} is the mean velocity of the wave between the Sun and the Earth normalized to 1 AU, and finally, V_0 represents the velocity of the coronal shock wave at the distance from the Sun at which the wave begins to decelerate.

(iii) the dependence of the local radial velocity V_{S-E} (illustrated by the curve composed of sequences of three dots and three dashes) and V_{S-P9} (illustrated by the dashed curve) of the shock waves on the heliocentric longitude of the associated flares.

The local velocities V_{S-P9} were computed by Dryer et al. (1976) from the plasma parameters measured by Pioneer 9. In order to compare the mean velocities of shock waves, measured at the heliocentric distance of the Earth, with the mean velocities, measured at a heliocentric distance of 0.77 AU, where Pioneer 9 was located, we normalized the mean velocities \bar{V}_{S-P9} to 1 AU assuming linear deceleration, which represents a first approximation. The dependence of the normalized mean velocity \bar{V}_{S-P9} of the shock waves on the heliographic longitude can also be seen in Figure 1 (dotted curve). For the purpose of other analyses we have illustrated the angular distribution of the radial velocities of flare-associated coronal shock waves in Figure 1, i.e. the initial velocities V_0 , from which the deceleration of the interplanetary shock wave begins (Pintér and Dryer, 1977). In some cases V_0 is identical with V_R , i.e. the velocity of the coronal shock wave is determined from the frequency drift of a type II radio burst. For the sake of completeness we have also included in Figure 1 the velocity of the coronal shock wave, determined from the frequency drift of a flare which occurred at the west limb at 1230 UT on August 11, 1975, but did not produce an interplanetary shock wave.

As indicated by Figure 1, the mean velocity of a flare-generated shock varies with the heliographic longitude of its source, as well as with the heliographic longitude of the point at which it is observed. If we were to assume that the curves, shown in Figure 1, express the mean angular characteristics of the propagation of shock waves, the above would mean that the shock waves do not always propagate spherically, or symmetrically relative to the flare meridian. This result suggests that the velocity of the shock wave induced by a flare varies with the direction of propagation. This anisotropic propagation of interplanetary shock waves was pointed out in the papers of Hirshberg (1968) and Sakurai (1974).

It should be noted that the result shown in the figure is peculiar and that it requires further research. We do not yet know how to determine the mechanism which controls the propagation pattern of shock waves. This mechanism may be associated with some of the characteristics of the flare source of shock waves itself, or with the conditions of propagation in interplanetary space.

Figure 1 also indicates quite good agreement between the shape of the curve, representing the angular distribution of the initial velocity V_0 of shock waves and the shape of the curves, representing the angular distributions of the velocities \bar{V}_{S-E} , V_{S-E} , and V_{S-P9} . It is interesting that the shape of the curve, representing the angular distribution of the local velocity V_{S-P9} of the shock waves observed by Pioneer 9, does not agree with the shape of the curve of the mean velocities \bar{V}_{S-P9} , but with the curves representing the angular distributions of the velocities \bar{V}_{S-E} , V_{S-E} , and V_0 . On the whole it may be concluded that the velocities of the coronal shock waves, as well as the mean and local velocities of the interplanetary shock waves are evidence for collimation of the plasma ejection from the flare region outward into interplanetary space (Hakura, 1975). It was found that the smaller the difference in heliographic longitude between the associated flare and the point at which the shock wave is observed, the more likely the tendency for the velocity to be relatively larger. The velocity of the shock waves is highest close to the plane of the meridian which crosses the appropriate flare region. In the events being studied, the flare observed at 9°E on August 4, 1972 at 0621 UT had the smallest relative distance between the longitude of the flare and the central meridian of the solar disk as observed from the Earth, and the interplanetary shock wave associated with it had the highest mean velocity $\bar{V}_{S-E} = 2864$ km/sec, measured close to the Earth. An exception to the general case may be illustrated by measurements from Pioneer 9. The largest mean velocity $\bar{V}_{S-P9} = 2120$ km/sec was recorded for the

shock wave which was associated with the flare of August 2 at 1959 UT, observed 17°W of the Sun-Pioneer 9 line, and not the shock wave generated by the flare on August 2, 1972 at 0316 UT, located 12°W of Pioneer, or only 5° closer to Pioneer 9. The deviation from the assumed "regularity" could, in this case, have been caused by a deformation of the wave with inhomogeneities in the solar wind at the time of propagation, and it is also a fact that the said shock waves were observed by Pioneer 9 in rapid sequence (0440 UT and 1117 UT on August 2, 1972), so that they could have influenced one another.

2.2 Spatial Distribution of Shock IV

Of the series of flare-generated interplanetary shock waves, which followed in sequence in August of 1972, given in Table 1, we investigated in greater detail the spatial distribution of the propagation velocities for shock IV. This shock wave was emitted by a flare which occurred at 1505 UT on August 7, 1972 at 14°N, 38°W and was accompanied by a combined type II/IV radio burst. A large amount of data was obtained on this shock wave from which information on its propagation at various heliocentric longitudes could be derived (Pintér and Dryer, 1977). Only such observations of interplanetary shock waves at various heliocentric longitudes are capable of providing an accurate picture of their propagation properties and shape of the shock surface.

Dryer et al. (1975) determined the trajectories and deceleration characteristics of this shock wave, which were further refined by Pintér and Dryer (1977). Figure 2, which shows the mean velocities of the shock wave as a function of helio-

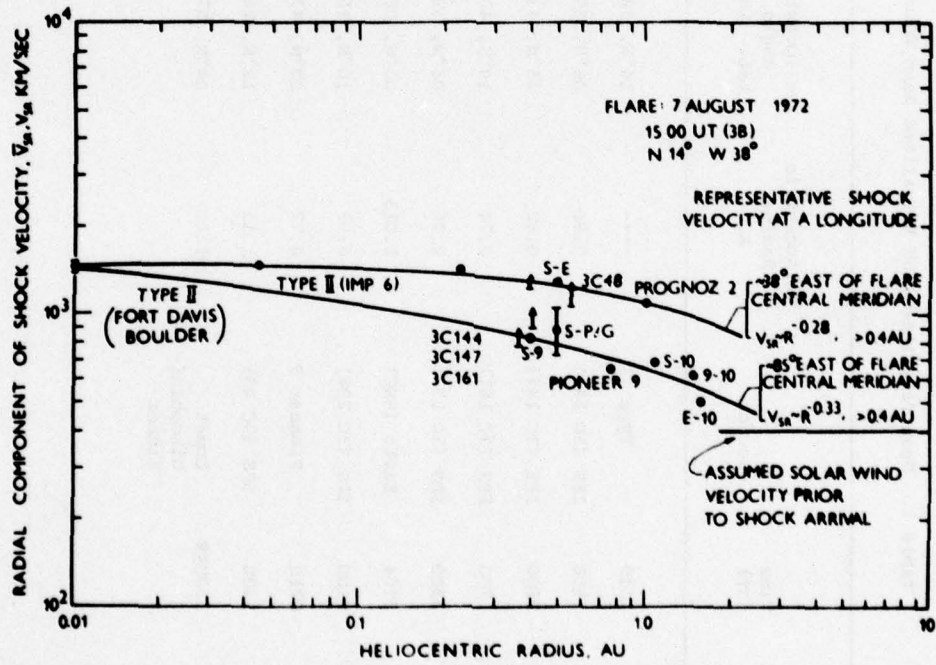


Figure 2. Average Velocity of Shock IV as a Function of Heliocentric Radius. The two solid curves are estimates for the asymmetrical shock velocity at two longitudes east of the flare's central meridian (Pintér and Dryer, 1977).

Table 2. Mean Velocities and Normalized Mean Velocities at 1 AU for Shock IV (August 1972)

Date 1972	Time (UT)	Source	Heliocentric Radius AU	Latitude Lat.	Longitude Long.	Average Shock Velocity km/sec	Normalized Shock Velocity km/sec	References
Aug. 7	1519	Type II	----	14°N, 38°W	1500	-----	-----	Maxwell (1973)
Aug. 8	1600	IPS (3C 144)	0.80	06°N, 39°W	1350	1076	1075	Rickett (1975)
Aug. 8	1600	IPS (3C 147)	0.82	25°N, 43°W	1383	1134	1134	Rickett (1975)
Aug. 8	1700	IPS (3C 161)	0.74	19°S, 40°W	1247	930	930	Rickett (1975)
Aug. 8	2300	IPS (3C 273)	0.76	06°N, 39°E	998	750	750	Rickett (1975)
Aug. 8	2354	Earth (SSC)	1.015	00°N, 00°E	1290	1290	1290	Dryer et al. (1975)
Aug. 9	0100	IPS (3C 298)	0.98	10°N, 15°E	1211	1180	1180	Rickett (1975)
Aug. 9	0710	Pioneer 9	0.77	00°N, 47°E	806	640	640	Dryer et al. (1975)
Aug. 9	1200	IPS (3C 48)	1.11	12°N, 16°W	1022	1135	1135	Rickett (1975)
Aug. 9	1500±9	Comet Giacobini-Zinner	~1.00	04°N, 57°W	906±171	906	906	Dryer et al. (1975)

centric distance, gives the more accurate trajectory of shock IV. The two solid curves are estimates for the asymmetrical shock velocity at two longitudes, 38° and 85°E of the flare's central meridian. This figure proves the fact that the shock wave propagates anisotropically in interplanetary space, i.e. the velocity of propagation of the shock is a function of the heliocentric longitude.

Table 2 gives a summary of the mean velocities and normalized mean velocities at 1 AU for shock IV, determined from spacecraft observations, IPS observations, both near and out of the ecliptic plane, as well as the mean velocity determined from observations of the periodic Giacobini-Zinner comet. The normalizing of the mean velocities to 1 AU was carried out by using the simple relation

$$\bar{V}_{(\text{average at 1 AU})} = \bar{V}_{(\text{average } R_i)} \frac{R_i}{R_{(1AU)}} \quad (1)$$

which represents a first approximation. By using the values in Table 2 we examined the normalized mean velocities of interplanetary shock waves as a function of the direction of their propagation, i.e. as a function of the heliocentric longitude of the point of observation. The angular distribution of the shock wave velocities are in Figure 3a, which also characterizes the contours of the shock front.

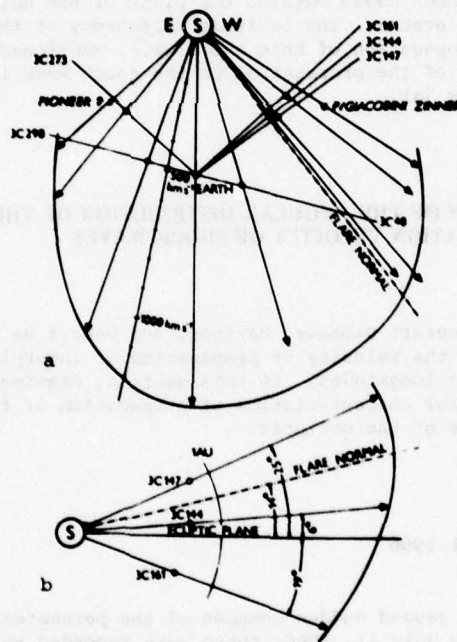


Figure 3. Part a: Configuration of the Interplanetary Shock Wave (Shock IV) of August 8-9, Derived from the Mean Velocity of Propagation at Various Heliocentric Longitudes and Distances. The velocities of the shocks were normalized to 1 AU. The line of sight to each of the radio sources 3C 161, 3C 144, 3C 48, 3C 298, and 3C 273 is indicated in projection onto the plane of the ecliptic. The positions of Pioneer 9 and the Earth are also shown. Part b: Configuration of the shock wave outside the plane of the ecliptic, determined from IPS observations.

Figure 3a shows that this interplanetary shock wave expanded non-spherically on a broad front and asymmetrically relative to the plane of the meridian which crosses the "associated flare". Of course, we are able to speak of a quasi-spherical symmetry, if the effective center of generation of the blast wave is shifted to a distance of about 0.4 AU and 15°W of the central meridian. This result would be in accordance with the findings of Taylor (1969) and Bavassano et al., (1973). One can explain this shift of the center of quasi-sphericity to 0.4 AU by the fact that, after the flare explosion, the ascending wave, directed into interplanetary space, has the nature of a piston-driven shock out to 0.4 AU, which may decelerate, or accelerate, and if so, it will decelerate quasi-spherically as a blast-like shock (Dryer et al., 1975). It should be pointed out that this example is not typical, as we shall see below, for the propagation of shock waves in interplanetary space.

Very little information is known on the velocity of propagation of shock waves outside the plane of the ecliptic. A first attempt to this effect was made by Watanabe (1975) in connection with shock IV, the result of which we shall specify below. Figure 3b shows the angular distribution of the mean velocity of shock IV determined from IPS observations. The velocities are also normalized to 1 AU. Only radio sources 3C 147, 3C 144, and 3C 161 were used; the mean velocities of the shock waves, determined from them, were close to the flare normal. The meridional cross-section shows the anisotropic distribution of the velocity outside the ecliptic plane, the largest velocity being observed in the direction of the flare normal, i.e. the velocity decreases with increasing angular distance from the heliocentric latitude of the flare. Whether this fact is a general property of the velocity of propagation of shock waves outside the plane of the ecliptic, will have to be examined on further events. The latitude anisotropy of the distribution of the mean velocity of propagation of this shock wave, mentioned above, could have distorted the contours of the propagation of the shock wave in the plane of the ecliptic (see Figure 3a).

3. CHARACTERISTICS OF THE ANGULAR DISTRIBUTION OF THE MEAN PROPAGATION VELOCITY OF SHOCK WAVES

Thanks to spacecraft Pioneer, Mariner, and Venera we are now able to examine the distribution of the velocity of propagation of interplanetary shock waves at various heliocentric longitudes. In this section, drawing on the individual events, we examine the spatial characteristics of propagation of flare-generated shock waves at 1 AU in the plane of the ecliptic.

3.1 Event of July 10-11, 1966

The shock wave caused sudden changes of the parameters of the solar wind plasma at 1542 UT on July 11, 1966; these were recorded by Explorer 33 (Lazarus and Binsack, 1969). At the same time an SSC was recorded in the geomagnetic field. The sudden changes of the plasma parameters and of the magnetic field at the time of the passage of the shock wave were also recorded by the Pioneer 6 space probe. At the time of the passage at 1800 UT on July 10, 1966, Pioneer 6 was located at a heliocentric distance of 0.84 AU, heliocentric longitude 45°W of the Earth. The source of this shock wave was a flare of importance 2B, which occurred at 0306 UT

JULY 10-11, 1966

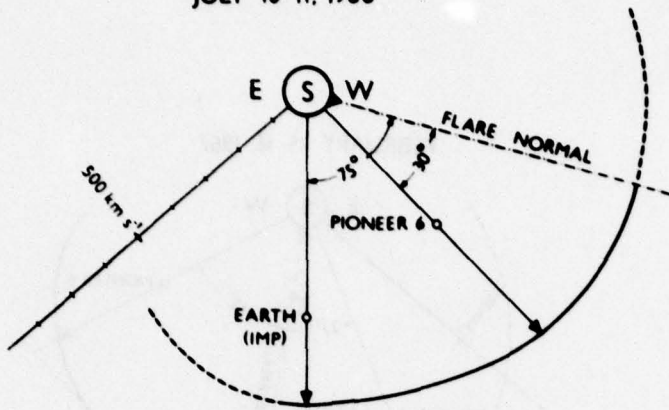


Figure 4. Estimated Angular Distribution of the Interplanetary Shock Wave Deduced from Multiple Spacecraft Observations. The shock wave was associated with the flare of July 9, 1966.

on July 9, 1966 at 35°N , 75°W (Pintér, 1975). The flare was also accompanied by a type II/IV radio burst.

This flare-generated interplanetary shock wave has already been analysed earlier in some papers (Ness and Taylor, 1969; Rao et al., 1969, Lazarus and Binsack, 1969). It is being mentioned here because the authors apparently incorrectly associated the shock wave, recorded by Pioneer 6 at 1822 UT on July 10, 1966, with the proton flare of July 7, 1966 beginning at 0025 UT. This would mean that the transit time of this flare to Pioneer 6 would have been 90 hours (Ness and Taylor, 1969). As can be seen in Figure 4, Pioneer 6 was located only 30°E of the flare normal, and it is very probable that the shock wave, generated by the flare of July 9 first passed the closer detector (0.8 AU) at the time of its quasi-spherical propagation and then reached the Earth's orbit. The mean velocity of the shock wave near the Earth (i.e. at 1 AU) is 700 km/sec, and the normalized velocity of the shock wave passing Pioneer 6 at 1 AU is 743 km/sec. One can see that quasi-isotropic propagation of the shock wave is involved, with a certain tendency to increasing the velocity towards the heliocentric longitude of the flare normal.

3.2 Event of February 15-16, 1967

With this event the shock wave was observed at 2352 UT on February 15 by Explorer 33 close to the Earth (Hirshberg et al., 1970) and later by Pioneer 7 at 1848 UT on February 16 (Lepping and Chao, 1976). Pioneer 7 was at a heliocentric distance of 1.13 AU and 23°E of the Sun-Earth line. The passage of the shock wave around Pioneer 6, which was at a heliocentric distance of 0.84 AU and 62°W of the Earth, was not observed directly because of a gap in the data. However, on the resumption of data acquisition at 1216 UT on February 15, a typical post-shock level of plasma and interplanetary magnetic field was observed. Lepping and Chao (1976) assumed that the shock wave passed Pioneer 6 just before the data acquisition

FEBRUARY 15-16, 1967

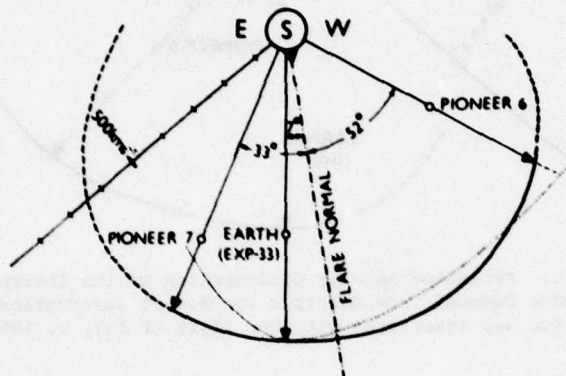


Figure 5. Estimated Angular Distribution of the Interplanetary Shock Wave at 1 AU for February 15-16, 1967. The shock wave was associated with the flare of February 13, 1976. The curve represents the positions of Pioneers 6 and 7 and Explorer 33 in the plane of the ecliptic during the passage of the flare-associated-shock.

was resumed at 1216 UT. The shock wave was associated with the 3B flare observed at 1745 UT on February 13, located at heliographic 21°N and 10°W . The flare was accompanied by a strong combined type II/IV radio burst. Lepping and Chao (1976) determined the ecliptical plane geometry of the shock surface near 1 AU. In Figure 5 the dot-dashed curve represents approximately the large scale interplanetary shock surface geometry, as determined by Lepping and Chao (1976), as it intersects the ecliptic plane. These authors determined the shape of the shock surface from the velocity of propagation of the shock waves in the direction of the individual cosmic objects. Their results indicate a spherical asymmetric shock, i.e. anisotropic propagation of the shock wave. Burlaga and Scudder (1975) mentioned that the event of February 15-16 is an example of a flare-associated driven shock, whose surface was distorted as the result of interacting with a co-rotating stream that happened to be passing near by.

We carried out a re-interpretation of the propagation of this flare-generated shock wave and drew a conclusion different to that of Lepping and Chao (1976) and Burlaga and Scudder (1975). In Figure 5 the solid curve represents the large-scale geometry of the shock-wave surface, determined from the velocity of propagation to the individual objects. The average velocities of propagation, determined with the help of Pioneers 6 and 7, were normalized to 1 AU. It can be seen that the shock wave indeed propagates anisotropically, but the geometry of the shock surface is not as distorted as indicated by the authors mentioned above. Instead the interplanetary shock wave has a behavior typical in the sense that it attains maximum velocity in the direction of the flare normal. We are of the opinion that in this case the shock-stream interaction, mentioned by Burlaga and Scudder (1975) did not affect the propagation characteristics of the shock wave.

3.3 Shock of May 6-7, 1968

In the interval between May 5 and May 8, 1968, three spacecraft, i.e. Pioneers 6, 7, and 8, were capable of recording the passage of the interplanetary shock wave. At 2123 UT on May 3, 1968 a solar flare was observed at 19°N , 50°E , importance 1B. The flare generated a coronal shock wave as indicated by the observations of a type II radio burst. The shock wave escaped from the corona into interplanetary space where it crossed Pioneers 7 and 8, and the Earth, all at a distance of roughly 1 AU.

Figure 6a shows the shape of the surface of the flare-generated shock wave, determined from the mean velocities of the shock as observed at various heliocentric longitudes in the plane of the ecliptic. The figure shows at first glance the strong asymmetric angular distribution of the propagation velocity of the shock wave with a maximum velocity around the plane of the flare normal. Pioneer 6 was located 139°W of the flare normal, and did not record the passage of this shock which is indicative of non-spherical propagation.

Further evidence of the anisotropic propagation of the shock was provided by Landt (1974) who determined the geometry of the dense plasma cloud from the values of the propagation of a radio signal between the Earth and Pioneer 8 and from comparison of these values with the observations of the plasma parameters made by Pioneer 8. This type of experiment with propagation of radio waves allows one to determine the electron content between the Earth and a distant space probe.

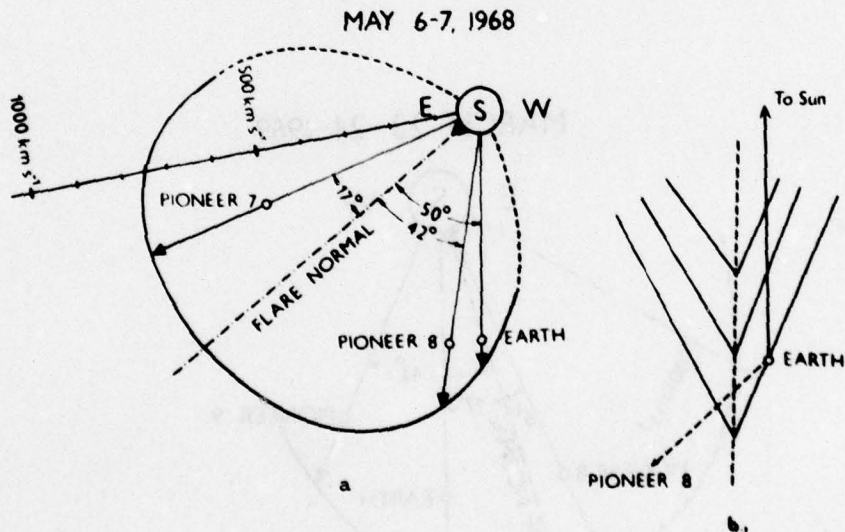


Figure 6. Part a: Estimated Angular Distribution of the Interplanetary Shock Wave of May 6-7, 1968 at 1 AU. The shock wave was associated with a flare observed on May 3, 1968. Part b: Possible shape of the plasma cloud (Landt, 1974). Pioneer 8 was 24×10^6 km away from the Earth and the Sun was 151×10^6 km from the Earth in the direction indicated.

Landt (1974) mentioned that the shock wave and the cloud, propagating behind it, were intersected by the radio signal before the shock was observed at the Earth; this is again indicative of the anisotropy of the propagation velocity of the shock. Figure 6b shows a sketch of the shape of the shock wave, determined according to Landt (1974), in the region between the Earth and Pioneer 8. In determining the shape of the disturbance, Landt (1974) assumed symmetry around a line extending radially from the Sun, and the contours were constructed concavely away from the Sun. If we compare the contours of the disturbance close to the Earth, shown in Figure 6 (part a and b) we can see that the shape we determined, as far as the central line of symmetry, agrees with Landt's. While the central symmetry shown in Figure 6b is incorrect, it does express the local nature of the disturbance.

3.4 Shock of March 23-24, 1969

Another example of the anisotropic propagation of a flare-generated shock wave at various heliocentric longitudes is shown in Figure 7. The largest mean velocity of 672 km/sec (at 1 AU) was determined from the passage of the shock wave around Pioneer 8, which was at 23°E heliocentric of the Earth, i.e. at a longitude very close to that of the flare which generated the shock wave. The smallest mean velocity of 518 km/sec was determined from the observations of Pioneer 9 which was located 42°W of the flare normal (Lockwood and Webber, 1975). Assuming a symmetric wave relative to the flare normal, the shape of the shock wave at 1 AU, determined from the angular distribution of the propagation velocity, is shown in Figure 7.

MARCH 23-24, 1969

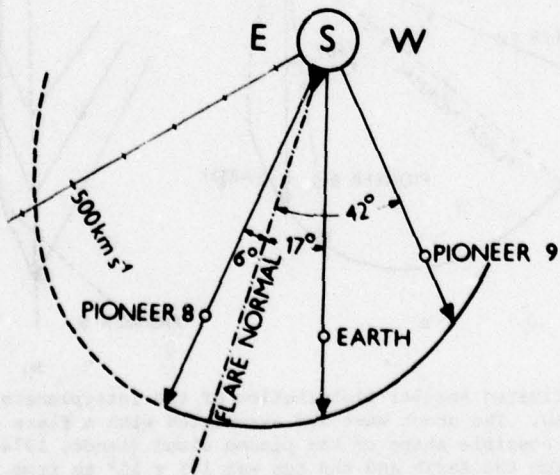


Figure 7. Velocity Distribution of the Interplanetary Shock Wave Observed on March 23-24, 1969. The shock was associated with a flare on March 21, 1969.

This interplanetary shock wave was associated with a flare observed at 0139 UT on March 21 at 20°N , 17°E , importance 2B. The flare was accompanied by a radio burst of type II/IV (Pintér, 1975).

3.5 Shock of April 12-13, 1969

The most representative example of the anisotropic angular distribution of the velocity of the propagation of flare generated interplanetary shock waves is shown in Figure 8. As can be seen the angular distribution of the velocity of the propagation of the flare-generated shock wave could be observed with the aid of spacecraft, located at various heliocentric longitudes over a range of 180° (Vernov et al., 1971; Lazarus et al., 1973; Bukata et al., 1971). This is one of the few cases for which the passage of the same shock wave was recorded at six different positions in space. In Figure 8 the locations of Pioneers 6, 7, 8, and 9, Venera 6, and the Earth (orbited by Explorer 33 and Vela 3 and 4) are marked with circles. The continuous curve in the figure represents the shock-wave front, determined from the mean velocities of wave propagation from the Sun to 1 AU.

The most probable solar source of this interplanetary shock wave was the flare which occurred just beyond the eastern limb of the solar disk (07°N , $>90^{\circ}\text{E}$) on April 10, 1969 in McMath region 10035. The first indication of this beyond-the-limb

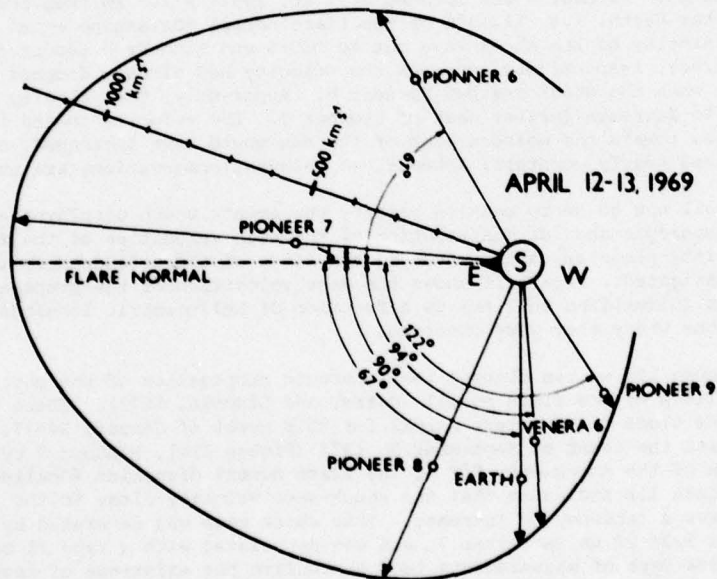


Figure 8. Estimated Angular Distribution of the Mean Velocity (Normalized to 1 AU) of the Shock Wave Observed on April 12-13, 1969 with Respect to the Position of the Associated Flare, Observed on April 10, 1969. This figure indicates a very good example of anisotropic propagation of a shock in interplanetary space. The highest velocity (1100 km/sec) can be observed in the meridional plane crossing the flare.

flare was observed at 0340 UT in the form of a surge. The very bright ascending surge occurred at 0355 UT and its rate of ascent amounted to 190 km/sec. A type II burst was recorded at the Culgoora Observatory, Australia, between 0356 and 0422 UT in the metre and decametre ranges. Figure 8 allows us to draw a brief conclusion about the nature of the propagation of this shock wave: The mean velocity of propagation of the shock wave, emitted by the flare, varies with the direction of propagation. The largest velocity is in the direction of the flare normal, and the mean velocity decreases with increasing angular distance from the flare. This is indicative of an anisotropic angular distribution of the mean velocity of propagation of the interplanetary shock wave.

3.6 Other Examples

We could go on to analyse in detail a number of other examples characterizing the anisotropic angular velocity distribution of the propagation of flare-generated interplanetary shocks. It was found that the regularities, determined with the studied examples, are generally quite valid as demonstrated by the examples given in Figure 9 and Figure 10. Figure 10 shows the angular distribution of the velocity of the propagation of a shock wave which was generated by a strong proton flare, observed on November 18, 1968 at the western limb of the Sun. The shock wave reached 1 AU at 0902 UT on November 20 and was recorded by the OGO-5 satellite. At that time Pioneer 9 was approximately 8.5 million km east of the Earth, also at 1 AU heliocentric, and the shock wave passed it at 0929.30 UT (Scarf et al., 1972). The passage of the shock wave was also recorded by Pioneer 8 at 2015 UT on November 20. Pioneer 8 was located at 1 AU, 149.7×10^6 km from the Sun, 22.3° E of the Earth, i.e. 112.3° E of the flare normal (Bavassano et al., 1973). The mean velocity of the shock wave out to OGO-5 and Pioneer 9 amounted to 879 and 872 km/sec, respectively, whereas the velocity had already dropped to 720 km/sec when the shock reached Pioneer 8. Apparently, the velocity would have continued to decrease further east of Pioneer 8. The velocity toward the flare normal, i.e. toward the western limb of the sun would have increased, or would have remained nearly constant; however, no relevant observations are available.

We shall now go on to mention briefly the events which displayed an isotropic or quasi-isotropic angular distribution of the mean velocities of the flare-generated interplanetary shock waves in the range of the heliocentric longitudes being investigated. Figure 11 shows the mean velocities of the propagation of shock waves (normalized to 1 AU) as a function of heliocentric longitudes of the positions where they were observed.

In Figure 11a we can observe the isotropic propagation of the shock wave as far as 116° W of the flare normal (Coffey and Lincoln, 1972). There were no observations close to the flare normal for this event of January 26-27, 1971; however, with the event of September 9, 1973 (Figure 11b), Pioneer 9 recorded the passage of the shock only 5° W of the flare normal direction (Gosling et al., 1975). Figure 11b indicates that the shock-wave velocity close to the flare normal does not have a tendency to increase. This shock wave was generated by a flare, observed at 1220 UT on September 7, and was associated with a type II radio burst. These type of measurements tend to confirm the existence of isotropically propagating flare-generated interplanetary shock waves over a wide range of about 100° . It is possible that the isotropic propagation of shock waves in the interplanetary medium is determined by the generation conditions on the Sun.

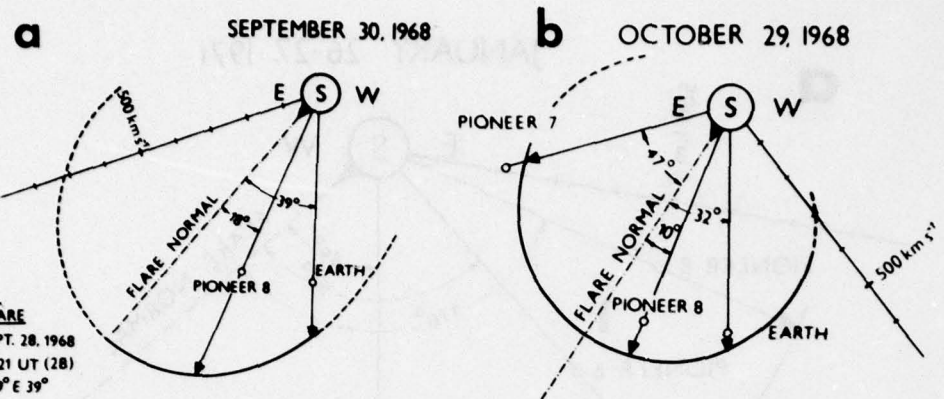


Figure 9. Pictorial Representation of the Velocity of Shock Waves as a Function of the Direction of their Propagation for the Events on September 30, 1968 (shown in Part a) and October 29, 1968 (shown in Part b). These mean velocities also indicate the gross features of the shape of the shock wave near 1 AU.

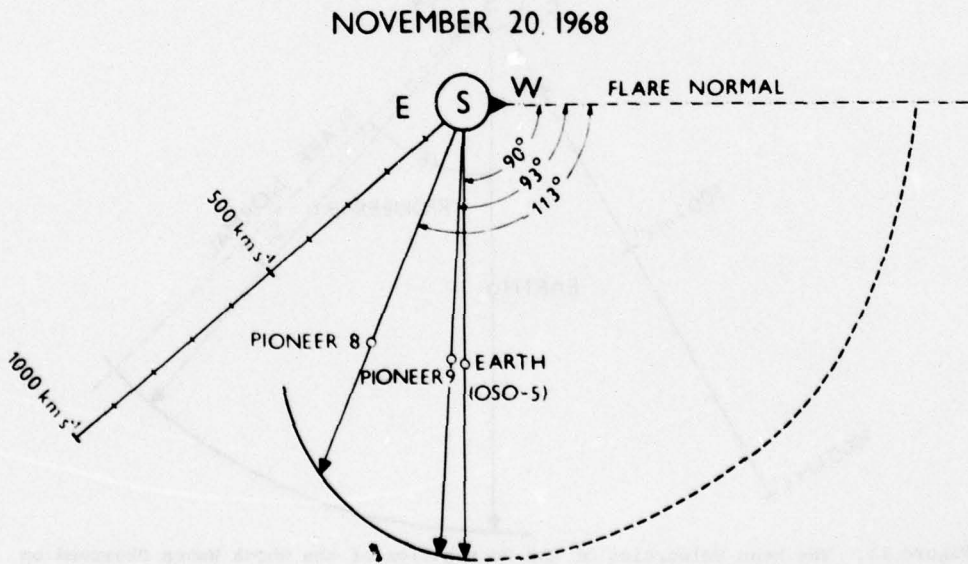


Figure 10. Angular Distribution of the Mean Velocity of Propagation of the Shock Wave Caused by the Flare of November 18, 1968 at the Western Limb of the Solar Disk

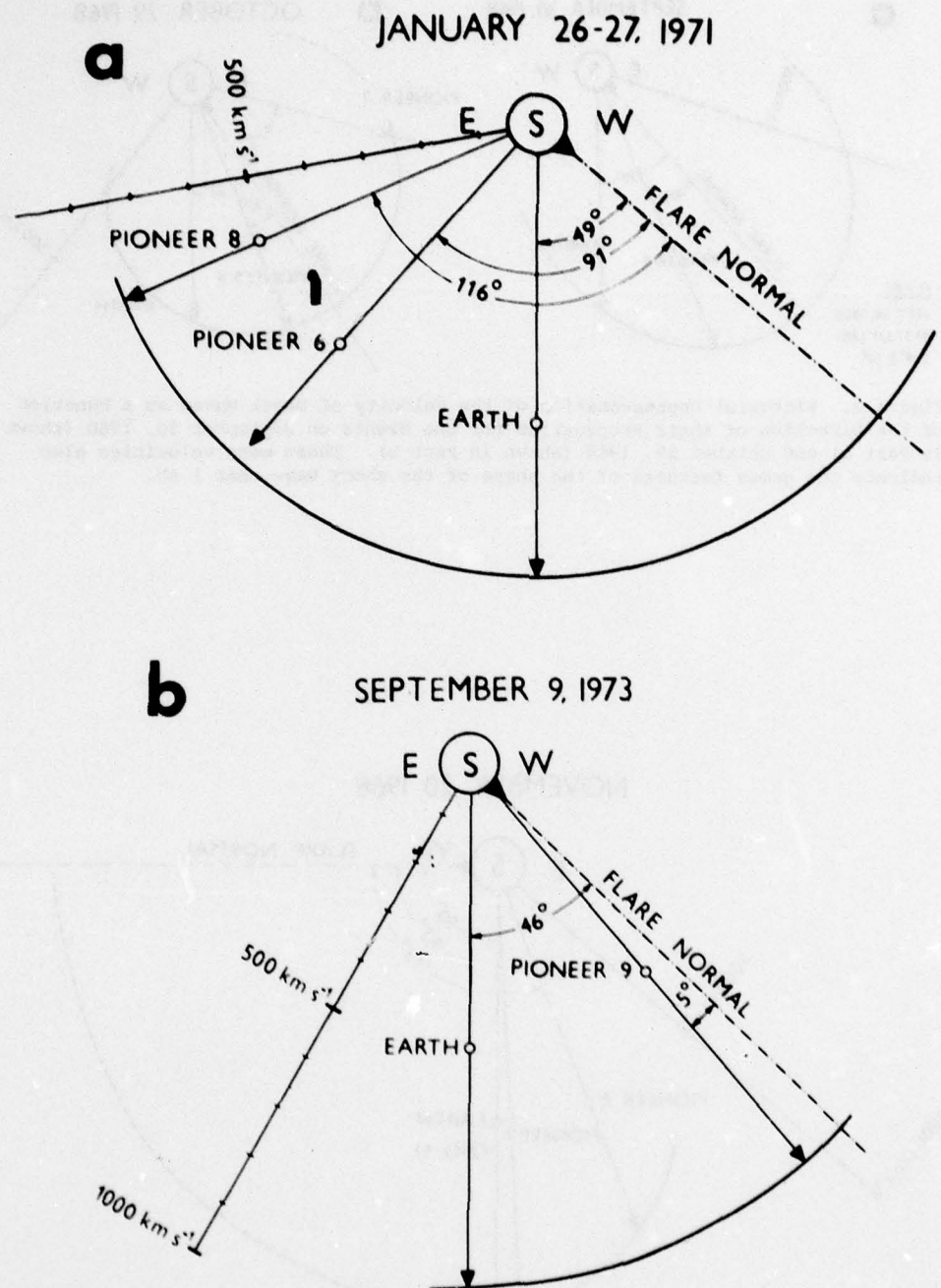


Figure 11. The Mean Velocities of the Propagation of the Shock Waves Observed on January 26-27, 1971 (shown in Part a) and on September 9, 1973 (shown in Part b). The mean velocities have been normalized to 1 AU. The figure indicates that the distribution of the propagation velocities was isotropic in both cases.

4. DISCUSSION OF RESULTS

There are a whole series of papers dealing with the theoretical and numerical propagation of flare-generated interplanetary shock waves (Hundhausen and Gentry, 1969; DeYoung and Hundhausen, 1971; Krimskij and Transkij, 1973; Dryer, 1974). However, there are few papers containing experimental evidence of the propagation of shock waves which either verify or disprove the major assumptions contained in the theoretical and numerical papers.

The purpose of this paper was to study the angular distribution of the mean velocity of the propagation of flare-generated interplanetary shock waves using multiple spacecraft observations. This research will provide the possibility of determining the real characteristics of the propagation of shock waves in interplanetary space, and also yield information on the shape of the shock front in the plane of the ecliptic close to 1 AU.

4.1 Characteristics of the Propagation of Flare-Generated Shock Waves

We shall now summarize the characteristics of the propagation of flare-generated interplanetary shock waves we have determined or adopted from earlier research:

(i) Flare-generated interplanetary shock waves in most cases propagate non-spherically, but there are also cases in which spherical or quasi-spherical propagation is quite evident.

(ii) Experimental multiple spacecraft observations enabled the angular distribution of the mean velocity of the shock waves to be determined with respect to the position of an associated flare. The mean velocity of the propagation of the shock wave, emitted by a flare, varies with the direction of propagation. The highest mean velocity is observed in the direction of the flare normal with the mean velocity decreasing with increasing angular distance (heliocentric longitude) from the flare. This is indicative of the anisotropic angular distribution of the mean velocity of the propagation of interplanetary shock waves in the plane of the ecliptic close to 1 AU.

(iii) By using IPS observations of discrete radio sources, in one case we were able to determine the angular distribution of the mean velocity of the propagation of an interplanetary shock wave outside the plane of the ecliptic. Anisotropic angular distribution of the mean velocity of the propagation was observed, the highest velocity being observed in the direction of the flare normal, i.e. at the heliocentric latitude of the flare, with the velocity decreasing in other directions.

(iv) The results indicate that in most cases the shape of the interplanetary shock wave is not spherical, but symmetric with respect to the meridional plane which crosses the position of an associated flare.

(v) The flare-generated interplanetary shock trajectories indicate a piston-driven character to about 0.3-0.6 AU, after which the shocks decay to blast-like motions (Dryer et al., 1975; Pintér and Dryer, 1977). Up to a heliocentric distance of 0.3-0.6 AU the piston-driven shock waves may accelerate, decelerate, or retain a constant velocity, but beyond 0.6 AU the blast-like wave has a decelerating nature. These properties of shock waves can be expressed in

plasma physics, as well as in astrophysics by means of the well-known parameter θ , defined as

$$\theta = \frac{R_s \dot{R}_s}{\dot{R}_s^2}, \quad (2)$$

where R_s is the distance of the shock front from the solar flare and \dot{R}_s is the shock velocity. Since R_s and \dot{R}_s are always positive, the sign of θ depends on the time rate of change of the shock velocity $\ddot{R}_s = d\dot{R}_s/dt$. Hence for:

- (i) Decelerating shock wave $\ddot{R}_s < 0$,
- (ii) Accelerating shock wave $\ddot{R}_s > 0$,
- (iii) Constant velocity wave $\ddot{R}_s = 0$.

For the case of a constant velocity shock front $\dot{R}_s = \text{constant}$, $\theta = 0$, the motion is isotropic.

4.2 Theoretical Explanation of the Characteristics Determining the Propagation of Shock Waves

We shall now try to explain the determined characteristics of the propagation of shock waves. The flares, generating the shock waves, mostly originate in the solar chromosphere and are of small angular dimension. In these layers of the chromosphere the density of the plasma depends strongly on the heliocentric distance ($\sim r^{-10}$) and the intensity of the magnetic field is high; we may, therefore, expect the disturbance from the flare explosion to be sufficiently directional. Moving away from the Sun the dependence of density on "r" decreases considerably and the disturbance front begins to develop. The deeper the layer of the solar atmosphere in which the initial explosion is generated, the more anisotropic the shock wave will be. This would then indicate that a flare, generated high in the corona, so-called coronal flares, would generate shock waves that propagate isotropically; i.e. spherically symmetrical. The propagation may also be affected by a number of other factors in the solar corona; in interplanetary space these factors may determine the isotropic or anisotropic nature of the propagation of the shock wave. If, for example, the flare explosion is completely encompassed by a high magnetic field region as on August 4, 1972 (Uchida, 1974), the wavefront emitted into interplanetary space will be strongly collimated. Also the existence of inhomogeneities in interplanetary space may cause the propagation of the shock wave to be strongly anisotropic. The occurrence of regions with increased density will hinder the propagation of the shock wave and, vice versa, a wave will propagate "more easily" in the direction of the "largest" decrease of density of the medium (Krimskij and Transkij, 1973).

In order to determine if a disturbance is collimated immediately after the flare explosion, we statistically investigated the dependence of the velocity of the disturbance on heliographic longitude. The velocity of the disturbance was determined from the time interval between the flare explosion, characterized by the beginning of the radio burst in the centimetre range, and the first onset of the type II radio burst at a certain frequency, which also yielded information on

the height of the disturbance above the chromosphere. The heavy solid curve shown in the polar diagram of Figure 12, derived from a point diagram (150 events were considered), characterizes the dependence of the highest disturbance velocity on heliocentric longitude. The velocity of the disturbances is highest 30°E and W of the central meridian; beyond these limits the velocity decreases towards the limb. Around the central meridian the velocity of the disturbances also decreases. It should be pointed out that, if this decrease around the central meridian is realistic, it remains unexplained. On the whole, Figure 12 indicates the expected fact that "the flare plasma and its shock wave are not travelling at the same velocity in all directions from the Sun".

5. DIRECTIONAL DIAGRAMS OF THE PROPAGATION OF FLARE-GENERATED SHOCK WAVES

As indicated by the experimental results in this paper and in the papers of Dryer et al. (1975), Pintér and Dryer (1977) and also in the theoretical papers of DeYoung and Hundhausen (1971), the flare-generated piston-driven shock waves proceed out to a distance of 0.3-0.6 AU (where they diffuse into the ambient plasma), i.e. the stream of ejected matter becomes collimated at that time and the continuing shock assumes the nature of a decelerating blast wave. At 1 AU the blast wave usually has a broad front and is symmetric to the flare normal. In these cases the effective region of forming of the shape of the shock wave is located at a distance of 0.3-0.6 AU from the Sun in a plane close to that of the flare normal.

Another alternative of the propagation of shock waves is also feasible: this assumes that the region where the characteristics of wave propagation are formed is

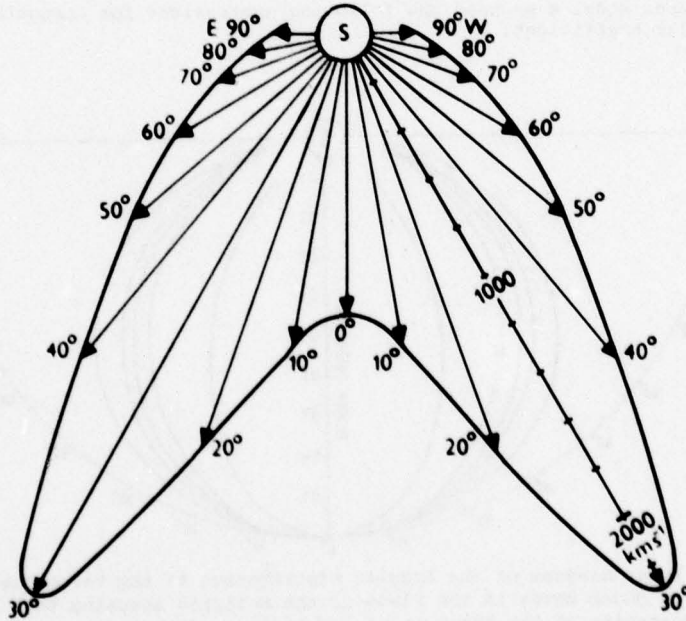


Figure 12. Polar Diagram Representing the Longitudinal Distribution of the Propagation Velocities of Coronal Shock Waves

directly on the solar surface. The propagation velocity of such a wave in the plane of the ecliptic will then depend on the zenith angle of the point where it leaves the flare region, i.e. under radial ejection of the plasma cloud on the heliographic longitude of the flare.

A polar diagram was used to investigate the directional, or angular properties of the mean velocity of the propagation of flare-generated shock waves. The polar diagram represents a geometric locus of the multiple coefficient of the mean velocity of the shock wave, emitted by the flare in various directions.

The mean velocity $\bar{V}(\lambda)$ of the front of the flare-generated wave at various angular distances, λ , with respect to the mean velocity $\bar{V}_{(\lambda=0^\circ)}$ in the direction of the flare normal can be determined from the expression $\bar{V}(\lambda)/\bar{V}_{(\lambda=0^\circ)} = D$ where $\bar{V}_{(\lambda=0^\circ)}$ is the axial mean velocity of the shock wave, i.e. in the direction of the flare normal, and $\bar{V}(\lambda)$ is the mean velocity at heliocentric distance, λ , from the axis of the shock, i.e. from the flare normal, and D is the angular coefficient.

The angular coefficient was computed for two cases:

(A) When the effective region of forming of the wave is at the solar surface or close to it, i.e. the angular coefficient for the heliocentric longitude $\lambda=90^\circ$ from the flare normal is equal to zero, $D(90^\circ) = 0$; and

(B) If we assume that the effective region of forming of the wave is at a distance of 0.3-0.6 AU, i.e. $D(90^\circ) \neq 0$.

We computed the propagation of the shock waves for both models, A and B, in accordance with the values of the angular coefficient, D , given above.

As regards Model A we used the following expressions for computing the values of the angular coefficient:

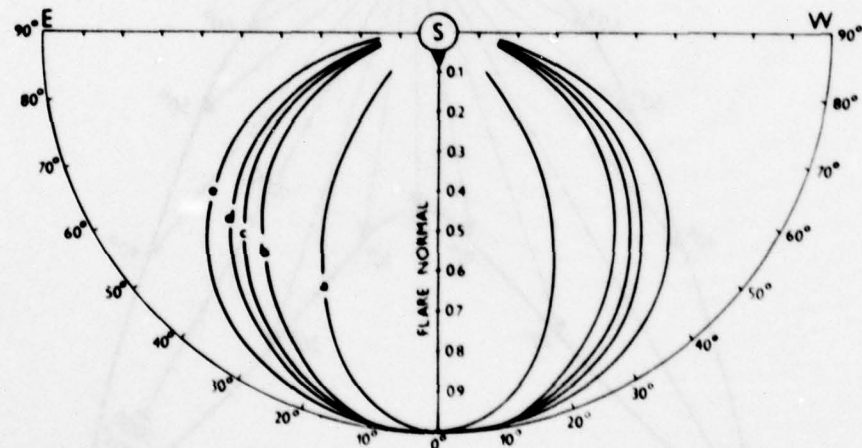


Figure 13. Polar Diagram of the Angular Distribution of the Velocities of Propagation of Shock Waves in the Plane of the Ecliptic Assuming that the Effective Region of Generation of the Shock is at the Surface of the Sun.

$$D = \begin{cases} k \sin(G \cos \lambda), \\ k \cos(G \sin \lambda) - \cos G / \cos \lambda. \end{cases} \quad (3)$$

(4)

The solution of these two equations for various heliocentric longitudes, λ , will provide an idea of the angular distribution of the propagation of flare-generated shock waves. In Figure 13 curves a-e represent a polar diagram of the values of the angular coefficient, computed from the above equations for the parameters given in Table 3. Figure 13 indicates that curve "a" yields a very "extended" shape of the angular distribution of the velocity of the shock wave, which could characterize the curves, determined experimentally, in Figure 2. Curves "d" and "e" can be used to model the distribution of the mean velocity of the shock wave which occurred on May 6-7, 1968 (Figure 6) and the velocity of the shock wave of October 29, 1968 (Figure 9, part b).

It seems that the model of the flare-generated shock wave that assumes the effective region of forming the shape of the wave is located at a distance, ρ , equal to 0.3-0.6 AU from the Sun is more realistic. We can thus use the relation

$$D = \frac{\bar{V}(\lambda)}{\bar{V}(\lambda=0^\circ)}, \text{ i.e.} \quad (5)$$

$$\bar{V}(\lambda) = \bar{V}(\lambda=0^\circ) k [1 + a^2 - 2a \cos(\psi - G \cos \lambda)]^{1/2}, \quad (6)$$

in which the parameter $a = \rho/R$, R being the distance from the Sun out to 1 AU, and G and ψ suitably chosen parameters. Table 4 gives the parameters used in computing the angular coefficient, D , plotted in Figure 14 as curves a-d.

If we want to illustrate the directional property in the ecliptic plane, the mean velocity $\bar{V}(\lambda=0^\circ)$ of the wave measured along the flare normal, is multiplied by the angular coefficient $D(\lambda)$, which is computed for various helio-graphic longitudes to the west and east of the flare normal. The directional properties of propagation of flare-generated symmetric shock waves, governed by

Table 3. Parameters Used to Determine the Curves Illustrated in Figure 13

Equation	Curve	k	G
(4)	a	0.5000	180°
(4)	b	1.0000	90°
(4)	c	5.2356	36°
(3)	d	0.8506	36°
(3)	e	0.61805	72°

Table 4. Parameters Used to Determine the Curves Illustrated in Figure 14

Curve in Figure 14	a	k	ψ	G
a	0.6	0.690264	340°	108°
b	0.5	0.732122	340°	108°
c	0.4	0.777903	340°	108°
d	0.3	0.827780	340°	108°

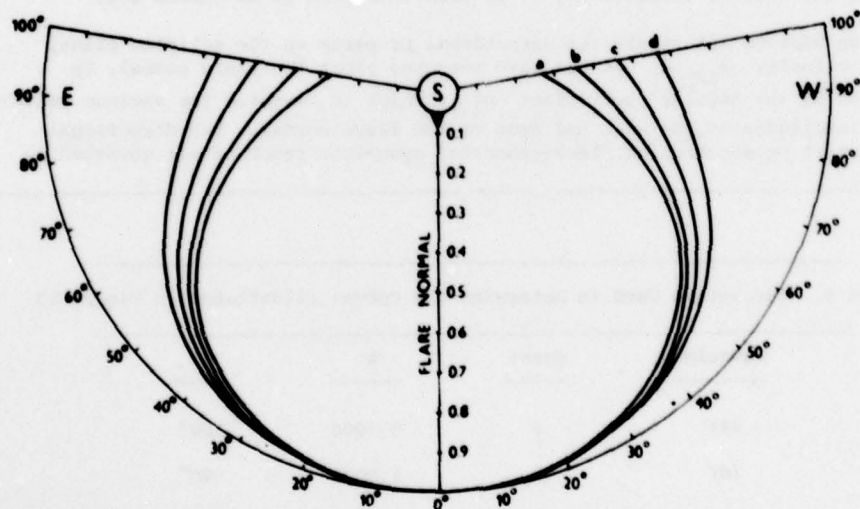


Figure 14. Polar Diagram of the Angular Distribution of the Propagation Velocity of Shock Waves in the Plane of the Ecliptic Assuming that the Effective Region of the Generation of the Shock is at a Distance of 0.3-0.6 AU from the Sun

Model B, are characterized by the waves expanding on a broad front (Figure 14); these waves can also be observed at larger heliocentric distances than 90° . This is demonstrated by the fact that we frequently observe the passage of the shock waves from beyond-the-limb flares in the neighbourhood of the Earth. The theoretical curves a-d in Figure 14 characterize the directional properties of the propagation of shock waves determined experimentally and as illustrated in Figures 4, 5, 8, and 9 (part a). It should be pointed out, of course, that with a suitable choice of the parameters a , ψ , and G , one can achieve a theoretical value of the angular distribution of the velocities of shock waves which fits very closely the values of velocities, determined experimentally by multiple spacecraft observations.

As a final note, measurements of flare-generated interplanetary shock waves from multi-spacecraft should be continued; this would enable us to study some of the detailed structure of the propagation of the shock waves in a wide range of heliocentric longitudes and latitudes.

Acknowledgments

The author wishes to thank all his colleagues who supplied him with the plasma and interplanetary magnetic field data from space probes Pioneers 6, 7, 8, and 9. He also wishes to thank Mr. A. Tlicik and Mrs. E. Kechesova for preparing the drawings and manuscript for publication.

References

- Bavassano, B., F. Mariani, and N. F. Ness, Pioneer 8 observations and interpretations of sixteen interplanetary shock waves observed in 1968, *J. Geophys. Res.*, 78, 4535, 1973.
- Bukata, R. P., U. R. Rao, K. G. McCracken, and E. P. Keath, Observation of particle fluxes over extended solar longitudes during the solar flare event of March 31 to April 10, 1969, 12th International Conference on Cosmic Rays, Hobart, Conference Papers (University of Tasmania), 2, 514, 1971.
- Burlaga, L. F., and J. D. Scudder, Motion of shocks through interplanetary space, *J. Geophys. Res.*, 80, 4004, 1975.
- Cambou, F., O. L. Vaisberg, H. Espagne, V. V. Temny, C. D'Uston, and G. N. Zastenker, Characteristics of interplanetary plasma near the earth observed during the solar events of August 1972, in *Space Research XV*, edited by M. J. Rycroft, p. 461, Academic-Verlag, Berlin, 1975.
- Chao, J. K., and R. P. Lepping, A correlative study of ssc's, interplanetary shocks, and solar activity, *J. Geophys. Res.*, 79, 1799, 1974.

- Coffey, H. E., and J. V. Lincoln (Compilers), *Data on Solar-Geophysical Activity Associated with the Major Ground Level Cosmic Ray Events of 24 January and 1 September 1971*, Report UAG-24, World Data Center A for Solar-Terrestrial Physics, Boulder, Colorado, 1972.
- DeYoung, D. S., and A. J. Hundhausen, Two-dimensional simulation of flare-associated disturbances in the solar wind, *J. Geophys. Res.*, **76**, 2245, 1971.
- Dryer, M., Interplanetary shock waves generated by solar flares, *Space Sci. Rev.*, **15**, 403, 1974.
- Dryer, M., A. Eviatar, A. Forhlich, A. Jacobs, J. H. Joseph, and E. J. Weber, Interplanetary shock waves and comet brightness fluctuations during June-August 1972, *J. Geophys. Res.*, **80**, 2001, 1975.
- Dryer, M., Z. K. Smith, R. S. Steinolfson, J. D. Mihalov, J. H. Wolfe, and J. K. Chao, Interplanetary disturbances caused by the August 1972 solar flares as observed by Pioneer 9, *J. Geophys. Res.*, **81**, 4651, 1976.
- D'Uston, C., Etudes des perturbations interplanetaires du mois d'Aout 1972 au moyen de l'expérience Calipso, Spec. Thesis No. 1788, Univ. Paul Sabatier, Toulouse, France, 1975.
- Gosling, J. T., E. Hildner, R. M. MacQueen, R. H. Munro, A. I. Poland, and C. L. Ross, Direct observations of a flare-related coronal and solar wind disturbance, *Solar Phys.*, **40**, 439, 1975.
- Hakura, Y., Summary of the major solar-interplanetary disturbances in early August 1972, *J. Radio Res. Lab.*, **22**, 95, 1975.
- Hirshberg, J., The transport of flare plasma from the Sun to the Earth, *Planetary Space Sci.*, **16**, 309, 1968.
- Hirshberg, J., A. Alksne, D. S. Colburn, S. J. Bame, and A. J. Hundhausen, Observation of a solar flare induced interplanetary shock and helium-enriched driver gas, *J. Geophys. Res.*, **75**, 1, 1970.
- Hundhausen, A. J., and R. A. Gentry, Numerical simulation of flare generated disturbances in the solar wind, *J. Geophys. Res.*, **74**, 2908, 1969.
- Krimskij, G. E., and I. A. Transkij, Shock-wave propagation in interplanetary space, *Geom. Aeron.*, **XIII**, 574, 1973.
- Landt, J. A., Dense solar wind cloud geometries deduced from comparisons of radio signal delay and in solar plasma measurements, *J. Geophys. Res.*, **79**, 2761, 1974.
- Landt, J. A., and T. A. Croft, Shape of a solar wind disturbance on July 9, 1966, inferred from radio signal delay to Pioneer 6, *J. Geophys. Res.*, **75**, 4623, 1970.
- Lazarus, A. J., and J. H. Binsack, Observations of the interplanetary plasma subsequent to the 7 July 1966 proton flare, in *Annals of the Iqsy*, **3**, Edited by A. C. Stickland, p. 378, The MIT Press, Cambridge, 1969.
- Lazarus, A. J., M. A. Heinemann, R. W. McKinnis, and H. S. Bridge, *Solar Wind Data from the MIT Plasma Experiments on Pioneer 6 and Pioneer 7*, NSSDC 73-08, 1973.
- Lepping, R. P., and J. K. Chao, A shock surface geometry: The February 15-16, 1967, event, *J. Geophys. Res.*, **81**, 60, 1976.

Lockwood, J. A., and W. R. Webber, Comparisons of ground-based monitor data with Pioneers 8, 9, 10 and 11 observations in 1968-1974, 14th International Conference on Cosmic Rays, Conference Papers, 12, 4229, 1975.

Mariani, F., B. Bavassano, and N. F. Ness, Interplanetary magnetic field measured by Pioneer 8 during the 25 February 1969 event, in *Intercorrelated Satellite Observations Related to Solar Events*, edited by V. Manno and D. E. Page, p. 427, D. Reidel Publishing Company, Dordrecht, Holland, 1970.

Maxwell, A., Dynamic spectra of four solar radio bursts during the period 1972 August 2-7, in *Collected Data Reports on August 1972 Solar-Terrestrial Events*, edited by Helen E. Coffey, World Data Center A for Solar-Terrestrial Physics Report No. UAG-28 (part I), 255, 1973.

Mihalov, J. D., D. S. Colburn, H. R. Collard, B. F. Smith, C. P. Sonett, and J. H. Wolfe, Pioneer solar plasma and magnetic field measurements in interplanetary space during August 2-17, 1972, in *Correlated Interplanetary and Magnetospheric Observations*, edited by D. E. Page, p. 545, D. Reidel Publishing Company, Dordrecht, Holland, 1974.

Ness, N. F., and H. E. Taylor, Observations of the interplanetary magnetic field, 4-12 July 1966, in *Annals of the IQSY*, 3, edited by A. C. Stickland, p. 366, The MIT Press, Cambridge, 1969.

Pintér, S., Flare-associated solar wind disturbances and Type II and IV M radio bursts, *Bull. Astron. Inst. Czech.*, 23, 69, 1975.

Pintér, S., and M. Dryer, On the solar-flare-generated coronal and interplanetary shock waves during August 2-13, 1972, *Izvestia Akademii Nauk SSR, Series FIZ*, 4, No. 9, 43, 1977.

Rao, U. R., K. G. McCracken, and R. P. Bukata, Pioneer 6 observations of the solar flare particle event of 7 July 1966, in *Annals of the IQSY*, 3, edited by A. C. Stickland, p. 329, The MIT Press, Cambridge, 1969.

Rickett, B. J., Disturbances in the solar wind from IPS measurements in August, 1972, *Solar Phys.*, 43, 237, 1975.

Sakurai, K., *Propagation Pattern of Interplanetary Shock Waves Associated with Solar Proton Flares*, National Aeronautics and Space Administration Report No. NASA/GSFC X-693-73-90, 1973.

Sakurai, K., *Physics of Solar Cosmic Rays*, University of Tokyo Press, Tokyo, 1974.

Scarf, F. L., R. W. Fredricks, and I. M. Green, Comparison of deep space and near-earth observations of plasma turbulence at solar wind discontinuities, in *Solar Wind*, edited by C. P. Sonett, P. J. Coleman, Jr., and J. M. Wilcox, p. 421, National Aeronautics and Space Administration, Washington, NASA SP-308, 1972.

Taylor, H. E., Sudden commencement associated discontinuities in the interplanetary magnetic field observed by IMP 3, *Solar Phys.*, 6, 320, 1969.

Uchida, Y., Manifestation of flare-induced coronal MHD waves and Type II bursts, in *Flare-Produced Shock Waves in the Corona and in Interplanetary Space*, edited by A. J. Hundhausen, and G. Newkirk, Jr., p. 53, National Center for Atmospheric Research, Boulder, 1974.

Vaisberg, O. L., G. N. Zastenker, F. Cambou, V. V. Temny, and M. Z. Khokhlov, Solar-wind parameters and shock waves generated by the strong flares of August 1972, *Cosmic Res.*, 13, 765, 1975 (English Translation from *Kosmich. Issled.*).

Venkatesan, D., T. Mathews, L. J. Lanzerotti, D. H. Fairfield, and C. O. Bostrom, Cosmic ray intensity variations during 0200-0700 UT, August 5, 1972, *J. Geophys. Res.*, 80, 1715, 1975.

Vernov, S. N., E. A. Chuchkov, N. N. Kontor, G. P. Lyubimov, A. G. Nikolaev, and N. V. Pereslegina, Solar cosmic ray bursts with proton energies $E_p > 30$ MeV observed aboard Venus 6, in *Space Research, XI*, edited by K. Ya. Kondrat'ev, M. J. Rycroft, and C. Sagan, p. 1213, Akademie-Verlag, Berlin, 1971.

Watanabe, T., T. Kakinuma, M. Kojima, and K. Shibasaki, Solar wind disturbances detected by the interplanetary scintillation of radio sources in early August 1972, *J. Geophys. Res.*, 78, 8364, 1973.

Zastenker, G. N., O. L. Vaisberg, F. Cambou, V. V. Temny, and M. Z. Khokhlov, Study of propagation of solar-glare-generated shock waves in August 1972 using solar wind measurements, in *Space Research, XVI*, Edited by M. J. Rycroft, p. 699, Akademie-Verlag, Berlin, 1976.

Discussion

Wu: Is the formula derived for the shock shapes completely empirical or has Dr. Pintér used the similarity theory?

Dryer (for Dr. Pintér): Dr. Pintér used the extensive number of multi-observed shocks (described in the text) to derive the piston-driven and blast-originated shock shapes in a completely empirical manner.

IV. COMETARY STUDIES

Viscous Interaction Between the Solar Wind and Cometary Plasmas

H. Pérez-de-Tejada * and A. Orozco
Univ. Nac. Autónoma de México
Mexico, D. F., Mexico

A. Ershkovich
Tel-Aviv University
Ramat-Aviv, Israel

M. Dryer
Space Environment Laboratory
ERL-NOAA
Boulder, CO 80302, USA

Abstract

A simplified 2-dimensional MHD analogue of the region of interaction between the streaming solar wind with cometary plasmas has been used to model numerically the trajectory of cometary fluid particles as they move downstream from the nuclear region. The invoked accelerating mechanism is viscous transfer of momentum imparted through wave-particle interactions in the cometary plasma environment. The model provides spatial trajectories as well as the velocity and acceleration vectors of fluid particles placed initially at different locations within the mixing region associated with the solar wind-cometary plasma interface. The numerically-computed velocities and accelerations are compared with those inferred from observational measurements of specific structures detected in cometary tails.

*On sabbatical leave at the Aerospace Eng. Sciences Dept., Univ. of Colo., Boulder.

The use of continuum flow mechanics has proved to be most useful to the interpretation of certain large-scale phenomena associated with the interaction of the solar wind with planetary and cometary objects. Such has been the case in regard to the inviscid MHD flow description of the shocked solar wind as it streams around magnetic and non-magnetic objects (see for example, Spreiter et al., 1970 and Dryer, 1977). Emphasis has also been put on viscous flow descriptions of such a flow as it streams around the boundary of the cavity associated with each obstacle (Faye-Petersen and Heckman, 1968; Cassen and Szabo, 1970; Pérez-de-Tejada and Dryer, 1976). In the present report some preliminary results of the application of viscous flow theory to the analysis of the interaction of the solar wind with cometary plasmas will be given with particular attention to the dynamics of the resulting mixing layer downstream from the stagnation-flow region.

A descriptive review of some peculiar features currently thought to be associated with the local plasma dynamics of cometary environments is presented in Figure 1 (reproduced from Würm and Mammano, 1972). Most notable is the presence of well-defined tail rays which are believed to originate from the so-called cometary plasma envelopes. These are features initially seen as patches in regions upstream from the nucleus and which exhibit a peculiar evolution by growing laterally in length while at the same time becoming thinner and receding toward the nucleus. Such structures gradually evolve into thin rays which are seen to collapse in the direction of the comet's tail axis. The motion towards the tail axis becomes more evident when one follows the path of specific plasma parcels as done by Öpik (1964) for a distinct structure observed in Halley's comet. The results of that study showed that the plasma particles move as if they were in fact affected by a force acting in the direction transverse to that of the tail axis as shown in Figure 1.

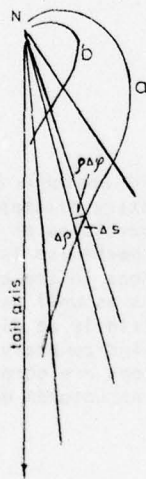


Figure 1. True orbit shapes (a and b) of two pieces of ionized matter in the tail rays of comets (from Würm and Mammano, 1972)

In order to study the motion of such cometary plasma particles, it is necessary to introduce a suitable MHD geometry which should represent the region of interaction between the solar wind and the cometary material. This is indicated schematically in Figure 2 where the shocked solar wind streaming by the flanks of the cometary plasma-cavity is replaced by a 2-D hypersonic MHD flow which interacts viscously with a stationary plasma. Thus, as a result of transverse transport of momentum, the cometary material will be subjected to an accelerating motion in the direction of the streaming flow, while at the same time will be exchanging thermal energy with it. A weak magnetic field aligned to the velocity vector will be allowed to exist throughout the region and its effect will be to reduce slightly the effective inertial force of the flow.

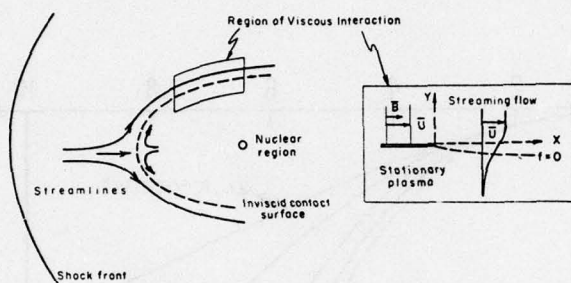


Figure 2. Schematic representation of the region of interaction between the shocked solar wind and the cometary plasma through a simplified 2-D geometry (insert)

The mathematical formulation of such a MHD mixing region takes its simplest form when conditions of perfect electrical conductivity are assumed to hold. In this case the aligned magnetic field " \bar{B} " is directly related to the density and velocity fields, " ρ " and " \bar{V} " respectively, through $B \sim \rho \bar{V}$, and the set of MHD equations that describe the motion (momentum and energy) can be reduced to a set of pseudo-gasdynamic equations (see Pérez-de-Tejada and Dryer, 1976 for an overall description of these equations). The most important aspect of such a formulation, however, lies in the selection of the proper boundary conditions, and it is in connection with this selection that some relevant physical implications are encountered. As discussed by Pérez-de-Tejada and Dryer (1976), the solution of the set of differential equations that describes the behavior of the MHD mixing region as defined above requires five boundary conditions, four of which are immediate and refer to the limiting values of the temperature and velocity imposed outside the region of interaction. The selection of the fifth boundary condition is obtained through a high-order analysis of the Navier-Stokes equation, and its form depends on the dynamic properties of both interacting media. For the particular case in which the streaming flow interacts with stationary material, the required boundary condition states that the transverse component of the velocity vector for the streaming flow is zero at the upper boundary of the mixing region (Ting, 1959). The implication of adopting this restriction as the appropriate form of the fifth boundary condition is that the dividing streamline between both interacting media

is not horizontal (along the X-axis) but will be laterally deflected into the region originally occupied by the stationary plasma. Calculations of such a displacement which affects the entire mixing region have been performed for flows of different physical properties. The results of these calculations are shown in Figure 3 where the lateral displacement (given in terms of a specific value of the variable of similarity $\eta = \hat{y}\sqrt{R/\hat{x}}$ where \hat{x} and \hat{y} denote the normalized distances along and transverse to the direction of the incident motion, and R is the Reynolds No.) is plotted as a function of the Mach number of the streaming flow using different forms of the viscosity function $\mu \sim T^n$ (where T denotes temperature and $n=0, 1, 2.5$) and of the Prandtl number P_r . It is seen that, while the displacement is very small for incompressible and subsonic flows, it grows at an ever increasing rate in the hypersonic range. The implication of such an accelerated lateral displacement is that we can expect a strong tendency for the hypersonic flow to force its way into the stationary material with which it interacts.

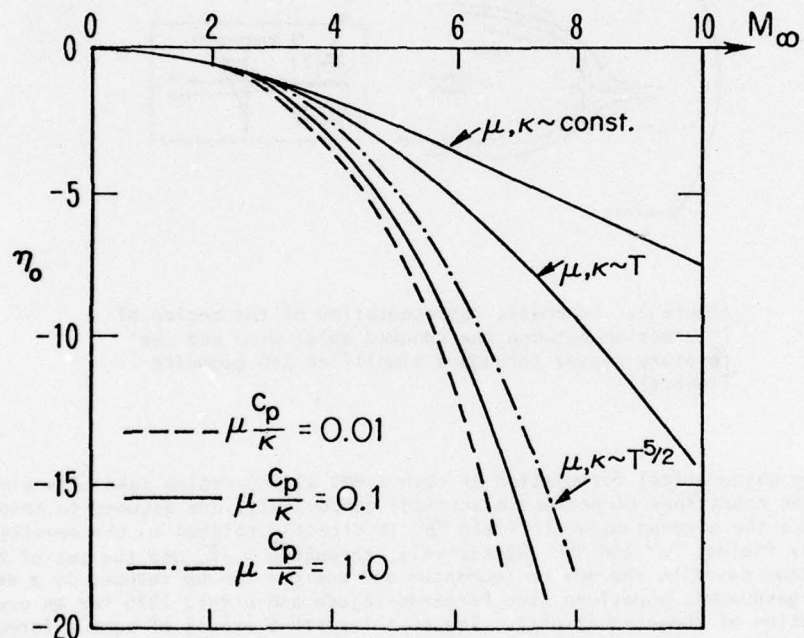


Figure 3. Lateral displacement, η_0 , of the dividing streamline between a streaming flow and a stationary plasma as a function of the Mach number, M_∞

A clearer picture of these concepts can be obtained by using flow diagrams which indicate the direction of the flow streamlines within the mixing region. An example of such diagrams (obtained from the numerical solution of the equations referred to above) is presented in Figure 4. Most notable is the marked transverse deflection of all the streamlines acting in such a way as to align the material along a narrow region centered around the dividing streamline. The overall

resemblance between this motion and that derived from the observational analysis of specific plasma structures in cometary plasma environments is evident. Thus, it demonstrates the usefulness of the proposed MHD viscous flow analogue to model the actual interaction processes taking place between the solar wind and cometary plasmas. Superimposed at specific locations, we have also traced sections of the local velocity profile in order to exhibit the accelerated growth of the transverse extent of the mixing region. An important consequence of this growth is the fact that in the far downstream regions of the mixing layer the fluid particles which were initially located at distinct sections within the mixing region have now very similar velocities. Finally, it is important to point out that the downward deflection of streamlines is effective to particles of both the stationary and the streaming flow, even though the former exhibits an initial upward motion. This is due to the fact that at $y = -\infty$, the boundary conditions on the longitudinal and transverse velocity components are, respectively: $u(-\infty) = 0$ and $v(-\infty) > 0$.

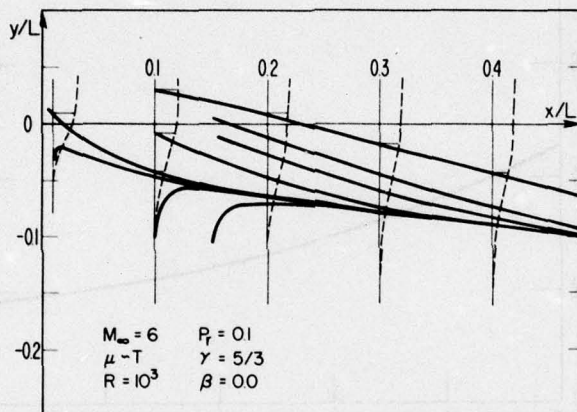


Figure 4. Flow diagram for the mixing region of a hypersonic flow in the x/L , y/L plane. L denotes the characteristic length of the flow, and R and β the Reynolds number and the ratio of the magnetic energy density to the kinetic energy density of the freestream flow, respectively. The rest of the parameters shown are discussed in the text.

By computing locally the longitudinal and transverse velocity components along different streamlines, it is possible to infer about the rate of acceleration of particles initially at rest as well as of the rate of deceleration of the particles of the streaming flow. The result of these computations show that for particles placed throughout the mixing region, the acceleration (or deceleration) is notably fast and leads to a well-defined terminal velocity which is predominantly a function of the Mach number of the streaming flow, although an additional (weaker) dependence is also exerted by the form of the transport properties of both media.

The basic relationship between the terminal velocity and the Mach number is shown in Figure 5 (the relative differences between various values of the Prandtl number or of the n-index in the viscosity function $\mu \sim T^n$ are minor and cannot be appreciated at the scale shown). Most significant in the resulting "universal" curve is the fact that in the hypersonic range we have $\hat{U}(x+1) \approx 0.2-0.3$. The velocity values implied by these numbers are within the 60-90 km/sec range which is satisfactorily consistent with a number of observationally-inferred velocities within cometary plasma tails.

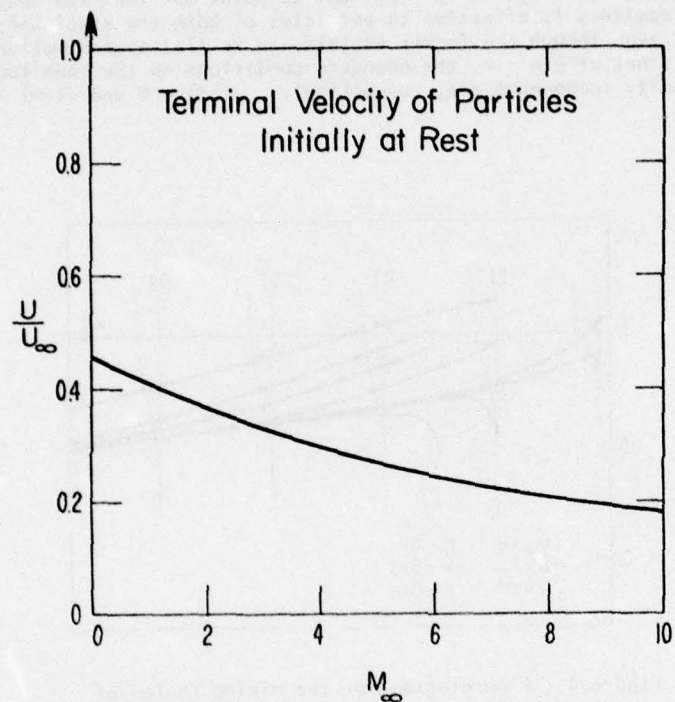


Figure 5. Terminal velocity of particles moving within the mixing region as a function of the Mach number of the streaming flow

Unlike the terminal velocity calculations, the plotting of local velocity vs distance does not lead into "universal curves" even if this is examined for streamlines corresponding to one same flow pattern. However, from the repeated comparison of such curves, it is found that (for each flow diagram) they can all be combined into one if the numerically computed velocity is plotted as a function of \hat{x}/\hat{x}_0 where \hat{x}_0 denotes the initial value of the normalized distance where the motion is initiated.

An example of how these curves can be employed to reproduce observationally-inferred acceleration curves of specific structures within cometary plasma tails is shown in Figure 6. We see here that the theoretical curves can be satisfactorily

used to account for the dramatic acceleration of cometary particles as it is observed along the plasma tails of some comets. The fact that the acceleration process is seen to occur in an abrupt manner at certain locations downstream from the nuclear region suggests that in some cases, at least, the convergence of the mixing region into the inner core of the tail may be slow, taking place at about 10^6 km downstream from the nucleus.

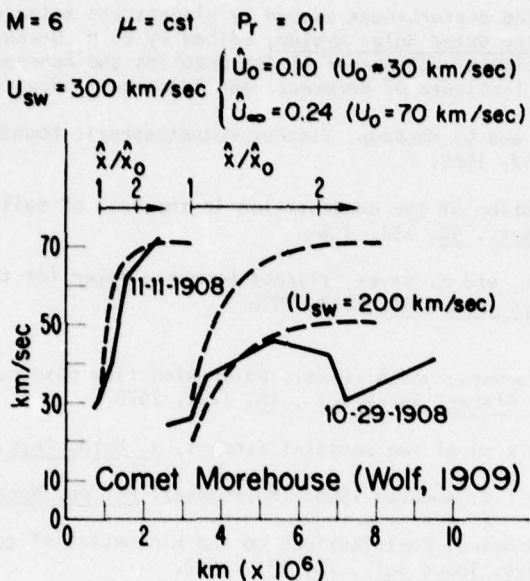


Figure 6. Comparison between theoretical and experimental "velocity vs distance" curves. The abscissa for the theoretical (dashed) velocities are given in the upper part of the figure. A solar wind velocity of $U_{sw} = 300 \text{ km/sec}$ fits the data of Nov. 11, 1908 for Comet Morehouse, but exceeds that of Oct. 29, 1908.

Acknowledgments

We wish to acknowledge financial support from the Aerospace Engineering Sciences Department of the University of Colorado (HPT) and the United States-Israel Binational Science Foundation (AE).

References

- Cassen, P., and T. Szabo, The viscous magnetopause, Planet. Space Sci., 18, 349, 1970.
- Dryer, M., Solar wind disturbances caused by planets and solar flares, in Exploration of the Outer Solar System, edited by E. M. Greenstadt, M. Dryer, and D. S. Intriligator, (Progress in Astronautics and Aeronautics, Vol. 50), p. 43, American Institute of Aeronaut. and Astronaut., New York, 1977.
- Faye-Petersen, R., and G. Heckman, Viscous magnetospheric boundary layer, Ann. Geophys., 24, 347, 1968.
- Öpik, E. J., The motion of the condensation in the tail of Halley's Comet June 5-8, 1910, Z. Astrophys., 58, 192, 1964.
- Perez-de-Tejada, H., and M. Dryer, Viscous boundary layer for the Venusian ionopause, J. Geophys. Res., 81, 2023, 1976.
- Spreiter, J., A. Summers, and A. Rizzi, Solar wind flow past nonmagnetic planets - Venus and Mars, Planet. Space Sci., 18, 1281, 1970.
- Ting, L., On the mixing of two parallel streams, J. Math. Phys., 38, 153, 1959.
- Wolf, M., D. Schweif d. Kometen 1908c (Morehouse), Astron. Nachr., 180, 4295, 1909.
- Würm, K., and S. Mamano, Contributions to the kinematics of type I tails of comets, Astrophys. Space Sci., 18, 273, 1972.

Discussion

- K. Jockers: I wonder why the speed at large distances downstream from the cometary head does not approach the solar wind speed?
- H. Perez-de-Tejada: Within the framework of the two dimensional semi-infinite geometry adopted in the model, there is a net transfer of momentum from the solar wind flow to the cometary plasma. This transfer results in a certain decrease of the directed velocity of the solar wind particles throughout the mixing region. This decrease in velocity is never recovered in the model in view of the assumed infinite transverse extent of the region occupied by the cometary plasma below the dividing streamline.
- S. Grzedzinski: Do your calculations on the viscous drag refer to the subsonic or supersonic case?
- H. Perez-de-Tejada: The analysis of the mixing layer as described in the model applies to situations in which a certain velocity shear exists between two parallel (subsonic or supersonic) flows. The thickness of the mixing region and the lateral displacement of the dividing streamline vary strongly with the Mach number. Throughout the subsonic range the geometry of the

mixing region is not very different from that of incompressible flows. In the supersonic range, on the other hand, the predicted thickness and orientation of the mixing layer change significantly with Mach number.

S. Grezedzinski: If your theory applies to the supersonic flow, how do you know where the supersonic region begins? One can well imagine a viscous drag effective in the subsonic region, which means that the position of the sonic line (beginning of the supersonic region) depends on the amount of drag in the subsonic region.

H. Perez-de-Tejada: Since the calculations are intended to provide a phenomenological description of the overall dynamics of the region of interaction between the shocked solar wind and cometary plasmas, it is necessary to regard the two-dimensional geometry adopted in the model as a suitable analogue of the actual boundary layer present at locations downstream from the subsolar region. Thus, effects associated with pressure gradients along the curved contact surface or with the position of the sonic line have not been considered. There is, indeed, a viscous drag in the subsonic region along this curved surface as you pointed out.

H. Eviatar: A real comet's tail has fine structure and looks like spaghetti. What refinement would your model need to reproduce this fine structure on a scale ~ 10⁵ km?

H. Perez-de-Tejada: The preliminary numerical modeling of arbitrary structures released near the leading edge of the mixing layer indicates that the material exhibits a certain tendency to concentrate in the vicinity of the dividing streamline. This gives the appearance of a thin filament with a non-uniform density distribution along its length. It is possible that structures resembling cometary tail rays could ultimately be constructed from the cumulative superposition of these numerically-generated filaments. This question is under current investigation.

M. K. Wallis: Have you considered the case of a homogeneous cylindrical tail, presumably with constant pressure as the 'lower' boundary condition?

H. Perez-de-Tejada: I have not considered three dimensional geometries which would, presumably, provide a better representation of the mixing region in the far downstream regions of the wake. The adoption of a constant pressure at the lower edge of the mixing region would be a desirable but insufficient modification to the present model in view of the assumed infinite transverse extent of both interacting media in the geometry employed.

"Secondary Tail Events" in the Plasma Tail of Comet Kohoutek 1973 XII

K. Jockers
Max-Planck-Institut für Physik und Astrophysik
Foehringer Ring 8, Postfach 401212
8000 Munich 40, FRG

Abstract

Pictures of Comet Kohoutek 1973 XII from all over the world have been collected for an atlas. This atlas, which will be published separately, will show the comet tail several times a day in the period from January 9 - 24, 1974. To correlate cometary events with solar events, in this paper orbital information on Comet 1973 XII is given together with the tail aberration angles and the (as yet tentative) onset of so-called secondary tail events, as they can be deduced from the pictures of the cometary atlas.

1. INTRODUCTION

It may not be accidental that in this session on comet-solar wind interaction there have as yet only theoretical papers been presented. It is difficult to obtain cometary tail data which are suited for correlation studies. Since comet tails change their appearance quickly it is desirable to have a picture of a comet tail every hour. As comets with plasma tails usually are close to the sun they can be seen from a single site only a few hours. Therefore a cooperation of cometary observers all over the world is necessary. Even then, because of the inhomogeneous distribution in geographic longitude of the countries with developed astronomy programs, gaps in the data will remain. In this talk I will present preliminary results obtained from pictures of Comet Kohoutek 1973 XII which I have collected from all over the world. These pictures will be published separately as an atlas. So far the following observatories have contributed data. They are listed in the order of increasing geographic longitude. The German-Spanish Observatory on Calar Alto mountain, Spain, the Joint Observatory for Cometary Research, Socorro, New Mexico, the Catalina Observatory of the University of Arizona, Tucson, Arizona, Lowell Observatory, Flagstaff, Arizona, Hale Observatories on Mt. Palomar, California, the Mauna-Kea Station of the Astronomical Institute of the University of Hawaii, the Dodeira Station of the Astronomical Institute of Tokyo University, Japan, the Kagoshima Station of the Japanese Institute for Space Research, the Astronomical Observatory of the Kasakh Academy of Sciences, USSR, Asiago Observatory of the University of Padova, Italy and the Observatoire Haute Provence of CNRS, France. In addition I have received many pictures from the Baker-Nunn satellite tracking network operated by the Smithsonian Astrophysical Observatory in Cambridge, Massachusetts. In particular, pictures from stations in Spain, Brazilia, Arizona, Hawaii, India and Ethiopia were useful. Some amateurs also have contributed pictures. The data cover the period January 9 - 24, 1974, when, at one hand, the comet was not too close to the sun and, on the other hand, moon light did still not interfere with the observations. In this time period Skylab was still operating.

2. THE ORBIT OF COMET KOHOUTEK 1973 XII

To interpret cometary data it is necessary to have some information on the cometary orbit. As the inclination of the orbit of Comet 1973 XII was low one can obtain a good picture by assuming the comet to move in the ecliptic plane. Figure 1 (next page) shows the comet orbit projected onto the ecliptic plane and the relative position of sun, comet and earth. During the period January 9 - 24 the heliocentric distance of the comet varied from .5 to .8 AU. The geocentric distance of the comet was always about .8 AU. As seen from the earth, the sub-solar point of the comet was always close to the east limb of the sun moving slowly onto the disk at the end of the observation period.

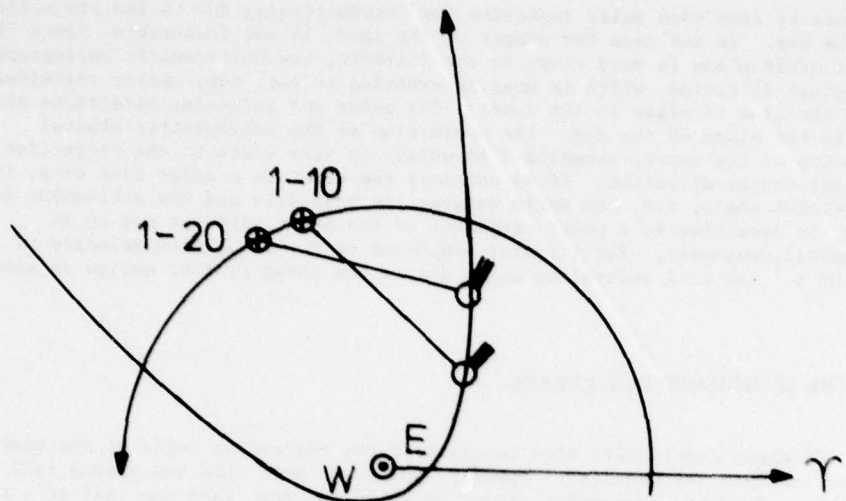


Figure 1: The Relative Position of Comet 1973 XII and Earth, January 1974

Cometary pictures only show the projection of the comet on the sky plane. Therefore it is necessary to know the projection of the relevant unit vectors on the sky plane. As there were only minor changes through the observing interval it is sufficient to consider the situation on January 17, in the middle of the observing period. Figure 2 shows the projection of some unit vectors drawn into the unit circle. The amount by which the length of the

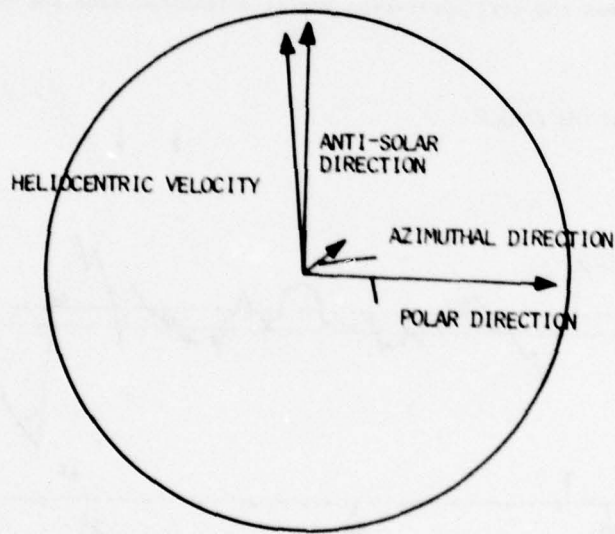


Figure 2: Projection of Unit Vectors on Sky Plane, January 17, 1974

vectors is less than unity indicates the foreshortening due to the projection on the sky. In our case the aspect of the comet is not favourable. Since the comet orbit plane is very close to the ecliptic, the heliocentric heliographic azimuthal direction, which is most interesting to see, very nearly coincides with the line of sight to the comet. The polar and antisolar directions almost lie in the plane of the sky. The projection of the heliocentric orbital velocity of the comet, normalized to unity, is very close to the projection of the anti-solar direction. If we consider the comet as a solar wind sock, the aberration angle, i.e. the angle between the tail axis and the anti-solar direction, is sensitive to a polar component of the solar wind but not to an azimuthal component. For a radial component of the solar wind velocity of about 400 km s^{-1} the tail aberration angle due to the comet orbital motion is about 1°.

3. THE SECONDARY TAIL EVENTS

To study comet-solar wind interaction the aberration angle of the comet tail is certainly a key quantity. However, sometimes more than one plasma tail is visible. The wind sock model cannot be valid for more than one tail at a time. The appearance of a secondary tail in Comet Bennett 1970 II has been studied by Burlaga et al. (1973), Jockers and Lüst (1973) and Wurm and Mammano (1972). Even though there was disagreement about the solar wind as a cause of the secondary tail the phenomenon itself is described similarly by the different authors. During a few hours a secondary tail develops out of a tail ray. This second tail quickly increases in brightness so that the role of primary and secondary tail interchanges. Therefore, if one determines the tail aberration angle from the most intense tail this angle changes suddenly when what was formerly considered to be a tail ray is taken to be the main tail. During further development this new tail assumes the normal aberration angle, i.e. moves into the position of the former tail.

Figure 3 shows the tail aberration angles determined from the comet tail

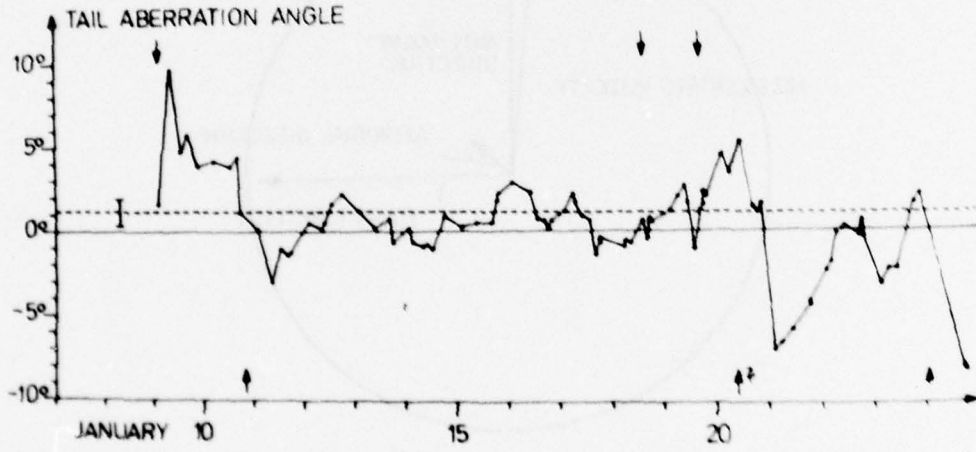


Figure 3: Tail Aberration Angles and Secondary Tail Events

noted below.

pictures. The angles are accurate to $\pm 1^\circ$ only. In case of a curved tail I have measured the tail close to the nucleus, i.e., the "primary tail" as it is called by Hoffmeister (1943). The dotted line gives the aberration angle produced by an undisturbed radial solar wind of 400 km s^{-1} speed. The arrows mark the onset of tail ray activity which later on produced a secondary tail. Arrows in the upper or lower part indicate that the activity started at the north or south side of the comet, respectively. Due to the data gaps some of the events may not have been recognized correctly, as some tail ray activity is always going on in the comet. Some of the strong changes in tail aberration angle which accompany the secondary tail events are caused by the subsequent interchange of main and secondary tail.

Due to the fact that solar observations (ground based and from Skylab) were not available to the author prior to the meeting, a detailed comparison of the secondary tail events with solar data could not be made as yet.

Acknowledgments

Without the cometary pictures obtained at the above-mentioned observatories, this study could not have been made. Part of this work has been done during the author's stay at Sacramento Peak Observatory when he was supported by a NAS/NRC fellowship.

References

- Burlaga, L. F., J. Rahe, B. Donn, and M. Neugebauer, Solar wind interaction with comet Bennett (1962), Solar Phys., 30, 211, 1973.
- Hoffmeister, C., Physikalische Untersuchungen an Kometen. I. Die Beziehungen des primären Schweifstrahls zum Radiusvektor, Z. Astrophys., 22, 265, 1943.
- Jockers, K., and Rh. Lust, Tail peculiarities in comet Bennett caused by solar wind disturbances, Astron. Astrophys., 26, 113, 1973.
- Wurm, K., and A. Mammano, Contributions to the kinematics of Type I tails of comets, Astrophys. Space Sci., 18, 273, 1972.

Discussion

Malaise: Do I understand that the observed aberration angle you showed is the observed angle of the tail with respect to the radius vector?

Jockers: Yes.

Malaise: The curve you showed for the aberration angle is continuous. Does this mean that it pertains to the same tail or is it the angle of the brightest feature?

Jockers: It pertains to the brightest feature. The large changes in tail aberration angle following some of the marked secondary tail events must have contributed to the discontinuity which arises when what was formerly a tail ray is now interpreted as the main tail.

Malaise: (This question was asked following the presentation of a movie on comet Kohoutek. The details on this movie were given at the IAU Conference No. 25, The Physics of Comets, Greenbelt, Maryland, 1974.) How difficult would it be to cancel the orbital motion of the head in the motion picture? I am asking this question because it seems that the features away in the ion tails move essentially parallel to the head, that is the ion tail moves with the head as if it were attached to it. This picture does not agree with theories in which the tail ions very quickly reach their terminal velocity with respect to the solar wind.

Jockers: It would not be very difficult to cancel the orbital motion of the comet, but it would not make much sense, as the eye would always take the stars as reference no matter if they remain fixed or if they move opposite to the comet's proper motion. The only useful step in this direction would be to remove the stars from the pictures completely by some kind of filtering technique. As a movie always gives only a subjective impression it cannot prove or disprove theories about motions of the cometary ions.

**V. COSMIC RAY MODULATION
AND ACCELERATION**

influence of disturbances of solar wind properties on cosmic rays. The influence of magnetic field fluctuations on solar wind velocity and density was also studied. Quiet solar regions associated with strong magnetic field were considered. The influence of solar wind velocity and density changes on cosmic ray intensity was also studied. The influence of magnetic field fluctuations on solar wind velocity and density was also studied. The influence of solar wind velocity and density changes on cosmic ray intensity was also studied.

Cosmic Ray Perturbations Produced by Fast Streams Coming From Quiet Solar Regions-Coronal Holes

N. Iucci

Istituto di Fisica - Università
Piazzale delle Scienze, 5 - 00185 Rome, Italy

S. Orsini, M. Parisi, M. Storini, and G. Villoresi

Laboratorio Plasma Spazio - C.N.R.
Istituto di Fisica - Università
Piazzale delle Scienze, 5 - 00185 Rome, Italy

Abstract

The satellite data on solar wind (density, bulk velocity and magnetic field) together with the solar activity data have been used to identify high-velocity, low-density streams emitted by quiet solar regions (coronal holes) in cycle n. 20. For the identified events, a small cosmic ray depression is generally observed, its time behaviour traces that of the solar wind speed (about 0.5% of intensity depression at high-latitude neutron stations for an increase of 100 km/sec in the solar wind velocity).

1. INTRODUCTION

We may assume, as suggested by Gosling et al. (1976a), that the most characteristic state of solar wind is the high-speed flow which is modulated by intrusions of low-speed gas. The high-speed flow is emitted by quiet solar regions of low density where the magnetic field is divergent (coronal holes), while the low-speed flow comes from regions where closed field line structures exist (Gulbransen, 1975; Sheeley et al., 1976; Nolte et al., 1976b). The high-speed streams mainly survive for long time and then they are often found to recur for several solar rotations; at the Earth's orbit the broadest and fastest streams are more frequent in years of declining solar activity near the minimum (Gosling, 1976a). Near the solar equatorial plane the low-speed flow, which comes from solar regions where activity phenomena may occur, is more frequently observed in the years of maximum solar activity; transient high-speed flow can be emitted by these active regions on occasion of energetic Type IV solar flares (Gosling et al., 1976b).

Cosmic ray decreases, not associated with solar flares in the visible hemisphere of the Sun, were interpreted as produced by a continuous emission of fast plasma by a restricted region of the Sun (McCracken et al., 1966; Bukata et al., 1968); in Iucci et al. (1977) it has been found that in the period 1957-1969 the majority of these events with amplitude $\Delta I/I > 1.5\%$ at high latitude neutron monitors can be produced by Type IV solar flares occurring beyond the East limb of the Sun, while the smaller and recurrent cosmic ray decreases can be mainly produced by fast streams coming from coronal holes.

The aim of the present work is to study the influence of the high-speed streams produced by coronal holes on the cosmic ray intensity in the period 1965-1974. For this purpose the following data are used: neutron monitor intensity at high latitude, solar wind density (Diodato et al., 1975) and velocity (Diodato et al., 1975; Gosling et al., 1976a), interplanetary magnetic field (King, 1975; Svalgaard, 1975).

2. FAST STREAMS FROM 1965 TO 1974

The high-speed streams coming presumably from coronal holes in the period July 1965 - October 1974 are identified under the following requirements:

- a) enhanced velocity ($V_{max} > 400 \text{ km/sec}$ and $\Delta V = (V_{max} - V_0) \geq 100 \text{ km/sec}$, where V_{max} is the maximum daily value in the fast stream and V_0 is the daily value immediately out of the stream) for ≥ 3 days;
- b) enhanced density and magnetic field intensity during the phase of increasing velocity;
- c) relatively low density and quiet magnetic field after the phase of increasing velocity;
- d) absence of active regions which produce energetic solar flares in the he-

longitude belt containing the possible coronal hole.

The transient high-speed streams associable with Type IV solar flares have been excluded; for these cases at least one of the requirements listed above is not fulfilled. At the end of each stream, after the phase of decreasing velocity, an increase in solar wind density is generally observed; the occurrence of a density peak inside a long period of enhanced velocity is used to separate subsequent streams.

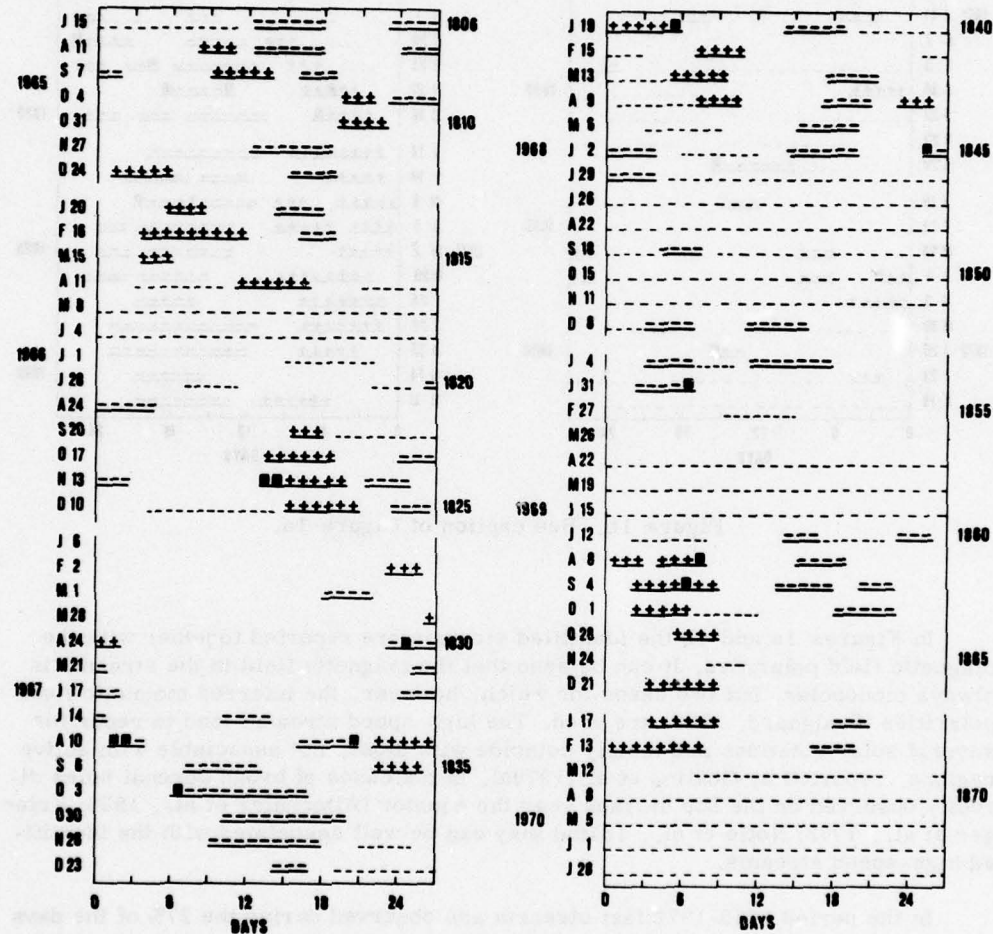


Figure 1a. High-speed Solar Wind Streams (horizontal bars) and Interplanetary Magnetic Field Polarities in the Streams Plotted According to 27-day Bartels Rotations. The gaps in the solar wind velocity lasting more than 2 days are reported (broken lines). The numbers on the right refer to the Bartels rotation numbers.

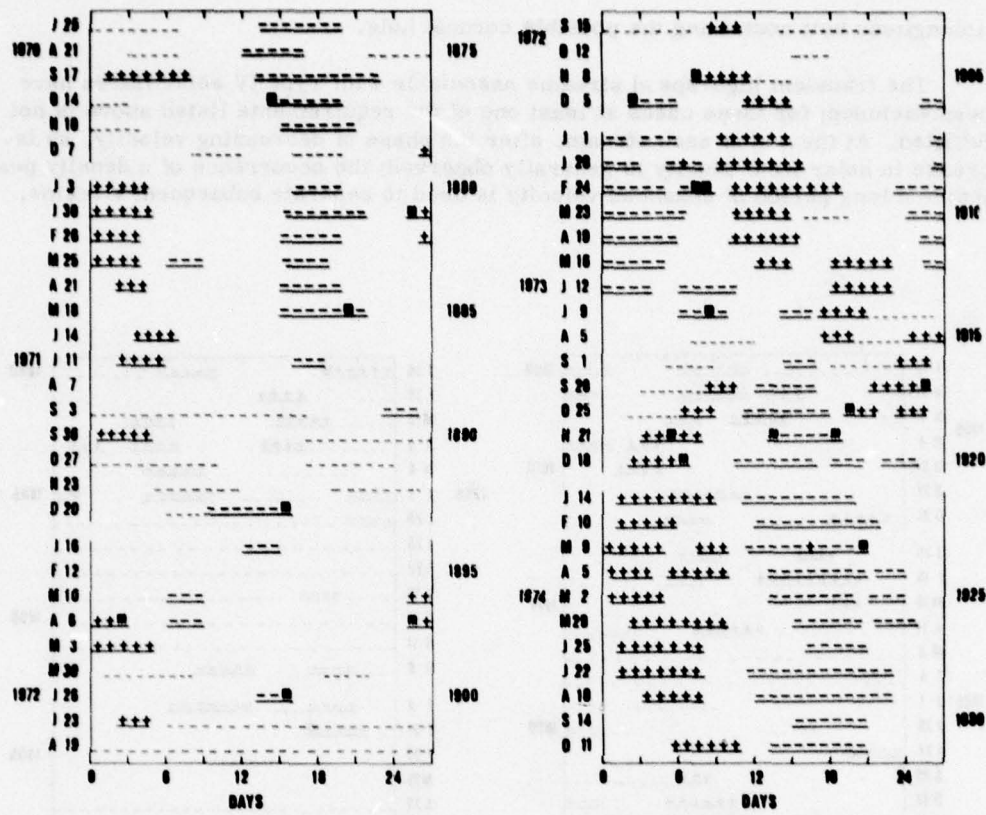


Figure 1b. See caption of Figure 1a.

In Figures 1a and 1b the identified streams are reported together with the magnetic field polarities. It can be seen that the magnetic field in the streams is always monopolar, but two cases for which, however, the inferred magnetic field polarities (Svalgaard, 1975) are used. The high-speed streams tend to recur for several solar rotations and mainly coincide with those, not associable with active regions, reported by Gosling et al. (1976a). In the cases of broad coronal holes directly observed on the Sun surface near the equator (Altschuler et al., 1972; Krieger et al., 1973; Nolte et al., 1976a) they can be well associated with the identified high-speed streams.

In the period 1965-1972 fast streams are observed during the 27% of the days in which the solar wind velocity is measured; this percentage increases to 56% in the years 1973-1974. Moreover, also the average value of ΔV increases from ~ 170 km/sec (in 1965-1972) to ~ 255 km/sec (in 1973-1974). Taking into account the relation between the area of the equatorial holes and V_{\max} reported by Nolte et al. (1976b), this increase of ΔV suggests that the broadest coronal holes devel-

op near equatorial regions mainly in the declining phase of solar activity near the minimum, in agreement with the long duration of the fast streams observed in the years 1973-1974.

3. THE INFLUENCE OF THE FAST STREAMS ON THE COSMIC RAY INTENSITY

When a fast stream ejected from a coronal hole envelopes the Earth, a decrease in the cosmic ray intensity, lasting the time spent by the Earth inside the stream, is observed in most cases. The time behaviour of such cosmic ray events, which represents the longitudinal variation of the cosmic ray density inside the stream, will depend on two effects: the outward convection produced by the enhanced solar wind velocity and the diffusion through the edges of the stream.

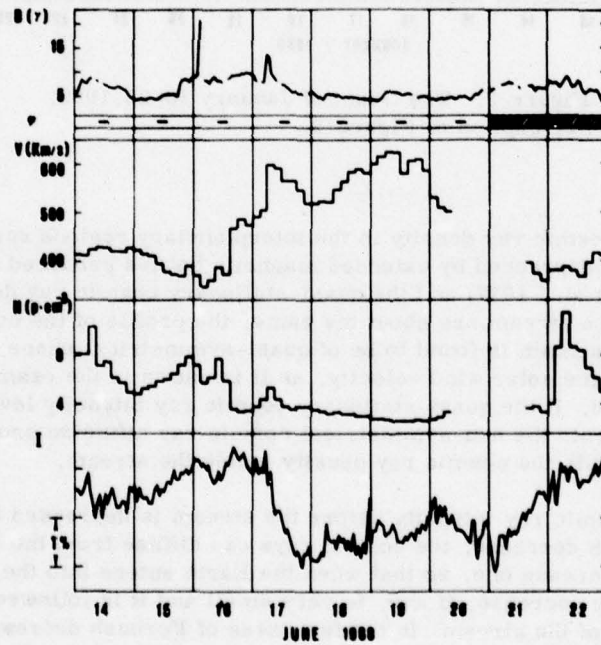


Figure 2. The Event of June 14-22, 1968. The intensity (B) and polarity (dashed area indicates mixed or undefined polarity) of the interplanetary magnetic field; the velocity (V) and density (N) of the solar wind and the average intensity of the Alert and McMurdo neutron monitors (I) are plotted.

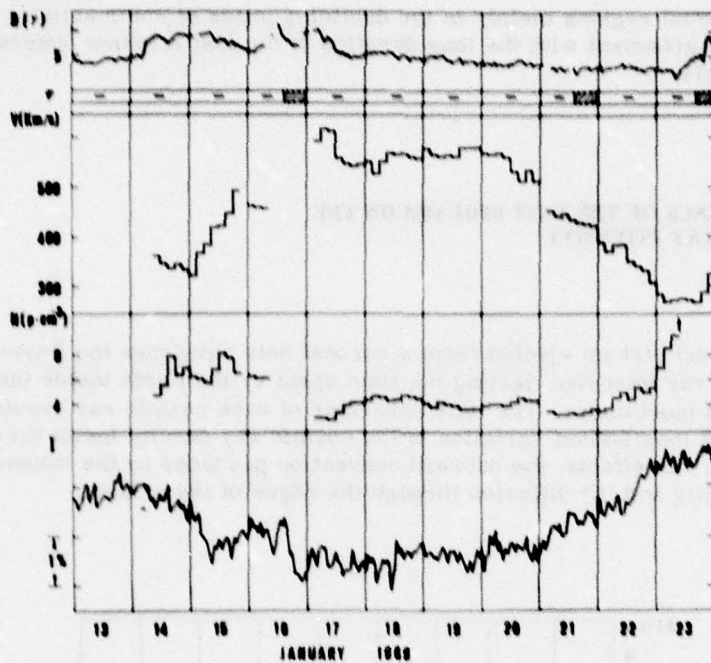


Figure 3. The Event of January 13-23, 1969.
See caption of Figure 2.

In case the cosmic ray density in the interplanetary regions surrounding the fast stream is not depressed by extended magnetic bottles produced by Type IV solar flares (Lucci et al., 1977) and the quasi-stationary cosmic ray density levels before and after the stream are about the same, the profile of the cosmic ray decrease inside the stream is found to be of quasi-symmetrical shape, following the time behaviour of the solar wind velocity, as it is shown in the examples reported in Figures 2 and 3. If the quasi-stationary cosmic ray intensity levels nearby the stream are different, the non-symmetrical cosmic ray diffusion produces the observed asymmetry in the cosmic ray density inside the stream.

When the cosmic ray intensity before the stream is depressed by the occurrence of a Forbush decrease, the cosmic rays can diffuse from the stream region to the Forbush-decrease one, so that when the Earth enters into the stream the observed cosmic ray decrease, if any, is very small and it is followed by a sharp recovery at the end of the stream. In the few cases of Forbush decreases occurring before and after the stream, the effect of the stream on the cosmic ray time behaviour appears to be highly confused.

Various examples of fast streams and their influence on the cosmic ray intensity can be found in Figures 4 and 5 for two series of solar rotations in 1968 and 1973-1974; the fast streams visible in Figure 5 are produced by coronal holes.

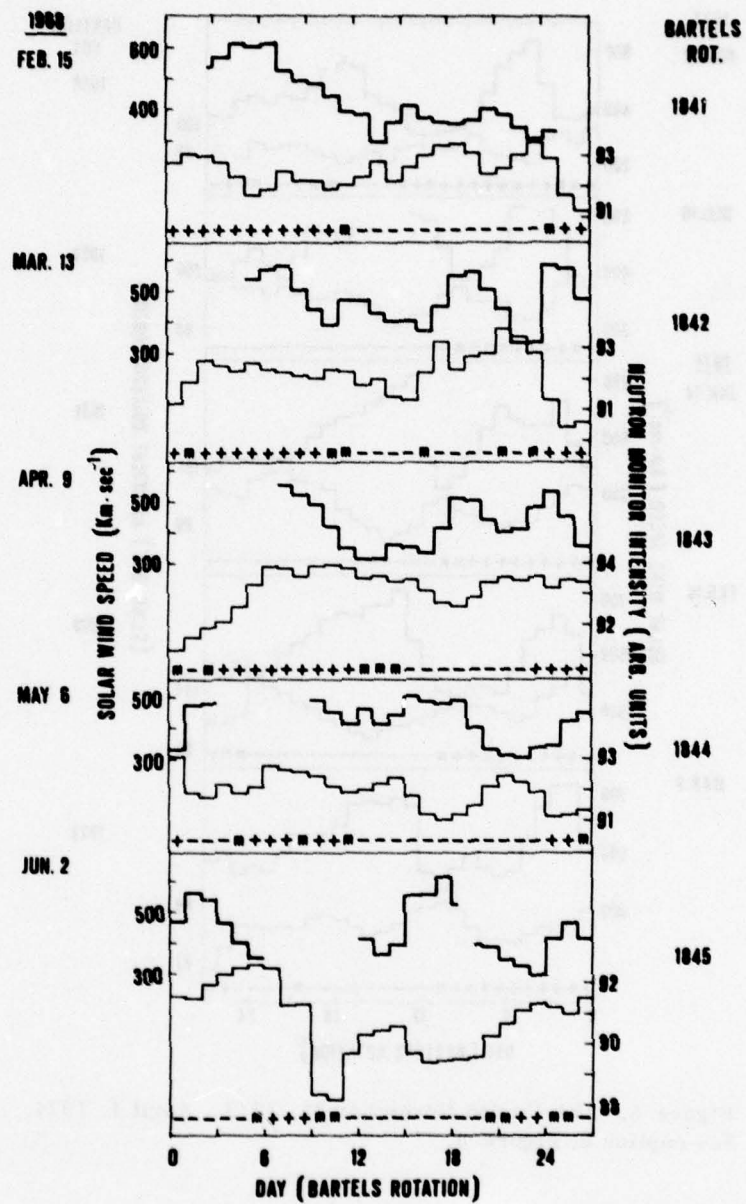


Figure 4. Solar Wind Velocity (heavy line), Neutron Monitor Intensity at High Latitude (light line) and Interplanetary Magnetic Field Polarity (m refers to mixed or undefined polarity). The period February 15-June 28, 1968 is plotted according to 27-day Bartels rotations.

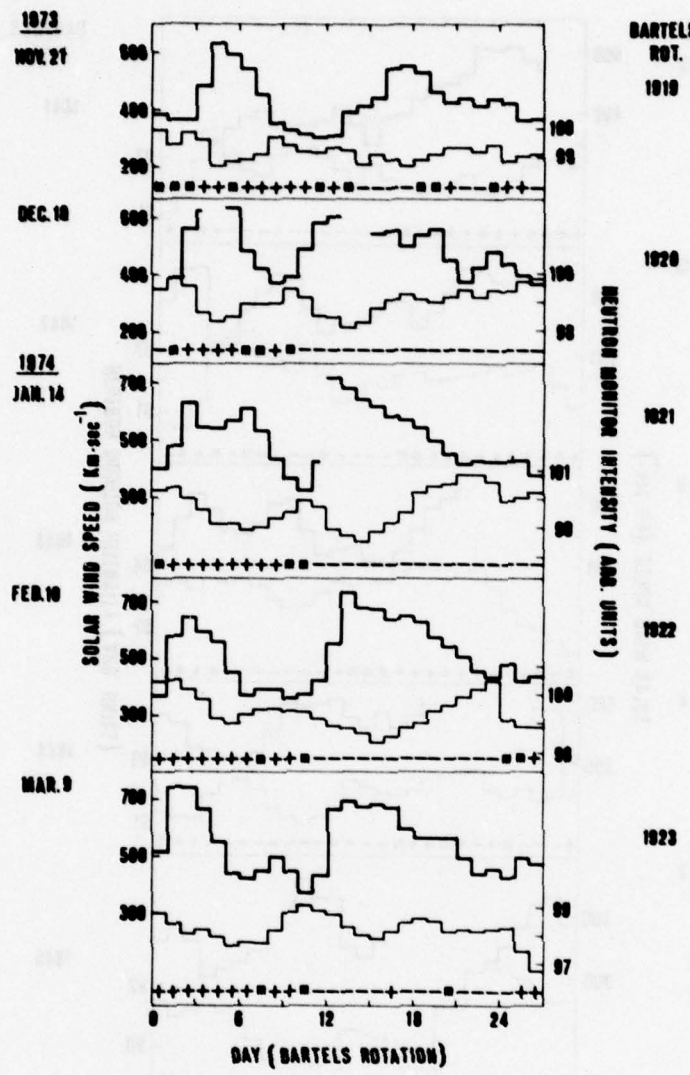


Figure 5. The Period November 21, 1973 - April 4, 1974.
See caption of Figure 4.

Small Forbush decreases can be observed at the end of the rotations 1919, 1921, 1922 and 1923. For the period reported in Figure 4 the fast streams associated with coronal holes can be identified by Figure 1.

For all the events not much perturbed by Forbush decreases, the maximum amplitudes of the relative cosmic ray decrease ($\Delta I/I$) and of the velocity increase

(ΔV) have been estimated and reported in Figure 6 ; the reference levels have been computed by averaging the values immediately before and after the stream. The distribution of the points in Figure 6 shows a linear relation between ΔV and $\Delta I/I$. The spread of the points can be due, besides to the errors in the estimate of the two variables, to the possible variations in the cosmic ray diffusion perpendicular to the field lines; in any case the relation between ΔV and $\Delta I/I$ does not seem to depend on solar cycle. As an average for $\Delta V = 100$ km/sec, $\Delta I/I = 0.52\%$.

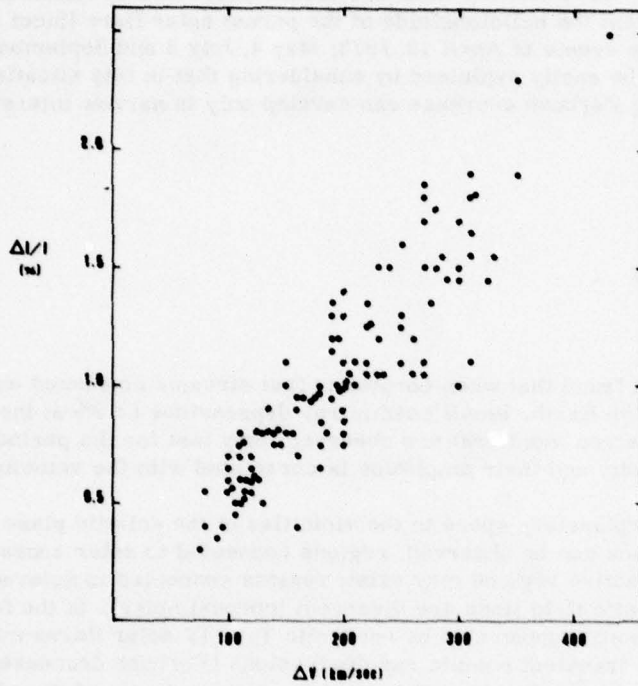


Figure 6. The Amplitude of the Cosmic-ray Intensity Decrease at High-latitude Neutron Monitors ($\Delta I/I$) is Plotted Versus the Increase in the Solar Wind Velocity (ΔV) of the Associated Fast Stream

4. ACTIVE REGIONS AND CORONAL HOLES

As it was suggested by Timothy et al. (1975) the large equatorial coronal holes are formed when the remnants of active regions fields, emerging in both hemi-

spheres, combine to form a large area of essentially unipolar field. This mechanism may explain the existence of the broadest equatorial coronal holes in the declining phase of solar activity near the minimum when the active regions are close to the equator. Moreover, we have found that in some cases the coronal holes appear in solar regions which were active and producing Type IV solar flares in previous solar rotations and there are also coronal holes which disappear when, close to them, Type IV solar flares producing Forbush decreases occur. In order to achieve understanding of this interconnection between active regions and coronal holes, a more detailed study must be pursued. Finally we remark that when the fast streams coming from coronal holes cover a large portion of the ecliptic plane, as in 1973-1974, the recovery time of Forbush decreases becomes shorter than that expected from the heliolongitude of the parent solar flare (Iucci et al., 1977) (for instance the events of April 12, 1973; May 4, July 6 and September 12, 1974). This effect can be easily explained by considering that in this situation the magnetic bottle producing Forbush decrease can develop only in narrow interstream regions.

5. CONCLUSIONS

It has been found that when corotating fast streams connected with coronal holes envelope the Earth, small cosmic ray depressions ($\lesssim 2\%$ at the energies of high-latitude neutron monitors) are observed; they last for the period of enhanced solar wind velocity and their amplitude is correlated with the velocity increase.

In the interplanetary space in the vicinities of the ecliptic plane two types of corotating regions can be observed: regions connected to solar zones where magnetic field loops and active regions may exist; regions connected to quiet solar zones where the magnetic field lines are divergent (coronal holes). In the former regions wide magnetic bottles generated by energetic Type IV solar flares may expand producing large transient cosmic ray depressions (Forbush decreases), whose maximum amplitude at the Earth's orbit depends on the velocity of the advancing front of the bottle (Iucci et al., 1977); in the latter regions the cosmic ray density is maintained depressed by the continuous outflow of enhanced solar wind and the amount of the quasi-stationary cosmic ray depression is linearly related with the increase in solar wind velocity. The amount of the cosmic ray decrease observed in presence of broad coronal holes, like those in 1973-1974, may offer a rough estimate of the cosmic ray intensity level over the solar poles where extended coronal holes are present.

For what concerns the possible relation between fast streams and long-term cosmic ray modulation (Intriligator, 1975) it should be noted that the fast streams increase the outward cosmic ray convection, but unfortunately this effect is larger near solar minimum. We think that the long-term cosmic ray modulation can be due mainly to the outward sweep mechanism on cosmic rays produced by the magnetic bottles generated by energetic Type IV solar flares (Iucci et al., 1975).

References

- Altschuler, M. D., D. E. Trotter, F. Q. Orrall, Coronal holes, Solar Phys., 29, 354, 1972.
- Bukata, R. P., K. G. McCracken, and U. R. Rao, A comparison of the characteristics of corotating and flare-initiated Forbush decreases, Can. J. Phys., 46, S 994, 1968.
- Diodato, L., G. Moreno, and C. Signorini, A compilation of normalized solar wind densities and velocities, Astron. Astrophys. Suppl., 20, 313, 1975.
- Gosling, J. T., J. R. Asbridge, S. J. Bame, and W. C. Feldman, J. Geophys. Res., 81, 5061, 1976a.
- Gosling, J. T., E. Hildner, R. M. MacQueen, R. H. Munro, A. I. Poland, and C. L. Ross, The speeds of coronal mass ejection events, Solar Phys., 48, 389, 1976b.
- Gulbrandsen, A., The solar M-region problem - an old problem now facing its solution?, Planet. Space Sci., 23, 143, 1975.
- Intriligator, D. S., The solar cycle variation in the solar wind and the modulation of cosmic rays, Proc. 14th Intern. Cosmic Ray Conf., Munich, 3, 1033, 1975.
- Iucci, N., M. Parisi, M. Storini, and G. Villoresi, The solar cycle modulation of the galactic cosmic rays and the solar flare activity, Proc. 14th Intern. Cosmic Ray Conf., Munich, 3, 958, 1975.
- Iucci, N., M. Parisi, M. Storini, and G. Villoresi, A study of the Forbush decrease effect: the origin and the development in the interplanetary space, Internal Report of Space Plasma Laboratory - 77-2, Rome, February 1977.
- King, J. H., Interplanetary Magnetic Field Data Book, National Space Science Data Center - 75-04, Greenbelt, April 1975.
- Krieger, A. S., A. F. Timothy, E. C. Roelof, A coronal hole and its identification as source of a high velocity solar wind stream, Solar Phys., 29, 505, 1973.
- McCracken, K. G., U. R. Rao, and R. P. Bukata, Recurrent Forbush decreases associated with M-region magnetic storms, Phys. Rev. Letters, 17, 928, 1966.
- Nolte, J. T., A. S. Krieger, A. F. Timothy, G. S. Vaiana, and M. V. Zombeck, An Atlas of coronal hole boundary positions May 28 to November 21, 1973, Solar Phys., 46, 291, 1976a.

Nolte, J. T., A. S. Krieger, A. F. Timothy, R. E. Gold, E. C. Roelof, G. Vaiana, A. J. Lazarus, J. D. Sullivan, and P. S. McIntosh, Coronal holes as sources of solar wind, Solar Phys., 46, 303, 1976b.

Sheeley N. R., J. W. Harvey, and W. C. Feldman, Coronal holes, solar wind streams, and recurrent geomagnetic disturbances: 1973-1976, Solar Phys., 49, 271, 1976.

Svalgaard, L., An Atlas of interplanetary sector structure 1957-1974, Institute for Plasma Research, SUIPR report - 629, Stanford University, California, 1975.

Timothy, A. F., A. S. Krieger, and G. S. Vaiana, The structure and evolution of coronal holes, Solar Phys., 42, 135, 1975.

Abstract. In the turbulent region behind interplanetary shock waves it is to be expected that solar flare particles can be trapped very efficiently. In order to study the intensity-time variation produced by such local propagating variations of the diffusion coefficient we have solved the time-dependent Fokker-Planck equation for the diffusive and convective transport in three dimensions (time, space and energy) numerically by a Crank-Nicholson method. The diffusion coefficient is allowed to be time, energy and space dependent. It is shown, that variations in the intensity-time profile at 1 AU are strongly dependent on the boundary condition near the sun, i.e. whether the particles are injected momentarily or whether they are stored in the corona and injected over a certain time period.

Modulation of Energetic Solar Particle Fluxes by Interplanetary Shock Waves

Manfred Scholer
Max-Planck-Institut für Physik und Astrophysik
Institut für extraterrestrische Physik
8046 Garching, FRG

Gregor Morfill
Max-Planck-Institut für Kernphysik
69 Heidelberg, FRG

Abstract

Due to the reduction of the cosmic ray diffusion coefficient in the turbulent region behind interplanetary shock waves it is to be expected that solar flare particles can be trapped very efficiently in that region. In order to study the intensity-time variation produced by such local propagating variations of the diffusion coefficient we have solved the time-dependent Fokker-Planck equation for the diffusive and convective transport in three dimensions (time, space and energy) numerically by a Crank-Nicholson method. The diffusion coefficient is allowed to be time, energy and space dependent. It is shown, that variations in the intensity-time profile at 1 AU are strongly dependent on the boundary condition near the sun, i.e. whether the particles are injected momentarily or whether they are stored in the corona and injected over a certain time period.

I. INTRODUCTION

Recently, Scholer and Morfill (1975) developed a numerical model in order to explain the large flux increases of low energy cosmic rays observed a few hours before the arrival of interplanetary shock waves - the so called energetic storm particle events. The model is based on the assumption that solar cosmic rays gain energy due to successive reflections at the moving interplanetary shock front by the first order Fermi process. With a reasonable mean free path in front of the shock (~ 0.07 AU for 1 MeV protons) Scholer and Morfill (1975) could simulate intensity increases by more than an order of magnitude in front of the shock and an intensity drop within about an hour after the shock passage. Quite often, however, the shock associated flux increase continues into the post-shock region and the subsequent decrease coincides more or less with the following tangential discontinuity separating the shocked interplanetary plasma from the driver gas. Other examples show the flux increase to be wholly contained between the shock and the tangential discontinuity (see, e.g., Kunstmann and Wibberenz, 1973). Reinhard (1975) proposed second order Fermi acceleration in the post-shock region in order to explain these intensity increases. Assuming a model for the interaction of outwardly propagating Alfvén waves (responsible for the particle scattering) with an interplanetary shock, Morfill and Scholer (1977a) showed that Fermi acceleration can compete with adiabatic deceleration only at energies below ~ 100 keV. They obtained, however, a reduction of the radial diffusion coefficient in the post-shock region by more than an order of magnitude. This (last) theoretical result has also been confirmed experimentally for certain interplanetary shock waves (Morfill and Scholer, 1977b). It is therefore of some interest to examine how such a (measured and theoretically predicted) reduction of the diffusion coefficient in the post-shock region will alter the over-all intensity-time profile. This report summarizes preliminary numerical calculations concerning the effect of localized travelling regions in the interplanetary medium, containing different diffusion coefficients, on solar particle intensity time profiles.

2. THE MODEL

We assume that the propagation of cosmic rays in interplanetary space can be described by a spherically symmetric diffusion-convection equation for the omnidirectional intensity $U(r, T, t)$ as a function of radial distance r , energy T and time t :

$$\frac{\partial U}{\partial t} = \frac{1}{r^2} \frac{\partial}{\partial r} \left(r^2 \kappa \frac{\partial U}{\partial r} - r^2 V_{SW} U \right) + \frac{4}{3} \frac{V}{r} \frac{\partial}{\partial T} TU \quad (1)$$

where κ is the radial cosmic ray diffusion coefficient and V_{SW} the solar wind velocity. Following Webb and Quenby (1973) we have solved Eq. (1) numerically by a Crank-Nicholson method. Since we include T as a third independent variable (in addition to r and t) we use the alternating direction modification of the Crank-Nicholson method as described, e.g. in Fisk (1976). Details of the numerical procedure can be found in Scholer (1977). We assumed a power law dependence of κ on T , writing $\kappa = \kappa_0(r, t)(T/T_0)^a$, where $T_0 = 1$ MeV and $\kappa_0(r, t)$ is the value of κ at 1 MeV. Quasilinear theory of particle-wave interaction shows that if magnetic field fluctuations have the spectral form $P \sim f^{-n}$ this results in the above energy dependence of the diffusion coefficient, where $a = (3-n)/2$. Since we want to study the influence of the low radial diffusion coefficient in the post-shock regime on the intensity-time structure of solar flare particles we assume that a region of reduced κ is propagating with a velocity V_S greater than the solar wind velocity through the interplanetary medium: At the time of the particle injection at the sun a shock front propagates with velocity V_g into the interplanetary medium. Behind this front, the diffusion coefficient is reduced from a value κ_1 in the undisturbed solar wind to a value κ_2 . This low value persists up to a second front which starts from the sun at the same time but with a lower velocity V_{TD} . Since we want to identify this second front with the tangential discontinuity, V_{TD} should be equal to V_{SW} , the solar wind velocity.

The numerical code can only handle smooth transitions between regions of different diffusion coefficients. Therefore we set (with some small value Δr):

$$\kappa_0(r,t) = \kappa_2 \text{ for } v_{TD}t \leq r \leq v_S t$$

$$\kappa_0(r,t) = \kappa_1 - (\kappa_1 - \kappa_2) \exp\{-(v_{TD}t - r)^2/\Delta r^2\} \text{ for } r < v_{TD}t$$

$$\kappa_0(r,t) = \kappa_1 - (\kappa_1 - \kappa_2) \exp\{-(v_S t - r)^2/\Delta r^2\} \text{ for } r > v_S t$$

We have not attempted to simulate any realistic post-shock flow pattern yet, so that $v_{SW} = \text{const.}$ everywhere. The program can be used with different initial conditions, i.e. we can either use a delta-function injection at the sun, or we have a continuous injection of the form $U \sim \exp\{-t/\tau\}$ with a time constant τ .

3. RESULTS

Some of the numerical results are presented in Figures 1 to 3. We used a solar wind velocity of 600 km/sec and a pre-to-post-shock ratio of the diffusion coefficient of 10. κ_0 is the diffusion coefficient in the pre-shock region at 1 MeV, the power law dependence of κ on T is given by $\kappa \sim T^{0.75}$ (power spectral index $n = 1.5$). Figure 1 shows in the upper panel the intensity-time profile at 1 AU for a continuous injection with $\tau = 10$ hours, in the lower panel τ was assumed to be 5 hours. Figure 2 shows in the upper panel the profiles for a delta function injection with the same parameters. The different profiles represent 0.4, 1.0, 2.0 and 4.0 MeV protons. In the lower panel we have again assumed a delta function injection but the pre-shock diffusion coefficient has the unrealistic low value of $10^{20} \text{ cm}^2/\text{sec}$ at 1 MeV. The time difference between the appearance of the "shock" and the "tangential discontinuity" is rather large in this model. We have therefore arbitrarily assigned a velocity v_{TD} greater than the pre-shock solar wind velocity v_{SW} to the sunward edge of the region of reduced diffusion coefficient. Results are shown in Figure 3 for a delta function injection (upper panel) and a continuous injection with $\tau = 5$ hours for 0.4 and 1 MeV.

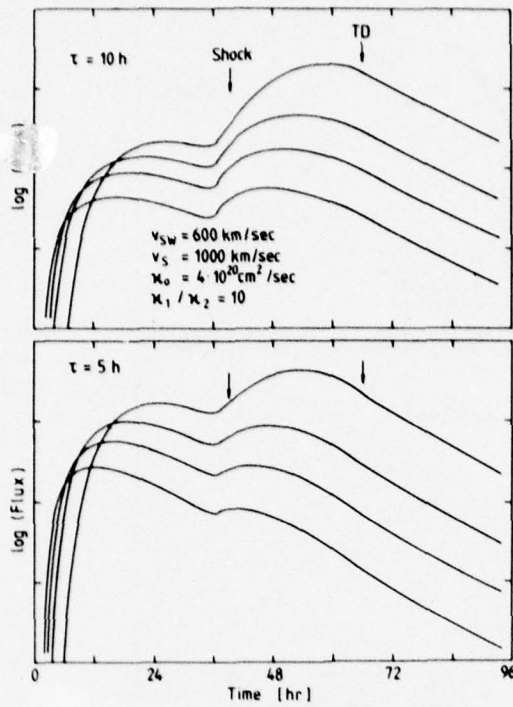


Figure 1. Intensity-time profile of 0.4, 1.0, 2.0 and 4.0 MeV protons at 1 AU. A continuous injection at the sun with an e-folding time of $\tau = 10 \text{ h}$ (upper panel) and $\tau = 5 \text{ h}$ (lower panel), was assumed.

4. DISCUSSION

The numerical results presented above show that a reduction of the diffusion coefficient in the post-shock region by an order of magnitude together with a long lasting injection can easily result in observable flux increases behind interplanetary shocks for solar particles in the 1 MeV region. A reduction of the radial diffusion coefficient of an order of magnitude has indeed been derived in some cases from interplanetary plasma and field data - see Morfill and Scholer, 1977b.

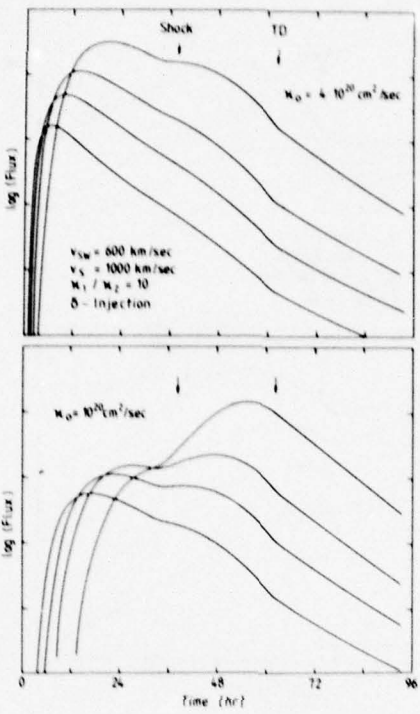


Figure 2. Intensity-time profile of 0.4, 1.0, 2.0 and 4.0 MeV protons at 1 AU. For this case a delta function injection was assumed.

A drop in the intensity at the "tangential discontinuity" can, of course, not be simulated by our simple model. This would require the introduction of an additional boundary condition at the sunward edge of the region with the reduced diffusion coefficient and, in addition, a longitudinal dependence. We have not tried to simulate the plasma flow in the post-shock region (which would, for instance, result also in enhanced adiabatic deceleration, as shown by e.g. Morfill and Scholer, 1977a). Since this is the main simplification of our present model further work is aimed at a more realistic shock - tangential discontinuity description, and although we expect the overall effects reported here to still be present in a more refined model, their magnitude may change somewhat. Figure 4 summarizes our view on shock associated particle intensity increases. We believe that ESP events

can be explained quite satisfactory by repeated reflections at the moving shock front. The short time intensity increases - the so-called shock spikes - are probably due to acceleration by repeated crossing of the shock front at almost perpendicular shocks (e.g. Chen and Armstrong, 1975).

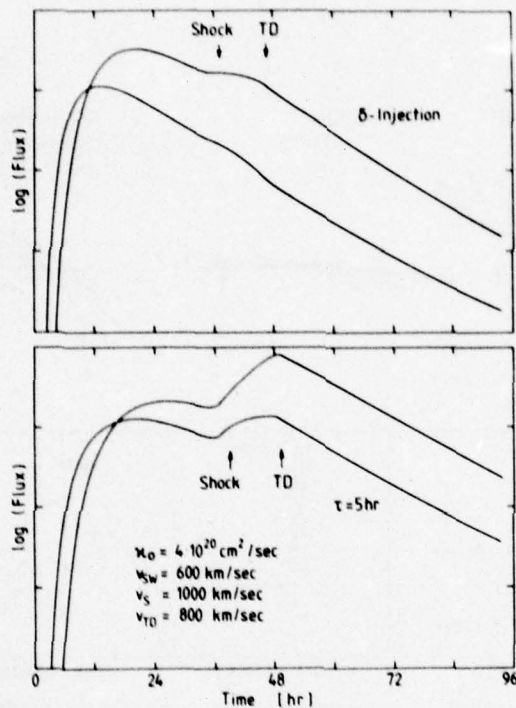


Figure 3. Intensity-time profile at 1 AU of 0.4 and 1.0 MeV protons for a δ -function injection (upper panel) and a continuous injection with $\tau = 5$ h (lower panel). The sunward side of the region of reduced diffusion coefficient has a higher velocity than the solar wind velocity.

It should be pointed out that the physical process is the same in both cases. For oblique shocks - and this should be the average case between the sun and 1 AU - one needs, however, repeated reflections in order to obtain a reasonable energy gain. If the shock is almost perpendicular one or a few reflections will be sufficient. Intensity

increases behind interplanetary shocks may in the case of low particle energies be due to second order Fermi acceleration in the post-shock turbulent region, or at the higher energies due to diffusive "trapping" of particles in the post-shock fluctuations, as shown in this report. The real situation, however, will be a weighted mixture of all cases.

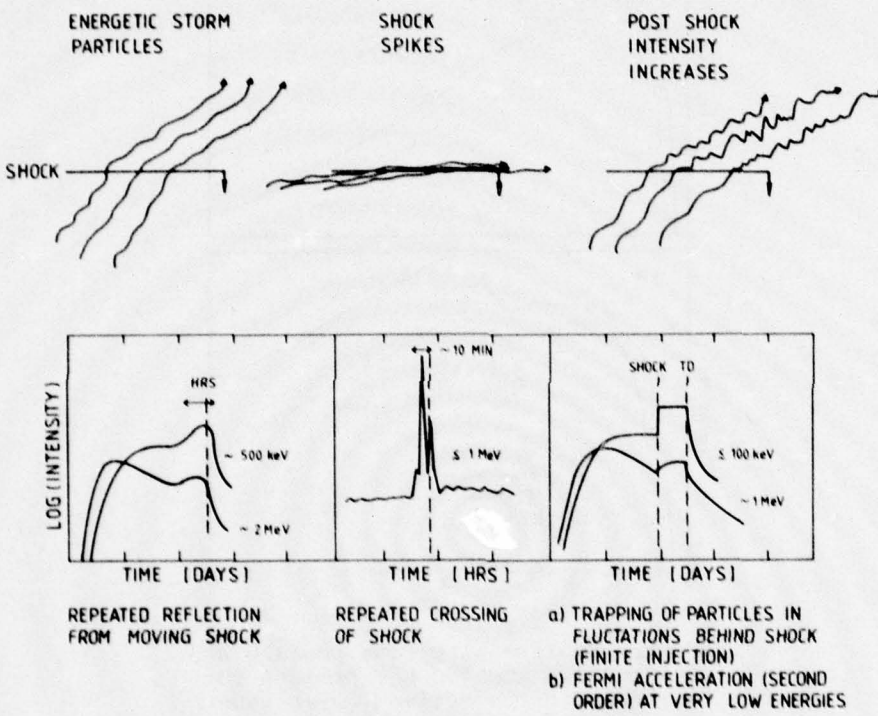


Figure 4. Schematic representation of different processes leading to shock associated intensity increases of solar energetic particles.

References

- Chen, G., and T.P. Armstrong, Acceleration of charged particles in oblique MHD shocks, in Proc. 14th Intern. Cosmic Ray Conference, p. 1814, Munich, Germany, 1975.
- Fisk, L.A., Solar modulation of galactic cosmic rays. 4. Latitude-dependent modulation, J. Geophys. Res., 81, 4646, 1976.
- Kunstmann, J., and G. Wibberenz, The connection of energetic storm particle events to interplanetary magnetic field discontinuities, in 13. Intern. Conference on Cosmic Rays, p. 1638, Denver, USA, 1973.
- Morfill, G.E., and M. Scholer, Influence of interplanetary shocks on solar particle events, Astrophys. Space Sci., 46, 73, 1977a.
- Morfill, G. E., and M. Scholer, Solar cosmic ray diffusion coefficient behind interplanetary shock waves, in Contributed Papers to the Study of Travelling Interplanetary Phenomena/1977, edited by M. A. Shea, D. F. Smart, and S. T. Wu, AFGL-TR-77-0309, p. 231, Air Force Geophysics Laboratory, Bedford, Massachusetts, 1977.
- Morfill, G.E., and M. Scholer, Solar cosmic ray diffusion coefficient behind interplanetary shock waves, these Proceedings, 1977b.
- Reinhard, R., Die solare Ausbreitung flarerzeugter Protonen im Energiebereich 10 - 60 MeV, PHD thesis, Univ. Kiel, Germany, 1975.
- Scholer, M., and G.E. Morfill, Simulation of solar flare particle interaction with interplanetary shock waves, Solar Phys., 45, 227, 1975.
- Scholer, M., On the exponential decay of western hemisphere solar particle events, Planet. Space Sci., 25, 1081, 1977.
- Webb, S., and J.J. Quenby, Numerical studies of the transport of solar protons in interplanetary space, Planet. Space Sci., 21, 23, 1973.

Discussion

- Sarris: Tangential discontinuities are convected with the solar wind velocity. In your model, how could you have the tangential discontinuity moving with respect to the solar wind?
- Scholer: We have not simulated a realistic plasma and field topology in the post-shock region but have examined the effect of localized travelling regions in the interplanetary medium, containing different diffusion coefficients, on the particle intensity profiles.

Sarris: You showed a smooth profile in the particle intensities across the tangential discontinuity. Does that mean that you have assumed cross-field diffusion? How did you obtain a smooth transition?

Scholer: We did not introduce any boundary condition in the numerical calculations at the sunward edge of the region with a reduced diffusion coefficient so that we have not really simulated a tangential discontinuity.

Armstrong: We do not see many large angle oblique shocks, and when they happen the energetic particle effects are small. You could have ESP also involved with a small-angle shock spike event.

Scholer: For near parallel shocks, the magnetic field enhancement behind the shock should be small. Thus we would not expect magnetostatic reflection to be important and would agree therefore with your comment. An association of ESP events (as inferred from our model) and shock spike events should also exist for shocks as they become more perpendicular.

Krimigis: An essential requirement for any ESP model is that it should adequately account for both the intensity and anisotropy profiles. Your model accounts for typical observed intensity profiles but cannot account for the observed anisotropies. A diffusion coefficient of $\sim 10^{19}$ to $10^{20} \text{ cm}^2/\text{sec}$ is incompatible with observed anisotropies with $\xi > 0.5$ and often > 1 . Thus, I do not believe that diffusion models for ESP events can adequately account for the observations. Would you comment on this point?

Scholer: Firstly, we obtained a typical intensity profile only for a radial diffusion coefficient of $\sim 5 \times 10^{20} \text{ cm}^2/\text{sec}$ (parallel diffusion coefficient - which is the important quantity for the field aligned anisotropy - of $\sim 10^{21} \text{ cm}^2/\text{sec}$) for 1 MeV protons. Secondly, the calculated radial anisotropy is about 50% directed away from the shock in front as well as behind the shock (for about one hour) in our calculations. The low value of the diffusion coefficient which you mention should, at times, occur in the post-shock region only, and does not influence the calculations for the ESP events greatly because they are due to scattering of the energetic particles in front of the shock in our model.

Solar Cosmic Ray Diffusion Coefficient Behind Interplanetary Shock Waves

Gregor Morfill

**Max-Planck-Institut für Kernphysik
69 Heidelberg, FRG**

Manfred Scholer

**Max-Planck-Institut für Physik und Astrophysik
Institut für extraterrestrische Physik
8046 Garching, FRG**

Abstract

We have analyzed interplanetary magnetic field and plasma data obtained during the passage of four flare generated shock waves with accompanying energetic solar particles. Using magnetic field power spectra the ratio of the parallel cosmic ray diffusion coefficients in the pre- and post-shock regions as well as the averaged radial cosmic ray diffusion coefficient is calculated. The results are discussed in terms of the location of the shock wave generating flare on the sun's surface.

1. INTRODUCTION

It is well known that the existence of an interplanetary shock wave during solar flare events can greatly alter the intensity time profile of the energetic flare particles. In addition to the energetic storm particles, which have been interpreted by, e.g. Scholer and Morfill (1975) as being due to repeated reflections at the shock, behind the shock the background plasma/field topology is greatly modified. Morfill and Scholer (1977) have argued on theoretical grounds that this leads to a considerable reduction of the radial cosmic ray diffusion coefficient in the post-shock region. Thus, sub-MeV particles injected in the post-shock region have little chance to "leak out", since diffusion will become smaller relative to the convection term.

It is therefore of great importance to verify the theoretically predicted reduction of the radial diffusion coefficient experimentally. This report is the result of an analysis of observations obtained during the passage of four interplanetary shocks.

2. OBSERVATIONS

We have chosen for our analysis four solar flare associated interplanetary shocks with accompanying energetic particles. The days of the shock occurrence and the pre-and post-shock plasma and magnetic field parameters are listed in Table 1. The plasma parameters (density n and solar wind velocity) of the March 8, 1970 shock are from Vela 5 (Montgomery and Bame, 1971). The plasma parameters of the March 6, 1972, May 15, 1972 and June 17, 1972 shocks are from Heos 2 and were generously supplied by H. Grünwaldt. Magnetic field vector measurements every 30 sec for the March 8, 1970 flare from Heos 1 and for the other three flares from Heos 2 were generously supplied by P.C. Hedgecock.

Table 1. The plasma and magnetic field parameters in the pre-(index 1) and post-shock region (index 2). n = solar wind density, V = solar wind velocity, B = magnetic field strength, P_0 = power at 1 Hz, q = exponent of magnetic field power spectrum.

	March 8, 1970	March 6, 1972	May 15, 1972	June 17, 1972
n_1 (cm^{-3})	8	5.8	21	4.5
V_1 (km/sec)	370	370	342	470
B_1 (γ)	8.0	3.9	8.7	7.4
n_2 (cm^{-3})	13	18.0	65	13.8
V_2 (km/sec)	860	590	480	610
B_2 (γ)	25.5	5.9	17.3	19.8
P_{01} (γ^2/Hz)	20.5	0.4	0.53	0.89
q_1	0.43	1.0	1.15	1.15
P_{02} (γ^2/Hz)	4.5	3.2	2.06	5.5
q_2	1.41	1.2	1.40	1.13
$\alpha(\vec{s}, \vec{r})$???	68°	36°	--	85°

We have calculated an average magnetic field \underline{B} during a \sim two hour interval in front of the shock (index 1) and behind the shock (index 2). In case the tangential discontinuity occurred within the two hour interval behind the shock we have taken only an average up to the appearance of the tangential discontinuity. The components of the magnetic field were then computed in a coordinate system with one vector parallel to \underline{B} and two other vectors perpendicular to \underline{B} and perpendicular to each other. These magnetic field data have been subjected to power spectral analysis by the Blackman and Turkey method.

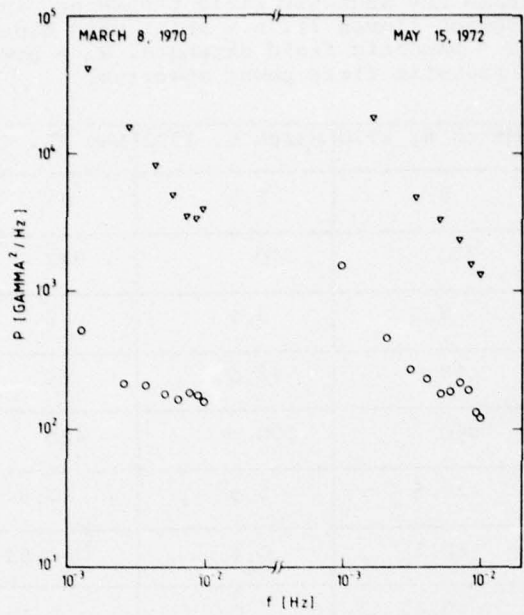


Figure 1. Magnetic field power spectra for the component perpendicular to the average magnetic field during the pre-(circles) and post-(triangles) shock time periods. Time periods are: 1200 - 1424 UT and 1424 - 1626 UT on March 8, 1970 and 1626 - 1835 UT and 1853 - 2030 UT on May 15, 1972.

Figures 1 and 2 show the power perpendicular to \underline{B} for the four shocks. Circles are for the power in the pre-shock, triangles for the power in the post-shock region. Representing the power by a power law in frequency f : $P = P_0 f^{-q}$, we have determined P_0 and q . The values are given in Table 1. From the average magnetic field vectors \underline{B}_1 and \underline{B}_2 in the pre-and post-shock region it is, in principle, possible to determine the shock normal by applying the coplanarity theorem. Such a determination is, however, highly uncertain and we have marked the angle between the shock normal \underline{s} and the radial direction \underline{r} in Table 1 with three question marks. As can be seen from Figures 1 and 2 the power in the post-shock region is generally larger by about an order of magnitude than the corresponding power in the pre-shock region.

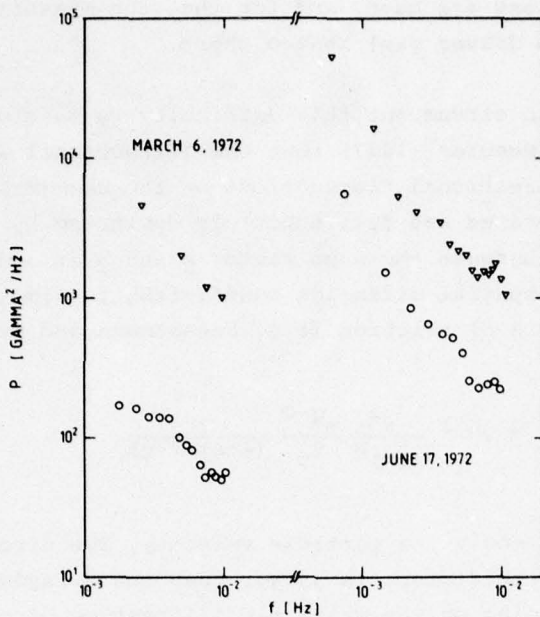


Figure 2. Magnetic field power spectra for the component perpendicular to the average magnetic field during the pre-(circles) and post-(triangles) shock time periods. Time periods are: 1800 - 2107 UT and 2108 - 2200 UT on March 6, 1972, and 1000 - 1314 UT and 1314 - 1700 UT on June 17, 1972.

The spectral exponent may also differ in the two regions, in contrast to the simple model used in Morfill and Scholer (1977).

3. COSMIC RAY DIFFUSION COEFFICIENT

In relation to energetic solar particles, which average over medium scale fluctuations as well as flux tubes, a similar average of the parameters influencing the diffusion coefficient is not possible using a single spacecraft. The reason for this is that suitable averaging accuracy is only obtained if sufficient flux tubes and/or medium

scale fluctuations are used, and for that the measuring period (between shock and driver gas) is too short.

In order to circumvent this difficulty we make use of the results of Morfill and Scholer (1977) that the "directional averaging" (averaging over the directional fluctuations of the background magnetic field \underline{B} over medium scales and flux tubes) is dominated by those instances when the angle between the wave vector \underline{k} and \underline{B} is less than 30° . In that case, the spatial diffusion coefficient is almost given by the axisymmetric ($\underline{k} \parallel \underline{B}$) solution (e.g. Hasselmann and Wibberenz, 1968)

$$\kappa_{\parallel \text{axi}} = v^{3-q} v^{q-1} \frac{B^2}{(2n)^q} \frac{\omega^{q-2}}{P_0} \frac{1}{(4-q)(2-q)} \quad (1)$$

where $\omega = eB/mc$ and v the particle velocity. The directionally averaged diffusion coefficient is larger than the axisymmetric value by an amount depending on the ratio $\eta = 1/($ fraction of cases where \underline{k} and \underline{B} have an angular separation $< 30^\circ$ $)$. If, therefore, the distribution of medium scale background field directions is fairly broad about the long term average value, $\langle \kappa_{\parallel} \rangle$ is proportional $\kappa_{\parallel \text{axi}}$ and $\langle \kappa_r \rangle$ is proportional to $\kappa_{\parallel \text{axi}} \cos^2 \chi$, where χ is the long term average field direction. Thus

$$\frac{\langle \kappa_r \rangle_{\text{before}}}{\langle \kappa_r \rangle_{\text{after}}} \approx \frac{\kappa_{\parallel \text{axi}(\text{before})} \cos^2 \chi_{\text{before}}}{\kappa_{\parallel \text{axi}(\text{after})} \cos^2 \chi_{\text{after}}} \quad (2)$$

Whilst most quantities in (1) are relatively straightforward to measure, the main problem occurs with χ and the assumption $\eta_{\text{before}} \approx \eta_{\text{after}}$. The latter is approximately (to within a factor 2) satisfied if the directional distribution of flux tubes and medium scale fluctuations is as wide as long term measurements in interplanetary space lead us to believe. The determination of χ is more difficult. As mentioned before, we cannot simply take long term average values if we want to investigate individual examples. On the other hand, we have only a limited sample of flux tubes and medium scale fluctuations for our determination of χ (at 1 AU), a sample which may not be represen-

tative of the situation as a whole - as seen by the energetic particles (which sample the fluctuations during their whole passage from the sun to the detector). There is nothing one can do about this uncertainty, except to take the measurements at face value and it may well be that the uncertainties in χ distort the calculations in such a way that expression (2) is too inaccurate for a reasonable microscopic description of the solar wind medium. Inserting the parameters given in Table 1 in Eq. 1 and 2 we obtain the ratios $\langle \chi_{\parallel} \rangle_{\text{axi}}^{\text{before}} / \langle \chi_{\parallel} \rangle_{\text{axi}}^{\text{after}}$ (dashed line) and $\langle \chi_r \rangle_{\text{before}} / \langle \chi_r \rangle_{\text{after}}$ (solid line) shown in Figures 3 and 4.

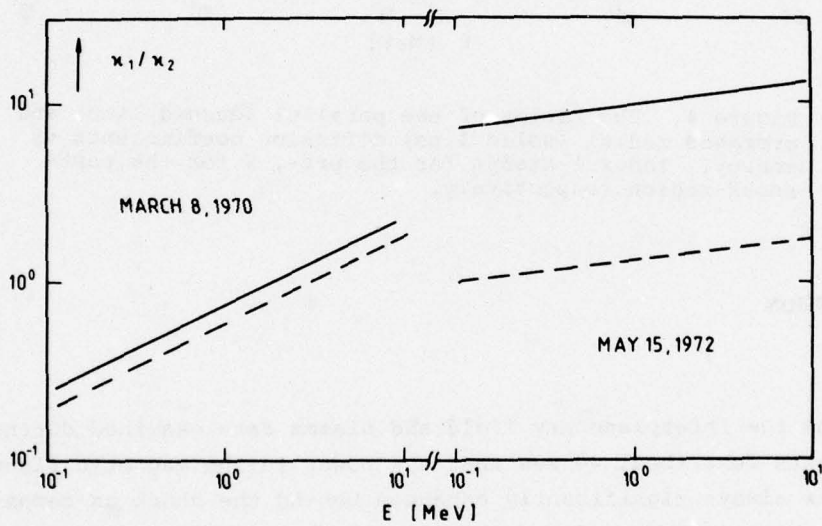


Figure 3. The ratios of the parallel (dashed line) and averaged radial (solid line) diffusion coefficients vs energy. Index 1 stands for the pre-, 2 for the post-shock region respectively.

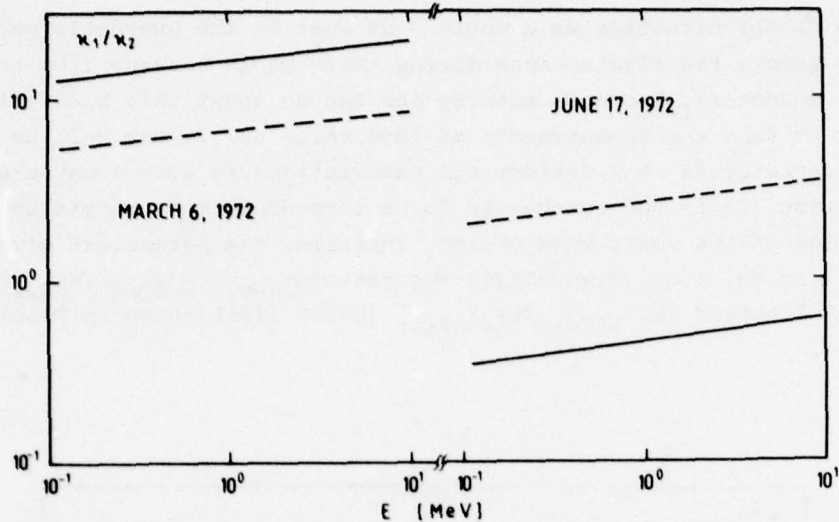


Figure 4. The ratios of the parallel (dashed line) and averaged radial (solid line) diffusion coefficients vs energy. Index 1 stands for the pre-, 2 for the post-shock region respectively.

4. DISCUSSION

From the interplanetary field and plasma data examined during the four events described, we see that the power in the magnetic fluctuations is always significantly enhanced behind the shock as compared to the region in front of the shock. All other things being equal, one would expect an appropriate reduction in the parallel spatial diffusion coefficient, since κ_{\parallel} is proportional to $1/P(f_{\text{res}})$. The fact that the calculations do not show this simple dependence (see especially the March 8, 1970 event) is attributed largely to the increase in the magnetic field strength behind the shock, which increases the resonant frequency f_{res} . Since $P \sim f^{-q}$ (with q typically > 1) is a good approximation, we see that those interplanetary shocks, which have a large increase in field strength associated with them, may not necessarily have a reduced parallel spatial diffusion coefficient in the post-shock region.

Second feature to notice is the relative magnitude of the radial diffusion coefficient κ_r , which depends on the direction of the average magnetic field relative to the radius vector. Clearly, the usual jump conditions at the shock require $B_{N1} = B_{N2}$ and $B_{T1} = 0.25 B_{T2}$, i.e. the tangential component of the IMF is enhanced by a factor 4 in the post-shock region. This, mainly, accounts for the observed changes in field direction. For κ_r , however, we are interested in the magnetic field direction relative to a fixed axis (\underline{r}) - and it is verified that different shock surfaces will also cause different values of χ in the post-shock region. As an example let us consider the following cases:

If the IMF in the pre-shock region is approximately given by the Archimedian spiral field, and if the shock normal is radially directed, χ (the angle between \underline{B} and \underline{r}) is larger in the post-shock region (see Morfill and Scholer, 1977) and thus $\kappa_r = \kappa_{||} \cos^2 \chi$ would be reduced even more relative to the pre-shock value. If, however, the shock front is placed in such a way that the shock normal makes a larger angle with the radius vector, then the Archimedian spiral, χ , would become smaller in the post-shock region, and thus κ_r would increase relative to the pre-shock value. (This latter case corresponds to the June 17, 1972 observations, where the ratio of the radial diffusion coefficient is smaller than that of the corresponding parallel diffusion coefficients.)

Clearly, each individual event has to be analyzed on its own merit, and one cannot make sweeping statements concerning the size of the radial diffusion coefficient in the post-shock region - although presumably the average situation (described by Morfill and Scholer, 1977) will apply in many cases. One trend is predicted by our analysis, however, which is open to further observations. If we take the shock surface in the ecliptic plane as that inferred by e.g. Taylor (1969) and Hirshberg (1968), it is clear that east limb flares would on average yield more perpendicular shocks (i.e. shock normal perpendicular to the quiet time average IMF) and west limb flares would on average yield more parallel shocks (i.e. shock normal parallel to the quiet time average IMF). Central meridian flares will have shock normals which are, on average, parallel to \underline{r} . Now, our preceding analysis has shown that both for perpendicular and parallel shocks

the angle χ cannot vary greatly (and is then, on average, given by the Archimedean spiral angle). We thus have:

	κ_{\parallel} (after) _____ κ_{\parallel} (before)	κ_r (after) _____ κ_r (before)
West limb flares	$\ll 1$ Increase in power not accompanied by increase in B for parallel shocks	$\ll 1$ About the same as parallel diffusion coefficients (χ unchanged)
Central Meridian	< 1	< 1 or $\ll 1$ due to increase in χ
East limb flare	> 1 Due to large increases in B for perpendicular shock	≥ 1 About the same as parallel diffusion coefficients (χ unchanged)

For solar energetic particles this would imply a greater chance of becoming trapped behind a shock (with κ_r (after) $\ll \kappa_r$ (before)) which belongs to a central meridian or west limb flare. Such flares should, on the basis of our calculations, have a statistically greater likelihood of enhanced (or at least not reduced) energetic solar particle fluxes in the post-shock region.

Acknowledgments

We are deeply indebted to P.C. Hedgecock for use of HEOS magnetic field data and to H. Grünwaldt for providing us with HEOS plasma data and to V. Domingo for pointing out an inconsistency in the original discussion.

References

- Hasselmann, K., and G. Wibberenz, Scattering of charged particles by random electromagnetic fields, Z. Geophys., 34, 353, 1968.
- Hirshberg, J., The transport of flare plasma from the sun to the earth, Planet. Space Sci., 16, 309, 1968.
- Montgomery, M.D., and S.J. Bame, Vela 5 solar wind observations during the geomagnetic storm of March 8, 1970, in Report UAG-12 part I, p. 122, US Department of Commerce, Boulder, 1971.
- Morfill, G.E., and M. Scholer, Influence of interplanetary shocks on solar particle events, Astrophys. Space Sci., 46, 73, 1977.
- Scholer, M., and G. Morfill, Simulation of solar flare particle interaction with interplanetary shock waves, Solar Phys., 45, 227, 1975.
- Taylor, H.E., Sudden commencement associated discontinuities in the interplanetary magnetic field observed by IMP 3, Solar Phys., 6, 320, 1969.

Discussion

Domingo: I would like to mention that for the particle flux profile (low energy protons) around the 6 March 1972 shock we have an alternate explanation based on the fact that the different flux levels observed come from different regions in the solar surface, that may be connected, more or less efficiently, to the particle sources by coronal transport. These results will be presented at the 15th International Cosmic Ray Conference to be held in Plovdiv, Bulgaria in August 1977.

Morfill: This statement amazes me a little bit, because in order to map the field lines back to the sun you would need a reliable two- (or maybe even three-) dimensional model of MHD shocks, and as far as I know such models are only very crude right now.

Acceleration of Low-Energy Solar Protons at Interplanetary Shocks

E. Amata¹⁾, V. Domingo, R. Reinhard and K.-P. Wenzel
Space Science Department of ESA
European Space Research and Technology Centre
Noordwijk, The Netherlands

H. Grünwaldt
Max-Planck-Institut für Physik und Astrophysik
8046 Garching bei München, FRG

Abstract

The shock spikes of 15 May, 6 June, 13 September and 18 October 1972 are discussed using the low-energy proton channels of the SSD/ESA detector systems onboard HEOS-2. It is found that the magnitude of the shock spike increases with the angle between the shock normal and the upstream interplanetary magnetic field, in agreement with theoretical predictions of particle acceleration at shock fronts. In addition to the shock spike a general increase of the particle fluxes is observed within a few hours of the shock passage. There is evidence that these increases, which are tentatively identified as ESP events, are due to the same acceleration mechanism. This follows from the correlation of the size of the ESP event with the size of the shock spike and also from anisotropy measurements.

¹⁾ Now at: Laboratorio Plasma Spazio, CNR, Frascati, Italy.

1. INTRODUCTION

Shock spikes are short-lived low-energy particle intensity increases observed within a few minutes of the passage of an interplanetary shock wave. Shock spikes are also known as LESP (low-energy storm particles) and should not be confused with ESP (energetic storm particles) events, which typically last several hours and are only loosely correlated with shocks. Shock spikes have been the subject of many studies and different mechanisms have been proposed to explain the observations. There is little doubt that shock spike particles are accelerated by the interaction with the plasma shock wave and it is also generally agreed that sweeping and albedo acceleration (single-step Fermi acceleration) can only explain moderate spike events (30-40% increase above the ambient flux level).

Therefore, a number of multi-encounter models have been discussed. Van Allen and Ness (1967) and Fisk (1971) considered acceleration by repeated reflections between the moving shock and upstream magnetic field irregularities. Axford and Reid (1963) and Ogilvie and Arens (1971) discussed acceleration by repeated reflections between the moving shock and the Earth's bow shock. Although these acceleration mechanisms may exist, the model predictions of anisotropies and spectra are in disagreement with some of the well-documented spike events.

Sonnerup (1969) and Singer and Montgomery (1971) pointed out the importance of the angle between the shock normal and the upstream interplanetary magnetic field and its relation to the energy gain in the acceleration. However, this is not a single-encounter process as these authors had assumed, but a multiple-encounter (Sarris and Van Allen, 1974; Chen and Armstrong, 1975). If the magnetic field stays almost perpendicular to the shock normal for several minutes the particles are confined to the shock and cross the shock front repeatedly, thus being accelerated within a few minutes. Clearly, the acceleration mechanism is only effective if, and as long as, the angle between the interplanetary magnetic field and the shock front normal is large.

It is the purpose of this paper to test this prediction with low-energy particle data from HEOS-2. Analysing all suitable shock spikes during the $2\frac{1}{2}$ years lifetime of HEOS-2 we find that the observations are in agreement with the prediction.

2. THE DATA

The particle data were obtained by the SSD/ESA experiment on HEOS-2 (Kohn et al., 1972) comprising two solid state detector systems. For this study we used the low and medium energy proton channels of the main telescope (0.8-1 MeV, 1-9 MeV, 9-12 MeV) which was mounted perpendicular to the spin axis, and the 0.5-5 MeV protons of another telescope, which was pointed antiparallel to the spin axis. Either spin-averaged data with a time resolution of ~ 2 minutes or 'angular' data in 4 sectors with a time resolution of ~ 8 minutes were obtained for the 1-9 MeV and 9-12 MeV protons. Due to this limited time resolution the detailed structure of the shock spikes cannot be resolved. Therefore, we restrict ourselves to determine the magnitude of the spike and its location with respect to the shock. A second limitation is given by the spectral resolution, which is insufficient to correct the particle fluxes for the Compton-Getting effect at times when the spectrum is not a simple power-law.

The HEOS-2 magnetic field data with a time resolution of 32 seconds were provided by Dr. P.C. Hedgecock. The direction of the shock normal was estimated using plasma and magnetic field data assuming the validity of the Rankine-Hugoniot conservation relations (Lepping and Argentiero, 1970, 1971; Grünwaldt et al., 1976).

3. OBSERVATIONS

During its $2\frac{1}{2}$ year lifetime (February 1972 - July 1974) HEOS-2 spent about 50% of the time outside the magnetosphere in interplanetary space. During that time we detected 6 short-lived particle increases associated with interplanetary shocks as identified from interplanetary magnetic field data and storm sudden commencements (SSC). In two of these the solar proton fluxes were so high that several particle channels were saturated. In the following we describe the main characteristics of the 4 remaining events.

In Figures 1 through 4 we display two low-energy particle channels and the magnitude and the two polar co-ordinates of the magnetic field vector in geocentric solar ecliptic (GSE) co-ordinates for a few hours around each shock spike. The time of the shock passage is marked by a vertical dashed line.

The events of 18 October and 6 June 1972 (Figures 1 and 2) are rather similar. They show a narrow spike of about 2-4 minutes duration within 2 minutes of the shock transit time, a 'pedestal' of about $\frac{1}{2}$ hour duration preceding the shock and an immediate decrease to the steady particle flux level after the shock. The increases in magnetic field intensity that occur during the two hours prior to the 6 June shock are short encounters of the Earth's bow shock moving past the satellite.

The event of 13 September 1972 (Figure 3) is by far the largest of the four. The 1-9 MeV proton intensity increases within $\sqrt{1\frac{1}{2}}$ hours by almost 3 orders of magnitude. Superimposed on the broad increase is a narrow spike just after the time of the shock.

The shock of 15 May 1972 (Figure 4) shows a particle flux increase of about 2 hours width with a narrow shock spike superimposed at the time of the shock encounter.

Summarizing the observations, we find in each of the 4 cases that

- (1) the presence of solar particles seems to be required for the production of the shock spikes,
- (2) within ± 2 hours around the shock there is a 'pedestal' of particles which is interpreted as an ESP event associated with the shock,
- (3) the shock spike is observed within a few minutes of the shock passage, either prior to (18 October, 6 June, 15 May) or after (13 September) the shock passage.

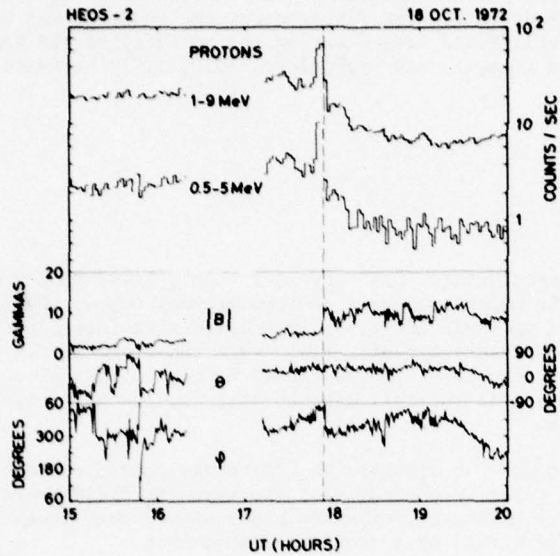


Figure 1. The shock event of 18 October 1972. Proton count rates and magnetic field vector components in geocentric solar ecliptic (GSE) co-ordinates, as measured by HEOS-2. The vertical line marks the transit time of the shock as seen in the magnetic field intensity

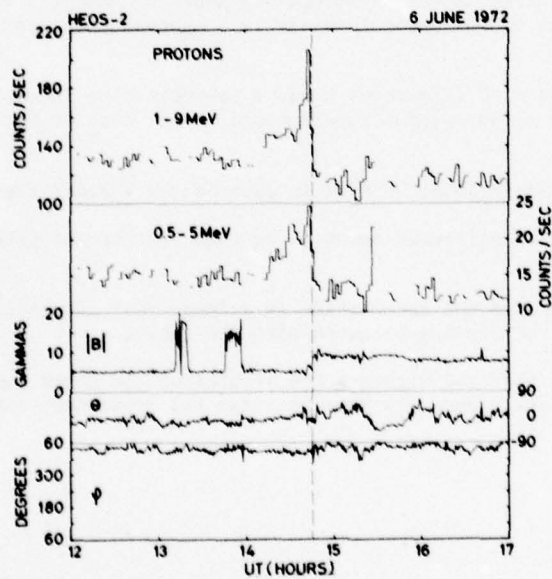


Figure 2. The shock event of 6 June 1972.
See Figure 1 caption

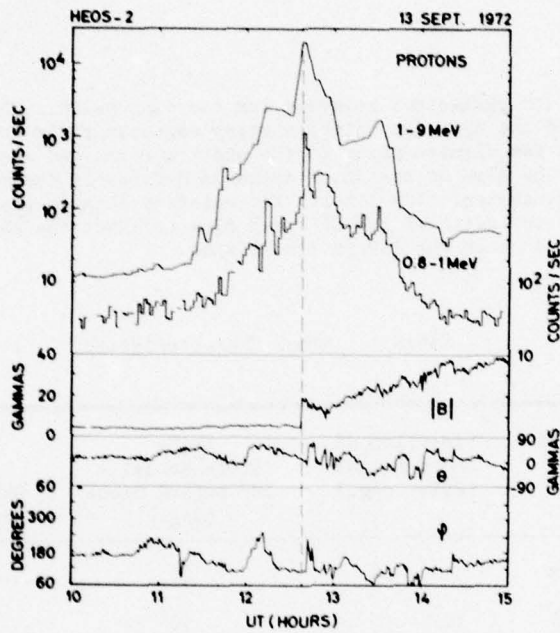


Figure 3. The shock event of 13 September 1972. The count rates of the 1-9 MeV proton channel are spin-averaged and have a time resolution of ~ 8 min. The 0.8-1 MeV channel has a sampling rate of ~ 2 min and measures the count rate at near random angles. Thus some differences in behaviour between both channels may be due to the differences in angular observation

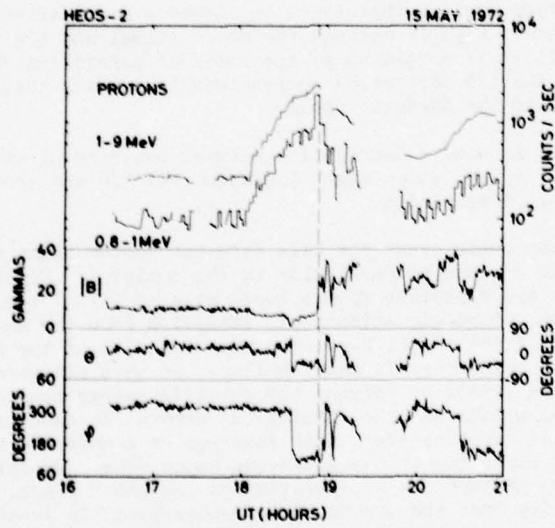


Figure 4. The shock event of 15 May 1972. See caption for Figure 3

4. DISCUSSION

Table 1 gives the parameters relevant for the discussion. The angle between the shock normal and the upstream interplanetary magnetic field does not vary significantly for a few minutes prior to the shock arrival and was averaged over that time period. The size of the shock spike is defined by the ratio of the 1-9 MeV peak flux to the ambient flux level. The relative flux increase of the ESP event as defined by the ratio of the ESP peak flux (without the shock spike) to the flux level before and after the ESP is also listed.

Table 1. Shock Characteristics

Date 1972	Time of Shock UT	Direction of Shock Normal (GSE, deg.)	Angle Shock Normal - IMF before Shock (deg.)	Size of	
				Shock Spike	ESP Event
15 May	1853	178 19	60	3	20
6 June	1445	162 -5	60	1.4	1.6
13 Sept	1238	202 -23	86	10	500
18 Oct	1754	167 28	71	3	4

It is evident from Table 1 that there is indeed a correlation between the size of the shock spike and the angle between the shock normal and the upstream interplanetary magnetic field as predicted by the model of Sarris and Van Allen (1974). The largest shock spike (13 September) corresponds to a shock that was propagating almost perpendicular to the magnetic field.

Apparently there is also a correlation between the size of the ESP event and the size of the shock spike, which might indicate that ESP and shock spikes are due to the same acceleration mechanism.

During the 13 September event the main detector system obtained angular information on the fluxes in a plane perpendicular to the ecliptic. Figure 5 shows the anisotropy magnitude and direction from a least-squares fit of the measurements to a cosine-distribution. Strongly anisotropic streaming from the Sun is observed prior to the passage of the shock, i.e. from the direction of the arriving shock. After its passage the anisotropy is much smaller. We have estimated the influence of the Compton-Getting effect by varying the particle energy spectrum within the limits of the channel widths and the statistical errors. In each case the post-shock anisotropy is either consistent with isotropy or a moderate sunward flow, i.e. a flow from the direction of the departing shock wave. We interpret these results as indicative of particle acceleration at the shock front. However, there is also the possibility that the strong 13 September particle event is a corotating solar particle stream originating in McMath plage 12021 at $\sim 30^\circ$. The possibility of a prompt flare induced event can be excluded because no H α or X-ray flare was

observed at that time and the anisotropy magnitude increases with time, in contrast to a flare event, where it generally decreases.

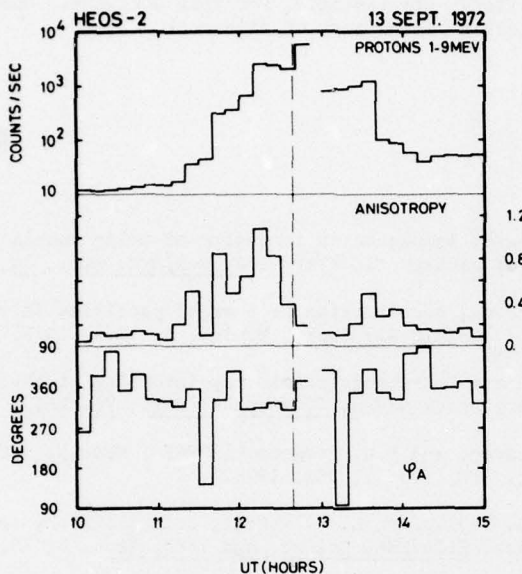


Figure 5. 10-minute averages of 1-9 MeV proton flux and anisotropy parameters A and ϕ_A as observed around the shock of 13 September 1972. ϕ_A is given in space-craft co-ordinates, $\phi_A = 360^\circ$ corresponds to particles coming from the Sun and $\phi_A = 90^\circ$ to those from ecliptic north

5. SUMMARY AND CONCLUSION

We have shown that there is a correlation between the shock spike magnitude and the angle between the shock normal and the upstream interplanetary magnetic field as predicted by the Sarris and Van Allen model (1974). The largest shock spikes are associated with almost perpendicular shock waves. We have also shown that apart from the shock spike there is a general increase of the particle intensity (ESP event), the magnitude of which is correlated with the size of the shock spike. We conclude that this is indicative that the same acceleration mechanism explains both the shock spike and the ambient ESP event. Our conclusion of interplanetary acceleration of low energy particles by the shock front is supported by anisotropy measurements available for the strongest event (13 September 1972).

Acknowledgments

We are grateful to Dr. P.C. Hedgecock, Imperial College, London, for providing us with HEOS-2 magnetic field data essential for this analysis. One of us (E.A.) was holding an ESA fellowship during part of this work.

References

- Axford, W.I., and G.C. Reid, Increases in intensity of solar cosmic rays before sudden commencements of geomagnetic storms, J. Geophys. Res., 68, 1793, 1963.
- Chen, G., and T.P. Armstrong, Acceleration of charged particles in oblique MHD shocks, Proc. 14th Int. Cosmic Ray Conf., Munich, 5, 1814, 1975.
- Fisk, L.A., Increases in the low-energy cosmic ray intensity at the front of propagating interplanetary shock waves, J. Geophys. Res., 76, 1662, 1971.
- Grünwaldt, H., H. Rosenbauer, and P.C. Hedgecock, HEOS-2 Messung interplanetarer Stosswellen, Verhandl. DPG (VI) 11, 383, 1976.
- Köhn, D., D.E. Page, B.G. Taylor, and K.-P. Wenzel, Interplanetary experiment (S 204) for the HEOS-A2 mission, ELDO/ESRO Scient. and Tech. Rev., 4, 19, 1972.
- Lepping, R.P., and P.D. Argentiero, Improved shock normals obtained from combined magnetic field and plasma data from a single spacecraft, NASA N70-35938 preprint, GSFC, Greenbelt, Maryland, 1970.
- Lepping, R.P., and P.D. Argentiero, Single spacecraft method of estimating shock normals, J. Geophys. Res., 76, 4349, 1971.
- Ogilvie, K.W., and J.F. Arens, Acceleration of protons by interplanetary shocks, J. Geophys. Res., 76, 13, 1971.
- Sarris, E.T., and J.A. Van Allen, Effects of interplanetary shock waves on energetic charged particles, J. Geophys. Res., 79, 4157, 1974.
- Singer, S., and M.D. Montgomery, Detailed directional and temporal properties of solar energetic particles associated with propagating interplanetary shock waves, J. Geophys. Res., 76, 6628, 1971.
- Sonnerup, B.V.D., Acceleration of particles reflected at a shock front, J. Geophys. Res., 74, 1301, 1969.
- Van Allen, J.A., and N.F. Ness, Observed particle effects of an interplanetary shock wave on July 8, 1966, J. Geophys. Res., 72, 935, 1967.

Discussion

Krimigis: You have stated that the Fisk model explains the "snow plow" effect upstream from the shock. Yet you have shown large anisotropies, which are not allowed by the Fisk model ($k < 10^{19} \text{ cm}^2/\text{sec}$). Can you comment on the basis for your statement?

Domingo: The events of 6 June and 18 October are rather similar in flux profile to those predicted by Fisk. For those events we do not have angular information. In the event of 13 September, I have mentioned that the spectra get harder around the shock as predicted by Fisk, but you are right, the observed anisotropy is incompatible with Fisk's model prediction.

Sarris: During shock waves we have dramatic "sweeps" in solar longitude; therefore we sample considerably different regimes of the solar corona before and after the shock. This should be taken into account before attempting to explain the change in the energetic particle intensities away from the shock.

Domingo: I agree with your considerations, but only a small fraction of the shocks are perpendicular shocks, and in the other cases a change in plasma regime needs not to be a change in particle regime unless the shock really acts as a barrier. A greater than 1 MeV proton travels much faster than the shock.

Storage of Solar Cosmic Rays by Shock Wave Ensemble

J. Otaola, R. Gall, and R. Pérez Enríquez
Instituto de Geofísica, U.N.A.M.
Mexico 20, D.F., Mexico

Abstract

Using a mathematical model for the magnetic field topology of a Dryer-type double shock ensemble, we analyze the propagation of energetic solar cosmic ray protons during the events of August 1972. The 8-hour delay between the 06:20 UT flare of August 4th and the arrival of particles at high level detectors is satisfactorily explained by the storage effect exerted by the ensemble. This interpretation associated the observations of particles with a δ -function type injection at the flare location and differs from other explanations which propose effects such as coronal convection, acceleration, etc.

I. INTRODUCTION

In this paper we consider the effect that a shock wave ensemble has on the propagation of high rigidity solar protons. We give a preliminary report of our

analysis of the ground level event (GLE) of August 4th, 1972, and propose a new interpretation of the GLE in terms of trapping of particles in a storage region behind a fast and wide shock ensemble, that was generated on August 3rd, at about 0.3 AU and passed by the earth late on August 4th. The event was detected at neutron monitor stations with $P_c \leq 2$ GV after an unusual 8-hour delay and had a sharp onset and a sharp decay.

2. SHOCK WAVE ENSEMBLE AND COSMIC RAY PROPAGATION

Extensive studies on the characteristics, generation, propagation and evolution of shock wave ensembles have been done by several workers (Dryer, 1972, 1974; Dryer et al., 1974a, 1974b; Steinolfson et al., 1975a, 1975b). These authors give values for the shock ensemble in the region less than 1.0 AU as ranging from 0.05 to 0.25 AU. We note that these widths are 3 to 4 orders of magnitude greater than the width of a simple shock.

Based on the work of Dryer et al., (1974a, b), we derived a simple model of the magnetic field within the ensemble; the strongly enhanced azimuthal component was modeled by a sine function (Figure 1). With the help of this model we have simulated, by numerical integration, the motion of protons of 0.5 to 5 GV and found that particles are reflected from the reverse shock and remain trapped behind the shock, bouncing between the reverse shock and the more intense IMF behind the shock (Pérez Enriquez and Gall, 1976); only particles with higher rigidity manage to cross the ensemble, deviated only slightly by the magnetic field of the ensemble (Figure 2). As the ensemble propagates outward, its field decreases; the widths of the ensemble and the storage region increase; and the ensemble becomes more and more transparent each time to lower rigidity particles.

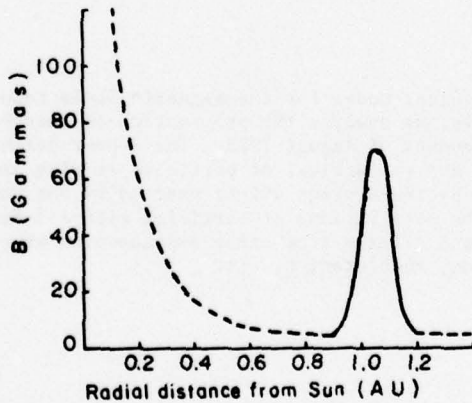


Figure 1. Assumed radial magnetic field associated with a double shock ensemble, modeled after the work of Dryer et al. (1974a, 1974b).

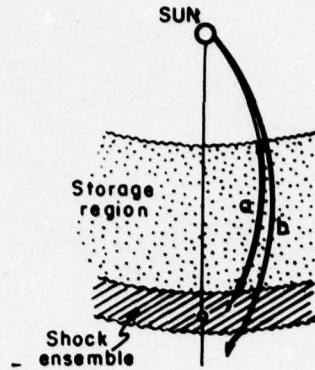


Figure 2. Schematic representation of trajectories of (a) trapped particle, and (b) non-trapped particle in the presence of a double shock ensemble.

3. THE AUGUST 3-4, 1972 SHOCK WAVES

In order to interpret the August 4th GLE, we must first study the generation and propagation of the forward (F) and reverse (R) shocks. Again, we use the results of the numerical simulation of the August disturbances derived by Dryer et al. (1975, 1976) and represented by the radius time diagram shown in Figure 3. The forward shocks, F_1 , F_2 and F_3 , generated in three different flares, reached the earth at 01:10, 02:20, and 20:54 UT, respectively, during August 4th, including SSC's and Forbush Decreases. The F_3 , a very fast shock, generated by the '3B flare was longitudinally very asymmetric, as indicated by its observation by Pioneer 9 (situated at 0.78 AU, 45° East of the Earth-Sun line) 3 hours after it reached the earth. The reverse shocks, formed in the early hours of August 3rd, evolved and formed, with the forward shocks, (the $R_2R'_2 - F'_2F_1$ shock ensemble), that, at the time of the 3B flare, was 0.2 AU wide and was located at .92 AU.

4. THE INTERPRETATION OF THE AUGUST 4TH, 1972, GROUND LEVEL EVENT

With the help of the magnetic field associated with the $R_2R'_2 - F'_2F_1$ ensemble, we have simulated about 200 proton trajectories impinging under a wide spectrum of directions of incidence. We have done this for different values of the field maximum. We found: (a) a 0.6 AU wide storage region lying behind the $R_2R'_2$ reverse shock; (b) a highly non-transparent ensemble to particles of rigidities below 2 GV;

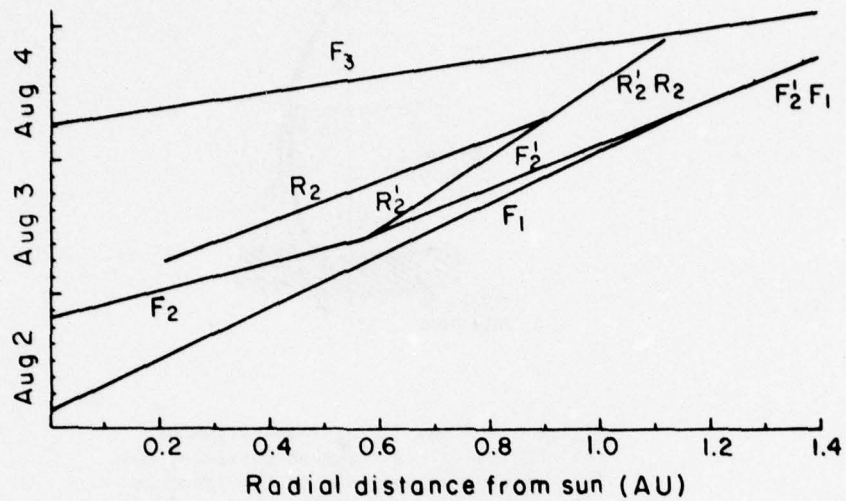


Figure 3. Radius-time diagram of the forward (F) and reverse (R) shocks produced during August 2-4, 1972. F_2' and R_2' were formed at ~ 0.6 AU by the interaction of F_2 with a rarefaction which followed F_1 . $R_2'R_2$ was formed by the interaction of R_2' with R_2 which overtook the former reverse shock wave at ~ 0.9 AU. Then, F_2' overtook F_1 at ~ 1.5 AU forming the new forward shock, $F_2'F_1$. The impending interactions of F_3 with $R_2'R_2$ and, at a later time, the altered F_3 with $F_2'F_1$ beyond 1.4 AU are also indicated.

and (c) only by lowering the maximum B value for the ensemble at 0.98 AU, to about 10 γ, did the ensemble become transparent to particles of rigidities $R \leq 1$ GV.

The interpretation of the GLE is illustrated schematically in Figure 4. In this compound figure, the upper part shows the I vs t curve of the South Pole station neutron monitor, while the lower part represents the propagation and evolution of the ensemble and the storage region. The sequence of events during August 4 is summarized as follows:

- (1) At $t_1 = 01:10$ and at $t_2 = 02:10$ UT the forward shocks F_1 and F_2' (respectively) reached the earth, causing consecutive sudden commencements.
- (2) At 06:21 UT a 3B flare occurred at $9^\circ E, 15^\circ N$; the cosmic rays ejected from the flare site promptly reach the $R_2'R_2$ wave and fill the storage region extending between .92 and .32 AU. At the time of the flare, the fast F_3 shock wave is generated. From the time of formation of the storage region until 14:00 UT the earth remains immersed in the ensemble and, due to the ensemble's lack of transparency, does not detect any CR enhancement.
- (3) At $t_4 = 11:30$ UT, F_3 reaches the outer boundary of the storage region and starts to compress it.

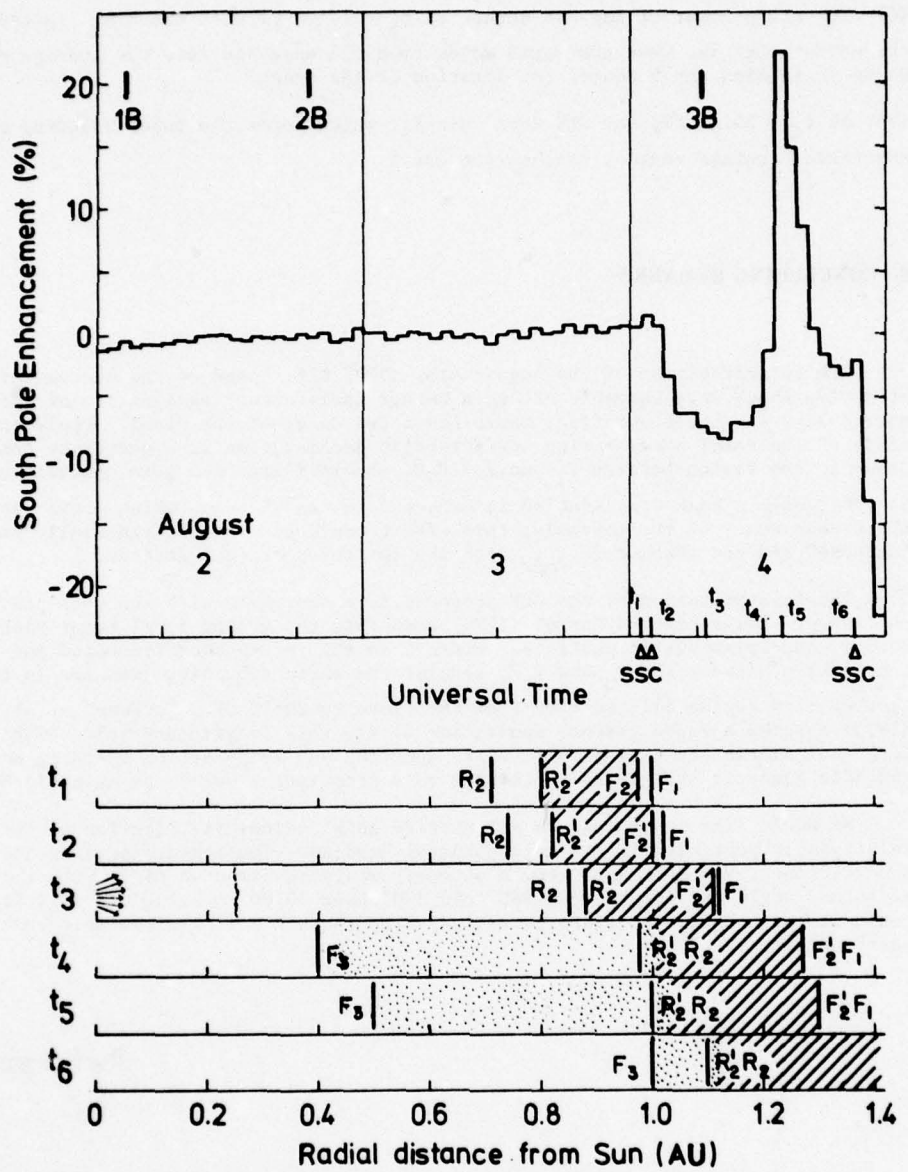


Figure 4. GLE and time diagram of shock fronts and storage region. (For detailed explanation, see text).

(4) The sharp onset of the GLE occurs at $t_5 = 14:00$ UT when the $R_2 R'_2$ passes by the earth; that is, when the earth moves from the ensemble into the storage region where it remains for 6 hours, the duration of the event.

(5) At $t_6 = 20:54$ UT, the GLE ends when F_3 , which forms the outer boundary of the compressed storage region, reaches the earth.

5. CONCLUDING REMARKS

The interpretation of the August 4th, 1972, GLE, based on the storage effect of a wide shock wave ensemble allows a rather satisfactory explanation of the eight hour delay, six hours duration, sharp onset and decay of the event. Preliminary study of the Fermi acceleration and adiabatic deceleration is expected to take place in the region between F_3 and the $R_2 R'_2$ shocks (Pérez and Lara, private communication); only a weak acceleration is expected in the GV range which would increase the transparency of the ensemble; this effect could account for the small "pre-increase" and the changes in t_{\max} with the latitudes of the stations.

The interpretation of the GLE proposed here contrasts with the ones previously published. Pomerantz and Duggal (1974) associate the ground level event with low energy, non-relativistic particles, present in the interplanetary medium and accelerated between the F_3 and $F'_1 F_1$ shocks; the earth remaining immersed in the acceleration region all the time from the flare to 20:50 UT. Lockwood et al. (1975) assumed a rapid coronal convection of the relativistic particles with strong longitudinal redistribution followed by ejection and long-lasting trapping on specific magnetic tube lines pertaining to a preexisting Gold-type magnetic bottle.

We would like to propose an alternative longitudinal distribution of the relativistic particles in the interplanetary medium. The measurements of the IMF aboard Pioneer 9 and Prognoz show a strongly westward directed field with the azimuthal angle varying between 180° and 320° from 10:00 to 21:00 UT; this field could indeed channel the flare particles, from the $9^\circ E$ meridian westward to the earth detectors.

References

Dryer, M., Interplanetary double-shock ensembles with anomalous electric conductivity, in Solar Wind, edited by C. P. Sonett, P. J. Coleman, Jr., and J. M. Wilcox, p. 453, NASA SP-308, Supt. of Doc., Washington, D.C., 1972.

Dryer, M., Interplanetary shock waves generated by solar flares, Space Sci. Rev., 15, 403, 1974.

Dryer, M., S. Frankenthal, P. Rosenau, and T. Chen, Theoretical aspects of solar flare-generated interplanetary shock waves, in Flare-Produced Shock Waves in the Corona and in Interplanetary Space, edited by A. J. Hundhausen and G. Newkirk, Jr., p. 163, National Center for Atmospheric Research, Boulder, Colorado, 1974a.

Dryer, M., A. Eviatar, A. Frohlich, A. Jacobs, J. Joseph, and E. J. Weber, Interplanetary shock waves from McMath Region 11976 during its passage in August 1972, in Coronal Disturbances, edited by G. Newkirk, Jr., IAU Symp., 57, 377, 1974b.

Dryer, M., A. Eviatar, A. Frohlich, A. Jacobs, J. H. Joseph, and E. J. Weber, Interplanetary shock waves and comet brightness fluctuations during June-August 1972, J. Geophys. Res., 80, 2001, 1975.

Dryer, M., Z. K. Smith, R. S. Steinolfson, J. D. Mihalov and J. H. Wolfe, Interplanetary disturbances caused by the August 1972 solar flares as observed by Pioneer 9, J. Geophys. Res., 81, 4651, 1976.

Lockwood, J. A., L. Hsieh, and J. J. Quenby, Some unusual features of the cosmic ray storm in August 1972, J. Geophys. Res., 80, 1725, 1975.

Pérez Enríquez and R. Gall, The influence of shock wave ensemble on propagation of solar cosmic rays, Book of Abstracts, p. 87, ISSTP, Boulder, CO., 1976.

Pomerantz, M. A. and S. P. Duggal, Interplanetary acceleration of solar cosmic rays to relativistic energy, J. Geophys. Res., 79, 913, 1974.

Steinolfson, R. S., M. Dryer, and Y. Nakagawa, Numerical MHD simulation of interplanetary shock pairs, J. Geophys. Res., 80, 1223, 1975a.

Steinolfson, R. S., M. Dryer, and Y. Nakagawa, Interplanetary shock pair disturbances: Comparison of theory with space probe data, J. Geophys. Res., 80, 1989, 1975b.

**VI. STUDY OF TRAVELLING
INTERPLANETARY PHENOMENA -
STIP INTERVAL I (SEPTEMBER-OCTOBER 1975)**

A Coronal Hole Observed by λ 8-cm Radioheliograph

Kiyoto Shibasaki, Masato Ishiguro and Shinzo Enome
Research Institute of Atmospherics
Nagoya University
Toyokawa, Aichi 442, Japan

Haruo Tanaka
Tokyo Astronomical Observatory
The University of Tokyo
Mitaka, Tokyo 181, Japan

Abstract

In the later part of the year 1975, including the STIP Interval I, a low brightness region was detected by λ 8-cm radioheliograph at Toyokawa over a period of three solar rotations. It was accompanied by a high-speed solar wind stream and was associated with recurrent-type geomagnetic storms. This region was identified as a coronal hole. The brightness temperature of this coronal hole was 6000 K lower than that of the normal quiet region of 22000 K.

The authors used a simple model of the solar atmosphere and calculated the brightness temperature at the wavelength of 8 cm in the coronal hole and in the normal quiet region. The electron pressures at the base of the corona obtained by EUV and soft X-ray observations are too high to explain the present radio observations of the coronal hole and the normal quiet region.

1. INTRODUCTION

There are sometimes low brightness regions in the corona, when the Sun is observed by EUV spectroheliographs (e.g. Burton 1968; Tousey et al. 1968; Reeves and Parkinson 1970; Withbroe et al. 1971) and soft X-ray telescopes (e.g. Underwood and Muney 1967; Vaiana et al. 1973; Timothy et al. 1975). These regions are called 'coronal holes'. It is known that in the coronal hole, electron density and temperature at the base of the corona are low and also the conductive heat flux in the transition region is small as compared with those quantities in the normal quiet region (Munro and Withbroe 1972; Krieger et al. 1973). At the photosphere, the coronal hole corresponds to a region of unipolar or weak magnetic field. In the corona, the magnetic field has an open structure (Altschuler et al. 1972). Coronal holes have been found to be associated with recurrent high-speed solar wind streams (e.g. Krieger et al. 1973; Nolte et al. 1976). Neupert and Pizzo (1974) found that large coronal holes causes recurrent-type geomagnetic storms.

Radio observations of coronal holes have been done in the meter and microwave region. Dulk and Sheridan (1974) observed a quiet sun with the Culgoora radioheliograph and found a low brightness region which corresponds to a coronal hole observed by the 284 Å spectroheliograph on board OSO-7. The brightness temperature of the coronal hole was 0.2×10^6 K and 0.4×10^6 K lower than that of the normal quiet region at 80 MHz and 160 MHz respectively. Lantos and Avignon (1975) obtained one dimensional quiet sun distributions from the lower envelopes of daily drift scans by the Nançay metric interferometers at 169 and 408 MHz. They showed that the quiet suns thus obtained correspond to the base level of coronal hole. Fürst and Hirth (1975) observed a coronal hole at 10.69 GHz and Kundu and Liu (1976) also observed a coronal hole at 85 GHz. At millimeter and short centimeter wavelength, corona does not contribute so much to the brightness temperature that depression of the brightness in the coronal hole is less than few percent of that in the normal quiet region. Dulk et al. (1977) combined EUV and radio (at 10.69 GHz, 1.42 GHz, 160 MHz and 80 MHz) observations of the coronal holes during the ATM experiments to find that no one standard model can explain both sets of observations.

We have been observing the Sun with Toyokawa λ 8-cm radioheliograph since June 1975. From September to December 1975, including STIP Interval I, the solar activity was low and it was convenient for observations of quiet phenomena. In Sections 2 and 3, we present our method of observations and observational results. In Sections 4 and 5, we discuss physical conditions of the coronal hole and compare our results with other observations.

2. OBSERVATIONS

The λ 8-cm radioheliograph at Toyokawa (Ishiguro et al. 1975) has been in operation since June 1975. This heliograph consists of T-shaped array of 3-m paraboloids, 32 elements in the E-W direction

and 16 elements in the N-S direction. The HPBW of the heliograph is $1.5' \times 1.5' \cdot \text{SEC}(ZD)$ (in N-S; where ZD is the zenith distance). The observations have been carried out at about 03 UT every day. The mode of the observation is skip scanning (Tanaka et al. 1970), and it takes 20 minutes to get one map. Each map covers the area of $40' \times 40' \cdot \text{SEC}(ZD)$ which is composed of $64 \times 64 = 4096$ picture elements. Output data are digitized and processed by a small computer. The main procedures of data processing (Shibasaki et al. 1976) are

- 1) Rearrangement of the picture elements in accordance with the skip scanning program,
- 2) Correction of the phase errors between three arms of the T-shaped array,
- 3) Smoothing by tapering higher Fourier components to reduce the sidelobes, which results in the broadening of the effective beam width to $2.25' \times 2.25' \cdot \text{SEC}(ZD)$, and
- 4) Calibration of the brightness temperature by use of the simultaneous total-flux observations.

Processed maps are displayed by a density modulation on a graphic terminal. Sidelobe level depends mainly on the phase errors of the radioheliograph. When there are no phase errors, we can reduce the sidelobe levels as low as -21 dB by the smoothing technique. Practically, however, it is hard to keep the system free from phase errors. From the calibration of phase errors, we estimate the error in the brightness temperature to be less than several percent of the quiet sun level when the Sun is not active.

3. OBSERVATIONAL RESULTS

In September 1975, a low brightness region was observed at Carrington Longitude 240° . This region became remarkable in the next solar rotation (Carrington rotation number 1633). It lasted over a period of three solar rotations. Figure 1 shows the radio maps of the Sun at 8 cm wavelength on October 3, 4, 5 and 6, 1975. We can recognize the low brightness region which extends from equator to 30° N in latitude. The central meridian passage of this region is about October 4. After Solar-Geophysical Data (SGD 1975), there are no optical counterparts to this region. The K-coronameter observations at Mauna Loa, Hawaii (Hansen; private communication) show that a weak emitting region corresponds to this region.

Nolte and Roelof (1973) found that the source longitude of quiet-time solar wind can be determined within the accuracy of 10° , assuming radial and constant velocity for solar wind propagation. In Figure 2, the solar wind speed observed by IMP-8 (SGD 1976) during this period are traced back to the solar surface on the same assumption. At around the longitude of 220° , there is a source of high-speed solar wind stream. Figure 3 shows that this high-speed stream caused a recurrent-type geomagnetic storm. During the Bartels rotation number 1944 to 1947, K_p index has recurrent peaks at around the middle of each rotation period and it corresponds to the peak in the solar wind speed. There is also a lower peak in the solar wind speed, but it corresponds to neither the peak of K_p index nor the distinct depression of the radio brightness in $\lambda 8\text{-cm}$ map.

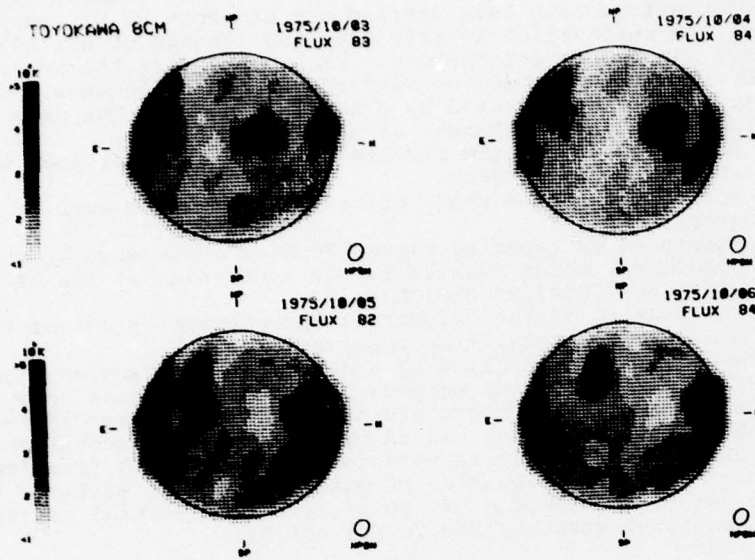


Figure 1. Radio maps observed at 3.75 GHz on October 3, 4, 5 and 6, 1975. The outline of the optical disk is shown by a circle. Total fluxes are adjusted to 1 A.U.

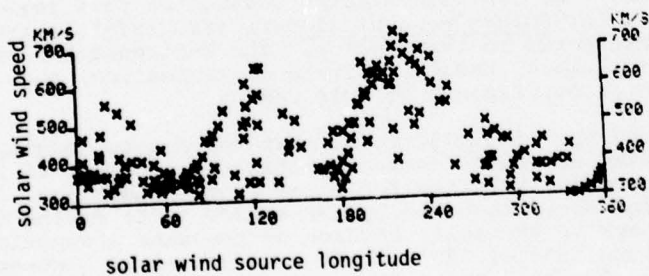


Figure 2. Solar wind speeds observed by IMP-8 (SGD 1976) are plotted against estimated source longitudes for the period of August - December 1975

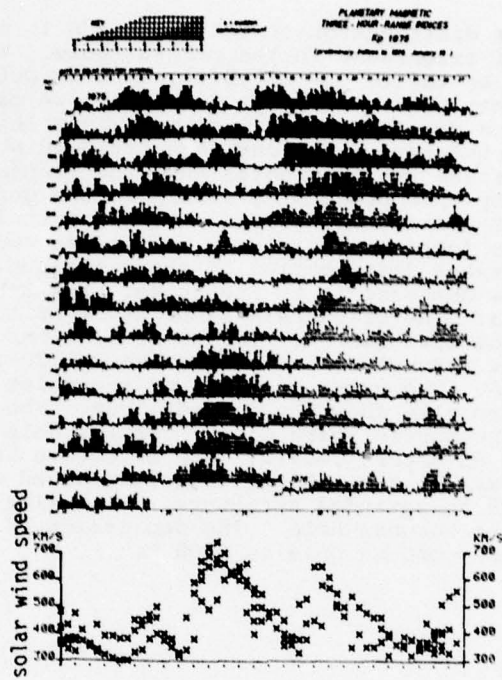


Figure 3. K_p index in 1975 (SGD 1976) and solar wind speed observed by IMP-8 (SGD 1976) during the period of August - December 1975

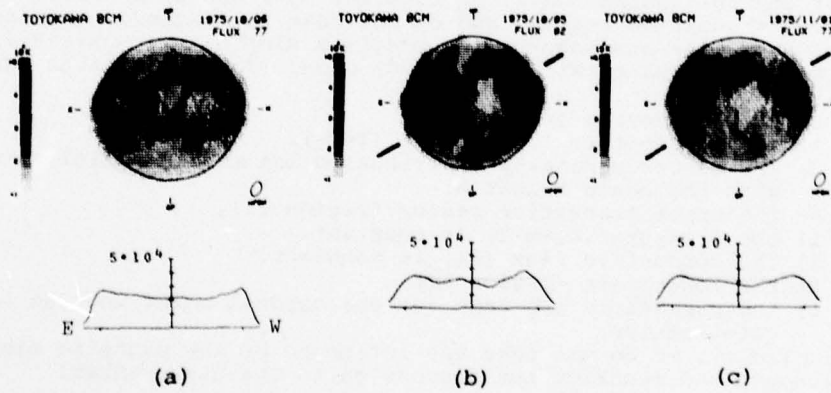


Figure 4. (a) Quiet sun of October 1975 (see in the text) and E-W cross section (b) Radio map on October 5, 1975 and the cross section at the position angle of 120° . Dotted line is the cross section of the quiet sun of October 1975 at the same position angle (c) Same as Figure (b), but for November 1, 1975

A brightness distribution of the quiet sun is necessary to know the depression of brightness in the coronal hole. We employed an iterative method by making use of thirty maps in October 1975 to obtain the quiet sun distribution. In the first run, we calculated mean and standard deviation for each picture element from thirty brightness data. In the second run, those data are excluded whose distance from the mean of the first run is greater than the standard deviation of the first run. By this procedure, errors in the quiet sun caused by the presence of S-components, coronal holes and their sidelobes are reduced. We have found by experience that three runs are sufficient to get the brightness distribution of the quiet sun. The quiet sun distribution thus obtained is in Figure 4a. The E-W cross section is also in Figure 4a. The brightness temperature of the quiet sun is 2.2×10^4 K near the disk center. The cross sections which pass through the center of the coronal hole (position angle 120°) are drawn in Figures 4b and 4c. The cross sections of the quiet sun at the same position angle are also shown by dotted lines. The brightness temperature of the central part of the coronal hole is 1.6×10^4 K on October 5 and on November 1, 1975. The effective HPBW is 2.25×3.45 . The structures smaller than this size are smoothed out. The coronal hole, however, is an extended structure, this value is the brightness temperature of the coronal hole. The depression of the brightness temperature in the coronal hole is 6000 K.

4. INTERPRETATION

In this section, we use a simple model of the solar atmosphere and investigate the electron density and temperature at the base of the corona in the coronal hole in contrast with the normal quiet region. Since coronal holes are thought to be mainly the phenomena of the upper part of the solar atmosphere, we consider only the lower corona and the upper transition region, and do not take into account the lower part of the solar atmosphere. We modify a simple three-parameter model of these regions which Withbroe (1970) used. The assumptions adopted here are,

- a) at the low corona (region I),
 - 1) the temperature is constant ($T=T_c$).
 - 2) The electron density distribution has an exponential structure with the scale height H .
- b) At the upper transition region (region II),
 - 1) the pressure ($P_c=N \cdot T$) is constant.
 - 2) The conductive flux (F_c) is constant.
- c) At the lower part (region III),
 - 1) the parameters are same for the coronal holes and the normal quiet region.

For simplicity, we do not take the influence of the magnetic field into account and restrict the discussion to the disk center.

The radio brightness temperature (T_b) is calculated by the following equation,

$$T_b = \int_0^T T e^{-T} dt. \quad (1)$$

In eq. (1), we can separate the contribution to the brightness temperature into three parts, corresponding to regions I, II and III.

$$T_b = T_{bI} + e^{-\tau_I} (T_{bII} + e^{-\tau_{III}} T_{bIII}), \quad (2)$$

where, $\tau_{I, II} = \int_{I, II} \kappa dr,$

$$T_{bI, II, III} = \int_{I, II, III} T e^{-\tau} dr.$$

By use of the above mentioned assumptions, we estimate the contribution of each region. The contribution left from region III is T_{bIII} . As it is shown later that $\tau_{I, II} \ll 1$, the brightness temperature can be written as follows;

$$T_b = \frac{\xi}{v^2} \frac{P_c^2}{T_c^{5/2}} \frac{H}{2} + \frac{\xi}{v^2} \frac{\alpha}{F_c} P_c^2 (T_c - T_o) + T_{bIII}. \quad (3)$$

where, $\xi = 0.2$ (Chambe and Lantos 1971),

n =refractive index,

v =observational frequency,

$\alpha = 10^{-6}$ (Spitzer 1956),

r_0 =the height of the top of the lower transition region, and

T_o =the temperature at the top of the lower transition region.

By use of this equation, we study the differences of the parameters in the coronal hole and in the normal quiet region. Munro and Withbroe (1972) found that P^2/F_c in the coronal hole does not differ from that in the normal quiet region. They also found that the ratio of the conductive flux in the coronal hole to that in the normal quiet region is 1/10. Huber et al. (1974) got the value of 1/6 independently.

Soft X-ray observations (Krieger et al. 1973) show that the pure gravitational hydrostatic equilibrium does not hold in the closed field region. We consider that the closed region corresponds to the normal quiet region and assume that the density scale height (H) in the normal quiet region is twice the hydrostatic one. In the coronal hole, we use the hydrostatic scale height. In the following, the superscripts Q and H stand for the parameters of the normal quiet region and for the coronal hole respectively. As for the pressure, the ratio is

$$\frac{P_c^H}{P_c^Q} = \left(\frac{F_c^H}{F_c^Q} \right)^{1/2} \approx 1/3. \quad (4)$$

The brightness temperatures in the normal quiet region and the coronal hole are,

$$T_b^Q = \frac{\xi}{v^2} \frac{k}{\mu m g_o} \frac{P_c^{Q2}}{T_c^{Q3/2}} + \frac{\xi}{v^2} \frac{\alpha}{F_c^Q} P_c^{Q2} (T_c^Q - T_o) + T_{bIII}, \quad (5)$$

$$T_b^H = \frac{\xi}{v^2} \frac{k}{\mu m g_o} \frac{P_c^c}{T_c^{Q3/2}} \left(\frac{1}{18R^{3/2}} \right) + \frac{\xi}{v^2} \frac{\alpha}{F_c^Q} P_c^{Q2} (T_c^Q - T_o) + T_{bIII}, \quad (6)$$

where, k =Boltzmann constant,

μ =mean molecular weight (0.62),
 m =weight of the proton,
 g_0 =gravity acceleration at the solar surface,
and $R=T_c^H/T_c^Q$.

The difference of the brightness temperature in the coronal hole and the normal quiet region is

$$T_b^Q - T_b^H = \frac{\xi}{v^2} \frac{k}{\mu m g_0} \frac{P_c^{Q2}}{T_c^{Q3/2}} \left(1 - \frac{1}{18R^{3/2}}\right) + \frac{\xi}{v^2} \frac{\alpha}{F_c^Q} P_c^{Q2} T_c (1-R). \quad (7)$$

Our observation at the frequency of 3.75 GHz gives the value,

$$T_b^Q - T_b^H = 6000 \text{ K}. \quad (8)$$

If we get the values of T_c^Q , P_c^Q and F_c^Q , we can determine the temperature and density in the coronal hole by use of the eqs. (7), (8) and (4). Since our observation is made at the single frequency, we cannot determine these values uniquely. The EUV line observations (Athay, 1966; Dupree and Goldberg 1967; Withbroe 1970) gave $F_c^Q = 6 \times 10^5 \text{ erg cm}^{-2} \text{ sec}^{-1}$. We use this value. As the optical depth at 3.75 GHz becomes larger than unity in the chromosphere, $T_{bIII} = 10^4 \text{ K}$. The brightness temperature observed at 3.75 GHz is $2.2 \times 10^4 \text{ K}$. If we assume $T_c^Q = 2 \times 10^6 \text{ K}$, P_c^Q can be calculated by the eq. (5),

$$P_c^Q = 4.2 \times 10^{14} \text{ K cm}^{-3}.$$

Putting these three values into eq. (7), we get $R=0.12$ and 0.75 . If we take $R=0.12$, the temperature in the coronal hole is too low, therefore we take $R=0.75$. The temperature in the coronal hole is $1.5 \times 10^6 \text{ K}$ and the electron density in the coronal hole is $9.3 \times 10^7 \text{ cm}^{-3}$. The optical depths are $\tau_I^Q = 2 \times 10^{-3}$, $\tau_{II}^Q = 1 \times 10^{-2}$, $\tau_I^H = 2 \times 10^{-4}$ and $\tau_{II}^H = 1 \times 10^{-2}$. The approximation used in deriving eq. (3) holds good.

5. DISCUSSION

The observations of the coronal hole have been carried out by EUV spectroheliographs, soft X-ray telescopes, and radio telescopes. Munro and Withbroe (1972) analyzed the EUV line observations on board OSO-IV and obtained temperatures, pressures, and conductive fluxes in a normal quiet region and a coronal hole. The values are listed in Table 1. At 3.75 GHz, these values give from eq. (6),

$$T_b^H = 1.4 \times 10^4 \text{ K} + T_{bIII}.$$

Table 1. Parameters of the solar atmosphere and the brightness temperature calculated at 3.75 GHz

	T_c^Q	P_c^Q	F_c^Q	$T_b^Q(T_{bI}^Q)$	T_c^H	P_c^H	F_c^H	$T_b^H(T_{bI}^H)$
EUV observation								
Munro & Withbroe(1972)	1.7×10^6	9.1×10^{14}	1.3×10^6	5.1×10^4	1.0×10^6	3.2×10^{14}	1.3×10^5	2.4×10^4
Soft X-ray observation								
Krieger et al.(1973)								
constant temperature model	1.3×10^6	3.8×10^{15}		(6.7×10^5)	1.3×10^6	3.5×10^{15}		(2.9×10^5)
constant density model	1.5×10^6	4.1×10^{15}		(6.3×10^5)	1.3×10^6	3.5×10^{15}		(2.9×10^5)
Meter wave observation								
Lantos & Avignon (1975)					9×10^5	1.1×10^{14}	7×10^4	1.3×10^4
Used in this paper	2×10^6	4.2×10^{14}	6×10^5	2.2×10^4				
Obtained parameters					1.5×10^6	1.4×10^{14}	6.7×10^4	1.6×10^4

Units: T_c ; K
 P_c ; K cm⁻³
 F_c ; erg cm⁻² sec⁻¹
 T_b ; K

This value is higher than the obtained brightness temperature (T_b (obs.) = 1.6×10^4 K). The coronal contribution to the brightness temperature in the normal quiet region is calculated to be

$$T_{bI}^Q = 2.7 \times 10^4 \text{ K} > T_b^Q(\text{obs.}) = 2.2 \times 10^4 \text{ K.}$$

These discrepancies are mainly due to the high pressure at the coronal base adopted by Munro and Withbroe.

The soft X-ray observation (Krieger et al. 1973) also gave the density and temperature at the base of the corona which are in Table 1. If we calculate the coronal contribution to the brightness temperature at 3.75 GHz with these parameters,

$$\begin{cases} T_{bI}^Q = 6.7 \times 10^5 \text{ K,} \\ T_{bI}^H = 2.9 \times 10^5 \text{ K,} \end{cases} \text{(constant temperature model)}$$

$$\begin{cases} T_{bI}^Q = 6.3 \times 10^5 \text{ K,} \\ T_{bI}^H = 2.9 \times 10^5 \text{ K.} \end{cases} \text{(constant density model)}$$

These are too high in comparison with the present observations, which is again due to the high pressure.

This trend, that EUV or soft X-ray results lead to higher radio brightness both in hole and in quiet region, agrees with that of Dulk et al (1976). They examined the several possibilities in their radio and EUV models that are open to question. They have reached a

conclusion that if the chemical abundances of heavy elements in some parts of the transition region and corona were increased by about a factor of ten, the coronal hole models derived from the radio and EUV data can be brought into agreement. In this paper, we assumed implicitly that the values of the parameters are equal for coronal holes observed at different periods of time. To remove this assumption, it is necessary to carry out the coronal hole observations at various frequencies simultaneously as done by Dulk et al. (1977), and to determine the values of parameters for the same coronal hole.

Acknowledgments

We would like to thank Messrs. T. Takayanagi, C. Torii, Y. Tsukiji, S. Kobayashi, N. Yoshimi, Misses R. Shirai and R. Masuda of TOYOKAWA observatory for their contribution to the construction of radio-heliograph and observations. Our thanks are also due to Drs. A. J. Lazarus and R. T. Hansen for providing us their data before publication.

References

- Altschuler, M. D., D. E. Trotter and F. Q. Orall, Coronal holes, Solar Phys., 26, 354, 1972.
- Athay, R. G., Theoretical line intensities. V. Solar UV emission lines of heavy elements, Astrophys. J., 145, 784, 1966.
- Burton, W. M., Extreme ultraviolet observations of active regions in the solar corona, in Structure and Development of Solar Active Regions, edited by K. O. Kiepenheuer, P. 395, D. Reidel Publishing company, Dordrecht, 1968.
- Chambe, G., and P. Lantos, Influence of helium and heavy elements on the radio absorbtion coefficient, Solar Phys., 17, 97, 1971.
- Dulk, G. A., and K. V. Sheridan, The structure of the middle corona from observations at 80 and 160 MHz, Solar Phys., 36, 191, 1974.
- Dulk, G. A., K. V. Sheridan, S. F. Smerd, and G. L. Withbroe, Radio and EUV observations of a coronal hole, Solar Phys., 52, 349, 1977.
- Dupree, A. K., and L. Goldberg, Solar abundance determinations from ultraviolet emission lines, Solar Phys., 1, 229, 1967.
- Fürst, E., and W. Hirth, A coronal hole observed at 10.7 GHz with a large single dish, Solar Phys., 42, 157, 1975.

- Huber, M. C. E., P. V. Foukal, R. W. Noyes, E. M. Reeves, E. J. Schmah., J. G. Timothy, J. E. Vernazza, and G. L. Withbroe, Extreme-ultraviolet observations of coronal holes: Initial results from SKYLAB. Astrophys. J., 194, L115, 1974.
- Ishiguro, M., H. Tanaka, S. Enome, C. Torii, Y. Tsukiji, S. Kobayashi, and N. Yoshimi, 8-cm radioheliograph, Proc. Res. Inst. Atmospheric, Nagoya Univ., 22, 1, 1975.
- Krieger, A. S., A. F. Timothy, and E. C. Roelof, A coronal hole and its identification as the source of a high velocity solar wind stream, Solar Phys., 29, 505, 1973.
- Kundu, M. R., and Sou-Yang Liu, Observation of a coronal hole at 85 GHz, Solar Phys., 49, 267, 1976.
- Lantos, P., and Y. Avignon, The metric quiet sun during two cycles of activity and the nature of the coronal holes, Astron. Astrophys., 41, 137, 1975.
- Munro, R. H., and G. L. Withbroe, Properties of a coronal "hole" derived from extreme-ultraviolet observations, Astrophys.J., 176, 511, 1972.
- Neupert, W. M., and V. Pizzo, Solar coronal holes as source of recurrent geomagnetic disturbances, J. Geophys. Res., 79, 3701, 1974.
- Nolte, J. T., A. S. Krieger, A. F. Timothy, R. E. Gold, E. C. Roelof, G. Vaiana, A. J. Lazarus, J. D. Sullivan and P. S. McIntosh, Coronal holes as sources of solar wind, Solar Phys., 46, 303, 1976.
- Nolte, J. T., and E. C. Roelof, Large-scale structure of the interplanetary medium, Solar Phys., 33, 241, 1973.
- Reeves, E. M., and W. H. Parkinson, An atlas of extreme-ultraviolet spectroheliograms from OSO-IV, Astrophys.J. Suppl., 21, 1, 1970.
- Shibasaki, K., M. Ishiguro, S. Enome, H. Tanaka, C. Torii, Y. Tsukiji, S. Kobayashi, and N. Yoshimi, λ 8 cm radioheliograms, Proc. Res. Inst. Atmospheric, Nagoya Univ., 23, 21, 1976.
- Spizer, L., Physics of Fully Ionized Gases, Interscience Publishers, Inc., New York, 1956.
- Tanaka, H., S. Enome, C. Torii, Y. Tsukiji, S. Kobayashi, M. Ishiguro, and M. Arisawa, 3-cm radioheliograph, Proc. Res. Inst. Atmospheric, Nagoya Univ., 17, 57, 1970.
- Timothy, A. F., A. S. Krieger, and G. S. Vaiana, The structure and evolution of coronal holes, Solar Phys., 42, 135, 1975.
- Tousey, R., G. D. Sandlin, and J. D. Purcell, in Structure and Development of Solar Active Regions, edited by K. O. Kiepenheuer, P. 395, D. Reidel Publishing Company, Dordrecht, 1968.
- Underwood, J. H., and W. S. Muney, A glancing incidence solar telescope for the soft X-ray region, Solar Phys., 1, 129, 1967.

Vaiana, G. S., A. S. Krieger, and A. F. Timothy, Identification and analysis of structures in the corona from X-ray photography, Solar Phys., 32, 81, 1973.

Withbroe, G. L., Solar XUV limb brightening observations: I. The lithium-like ions, Solar Phys., 11, 42, 1970.

Withbroe, G. L., A. K. Dupree, L. Goldberg, M. C. E. Huber, R. W. Noyes, W. H. Parkinson, and E. M. Reeves, Coronal electron density maps for 7 March, 1970, derived from Mg X λ 625 spectroheliograms, Solar Phys., 21, 272, 1971.

Solar Wind Parameters During STIP Intervals I and II According to Venera-9 and Venera-10 Measurements

G. N. Zastenker[†]
J. M. Bosqued^{††}
A. V. Djatchkov[†]
C. D'Uston^{††}
S. A. Romanov[†]
V. V. Temny[†]
O. L. Vaisberg[†]

[†]Space Research Institute, (I.K.I.)
USSR Academy of Sciences
Prosoyusnaya, 88
117810, Moscow, USSR

^{††}Centre d'Etude Spatiale des Rayonnements, (C.E.S.R.)
BP 4346
31029 Toulouse, France

Abstract

Solar wind velocity and temperature were measured by an RIEP-2801 electrostatic analyser on board VENERA-9 and VENERA-10 space probes during announced STIP Intervals. In the First Interval (September-October 1975) the probes were on their interplanetary EARTH-VENUS trajectory, in the second, on the VENUS-bound orbits. Data coverage is not complete but seems to show solar wind structures. During STIP Interval-I three major increases in solar wind velocity (from 300 to ~ 550 km/sec) were observed, two of which were apparently recurrent solar wind streams.

Solar wind parameters were measured aboard the Venera 9 and Venera 10 spacecraft in the course of other experiments during two periods of international study of Travelling Interplanetary Phenomena. Solar wind characteristics were recorded by means of a RIEP-B ion spectrometer.

1. INSTRUMENTATION

The Venera 9 and 10 spacecraft were launched on 8 and 14 June 1975 and were put into an orbit around Venus on 22 and 25 October, respectively. Figure 1 gives the Venera 9 and 10 trajectories between Earth and Venus and the orbits of Earth and Venus during the periods concerned.

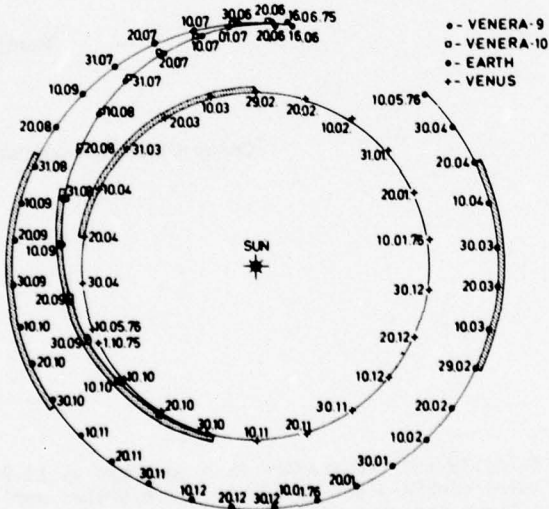


Figure 1. Trajectories of Venera 9 and 10 flights and orbits of the Earth and Venus from September 1975 to May 1976.

During the first STIP period (September-October 1975), the spacecraft were in transit between Earth and Venus and went into orbit around Venus only at the end of this period. During this time the Earth-Sun-spacecraft angle varied from 5° at the beginning to 40° at the end. During their transit between Earth and Venus the spacecraft were 200,000 to 500,000 km apart ; in Figure 1 these two positions coincide. During the second STIP period (15 March-15 May, 1976) the two spacecraft were moving around the Sun with the planet Venus ; the Earth-Sun-Venus angle was greater than for the first STIP period varying from 120° to 145° .

The RIEP-B apparatus consisted of several energy spectrometers (Vaisberg et al., 1976). The ion flux was measured by 6 identical electrostatic analysers with an energy resolution of $6\% \pm 3\%$ and angular resolution of $5^\circ \times 5^\circ$ (FWHM). Each of the electrostatic analysers provided a spectrum by sweeping its energy range in 8 energy steps in geometric progression. The total energy range studied was from 50 eV to 20,000 eV/Q. In order to increase the possibilities of the instrument, some analysers were turned in the directions of $+30^\circ$ and -15° on either side of the main axis of the experiment. During most of the trajectory from Earth to Venus the main axis was directed toward the Sun and the spacecraft rotated about this axis. In orbit around Venus, measurements were generally made with 3 axis stabilization ; the main axis changed its orientation 0.5° per day with respect to the solar direction. The solar wind spectra were generally measured for 10 minutes, and for several periods measurements were carried out during two minute periods.

Solar wind parameters were calculated independently for each analyser by using a least squares method and assuming an isotropic Maxwellian distribution with temperature T and transport velocity V. The ion concentration was not calculated due to the absence of information on the orientation of the detectors ; this absence of data does not alter the accuracy of either the velocity or temperature measurements (Romanov, 1975). The precision for the velocity is $\pm 5\%$, and the temperature is estimated to within a factor of 2 or less. Comparison of simultaneous data in several channels has shown a good agreement, particularly for solar wind velocity. For these measurements and for those which follow, the values have been averaged.

2. EXPERIMENTAL RESULTS

The data obtained were averaged over 3-hour intervals and are given in Figure 2 for the first STIP period and in Figure 3 for the second STIP period. It must be pointed out that the data do not completely cover the intervals and are fragmentary and incomplete for the second interval. The characteristic feature of the data is the good agreement of the results obtained by the two spacecraft in almost all cases of simultaneous measurement (particularly for the velocity). This means that the velocity and temperature gradients for the solar wind are not so high that they change the parameters measured over the distances between the two spacecraft. Another characteristic feature of the parameters recorded is the strong modulation both in the first and second STIP interval. The solar wind velocity varies in a wide range between 250 - 300 km (sec) $^{-1}$ and 500 - 600 km (sec) $^{-1}$, and the temperature varies from 10^4 °K and 5×10^5 °K. We can distinguish two periods during which the parameter values are constant.

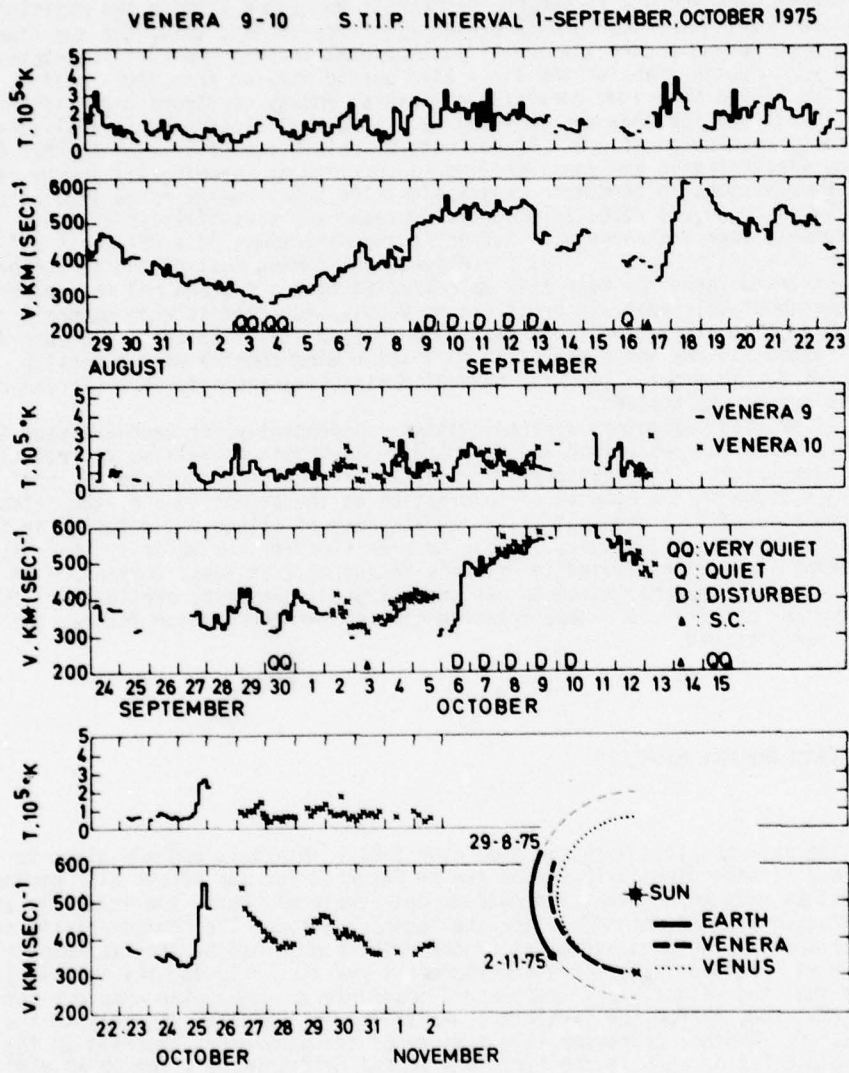


Figure 2. Ion velocity and temperature of solar wind as observed by spacecraft Venera 9 and 10 during first STIP interval. At lower right are shown corresponding parts of trajectories.

2.1 First STIP Period (September-October 1975)

The first STIP period begins with a slow decrease in velocity flow from $400 \text{ km}(\text{sec})^{-1}$ to $300 \text{ km}(\text{sec})^{-1}$, then a slow increase in solar wind velocity back up to the initial value. This basic phenomenon is followed by a high speed stream with values of $500 \text{ km}(\text{sec})^{-1}$ for 4 or 5 days from 9 to 13 September. Several days later, between 17 and 22 September, a high speed plasma flux is also recorded. The velocity increases more slowly than in the preceding case but reaches $600 \text{ km}(\text{sec})^{-1}$. The ion temperature during the increase in velocity rises to $3 \times 10^5 \text{ K}$. For more than 10 days velocity values ranging from 300 to $400 \text{ km}(\text{sec})^{-1}$ are recorded. A third high velocity flux is detected from 6 to 12 October with velocities from 500 to $550 \text{ km}(\text{sec})^{-1}$ and a well-defined onset. In the data following there are gaps from 13 to 23 October and in the final part of the first period we can see a strong increase in the velocity from $330 \text{ km}(\text{sec})^{-1}$ to $560 \text{ km}(\text{sec})^{-1}$, and in the temperature from $5 \times 10^4 \text{ K}$ to $2.5 \times 10^5 \text{ K}$. On 26 October the gradual decrease in values begins, and a new small increase appears on 29 October.

2.2 Second STIP Period (March-April, 1976)

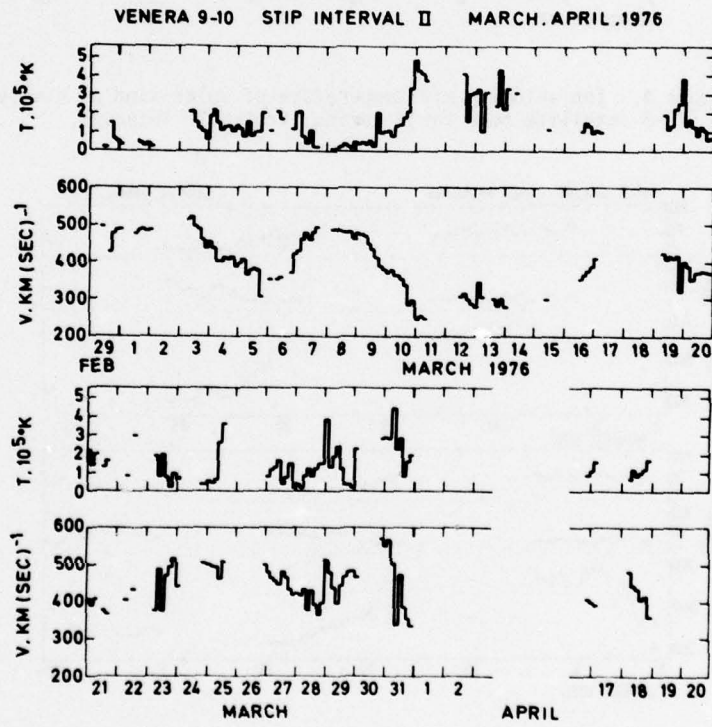


Figure 3. Same as figure 2 for second STIP interval

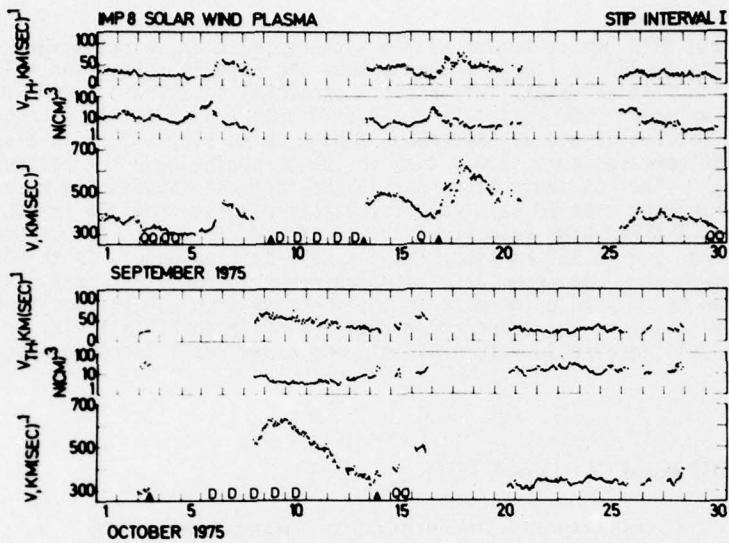


Figure 4. Ion velocity and temperature of solar wind as observed by IMP-8 satellite near Earth during first STIP interval.

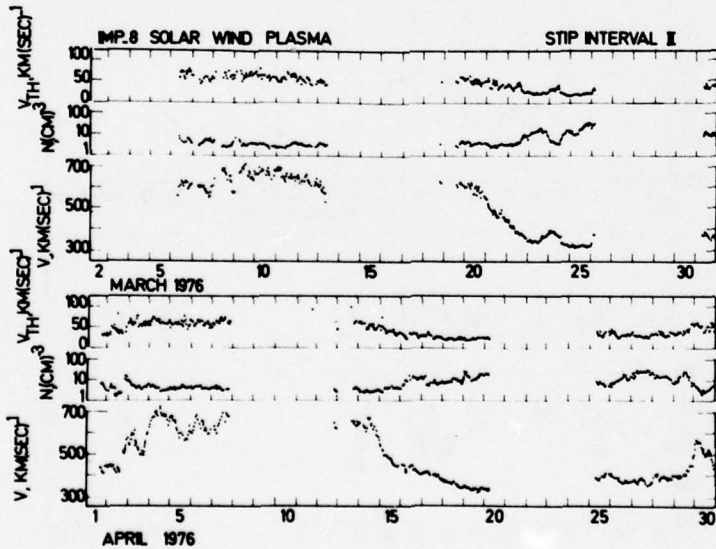


Figure 5. Same as figure 4 for second STIP interval.

The second STIP period begins with two high velocity flows from 1 to 4 and from 7 to 10 March, respectively ; between these the velocity decreases to 300-350 km/sec. At the end of the second stream we see a substantial increase in temperature to 4.5×10^5 K. The final data for this period are very fragmentary. We can only see that the velocity of the solar wind is as high as $500 \text{ km} (\text{sec})^{-1}$ from 23 to 26 March and 29-30 March. At the end of this period the velocity drops to 300 km/sec.

3. DISCUSSION

From the point of view of the STIP project these data can be analysed in two ways : a correlation between the variations observed in the solar wind parameters and solar activity or a comparison of observations in different points in interplanetary space. It must be noted that during the first STIP period solar activity was very low ; no class 1B or greater flare was reported. The analysis of the data for the first STIP period (Figure 2) shows that the high velocity solar wind flows from 9 to 13 September and from 6 to 12 October have similar shapes and that the time between the two is 28 days. The study of geomagnetic data¹ indicates that each of these periods is correlated with the observations of 5 disturbed days. On 9 September a sudden geomagnetic disturbance was indicated by a S.C. which may indicate the arrival of the high velocity structure, limited in front either by a shock or by a stationary discontinuity. These events are probably manifestations of the same recurrent high velocity streams whose lifetime is greater than the times of two solar rotations. We see no other recurrent structures in our data. The 25 October event is not recurrent ; prior to 25 October the plasma flow velocity was below $400 \text{ km} (\text{sec})^{-1}$ and we have no information on whether the events of 17-20 September and 1-10 March are recurrent.

A travelling interplanetary phenomenon can be studied by comparing data from Venera 9 and 10 with measurements of the solar wind made near the Earth by IMP 8. The preliminary solar wind velocity and temperature data for the STIP periods, obtained by means of this satellite, are given in Figures 4 and 5. These data are incomplete, but some of the events can be compared. The first of these events is evidenced by the increase in velocity observed 17 September near the Earth and by Venera 9. This increase occurs at about 18.00 U.T. at Venera 9 and at about 06.00 U.T. at the IMP 8 satellite. On 18 September the solar wind velocity increases to $650 \text{ km} (\text{sec})^{-1}$ near the Earth and to about $600 \text{ km} (\text{sec})^{-1}$ on Venera 9. For the two spacecraft the ion temperature was about $2-3 \times 10^5$ K. We can estimate the time delay Δt between the arrival times of the flux at each of the two positions by using the equation deduced from the solar wind corotation model,

$$\Delta t = \frac{R_{\text{IMP}} - R_{\text{Venera}}}{V_0} - \frac{\phi_{\text{Venera}} - \phi_{\text{IMP}}}{\Omega}$$

-
1. Solar Geophysical Data, NOAA, 1976
N° 381, part II, pages 38, 41 ;
N° 387, part II, page 28 ;
N° 385, part II, page 35 ;

where

R = heliocentric distance

ϕ = heliocentric longitude

Ω = angular velocity of solar rotation ($\Omega = 0.5515^\circ \text{ (hour)}^{-1}$)

For the 17 September event we obtain :

$$\Delta t = \frac{1.49 \times 10^8 - 1.18 \times 10^8}{800 \times 3600} - \frac{13}{0.55} \sim 10.6 \text{ hours.}$$

Thus in this model the high velocity particle flux must arrive at Venera 9 about 11 hours after its arrival at the Earth, which is in agreement with the 12-hour time interval actually recorded. A second argument favoring the corotation model can be seen in the similarity between the velocity decreases recorded by IMP 8 and by Venera 9 and 10 between 10 and 13 October.

Additional data on this type of discontinuity in the solar wind plasma can be acquired by comparing proton flux data for energies from 1-10 MeV measured aboard IMP 8. The increase in proton flux for energies between 0.97 and 1.87 MeV on 8 September and 16 and 17 September (see footnote 1) coincide with the increase in solar wind velocity aboard Venera 9 and 10. Similar facts are observed on 7 and 8 October and 18-19 October, 1975. During the August 1972 events the

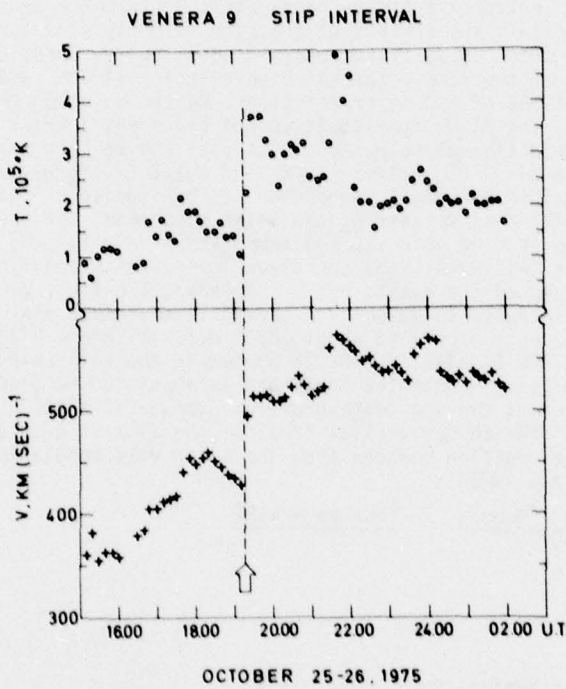


Figure 6. Solar wind velocity and temperature evolution from Venera 9 data, 25-26 October 1975

guided proton fluxes having energies up to 100 MeV were recorded within the high velocity current after crossing the shock wave front (Cambou et al., 1975). In the event of the first STIP period the guided proton energy was below 10 MeV.

An interesting event was measured by Venera 9 and 10 on 25 October, with an increase in velocity and temperature (Figure 2). In Figure 6 the most detailed features of this event are shown (one spectrum every 10 minutes). We can see a sharp increase in velocity from 420 to 500 km (sec)⁻¹ and in temperature from 10^5 to 2.8×10^5 K between 19.10 U.T. and 19.20 U.T. on 25 October; this phenomenon may be associated with the crossing of the interplanetary shock wave front. The measurement of the disturbance on 25, 26, and 27 October by two spacecraft is very typical. However, the measurements near Earth (Figure 4) show no increase in solar wind velocity above 350 km (sec)⁻¹ during this period. There are several data gaps aboard IMP 8 but not long enough to conceal disturbance phenomena. Since no disturbance was seen near the Earth we can assume that the measurements made by Venera 9 from 25 to 28 October indicate the presence of a very narrow high speed stream which does not extend east of the sun more than 35° from the Venera position.

4. CONCLUSION

The measurements of solar wind parameters made by Venera 9 and 10 during the first two STIP periods show the very variable structure of the interplanetary medium. During the first STIP period a series of high velocity recurrent fluxes was observed by the spacecraft and also recorded at Earth by the IMP 8 satellite. The time separating these observations corresponds to a solar wind model in corotation. However, Venera 9 also detected a very narrow high velocity flux which was not observed near Earth. The data for the second STIP period are not as complete and show no correlation with measurements made near Earth.

We emphasize that this analysis of the data is still in the preliminary stage and that it is desirable to study them in conjunction with measurements obtained using other spacecraft.

Acknowledgments

The authors thank their colleagues who have taken part in instrument construction, experiment preparation and data processing. They are also grateful to N.G. Havenson who has computed Venera 9 and 10 trajectories. This cooperative work was carried out as part of French-Soviet space science program. The French part of this project was supported by grant CNES 212 from the Centre National d'Etudes Spatiales.

References

- Cambou, F., O.L. Vaisberg, H. Espagne, V.V. Temny, C. d'Uston, G.N. Zastenker,
Characteristics of interplanetary plasma near the Earth during the solar events
of August 1972, Space Res., 15, 461, 1975.
- Intriligator D., M. Neugebauer, A search for solar wind velocity changes between
0.7 and 1 A.U., J. Geophys. Res., 80, 1332, 1975.
- Romanov S.A., Influence of characteristics of charges particles analysers on solar
wind measurements, Internal report (IKI), p.r. 211, Moscow, 1975 (in Russian).
- Vaisberg O.L., S.A. Romanov, V.N. Smirnov, I.P. Karpinski, B.I. Hazanov,
B.V. Polienov, A.B. Bogdanov, N.M. Antonov, Structure of interaction region
between solar wind and Venus from measurements of characteristics of ion flux
with automatic space probes Venera 9 and Venera 10., Kosmicheskie Issledovaniya,
14, 827, 1976 (in Russian).

**VII. STUDY OF TRAVELLING
INTERPLANETARY PHENOMENA -
STIP INTERVAL II (15 MARCH-15 MAY 1976)**

Type II Radio Bursts Originating From Well Behind the Solar Limb

G. J. Nelson and D. J. McLean
Division of Radiophysics, CSIRO
P. O. Box 76
Epping, N.S.W. 2121
Australia

Abstract

Observations have been made of two type II radio bursts originating from well behind the solar limb. The results support the previous conclusions that type II producing shock waves (a) can be refracted along curved paths, and (b) can move along magnetic field lines. An interesting new observation is that although the radial source size increases with height, the transverse size may decrease. The latter is ascribed to a decrease of the lateral extent of the shock wave with height, and the former to the increased scattering from coronal irregularities at greater heights (lower frequencies). The 40 and 21.5 MHz plasma levels were found to be at heights of at least 1.85 and 2.4 R_s , respectively.

1. INTRODUCTION

On 1976 March 20 the Culgoora radioheliograph (Wild, 1967; Sheridan et al., 1973) and radio spectrograph (Sheridan, 1967) recorded two type II bursts above the Sun's east limb. These events occurred at 0203 UT and 2255 UT; the first event has already been discussed by McLean and Nelson (1977). No H-alpha activity was visible near the east limb until about four days later, when McMath region 14143 rotated into view. There is little doubt that this region was the source of the bursts on March 20, in which case these bursts would have been caused by flares located about 55° and 44° behind the limb respectively. Events of this type have been observed before (e.g., Smerd, 1970), but not from such great distances behind the limb.

2. TYPE II BURST OF 1976 MARCH 20^d02^h03^m

The dynamic spectrum of this burst is shown in Figure 1 (upper). Important features to note include:

- (a) The three main emission bands in the type II burst. With the possible exception of some small features near 0216 UT, these emission bands are not harmonically related.

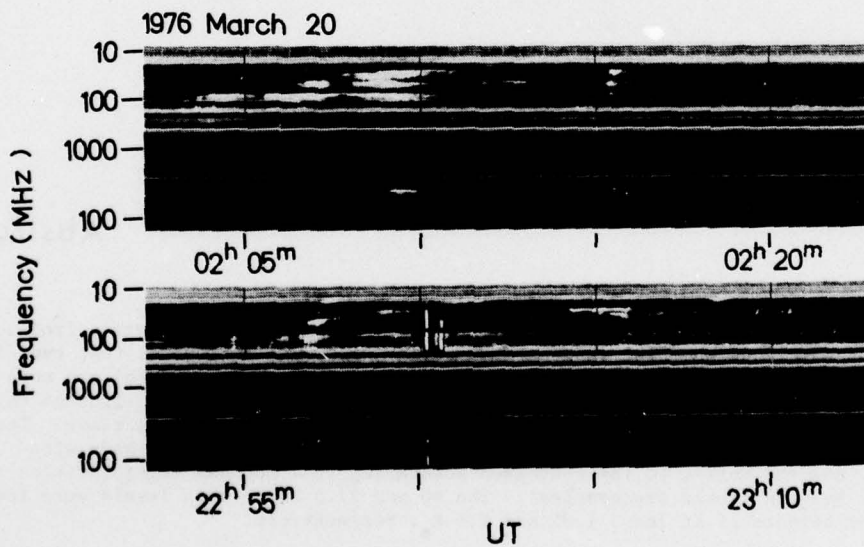


Figure 1. Dynamic spectra of the two type II bursts recorded 1976 March 20. For each frequency and time the intensity is shown by the whiteness of the record. Horizontal straight lines are due to interference. Below each spectrum the range from 25 to 200 MHz is repeated at lower sensitivity.

- (b) During the first 5 min of the burst the emission cuts off abruptly at low frequencies. The cut-off frequency drifts to lower frequencies much more rapidly than do the individual bands.
- (c) The irregular nature of the burst (a feature common among type II limb events).
- (d) The initial type III bursts at 80 MHz (e.g., at 02^h03^m38^s and 02^h03^m42^s). These appear stunted compared to normal type III bursts and presumably also come from 55° behind the limb.

Figure 2 gives the radial positions of the type II and type III bursts at 80 and 43 MHz and of an unrelated noise storm at 160 MHz. It can be seen that the type II sources (particularly at 43 MHz) after moving slightly outwards thereafter move inwards. This is taken to imply that the intersection of the shock front with the relevant plasma level moves from slightly behind the limb to possibly 40° in front of the limb (McLean and Nelson, 1977).

The centroids of all the observed sources are plotted in Figure 3. For type II bursts behind and at the limb it is expected that the emission is at the second harmonic of the plasma frequency because fundamental emission is severely attenuated (Riddle, private communication quoted by Dulk et al., 1976). The highest type II sources at 43 and 80 MHz in Figure 3 would therefore originate above the limb at the 21.5 and 40 MHz plasma levels respectively. Refraction and scattering however cause harmonic sources to appear nearer the Sun than their true positions. Thus the observed heights of 2.5 and 1.85 R_o are lower limits to the real heights of the 21.5 and 40 MHz plasma levels respectively. If the emission were fundamental the sources would appear further out than their true positions and the observed source heights would then be lower limits to the 43 and 80 MHz plasma levels.

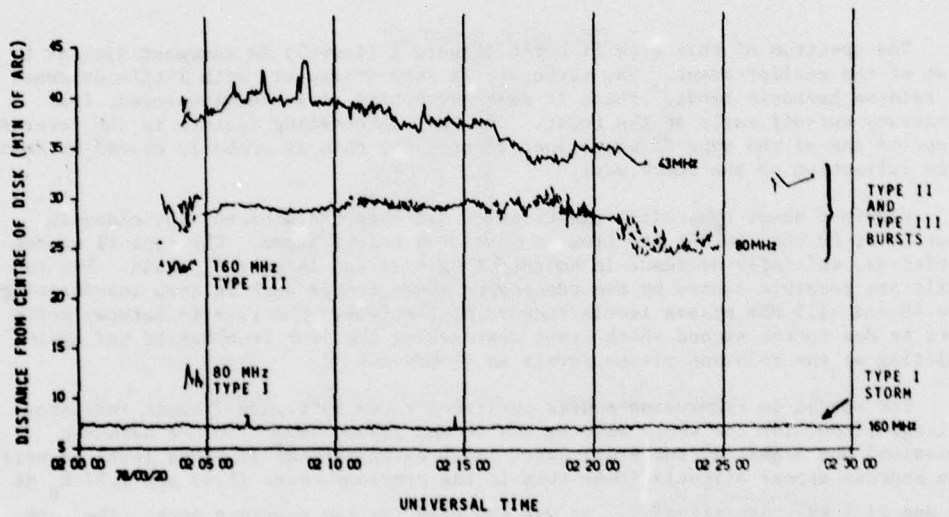


Figure 2. A plot showing the distances of the centroids of the different sources from the centre of the solar disk as a function of time.

Although they are not shown separately in Figures 2 and 3 the type III bursts at the beginning of the event are observed at 80 MHz in positions scattered amongst the type II burst positions. It is generally accepted that the type III electrons travel along magnetic field lines and it appears therefore that in this case the type II shock waves are also guided along the magnetic field. This is in agreement with observations of the 1969 March 30 "behind the limb" event (Dulk et al., 1971), in which the shock waves were found to have travelled along coronal field lines deduced from observed photospheric fields.

It is interesting to note the large transverse extent of the shock front at 80 MHz and the apparently much smaller extent at 43 MHz. This is illustrated further in Figure 4, which shows typical individual sources at each frequency. This observation suggests that the lateral extent of the particular shock front producing this type II burst decreases with height. However, while the transverse source size decreases with height the radial size increases, as in previous observations (Nelson and Robinson, 1975). This probably occurs because the scattering from irregularities in the corona increases as the frequency decreases. The sources typically cover a range of heights corresponding to a 2:1 range in plasma frequency.

Figure 5 shows two possible models of the shock paths which may explain the observation. The first of these assumes rectilinear outward paths for the disturbances; this explains the source positions but not the slow drift rates of the individual type II bands and the fast drift rate of the low-frequency cut-off at the start of the burst. To explain these as well, the second model with curved propagation paths is required. Thus it seems that the shock wave was refracted along a curved path, which was also the case in the 1969 March 30 event described by Smerd (1970).

3. TYPE II BURST OF 1976 MARCH 20^d22^h55^m

The spectrum of this type II burst (Figure 1 (lower)) is somewhat similar to that of the earlier event. The structure is very irregular, with little evidence of related harmonic bands. There is some suggestion of a steeply-sloped, low-frequency cut-off early in the burst. One very interesting feature is the reverse slope of one of the type II bands just after 2305; this is probably caused by downward refraction of the shock wave.

Figure 6 shows the radial positions of all observed sources. The close-in sources at 80 and 160 MHz are from an unrelated type I storm. The type II source positions, initially decrease in height, then rise and later fall again. The two falls are possibly caused by two successive shock fronts each in turn intersecting the 40 and 21.5 MHz plasma levels forward of the limb. The rise in between would then be due to the second shock front approaching the limb from behind and again emitting at the relevant plasma levels as it moves.

The spread in transverse source positions shown in Figure 7 again indicates a large extent for the shock wave at the 40 MHz plasma level (80 MHz harmonic emission) and a smaller but still quite large extent at the 21.5 MHz level as well. The sources appear slightly lower than in the previous event (1.83 and $2.27 R_{\odot}$ at 40 and 21.5 MHz respectively). As was the case for the previous event, the type II and type III positions are indistinguishable. This again suggests that the type II shock waves propagated along magnetic field lines.

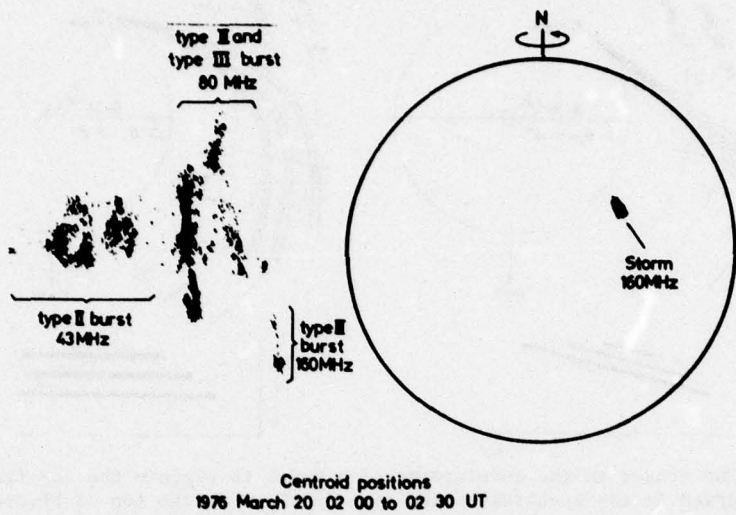


Figure 3. Map of centroid positions observed with the Culgoora radioheliograph. On this figure the position of the centroid of each source observed during a half-hour period is marked by a small symbol. The individual symbols cannot be distinguished but the superposition of many symbols marks clearly the positions of the important sources.

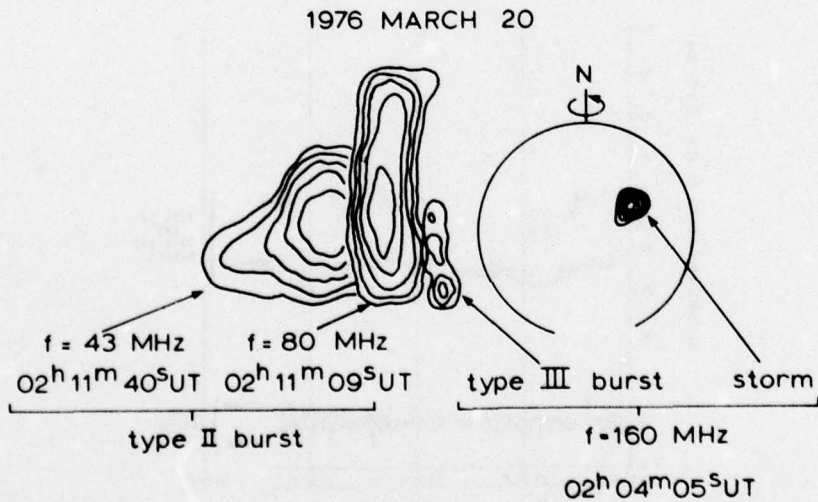


Figure 4. Composite contour diagram showing typical sizes and positions of sources observed at the three observing frequencies of the Culgoora radioheliograph during the first type II event.

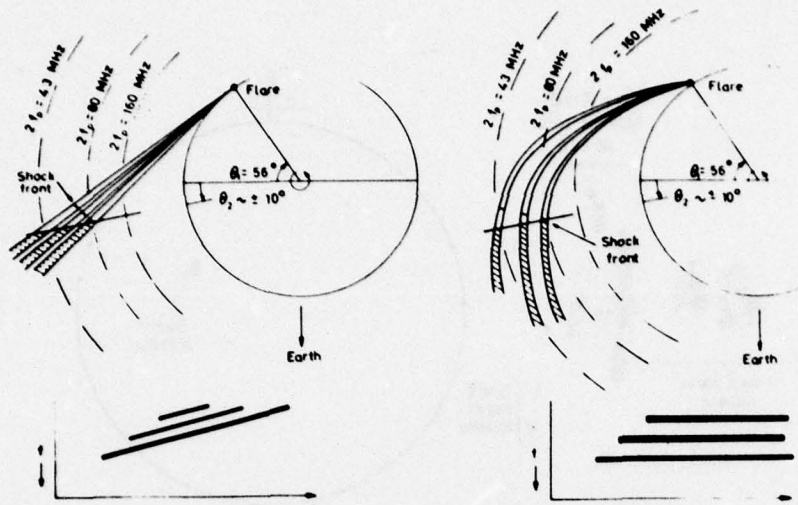


Figure 5. Two stages in the development of a model to explain the low-frequency cut-off observed in the spectrum of the type II shown at the top of Figure 1. Left: a shock front, broken into about three fragments, propagates away from the flare along straight paths. Because of scattering and refraction only the part of the path of the shock front (shown cross-hatched) after it crosses some surface near the limb is visible from the Earth. The dynamic spectrum of the type II burst predicted by this model is indicated below the model. Right: If we assume that the shock disturbance travelled along curved paths (as in the 1969 March 30 event) the predicted spectrum is in better agreement with the observations.

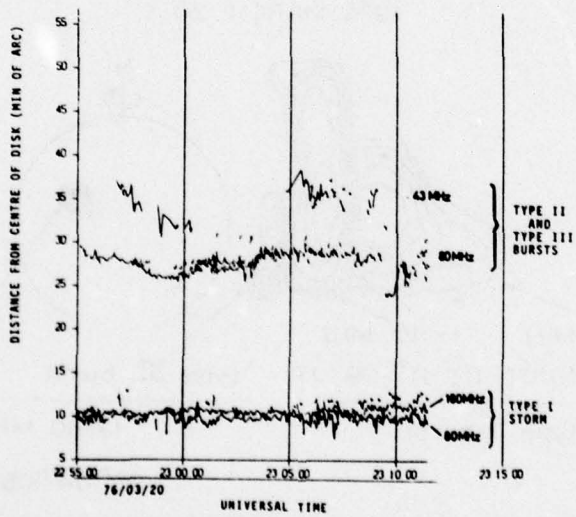
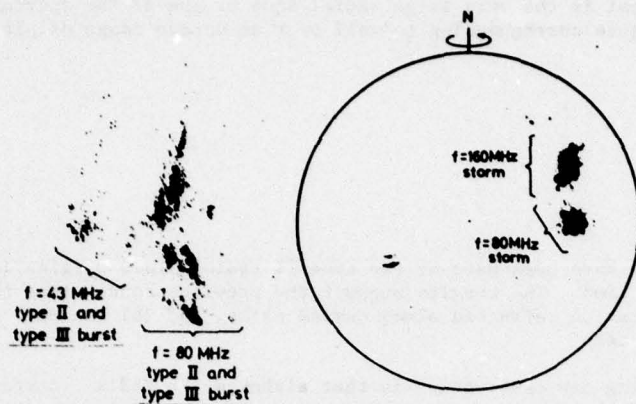


Figure 6. A plot showing the distance of the centroids of the different sources from the centre of the solar disk as a function of time.



Centroid Positions (corrected for ionospheric refraction)
1976 March 20 22 55 to 23 11 UT

Figure 7. Map of centroid positions observed with the Culgoora radioheliograph. On this figure the position of the centroid of each source observed during a half-hour period is marked by a small symbol. The individual symbols cannot be distinguished but the superposition of many symbols marks clearly the positions of the important sources.

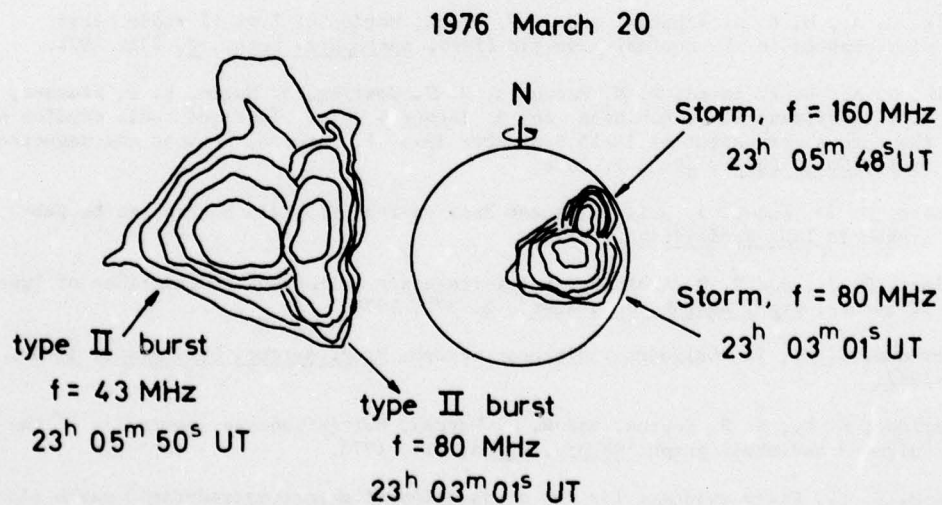


Figure 8. Composite contour diagram showing typical sizes and positions of sources observed at the three observing frequencies of the Culgoora radioheliograph during the second type II event.

Typical contours for the different sources are shown in Figure 8. Of particular interest is the very large radial size of the 43 MHz source, which extends over heights corresponding to well over an octave range of plasma frequency.

4. SUMMARY

Observations have been made of two type II radio bursts originating from well behind the solar limb. The results support the previous conclusions that type II-shock waves (a) can be refracted along curved paths, and (b) can move along magnetic field lines.

An interesting new observation is that although the radial source size increases with height the transverse size may decrease. The latter is ascribed to a decrease of the lateral extent of the shock wave with height, and the former to the increased scattering from coronal irregularities at greater heights (lower frequencies).

The 40 and 21.5 MHz plasma levels were found to be at heights of at least 1.85 and $2.4 R_{\odot}$ respectively.

References

- Dulk, G. A., M. D. Altschuler, and S. F. Smerd, Motion of Type II radio burst disturbances in the coronal magnetic field, Astrophys. Lett., 8, 235, 1971.
- Dulk, G. A., S. F. Smerd, R. M. MacQueen, J. T. Gosling, A. Magun, R. T. Stewart, K. V. Sheridan, R. D. Robinson, and S. Jacques, White light and radio studies of the coronal transient of 14-15 September 1973. I. Material motions and magnetic field, Solar Phys., 49, 369, 1976.
- McLean, D. J., and G. J. Nelson, Recent data on Type II radio bursts, to be published in IVUZ Radiofizika, 1977.
- Nelson, G. J., and R. D. Robinson, Multi-frequency heliograph observations of Type II bursts, Proc. Astron. Soc. Aust., 2, 370, 1975.
- Sheridan, K. V., The Culgoora radiospectrograph, Proc. Astron. Soc. Aust., 1, 58, 1967.
- Sheridan, K. V., N. R. Labrum, and W. J. Payten, Multi-frequency operation of the Culgoora radioheliograph, Nature, 238ps, 115, 1973.
- Smerd, S. F., Radio evidence for the propagation of magnetohydrodynamic waves along curved paths in the solar corona, Proc. Astron. Soc. Aust., 1, 305, 1970.
- Wild, J. P. (Ed.), The Culgoora Radioheliograph, Proc. IREE Aust., 28, No. 9, 1967.

Evolution of the X-ray Emitting Corona Preceding and After Major Solar Events

C. J. Wolfson, L. W. Acton, D. T. Roethig, and M. Walt
Lockheed Palo Alto Research Laboratory
3251 Hanover Street
Palo Alto, CA 94304, USA

Abstract

Soft X-ray emission from the sun during STIP Interval II, observed with the Lockheed Mapping X-ray Heliometer on the NASA OSO-8 satellite, is presented. In examining the emission versus time for extended intervals around the times of the Class 1B flare on March 28, 1976, and the Class 1B flare on April 30, 1976, we find significantly more low level flare activity prior to the major flares than after. Twelve modest X-ray bursts are investigated and no compelling case of a preflare brightening phase is observed. Preliminary correlations with the time history of emitted solar particles are discussed.

I. INTRODUCTION

This study examines the condition of the solar corona prior to, during, and following two large solar flares which occurred during STIP Interval II. The principal observations which will be used are at X-ray wavelengths, and therefore provide an indication of the processes taking place in the high temperature plasma. Correlations with other related phenomena, to the extent presently available, will also be used to help elucidate the entire flare phenomena.

The X-ray observations were obtained with the Lockheed Mapping X-ray Heliometer (MXRH) on the NASA Orbiting Solar Observatory-8 (OSO-8) satellite. The MXRH became operational on June 24, 1975, and obtained data through STIP Intervals I, II and III. A brief description of the MXRH instrument, the data coverage during STIP Interval II, and several sets of data for periods of major activity during this interval will be published in the UAG Special Report on the Retrospective World Interval 20 March to 5 May 1976 (Wolfson, Acton, Roethig, and Smith, 1977). That article will hereafter be referred to as Paper I and information in Paper I will in general not be restated in this paper.

The MXRH instrument responds to X-rays in the 1.5 - 30 keV energy range although the effective high energy limit for solar observations is usually substantially lower than 30 keV due to the steepness of the solar spectrum.

The instrument looks radially outward from the rotating wheel section of the OSO-8 satellite. It contains three detection systems, each collimated in one dimension with mechanical collimators. The collimators have a full width at half maximum transmission of 2 minutes of arc, although other instrumental effects broaden the instrument response function to about 4 minutes of arc under some conditions. Each field-of-view is tilted 120° with respect to the others. These three systems are called Vertical, Slant A and Slant B, with the Vertical system field-of-view parallel to the satellite spin axis. As the wheel rotation sweeps these fields of view across the sun, three one-dimensional count rate distributions are obtained. These distributions permit the location and isolation of emitting X-ray regions. Each spatial distribution consists of 31 successive strips, or area segments, parallel to a system's field-of-view.

An example of these distributions is shown in Figure 1, where the map for 1521-1524 UT on March 28 is presented. This example demonstrates how active regions which are overlapping in one detection system may be clearly resolved in a different system. The instrument maps the entire solar disk every 40 seconds. Longer integration times are required to detect regions of weak emission. Temporal information is obtained by monitoring the intensity versus time for selected area segments. Spectral information is obtained by 15 channel analysis of the proportional counter signals.

A more complete description of the MXRH may be found in Paper I and detailed information is given in the Technical Manual for the Mapping X-ray Heliometer Instrument on OSO-8 (Wolfson, Acton, and Gilbreth, 1975). Daily MXRH maps of the sun since August 1975 have been published in Solar Geophysical Data (SGD). It is anticipated that the MXRH will continue operation until at least October 1978.

The three largest solar flares observed by the MXRH between July 1975 and January 1977, as defined by either the magnitude of the resultant geomagnetic storm or the maximum intensity of the soft X-ray emission, occurred during STIP Interval II. In this paper we will study the time periods around the flare which occurred near 1930 UT on March 28 and the flare near 2115 UT on

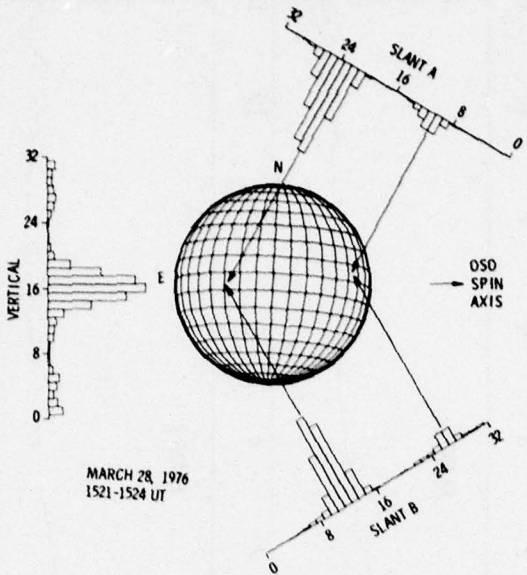


Figure 1. The X-ray Sun Prior to the Large Flare of McMath 14143 Near 1930 UT. The MXRH data are collected and displayed in terms of 32 numbered area segments, each 1.3 arc minutes in width. Each histogram is normalized to the peak intensity for that detection system. The arrows converge on McMath 14143 ($\sim S7 E28$) and McMath 14146 ($\sim N5 W55$).

April 30. These two events were chosen in preference to the event near 0900 UT on March 23 since these two flares occurred well away from the solar limb thereby increasing the likelihood of the correlation with data from other observing instruments. The event of March 23 was at, or slightly behind, the visible east limb.

2. EVOLUTION OF X-RAY EMISSION

Figures 2 and 3 show soft X-ray intensity light curves for extended intervals around the times of the two major flares. The solid portion of the curve is a normalized MXRH count rate from the region which produced the major flare. OSO-8 views the sun for approximately 60 minutes out of every 90 minute orbit. Additionally, data losses result when the satellite is in the high background environment of the South Atlantic Anomaly radiation zone. We have drawn dashed curves through the MXRH data gaps based on the NOAA 1-8 \AA full sun X-ray observations (Donnelly, private communication, 1977). Minor variations, and variations known to be from a different region by optical observations, were eliminated from the NOAA data. Reported (SGD) optical flares and subflares are also indicated. Except for the two class 1B flares, one on March 28 and one on April 30, all of the H α enhancements were classified as subflares. Some higher time resolution data may be seen in Paper I.

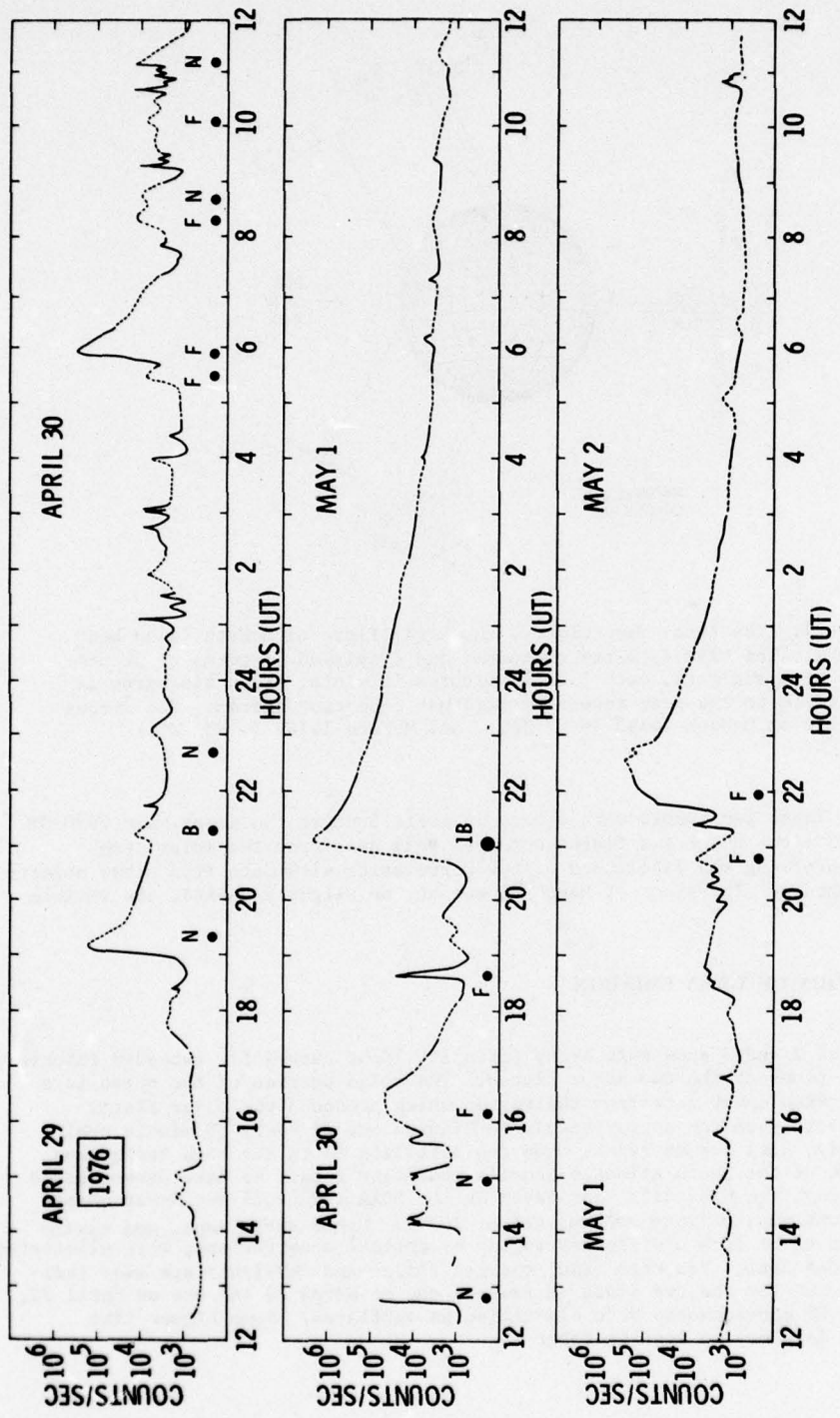


Figure 2. Light Curve of X-ray Emission from McMath 14179. The data were collected from various MRH detectors and normalized to the equivalent rate for the vertical large detector. The gaps in the MRH data have been sketch-d-in based on data from the NOAA full sun X-ray monitors. Optical Flares and subflares, as reported in Solar Geophysical Data, are also indicated.

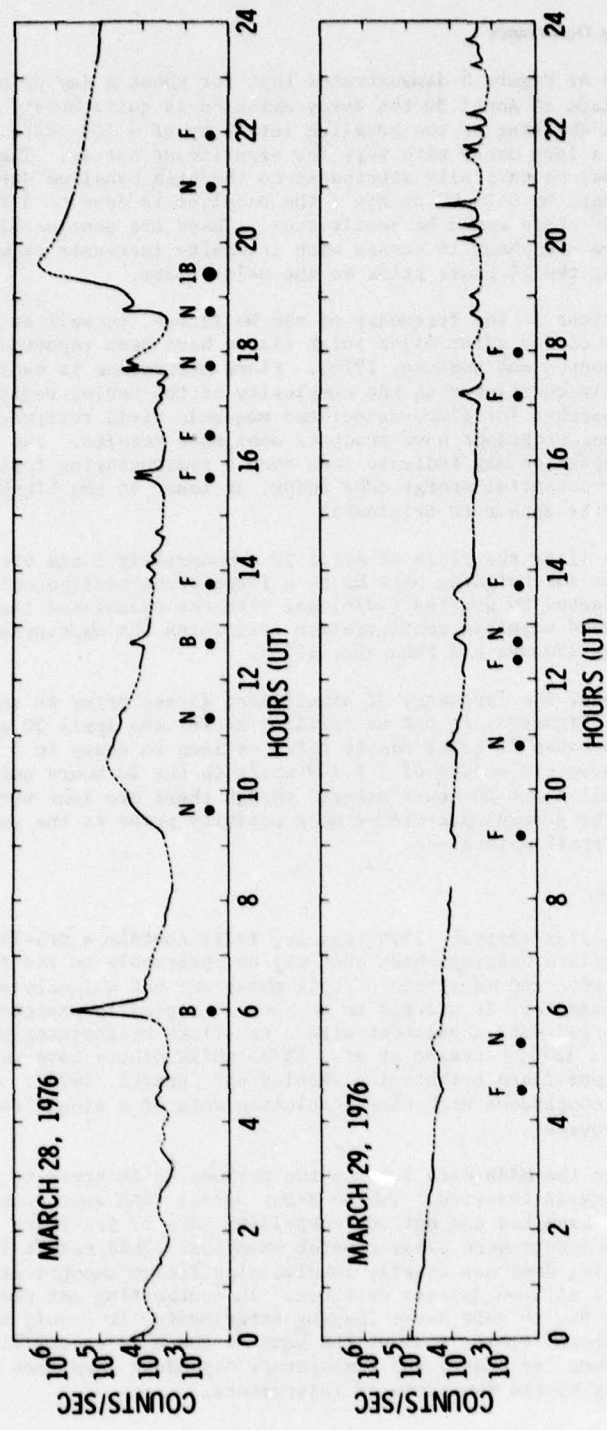


Figure 3. Light Curve of X-ray Emission from McMath 14143

2.1 Frequency of Flare Occurrence

An examination of Figure 2 demonstrates that for about a day prior to the proton producing flare of April 30 the X-ray emission is quite bursty with the emission seldom dwelling at the baseline intensity of $\sim 10^3$ cts/s. After the flare there is a long decay with very few significant bursts. The lack of post flare bursts may be partially attributed to the high baseline during the early decay. However, by 0400 UT on May 1 the baseline is down to 5×10^3 cts/s and bursts of 5×10^3 cts/s would be easily seen. There are none until 2120 UT. In comparison, there are about 16 bursts with intensity increases of more than 5×10^3 cts/s during the 24 hours prior to the major flare.

Similar variations in the frequency of the H_α flares, as well as full disk X-ray bursts, prior to and after major solar flares have been reported previously (Krivský, 1973; Dodson and Hedeman, 1976). Flare occurrence is usually considered to be closely correlated to the complexity of the active region magnetic field. However, searches for flare-associated magnetic field restructuring with photospheric magnetographs have produced ambiguous results. The above MXRH burst frequency comparison may indicate that such a restructuring toward a configuration of lower potential energy does occur, at least at the higher levels where the X-ray bursts appear to originate.

About 24 hours after the flare of April 30 a moderately large event is observed. This time for building back up to a flare-prone configuration is consistent with that stated by Svestka (1976) and with the calculated times for building up a stressed magnetic configuration containing the appropriate quantities of energy (Tanaka and Nakagawa, 1973).

The comparison of the frequency of significant flares prior to and after the March 28 event (Figure 3) is not as striking as for the April 30 event. This is partially because it takes nearly twice as long to decay to 5×10^3 cts/s. However, we do observe six bursts of 5×10^3 cts/s in the 20 hours prior to the event, and none until about 24 hours after; though there are four bursts of $\sim 2 \times 10^3$ cts/s. The general pattern of more activity prior to the event than after is therefore still maintained.

2.2 Pre-Flare Brightening

Some flare theories (Priest, 1976; Spicer, 1976) contain a pre-flare brightening or pre-flare heating phase that may be observable in the soft X-ray emission. The duration and magnitude of this phase are not uniquely specified, but a time of approximately 10 minutes to an hour is typically expected. Some observers have reported data consistent with a pre-flare brightening phase (Pallavicini et al., 1975; Petrasco et al., 1975) while others have reported a systematic lack of pre-flare brightening (Kahler and Buratti, 1976). None have had access to continuous high time resolution data of a single region such as the MXRH provides.

We have studied the MXRH data for the two periods of interest to see if pre-flare brightening is observed. Twelve X-ray bursts with appropriate pre-flare data were examined and not one compelling case of pre-flare brightening was found. Six bursts were clear counter examples. This result indicates that pre-flare heating does not usually involve significant amounts of material at temperatures of 2 million degrees or above. In contrasting our results with those from the Skylab soft X-ray imaging experiments, it should be noted that the MXRH low energy limit is about the same as the high energy limit of the Skylab instruments, so energy and temperature dependent phenomena may be observed differently by the two types of instruments.

A related observation is that flares from the same region show a wide variation in rise times and fall times, and that two (or more) bursts are frequently superimposed. A statistical evaluation of causality is beyond the scope of this paper. It is possible that some reported pre-flare brightenings were actually double flares where the early flare had a very slow rise time.

3. ENERGY OUTPUT

To obtain the X-ray energy radiated from the two major flares we first determine the parameters of the isothermal hot plasma which most closely reproduce the observed pulse height distributions during the flares. An updated version of the code developed by Tucker and Koren (1971) for the emission from a low density, high temperature plasma is used for this determination. Two parameters, temperature and emission measure ($\int n_e^2 dV$), are derived. The radiation predicted by the model for any wavelength interval can then be calculated. The 1-8 Å wavelength band was chosen because it corresponds reasonably well to the MXRH sensitivity range and is the commonly used interval for the SOLRAD and NOAA full sun monitors. The resultant MXRH fluxes are typically consistent with the NOAA monitor fluxes when the region of interest dominates the disk and is non-flaring, while the MXRH values are somewhat lower near the peak of large flares.

The MXRH did not observe the peak of either major flare. For the April 30 flare our observations began at 2121 UT, about 7 minutes after peak emission. For the March 28 flare our observations ended at 1918 UT and began again at 2004 UT while flare maximum was about 1940 UT. The MXRH fluxes were extrapolated through these gaps. We obtain a total X-ray output (1-8 Å) of 6×10^{29} ergs for the April 30 flare and 1×10^{30} ergs for the flare of March 28.

4. RELATED OBSERVATION

The possibility of combining the X-ray data with information from other experiments should be greatly enhanced by interactions at this symposium. Our preliminary efforts in this direction have centered around examining particle observations for the April 29 to May 2 interval. This interval was selected because it contained a high energy proton event and because the source, McMath 14179, was on the western portion of the disk and thus had good access to the interplanetary magnetic field lines leading to the earth. The non X-ray data thus far examined are: 1) the IMP 7 and 8 relativistic electron fluxes as provided to us by T.M. Krimmingis of John Hopkins Applied Physics Laboratory, 2) the IMP 7 and 8 high energy proton fluxes as presented in SGD, and 3) radio observations from SGD.

The high energy proton data show a five order of magnitude increase correlated with the major flare of April 30, but no detectable increases with any of the other flare activity. These data will not be discussed further.

The > 0.22 MeV electron data from IMP-7 and IMP-8 are shown in Figure 4 along with a compressed version of the X-ray fluxes previously presented in Figure 2. Periods when Type II and Type IV radio noise was detected, indicative of significant particle acceleration, are also shown. The electron curve is dominated by the major event at 2115 UT on April 30. Increases are also seen associated with the modest X-ray bursts (Hα subflares) at 0600 UT

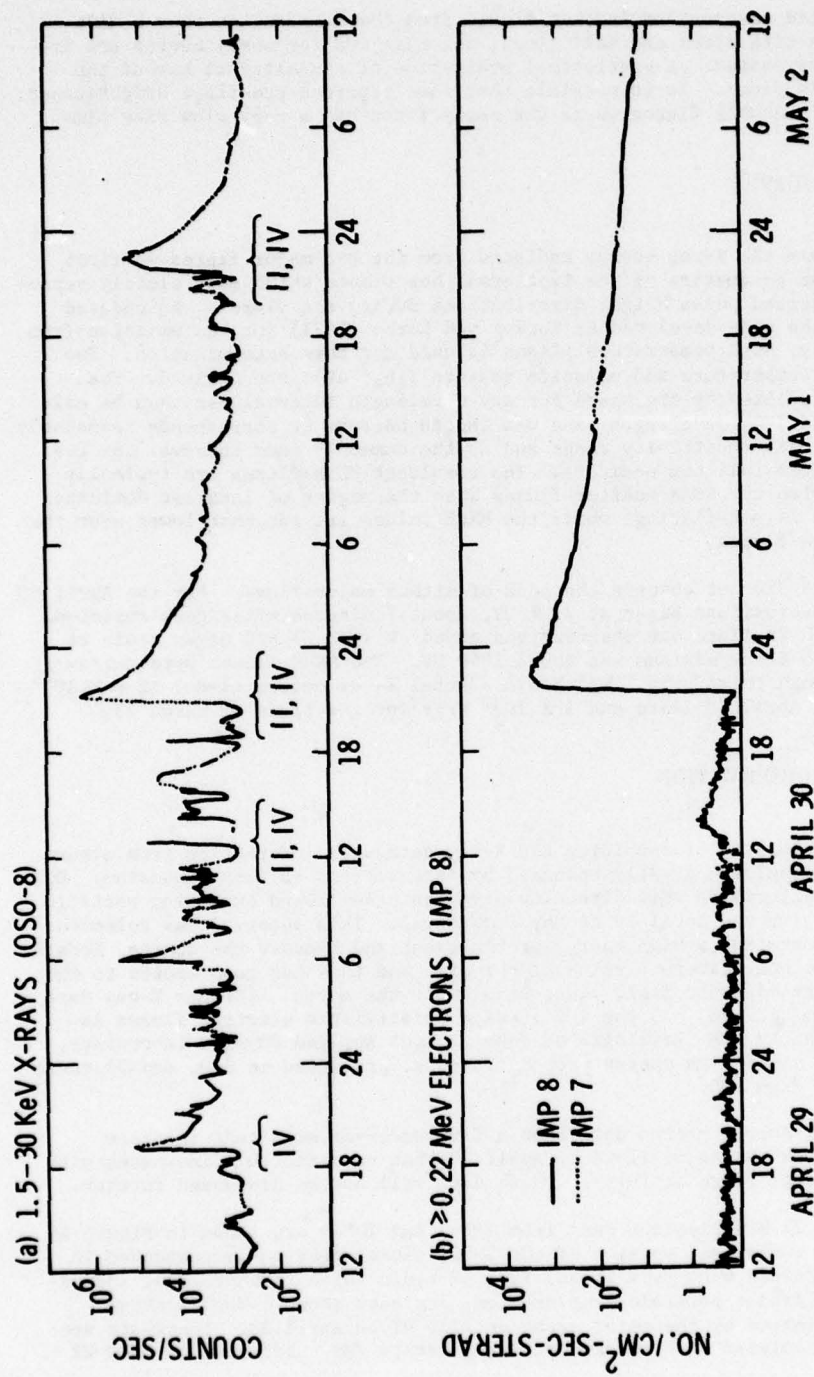


Figure 4. Light Curves of X-ray Emission and Electron Fluxes. Type II and Type IV radio events, as reported in Solar Geophysical Data, are also indicated.

and 1250 UT on April 30. However, no detectable electron enhancements occurred in conjunction with the burst at 1930 UT on April 29 or with the flare at 2200 UT on May 1.

It is interesting to note that the time dependence of the electron flux for the subflare at 1250 UT resembles the major flare both in rise time to maximum and decay rate, indicating that the interplanetary propagation conditions and injection rates were similar at both times. The similarity in shapes also adds confidence to associating the electron enhancement with the subflare. The short time intervals (1.1 to 1.5 hr) required for the electron flux to reach maximum is consistent with a direct magnetic connection and a relative long scattering mean free path in the interplanetary medium (Lanzerotti et al., 1973). The electron flux increase following the subflare at 0600 UT is much less pronounced and is too uncertain to provide propagation information.

The lack of a significant electron enhancement from the subflare at 1930 UT on April 29 is surprising, as this event was comparable in X-ray yield with the two subflares which did produce electrons. The active region was somewhat less favorably situated at that time (W30), but it seems unlikely that this is the dominant difference.

No electron enhancement was observed accompanying the flare late on May 1 although the flare was very favorably located (W60) for propagating electrons to earth and it might have been expected that the major flare a day earlier would have smoothed out inhomogeneities in the interplanetary field and improved the propagation characteristics (Bukata and Palmeira, 1967). However, at the time of the May 1 flare the decaying electron flux from the April 30 event was still two orders of magnitude above the quiet time background values and a moderate electron flux increase would not have been noted.

5. SUMMARY

Using data which were obtained with the Lockheed MXRH experiment on OSO-8, we have studied the solar soft X-ray emission for periods including the major flares of March 28 and April 30, 1976. Our data are consistent with models which predict significantly more activity prior to a major flare than after, and with approximately one day as the time required to build up the configuration for a subsequent large flare. The data are, in general, not consistent with a pre-flare X-ray brightening phase on the time scale of 5-60 minutes.

Examination of >0.22 MeV electron data for a period including the April 30 event shows that small enhancements were detected from two subflares prior to the LB flare and that a large flux was promptly detected in correlation with the LB flare. Somewhat surprisingly no electron enhancements were detected from the flares about a day earlier (1930 UT on April 29) and a day later (2200 UT on May 1). The lack of an enhancement on May 1 may be simply because the intensity was still quite high due to the major event.

Acknowledgments

The authors wish to acknowledge the team that conceived, designed, fabricated and presently operate the MXRH instrument, especially Project Engineer, C.W. Gilbreth and ground station scientist, K.L. Smith. Useful scientific discussions with J.W. Leibacher and J.M. Mosher are gratefully acknowledged. Special thanks are extended to R.F. Donnelly of NOAA and S.M. Krimigis of Johns Hopkins Applied Physics Laboratory for providing us with their data. This program has been supported by the National Aeronautics and Space Administration under Contracts NAS5-22411, NAS5-11360, and by the Lockheed Independent Research Program.

References

- Bukata, R. P. and R. A. R. Palmeira, The effects of the filamentary interplanetary field structure on the solar flare of May 4, 1960, J. Geophys. Res., 22, 5563, 1967.
- Dodson, H. W., and E. R. Hedeman, Some comments on flares after many years of observations, Solar Phys., 47, 267, 1976.
- Kahler, S. W., and B. J. Buratti, Preflare X-ray morphology of active regions observed with the A S and E telescope on Skylab, Solar Phys., 47, 157, 1976.
- Křivský, L., Sudden changes of activity before proton flares (events of August 1972), Bull. Astron. Inst. Czec., 24, 375, 1973.
- Lanzerotti, L. J., D. Venkatesan, and G. Wibberenz, Rise time to maximum flux of relativistic solar electron events and its relation to the high frequency component of the interplanetary field power spectrum, J. Geophys. Res., 78, 7986, 1973.
- Pallavicini, R., G. S. Vaiana, S. W. Kahler, and A. S. Krieger, Spatial structure and temporal development of a solar X-ray flare observed from Skylab on June 15, 1973, Solar Phys., 45, 411, 1975.
- Petrasso, R. D., S. W. Kahler, A. S. Krieger, and J. K. Silk, The location of the site of energy release in a solar X-ray subflare, Ap. J. (Letters), 199, L127, 1975.
- Priest, E. R., Current sheet models of solar flares, Solar Phys., 47, 41, 1976.
- Spicer, D. S., An unstable arch model of a solar flare, NRL Report 8036 (Naval Research Laboratory, Washington, D.C.) 1976.
- Švestka, Z., Solar Flares, D. Reidel, Dordrecht, The Netherlands, 1976.
- Tanaka, K., and Y. Nakagawa, Force-free magnetic fields and flares of August 1973, Solar Phys., 33, 187, 1973.
- Tucker, W. H., and M. Koren, Radiation from a high temperature, low-density, plasma: the X-ray spectrum of the solar corona, Astrophys. J., 168, 283, 1971.

Wolfson, C. J., L. W. Acton, and C. W. Gilbreth, Mapping X-ray Heliometer for OSO-8, Final Report, NASA-CR-144710, 1975.

Wolfson, C. J., L. W. Acton, D. T. Roethig, and K. L. Smith, 2-30 keV X-ray data from OSO-8, Collected Data Reports for STIP Interval II 20 March - 5 May 1976, Edited by H. E. Coffey and J. A. McKinnon, World Data Center A for Solar-Terrestrial Physics Report No. UAG-61, 187, 1977.

Discussion

Kaufmann: In high sensitivity tracking of an active solar center at 13 mm wavelength, in July 1974, we observed time features very much comparable to the soft X-ray results presented here.

Wolfson: Thank you for that interesting comment. Kundu of the University of Maryland has told me that he does see evidence of preflare heating for some radio events.

Fast Flux and Polarization Periodic Time Structure of Microwave Solar Bursts*

Pierre Kaufmann, L. Rizzo Piazza, and J. C. Raffaelli
CRAAM-Centro de Rádio-Astronomia e Astrofísica "Mackenzie"**
CNPq-Observatório Nacional
São Paulo, SP, Brazil

Abstract

Microwave bursts (7 GHz) that occurred in McMath 14143 (March 1976) have shown fast time structures in flux without corresponding structures in circular polarization degree. The great burst of 28 March 1976 displayed a superimposed oscillation, with a period of 4.7 ± 0.4 seconds, and amplitude proportional to the flux, lasting the entire event duration.

* This is an extended summary of two papers being published in Solar Physics.
** Provisional mailing address: R.Aibi 215, apt. 1102A, 05054-São Paulo, SP, Brazil

Important solar activity occurred in 1976 being associated with McMath plage 14143. The Sun was monitored at 7 GHz by a solar polarimeter at Itapetinga Radio Observatory, Atibaia, SP, Brazil. The instrument's sensitivity and time resolution were greatly improved previously to these measurements. In Figure 1 we show the average daily measurements of the Sun at 7 GHz. The S-component associated with McMath 14143 produced an excess contribution of nearly 20 percent in flux at its central meridian passage (CMP), in the last days of March 1976. The polarization of the S-component remained left-handed in the entire half-rotation, displaying an apparent dependence on heliographic longitude. The lack of polarization sense reversal, or magneto-ionic coupling at the source (Takakura, 1960) after CMP is not an unusual effect (Paes de Barros and Kaufmann, 1972). This effect and the suggested dependence of polarization degree on heliographic longitude might be explained in terms of Zheleznyakov's (1970) model that takes into account the gyro absorptive layers influence on emerging ordinary and extraordinary rays. In this case the source should be optically thick for ordinary rays, and most of the contribution corresponds to extraordinary rays.

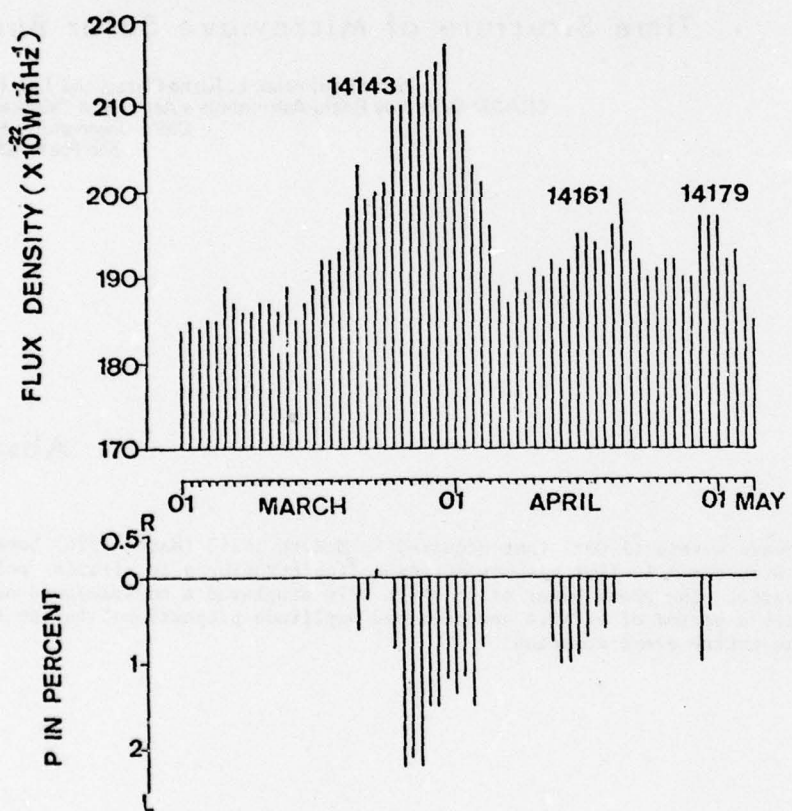


Figure 1. Daily Average Flux and Circular Polarization for the Overall Sun, at 7 GHz, in March-April 1976

Several events occurred in this period. All of them presented left-handed sense of polarization, agreeing with the S-component sense of polarization as expected (Scalise and Kaufmann, 1974). We will restrict ourselves to describing briefly two events of major interest. The event of 26 March 1976, shown in Figure 2, was analysed elsewhere (Kaufmann, 1976). The quasi-periodic structure in flux of 17 seconds is similar to events of this kind studied by Janssens et al. (1973).

On 28 March 1976 we recorded a Great Burst; the overall development with time is shown in Figure 3, together with a sudden phase advance in a very low frequency transmission received at the same site. A complete study of this event is being published elsewhere (Kaufmann et al. 1977). The large time scale polarization degree features, compared to the flux features, behave approximately as described in other works (Wassenberg, 1971). But we wish to draw the attention to the existence of a fast oscillation superimposed on the flux development with time, which cannot be shown in the scale used in Figure 3. The fast oscillations lasted the entire event duration, during which we were able to establish a period of 4.7 ± 0.9 seconds. This phenomenon appears to be different from known cases of pulses in microwave bursts (Janssens, et al., 1973). It is also remarkable that the polarization remained stable in relation to the oscillation similar to the event of 26 March 1976. The accuracy of polarization degree determination depends on the flux density level. At the maximum of the event, shown in Figure 4, the polarization was 24 ± 0.5 percent.

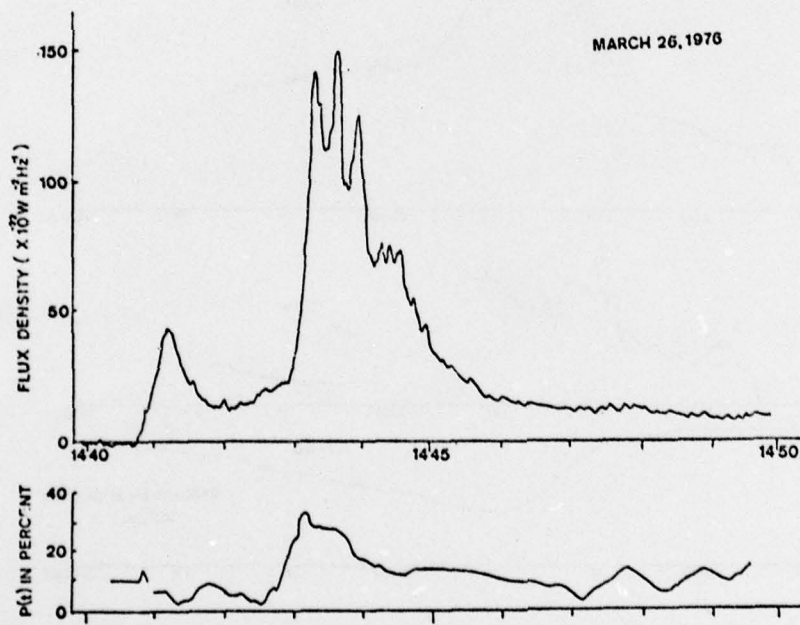


Figure 2. The Event of 26 March 1976 has shown a 17 Second Quasi-periodic Structure in Flux Without Any Counterpart in Polarization Degree

The amplitude of the oscillation A in any instant of the event was proportional to the flux density S at that instant

$$A/S \sim a \quad (\text{constant})$$

(1)

and the burst development with time could be described by the function

$$S(t) \approx A(t) (1 + a \cos \omega t), \quad 50 < S < 3000 \text{ s.f.u.}^*$$

where $a \approx 0.1$, $\omega = 2\pi/T$, $T \approx 4.7$ seconds.

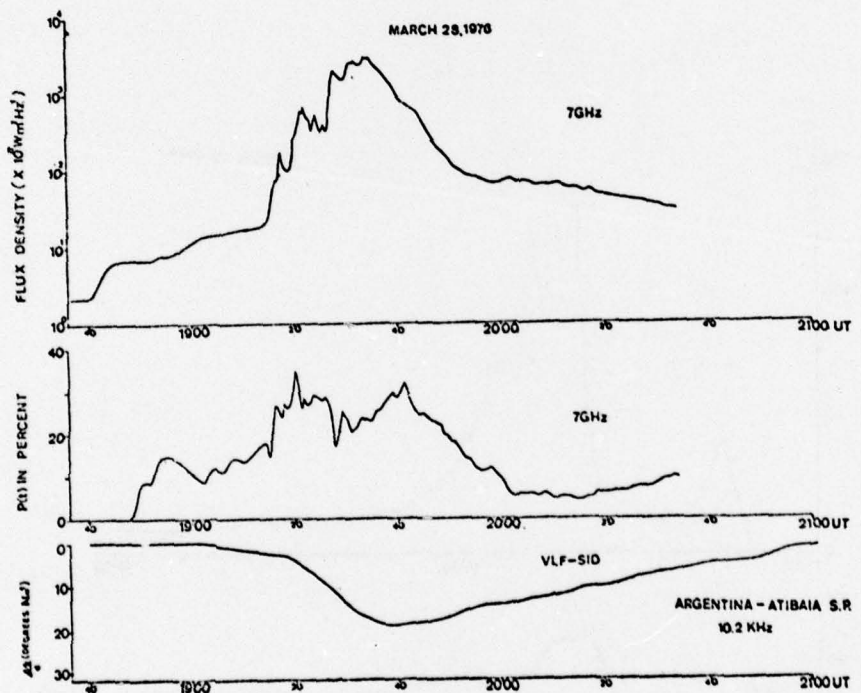


Figure 3. The overall time development of the Great Burst of 28 March 1976

*One solar flux unit (s.f.u.) = $1 \times 10^{-22} (\text{W/m}^2 \cdot \text{Hz} \cdot \text{sec})$.

Changes of polarization degree with time in the course of a microwave burst can be attributed to the movement of the emitting source in the magnetic field, or to change of the magnetic field applied to the source - or to both effects combined. This is seen for the large time structures, but it doesn't exist for the fast oscillations. It is difficult to reconcile the lack of polarization time structures for the fast oscillations to models assuming the bouncing of emitting electrons in magnetic loops at the active center (Janssens, et al., 1973, Chiu, 1970). The emitting source might be deeper in the flaring region, and thus observed under optically thick conditions. But in this case the event should be unpolarized, which was not the case. The observed oscillations might be tentatively attributed to the emission mechanism at the microwave source, regulated by the qualitative proportionality $S(t) \propto A(t)$.

Acknowledgments

This work was partially supported by Brazilian research agency FAPESP and by US AFOSR.

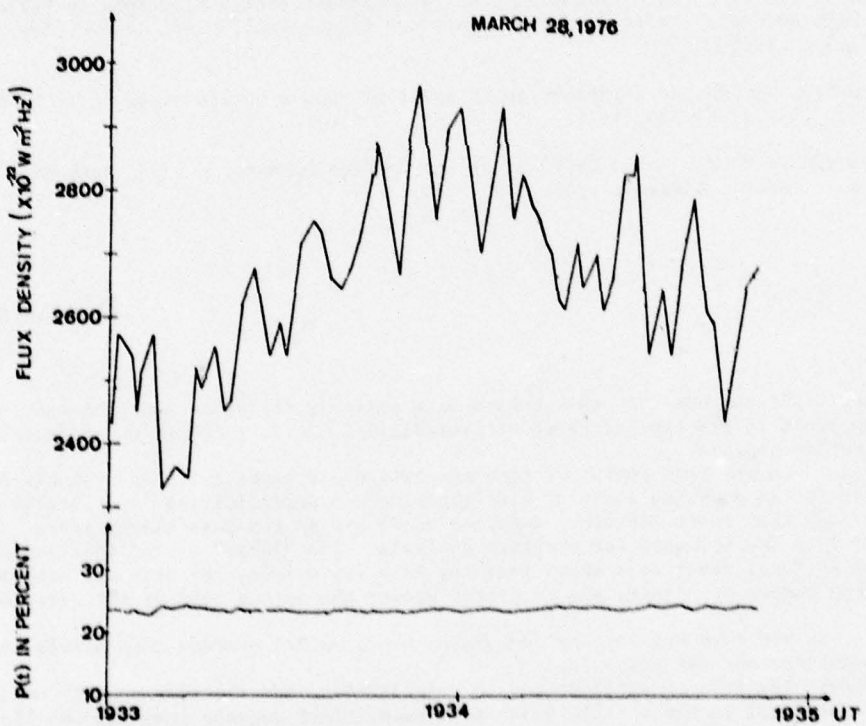


Figure 4. An Example of Two Minutes in Expanded Scale, Near the Maximum of the Great Burst of 28 March 1976. The polarization degree remained nearly stable in spite of the rather strong flux oscillation (of nearly 300 solar flux units).

References

- Chiu, Y. T., Theory of solar radio pulsation, *Solar Phys.*, 13, 420, 1970.
- Janssens, T. J., K. P. White, III, and R. M. Broussard, Quasi-periodic structure in solar microwave bursts, *Solar Phys.*, 31, 207, 1973.
- Kaufmann, P., Polarization of a periodic solar microwave burst, *Solar Phys.*, 50, 197, 1976.
- Kaufmann, P., L. Rizzo Piazza, and J. C. Raffaelli, 4.7 s nearly periodic oscillations superimposed on the solar microwave great burst of 28 March 1976, *Solar Phys.*, 54, 179, 1977.
- Paes de Barros, M. H., and P. Kaufmann, On the long-term behaviour of the circular polarization from coronal condensation radio emission at 4.3 cm wavelength, *Solar Phys.*, 27, 203, 1972.
- Scalise Jr., E., and P. Kaufmann, Coupling of microwaves at a selected solar active centre, *Solar Phys.*, 34, 189, 1974.
- Takakura, T., Synchrotron radiation from intermediate energy electrons in helical orbits and solar radio bursts at microwave frequencies, *Publ. Astron. Soc. Japan*, 12, 352, 1960.
- Wassenberg, W., On the polarization of solar microwave bursts observed at 17 GHz, *Solar Phys.*, 20, 130, 1971.
- Zheleznyakov, V. V., *Radio Emission of the Sun and Planets*, p. 538, Pergamon Press, Oxford, England, 1969.

Discussion

Schanda: Did you observe other bursts with periodic structure superimposed, and if yes, what is the typical range of periodicity? In particular, what are the shortest periods?

Kaufmann: In the past years our time resolution and sensitivity was relatively poor for an adequate study of fast superimposed periodicities. Qualitatively, I may say that there are other examples at 7 GHz, in the past eleven years, but the data are not good for accurate analysis. The "large" period oscillation of the 26 March event is a known feature, with few pulses. We have not analyzed a large number of events, and we cannot answer the second part of the question.

Dryer: Do you have suggestions concerning the physical process responsible for the amplitudes and periodicities?

Kaufmann: The lack of oscillations in polarization, and the flux density being proportional to the oscillations' amplitude, might suggest that the oscillatory phenomena are connected to the flaring mechanism itself, i.e., the original acceleration might be discontinuous in time. We have been studying this possibility as a general process connected to initial phases of solar flares.

**Estimation of Exciter Length of
Type IIIb Bursts Near Two Solar Radii
Derived From Microscopic Solar
Decametric Spectral Features**

H. S. Sawant, R. V. Bhonsle, S. S. Desonkar and S. K. Alurkar
Physical Research Laboratory
Ahmedabad-380009, India

Abstract

A high resolution spectroscope, with a time and frequency resolution of 10 ms and 5 kHz respectively, has been in operation at Ahmedabad over the frequency range from 35 to 34 MHz. This spectroscope is capable of obtaining spectra simultaneously in right-handed and left-handed circular polarization on a continuously moving 35 mm film.

We report here an unusual observation of the occurrence of a microscopic "U" burst almost simultaneously with a type IIIb burst with duration less than that of the former, recorded during the solar radio noise storm on 29 March 1976 (STIP Interval-II).

Recently, Sawant et al. (1976) have estimated the length of the density irregularity required for the generation of these microscopic "U" bursts to be $\sim 10^4$ km on the assumption that the exciter travels with velocity of the order of $0.3 c$, where c is the velocity

of light, the total duration of the microscopic "U" burst being 0.6 s.

The fact that the microscopic "U" burst appears on the record as one of the elements in the type IIIb burst and also shows intensity variation as a function of frequency and time implies that the large scale electron density irregularity which has generated this unusual burst may have a fine structure ($\leq 10^4$ km). The time interval between the beginning of the type IIIb and the beginning of the last element of the microscopic "U" burst enables determination of the exciter length of $\sim 10^3$ km.

1. INTRODUCTION

A high resolution Spectroscopic having time and frequency resolutions of 10 ms and 5 kHz respectively operating at Ahmedabad, records spectra of solar radio bursts over a frequency range 35 to 34 MHz simultaneously in right-handed and left-handed circular polarizations on a continuously moving 35 mm film.

We report here a rare event recorded during the solar radio noise storm on 29 March, 1976. Although the type IIIb burst is a common spectral feature associated with type III in the meter and decameter solar noise storm (de la Noë and Boischot, 1972; Baselyan et al. 1974a, b; Takakura and Yousef, 1974) we have observed a microscopic "U" along with a type IIIb burst (Sawant et al. 1976).

2. OBSERVATIONS

Figure 1(a) shows the event observed in the frequency range 34.5 - 35 MHz on 29 March, 1976 at 051625 UT. A microscopic "U" burst at about 35 MHz can be seen clearly as one of the elements of type IIIb burst. An intensity variation is also seen as a function of frequency and time in both the branches of the "U" burst. The frequency range, total duration, and time of the individual branches are respectively 150 kHz, 1.1 s and 0.4 s. The frequency drift rates of the first and the second branches are -200 kHz/s and +150 kHz/s respectively. One more event of this type has been recorded on the same day.

3. DISCUSSION

Recently, Sawant et al. (1976) have reported isolated microscopic "U", "inverted U" and "partial U" solar radio bursts. They have

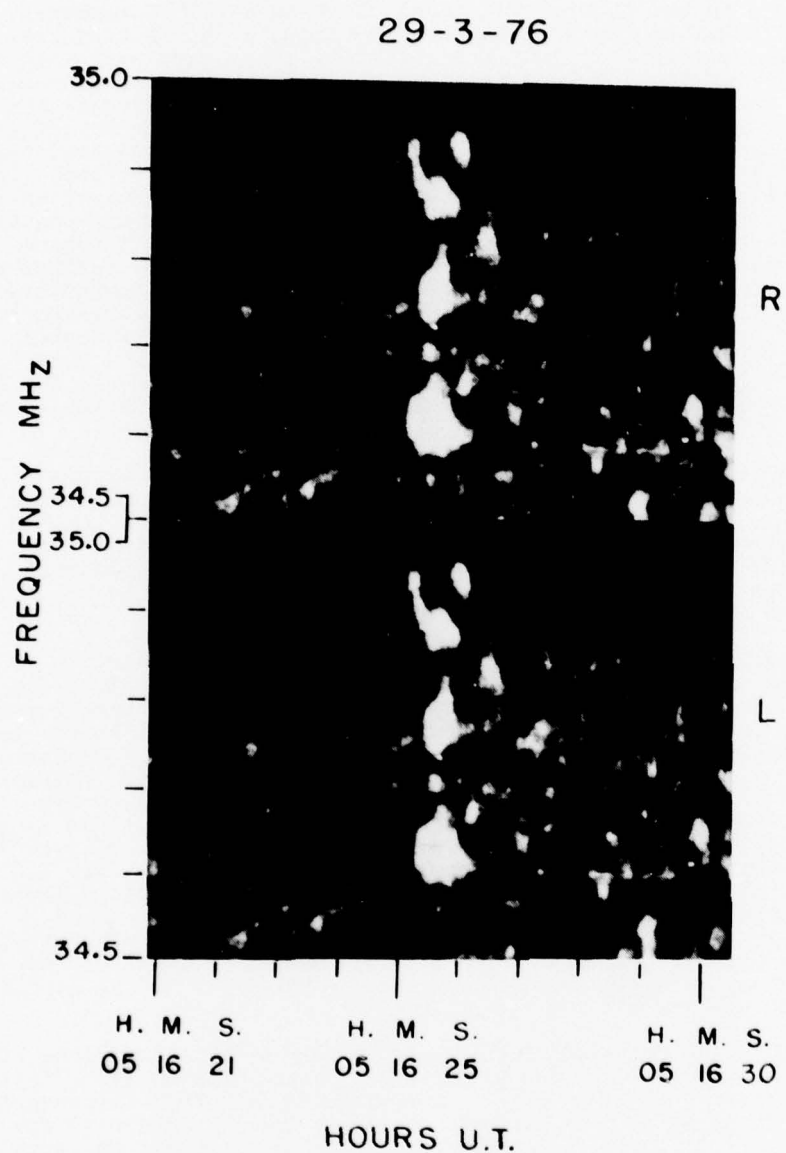


Figure 1(a). Dynamic spectra of solar microscopic "U" burst showing striations, observed over a range of 150 kHz simultaneously with type IIIb burst at 051625 UT, in R(upper) and L(lower) polarizations.

explained the frequency drift rates of these microscopic bursts by the change in the sign of the local electron density gradients which the exciter electron beam would encounter as it traverses an individual electron density irregularity. They have explained the generation of these bursts assuming the mechanism of induced scattering for the conversion of Langmuir waves to electromagnetic waves using the theory developed by Melrose (1974) for brightness temperature of type III bursts. Further they estimated from the observed total duration of 0.6 s of the microscopic "U" burst the length of the density irregularity required for the generation of those microscopic "U" bursts to be $\sim 10^4$ km on the assumption that the exciter travelled with an average velocity $\sim 0.3 c$ (where c is the velocity of light). Takakura and Yousef (1974) earlier had given estimates of the length of this order for the filamentary irregularities responsible for the generation of the stria bursts (type IIIb). In general, a low electron density gradient will provide larger interaction length for induced scattering than the steep density gradient and hence enhanced radiation due to the former and emission gaps due to the latter are observed in the microscopic "U" burst.

The fact that the microscopic "U" burst shown in Figure 1(a) occurred as one of the elements of a type IIIb burst and showed intensity variation as a function of frequency and time implies that the electron density irregularity itself had a fine structure ($\leq 10^4$ km) within it. From theoretical considerations Melrose (1975) has indicated the scale size of irregularities to be about 300 km at $2 R_\odot$.

A possible mechanism for the near simultaneous emission of stria and microscopic "U" bursts, assuming a single exciter beam responsible for them, is sketched in Figure 1(b). A density irregularity of size 10^4 km is shown to exist along a kink in the magnetic field line in the corona. The different density gradients labelled 1, 2, 3 and 4 within the kink correspond to the emissions observed in the first half of "U" and the two elements of type IIIb representing a total length of about 5×10^3 km. Also, the appearance of a microscopic "U" burst as one of the elements of type IIIb burst permits us to estimate the exciter length of the type IIIb burst which turns out to be of the order of 10^3 km. It is important to note that emissions at 2, 3 and 4 appear almost simultaneously whereas the emission at 5 appears about 50 ms after that at 4. This time delay permits us to obtain an upper limit to the length of an exciter beam which works out to $\sim 5 \times 10^3$ km assuming $0.3 c$ for the velocity of the exciter.

Aubier and Boischot (1972) have estimated time durations of the exciter of type III burst and their decay time constant to be of the order of 4 - 8 s and 1 - 2 s respectively from the recorded time profiles of type III bursts at three fixed frequencies viz., 60, 36.9 and 29.3 MHz. Recently, following the method suggested by Aubier and Boischot (1972), Barrow and Achong (1975) obtained the exciter time durations and decay time constants of type III bursts from fixed frequency time profiles of 103 bursts recorded at Kingston, Jamaica during 1970-74 at frequencies 18, 22, 26 and 36 MHz. These authors estimated the exciter length to be 5×10^5 km taking the velocity of the exciter of type III burst of $\sim 0.3 c$. The observational evidence presented in this note indicates that the exciter length responsible for the generation of type IIIb bursts

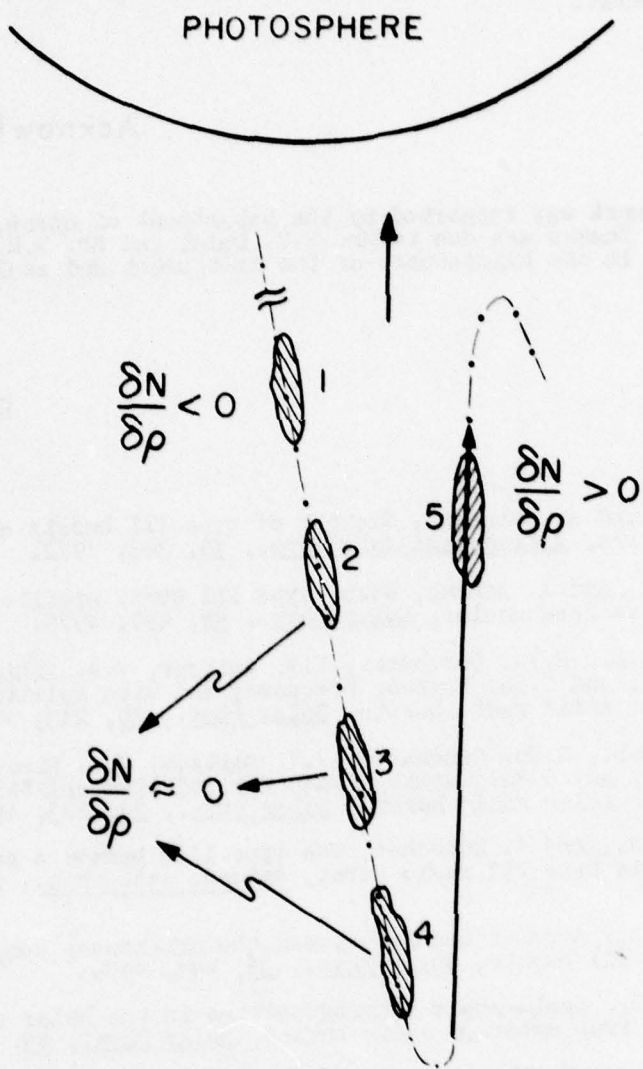


Figure 1(b). Schematic for simultaneous generation of "U" burst and type IIIb burst. 1, 2, 3, 4 and 5 represent the irregularities. Thin dotted line represents kink in solar magnetic field line. Thick line with arrow indicates the possible length of exciter. $\frac{\delta N}{\delta p}$ is the electron density gradient of the irregularity.

turns out to be two orders of magnitude smaller than that of the type III burst.

Acknowledgments

This work was supported by the Department of Space, Government of India. Thanks are due to Mr. N.V. Dalal and Mr. A.H. Desai for assistance in the maintenance of the instrument and scaling of the records.

References

- Aubier, M., and A. Boischot, Exciter of type III bursts and coronal temperature, Astron. and Astrophys., 12, 343, 1972.
- Barrow, C.H., and A. Achong, Solar type III burst profiles at decametre-wave frequencies, Solar Phys., 45, 459, 1975.
- Baselyan, L.L., N.Vu. Goncharov, V.V. Zaitsev, V.A. Zinichev, V.O. Rapoport, and G.Ya. Tsybko, Frequency and time splitting of decameter solar radio bursts, Solar Phys., 39, 213, 1974a.
- Baselyan, L.L., N.Vu. Goncharov, V.V. Zaitsev, V.A. Zinichev, V.O. Rapoport, and G.Ya. Tsybko, Frequency and time splitting of decameter solar radio bursts, Solar Phys., 39, 223, 1974b.
- de la Noë, J., and A. Boischot, The type IIIb burst: A precursor of decametric type III radio burst, Astron. Astrophys., 20, 55, 1972.
- Melrose, D.B., A relationship between the brightness temperature for type III bursts, Solar Phys., 35, 141, 1974.
- Melrose, D.B., Small-scale inhomogeneities in the solar corona: Evidence from meter- λ radio bursts, Solar Phys., 43, 79, 1975.
- Sawant, H.S., R.V. Bhonsle, and S.K. Alurkar, Microscopic spectral features in solar decametric bursts and coronal irregularities, Solar Phys., 50, 481, 1976.

Discussion

Steinberg: I am tempted to question the very existence of a type U component in your type III-b record. In my opinion, this type of U is made of several (2 to 3) components clearly resolved in the time-frequency domain.

Alurkar: The two wings of the type U are seen to have different signs of the frequency drift-rates together with brightening at the turnover. We have observed one more event of this type.

Steinberg: You invoke electron density inhomogeneities along the electron path to explain your findings. I do not understand what maintains such electron density deviations along the electron path, i.e. along a given line of force.

Alurkar: We know from coronal scattering of radio waves, IPS observations, etc. that field-aligned density irregularities do exist in the solar corona. These are connected outward by the coronal expansion (as discussed in the next paper "Radio Evidence of Travelling Coronal Electron Density Irregularities Near Two Solar Radii").

Dryer: (Comment following Dr. Steinberg's skepticism - as noted in his comment.) Is it possible that a periodic, pulsating mechanism at the flare source (as suggested by Dr. P. Kaufmann in the paper "Fast Flux and Polarization Periodic Time Structure of Microwave Solar Bursts" might be responsible for the generation of inhomogeneous plasma blobs which travel outward?

Alurkar: We know from radio observations that field-aligned plasma density irregularities exist in the corona, but it is not certain which particular mechanism is responsible for their generation.

Radio Evidence of Travelling Coronal Electron Density Irregularities Near Two Solar Radii

R. V. Bhonsle, H. S. Sawant, S. S. Degaonkar and S. K. Alurkar
Physical Research Laboratory
Ahmedabad-380009, India

Abstract

We report here new observations of "echo-like" bursts which have spectral "signatures" similar to those of the original bursts such as stria, split pairs and type IIIb but are observed after a certain time delay. The centre frequency of the echo-like burst is observed to differ by as much as ± 300 kHz from that of the original burst with time delays from a few milliseconds to a few seconds. Thirty two such echo-like bursts associated with different spectral types of bursts have been analyzed.

Some of these echo-like bursts may be explained if the same electron density irregularity in the corona is excited into plasma oscillations by two successive excitors. From the observed time delays and shifts in the centre frequency of these echo-like bursts, it is possible to estimate the velocity of coronal irregularities near 2 solar radii from the photosphere. These estimates, which are coronal model dependent, range from 100 to 1000 km/s. This

suggests that probably MHD disturbances might be responsible for the travelling coronal irregularities.

1. INTRODUCTION

Occurrence of an echo of a solar radio burst at meter and decameter wave lengths has been reported earlier (Roberts, 1958; Ellis, 1969; de la Noë and Möller-Pedersen, 1971; Baselyan et al., 1974). In addition to the conventional echo-type events such as drift pairs (Roberts, 1958) also, stria, split pairs, triplets and type IIIb bursts have been reported as echo events (Baselyan et al., 1974). The drift pair burst contains two identical elements, the second being repetition of the first and is observed after a typical delay of 1 to 2 seconds. The frequency shift of the second element is of the order of ± 1.5 MHz (Roberts, 1958).

High frequency-resolution observations in the decameter range (Baselyan et al., 1974) led to estimates of frequency-shift and time delays for different varieties of the echo events; on an average, the frequency-shift of the second element was of the order of ± 10 to 30 kHz and the delays ranged from 0.5 to 6 seconds. Moreover, they also observed that the instantaneous bandwidths and frequency drift rates were an order of magnitude less in the case of the echo-type events compared to those events without an echo.

We present here observations of "echo-like" bursts carried out by a high resolution solar decametric spectroscope, which has enabled accurate measurements of the differences in the frequency and time of the first and second components of echo-like events. An attempt has been made to calculate the velocity of moving coronal irregularities, which are responsible for the generation of echo-like bursts.

2. OBSERVATIONS

During November 1975 and March 1976 noise storms, 78 conventional echo-type and 32 echo-like bursts were observed with the help of a high resolution spectrograph operating near 35 MHz at Ahmedabad, India. The frequency and time resolution of this spectrograph are 5 kHz and 10 ms respectively. Some of the important characteristics of these "echo-like" bursts are as follows:

- a) Different varieties of the bursts such as stria, split pair, type IIIb, fast drift burst and a microscopic inverted "U" bursts were observed in the echo-like events.
- b) The parameters of these bursts such as instantaneous bandwidths and drift rates do not differ from those without echoes.

c) The observed frequency difference between the first and second component is of the order of ± 300 kHz or more with respect to the first component.

In 60 per cent of the echo-like events the shift in frequency was lower ($-\Delta f$) and in 40 per cent it was higher ($+\Delta f$). As shown in Figure 3, a convincing example of a microscopic inverted "U" burst, as an echo-like event, has been observed on 20 November 1975 at 0603:30 UT. It may be noted that there is a striking similarity between the two components except the shift in frequency at the "turnover" point. If the same electron density irregularity in the corona is excited into plasma oscillations by two different excitors then the same spectral features with almost the same properties will be observed but shifted in the frequency if the irregularity has moved during the period. This is valid under the assumption that the density structure of the irregularity remains unchanged at least for the time interval between the two excitors.

Assuming the coronal density model Hansen et al. (1969) and the observed time delays and shifts in the centre frequency of these "echo-like" bursts, it is possible to estimate the velocity of the coronal irregularities near two solar radii (35 MHz plasma level) from the photosphere.

Electron densities 2 to 3 per cent in excess of the background are assumed to be responsible for the generation of varieties of bursts which are located at corresponding plasma levels (Takakura and Yousef, 1974; Sawant et al. 1976). The height of the irregularities above photosphere has been estimated using the coronal electron density model of Hansen et al. (1969) as given by

$$N(\rho) = 4 \times 10^4 + 4.3\rho$$

where ρ is heliocentric altitude in solar radii. Thus, knowing the distance that the electron density irregularity might have travelled during the delay time, the outward motions of these irregularities are estimated. In case of ($-\Delta f$) i.e. negative frequency shift of the second component, the estimated motions of irregularities lie between 100 to 1000 km/s.

3. DISCUSSION

Three types of "echo-like" bursts were observed. They are:

- (1) The events in which the second component started at a lower frequency than that of the first. This difference in their starting frequencies is denoted as ($-\Delta f$) (Figure 1).
- (2) The events in which the second component started at a higher frequency than that of the first. This frequency difference is denoted as ($+\Delta f$) (Figure 2).

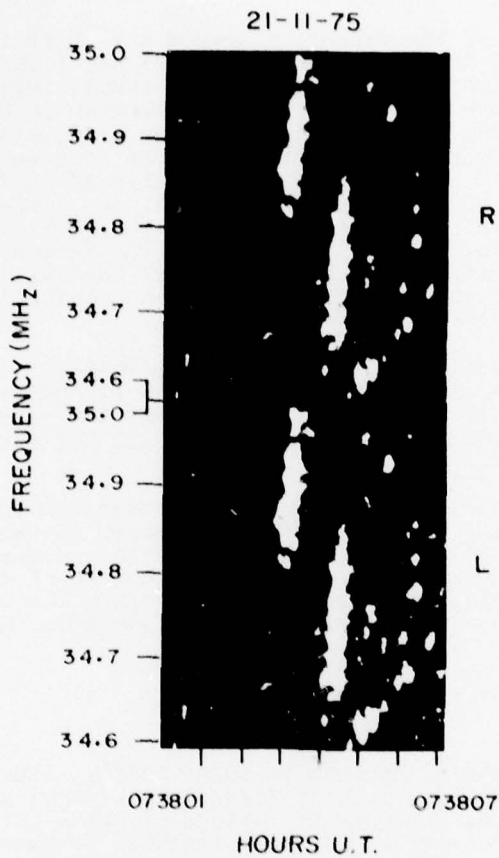


Figure 1. Dynamic spectra of "echo-like" reverse drift pair observed at 073802 UT. In this case the starting frequency of the second element is lower ($-\Delta f$) by ~ 150 kHz.

It may be noted that, if $\Delta f \leq 30$ kHz, then the event is called a conventional "echo-type" (Baselyan et al., 1974). In the cases (1) and (2), the two components may overlap in time duration or the second component may start after the end of the first component.

The cases (1) and (2) may be explained by assuming a single exciter beam traversing two coronal irregularities situated along the path of the exciter. If the length of the exciter beam is longer than the spatial separation of the two irregularities, then this would give rise to an overlap in time of the emission of the two components of the burst. It may also happen that the length of the

21-11-75

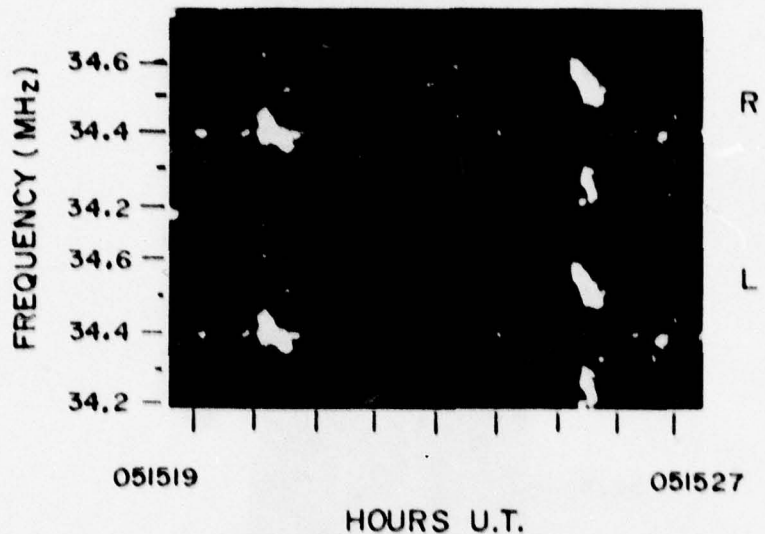


Figure 2. Dynamic spectra of "echo-like" split pair. At 051520 UT a single element of split pair is observed. In this case starting frequency of the second component is higher by ($\pm \Delta f$) by ~ 100 kHz. Weak horizontal emission is local transmission.

exciter is smaller than the inter-irregularity gap, then this will cause no overlap in time of the two components. The small frequency difference Δf (± 300 kHz) between the two components may arise due to (i) difference in the deviations of electron densities of the two irregularities or (ii) change in the electron density at the point of reflection of the radiation which later appears as the second component of the conventional echo phenomenon. In the latter case, one should expect a change of polarization of the reflected second component. Since no such change has been observed, this possibility is ruled out.

We now consider "echo-like" events, in which there is no overlap of emission of the two components in time. Such events may be thought of as being produced by two successive exciter beams traversing the same density irregularity after a finite interval of time. The frequency shift of the second component may be attributed to the temporal change in the magnitude of the electron density deviation of the irregularity during the time interval between the two successive excitations. Secondly, it is to be expected that the irregularity would be convected by the coronal expansion, as is evidenced in

20-11-75

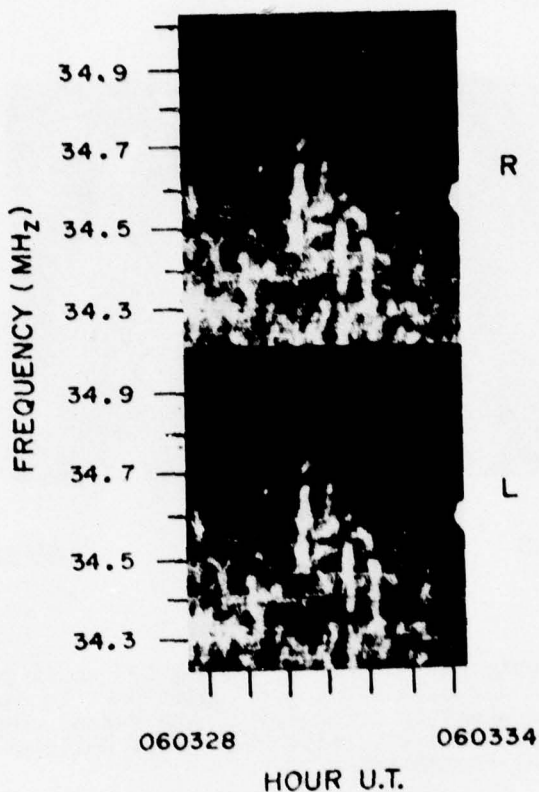


Figure 3. Dynamic spectra of "echo-like" inverted "U" burst observed at 060330 and 060331.5 UT in R(upper) and L(lower) polarization. Range of inverted "U" burst is ~ 250 kHz.

the case of microscopic inverted "U" burst (Figure 3) displaying decrease in frequency. This implies that the irregularity has moved outward to a level where the local electron density is less than that at the level where it was traversed by the first exciter. This difference between the two coronal levels has been estimated using the model of Hansen et al. (1969). Thus the velocity with which the density irregularity travelled turns out to be 1793.16 km/s. There is no reason why the effect of more than two excitors should not have been observed. This may partly be due to the narrow spectral range of the spectroscope. This limitation is being overcome by widening the spectral range so as to accommodate larger frequency

shifts due to a greater number of exciter beams.

4. CONCLUSION

We have discussed different types of "echo-like" bursts recorded with the high resolution spectrometer at 35 MHz. It has been observed that the second component of the "echo-like" burst may display difference in frequency with respect to the first one and either partially overlap in time or does not overlap at all. The latter variety of the "echo-like" events has been interpreted in terms of excitation of a moving density irregularity by two successive exciter beams. This effect has been clearly demonstrated by an event of a pair of a microscopic inverted "U" bursts, the differences in frequency and time between which have been used to estimate the velocity of the irregularity using a spherically symmetrical corona.

Acknowledgments

This work was supported by the Department of Space, Government of India. Facilities provided at the Radio Astronomy site by the Space Applications Centre, ISRO are gratefully acknowledged. Thanks are due to Mr. N.V. Dalal and Mr. A.H. Desai for assistance in the maintenance of the instrument and scaling of the records.

References

- Baselyan, L. L., N. Vu. Goncharov, V. V. Zaitsev, V. A. Zinichev, V. O. Rapoport, and G. Ya. Tsibko, Frequency and time splitting of decameter solar radio bursts, Solar Phys., 39, 213, 1974.
- de al Noë, J., and B. Möller-Pedersen, Relationship between drift pair bursts and decameter type III solar radio emission, Astron. Astrophys., 12, 371, 1971.
- Ellis, G. R. A., Fine structure in the spectra of solar radio bursts, Australian J. Phys., 22, 177, 1969.
- Hansen, R. T., C. J. Garcia, and S. F. Hansen, Brightness variations of white light corona during the years 1964-67, Solar Phys., 7, 417, 1969.

Roberts, J. A., Evidence of echoes in the solar corona from a new type of radio burst, Australian J. Phys., 11, 215, 1958.

Sawant, H. S., R. V. Bhonsle, and S. K. Alurkar, Microscopic spectral features in solar decametric bursts and coronal irregularities, Solar Phys., 50, 481, 1976.

Takakura, T., and S. Yousef, The third harmonic of type III solar radio bursts, Solar Phys., 36, 451, 1974.

Solar Radio Burst Energies for March-April 1976

J. P. Castelli and *G. L. Tarnstrom
Air Force Geophysics Laboratory
Hanscom AFB
Bedford, MA 01731, USA

Abstract

For the three principal solar radio events of the March 20 - May 3, 1976 period on March 23 at 0845, March 28 at 1930 and April 30 at 2100 UT, the energy transformed to radiation was about 0.64, 2.4 and 1.7×10^{24} ergs respectively for a 600 to 8800 MHz band. Surprisingly, the first event to which the high A_p value on March 26 was somehow related, was weaker than the later 2 events. The April 30 event with a significant PCA and GLE had considerably less energy than the March 28 burst in the same bandwidth. In comparison with some of the most outstanding bursts of sunspot cycle #20 on e.g. May 23, 1967, March 30, 1969 and August 4, 1972, the 1976 events were 20 to 50 times weaker and about 10 times weaker than moderate outbursts such as that of July 23, 1970. It is shown that the spectra of the bursts play an important role. When radio emission to 35000 MHz is considered, energies may be 2 to 4 times the above values depending on the spectral hardness in the millimeter range. Noise storm energy and uses of energy data are also discussed.

* NAS-NRC Resident Research Associate

1. INTRODUCTION

Sunspot cycle #20 was a disappointment to many researchers in Solar-Terrestrial Physics. It is true that the maximum daily sunspot index was much lower than that for cycle #19. The number of important geophysical events was also greatly reduced. Consider that in one year, 1960, on 9 different occasions the A_p exceeded 100, and three times it exceeded 200. Neither such magnitude nor frequency of activity have been attained in this cycle. However, great strides have been made in sunspot cycle #20 in development of sensors for various satellite measurements.

In the ground based observation area, we could cite the progress made in continuity, bandwidth and accuracy of discrete frequency solar radio observations from 100 to 70,000 MHz [Castelli, et al. 1973]. Because of this, it is now possible to discuss solar radio burst energy measurements with confidence for scientific applications.

In terms of total energy from the sun at the time of a flare/burst, the radio energy may be small. However just as radio burst emission is producing valuable signatures for predicting the occurrence, intensity and spectra of proton events, it is believed that accurate radio burst energy measurements may serve scientists in the solar-terrestrial effects area in relating to interplanetary parameters, [Dryer, 1974 and Pinter and Dryer, 1976], and physical mechanisms.

2. BURST ENERGY INPUTS MARCH-MAY 1976

2.1 Peak Flux Density Spectra

During the March-May 1976 period, from the radio viewpoint there were three principal events which occurred on March 23, March 28 and April 30, [Castelli and Barron, 1977]. The first two events occurred during one disk passage of the active region, McMath #14143. Associated A_p 's of 138 and 107 occurred on March 26 and April 1 for these first two events. The April 30 event took place during the following disk passage. The radio burst profiles are shown in Figures 1, 2, and 3. The first was observed at Manila (P.I.) Observatory while the 2nd and 3rd were observed at the Sagamore Hill Radio Observatory. Note that there are certain similarities of burst complexity and structure. Note the superposed spikes on the 1415 MHz records. The slow rise to maximum (> 5 minutes) at centimeter wavelengths is noteworthy. In terms of total duration, the March 28 event was the longest at meter wavelengths.

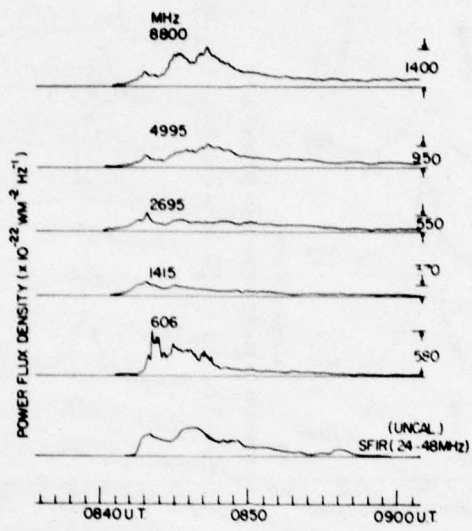


Figure 1. Great Radio Burst Observed on March 23, 1976 at Manila Observatory, P. I.

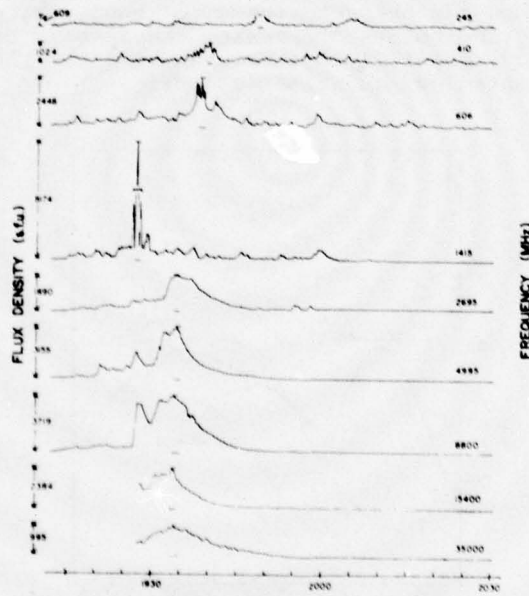


Figure 2. Great Burst Observed 28 March 1976 at Sagamore Hill Radio Observatory, Hamilton, Mass.

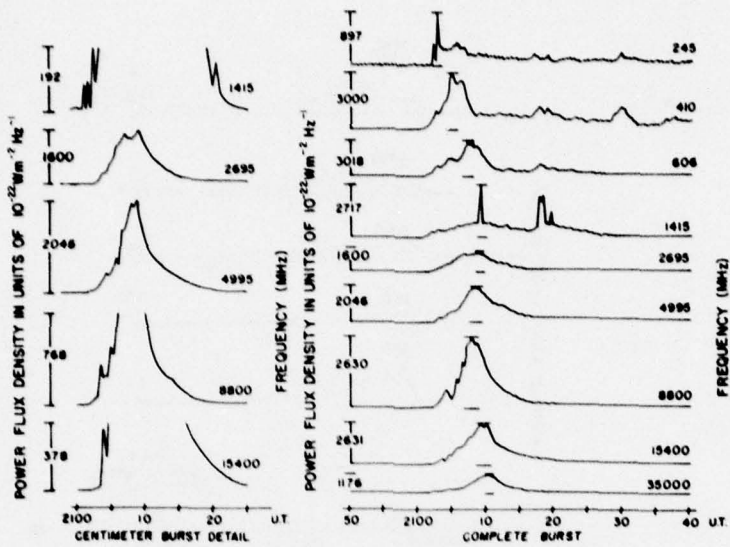


Figure 3. Great Burst Observed on 30 April 1976 at Sagamore Hill Radio Observatory, Hamilton, Mass.

The peak flux density spectra of the events are shown in Figure 4. The curves show the characteristic "U" spectrum, predictive of proton emission. The points comprising the spectra can be measured with good accuracy, generally better than 10-15%. Thus, spectral information presented has quantitative merit.

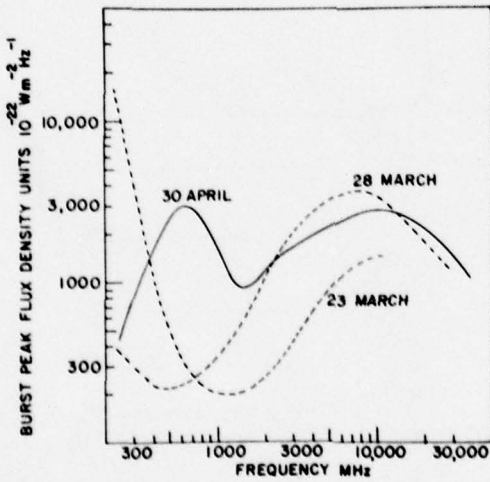


Figure 4. Burst Peak Flux Density Spectra for Events of 23 March, 28 March, and 30 April 1976.

2.2 Integrated Flux Density

If one determines the area under any of the burst curves as in Figures 1, 2, 3 one thereby derives burst integrated flux density ($\text{Joules } \text{m}^{-2} \text{Hz}^{-1}$). Briefly one multiplies the burst duration in seconds by the burst mean amplitude. (A value of about $10^{-17} \text{ J m}^{-2} \text{Hz}^{-1}$ is the statistical threshold for a small PCA or proton event). The integrated flux density spectra for the three events in question are shown in Figure 5. Note that while the spectra are quite different, the curves are reasonably smooth. (Note that spectra with large values at the highest frequencies will produce the largest mean integrated flux density over specified bands and in turn greatest energy.)

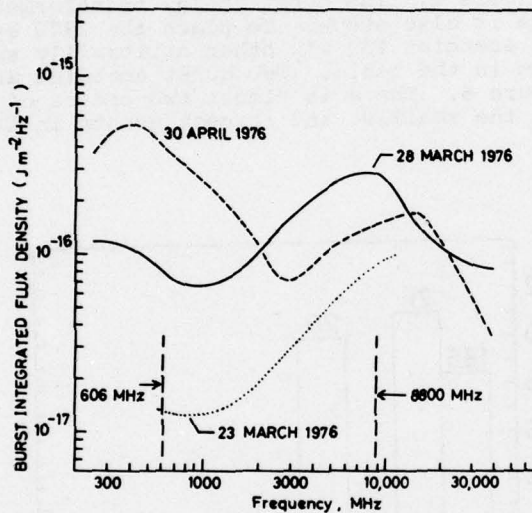


Figure 5. Burst Integrated Flux Density Spectra for March 23, March 28, and April 30, 1976, Events.

Whereas at one time the problem was to determine the burst mean amplitude over the duration of the event, now with a system of automation for sampling the burst at all frequencies every few seconds and maintaining a running summation of the area of the multiple rectangles, [Guidice, 1975] it is possible to have an accurate burst integrated flux density value at any instant during the burst and certainly at the end of the event.

At different times burst integrated flux density at different frequencies has been used as a quantitative predictor of 10 MeV proton flux. Early in cycle #20, 1415 MHz seemed better correlated [Straka and Barron, 1970], while for later cycle events, 8800 MHz seemed to provide better correlation [Castelli and Guidice, 1976]. Possibly the mean integrated flux density over the band, say from 1000 to 10,000 MHz, will provide the best correlation from an experimental viewpoint. This is being addressed.

3. BURST ENERGY TRANSFORMED TO RADIATION

The radiated energy per unit bandwidth at the sun may be computed from the burst integrated flux density at a given frequency recorded at the earth and multiplied by the area of a sphere, $4\pi R^2$, where $R = 150 \times 10^6 \text{ km}$ ($1.5 \times 10^{11} \text{ meters}$), the earth-sun mean distance. Perhaps hemispheric geometry is more appropriate. We have assumed this. The total microwave energy radiated at the sun in a given band after converting Joules to Ergs is: $E = (\text{mean integrated flux density in } \text{Jm}^{-2} \text{ Hz}^{-1}) (\text{Bandwidth in Hz}) (k=10^7) (2\pi R^2 = 14.14 \times 10^{22})$. Equation 1.

Table 1 shows burst mean integrated flux density for the three events noted for the 600 to 8800 MHz band. These data are derived essentially from Figure 5. The burst energy transformed to radiation for the same events is also shown. To place the 1976 events in proper perspective, burst energies for six other arbitrarily selected cycle 20 events are shown in the table. The burst energies are compared graphically in Figure 6. There is almost two orders of magnitude difference between the smallest and largest events in Table 1.

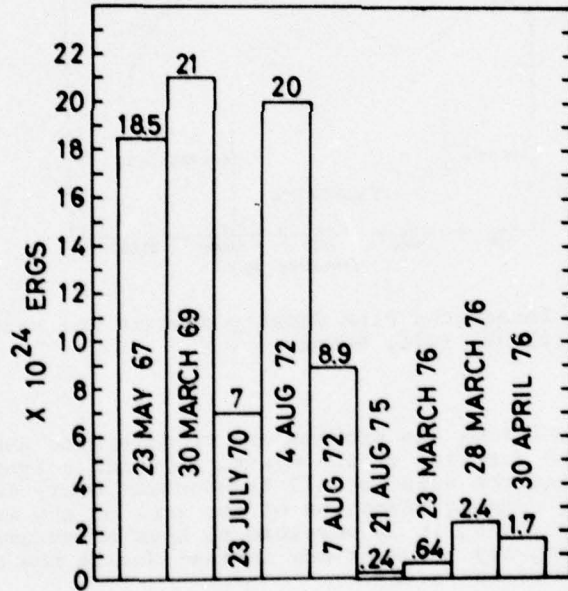


Figure 6. Comparison of Burst Energy at 606-8800 MHz in Selected Events

Table 1. Burst Energy Transformed to Radiation

Event Date	Mean Integrated Flux Density 600-8800MHz, $J \text{ m}^{-2}\text{Hz}^{-1} \times 10^{-16}$	Burst Energy 600-8800 MHz ERGS $\times 10^{24}$
23 March 1976	0.55	0.64
28 March 1976	2.2	2.4
30 April 1976	1.47	1.7
23 May 1976	16.0	18.5
30 March 1969	18.5	21.0
23 July 1970	6.0	7.0
4 August 1972	17.4	20.0
7 August 1972	7.7	8.9
21 August 1975	0.21	0.24

4. BURST ENERGY APPLICATIONS

The burst energy provides a measure of the energy contained in the non-thermal distribution of flare-accelerated electrons. A significant portion of the energy contained in >100 KeV electrons is radiated as synchrotron emission [H.C. Ko, Private Communication, 1976] predominantly at cm-and mm-wavelengths, and makes up most of the energy radiated at radio wavelengths. Electrons of lower energy lose almost all of their energy through elastic collisions heating the solar atmosphere.

Impulsive (non-thermal) X-ray bursts indicate that the non-thermal electrons have a power-law distribution $E^{-\gamma} (dN/dE) E^{-\gamma}$ with $\gamma \sim 4$, commonly extending down to ~ 10 keV and occasionally down to at least 3 keV, [Kahler and Kreplin, 1971].

Different flares, thus, have similar non-thermal electron distributions and measurement of the energy contained in >100 keV electrons serves to scale the total energy contained in the non-thermal electrons (at least in >10 keV electrons). Since the relationship between accelerated electrons and protons should be systematic, burst energy should serve as an index of the terrestrial effects of a flare, as has indeed been shown for peak PCA absorption [Straka and Barron, 1970]. Since non-thermal electrons may contain a major portion of the total energy of a flare [Syrovatskii and Shmeleva, 1972; Brown, 1973; Lin, 1975], burst energy should serve as a general flare index.

The application of the burst energy as a general flare index is illustrated in Figure 7. Figure 7 compares the burst energy (606-8800 MHz) of the 23 March, 28 March, and 30 April 1976 flares with the energy radiated by these flares in soft x-rays and H α [Marková, 1977]. The radiated energies are plotted according to the energies of the radiating electrons. There is good agreement between the relative amounts of energy radiated in each wavelength range. The wide spread of H α energies may be due to difficulty in observing the 23 March flare at the East limb or to limitations of the method employed to estimate the H α energy from flare durations.

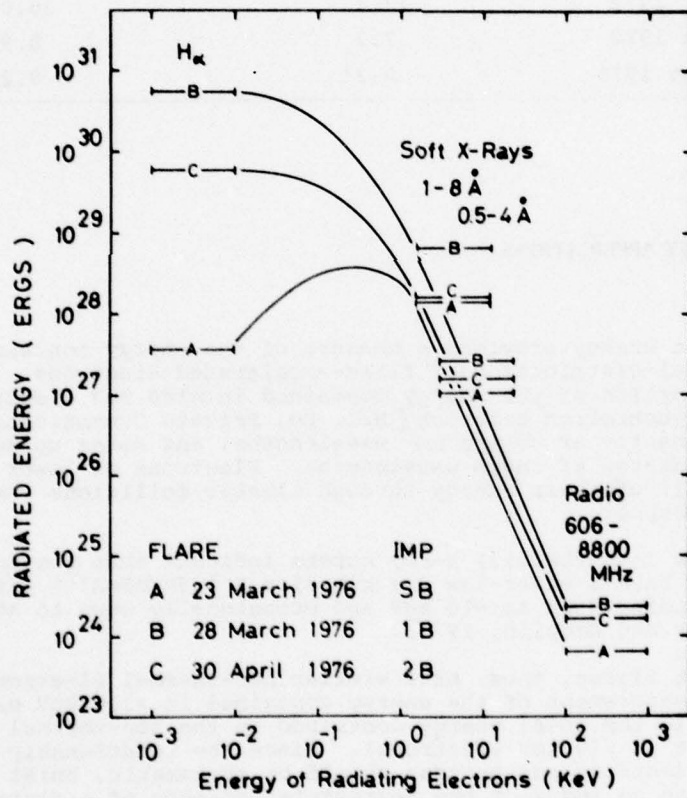


Figure 7. Comparison of Energy Radiated at Different Wavelengths.

Figures 7 also illustrates an application of burst energy to flare energetics. If the flare acceleration mechanism were efficient, H α and soft x-ray energies would come largely from heat produced by the accelerated, non-thermal electrons. The electron distribution must then extend down to a low-energy cut off $E_0 \sim 1$ keV to contain sufficient energy. Soft X-ray energy should correlate well with burst energy. Small variations of γ and E_0 between flares would produce large differences in H α energy and reduce the correlation between H α and burst or soft X-ray energies. If the acceleration mechanism were inefficient, H α and soft X-ray energies would come from heat produced while accelerating the electrons. In the inefficient case, H α and soft X-ray energies should correlate well. Small variations in efficiency would produce large differences in burst energy and reduce the correlation between burst energy and H α or soft X-ray energy. If the nature of the acceleration mechanism could be identified, burst energy could contribute to more detailed analyses of the distribution and redistribution of flare energy.

5. OTHER CONSIDERATIONS

Earlier in Figure 5, the integrated flux density spectra for several bursts was shown. The total energy transformed to radiation in the band from 600 to 8800 MHz was also given. Obviously this energy is highly dependent on the shape of the spectrum at the high frequency end because of the bandwidth term shown in equation 1. It is easy to see that when bursts which have the spectral maximum in the very short cm wavelength range, the integrated flux density spectral maximum considerably above 10,000 MHz and with a moderate slope in the high frequency direction (i.e., the spectrum not dropping off sharply), the burst energy from 600 to 35000 MHz can be easily 2 to 4 times that found in the 600-8800 MHz range.

While we have especially addressed burst energy in the centimeter band and have cited its application to the prediction of > 10 MeV proton flux, other parts of the radio spectrum and other times than during bursts should be considered for other applications. For example, extremely high A_p's on March 26 and April 1, 1977 were noted. We do not wish to imply a unique correlation between high A_p's and sporadic bursts or cm burst energy. The A_p may be high in association with bursts. It may also be high without bursts. In either case the disturbance causing the magnetic effect probably propagates radially from the sun. For the former case (with burst association) disk position of the flare/burst is not particularly important; i.e., a magnetic storm and a high A_p may occur when the flare/burst occurs at any visible solar disk position. A fairly broad cone of propagation of the causative shock wave seems essential. For the latter (no flare/burst), the source of the high A_p must originate from close to the central meridian of the sun. A more narrow cone of propagation is implied from data.

A radio signature (sometimes used) for recurrent magnetic storms is the noise storm energy in the 100 to 300 MHz range. The noise storm activity (not flare associated) lasts generally several days and for large A_p's may have a mean flux density of 50 to 100×10^{-22}

$\text{W m}^{-2}\text{Hz}^{-1}$ for 24 hours. This is equivalent to about 6 to 12×10^{22} Ergs. Such was measured April 1, 1976 when the A_p reached 107.

It is risky to invoke noise storm correlation quantitatively with sporadic events since it is still uncertain in how much meter wavelength radio noise is attenuated as a function of disk position. Nevertheless, an assumed attenuation of 3 dB for a reported noise storm flux of $46 \times 10^{-22} \text{ W m}^{-2}\text{Hz}^{-1}$ at 200 MHz on March 26 would easily yield a corrected energy in excess of that on 1 April - in coarse correlation with the A_p of 137 on March 26.

Acknowledgments

We wish to express our gratitude to D. F. Smart and M. A. Shea of AFGL and Murray Dryer of NOAA's Space Environment Laboratory for their encouragement in this area of research. We also acknowledge their help in discussions and research material furnished.

References

- Brown, J. C., The temperature structure of chromospheric flares heated by non-thermal electrons, Solar Phys., 31, 143, 1973.
- Castelli, J. P., J. Aarons, D. A. Guidice, and R. M. Straka, The solar radio patrol network of the USAF and its application, Proc. IEEE, 61, 1307, 1973.
- Castelli, J. A., and D. A. Guidice, Impact of current solar radio patrol observations, Vistas in Astronomy, Vol. 19, Pergamon Press, Oxford, 355, 1976.
- Castelli, J. P., and W. R. Barron, Highlights of solar radio data, 20 March - 5 May, 1976, Collected Data Reports for STIP Interval II 20 March-5 May 1976, Edited by H. E. Coffey and J. A. McKinnon, World Data Center A for Solar-Terrestrial Physics Report No. UAG-61, 39, 1977.
- Dryer, M., Interplanetary shock waves generated by solar flares, Space Science Reviews, 15, 403, 1974.
- Guidice, D. A., Sagamore Hill Radio Observatory, Bulletin of the AAS, Vol. 7, No. 1, 199, 1975.

Kahler, S. W., and R. W. Kreplin, The observation of non-thermal solar X-radiation in the energy Range $3 < E < 10$ Kev, Astrophys. J., 168, 531, 1971.

Lin, R. P., Fast electrons in small solar flares, Solar Gamma-, X-, and EUV Radiation, Edited by S. Kane, D. Reidel Publishing Company, Dordrecht, Holland, 385, 1975.

Marková, E., Energy content of flares in McMath Regions 14143 and 14179 (March 1976), Collected Data Reports for STIP Interval II 20 March-5 May 1976, Edited by H. E. Coffey and J. A. McKinnon, World Data Center A for Solar-Terrestrial Physics Report No. UAG-61, 35, 1977.

Pintér, S., and M. Dryer, On the solar-flare-generated coronal and interplanetary shock waves during August 2-13, 1972, Izvestia Akademii Nauk SSR, Series FIZ, Vol. 4, No. 9, 43, 1977.

Straka, R. A., and W. R. Barron, Multifrequency solar radio bursts as predictors for proton events, AGARD, Proc. of Symposium on Ionospheric Forecasting No. 49, 10-1, 1970.

Syrovat-skii, S. I., and O. P. Shmeleva, Heating of plasma by high-energy electrons and non-thermal X-ray emission in solar flares, Soviet Astronomy-AJ, 16, 273, 1972.

**Radio and Optical Evidence of
Mass Ejections From Solar Flares and
Solar Decametric Noise Storm Activity
During March 1976 (STIP Interval-II)**

A. Bhatnagar,* G. M. Ballabh, Rajmal Jain and S. S. Rao
Vedhshala (Udaipur Solar Observatory)
Ahmedabad-380013, India

R. V. Bhonsle and H. S. Sawant
Physical Research Laboratory
Ahmedabad-380009, India

Abstract

This paper describes time lapse H-alpha observations made at Udaipur Solar Observatory and solar radio emissions observed from the Physical Research Laboratory, Ahmedabad, during March 1976 (STIP Interval-II). Evidences are presented for mass ejections from flaring regions. Transverse velocity of propagation of disturbances was found to range from 200 to 500 km/s. A tendency for the flares and surges to occur in quick succession was observed. A moving wave with a speed of 500 km/s was observed associated with the flare on 26th March, but no type II radio bursts were reported accompanying this event. This may indicate that the shock wave detected from optical observations travelled predominantly in transverse direction. However, a few type IIIb, many type III bursts and a noise storm at

* Present address: Nehru Centre, Bombay-400018, India.

meter and decameter wavelengths were observed associated with the March 26 event. It is therefore concluded that only fast electrons escaped into the corona and not the flare-generated shock wave which was detected optically.

1. INTRODUCTION

This report is a result of analysis of observations obtained during the "Study of Travelling Interplanetary Phenomenon (STIP) Interval-II", from the Udaipur Solar Observatory located on an island in the Fatehsagar lake at Udaipur ($73^{\circ}8'E$, $24^{\circ}5'N$) and simultaneous radio observations from Physical Research Laboratory (PRL), Ahmedabad ($72^{\circ}6'E$, $23^{\circ}0'N$). The solar observatory has a 12-foot spar with a solar guider and two 6-inch refractors, one of which is being used for photographing full disk pictures of the sun in white light and the other for high resolution photography in H-alpha using, a $\frac{1}{2}$ R pass band birefringent filter built by Ramsey and Bhatnagar. Time lapse movies are regularly made for study of transient solar events. A study of such movies made during STIP Interval-II, has revealed interesting solar events on 21st, 22nd, 24th and 26th March, 1976. In particular on 26th March, a flare-generated wave disturbance was observed, which incidentally did not give rise to type II radio bursts. We report here the transient optical phenomena observed in McMath regions 14127 and 14143 during STIP Interval-II along with the corresponding radio observations. The radio observations were made at PRL, Ahmedabad, India, with the help of 35.2 - 34.2 MHz spectroscope, which has a time resolution of 10 ms, and a frequency resolution of 5 kHz, simultaneously in right-handed and left-handed circular polarizations. During this period a strong radio noise storm was in progress.

2. EVENTS OF 21ST MARCH 1976

In McMath region 14127 (N05, W32) a subflare occurred at 0836 UT near the preceding spot-A at position marked F1 in Figure 1. Following the subflare a dark filament D1 showed considerable activity and finally got disrupted. A bright surge starting near this spot-A was observed soon after the flare. Another surge was observed at 0324 UT near the spot-A in which the material moved swiftly along an arch and appeared to fall back around 0345 UT. In this case we did not observe any brightening at the feet of the falling surge material as is suggested by Hyder's (1967a,b) in fall-impact theory.

On the same day, Culgoora Observatory, Australia, reported type III bursts of intensity 1 in metric band from 0000 UT. It is also well known that type III bursts are closely associated with flares but some remote relation between type III bursts and surges can not be excluded (Svestka, 1976). The observed type III bursts therefore might have been caused by the flare-surge activity.

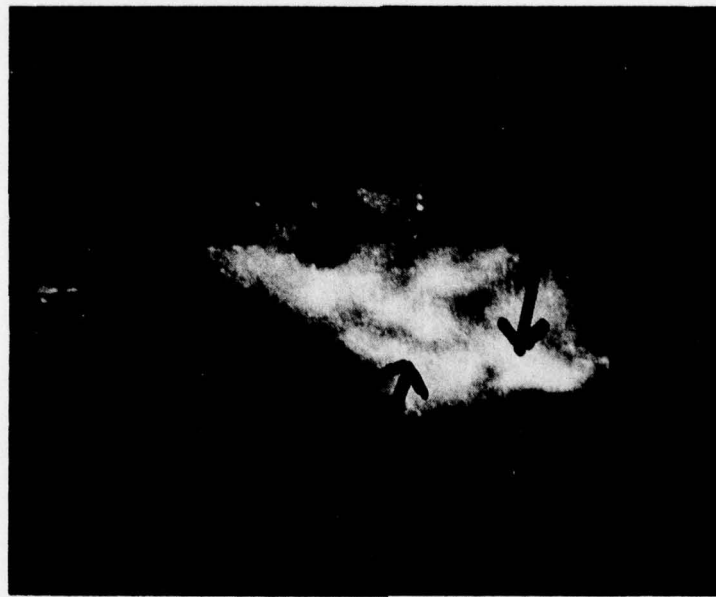


Figure 1. McMath region 14127 on 1976 March 21, showing the place of flare occurrence and the dark filament, which showed considerable activity.

3. EVENTS OF 22ND MARCH 1976

On 22nd March 1976, McMath region 14127 (N05, W43) was well developed with much activity giving rise to several surges, filament activity and a sequence of sub-flares. The first sub-flare observed at 0349 UT near F1, as shown in Figure 2, attained maximum at 0351 UT. During the rising phase of this flare a bright surge was seen ejected from the flaring region. After a minute another flare was seen in the same region. Just before and during the development of these flares a bright loop-like structure, slightly away, in the same plage region was seen forming, breaking-up and forming once again. At 0456 UT and 0509 UT two more flares were observed in the same region in quick succession.

A series of dark surges was observed starting near the feet of the bright loop-like structure indicated by BL in Figure 2. The trajectories of these surges appeared to be tangential to the bright loop but did not follow the close loop structure, this suggests that the surge material was thrown out along the open field lines. The velocities of these surges range from 40 to 150 km/s. Many observers have reported that surges have a strong recurrence tendency with a frequency of the order of one hour, to appear around the same place (Svestka, 1976). However, in this case we have observed much higher frequency of recurrence of surges from the same region.



Figure 2. McMath region 14127 on 1976 March 22, showing the bright loop, places of surge and flare occurrence.

Swarup et al. (1960) have shown that the probability of a fast radio drift burst increases, if the flare is followed by a surge. On 22nd March, the Physical Research Laboratory, Ahmedabad, reported groups of type III and IIIb bursts in decametric and metric bands between 0419 and 0722 UT. Culgoora Observatory, Australia, also reported metric noise storm activity on the same day. These type III & IIIb radio bursts correspond to the same period during which we have observed the flare-surge activity. As there was only one active region on the sun during this period, it is evident that these radio bursts were associated with the observed flare-surge activity.

4. EVENTS OF 24TH MARCH 1976

In the same McMath region 14127, which moved now close to the western limb of the sun (N06, W72), several sub-flares associated with mass ejections were observed. At 0343 UT a sub-flare occurred, which attained maximum phase at 0346 UT. Two more flares were observed in quick succession, at an interval of two minutes with maximum at 0347 and 0349 UT respectively.

Figure 3 shows the development of another flare in the same

DEVELOPMENT OF SOLAR FLARE
24 MARCH 1976

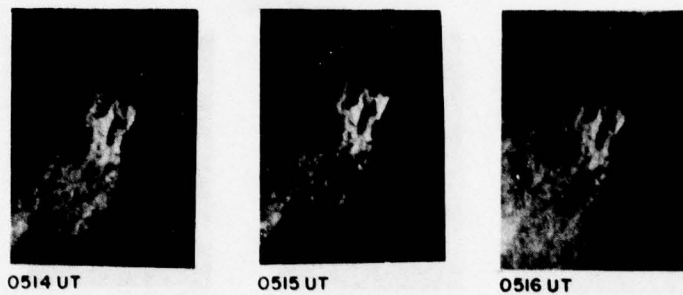


Figure 3. Development of solar flare in McMath region 14127 on 1976 March 24.

McMath region 14127 from 0514 to 0516 UT. After the flash phase (middle frame) part of the flare detached from the main body of the flare and disappeared very fast like a bright spray.

In Figure 4 is seen a small V-shaped loop along which the bright material moved and caused maximum brightness at the vertex of the loop. It appears that the vertex of this loop represents the region of the reconnection of the magnetic field lines. The brightness of the loop disappeared after a minute.

Type III and IIIb bursts in metric band were reported on this day between 0000 and 0357 UT, and were probably associated with the above observed flares. These flares excited the surge activity and ejected material from this active region with a velocity range of 150 - 200 km/s, similar to those occurred in the same region on 22nd March, 1976. No flare generated wave effects were detected and also no type II/IV radio bursts were reported.

5. EVENTS OF 26TH MARCH 1976

On 26th March the only region visible on the solar disk was McMath region 14143 (S07, E58). This region showed considerable activity involving filaments, surges and flares. During our

DEVELOPMENT OF SOLAR FLARE
24 MARCH 1976



Figure 4. Development of solar flare in McMath region 14127 on 1976 March 24.

observing period from 0240 to 1140 UT, three flares were observed at an interval of about an hour, many surges, bright knots of short duration and filament activity were also observed.

On the following side of the spot, nearby plage regions were observed to develop into bright knots. These bright knots soon joined together to give rise to the first flare which started at 0348 UT and attained maximum brightness at 0400 UT. This flare was followed by a bright surge from the same region. A second flare, which attained maximum brightness at 0718 UT and decayed around 0733 UT occurred at exactly the same place as the first flare. The development of this second flare along with the corresponding radio observations in right-handed and left-handed polarizations, made at PRL, Ahmedabad, are shown in Figure 5. The sequence of pictures in Figure 5, clearly show the formation, expansion and the decay phase of this flare. The maximum phase is indicated by the arrow.

The other flare which occurred towards the preceding side of the spot, and attained the maximum phase at 0832 UT was caused by joining of few bright knots which had developed along the filament. This flare is very interesting as it generated a travelling wave front disturbance which propagated outwards perhaps during the flash phase of the flare, with a velocity of about 500 km/s. The development of this flare and the wave phenomena is shown in Figure 6 through a sequence of pictures. The arrow in Figure 6 shows the travelling wave front. The wave front of this disturbance started in a radial sector of about 70° on the disk, around the flare region.

DEVELOPMENT OF SOLAR FLARE
AND ASSOCIATED TYPE III RADIO
EMISSION IN L & R POLARIZATION
MARCH 26, 1976

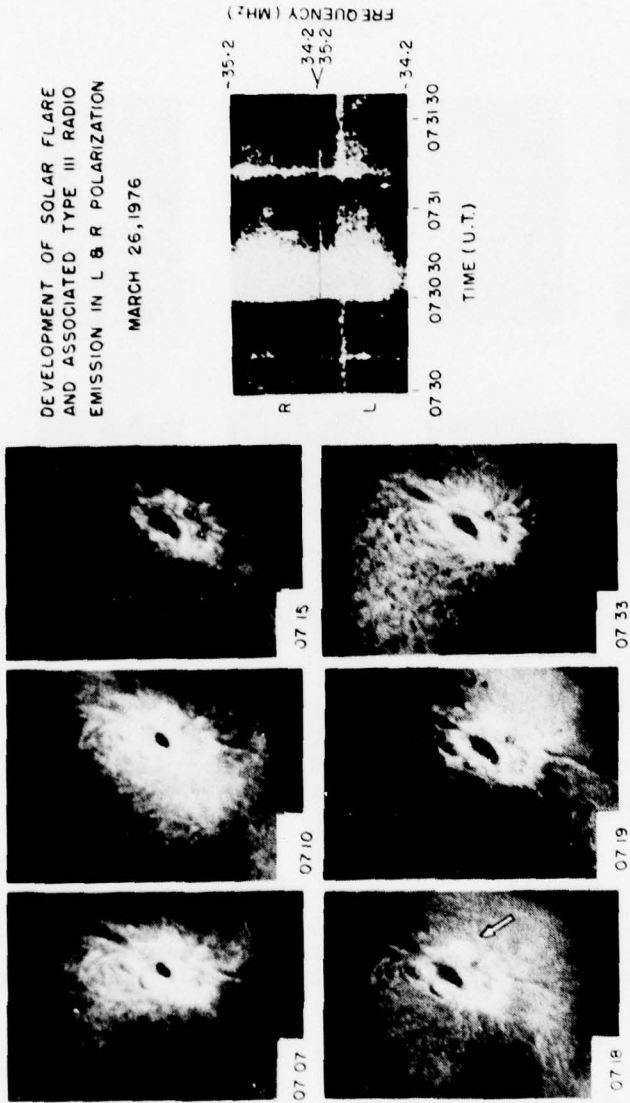


Figure 5. Development of solar flare and associated type III radio bursts in KCMa3 region 14143 on 1976 March 26.

DEVELOPMENT OF FLARE GENERATED WAVE
26 MARCH, 1976

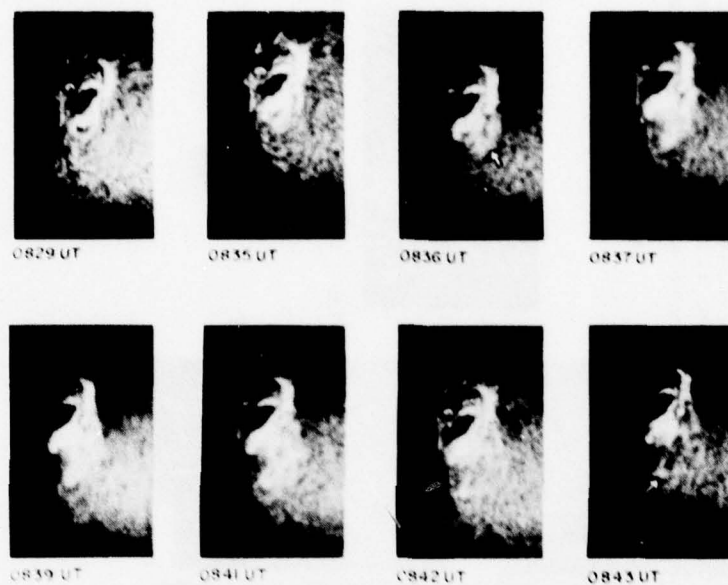


Figure 6. Development of flare generated wave disturbance in McMath region 14143 on 1976 March 26.

After moving some distance outwards this wave front channelled in two directions. Along one of these directions, at a distance of about 54,000 kms from the spot, the moving front caused a brightening shown in Figure 6. The other wave front simply faded out on the disk.

A major noise storm associated with this event was reported from PRL, Ahmedabad, India, and Culgoora Observatory, Australia, consisting of type I continuum, type III and type IIIb bursts at meter and decameter wavelengths, from 26th March to 2nd April 1976 (Sawant et al. 1976), but no type II/IV bursts were reported which are generally associated with such flare-triggered wave disturbances.

In particular on 26th March, 1976, most of the activity was of type IIIb bursts, a few isolated type IIIb and associated type IIIb-III bursts. Also Weissenau Radio Astronomy Observatory (F.R.G.) and

Dwingeloo Observatory (Netherlands) reported groups of type III and IIIb bursts between 0735.1 - 0735.4 UT, 0747.5 - 0748.1 UT, 0821 - 0930 UT, 0929.5 - 0930.5 UT and 0933.2 - 0933.3 UT, in metric band.

Incidentally type IIIb - type III activity associated with 0718 UT flare was also observed at PRL. This type IIIb burst was intense and unpolarized. On 26th March, type IIIb activity was also reported by the Culgoora observatory, extending up to 80 MHz. These evidences together with the noise storm suggest that these bursts are most likely to be "Off-fringe" type III bursts (Gergley and Kurdu, 1975). It is significant that the type IIIb burst was observed over the entire band from 80 MHz down to at least 34 MHz and was unpolarized. Therefore, it is felt, that this type IIIb burst might also be of "Off-fringe" type, since it meets all the criteria necessary for such identification as follows:-

- (i) Association of "Off-fringe" type IIIb bursts with a flare.
- (ii) Weak or no polarization, and
- (iii) Wide spectral range.

A positional information of these bursts (IIIb and III) might have been useful to verify this suggestion.

6. DISCUSSION

Observations on 21, 22 and 24 March, of surge activity associated with flares, indicate that the frequency of surge recurrence is about 15 minutes which is higher than the earlier estimates of the order of one hour.

If one considers the energetics of solar flares that give rise to interplanetary shock waves, more than half of the total energy is carried away by them in the interplanetary medium at least up to 1 AU (Hundhausen, 1972; Dryer, 1975). When one tries to identify an optical flare, responsible for interplanetary shock waves, the causal relationship is not always unambiguous, as it may happen that even a large H-alpha flare may not always produce such shock waves. It is well known that the ground-based radio observations of type II/IV bursts associated with an optical flare facilitates unambiguous identification of the flare responsible for the shock wave generation.

It is generally accepted that type II bursts are generated by plasma oscillations caused by the outward passage of MHD shock wave through the corona and type IV bursts by synchrotron mechanism of near-relativistic electrons trapped in a suitable magnetic field configuration.

Now according to our observations, we see that the H-alpha flare of 26th March, generated a shock wave. If this shock wave had travelled outward through the corona then type II bursts should have been observed, but in fact type II bursts were not observed on 26th March, as is evident from radio observations made at PRL, Ahmedabad. Failure

to observe type II bursts associated with this event, implies that the shock wave probably travelled predominantly in the transverse direction with a velocity of the order of 500 km/s in region of weak magnetic field. Hence it is concluded that only fast electrons escaped into the corona and not the flare-generated primary disturbance.

Acknowledgments

The authors express their gratitude to Professor K.R.Ramanathan for his keen interest in this work. The Vedhshala, Ahmedabad, gratefully acknowledges the financial support received from the Department of Science and Technology, Government of India, for this inter-institutional project. One of us (Rajmal Jain) is thankful to CSIR, New Delhi, India, for a Junior Research Fellowship. Solar radio astronomy programme at PRL, Ahmedabad is financially supported by the Department of Space, Government of India. Operational facilities provided by the Space Applications Centre, ISRO, Ahmedabad, for solar radio astronomy programme of PRL are highly appreciated.

References

- Dryer, M., Interplanetary shock waves: recent developments, Space Sci. Rev., 12, 277, 1975.
- Gergley, T.E., and M.R. Kundu, Decameter storm radiation, II, Solar Phys., 41, 163, 1975.
- Hundhausen, A.J., Coronal Expansion and Solar Wind, Springer-Verlag, New York, 1972.
- Hyder, C.L., A phenomenological model for disparities brusques followed by flare-like chromospheric brightening-I, Solar Phys., 2, 49, 1967a.
- Hyder, C.L., A phenomenological model for disparities brusques followed by flare-like chromospheric brightening-II, Solar Phys., 2, 267, 1967b.
- Sawant, H.S., R.V. Bhonsle, and S.K. Alurkar, Microscopic spectral features in solar decametric bursts and coronal irregularities, Solar Phys., 50, 481, 1976.
- Svestka, Z., Solar Flares, Geophysics and Astrophysics Monograms, Vol. 8, D. Reidel Publ. Co., 1976.
- Swarup, G., P.H. Stone and A. Maxwell, The association of solar radio bursts with flares and prominences, Astro. Phys. J., 131, 725, 1960.

**The Solar Wind During STIP II Interval:
Stream Structures, Boundaries, Shocks
and Other Features as Observed by
the Plasma Instruments on
Helios-1 and Helios-2**

R. Schwenn, H. Rosenbauer, and K. H. Mühlhäuser
Max-Planck-Institut für Physik und Astrophysik
Institut für extraterrestrische Physik
8046 Garching b. München, FRG

Abstract

The solar wind stream structure in early 1976, as observed from the Helios solar probes, was still governed by well developed high speed streams. The front of the big stream associated with the north polar coronal hole happened to be observed around day 74 (14 March) when Helios-1 (at 0.45 AU), Helios-2 (at 0.68 AU) and the earth were within a 15 degree-range of heliographic longitude. The spiral angle of the stream front can be determined without ambiguities caused by temporal or latitudinal effects. An usually sharp stream interface was observed in the same edge, but only from Helios-2. This discontinuity shows a density increase and a proton temperature decrease, both by a factor of three, and a velocity increase by 60 km/sec within only 40 seconds. The northern stream was observed again when Helios-2 was close to perihelion (at 0.29 AU). The whole course of observations now confirms that the boundaries between low and high speed streams inside 0.4 AU are characterized by speed gradients of the order of 100 km/sec per degree. The flare activity around April 1st resulted in several interplanetary shocks which could be detected from Helios-2 (10° west of the earth at 0.45 AU) but not at all from Helios-1 (at 90° west at 0.31 AU).

In this summary a brief survey is given on some important features of the solar wind during STIP II Interval as measured by the plasma instruments onboard the Helios solar probes (Rosenbauer, et al., 1977).

In Figure 1 the orbits of the Helios probes and the earth are given, showing that several line-up configurations occurred during STIP II Interval, specifically between Helios-1 and Helios-2, on day 69 (9 March) and day 124 (3 May), between Helios-1 and the earth, on day 74 (14 March), and between Helios-2 and the earth, on day 85 (25 March).

The solar wind stream structure in early 1976 was still governed by well-developed high speed streams (see Figures 2 and 3). They can readily be related to their probable sources, the coronal holes, as observed by means of white light coronagraphs (courtesy of R. T. Hansen, HAO, Boulder).

The existence of quite sharp latitudinal boundaries of high speed streams in the sun's equatorial regions (Schwenn, et al., 1976) could be confirmed. The favorable configuration of the Helios orbits (see Figure 1) caused a separation of the Helios probes with respect to both heliocentric longitude and latitude in the perihelion phase. The latitudinal boundaries of two different streams happened to be in such a location that the boundary could be observed from both sides, Helios-1

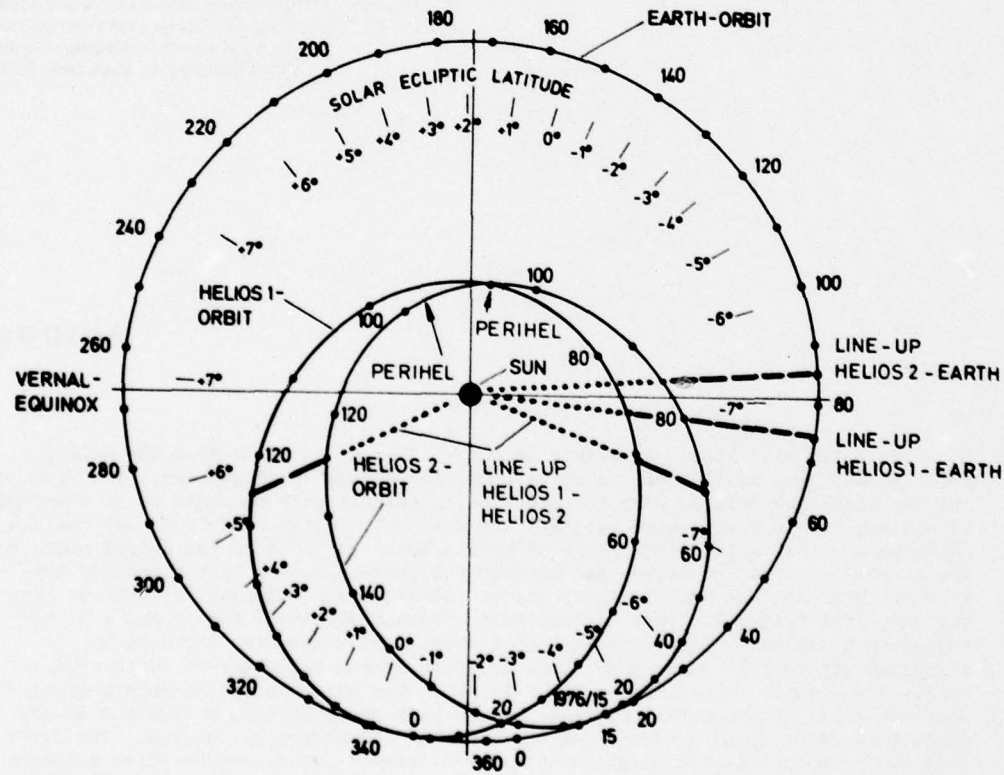


Figure 1. The orbits of Helios-1, Helios-2 and the earth around the sun in the first six months of 1976

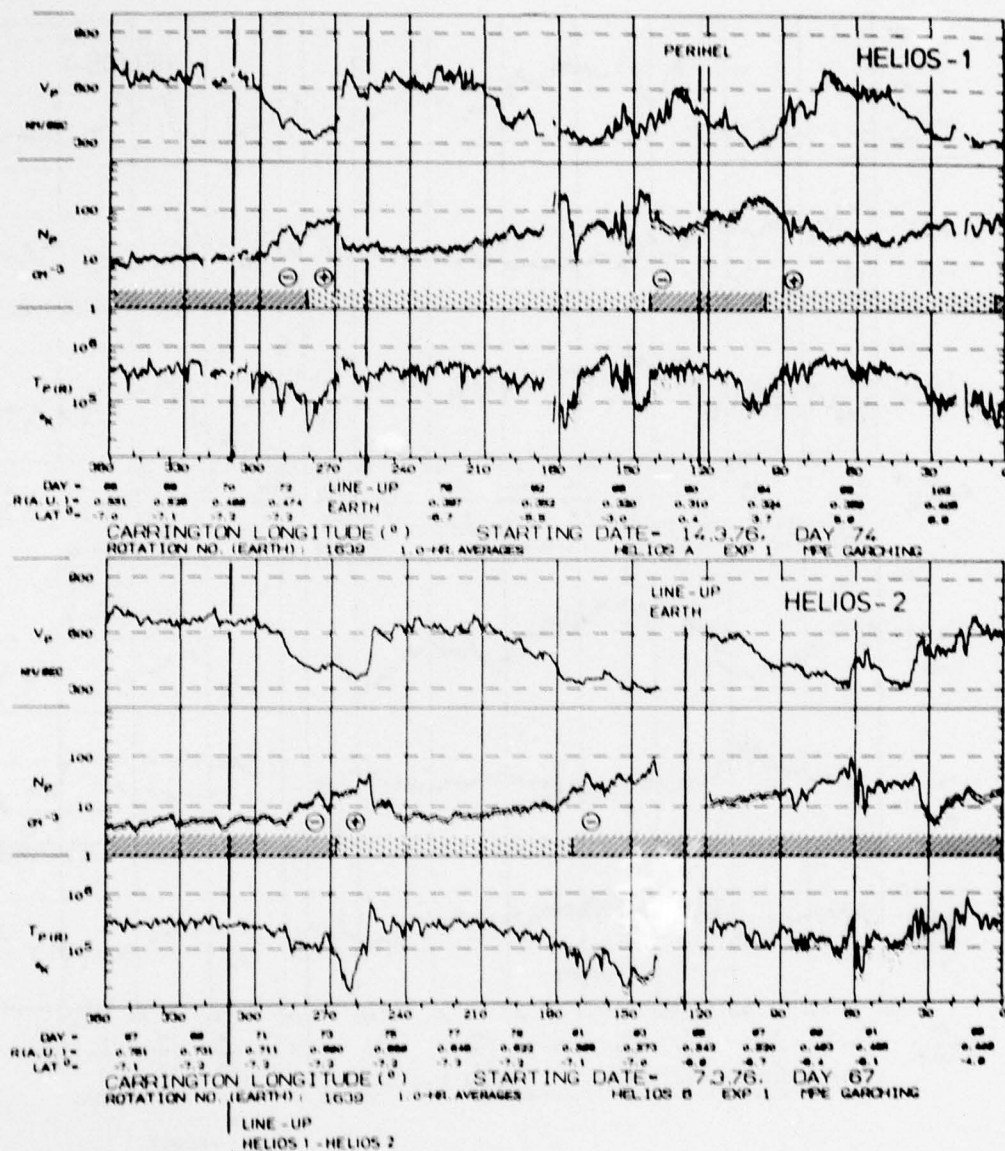


Figure 2. The solar wind proton bulk speed V_p , density n_p , and temperature T_p , plotted as one-hour averages, during Carrington rotation 1639 as measured from Helios-1 (upper panels) and Helios-2 (lower panels). The magnetic sectors as determined from preliminary magnetic field data (courtesy of F. M. Neubauer, TU Braunschweig) are indicated by different shadings for positive and negative polarities.

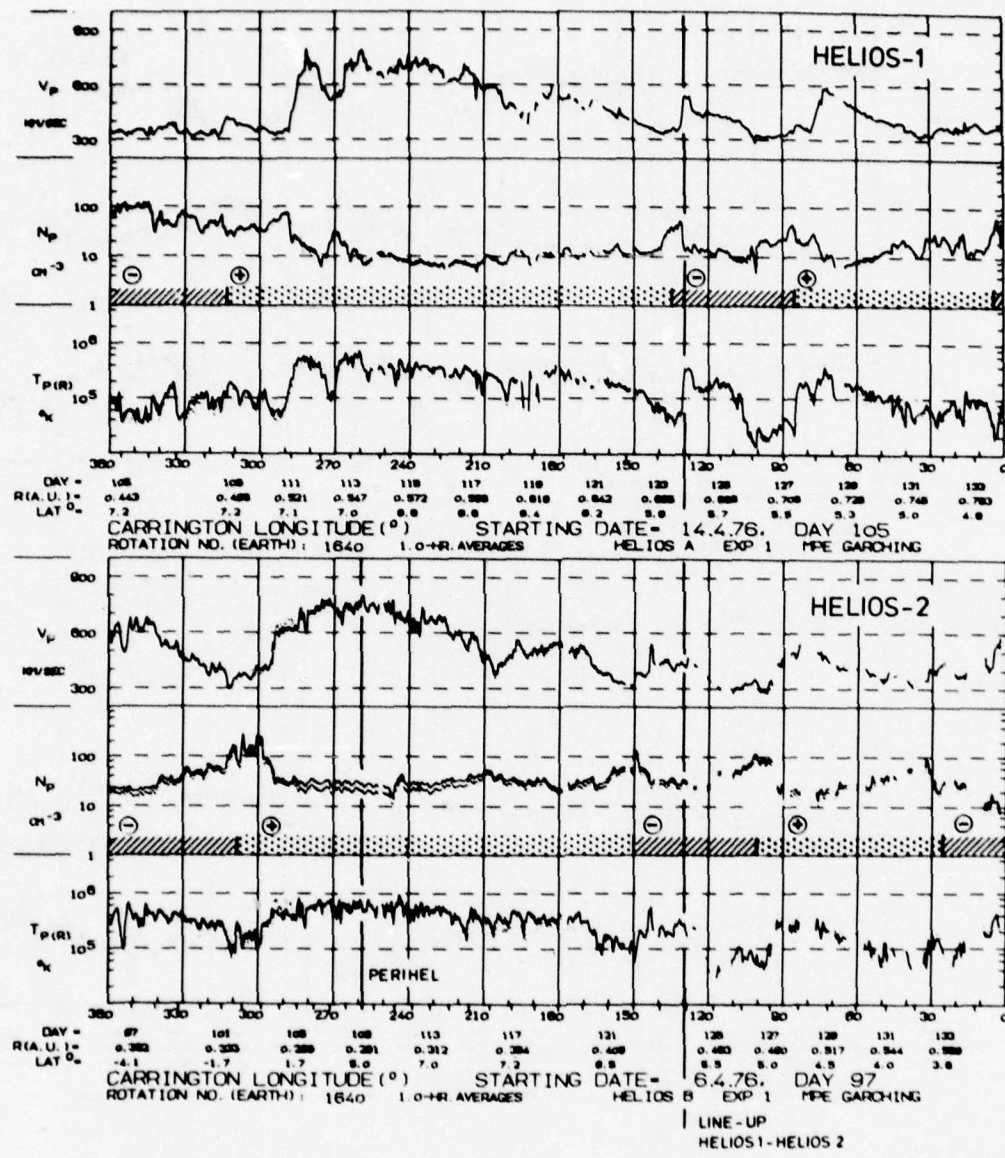


Figure 3. The solar wind proton bulk speed v_p , density n_p , and temperature T_p , plotted as one-hour averages, during Carrington rotation 1640 as measured from Helios-1 (upper panels) and Helios-2 (lower panels). The magnetic sectors as determined from preliminary magnetic field data (courtesy of F. M. Neubauer, TU Braunschweig) are indicated by different shadings for positive and negative polarities.

being "in" the stream and Helios-2 "out", and then vice versa. At the end of Carrington rotation number 1639 the two spacecraft, in addition to being on two sides of a stream boundary, were also on different sides of a magnetic sector boundary for about a quarter of a solar rotation.

In several cases when Helios-1 and Helios-2 were nearly lined up radially, the spiral angle of high speed stream fronts could be determined without ambiguities caused by temporal or latitudinal effects. Figure 4 shows what the stream front as measured from Helios-1 at 0.45 AU should look like when arriving at the location of Helios-2 at 0.67 AU, assuming a purely radial flow. The comparison to the actually

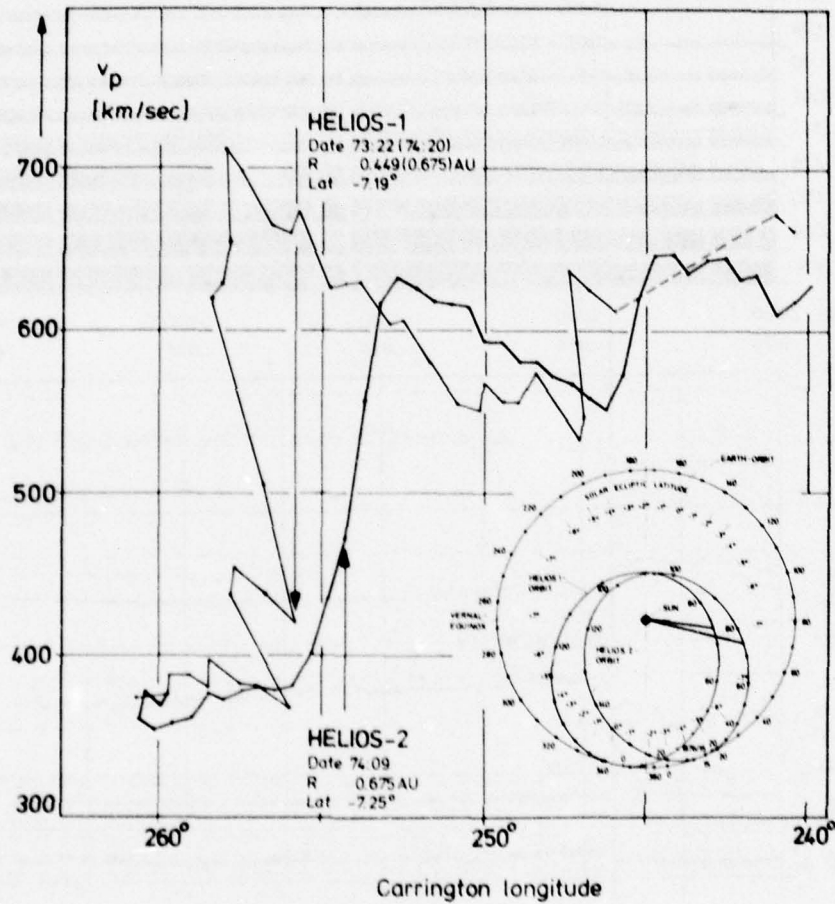


Figure 4. The speed profile of a high speed stream leading edge as measured directly from Helios-2 at 0.67 AU, is compared to a profile calculated from measurements of Helios-1 taken at 0.45 AU assuming a purely radial flow at the measured speed. (The speed values are given as one-hour averages.) The insert shows the locations of Helios-1 and Helios-2 on day 74 (14 March).

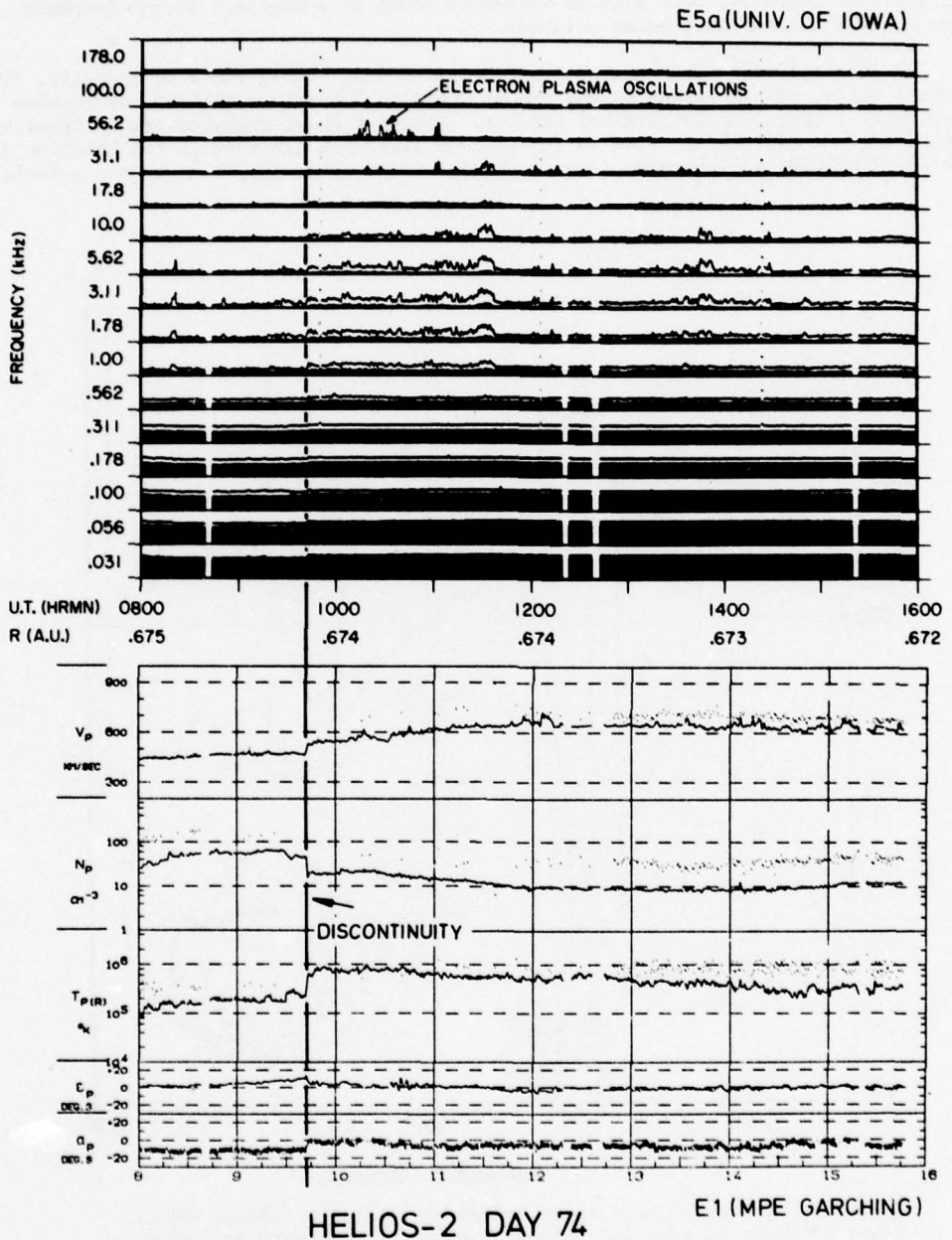


Figure 5. The high speed stream leading edge of day 74 (14 March) as observed in a finer time resolution. The unusually distinct discontinuity at 0942 UT is correlated to the onset of ion-acoustic waves (courtesy of D. A. Gurnett, University of Iowa).

measured stream at Helios-2 indicates an eastward deflection of the fast stream by 5° over a distance of 0.22 AU. Similar values were obtained in three more cases.

Figure 5 shows the stream edge as observed from Helios-2 on day 74 (14 March) at 0.67 AU in more detail. This stream-interface shows an unusually distinct discontinuity in all plasma parameters, associated with the onset of ion-acoustic wave activity as observed by the University of Iowa plasma-wave instrument (Gurnett and Anderson, 1977). The occurrence of a similar discontinuity within the same stream front at the location of Helios-1 could not be confirmed, because of a gap in the ground station coverage.

On day 91 (31 March) at 1146 UT a 1N-flare occurred on the sun at N07 W10 in McMath region 14143. The positions of Helios-1, Helios-2 and the earth as well as the longitudinal position of the flare are given in Figure 6. A strong interplanetary shock reached Helios-2 at 0.44 AU on day 92 (1 April) at 1325 UT (see Figure 7). The mean propagation speed was 720 km/sec, while the local shock speed, assuming a radial shock normal, was approximately 650 km/sec. A detailed analysis of the whole event, including the several discontinuities some hours later, will be performed when the final magnetic field data are available. At the location of Helios-1 (~70° West of Helios-2 at 0.32 AU) the solar wind remained undisturbed.

At 2048 UT on day 121 (30 April) a 2B-flare occurred at S08 W46 originating from the same region, 14179, albeit one solar rotation later (i.e. McMath region 14143 was re-numbered as 14179 for the second solar rotation of STIP II Interval). As illustrated in Figure 8, Helios-1 and Helios-2 were separated from the flare site by about 120° in longitude. No forward shock was observed. However, Figure 9

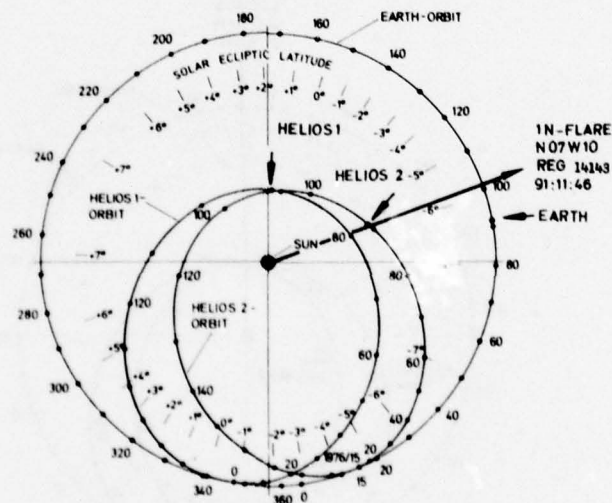


Figure 6. The locations of Helios-1, Helios-2, and the earth as well as the longitudinal position of the 1N-flare in McMath Region 14143 on day 91 (31 March).

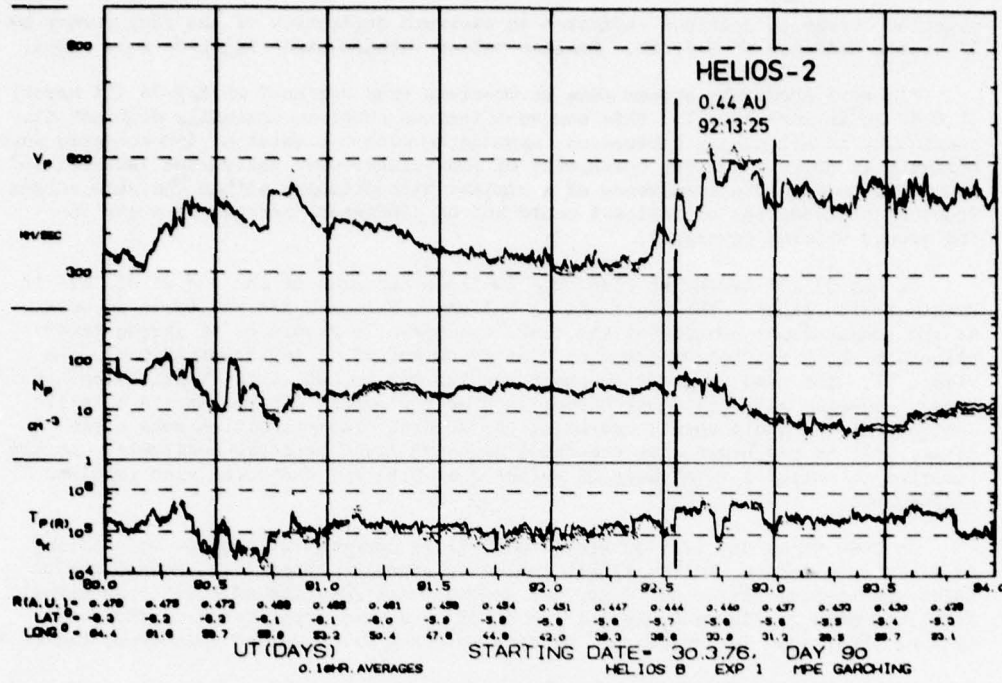


Figure 7. The solar wind proton parameters as measured from Helios-2, plotted as 10-minute averages, during the time period of the flare activity around 31 March.

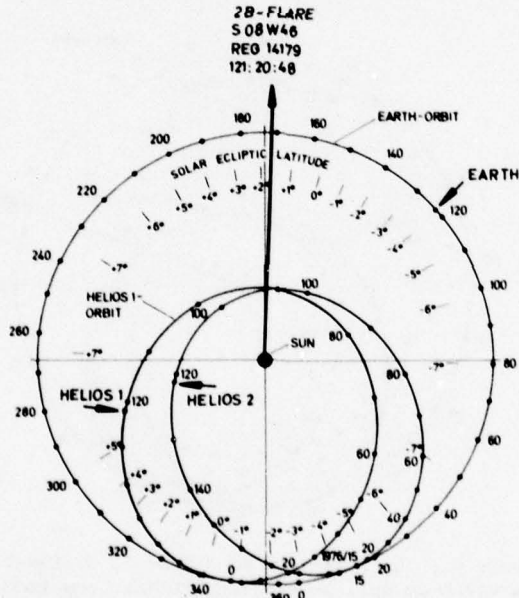


Figure 8. The locations of Helios-1, Helios-2, and the earth as well as the longitudinal position of the 2B-flare in McMath Region 14179 on day 121 (30 April).

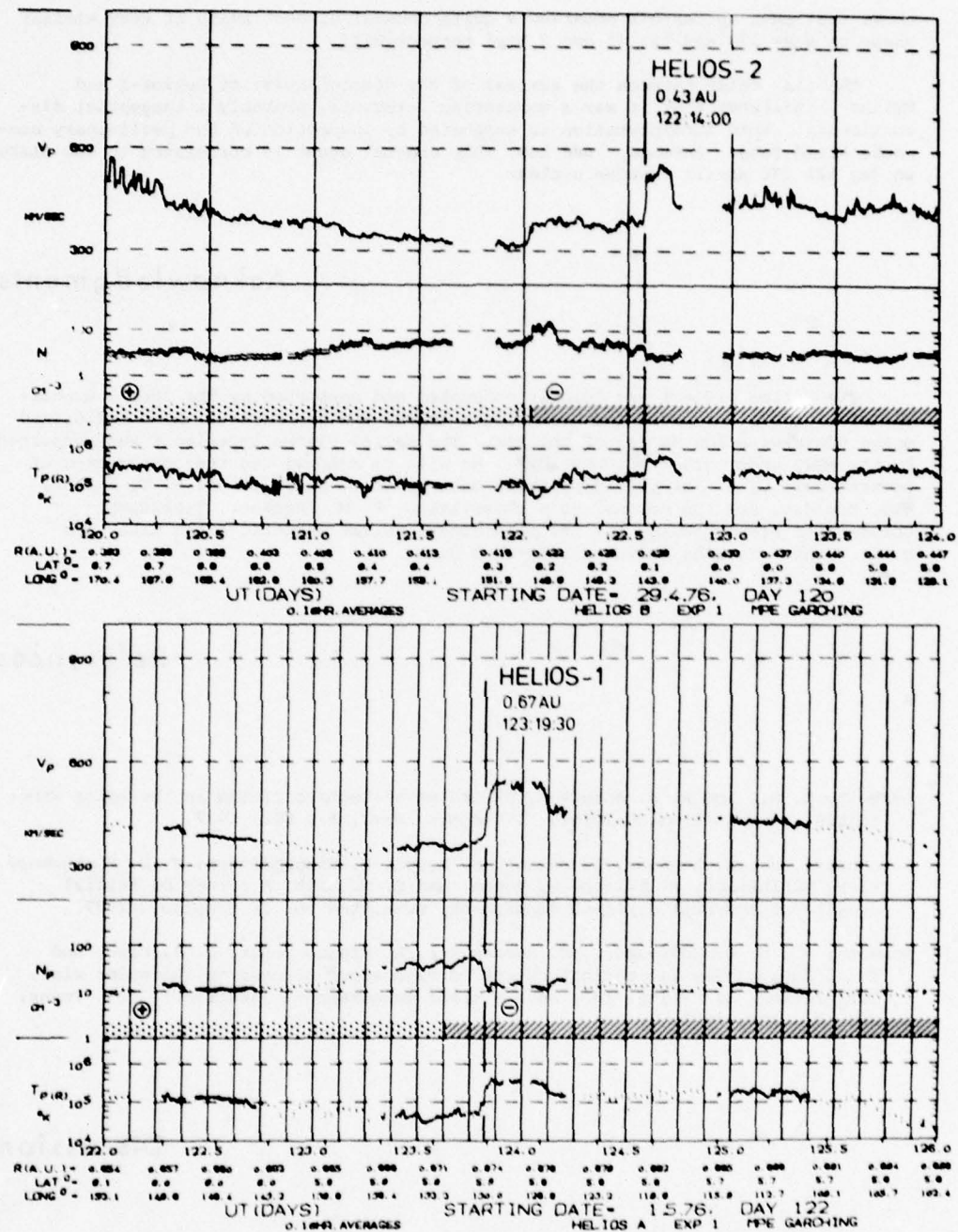


Figure 9. The solar wind proton parameters as measured from Helios-1 and Helios-2 (10-minute averages) showing the unusual discontinuities possibly related to the flare on day 121 (30 April).

shows that each spacecraft observed a quite unusual discontinuity of very similar shape on days 122 and 123 (1 and 2 May) respectively.

The time delay between the arrival of the discontinuity at Helios-1 and Helios-2 indicates that it was a corotating structure, probably a tangential discontinuity. This interpretation is supported by inspection of the preliminary magnetic field data. Whether, and how, this unusual event is correlated to the flare on day 121 (30 April) remains unclear.

Acknowledgments

The Helios project was jointly conducted and supported by the German Bundesministerium für Forschung und Technologie (BMFT) and the National Aeronautics and Space Administration (NASA) of the USA. The Helios plasma experiment was supported by the BMFT under grant No. WRS 10/7. We wish to acknowledge the cooperation of several colleagues for providing their data prior to publication: R. T. Hansen, HAO, Boulder, for the coronal hole observation, F. M. Neubauer, Technische Universität Braunschweig, for the preliminary Helios magnetic field data, and D. A. Gurnett for the Helios plasma-wave data.

References

- Gurnett, D. A., and R. R. Anderson, Plasma wave electric fields in the solar wind: Initial results from HELIOS-1, *J. Geophys. Res.*, 82, 632, 1977.
- Rosenbauer, H., R. Schwenn, E. Marsch, B. Meyer, H. Miggenrieder, M. D. Montgomery, K. H. Mühlhäuser, W. Pilipp, W. Voges, and S. M. Zink, A survey on initial results of the HELIOS plasma experiment, submitted to *J. Geophys.*, 1977.
- Schwenn, R., M. D. Montgomery, H. Rosenbauer, H. Miggenrieder, S. J. Bame, and R. H. Hansen, The latitudinal extent of high speed streams in the solar wind: Correlations of HELIOS, IMP, and K-Corona measurements (abstract), *EOS, Trans. AGU*, 57, 999, 1976.

Discussion

Alurkar: How good is the association between high velocity streams and coronal holes? Based on IPS observations these streams are not always seen to associate

with coronal holes.

Schwenn: The association of high speed streams as observed from Helios with coronal holes as derived from R. Hansen's (HAO) white light coronagraph measurements was always very close.

Villoresi: I think that the flare-associated event that you find to corotate can be explained by the corotative model of Forbush decreases - the relative positions of Helios-1 and Helios-2 with respect to the flare position may clarify this possibility.

Schwenn: Maybe. Note that the longitudinal separation of the flare site and both Helios space probes was very large, with one magnetic sector boundary in between.

Villoresi: You mentioned only three energetic flares occurring in the STIP II Interval. What happens in the solar wind data on the occurrence of the other flares?

Schwenn: (a) Helios-1 found some "turbulence" from day 82 to day 87 (22-27 March); a correlation to solar events has not yet been done. The flare of day 91 (31 March) did not at all show up in the Helios-1 plasma data.

(b) Helios-2 found no plasma response to flare activity until about day 90 (30 March). The events that followed have not yet been correlated since reliable magnetic field data are not yet available.

Dryer: Were the field components on each side of the tangential discontinuity parallel to each other?

Schwenn: Reliable magnetic field data are not yet available.

Dryer: Was there any azimuthal velocity change across the tangential discontinuity?

Schwenn: Yes.

Characteristic Features of Coronal Propagation as Derived From Solar Particle Observations by Helios 1 and 2 During STIP Interval II

H. Kunow, G. Wibberenz, G. Green, R. Müller-Mellin,
M. Witte, H. Hempe, and J. Fuckner
Institut für Reine und Angewandte Kernphysik
der Christian Albrechts Universität
Olshausenstr. 40 - 60
2300 Kiel, FRG

Abstract

On March 23 and 28, 1976, solar flares occurred in McMath region 14143. Energetic particles of these flares were observed by the University of Kiel experiments on board Helios 1 and 2 at distances less than 0.35 AU and 0.6 AU respectively. The first event showed a very long lasting decay of more than 10 days during which the complete coronal connection longitude range of 120° west to 40° east of the active region was covered by the 2 space probes. Temporal, longitudinal, and radial effects of the observed intensity time profiles of 4-13 MeV protons were separated resulting in an exponential decay time constant of 30 hours and an e-folding characteristic longitude of 40° for the coronal distribution. The March 28 event was observed only by Helios 2 at 65° off the flare site but not by Helios 1 at about 105° off. The effects of solar sector boundaries on coronal propagation are discussed.

I. INTRODUCTION

With the launch of Helios 2 on January 15, 1976, two solar probes Helios 1 and 2 scan the interplanetary medium with only relatively small separation in radius and heliographic longitude. Figure 1 shows both orbits relative to a fixed earth-sun line beginning with the launch day of Helios 2. The orbits of Helios 1 with a perihelion of 0.31 AU and Helios 2 with a perihelion of 0.29 AU are represented by dashed and solid lines. The circles denote the position of Helios 1 and Helios 2 respectively at times when major intensity enhancements were observed during the STIP Interval II by the University of Kiel cosmic ray experiments on board Helios 1 and Helios 2.

Both Helios instruments are identical and consist of 5 semiconductor detectors, one sapphire Cerenkov detector, and an anticoincidence scintillator. This allows observation of protons above 1.3 MeV heavier nuclei above 1.7 MeV/N, and electrons above 0.3 MeV up to relativistic energies. Further details of the instruments are given by Kunow et al. (1977a) and Kunow et al. (1975).

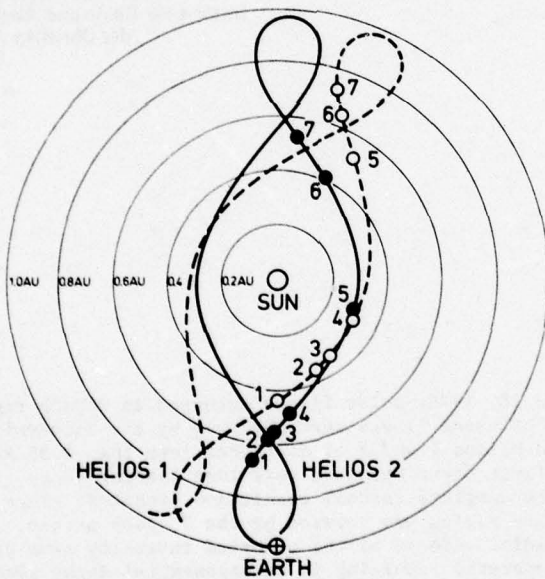


Figure 1. Orbits of Helios 1 and Helios 2 spacecraft relative to a fixed earth-sun line starting from the Helios 2 launch on January 15, 1976. Open and solid circles denote spacecraft positions at the times of major events during STIP Interval II.

2. SURVEY OF EVENTS DURING STIP INTERVAL II

A survey of the intensities as measured on board Helios 1 and 2 between March and May 1976 is presented in Figure 2. Hourly averaged intensities of electrons (E), alpha particles and heavier nuclei (A), and protons (P) of different energy intervals are shown. The corresponding logarithmic scales appear on alternate sides. The numbers labeling the different events correspond to the notation of the spacecraft positions in the orbit plot (Figure 1).

From the plots in Figure 2 the characteristics of each event can be read, e.g., maximum intensities, rise and decay time constants, coarse spectral information, and Helium or electron contributions. Events No. 1 and 5 have been identified as corotating events and will be discussed elsewhere (Kunow et al., 1977b). Most of the other events are prompt solar particle events originating from the same active region. Nevertheless their characteristics differ largely from one event to the other and between both space probes. This will be discussed in more detail by Witte et al. (1977).

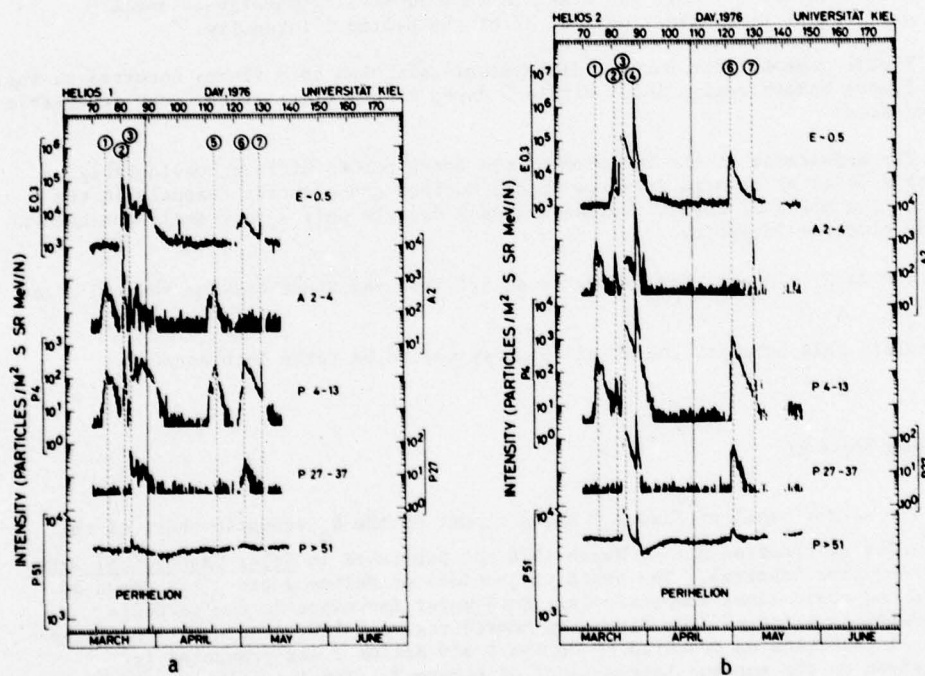


Figure 2. Survey of intensity time profiles during STIP Interval II (March-May 1976) measured by Helios 1 (a) and Helios 2 (b). The different panels show hourly averages of electrons (E) of about 0.5 MeV, alpha particles and heavier nuclei (A) of 2-4 MeV/N, and protons (P) of 4-13, 27-37, and > 51 MeV.

3. LATE MARCH 1976 EVENTS

3.1 Time Profiles

In the following we shall concentrate on the solar events on March 23 and 28, 1976, which are labeled 3 and 4 in Figure 2. We start the discussion of the intensity time profiles in late March with Helios 1 measurements. Both, the ~ 0.5 MeV electrons and the 4-13 MeV proton intensity show a very fast rise on March 23 which is followed by multiple peaks. These peaks are not associated with the flare in McMath region 14143 which occurred at 0837 UT on March 23 behind the east limb and shall be neglected for the purpose of this investigation.

The dominant feature is the very long decay phase. It starts in the proton profile on March 27 after the effects of some local interplanetary magnetic field disturbances on the previous day and lasts for more than 10 days. Helios 2 shows a similar profile: The maximum occurs on March 24, and is followed by a similar long decay of 10 days. However, sitting on top of the decay phase, the March 28 event exhibits very fast increases, and a decay time constant of about 6 hours in contrast to the underlying event. The increase coincides with a 1b flare in McMath region 14143. Note, that this event was not seen in any of the nucleon channels of Helios 1. Only the electron rate shows a comparatively small increase at that time with a peak of 2% of the Helios 2 intensity.

Please remember for further discussion: although both flares occurred in the same famous McMath region 14143 within 5 days, the particle events show remarkable differences:

1. The appearance at the location of the space probes differs considerably. Helios 2 observes a large increase in all nucleon and electron channels in the case of the March 28 event, whereas Helios 1 detects only a very small enhancement of the electron intensity.
2. The decay times differ by nearly an order of magnitude between the two major events.

To explain this behavior the solar topology has to be taken into account.

3.2 Solar Topology

The center panel of Figure 3 shows a part of the H_{α} synoptic chart of the solar disk as observed during March 1976 and published in Solar Geophysical Data (Comprehensive Reports). The orbit projections of Helios 1 and 2 are drawn by dashed and solid lines respectively. Both major increases in the particle intensities originated from flares in McMath region 14143. The hourly averaged proton intensities as measured by Helios 1 and Helios 2 are presented for comparison on the top and bottom panel of Figure 3. The intensities are shown versus Carrington longitude of the relevant magnetic field line connection point as first suggested by Nolte and Roelof (1973).

Let us first concentrate on the "fast" event on March 28, which was seen mainly by Helios 2. This spacecraft is connected to 110° Carrington longitude at the onset time with a distance of 65° to the flare site.

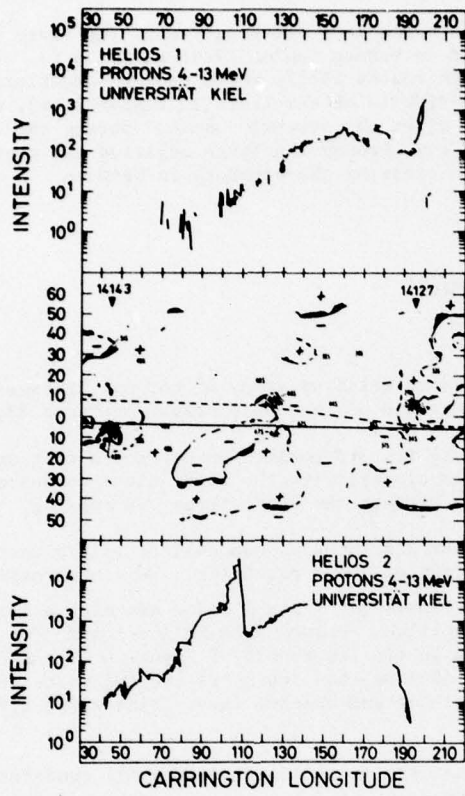


Figure 3. Center panel: H_{α} synoptic chart of the solar longitude range which was scanned by the Helios space probes between March 23, and April 5, 1976. Most particles originated from McMath region 14143. Upper and lower panel: 4-13 MeV proton intensities measured by Helios 1 and 2, and plotted at their calculated coronal connection longitudes.

The other probe, Helios 1, is only 40° behind at 150° . Both spacecraft are connected to areas of negative magnetic polarity, which seem to be connected.

However, from the Helios data we derive the following: A coronal sector boundary must run along the northern border of the negative area and across the bottleneck. This boundary is very efficient in preventing the particles from invasion into the adjacent areas; only 2% of the electrons managed somehow to enter the area across the sector boundary.

Furthermore, very effective loss processes are at work within this closed area containing the Helios 2 connection point, which account for the fast decay times. It seems possible that open field lines are responsible for the fast

evacuation of this area. The end of the decay coincides with the crossing of the north eastern boundary by Helios 2.

Let us now switch to the long decaying event. The flare being responsible for the long decay occurred in McMath region 14143 on March 23. Both spacecraft were at that time near McMath region 14127, which showed some flaring activity. As we consider here only the effects of the flare in region 14143, we neglected the period of about 2 days after the observed onset. During the long decay phase Helios 1 moved all the way through the large negative and positive areas without severe disturbance when crossing the boundary in between.

4. CORONAL PROPAGATION

Before starting a more detailed study of coronal propagation, the reader is reminded of the configuration of the space probes on March 23, 1976.

Helios 1 is close to its 3rd perihelion and moves fast as the event proceeds. Helios 2 at 0.6 AU moves slower, with the solar distance decreasing, and the longitudinal separation between the space probes increasing.

At those close solar distances we can neglect interplanetary scattering when discussing the propagation of solar particles. We can normalize the intensities obtained at various distances by Helios 1 and 2 assuming a $1/r^2$ dependence. The distance independent profiles, derived from Helios 1 and 2, i.e., the injection profiles, are presented in the lower part of Figure 4 versus Carrington longitude. With a time difference of more than 100 hours the two space probes sample the corona at the same longitude and observe intensities which differ by orders of magnitude.

This indicates, that the injection profile still contains temporal and longitudinal dependences.

Separation is possible if we assume the intensity to be proportional to a function of longitude times an exponential decay with time:

$$j(\phi, t) \sim F(\phi) \exp\left\{-\frac{t}{\tau}\right\}.$$

Comparison of intensities at the same longitude for a small number of samples between 142° and 111° results in a decay time constant

$$\tau = (30 \pm 3) \text{ hours.}$$

Since the slope of both profiles shows no significant changes we assume that the above time dependence is valid over the entire period. This allows the derivation of a coronal intensity profile at fixed times from the injection profiles. The upper part of Figure 4 shows, for a limited number of hourly averaged samples, the coronal intensity as a function of longitude for a fixed time 40 hours after the flare. Within the statistical uncertainties this method yields the same coronal intensities, no matter which spacecraft they were derived from. This supports the validity of our assumptions. Approaching the flare region we

observe a clear trend towards higher intensities in contrast to what we had observed before we eliminated the time dependence.

A fit by a straight line in this log-linear diagram suggests an exponential longitudinal dependence

$$F(\phi) \sim \exp \left\{ -\frac{\phi}{\phi_0} \right\}$$

with an e-folding characteristic longitude of

$$\phi_0 = (40 \pm 8)^\circ$$

for the range $160^\circ \dots 60^\circ$ Carrington longitude.

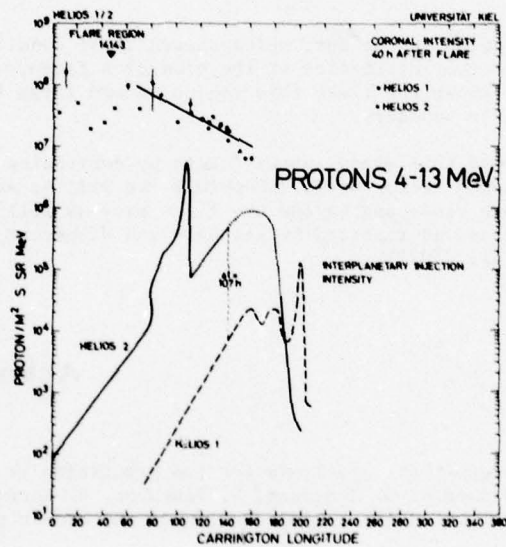


Figure 4. Distant independent intensities of 4-13 MeV protons, measured by Helios 1 and 2 and plotted at their calculated coronal connection longitudes. The lower curves, labeled interplanetary injection intensity, still contain the time dependences. The upper plot represents the estimated coronal intensities 40 hours after the flare.

Unfortunately the statistical uncertainties in the vicinity of the flare region became too large to decide from this small data sample whether a rarefaction region appears near the flare site and whether the slope changes beyond.

5. SUMMARY AND CONCLUSION

We described a very long lasting solar particle event with a smooth decay over 10 days and 120° longitude with both Helios space probes close to the sun. Clear separation of temporal and longitudinal effects was possible. The exponential decay time constant was 30 hours and the e-folding characteristic longitude $\phi_0 = 40^\circ$. ϕ_0 is larger than the previously reported values between 8° and 28° by Roelof et al. (1975), van Hollebeke et al. (1975), and Wibberenz (1976).

Both relatively large values of 30 hours and 40° imply a very effective particle transport through the corona, unobstructed by neutral lines or sector boundaries, and an efficient particle storage, e.g., due to mainly closed field lines.

We observed a region on the sun, which showed first conditions as described above but changed its characteristics at the time of a flare, which was about 60° off the flare site. After the flare this region showed large loss processes and a very effective sector boundary.

We hope to improve this study in the future by decreasing the statistical uncertainties by about a factor of 10. Hopefully we will be able to derive the latitudinal dependence close and beyond the flare site as well as to detect possible drift processes as reported by Reinhard and Wibberenz (1974), Roelof (1976), and Gold et al. (1977).

Acknowledgments

The authors express their gratitude for the permission to use Helios magnetic field and solar wind data of G. Mußmann, F. Neubauer, H. Rosenbauer, and R. Schwenn prior to publication for interpretation of the cosmic ray measurements.

References

Gold, R. E., E. P. Keath, E. C. Roelof, and R. Reinhard, Coronal structure of the April 10, 1969 solar flare particle event, 15th International Cosmic Ray Conference, Conference Papers, 5, 125, 1977.

Kunow, H., G. Wibberenz, G. Green, R. Müller-Mellin, M. Witte, and R. Hempe,

Raumfahrtforschung, 19, 253, 1975.

- Kunow, H., G. Wibberenz, G. Green, R. Müller-Mellin, M. Witte, H. Hempe, R. A. Mewaldt, E. C. Stone, and R. E. Vogt, Simultaneous observations of cosmic ray particles in a corotating interplanetary structure at different solar distances between 0.3 and 1 AU from Helios 1 and 2 and IMP 7 and 8, 15th International Cosmic Ray Conference, Conference Papers, 3, 227, 1977b.
- Kunow, H., M. Witte, G. Wibberenz, H. Hempe, R. Müller-Mellin, G. Green, B. Iwers, and J. Fuckner, to be published, J. Geophys. Res., 42, 1977a.
- Nolte, J. T., and E. C. Roelof, Large-scale structure of the interplanetary medium. I: High coronal source longitude of the quiet-time solar wind, Solar Phys., 33, 241, 1973.
- Reinhard, R., and G. Wibberenz, Propagation of flare protons in the solar atmosphere, Solar Phys., 36, 473, 1974.
- Roelof, E. C., Solar particle emission, in Physics of Solar Planetary Environments, Edited by Donald J. Williams, p. 214, American Geophysical Union, Washington, D.C., 1976.
- Roelof, E. C., R. E. Gold, S. M. Krimigis, A. S. Krieger, J. T. Nolte, P. S. McIntosh, A. J. Lazarus, and J. D. Sullivan, Relation of large-scale coronal X-ray structure and cosmic rays: 2. Coronal control of interplanetary injection of 300 keV protons, 14th International Cosmic Ray Conference, Conference Papers, 5, 1704, 1975.
- Van Hollebeke, M. A. I., L. S. MaSung, and F. B. McDonald, The variation of solar proton energy spectra and size distribution with heliolongitude, Solar Phys., 41, 189, 1975.
- Wibberenz, G., Coronal propagation: Variations with solar longitude and latitude, in Proceedings of the Symposium on the Study of the Sun and Interplanetary Medium in Three Dimensions, Edited by L. A. Fisk and W. I. Axford, p. 261, Goddard Space Flight Center, Greenbelt, Maryland (NASA X-660-76-53), 1976.
- Witte, M., H. Hempe, G. Green, H. Kunow, R. Müller-Mellin, and G. Wibberenz, Variation of alpha to proton ratios for solar events observed during STIP Interval II, Preprint: University of Kiel, Kiel, FRG, IFKKI 77/3, 1977.

**The Composition of
Low Energy Solar Cosmic Rays During
the Active Period March 76 - May 76**

M. Scholer, B. Klecker, and D. Hovestadt
Max-Planck-Institut für Physik und Astrophysik
Institut für extraterrestrische Physik
8046 Garching, FRG

G. Gloeckler
Department of Physics and Astronomy, University of Maryland
College Park, MD 20742, USA

C. Y. Fan
Department of Physics, University of Arizona
Tucson, AZ 85721, USA

Abstract

We have analyzed the low energy (> 0.6 MeV/nucl.) solar particle composition during the active period from March 1976 through May 1976. The measurements were made aboard the IMP 8 satellite near the earth orbit. Large variations of alpha particles, oxygen, carbon and iron ions have been measured from one event to the other within this active period. A corotating event has been tentatively identified and it has been found that the composition within this corotating event is changing with time.

I. INTRODUCTION

Recent measurements of the $Z > 2$ composition of solar particle fluxes in the lower energy range have shown that solar particle events do not represent a uniform and well-mixed sample of solar material. Composition measurements can therefore contribute in understanding the origin and/or acceleration processes of these particles.

Close to the last solar minimum a period of increased solar activity occurred between March and May 1976. We report in this paper measurements of protons, alpha particles and heavy particles obtained on board the IMP 8 spacecraft within this time period.

2. INSTRUMENTATION AND SATELLITE

The measurements were made with the ULET sensor and the Electrostatic Analyzer of the University of Maryland/Max-Planck-Institut experiment on board the earth-orbiting spacecraft IMP 8. The IMP 8 spacecraft achieved an elliptical orbit with a mean apogee of about 45 earth radii and a perigee of $\sim 28 R_E$, inclined 29° to the ecliptic. The ULET sensor is a three element dE/dx vs. E telescope with a geometrical factor of $0.53 \text{ cm}^2 \text{ ster}$, a $130 \mu\text{g}/\text{cm}^2$ flow through proportional counter, D1, as the ΔE element, a conventional surface barrier Au-Si detector, D2, as the total energy detector and a plastic scintillator anticoincidence cup, A, (Hovestadt and Vollmer, 1971). This design enables us, to obtain a unique identification of heavy particles of energies between 0.5 and 21 MeV/nucl. Every three hours the instrument is automatically switched between a low and high threshold mode of operation for counting and analyzing all elements or only nuclei heavier than helium, respectively. The Electrostatic Deflection Analyzer uniquely identifies low energy protons, alphas and heavy ions by simultaneously measuring the kinetic energy and amount of deflection of collimated incoming particles in a known electrostatic field. Energy per charge limits of the various counting rate channels are determined by the width and relative positions of the

rectangular solid state detectors which are also used to measure the particle kinetic energy (Fan et al., 1971).

3. RESULTS

The top panels of Figures 1 and 2 show ~3 hour averages of the D1 D2 coincidence rate in the low threshold mode for the time period Day 60 - Day 156, 1976, thus representing 0.43 - 1.50 MeV protons. There are at least eight well-defined intensity increases within this time period, which we have numbered 1 through 8 in the top panel of Figure 2.

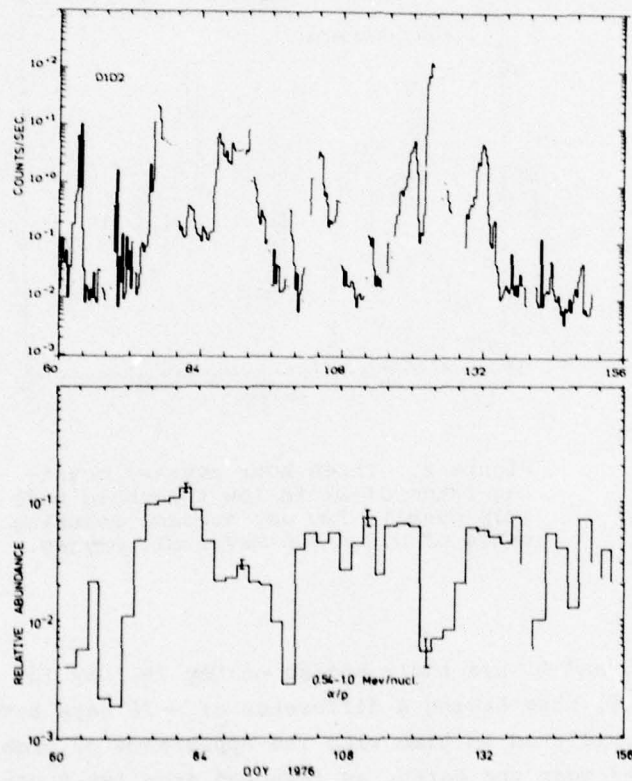


Figure 1. Three hour average counting rates D1 D2 in low threshold mode (top panel). Alpha particle to proton ratio at 0.54 - 1.0 MeV/nucl. (bottom panel).

The bottom panel of Figure 1 shows two day averages of the alpha particle to proton ratio at 0.54 - 1.0 MeV/nucl. In the bottom panel of Figure 2 we show two day average counting rates of 0.6 - 4.6 MeV/nucl. oxygen ions.

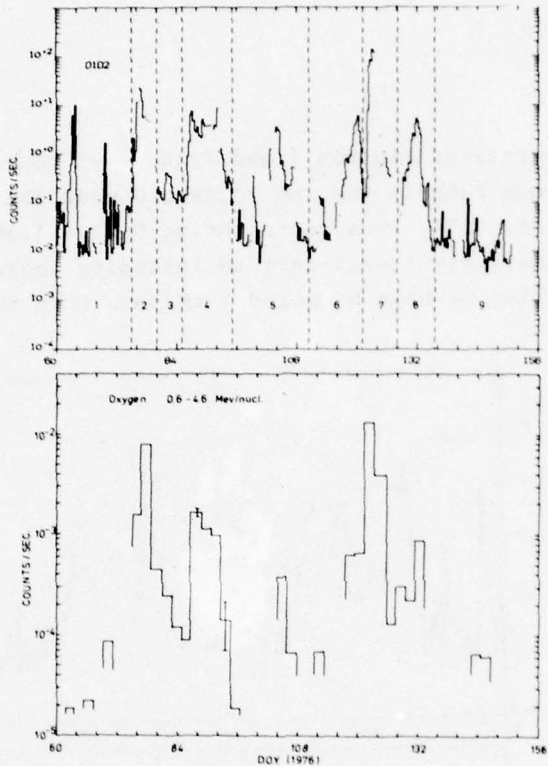


Figure 2. Three hour average counting rates D1 D2 in low threshold mode (top panel). Two day average counting rates of 0.6 - 4.6 MeV/nucl. oxygen.

Events 2, 5 and 8 have their maxima on Day 76, Day 104 and Day 132, respectively, thus having a difference of ~ 28 days between each other. They are correlated in time with the appearance of high velocity solar wind streams near the earth, as inferred from IMP 8 plasma measurements (W.C. Feldman, private communication). It is therefore very likely that these events are associated with the same corotating

interplanetary structure and can be classified as recurrent events. From Figure 1 it can be seen that the alpha to proton ratio is decreasing from event 2 to event 5 by about a factor two; it has about the same value during event 8 as during event 5. The change in oxygen content between event 2 and its reoccurrence as event 5 is more dramatic: As can be seen from the bottom panel of Figure 2 the oxygen counting rate changes by about a factor 20 and slightly increases again when the event reoccurs as event 8. This decrease by a factor 20 has, of course, to be compared with a decrease of a factor 5 in the proton count rate. Nevertheless, it seems that the composition is changing within the corotating event.

Table 1 shows relative abundances of the heavy ions carbon, oxygen, neon, magnesium, silicon and iron during events 1 to 8; i.e. we give an average abundance for each event during the time period indicated by the vertical bars in the top panel of Figure 2. It seems (at least for C/O and Fe/O) that the abundances do not change greatly from event 2 to event 8, so that we may say that in the corotating event the contribution of all heavy ions is decreasing.

Note the low Fe/O ratio during the corotating event (0.045 during event 2); low when compared with solar flare abundances: For a typical medium strong flare Hovestadt et al. (1973) report an Fe/O ratio of ~ 0.17 and during the event 7 the Fe/O ratio was as high as 0.31. The Fe abundance in the corotating event is, however, almost equal to the solar system abundance of 0.04 (Cameron, 1973) and the "best averaged" solar atmosphere value of 0.035 (Webber, 1975).

Event 7 shows the highest proton intensities during the time period under discussion. The event is probably the result of an importance 2B flare which occurred at 2048 UT, 1976 April 30 (Day 121) at W47. The location of this flare lies in the so-called "preferred connection region" (Van Hollebeke et al., 1975), which explains the extremely fast rise. As can be seen from Figure 1 the event exhibits a very small alpha particle to proton ratio (only $\sim 0.5\%$ alpha particles in the 0.54 - 1.0 MeV/nucl. energy range). The event shows also the highest oxygen count rate during the time period under discussion (Figure 2) and from Table 1 it can be seen that the event falls already into the "iron rich" category, i.e. the relative

Table 1. Relative abundances of heavy ions (C, O, Ne, Mg, Si and Fe) during 8 selected time periods as indicated in figure 2.

TIME NO	PERIOD D.O.Y.* (1976)	C / O		Ne / O		Mg / O		Si / O		Fe / O	
		0.6-3.4 MeV/nuc	1.-3.4 MeV/nuc	0.6-3.4 MeV/nuc	0.6-3.4 MeV/nuc						
1	60 - 75	< 0.35	0.33 ± 0.33	-	-	-	-	-	-	-	-
2	75 - 80	0.85 ± 0.09	0.23 ± 0.05	0.14 ± 0.04	0.044 ± 0.020	0.045 ± 0.015	-	-	-	-	-
3	80 - 85	0.85 ± 0.3	-	0.23 ± 0.18	0.19 ± 0.15	0.58 ± 0.23	-	-	-	-	-
4	85 - 95	0.69 ± 0.09	0.22 ± 0.05	0.10 ± 0.03	0.057 ± 0.026	0.15 ± 0.03	-	-	-	-	-
5	95 - 110	0.45 ± 0.45	-	-	-	-	-	-	-	-	-
6	110 - 121	0.75 ± 0.26	0.23 ± 0.18	0.23 ± 0.18	0.13	< 0.05	-	-	-	-	-
7	121 - 128	0.54 ± 0.09	0.075 ± 0.03	0.11 ± 0.04	0.10 ± 0.04	0.31 ± 0.06	-	-	-	-	-
8	128 - 135	0.68 ± 0.26	0.34 ± 0.23	< 0.06	0.11 ± 0.11	< 0.06	-	-	-	-	-

* D.O.Y. = Day of Year

abundance of iron is considerably increased as compared to the solar system abundance or "usual" flare abundance, respectively. Figure 3 shows the temporal profile in two energy ranges on an expanded time scale. Note that Figure 3 shows only the event 7 of Figure 2.

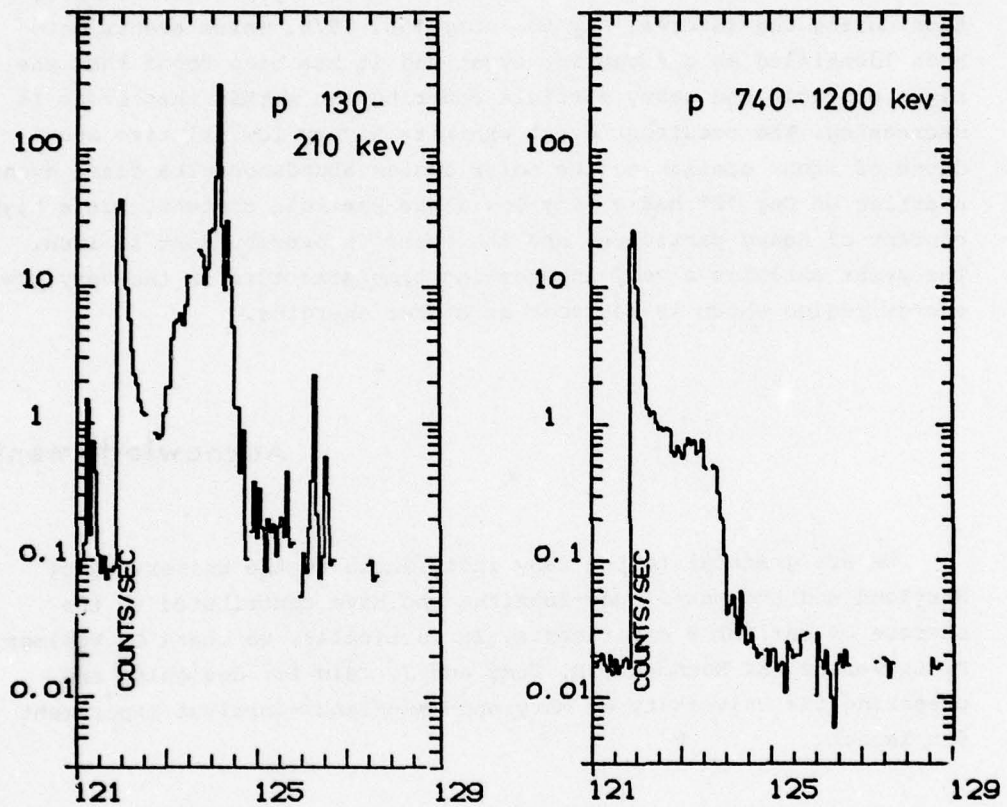


Figure 3. Variations of the 85 minute average counting rates of protons with time.

The hump starting on Day 123 is only seen in the lowest energy channel and may represent an ESP event: On May 2, 1829 UT (Day 123) a sudden commencement was observed (Solar Geophysical Data, July 1976).

4. SUMMARY

We have measured the proton, alpha and heavy particle composition during the interval Day 60 - Day 156, 1976. Three events have been identified as a recurrent event and it has been found that the alpha particle and heavy particle contribution within this event is decreasing. The recurrent event exhibits a very low relative abundance of iron, similar to the solar system abundance. The flare event starting on Day 121 has a very low alpha particle content, but a high content of heavy particles, and the event is overabundant in iron. The event exhibits a very interesting time structure in the very low energy region which is not seen at higher energies.

Acknowledgments

We are grateful to the many individuals at the University of Maryland and the Max-Planck-Institut who have contributed to the success of our IMP 8 experiments. In particular, we thank O. Vollmer, P. Laeverenz, E. Kuenneth, E. Tums and J. Cain for designing and preparing the University of Maryland-Max-Planck-Institut experiment for launch.

References

Cameron, A. G. W., Abundances of the elements in the solar system, Space Sci. Rev., 15, 121, 1973.

Fan, C. Y., G. Gloeckler, and E. Tums, An electrostatic detection vs. energy instrument for measuring interplanetary particles in the energy range 0.1 to ~ 3 MeV/charge, 12th International Conference on Cosmic Rays, Hobart, Conference Papers (University of Tasmania), 4, 1602, 1971.

Hovestadt, D., and O. Vollmer, A satellite experiment for detecting low energy heavy cosmic rays, 12th International Conference on Cosmic Rays, Hobart, Conference Papers (University of Tasmania), 4, 1608, 1971.

Hovestadt, D., O. Vollmer, G. Gloeckler, and C. Y. Fan, Measurement of elemental abundance of very low energy solar cosmic rays, 13th International Conference on Cosmic Rays, Conference Papers, 2, 1498, 1973.

Van Hollebeke, M. A. I., L. S. Ma Sung, and F. B. McDonald, The variation of solar proton energy spectra and size distribution with heliolongitude, Solar Phys., 41, 189, 1975.

Webber, W. R., Solar and galactic cosmic ray abundances - A comparison and some comments, 14th International Conference on Cosmic Rays, Conference Papers, 5, 1597, 1975.

Discussion

Dryer: Was that double-humped proton structure bounded by a forward and reverse shock?

Armstrong: Did you find velocity dispersion in the day 121 event? I think that the second spike of the day 121 event is shock spike plus ESP.

Scholer: In answer to both Dr. Dryer's and Dr. Armstrong's questions, the first spike on Day 121 in the low energy channels is due to penetrating protons ($E \geq 10$ MeV). It is therefore not possible to analyse the velocity dispersion from our data. The intensity of the 740 - 1200 keV protons decreases after the passage of the shock (as inferred from the SSC), whereas the second spike in the 130 - 210 keV appears ~ 10 hours after the SSC. This second spike may represent a magnetospheric burst event.

**The Time Behaviour of
the Galactic Cosmic Ray Intensity During
the Period, March 20-June 8 , 1976**

N. Iucci
Istituto di Fisica - Università
Piazzale delle Scienze, 5 - 00185 Rome, Italy

M. Parisi, M. Storini, and G. Villoresi
Laboratorio Plasma Spazio - C.N.R.
Istituto di Fisica - Università
Piazzale delle Scienze, 5 - 00185 Rome, Italy

Abstract

In the investigated period all the solar flares accompanied by Type IV radio-emission occur in the same solar active region which lasts for the three solar rotations under study. The cosmic-ray time behaviour, observed when the Earth is inside the portion of interplanetary space magnetically connected with this active region, is fully explained by means of the corotative model of Forbush decreases.

I. INTRODUCTION

In the interplanetary regions connected to solar zones where closed magnetic field structures and active regions exist, wide magnetic bottles, which produce Forbush decreases (Fds) on the cosmic ray (c. r.) intensity, may expand in the occasion of solar flares (s. f.) accompanied by Type IV radio emission extended in frequency from micrometric to metric wavelengths. The front of the bottle advances radially and the base, being connected to the Sun, corotates. By studying all the c. r. Fd-events and all the Type IV s. f. in the period 1957-1969 this simple model has been confirmed (Iucci et al., 1977a) and the event to event differences of the basic parameters of the Fds (Sun-Earth transit time of the perturbation, Fd-amplitude, recovery time) have been interpreted in terms of the energy involved in the radio emission and of the s. f. heliolongitude. In Figure 1 a sketch of the structure of a magnetic bottle generated by a Type IV s. f. is shown. The magnetic field configuration inside the modulated region will depend on the relative locations of the two polarities of the active region: when they lie about on the same latitude, both will be observed in the ecliptic plane, while, when the heliolatitudes of the sunspot polarities are much different, only the polarity nearest to the ecliptic plane will be observed.

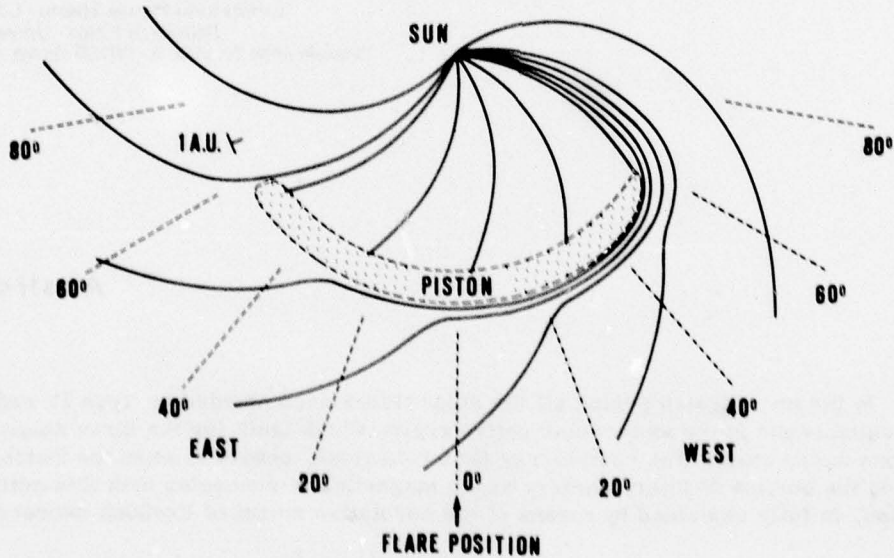


Figure 1. Sketch in the Ecliptic Plane of the Magnetic Configuration of the Perturbation Produced by a Type IV s. f.. The field inside the piston is inclined with respect to the ecliptic plane in a way depending on the locations of the magnetic polarities in the active region.

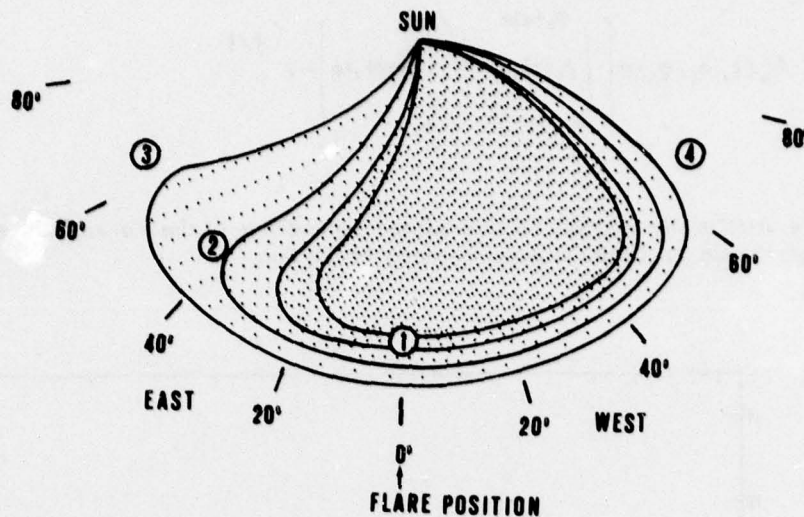


Figure 2. Sketch of the c.r. Density Distribution Inside a Typical Fd-region. The darkest shading indicates the lowest density. Four different positions of the Earth are indicated.

The c.r. depression inside the bottle is given in Figure 2 and it is derived mainly from the average dependence of the Fd-amplitude upon the s.f. heliolongitude (see Figure 3). The longitudinal extent of the bottle depends on the energy of the Type IV s.f. and on the dimensions of the interstream regions (regions not occupied by fast streams produced by coronal holes) (Iucci et al., 1977c), and it has been found to encompass as an average $\approx 130^\circ$ in the period 1957-1969 in which broad fast streams were seldom observed. Inside this bottle the region of maximum c.r. modulation (core) extends for $\approx 70^\circ$ and it is shifted towards the leading edge of the perturbation. The maximum c.r. depression inside the "core" at the Earth's orbit is found to be linearly correlated with the average velocity \bar{v}_f of the front of the perturbation from the Sun to the Earth's orbit:

$$\Delta I/I = 1.15 \times 10^{-2} (\bar{v}_f - 400) \quad (1)$$

where \bar{v}_f is given in km/sec and $\Delta I/I$ in percent.

The c.r. intensity recovers inside the bottle with a time constant $\tau \approx 10$ days; for a Fd observed at the Earth the recovery behaviour will depend on τ and on the longitudinal displacement of the Earth inside the magnetic bottle, therefore for s.f. occurring in the heliolongitude interval (ϕ_1, ϕ_2) it can be written as:

$$A_N(t, \phi_1, \phi_2) = \left[\int_{\phi_1 + \Omega t}^{\phi_2 + \Omega t} A(\phi) d\phi \right] / \left[\int_{\phi_1}^{\phi_2} A(\phi) d\phi \right] \times e^{-t/\tau} \quad (2)$$

where $A(\phi)$ is the average heliolongitude dependence of the Fd-amplitude shown in Figure 3 and Ω is the angular velocity of the Sun.

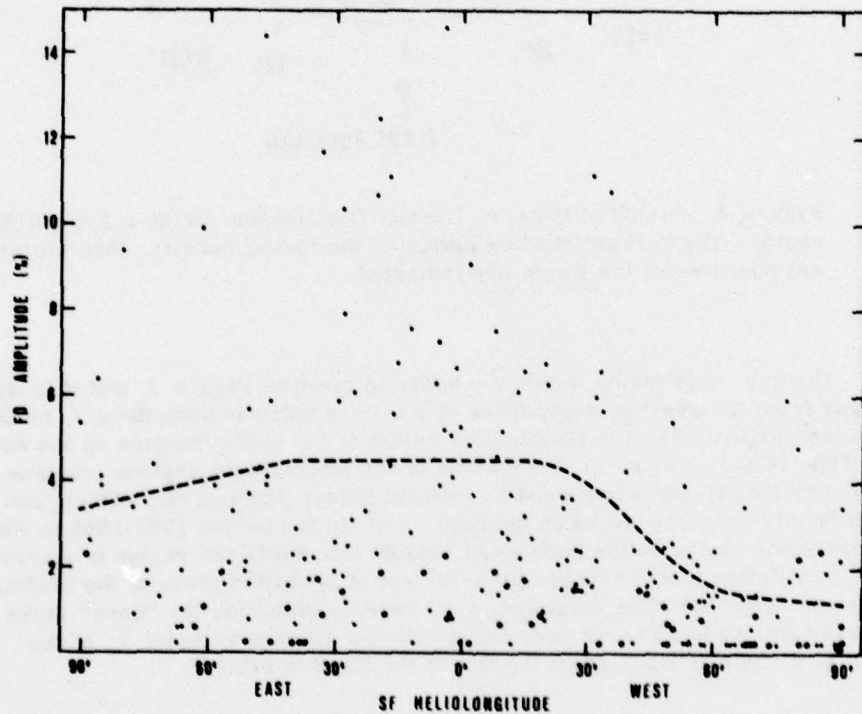


Figure 3. The Fd-amplitude versus the Heliolongitude of the Parent Type IV s.f.. The average behaviour is also reported (dashed curve).

In Figure 4 the average time behaviours of Fds associated with Type IV s.f. in four different heliolongitude intervals are compared with those computed by Eq. (2).

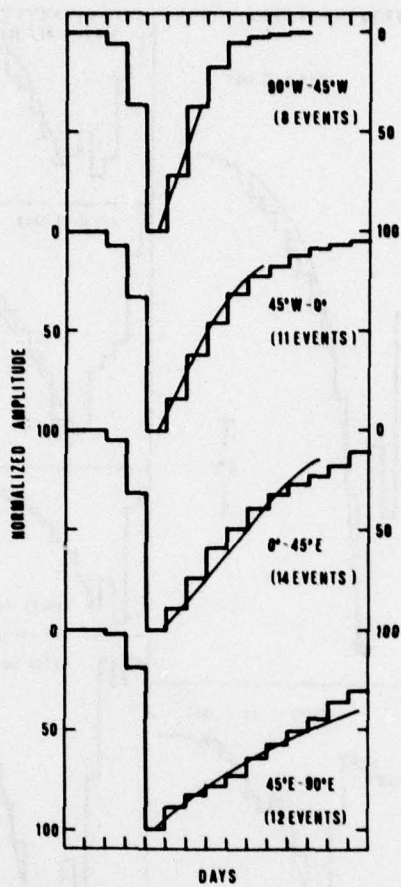


Figure 4. The Average Normalized Time Behaviours of Fds for Different Heliolongitude Intervals of the Associated Type IV s.f.. For 45° E- 90° E the exponential recovery ($\tau = 11$ days) best fitting the first five days (Earth inside the "core") is reported. For the other intervals the expected behaviours (see Eq.(2)) are reported (full curves).

When successive Type IV s.f. occur in the same active region, they depress the c.r. intensity in subsequent steps inside the same region corotating with the Sun, so that the recovery of such a set of Fds towards the unperturbed c.r. level depends only on the heliolongitude of the last Type IV burst which produces Fd. In Figure 5 some examples of series of Fds associated with the same active region are shown together with the recoveries computed by Eq. (2).

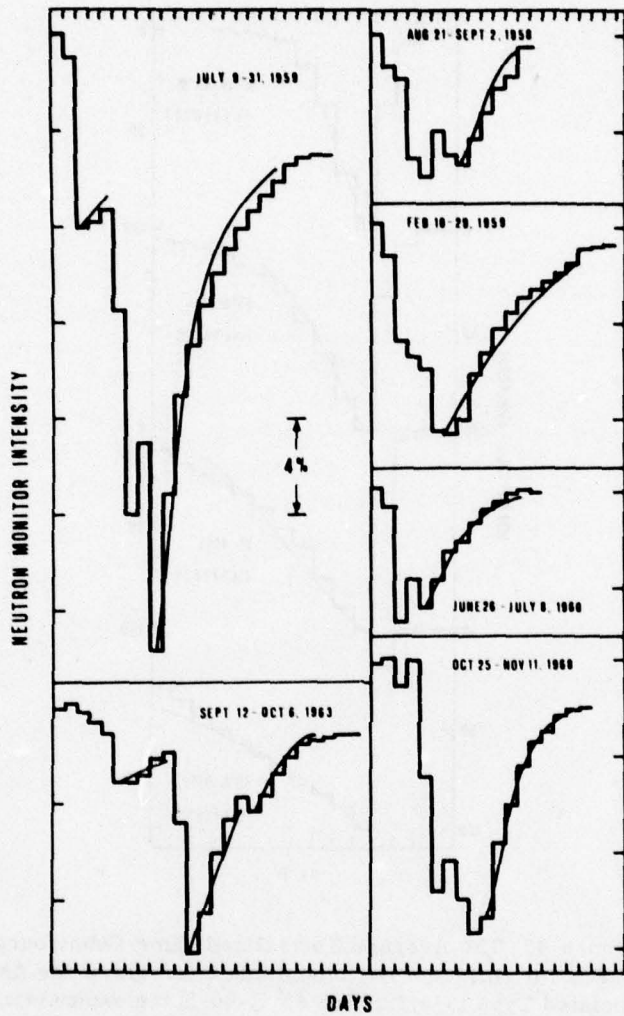


Figure 5. Series of Fds produced by the Same Active Region. The full lines are computed by Eq. (2).

Moreover, when a Type IV s.f. occurs beyond the East limb of the Sun, a Fd will be observed at the Earth when the leading edge of the modulated region reaches the Earth after a proper corotation time. On this line it has been found that nearly all the Fd-events not associated with Type IV s.f. in the visible hemisphere of the Sun, with amplitude $\geq 1.5\%$ at high-latitude neutron monitors, can be produced by Type IV s.f. occurring in the invisible hemisphere, as indicated by the amplitude distribution of these Fds and their average time profile.

This corotative model of Fds has been found to be consistent with what is observed in the solar wind, in the interplanetary magnetic field data and with the locations of the magnetic polarities in the parent active regions, for the few events for which the interplanetary data were available and the magnetic fields of the active regions showed a simple configuration (Iucci et al., 1977b). As an example the July 1968 events as observed in the c. r. intensity at high latitude and in the interplanetary magnetic field data near the Earth (SAT) (King, 1975) and at Pioneer 8 (P8) (Mariani et al., 1971) are reported in Figure 6. The perturbation produced by the Type IV s.f. occurring on July 5 at E89 is observed at P8, which is located at 13° East relative to the Sun-Earth line, one day earlier than the Earth, this suggesting that the leading edge of the modulated region envelopes P8 and the Earth successively. For the second perturbation (Type IV s.f. at E58), the radially advancing front envelopes P8 and the Earth at about the same time. The size of the magnetic bottle associated with this active region can be then estimated $\approx 140^\circ$ which is in agreement with the time spent by the Earth inside the modulated region (≈ 10 days). Moreover the magnetic polarities of the active regions, which lie on the same latitude, are observed successively in the interplanetary magnetic field data inside the bottle.

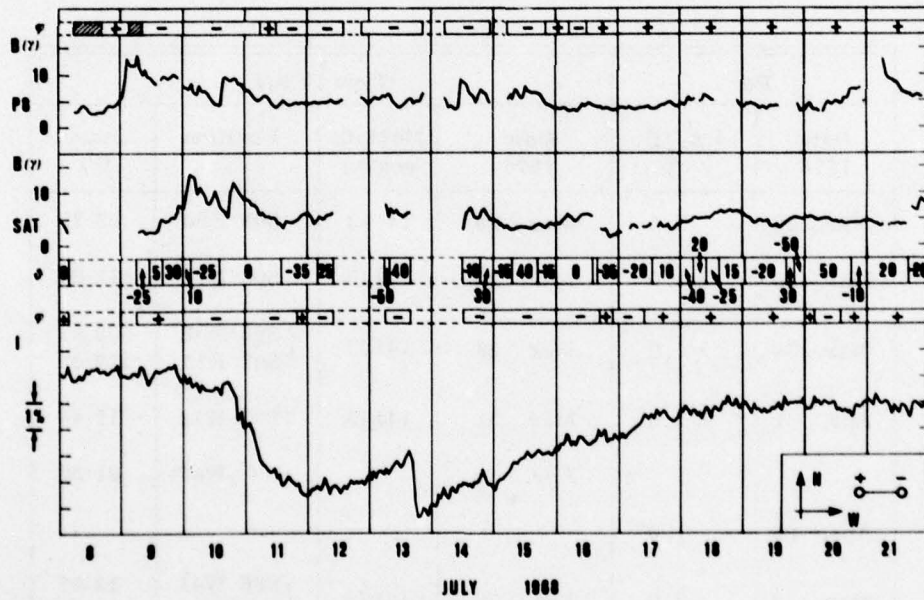


Figure 6. The Forbush Decrease of July 1968. Solar flares in McMath region 9503 accompanied by Type IV emissions occurred on July 6 (at N13, E89), July 8 (at N13, E58) and July 9 (at N13, E40). The interplanetary magnetic field at Pioneer 8 (indicated by P8) and near the earth (indicated by SAT) are shown on the top of the figure.

This corotative model of Fds is here applied to the events associated with the long-living McMath region 14143 in the period March 20-June 8, 1976.

2. ANALYSIS

In the period under study all the Type IV s.f. are produced by the same active region; the list of the Type IV s.f. widely extended in frequency (Solar Geophysical Data, 1976) and Fds associative with this active region are reported in Table 1. The Fd-amplitudes are determined from the daily intensities of the Deep River neutron monitor data (Solar Geophysical Data, 1976); for events occurring during the recovery phase of preceding Fds a tentative correction is applied. The hourly intensities for the Deep River and Rome NM-64 are plotted in Figure 7 and 8 respectively.

Table 1. Forbush Decreases and Type IV Solar Flares

Fd		Type IV s.f.			
Date 1976	($\Delta I/I$) %	Date 1976	McMath region	Position	Start UT
Mar. 26	2.5	Mar. 23	14143	S05 E90	08 37
Mar. 28	≈ 1.0	Mar. 25	14143	S06 E75	<12 03
Mar. 30	≈ 3.0	Mar. 28	14143	{ S08 E31 S07 E28	<09 22 <19 05
Apr. 1	≈ 1.5	Mar. 31	14143	S07 W12	11 44
		Apr. 5		(\approx W80)	21 50
Apr. 26	1.0				
May 2	2.0	Apr. 30	14179	{ S06 W41 S09 W47	12 43 20 48
		May 1	14179	S08 W61	21 55
May 21	2.0				

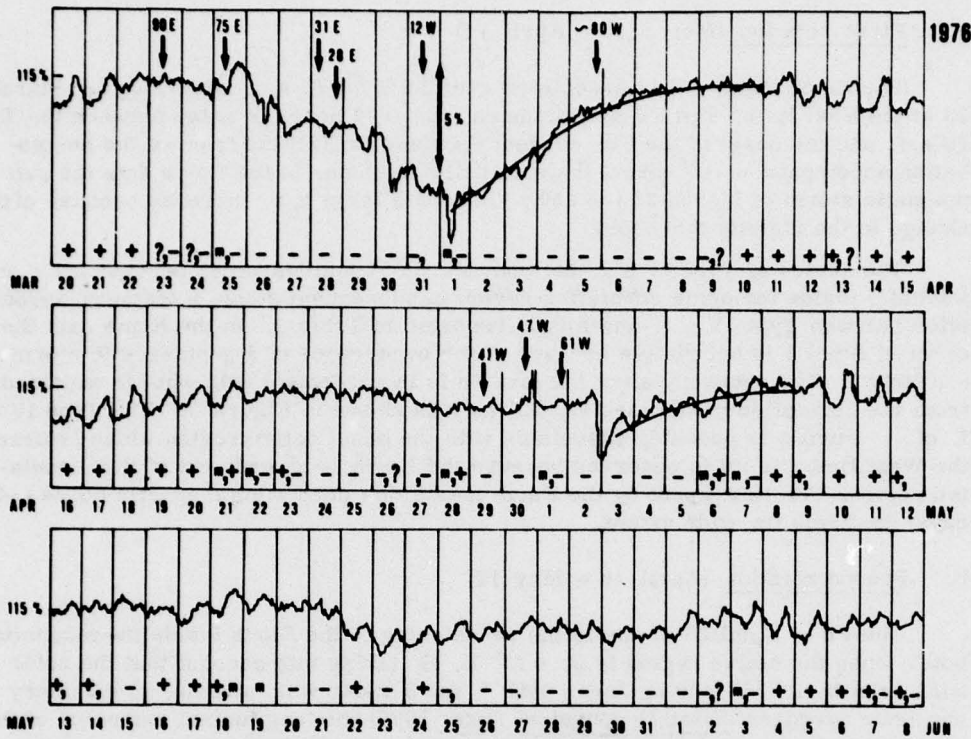


Figure 7. Deep River NM-64 Intensity. The occurrences of Type IV s.f. at the given heliolongitudes are indicated. The inferred interplanetary magnetic field polarities (Solar Geoph. Data, 1976) are reported; m indicates the mixed polarity.

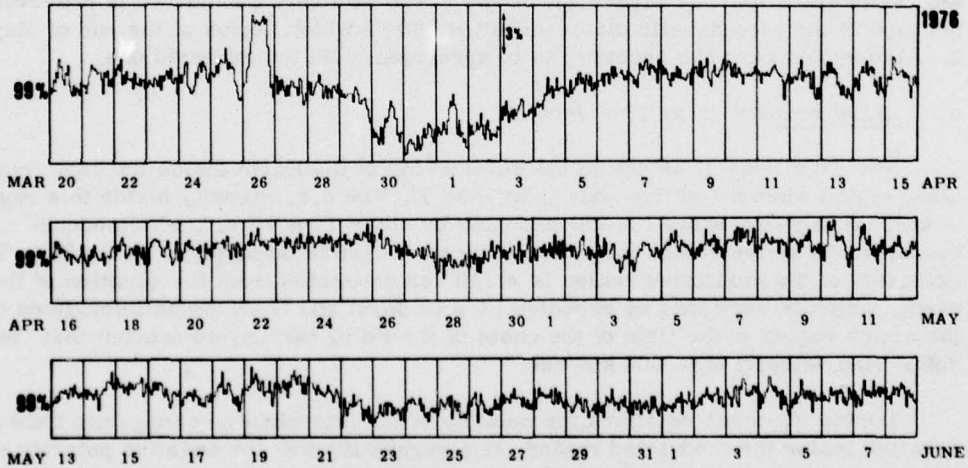


Figure 8. Rome Neutron Monitor Intensity.

a. First rotation (March 20 - April 15)

The Fd of March 26 is associated with the Type IV s.f. occurring on March 23 at the East limb. The Fd-amplitude and the ≈ 72 hours of delay between the Type IV s.f. and the onset of the Fd, suggest that (see Eq.(1)) the front of the perturbation encompass $\approx 160^\circ$ about the s.f. heliolongitude. In the Rome data the geomagnetic storm of March 26 ($\approx 250 \gamma$) causes a large c.r. increase because of the change in the rigidity threshold.

The series of Type IV s.f. between March 25 and March 31 depress the c.r. intensity inside the same corotating region in subsequent steps; a tentative association between Type IV s.f. and Fds is reported in Table 1. In the Rome data the event of April 1 is not visible because of the occurrence of a geomagnetic storm ($\approx 200 \gamma$). The recovery after the last Fd is in agreement with what is expected from the corotative model (see Eq.(2)) as it is shown in Figure 7. The Type IV s.f. of April 5 is probably associative with the same active region which is near the West limb; no Fd is observed because the Earth is already out of the modulated region. The time spent by the Earth inside this corotating magnetic bottle (≈ 13 days) confirms its wide extent.

b. Second rotation (April 16 - May 12)

The Fd of April 26 is due to the re-entering of the Earth inside the magnetic bottle when the active region is at $\approx 10^\circ$ E. By taking into account that the solar wind velocity is 350-400 km/sec (IMP 7 and 8 solar wind plasma, preliminary one-hour averages: Solar Geophysical Data, 1976) the longitudinal extension of the modulated region can be estimated of the order of 140° - 130° . The recovery is very slow as expected, with a time constant $\tau \approx 10$ days.

The Fd of May 2 is produced by the Type IV s.f. occurring on April 30 and May 1. The observed amplitude is presumably smaller than that existing inside the "core" because the Earth is now situated near the trailing edge of the modulated region (position 2 in Figure 2). In the Rome data only a small Fd is observed because of the geomagnetic disturbance ($\approx 100 \gamma$) which begins at the end of May 2. Also in this case the recovery is in agreement with the expected one.

c. Third rotation (May 13 - June 8)

The Fd of May 21 is due to the re-entering of the Earth inside the same modulated region when the active zone is at $\approx 30^\circ$ E. The c.r. intensity inside this region is still largely depressed ($\approx 2\%$) probably by other Type IV s.f. which occurred when the active region was situated in the invisible hemisphere of the Sun. The extension of the modulated region is $\approx 150^\circ$ as estimated from the duration of the event, which is very long as expected ($\tau \approx 10$ days) and from the heliolongitude of the active region at the time of the onset of the Fd by taking into account that the solar wind velocity is ≈ 500 km/sec.

During the three rotations the polarity of the interplanetary magnetic field is negative inside the modulated region, this suggesting that the negative polarity of the active region is nearer to the Sun equator than the positive one and that the closed lines of force of the magnetic bottle lie on surfaces quasi-perpendicular to the

ecliptic plane.

The small recurrent c. r. decrease observed inside the positive sector is produced by a fast stream which is observed to recur for several solar rotations. When the solar region which produces the fast stream is in the visible hemisphere of the Sun and significant radio bursts are not detected, then it is reasonable to assume that this region is a coronal hole. For all these recurrent events the ratio $(\Delta I/I)/\Delta v$ is $\sim 5 \cdot 10^{-2} \text{ \% (km/sec)}^{-1}$, in agreement with the average value reported in Lucci et al., 1977c.

References

- Lucci, N., M. Parisi, M. Storini, and G. Villoresi, A study of the Forbush decrease effect: the origin and the development in the interplanetary space, Internal Report of Space Plasma Laboratory - 77-2, Rome, February 1977a.
- Lucci, N., S. Orsini, M. Parisi, M. Storini, and G. Villoresi, The interplanetary perturbation associated with Forbush decreases, in Conference Papers of 15th International Cosmic Ray Conference, 3, 341, 1977b.
- Lucci, N., S. Orsini, M. Parisi, M. Storini, and G. Villoresi, Cosmic ray perturbations produced by fast streams coming from quiet solar regions, in Contributed Papers to the Study of Travelling Interplanetary Phenomena/1977, edited by M. A. Shea, D. F. Smart, and S. T. Wu, AFGL-TR-77-0309, p. 209, Air Force Geophysics Laboratory, Bedford, Massachusetts, 1977c.
- King, J. H., Interplanetary Magnetic Field Data Book, National Space Science Data Center-75-04, Greenbelt, April 1975.
- Mariani, F., N. F. Ness, and B. Bavassano, Magnetic field measurements by Pioneer 8, Internal Report of Space Plasma Laboratory - 71-22, Rome, July 1971.
- Solar Geophysical Data, Reports issued by the Environmental Data Service of National Oceanic and Atmospheric Administration, Boulder, 1976.

Discussion

Dryer: Your model has interplanetary magnetic field lines connected back to the sun (as shown in Figures 1 and 2). Would it make any difference if the lines were not connected to the sun?

Villoresi: A closed magnetic structure seems to be preferable for explaining the cosmic-ray anisotropies during Forbush decreases (see Barnden, L. R., The large scale magnetic field configuration associated with Forbush decreases, 13th International Conference on Cosmic Ray, Conference Papers, 2, 1277, 1973) and the large Forbush-decrease amplitudes, but it is not necessary for explaining the corotation of the modulated region which is the basic feature of our model.

Multidisciplinary Event-Oriented Data Collection for 30 April 1976

D. B. Bucknam and H. E. Coffey
World Data Center A for
Solar-Terrestrial Physics
Boulder, CO 80302, USA

Abstract

A multidisciplinary collection of data relevant to the ground level solar cosmic ray event of 30 April 1976 (STIP Interval II) is presented. This is a sample collection to illustrate a new service being initiated by World Data Center A for Solar-Terrestrial Physics. Event-oriented data collections for specific time periods have a particular value, especially for multidisciplinary investigations. World Data Center A for Solar-Terrestrial Physics has, from time to time over the years, published detailed data collections for specific events in the UAG Report series. The World Data Center A for Solar-Terrestrial Physics now offers to make available to any researcher its capabilities and facilities for collecting data and organizing them in a variety of useful formats to satisfy the researcher's needs. Special event-oriented data collections of this type can be as comprehensive or as narrow, in terms of data from associated disciplines, as the researcher desires.

Research workers in solar-terrestrial physics frequently require correlative data pertinent to the particular event they are studying. Examples are the hydrogen-alpha light-curve characterization of the solar flare to compare with, say, helium studies, or the level of geomagnetic activity at the time of a rocket launch, or the interplanetary magnetic field structure. Because of the data exchange arrangements through the World Data Centers (WDC), each WDC has a large amount of correlative solar-terrestrial physics (STP) data. Some of the key data are published in one place or another and are extensively, almost automatically, used in a wide variety of STP research studies. Other data flow to the WDCs and are cataloged and made available to requesters. But many scientists are not familiar enough with what data are available to know what to request. The purpose of this paper is to describe a standard set of correlative data, which as almost a routine can be compiled by World Data Center A for Solar-Terrestrial Physics (WDC-A for STP) in Boulder, CO, U.S.A., and to illustrate this by a correlative data set for the time of the solar flare of 30 April and the ensuing geomagnetic storm, all within STIP Interval II.

In the past, data on selected STP events have been collected for publication in special data reports, in the "UAG Report" Series by WDC-A for STP. Many of these collections were more complete than the type of event package now being proposed, but took longer to compile since they involved data which were not normally exchanged and editing of discussions by many authors. Usually they dealt with the very major events which were recommended for detailed study by one or more scientific organizations and which were declared to be "Retrospective World Intervals". These published data reports on STP events invariably involved extensive worldwide interchange with the many scientists contributing data analysis reports.

The new service of WDC-A for STP is aimed at packaging standard data for any events of interest to one or more STP research workers, but probably not to the community as a whole. It would not be economical to publish these packages, but rather they would be provided separately at the cost of compilation.

Along with WDCs "B" and "C", WDC-A for STP routinely collects data in several solar-terrestrial physics disciplines for the purpose of making these data readily available to the scientific community. Many of the key data are published in the monthly "Solar-Geophysical Data", one to six months after date of observation. Thus, "Solar-Geophysical Data" (SGD) is a rapid source for detailed information of solar-terrestrial events. But for any given short event interval, four to six issues of SGD would have to be searched to extract all the relevant information. Thus, part of the "event package" would be extracts from SGD.

Some data in SGD are published in the format received. Other data are extensively reformatted. A simple example of reformatting is the compilation of data reports from several observatories into one chronologically-ordered listing such as the listing of solar radio bursts. Another more elaborate example is the digitizing of analog geomagnetic records from several observatories to produce computer-generated common-scale magnetograms having the same time and intensity scales. A similar technique is used to produce the derived AE magnetic indices. Some degree of data quality control is possible as in the processing of the observatory reports of solar flares; we try to verify apparently discordant data.

As a first step a Multidisciplinary Event-Oriented Data Collection is compiled of all the data regularly published in SGD into one package. This will eliminate the need for searching many issues of SGD for the relevant data for the event. But further, most events are especially significant for one particular reason; in the event of 30 April 1976 which we are using as illustration, many scientists are particularly interested in the cosmic ray ground-level increase which followed the flare. The WDC-A for STP has many data sets which are not routinely published in

SGD, but which may be extracted to be included in such event data packages. (Appendix A shows the Table of Contents for this event data package.) Furthermore, the WDC is able to request from the monitoring stations faster reporting or more detailed data than are normally submitted to the center, once the key data parameters of an event are recognized. In the case of the 30 April 1976 event, we specifically requested more detailed cosmic ray data. The index to the detailed cosmic ray neutron monitor data is shown in Appendix B, and a stacked plot showing the ground level increase as seen by ten of these stations is shown in Appendix C. Thus, the WDC can make an initial selection of data of special interest beyond those normally published in SGD. The final choice, however, can be left to the scientist requesting the data. To the best of the capabilities available to the center the data package will be tailored to meet his needs.

WDC-A for STP must make a nominal charge for preparation of these data sets, currently established at \$50 U.S. for basic data from SGD plus routine "add-ons", as selected by WDC-A for STP. If additional requirements are imposed by the requester, the cost of preparation and copying may be greater. Perhaps an extended event data package can be cost effective only if several scientists request the same package and in effect share the extra cost. Sometimes we will try to anticipate requests, as we have done for the 30 April 1976 event, compile the data packages and announce their availability to the STP community.

WDC-A for STP is able to undertake providing a service of this scope only because of the contacts established through the World Data Center system over the past 20 years. In many scientific areas the data center has been recognized as a necessary and valuable intermediary between the data collectors and the research scientists. Often scientists would have great difficulties in collecting required data if the World Data Centers did not exist. The continued value of the data center facility, however, depends upon its ability to keep up with the ever changing and ever increasing data collections and increasing data needs. The WDCs try to stay alert to new data, data users, and new emphases and trends. In this they need continuing advice and stimulation from the users of the WDC data exchange.

APPENDIX A

TABLE OF CONTENTS

	Page
<u>General</u>	
Solar Indices	1
Sunspot Cycle	4
Solar Wind (Interplanetary Scintillations)	5
Inferred Interplanetary Magnetic Field.	7
<u>Region Information</u>	
H _α Synoptic Carrington Chart April 1976	8
Synoptic Carrington Solar Map (Meudon) April 1976	9
Regions of Solar Activity April 1976.	11
Solar Activity Centers - April 29 through May 2	12
East-West Solar Radio Emission Scans	
10.7 cm April and May 1976	20
21 cm April and May 1976	22
43 cm April and May 1976	24
Solar Radio Emission 169 MHz Inferometer.	26
<u>Flare Event of April 30, 1976</u>	
H _α Flare (Print).	27
H _α Flare Tabulations April 20 through 30.	29
Daily Flare Indices April	31
Solar Noise Burst Graphs	
2800 MHz April 30.	32
9400 MHz April 30.	33
Solar Radio Emission	
Outstanding Occurrences April 30	34
Spectral Observations April 26-30.	35
Sudden Ionospheric Disturbances April	37
Solar X-rays SMS/GOES	
Event Table and Graph April 30	38
Hourly Values (0.5 to 4 Å) April.	39
Hourly Values (1-8 Å) April	40
Provisional Solar Proton Event April 30-May 1	41
IMP 7 and 8 Interplanetary Data April and May	
Solar Wind Plasma.	42
Electrons.	44
Low Energy Protons	46
Intermediate Energy Protons.	48
High Energy Protons.	50
Alpha Particles.	52
Cosmic Ray Neutron Monitor Data	
Daily Values April and May	54
Hourly Graphical Values April and May.	56
Sulphur Mt. and Calgary 5-minute Graphical Values April 30	58
Stacked Plot for 10 stations	59
Riometer 15-minute Graphical Values April 30-May 2.	60

APPENDIX A (continued)

	Page
<u>Geophysical Events of May 2-4, 1976</u>	
Geomagnetic Data	
Ap Indices January 1975 through May 1976	61
Principal Magnetic Storms and Sudden Commencements May 1976	62
Kp 3-hr Values by Bartels Solar Rotation	63
Common-scale Magnetograms May 1-3	64
Hourly Equatorial Dst Values May	66
Dst Graphical 27-day Chart	67
Kp, Km, Ap, aa, Cp, Kn, Ks Indices April and May	68
Auroral Data	
DMSP Precipitating Electron Example	70
DMSP Auroral Imagery Print May 3	71
Ionospheric Data	
Wallops Island Composite N(h) Profiles April and May at 1200 UT.	72
Wallops Island N(h) Profiles April 30, May 1 and May 2 at 1200 UT.	73
Wallops Island Composite Tabulations April and May	74
Wallops Island N(h) Tabulations April 30, May 1 and May 2.	75
Churchill f plots April 30 through May 3	76
<u>April 30 Detailed Cosmic Ray Neutron Monitor Data</u>	
Detailed Index.	80
Alert 5 min Values.	81
Apatity 15 min Values.	82
Deep River 5 min Values.	83
Durham 5 min Values.	84
Goose Bay 5 min Values.	85
Hafelekhár 10 min Values.	86
Hermanus 10 min Values.	87
Inuvik 5 min Values.	89
Jungfraujoch 6 min Values.	90
Kerguelen 5 min Values.	92
Kiev 5 min Values.	93
McMurdo 6 min Values.	94
Mt. Washington 5 min Values.	95
Oulu 5 min Values.	96
Potchefstroom 10 min Values.	97
Sanae 10 min Values.	97
Terre Adelie 15 min Values.	98
Thule 6 min Values.	94
Tixie 5 min Values.	99
Tokyo 10 min Values.	100
Utrecht 5 min Values.	101
*Chacaltaya 5 min Values.	104
*Kiel 5 min Values.	105

*Received late and out of sequence.

APPENDIX B

INDEX TO DETAILED COSMIC RAY NEUTRON MONITOR DATA

Station	Cutoff Rigidity GV	Minutes Between Readings	Dates Available	Corrected Values	Uncorrected Values	Pressure
Alert	0.00	5	4/29-5/2	✓ {4/30-5/2}	X	X
Apatity	0.61	15	4/25-5/5	✓ {4/30-5/3}	X	X
Chacaltaya	12.64	5	4/25-5/5	✓ {4/30-5/1}		X
Deep River	1.07	5	4/29-5/2	✓ {4/30-5/2}	X	X
Durham	1.56	5	4/30	✓	✓	✓
Goose Bay	0.59	5	4/29-5/2	✓ {4/30-5/2}	X	X
Hafelekar	4.36	10	4/29-5/2	✓		
Hermanus	4.68	10	4/30-5/1	✓		✓
Inuvik	0.17	5	4/29-5/2	✓ {4/30-5/2}	X	X
Jungfraujoch	4.49	6	4/30-5/2	✓ {4/29-5/2}	X	
Kerguelen	1.12	5	4/30	✓		✓
Kiel	2.30	5	4/25-5/5	✓ {4/30-5/2}	X	X
Kiev	3.53	5	4/25-5/5	✓ {4/29-5/2}		
McMurdo	0.00	6	4/30	✓		
Mt. Washington	1.35	5	4/30	✓		✓
Oulu	0.84	5	4/29-5/2	(4/30-5/2)	✓	✓
Potchefstroom	7.04	10	4/30-5/1	✓		
Sanae	0.94	10	4/30-5/1	✓		
Terre Adelie	0.01	15	4/30	✓		✓
Thule	0.00	6	4/30	✓		
Tixie	0.49	5	4/30	✓		
Tokyo	11.55	10	4/30-5/2	✓	X	X
Utrecht	2.78	5	4/30-5/2	✓ {4/30}	X	X

✓ = attached

X = available

() = dates presented

APPENDIX C

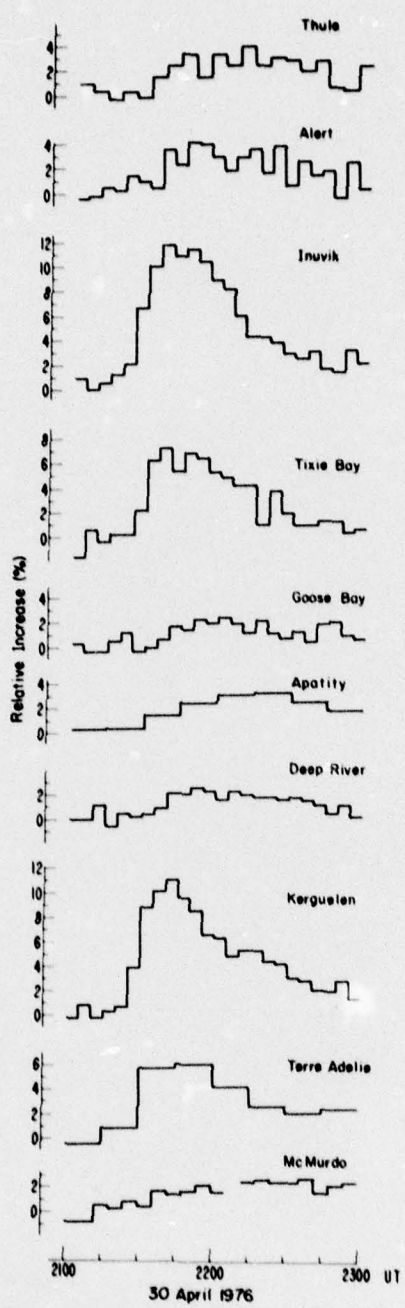


Figure 1. Relativistic Solar Cosmic Ray Event of 30 April 1976 as Observed by Various Ground-Based Neutron Monitors